# Mechanistic-Empirical Pavement Design Procedure For Geosynthetically Stabilized Flexible Pavements

**Salman Ahmed Bhutta**

**Dissertation submitted to the Faculty of the
Virginia Polytechnic Institute and State University
in partial fulfillment of the requirements for the**

**Doctor of Philosophy
in
Civil Engineering**

**Approved**

**Imad L. Al-Qadi, Chair
Thomas L. Brandon
Kenneth L. Reifsnider
Antonio A. Trani
Richard D. Walker**

**April 10, 1998
Blacksburg, Virginia**

**Keywords: geosynthetics, flexible pavement design, separation**

# MECHANISTIC-EMPIRICAL PAVEMENT DESIGN PROCEDURE FOR GEOSYNTHETICALLY STABILIZED FLEXIBLE PAVEMENTS

**Salman Ahmed Bhutta**
**Department of Civil Engineering**
**Virginia Polytechnic Institute and State University**
**Blacksburg, VA 24060, 1998**

## ABSTRACT

In June 1994, a 150-m-long secondary road pavement section was built as part of the realignment of route 616 and 757 in Bedford County, Virginia to evaluate the performance of geosynthetically stabilized flexible pavements. The California Bearing Ratio (CBR) of the subgrade after construction was approximately 8%. The pavement section is was divided into nine individual sections, each approximately 15 m long. Sections one through three have a 100-mm-thick limestone base course (VDOT 21-B), sections four through six have a 150-mm-thick base course, and sections seven through nine have a 200-mm-thick base course. Three sections were stabilized with geotextiles and three with geogrids at the base course-subgrade interface. The remaining three sections were kept as control sections. One of each stabilization category was included in each base course thickness group. The hot-mix asphalt (HMA), SM-2A, wearing surface thickness was 78-90 mm. The outside wheel path of the inner lane was instrumented with strain gages, pressure cells, piezoelectric sensors, thermocouples, and moisture sensors. Section performances based on the instrumentation response to control and normal vehicular loading indicated that geosynthetic stabilization provided significant improvement in pavement performance. Generally, the measured pressure at the base course-subgrade interface for the geotextile-stabilized sections was lower than the geogrid-stabilized and control sections, within a specific base course thickness group. This finding agreed with other measurements, such as rut depth, ground penetration radar survey, and falling weight deflectometer survey. The control section (100-mm-thick base course) exhibited rutting that was more severe than the geosynthetically stabilized sections. Falling weight deflectometer back-calculation revealed consistently weaker subgrade strength for the geogrid-stabilized and control sections than for the geotextile-stabilized sections over the three year evaluation period. To quantitatively assess the extent of contamination, excavation of the first three sections in October 1997 revealed that fines present in the base course were significantly greater in the control and geogrid-stabilized section than in

the geotextile-stabilized section. These findings led to the conclusion that the subgrade fine movement into the base layer when a separator is absent jeopardizes its strength. Further analysis of the field data showed that geotextile-stabilization may increase the service life of flexible secondary road pavements by 1.5 to 2 times.

Finally, a new mechanistic-empirical flexible pavement design method for pavements with and without geosynthetics has been developed. Elasto-viscoelastic material characterization is used to characterize the HMA layer. The field results from Bedford County, Virginia project have been used to calibrate and validate the final developed design procedure. The concept of transition layer formed at the interface of base course and subgrade is also incorporated into the design approach. Powerful axisymmetric linear elastic analysis is used to solve the system of equations for mechanical and thermal loading on the pavement structure. Elasto-viscoelastic correspondence principle (EVCP) and Boltzman superposition integral (BSI) are used to convert the elastic solution to its viscoelastic counterpart and also to introduce the dynamic nature of vehicular loading. Pseudo-elastoplasticity is introduced into the problem by determining the extent of plastic strain using laboratory experimentation results and estimating the failure mechanisms, based on accumulated strains as opposed to the total strain (recoverable and non-recoverable). The pavement design approach presented in this dissertation is a hybrid of already existing techniques, as well as new techniques developed to address the visco-plastic nature of HMA.

**In the Name of Allah the Most Beneficent the Most Merciful**

**Dedicated To My Parents**

# Acknowledgements

I would like to express my deepest gratitude to my friend and advisor, Dr. Imad L. Al-Qadi, who has provided me with numerous opportunities to perform research in the area of geosynthetic-stabilization, pavement design and non destructive testing. I am greatly indebted to him for the challenges he has placed upon me as well as his invaluable guidance throughout this research.

I would also like to thank the Government of Pakistan Virginia Center of Innovative Technologies (CIT), the Civil Engineering Fabrics Division of the Amoco Fibers and Fabrics Co. (AMOCO), and Atlantic Construction Fabrics, Inc (ACF) for their financial support to complete this study. Their support increased my understanding and knowledge of civil engineering materials as well as various other emerging technologies.

I would also like to express my appreciation to my committee members, Dr. Tomas L. Brandon, Dr. Kenneth L. Reifsnider, Dr. Antonio A Trani and Dr. Richard D. Walker, for their suggestions and advice throughout this research. Their suggestions and guidance helped me enhance the quality of this research.

I would also like to thank my parents brothers and sisters for their support and care provided to me throughout my education. Their support has been invaluable and the reason I have succeeded to be where I am today as a person and scholar.

I finally would like to thank my friends and research associates who assisted in this research over the past four years: Barney Barnhart, Jeff Kessler, Dale Grigg, Louis Pettigrew and David Thacker of Virginia Department of Transportation (VDOT); Amara Loulizi, Jeff Sexstone, Brian Diefenderfer, James Bryant, Stacey Reubush, Kiran Pokkuluri, Ramzi Khuri, Bruce Lacina, Michael Scarlett, Sherri Hoffman, David Weisz, Kessi Perkins, Dennis Huffman, Brett Framer and Clark Brown from the Via Department of Civil Engineering at Virginia Tech. Thanks everyone.

# Table of Contents

# List of Tables

# List of Figures

# 1 INTRODUCTION

## 1.1 Background

During the past two decades, the use of geosynthetics in pavements has increased dramatically (Barksdale *et al.,* 1989; Dass, 1991; Austin and Coleman *et al.,* 1993; Koerner *et al.,* 1994; Al-Qadi *et al.,* 1994, 1996, 1997). Various studies have been performed in the past few years to validate the performance of geosynthetics in highway pavements (Li *et al.,* 1992; Al-Qadi *et al.,* 1994; Koerner and Koerner, 1994). Attempts were made to develop design methods for pavements stabilized with geotextiles and geogrids (Hass, 1986; Carroll *et al.,* 1987; Barksdale *et al.,* 1989; Koerner *et al.,* 1994), but with little success. Several field and laboratory studies using static and dynamic loading conditions were conducted to validate the various claims of improving pavement performance due to geosynthetic inclusion. In 1993, researchers at Virginia Tech undertook a laboratory study to validate the performance of geogrids and geotextiles under controlled laboratory conditions using dynamic loading (Al-Qadi *et al.,* 1994; Smith *et al.,* 1995). The conclusions from that study supported the idea that geotextiles do improve flexible pavement performance due to the separation mechanism they introduce in a layered system, and not by reinforcement, as previously believed (Koerner and Koerner 1994; Al-Qadi *et al.,* 1994; Koerner, 1994; Carroll *et al.,* 1987; Smith *et al.,* 1995; Jorenby *et al.,* 1986; Lair and Brau, 1986). To validate this finding, a comprehensive field study was conducted.

In June 1994, a 150-m-long secondary road flexible pavement section in Bedford County, Virginia was instrumented. The test section, which consists of aggregate base and hot-mix asphalt (HMA) layers, is part of the realignment of intersection of Routes 757 and 616. The pavement section is located on a curve of constant radius with an intersection at mid-length. The average daily traffic on the pavement section is approximately 530 (700 in summer) vehicles, with approximately 8% trucks. The pavement section is composed of nine individual sections, each 15-m-long. Sections one through three have a 100 mm-thick limestone base course (VDOT 21-B); sections four through six have a 150 mm-thick base course; sections seven through nine have a 200 mm-thick base course. Three sections were stabilized with geotextiles and three with geogrid. The other three were kept as control sections. Geosynthetic stabilization was placed at the base course-subgrade interface. One of each stabilization category was

included in each base course thickness group. The non-stabilized sections served as the basis of comparison of the benefits of incorporating geosynthetics in the flexible pavement system.

The outside wheel path of the inner curve lane is instrumented with strain gages, pressure cells, surface piezoelectric sensors, thermocouples, and moisture sensors. A Keithley 500-A data acquisition system was used to collect instrument responses on-site. Data was collected and analyzed from the various instruments over three years. In addition to instrument responses from the pavement, laboratory testing on specimens obtained from the field was conducted, such as resilient modulus, creep compliance, dynamic accumulated plastic strain for HMA, and resilient modulus and characterization of base course and subgrade. Rut measurements, ground penetrating radar survey, and Falling Weight Deflectometer (FWD) tests were also performed on the test section. The collected data were analyzed to determine sectional performance and the effectiveness of geosynthetics at the base course-subgrade interface.

## 1.2 Objective and Scope

The objective of this study was to validate the Virginia Tech laboratory investigation as to the geosynthetic effectiveness in flexible pavements and to determine the extent of its benefit. It is an important objective of this study to quantify this effectiveness and provide a better understanding of the geosynthetic mechanism in pavements. In order to achieve these objectives, the test section in Bedford County, Virginia was selected, because, it presented a freshly constructed test section with optimal characteristics to study short-term and long-term performance of geosynthetically stabilized pavements in the field. Approximately 150 instruments of various functions were used to monitor the vehicular and environmental effects on the pavement.

In addition to subjecting the test section to accelerated heavy vehicular loading, periodic performance evaluations were conducted, including measuring subgrade resilient modulus using FWD and rut measurements. The collected data were analyzed and correlated to sectional performance. This step involved data reduction, which included sorting and analysis of raw data. A set of computer programs to visually reduce the raw data were developed for this purpose. The FWD data was also used to quantitatively estimate the development of a “transition layer” at the base course-subgrade interface.

The measured field data were also used to calibrate and check a pavement design method developed under this project. This method is transient elastic viscoelasto-plastic method and uses mechanical and thermal loading to determine cumulative strains and deformations in the HMA and subgrade.

## 1.3 Report Structure

This report addresses field testing of geosynthetically stabilized pavement and includes site selection, construction, instrumentation, field testing, and data analysis. It also discusses the development and testing of a mechanistic pavement design approach that considers geosynthetics in the design.

Chapter 2 discusses state-of-the-art knowledge in the area of pavements, which covers pavement analysis and design, geosynthetic stabilization and case studies of various projects involving the use of geosynthetics and instrumentation

Chapter 3 presents details of the site and the pavement construction process. It also includes details on the material characterization and pre-construction field testing.

Chapter 4 discusses the instrumentation types, calibration, installation, and sectional performance.

Chapter 5 details the data collection from instruments under normal and controlled traffic, rut depth, FWD measurement, and ground penetration radar (GPR) survey. It also presents a comparison of subgrade and base course material gradations after three years of in-field testing and monitoring.

Chapter 6 discusses new pavement analysis and design approach including basic equations and overall formulation. This method allows the inclusion of geosynthetics in the design procedure.

Chapter 7 presents the findings and conclusions of this study.

## 2 PRESENT STATE OF KNOWLEDGE

This section outlines the development of pavement design and research from the earliest times to the present. It proceeds from the nominal through the empirical and the semi-empirical, and finally to the semi-mechanistic approaches.

### 2.1 Pre-Modern Pavement Design

The earliest examples of highways and pavements have been identified in ancient Babylon and Egypt. However, little is known of these structures, because the ravages of time and environment have left few for modern examination. The greatest of the ancient road-builders were without doubt the Romans, who had established an efficient highway system throughout their empire by the year 200 BC. This system was established to permit the rapid movement of military forces and support materials anywhere within the imperial boundaries. Later, the same system was used to facilitate the administration of government throughout the empire and to enhance the system of commerce needed to support such a large economy.

The Roman concept of pavement massive at very best, required a vast amount of labor and materials. The construction was based upon erecting a pavement structure over the existing ground of such strength that all conceivable loads could be carried with minimum post-construction maintenance. Typically, a foundation of large stones was placed over the natural ground, and a matrix of finer stones and limestone dust was placed over them. Finally, a surfacing of carefully dressed hard stone provided a wearing surface. These structures were frequently as thick as one meter, and therefore well-raised above the surrounding topography, which mitigated against poor drainage. The height of these structures above the natural ground indeed provides the origin of the term “highway.”

There is little to term “design” in this process of early road building: these pavements were constructed “by the book,” an archetypal military manual. However, it is recognized that early field engineers did have to exercise judgment in selecting the appropriate structure in consideration of two situations: available materials and ground support. A number of different cross-sections (*Viae terrenae, Viae glaraetae, and Viae munitae*) are reported in various archaeological excavations and in contemporary literature (Caesar, 1996; Vitruvius, 1960). Of particular note are the pavement structures used in Roman Britain to carry highways over marshy or boggy areas. Mats of logs and

planking were first laid down (sometimes supported by timber piles) and bound into flexible rafts, over which the more traditional solid Roman pavements were constructed -- the first “raft foundations.”

That many of these pavement structures were over-designed for the traffic and environments under which they were to operate is evidenced by the fact that many are still in existence, and indeed many form part of existing highway systems (e.g., the M-1 Motorway in UK follows much of the alignment of “Watling Street,” a Roman road, and frequently incorporates the original Roman pavement within the modern infrastructure).

Following the fall of the Roman Empire (circa 400 AD), the highway system fell into disrepair, and as Europe fractionated into small, independent fiefdoms, parts were actually destroyed to prevent the easy movement of armies and troops. Throughout the Middle Ages, travel and commerce were essentially local in nature, and no effort was applied to re-establish any systematic network. Not until the time of Napoleon was any concerted effort made to enhance the condition of a ground transportation network. This was prompted by the same needs that initiated the Roman road system.

## 2.2 Modern Pavement Design

Modern pavement design falls into two periods: (i) early modern (1775 - 1900), and (ii) modern (20th century). The early modern period reflects a reawakening of the critical examination of the state and function of existing highways, and the initiation of “engineered” pavement structures, designed to ensure trafficability in all weather for wheeled vehicles. The modern period, which more or less coincides with the advent of the internal combustion engine, started with the early modern legacy of fixed designs and developed significantly throughout the twentieth century as engineers tried to address specific types of failure. Thus the modern period of pavement design has seen the transition from purely “catalog” design through empirical design and semi-empirical design to a more rational, semi-mechanistic approach.

### *2.2.1 Early Modern Pavement Design (~1775 to ~1900 AD)*

Pavement technology during the late colonial period in the US reflected that in Great Britain and much of Europe in general. Responsibility for roads was vested in the local communities through which they passed. Frequently, highway maintenance was undertaken by citizens as part of their fealty requirements (similar to a tax). This highly

unpopular obligation was rarely conducted with any enthusiasm or applied intelligence and largely consisted of burrowing crushed rock into particularly bad soft spots and puddles. Little was done of any enduring quality either to maintain or improve a road.

In France, as the nation moved toward revolution, the highway "system" became more strategically important to the maintenance of order. Consequently more attention was paid to it. However after the French Revolution when Napoleon required an efficient system upon which to move his Grande Armée for both internal and external action, the early modern highway system became more formalized. Napoleon called upon the expertise of the engineer Tresaguet, who had been active in the latter days of the kingdom, since 1764, to formalize a pavement structure that could be laid down and used by his corps of engineers. Tresaguet's design borrowed heavily from the Romans, but was much less massive. It consisted of a foundation composed of large rock fragments set close together and locked with smaller stones set within the interstices. Over this foundation was placed a relatively thin layer of smaller broken stone or gravel (Shaler, 1896).

The advantages of the French model were quickly seen by the British, who in their own response to the Napoleonic incursions adopted their enemy's pavement design to facilitate the movement of their own troops. The civilian application of this pavement was quickly modified by Thomas Telford (~1820), who introduced the crowned cross-section to improve the surface drainage, thickened the upper layer of crushed rock, and limited the size of the crushed rock to a maximum of about 60 mm.

This philosophy was again modified by "Blind Jack of Knaresborough" (John Metcalf) who, recognized the benefits of good drainage, and John Macadam, who recognized that the value of the crushed rock layer would be greatly enhanced if it were graded such as to "lock" into an effectively solid mass. With this advance came the realization that the underlying foundation of large rock fragments was not universally necessary, and that it should only be used where the subgrade was of an unstable nature. Thus, three advances were made: (i) a realization that the pavement design should reflect subgrade conditions, (ii) the development of a "new" material, i.e., rock macadam, whose properties provided enhanced performance, and (iii) a recognition of the need for positive and effective drainage.

The design philosophies of Tresaguet, Telford, and Macadam rapidly crossed over the Atlantic to the USA, where they were adopted in varying degrees throughout the new

States (Shaler, 1896; Blanchard *et al.*, 1919). The greatest application of these methods was made on some of the toll roads then in use. While great improvements were thus made to the existing highways, the general quality still remained somewhat poor. Incremental improvements in the consideration of drainage and material selection were made throughout the latter years of the nineteenth century, more especially in and around the larger cities; however, the majority of roads were still subject to dusting in summer and disintegration in winter and spring.

In the latter two decades of the 19th century, many urban pavements were surfaced with concrete or asphaltic materials. These were not intended to function as structural elements, but were provided to mitigate the effects of weather (dusting in summer and disintegration in winter and spring), and provide a smooth and comfortable riding surface.

Notwithstanding the incremental improvements in pavement technology, there was still no significant improvement over the concepts of Tresaguet, Telford, and Macadam until the advent of the automobile.

### *2.2.2 Modern Pavement Design (20th Century)*

Automobile traffic did not become significant until well into the 20th century. The major changes brought about by the transition from horse-drawn to self-propelled vehicles were those of mobility and number (volume). The automobile was much more autonomous than the horse-drawn carriage and could travel significantly further and usually at greater speed. These features quickly led to its popularity, which increased the number of cars on the roads. With this change came the need for reliable all-weather pavement surfaces. A horse-drawn carriage bogged down in the mire could usually be pulled out, albeit with great effort, by its team of horses, whereas the automobile in a similar situation and without the benefit of an equine prime-mover was more at the mercy of the state of the road.

In urban areas, the crushed rock surfacing had, in many places, been replaced by stone or wood setts (blocks), or by Portland cement or asphalt concrete. These materials had not been introduced with any great concern for pavement strength, but more as surface treatments to mitigate against summer dust and winter mire. Papers from the 3rd International Road Congress, held in London in 1913, report the main concerns of highway engineers from all over the world were the “wear” of pavement

surfacing (granular) and the benefits to be derived from binding these materials using concrete or asphaltic cements. There was still no true consideration of the engineering design of a structure to provide explicit performance.

## 2.3 Flexible Pavement

As recently as 50 years ago, most flexible pavements were designed on the basis of experience and "engineering judgment." In his comprehensive work on American highway practice published in 1942, Hewes makes no reference to flexible pavement thickness design. The first major step in flexible pavement design technology came with the Casagrande and AASHO soil classification systems, which led to catalog designs based upon the subgrade soil classification. In the 1930s, these soil classification methods were complemented by more utilitarian tests, including the development of the California Bearing Ratio (CBR) test.

### *2.3.1 Methods Based on Soil Properties*

*The Group Index Method:* This method evolved from the soil classification methods and was entirely empirical in its approach. The Group Index (GI) is defined as:

$$GI = 0.2a + 0.005ac + 0.01bd \quad (2.1)$$

where,

a = That portion of percentage passing the 75μm opening (ASTM #200 sieve) greater than 35% and not exceeding 75%, expressed as a positive integer (1 to 40);

b = That portion of percentage passing the 75μm opening (ASTM #200 sieve) greater than 15% and not exceeding 55%, expressed as a positive integer (1 to 40);

c = That portion of the numerical liquid limit (LL) greater than 40 and not exceeding 60, expressed as a positive integer (1 to 20); and

d = That portion of the numerical plasticity index (PI) greater than 10 and not exceeding 30, expressed as a positive integer (1 to 20).

First published in 1942, the *CBR Design Method* uses correlations between soil CBR results and observed performance. Its original is based upon correlation of CBR against pavement thicknesses. It was later justified and corrected by the US Army Corps of Engineers by recalibrating the empirical results against a soil model of shear failure in the subgrade. This method relies upon an appropriate CBR estimate for the subgrade

soil, and a representative wheel load. The CBR method, or its derivatives, is still the most common flexible pavement design method in the world. A number of states have modified the original CBR method and developed regional-specific designs (Colorado, Wyoming, Virginia, and others).

California abandoned the CBR method named after it, and adopted a method based upon the Hveem Stabilometer and Cohesiometer tests (*The Hveem Method*). The Stabilometer measures the ability of a material (base, subbase, or subgrade) to resist deformation, and the Cohesiometer provides an estimate of its cohesive resistance or tensile strength. The California Stabilometer Method was also the first to incorporate the concept of reducing mixed traffic to an equivalent number of repetitions of a standard (1125 N) load. This method estimates the number of equivalent 1125 N dual-tire loads to be expected in a 10-year design life, the logarithm (base 10) of which is referred to as the Traffic Index (TI). A further parameter derived from this method was the concept of the Gravel Equivalent (GE), which equates the structural value of a particular material to an equivalent thickness of granular material.

In the 1940s and 1950s, a number of design methods were developed based on various soil tests and correlated against local materials and performance; among these are:

*The Kansas Triaxial Method*: This method relies on triaxial tests of all materials incorporated within the pavement, tested in a saturated condition and adjusted for traffic and anticipated degree of saturation. The final design equation, derived from theory by Palmer and Barber (1940), is given as follows:

$$T = \left[ \sqrt{\left( \frac{3Pmn}{2\pi CS} \right)^2 - a^2} \right] \sqrt[3]{\frac{C}{Cp}} \qquad (2.2)$$

where,

T = Total thickness of pavement required (in);

Cp= Modulus of deformation of the wearing surface (psi);

C = Modulus of deformation of the subbase or subgrade (psi);

P = Design wheel load (typically 9,000 lb);

m = Traffic coefficient, based on traffic volume;

n = Saturation coefficient, based on rainfall;

a =Radius of tire contact (in); and

S = Allowable deflection on the surface (typically 25 mm).

* 1 in = 25.4 mm, 1 lb = 4.448 kN and 1 psi = 6.91 kPa

*North Dakota Cone Method*: The required cover over the subgrade is simply estimated from the subgrade bearing value (psi) measured by a cone penetration test (Wise, 1955.)

*Texas Triaxial Method*: Material samples are tested in a triaxial apparatus and the failure envelope is defined (shear stress, $\tau$, against normal stress, $\sigma$). The material is then identified as belonging to one of six material classes (Class 1 through 6). Using a design chart, the soil class and the anticipated wheel load provided an estimate of the depth of cover required to protect the subgrade (McDowell, 1954)

*North Carolina Method*: Using laboratory plate-bearing tests on the subgrade soils, estimates of a subgrade bearing value are obtained and applied to design charts based on work by Vokac (1943). A depth of cover to protect the subgrade from the design wheel load is obtained by Hicks (1946).

*Asphalt Institute Method (1954):* The original Asphalt Institute method (1954) is a mixture of the CBR method and the Soil Classification method. It relies on identifying the appropriate subgrade soil type from any one of a number of tests (e.g., AASHTO, Unified, CBR, etc.), a representative wheel load, and a traffic volume classification. This renders an estimate of the thickness of pavement required over the subgrade. Each structural layer has default minimum thickness values depending upon traffic intensity.

### *2.3.2 Performance-Based Pavement Design Methods*

Following World War II, it was recognized that the large increase in highway traffic, both in volume and weight, was rendering these various design methods obsolete. Designs that provided acceptable performance prior to this period were now failing on both old and new construction. A number of pavement trials and experimental road sections were constructed and monitored in the years after World War II. These included (a) the Maryland Road Test (1-MD), undertaken in 1950, in which an existing concrete pavement was tested under repeated application of two single- and two tandem-axle loads (HRB Special Report 4); and (b) the WASHO Road Test, undertaken

in Idaho in 1953-54, in which a number of specially constructed flexible pavements were tested under the same loads used in the Maryland test (HRB Special Reports 18 and 22). The impetus of these special tests, coinciding with the Federal Government legislation authorizing the Federal Interstate Highway system, led to the proposal to undertake a more comprehensive road test sponsored by AASHO; this ultimately resulted in the now-famous AASHO Road Test (1958-60)

*AASHTO Interim Guide (1972) and Guide (1985 and 1993).* The impending construction of 51,200 km of the Interstate System led to the establishment of the AASHO Road Test in Ottawa, Illinois, between 1958 and 1960. This landmark research yielded a new method of flexible pavement design, but more significantly defined two very important concepts, Equivalent Single Axle Load (ESAL) and serviceability.

*ESAL - Equivalent Single Axle Load.* Recognizing that real traffic comprises a mixture of axle weights and configurations, the mixed traffic of the Road Test provided a calibrated method of reducing mixed traffic to an equivalent number of standard (80 kN single axles) loads. Prior to this, the only method of making this transformation had been the concept of Equivalent Single Wheel Loads (ESWL), borrowed from Airfield pavement technology. The ESAL method is based on theoretical computations to equilibrate stress or deflection using Boussinesq theory. The AASHO Road Test provides the first real measure of equivalence based on performance.

Serviceability or Condition. Prior to the AASHO Road Test, most design methods had been based on a single wheel load, or in a few cases, upon a given number of applications of such a load. No attention was paid to the condition of the pavement, either through the design period or at the end of the design period. By recognizing that pavement deteriorates gradually (hopefully), rather than suddenly collapsing, the AASHO Road Test defines a measure of condition, or the serviceability index. This index, or more accurately, the serviceability rating upon which it is based, is designed to be an objective measure of the state of the pavement. The resulting design method relies not only on the decay of pavement serviceability, but also on the rate of such deterioration.

The design method that resulted from the AASHO Road Test is based on a natural decay curve. The resulting relationships that were derived by correlating the components of the decay expression with observed performance and structural measures are given as follows:

$$\log(W) = \log(\rho) + \frac{G}{\beta}$$
$$\log(\rho) = 5.93 + 9.36\log(D+1) + 4.33\log(L_2) - 4.79\log(L_1 + L_2)$$
$$G = \log\left(\frac{p_0 - p}{p_0 - p_t}\right) \qquad (2.3)$$
$$\beta = 0.4 + \frac{0.081(L_1 + L_2)^{3.23}}{(D+1)^{5.19} L_2^{3.23}}$$
$$D = 0.44D_1 + 0.14D_2 + 0.11D_3$$

The serviceability trends (p, $p_0$, $p_t$) are determined from field measurement of roughness, cracking, etc. and represent measures of pavement condition. The empirical correlation coefficients, $\rho$ and $\beta$, are defined as functions of a nominal pavement thickness (D), axle weight ($L_1$) and axle type ($L_2$). It was found that the nominal pavement thickness was not, as originally anticipated, a simple addition of layer thicknesses, but was, as shown above, a linear combination of layer thicknesses. It was assumed that the regression coefficients that resulted reflected a sort of unit strength for each material represented. With this change came a redefinition of the way in which the pavement layers were represented in combination. The composite design thickness, D, was renamed the Structural Number, SN, and the combination of layer thicknesses and material contributions (layer coefficients, $a_i$) are given as: $SN = a_1t_1 + a_2t_2 + a_3t_3$, where $a_i$ is the layer coefficient for the material in layer i, and $t_i$ is the thickness of layer i (inch). The design equation that resulted from the Road Test is given by:

$$\log(W_{18}) = 9.36\log(SN+1) - 0.2 + \frac{\log\left(\frac{p_0 - p}{p_0 - p_t}\right)}{0.4 + \frac{1094}{(SN+1)^{5.19}}} \qquad (2.4)$$

However, by the time the first interim design guide was issued in 1972, the relationship had been modified to allow for subgrades different from that at the Road Test and for different climatic environments. These two adjustments to the above relationship were never truly validated, and as initially published, are very vague and ill-defined. The final 1972 design equation was given as:

$$\log(W_{18}) = 9.36\log(SN+1) - 0.2 + \frac{\log\left(\frac{p_0 - p}{p_0 - p_t}\right)}{0.4 + \frac{1094}{(SN+1)^{5.19}}} + \log\left(\frac{1}{R}\right) + 0.372(S-3) \qquad (2.5)$$

where, R = Regional Factor, to adjust for different regional environments, and S = Soil Support Value. This was based upon a value of 3 with a subgrade CBR of 3 (as at the Road Test) and a nominal value of 10 for a well-graded compacted crushed aggregate material.

The 1972 Interim Guide maintained its currency until 1985, when AASHTO issued a revised and "final" edition. This new and improved version (revised and re-issued in 1993) makes a number of changes to the above design equation, some useful and some cosmetic.

The Regional Factor term was replaced by a Reliability term to allow for the uncertainties in the design equation and process. The reliability term comprises the design standard deviation, $S_0$ = 0.45, and a Reliability Factor, $Z_R$, based upon a set of recommended design reliabilities, which in turn reflect the importance of the highway type (e.g., urban interstate - 85-99.9%, through local roads - 50-80%).

The Soil Support Value term has been replaced by a weighted subgrade resilient modulus term, $M_R$ (in psi). The subgrade resilient modulus, $M_R$, varies seasonally with rainfall and freeze events. This is explicitly adjusted by weighting a 12-month-by-month estimate (few states measure the resilient modulus of the subgrade). The actual term that replaces the Soil Support Value term is simply a correlated transformation of information encoded in the nomograph given by McCullough *et al.* (1972) and, as such, remains unsubstantiated. A number of States still use CBR rather than resilient modulus as a design parameter to characterize the subgrade.

The Structural Number relationship ($SN = \Sigma a_i t_i$) was modified to include a moisture coefficient ($m_i$) based on the drainability of the base and subbase materials, i.e., $SN = a_1t_1+a_2m_2t_2+a_3m_3t_3$. The values attributed to the drainage coefficients, $m_i$, are based on an estimate of the quality of drainage within the layer material (excellent, good, fair, poor, very poor), and on an estimate of the percentage of time that the layer material is exposed to moisture levels approaching saturation. Thus, in most cases, the value of the drainage coefficient used results from an objective assessment of the material and

its in-place environment rather than from any direct measurement. The final, revised (1985) design equation is thus given as:

$$\log(W_{18}) = 9.36\log(SN+1) - 0.2 + \frac{\log\left(\frac{p_0 - p}{p_0 - p_t}\right)}{0.4 + \frac{1094}{(SN+1)^{5.19}}} + Z_R S_0 + \left(2.32\log_{10} M_R - 8.07\right) \qquad (2.6)$$

Many state agencies have adopted the various AASHTO Guides, either in full or in part. Most have also amended these recommendations to suit local conditions. For example, many still use the 1972 version with adjusted layer coefficients and regional factors, while others have adopted the 1985 version but do not perform the full resilient modulus evaluation of the subgrade material. Still others have adopted the concept, but have redefined it entirely to reflect their own experience, environment, and materials.

*The Virginia DOT Method*. Vaswani re-examined the AASHO Road Test data and simplified the design relationship above. In so doing, he redefined the Soil Support Value and the layer coefficients, $a_i$, so that a value of unity is assigned to asphaltic concrete, and all other values are adjusted so that the layer coefficient reflects the relative contribution of one inch of that material to one inch of asphaltic concrete (similar in concept to the gravel equivalent, GE). He also reduced the traffic value ($W_{18}$) from the cumulative traffic over the design period to the projected daily ESALs in the mid-year of the design period. The Soil Support Value, SSV, is defined by two parameters, the CBR and the Resiliency Factor (RF). This modification to the AASHTO method recognizes that the CBR test is, by itself, an insufficient measure of subgrade response, and takes into account the degree to which subgrade deformation is recoverable. A subgrade with a high RF will not contribute to deep rutting to the same extent as one with a low Resiliency Factor, because the cumulative permanent, or irrecoverable, deformations differ significantly. These factors are defined on a regional basis within the Commonwealth. These revised relationships have been validated in a number of studies on fifty-four projects throughout the Commonwealth and reported in HRB Record 291 (1969). The VDOT design relationship is given by:

$$\log_{10}(D) = (0.003SSV + 0.160)\log_{10} L - 0.011SSV + 0.75 \qquad (2.7)$$

where, D is the Thickness Index = $\Sigma a_i t_i$; SSV is the Soil Support Value = 2/3 CBR x Resiliency Factor (RF); and L is the Daily traffic in 80-kN equivalents in the mid-year of the project.

It is to be noted that the 1993 NCHRP Synthesis of Highway Practice Report 189 reports that 23 states use the 1972 AASHTO Guide and 19 states use the 1985 AASHTO. By far the greater number of states (42 out of 50) therefore currently use one or the other of the two AASHTO Guides (or modified versions thereof) for the design of flexible pavements.

### *2.3.3 Empirical-Mechanistic Methods*

Over the years since the AASHTO Road Test, a number of "mechanistic" design methodologies have been developed. These rely on more fundamental models of vehicular loading, material, and structural system response and environmental interaction. Typically, with this more "scientific" approach, a far greater number of material and system parameters are needed to model the system, and specific failure mechanisms may be addressed. These methods have typically been the domain of the research engineer rather than the state highway agency; however, that is changing as is evidenced by the five states (IL, KS, KY, OR, and WS; MN uses the Asphalt Institute method to check AASHTO design) that have adopted a mechanistic-based design method. Other countries, such as Canada, the United Kingdom, the Netherlands, Australia, and South Africa, have adopted mechanistic design methods in whole or in part, although in many cases, these have been used to set up a catalog of pre-designed sections based on traffic loading, subgrade type, environment, and standard material specifications.

The two oldest mechanistic programs in use are the SHELL method (1963, 1977) and the Asphalt Institute method (1981, 1991). Other methods are hereafter outlined and differentiated with respect to the SHELL method.

*The SHELL Method.* The early SHELL method (1963) is essentially the same as the later 1977 method, with the exception that many elements of the model have been updated with later research, and the material models have been improved. The method is based on a layered linear-elastic system, with viscoelastic asphalt layers treated in a step-wise incremental linear fashion to simplify the nonlinear viscous effects. The original method relies heavily on the program BISAR (and its predecessor BISTRO) for the analysis of the layered systems.

The SHELL model (pavement model) essentially treats the pavement as a three-layer structure: an HMA surface (which may comprise more than one physical layer),

unbound, or cementitious base and subbase layers, and a subgrade. The HMA surfacing is characterized by a stiffness modulus, $E_1$ ($S_{mix}$), Poisson's ratio, $\nu_1$, and thickness, $h_1$. The model of Bonnaure *et al.* (1977) is used to predict the stiffness modulus. This is justified as "...a fairly good approximation at short loading times of moving vehicles and the relatively small deformations occurring." The base and subbase layers are characterized by elastic moduli, $E_i$, Poisson's ratios, $\nu_1$, and thicknesses, $h_i$. These can be combined into an equivalent single layer with elastic modulus, $E_2$, Poisson's ratio, $\nu_2$, and thicknesses, $h_2$. Subgrade materials are similarly defined by $E_3$ and $\nu_3$. Based on field data from instrumented test sections, a restriction on the modulus of an unbound layer is required such that $E_2 = k_2E_3$, where $k_2 = 0.2h_2^{0.45}$ with $h_2$ in millimeters in the range $2 < k_2 < 4$.

Traffic is modeled as an equivalent number of standard single axle loads of 80 kN, each having two dual 20 kN wheels with a contact stress of 600 kN/m$^2$ and a loaded radius of 105 mm. Conversion from other axle weights (L, kN) to an equivalent number of this standard axle is given by: $n = 2.4 \times 10^{-8} L^4$, where L = Axle loads in kN other than the 80 kN standard.

The environmental model allows two methods: (i) using the Mean Monthly Air Temperature (MAAT) for each of the twelve months of the year, the analysis can be effected in twelve increments, and (ii) using the Mean Annual Air Temperature, MAAT, a single analysis may be made. The computation of the MAAT is based on work by Witczak (Witczak, 1972).

Three major performance-related criteria are defined: (i) compressive vertical strain at the surface of the subgrade which controls the permanent deformation of the subgrade, (ii) horizontal tensile strain in the HMA layer, generally at the bottom, which controls the fatigue cracking of the layer, and (iii) permanent deformation (rutting) of the asphalt layers. The subgrade strain criterion is based on the Edwards and Valkering (1974) analysis of the AASHO Road Test data, and is given by:

$$\varepsilon_3 = 2.8 \times 10^2 \times N^{-0.25} \tag{2.8}$$

The HMA surfacing tensile strain criterion is mixture specific, and is based on a number of laboratory fatigue tests conducted at the Koninklijke/Shell-Laboratorium in Amsterdam. The rut depth calculations are based on estimating the reduction in layer thickness, $\Delta h_1$(mm), resulting from the viscous part of $S_{bit}$ (N/mm$^2$), as follows:

$$\Delta h_1 = C_M \cdot h_1 \frac{\sigma_{av}}{S_{mix}}$$

$$S_{bit,visc} = \frac{3}{\sum_{T,t} \frac{Wt}{\eta}} \qquad (2.9)$$

where,

$C_M$ = A correction factor for dynamic effects, $1 < C_M < 2$;

$\sigma_{av}$ = The average vertical stress in the HMA thickness, $N/mm^2$;

$S_{mix}$ = Elastic stiffness of the HMA, a function of $S_{bit,visc}$, T, t, $V_b$ and VMA;

$S_{bit,visc}$ = Viscous part of $S_{bit}$;

W = Number of design loads;

t = Time of loading of each wheel pass, sec;

$\eta$ = Bitumen viscosity at T, $N/m^2$; and

T = Design pavement temperature, °C.

In principle, the method varies the thickness of the HMA layer ($h_1$) and of the base/subbase layer ($h_2$) by using an embedded BISAR coding. Critical strains are then computed until the three design criteria are satisfied for a design specific to the materials, loading, and environment appropriate to the project.

*The Asphalt Institute Method* is similar in principle to the SHELL method. The major differences are: (i) the definition of the traffic (ESAL), using a simplified AASHTO equivalency relationship; (ii) the treatment of the HMA elastic stiffness is based on the Witczak equations; and (iii) the failure criteria are based upon the Asphalt Institute equations, which differ from those used by SHELL. The Asphalt Institute method is available as a software program, DAMA.

The program suite *VESYS* was developed by W. Kenis at the FHWA Turner-Fairbanks Laboratory. It relies on a full viscoelastic characterization of the HMA layers. It also treats the problem as a probabilistic rather than a deterministic exercise. In most respects, it is similar in outline to both the Asphalt Institute and SHELL methods. However, with the viscoelastic consideration and the treatment of input data as probabilistic (i.e., data is input as mean values ($\mu$) and standard deviations ($\sigma$)), the

method is simultaneously both more realistic and conservative. It treats rutting explicitly using a two-parameter model: $\varepsilon_p(N) = \mu\varepsilon N^{-\alpha}$ where $\alpha$ and $\mu$ are determined from laboratory testing. VESYS, which has gone through a number of revisions and enhancements, remains a primary research tool.

*KENLAYER* was developed by Huang at the University of Kentucky (1993). This method is similar in outline to all of the mechanistic methods described above, however, a number of significant differences exist, including more material models can be used (linear-elastic, non-linear elastic, viscoelastic, and combinations thereof); different material parameters may be entered for each seasonal period; more flexibility exists with regard to the sub-division of the seasonal variations; there is more detailed characterization of traffic loading with respect to number and speed; up to 19 material layers can be explicitly examined; and the user can specify the parameters of the critical failure criteria.

Michigan DOT, in conjunction with Michigan State University, developed a mechanistic flexible pavement design method based on the same overall methodologies as described above (*MICHPAVE,* 1989). However, the various sub-models have been re-calibrated from field results obtained from various material (laboratory) and field trial sections within the state of Michigan. This program has been adopted by the Michigan DOT as an approved alternative to the AASHTO method. Development and calibration of the models is on-going based on a periodic field evaluation and assessment of actual versus predicted performance. This program suite was developed by Harichandran *et al.* (1989).

In summary, flexible pavement design has progressed from the nominal through the static, single load-based structure and the empirical performance-based analysis to the more empirical-mechanistic methods. Due to the reticence of highway agencies, the vital step from the semi-empirical methods in common use (AASHTO-based methods) to the more fundamental mechanistic methods is slow. Only five states currently use “empirical-mechanistic” methods. However, NCHRP Synthesis 189 reports that 22 state DOT’s have indicated their intention to proceed to mechanistically-based methods in the short- and medium-term future.

### *2.3.4 Other Attempts at Empirical-Mechanistic Design Methods*

For many years, the elastic solutions to the pavement analysis and design problem were considered as the optimal solution. Recent advances in material characterization have shown that a purely elastic solution always over predicts the pavement thicknesses and thus leads to an uneconomical design. The true behavior of the pavement constituent materials will predict the pavement thicknesses in a more precise manner.

For a pavement design procedure to be completely rational in nature, consideration should be given to three elements. These elements are prediction of the failure of distress parameter, evaluation of the pertinent material properties, and determination of the magnitude of the parameter in question to the failure or the performance level desired.

The comparative parameters are primarily stresses and strains of the material. For a safe design, a particular material should reveal a certain magnitude of stress and corresponding strain less than the strength of the material. This discussion reveals that calculation of stresses and strains at different intervals in time is necessary for any mechanistic design procedure. During the early stages of pavement design, Brown (1972) suggested a method based on regression for the calculation of stresses and strains in a three-layered system. In his analysis, all layers are considered to exhibit linear elastic behavior, based upon interpolation of the charts developed by Jones *et al.* (1962). The methodology adopted is appropriate, but the material behavior is considered lacking in the area of accurately depicting the response to dynamic-mechanical and thermal loading. Lister *et al.* (1967) introduced transient stress-strain behavior under linear elastic conditions in his solution approach, but this method is outdated and cumbersome by today's standards.

True behavior of HMA is viscoelasto-plastic and the base and subgrade is nonlinear elasto-plastic. This introduces complexity of solution into the problem. At this level of material complexity, the problem becomes so difficult that only solution techniques like finite element method can handle the issue. Another consideration, which plays a major role, is the inability to translate these procedures into simple nomographs and closed form solutions. Also, high-powered computers, which even at the current rate of development, are unable to perform the task in a reasonable amount of time.

The nature of the viscoelasto-plastic material is to dampen the vibrations from the material system. The most simplified form of a viscoelastic model is to have an elastic spring and dashpot in series. The spring is depicting the linear elastic or elasto-plastic nature of the material, where as the dashpot is depicting the viscous part of the material behavior. The combined effect of the two constituents is a material which under applied loading undergoes some instantaneous deformation, which is completely or partially recoverable (linear or nonlinear spring), and an infinite deformation (dashpot). Figure 2.1 shows the load deformation curve for a linear viscoelastic material. It also shows a series and parallel combination of spring and dashpot (Maxwell and Kelvin models).

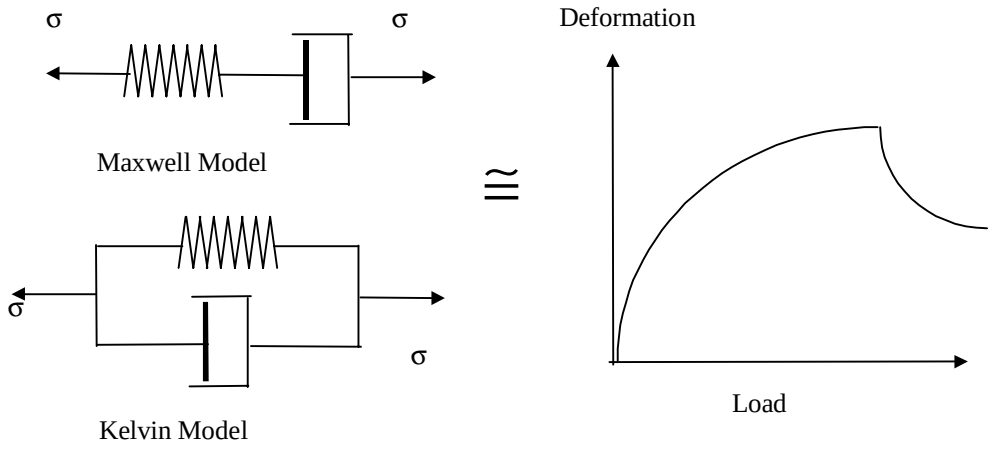


**Figure 2.1 Kelvin and Maxwell Model representation for viscoelastic materials.**

Several authors studied the viscoelastic and elasto-plastic nature of the constituent materials in pavement design. The studies performed resulted in varying conclusions and theories, but no complete pavement design method was developed. Most of the studies use existing pavement analysis and design methods and programs like MICHIPAVE, ILLIPAVE, KENLAYER and VESYS. Notable among these studies are Barksdale, 1967; Barksdale, 1970; Marchionna *et al.,* 1981; Smith *et al.,* 1981; Gomez-Achecar and Thompson, 1986; Sharma *et al.,* 1987; Barksdale *et al.,* 1989;Rao, 1991; Chen *et al.,* 1995; Jouve *et al.,* 1987; Khanna *et al.,* 1982; Zaghloul and White, 1993; Van Schelt *et al.,* 1994, and White *et al.,* 1995. Some of these researchers used high-

powered finite element programs like ABAQUS to perform the elasto-plastic analysis of the constituent layers.

Some of the important investigations are reported in Table 2.1, such as Ku, 1967; Moavenzadeh *et al.,* 1967, Verga *et al.,* 1976; Battiato *et al.,* 1977; Carpenter and Lytton, 1978; Lai, 1979; Battiato and Verga, 1982; Luhr *et al.,* 1982; Abdulshafi and Majidzadeh, 1984; Gillespie *et al.,* 1993; Zienkiewicz and Taylor, 1994; Collop *et al.,* 1995, and Rowe *et al.,* 1995. It was clear from the literature review that a complete pavement design based on mechanistic approach has not yet been developed. Most of the research to date has not incorporated the dynamics of mechanical and environmental loading on the pavement. In addition, no empirical-mechanistic design approach has incorporated geosynthetics.

## 2.4 Geosynthetics

Geosynthetics are used to provide reinforcement, separation, drainage, and filtration in civil engineering projects. The different types of geosynthetics include geotextiles, geogrids, geonets, geomembranes, geocells, and geocomposites.

Geotextiles are thin permeable sheets of synthetic, polymer-based materials used to stabilize and improve the performance of soil (Ingold and Miler, 1988). Geogrids are high-strength extruded sheets of polymer-based material characterized by a grid pattern of openings throughout the structure. Geonets have a netlike structure joined only at the intersections and are used primarily for drainage purposes. Geomembranes are used as a fluid or vapor barrier because of their ability to act as an impermeable membrane. The combination of a number of these can be used as geocomposites. The geometrical design and strength characteristics of geotextiles and geogrids make the integration of these products into flexible pavement construction process easy, therefore they are of primary focus in this research. A brief discussion of the two types of geosynthetics most commonly used in pavements follows.

The geotextiles industry originated because of a shrinking demand for organic textiles. As other world markets established self-sufficient textile production plants in organics like cotton and wool, the European and United States textile industries, which had been the previous textile suppliers, needed to adapt. With a surplus production capability and limited demand, the textile industries began to develop advances in textile

**Table 2.1 Brief description of literature review.**

| Title | Procedure and Mechanism | Remarks |
|---|---|---|
| Ku A. B. "Stress Strain Law For Viscoelastic Flexible Pavements Under Temperature Variations" | Linear viscoelastic theory for calculation of temperature effects and its mathematical formulation is presented in this paper. The presented formulations are based upon closed form mechanical solutions and involve significant effort in terms of integration procedures to achieve viscoelastic response to stress/strain under thermal effects. | This is the beginning of viscoelastic modeling in pavement design. However, the theory has been refined in later researches where effect of mechanical loading has been also introduced. The theory presented here has one problem in terms of its applicability to pavement design and presents a complex solution technique. |
| Lister *et al. "*The Behavior of Flexible Pavements under Moving Loads" | All layers are considered as linear elastic, and transient stress/strain analysis is performed to handle the dynamics of the problem. The loading on the pavement system is mechanical in nature. | The calculation of stresses and strains is cumbersome and somewhat complicated. An easier approach would be to use finite elements. The layers are considered linear elastic, which is a misrepresentation of actual material behavior, especially for HMA. |
| Barksdale *et al. "*Predicting Performance of Bituminous Surfaced Pavements" | Initially the problem is solved using linear elastic approach. Method of collocation, and elastic viscoelastic correspondence principle are then used to convert the linear elastic solution to the corresponding viscoelastic solution. The problem uses inverse of the creep compliance of the HMA as the instantaneous creep modulus. | Surprisingly, the procedure is exactly the same as that used by Huang (1993) in the KENLAYER program and described in his book "Pavement Analysis and Design". However there are two drawbacks: (i) dynamics of the problem are neglected, (ii) no failure mechanism determination is specified. |
| Moavenzadeh, F. "Analysis of Stresses and Displacements in A Three Layered Viscoelastic System" | All the layers are considered as linear viscoelastic in nature. The method uses closed form and numerical integration techniques for the stress state under linear viscoelastic conditions based on creep compliance of the HMA and underlying layers. | The load application is static and this would result in over-estimation of individual layer thickness. There are also questions as to the experimental accuracy of creep compliance determination for the underlying layers such as base course and the subgrade. |

| Title | Procedure and Mechanism | Remarks |
|---|---|---|
| Barksdale R. D. "A Nonlinear Theory for Predicting The Performance of Flexible Highway Pavements" | This procedure considers all layers to be initially linear, with incremental load applications. It involves transferring the nonlinear effects into the load matrix, thus essentially leaving the stiffness matrix unchanged. The computational time used in this procedure is dramatically reduced. Extensive use of finite element method is employed. | The solution is pseudo-nonlinear. The concept of transferring the nonlinear part of the problem into the load matrix may lead to some inconsistencies. Current elasto-plastic finite element procedures do not use increments in the load matrix, but rather change the stiffness matrix. Even when considering material nonlinearity, the recalculation of stiffness matrix is always performed. |
| Brown S. F. "Computation of Stresses and Strains for Design of Flexible Pavements" | All layers considered elastic, with a Poisson's ratio of 0.5. The charts developed by Jones are used to predict stresses and stains by using a regression curve. | The method is outdated and uses regression fitting for prediction of stresses and strains. Also, all the layers are linear elastic. During the 1970's and 1980 regression fitting the mechanistic response was a principal method of predicting the mechanical response like stresses and strains. If actual material behavior is considered, this probabilistic approach may be considered inefficient and misleading. |
| Verga *et al.* "Deformability of Flexible Pavements Subjected to Repeated Moving Loads" | A linear viscoelastic half space analysis of single layer is performed. A general procedure to incorporate the transient kernel into the viscoelastic solution is also established. The final results are mechanistic equations to predict the stress and strains in an viscoelastic half-space in the form of closed form solutions. | The mechanistic model proposed is not feasible due to the difference in mechanical and physical properties of the pavement layers |
| Carpenter *et al.* "Procedure for Predicting Occurrence and Spacing of Thermal Susceptibility Cracking in Flexible Pavements" | This method uses the linear viscoelastic concepts to analyze pavements with thermal cracking problem. The detailed procedure to calculate crack spacing and number of thermal applications to failure is also explained. The theory uses Minors rule for crack propagation in an elastic material, and generalizes it to encompass linear viscoelastic half-space. | The procedure is very straight forward and is based on a combination of fracture mechanics and statistics. The draw back in this type of approach is again the solution technique. Closed form solutions for this type of problems do not exist. The only possibility to approximate the solution is to use finite elements. If numerical integration is to be applied, then a simple finite element thermal problem is sufficient to predict the various responses under thermal loading. |

| Title | Procedure and Mechanism | Remarks |
|---|---|---|
| Smith *et al.* "Equivalent Granular Base Moduli Prediction" | This paper deals with modeling of nonlinear behavior in granular materials. A bulk stress approach to the problem is used, where the modulus is recalculated every time in an iterative manner to satisfy the vertical and the horizontal stresses within tolerable limits. A multi-layer elastic theory along with regression equations is developed and used to predict an equivalent layer modulus. | The method is pseudo-nonlinear, and has some serious drawbacks in mathematical modeling and reliability of results. The procedure has been used by other researchers especially in soil mechanics. |
| Khanna *et al.* "Characterization Design and Analysis of Bituminous Pavements" | All layers are considered as nonlinear elastic with static loading under axisymmetric conditions. A nonlinear stress strain behavior is used, and a finite element program was developed to handle the calculations. Data from laboratory tests was used to calibrate the finite element model. | The laboratory tests were under static loading and do not account for the dynamic loading of the pavements and their subsequent response. In addition, all the layers were considered non-linear elastic. This will lead to incorrect characterization of the HMA layer material behavior, which is viscoelastic in nature. |
| Battiato *et al.* "Viscoelastic Deformations in A Two Layered Paving System Predicted from The Laboratory Creep Results" | The procedure uses two viscoelastic layers and calculates the stresses and strains due to moving loads. It also includes the velocity and waiting time between consecutive vehicles. | This is one of the earlier attempts at modeling a linear viscoelastic system under the influence of dynamic loads. The solution as described in the paper is difficult to incorporate into a standard design procedure. The maximum number of layers that can be solved are two, and they have to be viscoelastic, thus reducing the applicability of the procedure in pavement design to a large extent. |
| Marchionna *et al.* "Pavement Elastic Characteristics Measured by Means of Falling Weight Deflectometer" | Falling weight deflectometer tests were performed on a four-layer pavement section. A finite element model with statistical corrections was developed to incorporate the nonlinear effects into the problem. The nonlinearity introduced into the problem is based on regression models and the finite element program results are corrected based on these results. | The procedure considers HMA as linear and the unbound layers as nonlinear. This is an attempt at characterizing the pavement response to loading using FWD and probabilistic techniques using finite element method. Correction of the finite element model based upon regression results is incorrect and may result in inaccuracies. |

| Title | Procedure and Mechanism | Remarks |
|---|---|---|
| Gomez-Achecar *et al.* "ILLIPAVE Based Response Algorithms for Full-Depth Asphalt Pavements" | ILLIPAVE finite element package was used to model full depth pavements. HMA was considered as linear elastic, and the variables studied were HMA radial strain, surface deflection and subgrade resilient modulus. Response algorithms for predicting all the stresses and strains were developed. | HMA is considered linear elastic, where in real life it is viscoelastic in nature. Results are usually over-prediction of stresses and strains. Some effort was made to check for nonlinearity of layers, by varying the HMA and subgrade resilient modulus (purely for sensitivity analysis). |
| Luhr *et al.* "Structural Analysis of AASHO Road Test Flexible Pavements for Performance Evaluation" | Pseudo nonlinear elastic finite element procedure was used to model a pavement structure. Modifications to incorporate nonlinearity were made to the existing linear elastic computer program. The procedure uses the bulk stress approach to the problem where the material property (resilient modulus) is a function of stress state. Good correlation between measured (Road test) and calculated results was obtained | The procedure is similar to KENLAYER program as it deals with the nonlinear elastic problems, where the material properties are functions of stress state. The tolerance limit set in this procedure dictates the accuracy of the results. |
| Battiato *et al.* "The AGIP Viscoelastic Method for Asphalt Pavement Design" | This is an extension of the work done previously by the authors to extend the 2 layered pavement design procedure proposed earlier by Battiato *et al.* (1977) to a three layered system. A computer program MOREL was developed by the authors to calculate the extent of permanent deformation based upon analytical formulations. The load is assumed to be uniformly distributed over a circular area. The major observations are:<br>• Lack of symmetry between the calculated strains on either side of the applied load.<br>• Influence of speed on strains.<br>• Difference between the longitudinal and transverse strain magnitudes at the bottom of HMA. | It is restricted to three layers. The problem seen in the analysis is the lack of symmetry between calculated strains. This non-symmetric behavior has been observed earlier in other researches, but usually is caused by the effect of dual tires, where pressure bulbs overlap. In this research, the inconsistency is related to some mathematical error in the computer program. However, the method has good potential for further use. |

| Title | Procedure and Mechanism | Remarks |
|---|---|---|
| Abdulshafi *et al.* "Combo Viscoelastic-Plastic Modeling and Rutting of Asphalt Mixtures" | A one dimensional combo visco-plastic constitutive model composed of Burger type 1-D mechanical elements connected in series and having a friction slider is used. The friction slider uses a set value, indicating the elasto visco-plastic threshold boundary. Once the calculated stress exceeds the level set for friction slider, the viscous dashpot is introduced into the system, thus making it visco elasto-plastic. The two failure criteria used are Druger-Prager, and Mohr-Coloumb. Results are also compared with VESYS to estimate the level of accuracy. | The HMA is assumed to behave as visco-elastoplastic, and base and subgrade as linear elastic or visco-elastoplastic. The method was later used by Rowe *et al.* (1995). The only drawback of this method is the complexity of the problem. Finite element is perhaps the best approach to use this procedure. Also, to model real visco-elastoplastic behavior, large number of 1-D elements have to be used, which increases computational time to a large extent. |
| Sharma *et al.* "Evaluation of Mechanical Parameters of In-Service Pavements from Field Data" | In this paper the authors use a nonlinear optimization technique called Simplex method. They also use an elasto-plastic back-calculation procedure to predict fatigue and rut equation constants for the failure equations from which life estimates can be obtained. This method uses a materially nonlinear model for the determination of mechanical properties of pavement layer materials from the field measured data such as vertical deflections, rutting, and cracking. | The procedure is pseudo-nonlinear elastic procedure, in which the calculated values are optimized to within a tolerable range of the field results. Some initial trial values for input are required. Static load conditions are considered, which may significantly affect the results. The overall approach is time consuming, and the authors acknowledge that large databases are the culprit in this case. Also, the nonlinear model used is complicated and difficult to adopt in real life field conditions. |
| Zienkiewicz, O. J. The Finite Element Method, Volume II, Fourth Edition | A procedure based on viscoelasticity using finite elements is discussed. The author acknowledges that the phenomenon of creep is in fact the building block of the viscoelastic behavior. The change in creep modulus over time, and its successive use in finite element coding to evaluate the time dependent stresses and strains is discussed in detail. The author outlines a procedure for linear elastic analysis and then correlates it to the closed form viscoelastic solution. | The book is a general reference text for any finite element program development. The procedure outlined is similar to Airy stress function closed form solutions techniques when accuracy is desired. Using finite element procedures, modeling multiple loadings (influencing each other) under axisymmetric conditions is not possible. Reverting to 3-D finite element solutions is one way to overcome this problem. |

| Title | Procedure and Mechanism | Remarks |
|---|---|---|
| Barksdale *et al.* "Potential Benefits o Geosynthetics in Flexible Pavements" | Several test sections were built in the laboratory and dynamically loaded. Finite element method was used to correlate the measured responses to the analytical results. Linear and nonlinear finite element results were compared in this study. The study also involves modeling of geosynthetics at the interface of base and subgrade as tensioned members. | Linear finite element results are in close proximity of the measured responses as compared to nonlinear elastic modeling. However, the modeling of geotextiles as a structural member of the overall pavement, with tensile strength and stiffness, is not proper. The authors do not provide enough detail as to the mechanical modeling of the pavement section. The dynamics of the problem is also neglected. The test sections were under controlled environmental conditions, and major influences like temperature and moisture effects were neglected in the analytical study. |
| Jouve *et al.* "Rational Modeling for The Flexible Pavement Deformations" | Nonlinear stress-strain behavior determined experimentally was used in this study to analyze pavement structures. All the layers are modeled as nonlinear elastic including the HMA. | The method considers HMA as nonlinear elastic. However, some errors may result due to ignoring the time effect on material properties. |
| Zaghloul *et al.* "Use Of 3-D Dynamic Finite Element Program for Analysis of Flexible Pavements" | The finite element results were compared to field strains from 8 sections located in Quebec, Canada, and high levels of correlations were obtained. Nonlinear and linear analysis of the pavement sections revealed that under dynamic loading the base and the subgrade behavior is linear elastic. Simpler programs like BISAR were also used and it was observed that the reduction in accuracy was negligible. | The conclusion regarding the material characterization of base and subgrade acting as linear elastic materials is quite reasonable, and supported by other authors such as Barksdale *et al.* (1989). |
| Rao C. S. "Finite Element Method for Structural Design of Heavy Duty Granular Pavements" | Nonlinear finite element method was used to calculate the structural response of granular pavements. A table was developed to predict the Poisson's ratio and stiffness of the pavement section. Deflection measurements were performed on 15 pavements and compared with the calculated results. CBR and Liquid Limit test results were | The predicted and measured deflections were in close agreement with each other (based on nonlinear elastic theory). The method was greatly simplified by the development of charts. The authors also have a varying base course and subgrade material combination in the field sections. |

| Title | Procedure and Mechanism | Remarks |
|---|---|---|
| | related to the stiffness and Poisson's ratio of the underlying layer. The final design for flexible pavements was presented in the form of a chart. | |
| Gillespie *et al.* "Effects of Heavy-Vehicle Characteristics on Pavement Response and Performance" | VESYS is used to determine the damage in pavements based on fatigue and rutting. The author considers the HMA as viscoelastic and the base and subgrade as elastic. The problem was also evaluated and checked for accuracy considering all the layers to be elastic and viscoelastic. | This study is used to verify the use of computer programs like VESYS in current pavement design procedures. Comparison of results from viscoelastic HMA and elastic HMA shows a considerable difference in the results. |
| Chen *et al.* "Assessment of Computer Programs for Analysis of Flexible Pavement Systems" | 2-D axisymmetric and 3-D Finite Element programs are compared to simpler elastic layered analysis programs like ELSYM5 and BISAR. The results from each simulation were checked with field measurements to determine prediction accuracy. Good level of accuracy is obtained in all cases especially when nonlinear elastic base and subgrade are considered. | The authors prefer the method, that considers nonlinear base and subgrade with linear elastic HMA. Results showed significant errors when linear elastic behavior is considered for underlying layers. |
| Van Schelt *et al.* "FE Analysis in Road Pavement Design in Netherlands" | HMA is considered viscoelastic, the base and subgrade are considered as nonlinear elastic and elastic. 2-D finite element program is used to analyze a primary road section, and the results are compare with field measurements. The primary comparison is in the area of deformations. Stresses and strains were also measured in the test section under dynamic loading and compared with the analytical results. Field stresses and strains have a wide spectrum of variation under dynamic loading. | Base layer is designed as nonlinear elastic, but the final results yield that stress fluctuations in the granular bases of primary roads are in the elastic range. Barksdale *et al.* (1989) and Zaghloul *et al.* (1993) have reported similar conclusions. |

| Title | Procedure and Mechanism | Remarks |
|---|---|---|
| Collop *et al.* "Viscoelastic Approach to Rutting in Flexible Pavements" | It was determined that the extent of permanent deformation under dynamic load is directly proportional to the static load, and inversely proportional to the vehicle speed. A new method for predicting rut depth was developed, which requires only one material parameter as input. The predicted results were compared with the field measurements in France, and good agreement was obtained. Extensive use of VESYS is employed in this study. | The authors got around the problem of dynamic loading by evaluation of a unique parameter from field data. The advantage is speed of calculation. However, this procedure can be better simulated by using Boltzman Superposition Integral in an equally fast manner. |
| Rowe *et al.* "Viscoelastic Analysis of Hot Mix Asphalt Pavement Structures" | Calculates the fatigue and rutting behavior of the pavement using elasto viscoplastic finite element procedure. Druker-Prager and Mohr-Coloumb failure criteria are used. The concept of a friction slider is also incorporated into the system. This provides the ability to introduce viscous part of the mechanical model in the system, thereby making the system visco elasto-plastic, or linear elastic. | The procedure uses a core finite element program and divides the year into 24 periods and calculates damage ratio and remaining life under explicit time stepping. The procedure is the same as that described by Abdulshafi *et al.* (1984). However, the authors do not provide enough information as to the mechanical loading condition. |
| White *et al.* "Use of Three Dimensional Dynamic Finite Element Model to Study the Effect of Unbound Layer Characteristics on Pavement Response to a Moving Load" | The load in this research is considered as 300,000 lb. at 4 mph. This high load level and low speed lead to the requirement of dynamic elasto-plastic finite element procedures. All the layers in this model are considered elastoplastic. | The need for introducing elasto-plasticity is generated by the effect of extremely high loads and low speeds. These high intensity loads are not encountered on highway pavements, and therefore such complex analysis is not needed. In the analysis, the authors consider all the layers as geometrically nonlinear in nature, which is especially not true for HMA, where visco elasto-plastic material characterization would be warranted. |

science. This new science involved the manufacturing of textile products using synthetic plastics. Modern geotextiles do not come into the technology picture until the late 1960's. The infrastructure and the interstate system provided a potential area where geotextiles could be used. Infact, the use of geotextiles has increased from 8.4 million square meters in 1977 to 336 million square meters in 1992 (Koerner 1994).

On the other hand, the development of high density polymer materials was the first step in the evolution of geogrids. The geogrid manufacturing industry originated and grew under the guidance of F. B. Mercer (Dass, 1991). Mercer was the first to introduce the idea of using polyurethane or polypropylene to create a grid-like, very stiff structure in 1960. Full-scale production of geogrids started in 1982, and its use in the construction industry evolved much in the same manner as that of geotextiles.

### *2.4.1 Manufacturing Process*

The general performance of a geosynthetic is dictated by the characteristics of the polymer from which it is created. The properties can be altered by chemical (additives) or mechanical (stretching) adjustment. This mechanical alteration is principally done to geogrids because they have enough thickness to sustain the tensile forces. This results in greater strength at a reduced strain in the final geogrid product, effectively increasing the stiffness of the material.

The overall production of geotextiles can be summed up by three basic manufacturing stages; production of the polymer with its various additives, production of a component, and conversion of the component into the finished geotextile

The production of the original polymer with possible additives is completed at a chemical plant before any type of mechanical alterations are made or component shapes are formed. For ease of packing and shipping, the polymer is shipped from the chemical plant to the manufacturer as pellets or granules. The manufacturer reheats the pellets to form the components of the geosynthetic. The three basic forms of components produced by heated extrusion include a circular cross-sectional filament with a diameter less than one millimeter, a flat tape with a width of a few millimeters and a thickness less than one millimeter, and a sheet or film with a width of several meters and a thickness of several millimeters (Ingold and Miler, 1988).

Koerner (1994) also states that a vast majority of geotextiles are made from polypropylene or polyester polymers formed into fibers or yarns (the choices are mono-

filament, multi-filament, staple, slit-film monofilament, or slit-film multi-filament), and finally into a woven and non-woven fabric, which, when placed in the ground, is a geotextile. In general, the words geotextile and fabric are used interchangeably. The choice of fabric styles is as following:

- Woven monofilament
- Woven multi-filament
- Woven slit-film monofilament
- Woven slit-film multi-filament
- Nonwoven continuous filament heat-bonded
- Nonwoven continuous filament needle-punched
- Nonwoven resin-bonded
- Other woven or non-woven combinations

The common polymers used in the manufacture of geogrids are high-density polyethylene, high-tenacity polyester and polypropylene (Koerner, 1990). These polymers are initially in a sheet form, holes are punched into the sheeting in a regular pattern, and then the sheet is drawn uniaxially or biaxially to obtain the desired geogrid. Drawing is done under controlled temperature and strain rate, so as to avoid fracture while allowing free flow of molecules into an elongated condition. During this drawing process, there is an increase in modulus and strength and a reduction of creep sensitivity of the ribs.

### *2.4.2 Functions in Pavements*

Four specific functions that geosynthetic materials may provide are separation, reinforcement, filtration, and moisture barrier. The following is a brief description of each one of these functions (Koerner, 1994).

- **Separation**: The placement of a flexible porous geosynthetic between dissimilar materials so that the integrity and the functioning of both materials can remain intact or can be improved.

- **Reinforcement**: The often synergistic improvement of a total system created by the inclusion of a geosynthetic (that is good in tension) into a soil (that is usually poor in tension) or other disjointed and relatively weak material.
- **Filtration and Drainage**: The equilibrium soil-to-geosynthetic flow regime that allows adequate liquid flow across the plane of geosynthetic with limited soil loss.
- **Barrier**: The introduction of a flexible non-permeable geosynthetic for the purpose of containment and/or isolation of liquids, solids, or gases.

As shown in Table 2.2, all types of geosynthetic materials can fit into one or more of these five functions The two terms that are most frequently used to describe the mechanisms provided by geosynthetics in roadway applications are separation and reinforcement. When geotextiles are used to stabilize pavement sections, they are generally regarded as being very effective in providing separation, but less effective in providing reinforcement. Conversely, research has shown geogrids to be effective in reinforcement, but not effective in separation.

**Table 2.2 Customary functions that different geosynthetics provide (after Koerner and Koerner, 1994).**

| Type of Geosynthetic | Separation | Reinforcement | Filtration | Drainage | Barrier |
|---|---|---|---|---|---|
| Geotextile | Yes | Yes | Yes | Yes | No[1] |
| Geogrid | No[2] | Yes | No | No | No |
| Geonets | No[3] | No[3] | No | Yes | No |
| Geomembranes | No[4] | No[5] | No | No | Yes |
| Geosynthetic Clay Liners | No[4] | No[6] | No | No | Yes |
| Geocomposites | Yes[7] | Yes[7] | Yes[7] | Yes[7] | Yes[7] |

Notes:
[1] Unless impregnated with bitumen, elastomer, etc.
[2] Unless very large particle sizes are involved.
[3] May be a secondary function.
[4] Always a secondary function.
[5] When fabric reinforced, high strength may be a secondary function.
[6] May be a secondary function when high strength fabric layers are involved.
[7] Depends upon the particular type of geocomposite product.

#### *2.4.2.1 Separation*

A typical secondary road comprises of HMA wearing surface, aggregate stone base course, and soil subgrade. The successful performance of each component is critical to the overall performance of the pavement system. The primary design requirement of the base course in a flexible pavement system is to reduce the stress of traffic loading at the elevation of the underlying subgrade to a level that can be supported by the subgrade (Yoder and Witczak, 1975). If the stress reduction function is not accomplished, excessive subgrade deformation may occur, resulting in pavement rutting and other distresses. For the base course to be effective in its role of distributing stress from surface loading, it must remain relatively permeable and its design thickness must be maintained.

Virtually all design theories of layered pavement systems assume that the construction materials will remain as they are initially placed. However, there are two mechanisms that may effectively reduce the thickness of the base course layer if it is constructed over a soft subgrade soil (Christopher and Holtz, 1991, Al-Qadi *et al.,* 1994).

One of these is the tendency for the subgrade fines to move into the voids between the aggregate particles via subgrade pumping, particularly when the soil is wet. If the soil fines are relatively non-plastic, such as with silt or lean clay, the soil particles may be carried upward into the base course aggregate voids as excess pore water pressures dissipate due to dynamic vehicular loading. If the subgrade soil fines are relatively plastic, such as with elastic silt or fat clay, pore water pressure dissipation may occur very slowly, and resulting migration of soil fines may be insignificant. However, as observed by Bell *at al.* (1982), contamination by soil fines can still occur as a result of subgrade softening. Water that resides in the base course, infiltrates from the road surface, or results from lateral flow may pool in local depressions or indentations created by compaction of aggregate particles. At these locations, water may combine with the cohesive soil to form a slurry. When surface loads are applied, it may be extruded upward into the aggregate layer.

Pumping results in the accumulation of fines beginning near the bottom of the base course and continuing upward. As the fines accumulate in the lower portion of the base course layer, particle-to-particle contact of the aggregate may be reduced, and thus the aggregate's stability and strength may be decreased. The result of this process is a reduction in the effective thickness of the aggregate layer.

The second mechanism by which the thickness of the base course may be effectively reduced is the penetration of aggregate stone particles into soft subgrade soil as local shear failure of the soil occurs. This process also begins at the bottom of the base course layer and also may lead to reduced particle-to-particle contact of the aggregate. The degradation is greatly accelerated if the aggregate is compacted over a wet subgrade or if the subgrade remains wet for extended periods during road use. Under these wet conditions, soil softening may occur and the resistance to aggregate penetration is reduced. Figures 2.2a and 2.2b illustrate the reduction of base course thickness as a result of soil migration and aggregate penetration.

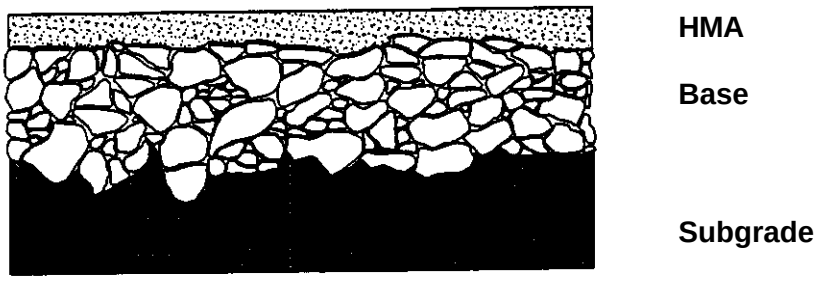


**Figure 2.2 a Typical subgrade and base course interface before migration of fines or penetration of aggregate (after Valentine, 1997).**

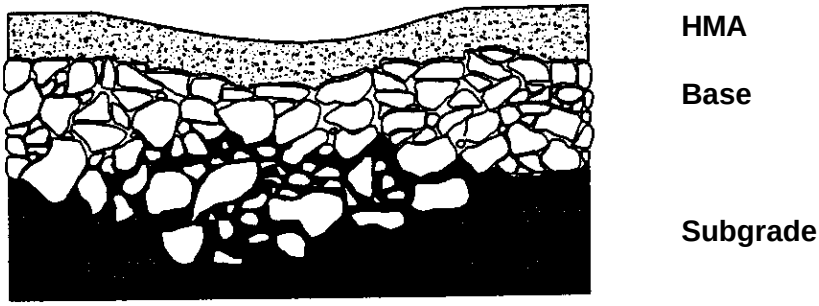


**Figure 2.2 b Typical subgrade and base course interface showing surface rutting as a result of the migration of fines and penetration of aggregate (after Valentine, 1997).**

The same contamination process that leads to a reduced base course thickness also degrades the drainage capability of the base course. Soil fines that are pumped into a formerly free-draining aggregate result in lower permeability. As the permeability

decreases, the time required for water to evacuate from the base course increases. As levels of saturation are reached, the base course becomes less capable of distributing the stress of surface loading, resulting in increased subgrade deformation and pavement distress.

Cedergren (1977) has observed that the presence of water in a base course section drastically changes the pattern by which surface loading pressures are distributed. He notes that lateral spreading of surface loads provided by a structurally sound base course can only occur if the base course is well-drained, and that stress distribution occurs as a result of the inter-granular stresses developed. However, when a base course is saturated with incompressible water, the applied surface pressures are transmitted downward to the subgrade with little or no reduction in intensity. Under this saturated condition, the normal stress distribution assumed in initial road design does not occur, and instead subgrade deformation and pavement distress can result. Figure 2.3 illustrates these two stress distribution conditions.

Field and laboratory experience has shown that it is possible to prevent the degradation of the base course by providing a geosynthetic barrier between the base course and the subgrade. The barrier must meet three general criteria if it is to be effective. First, it must meet the requirements for survivability. Survivability has been defined by the Federal Highway Administration (FHWA) as the geosynthetic's resistance to damage during installation, road construction, and initial operation. Survivability requirements have been established by the FHWA as a function of subgrade conditions, cover material, and construction equipment (Christopher and Holtz, 1985).

Damage to the geosynthetic may occur as a result of many actions during the construction process. For example, aggregate is often dropped onto the prepared subgrade and then spread to obtain the lift thickness required by the road design. If the aggregate is dropped onto a geosynthetic barrier, the geosynthetic may experience puncture damage. Inaddition, subgrade material that is not completely free of rocks and debris may cause puncture or tearing of the geosynthetic as it is installed and the overlying material is compacted. Further, as the aggregate is being spread, it is possible to abrade and tear the surface of the geosynthetic. If the geotextile sustains even localized damage, its ability to serve as an effective barrier in these locations may be compromised, possibly resulting in localized pavement failure.

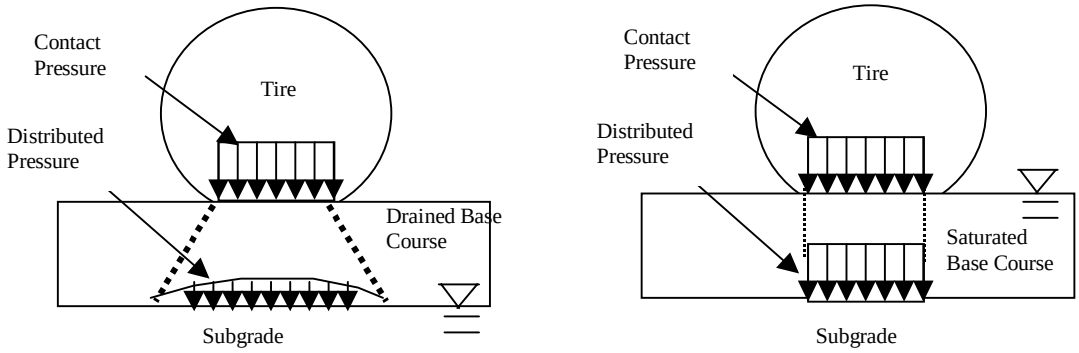


a) Drained base Course b) Saturated base course

**Figure 2.3 Idealized surface load stress distribution through drained aggregate base course and saturated aggregate base course (after Cedergren, 1977).**

The second and third criteria that the geosynthetic must meet are requirements for filtration and permeability. The openings between the geosynthetic fibers must be such that subgrade soil migration is restricted while an adequate flow of water is permitted. The migration of soil fines must be restricted to prevent the contamination of the base course aggregate. However, the geosynthetic must remain sufficiently permeable to permit the dissipation of excess pore water pressures which may develop under traffic loading. When a geosynthetic can meet both the criteria for filtration and permeability, the mechanisms it provides are referred to as separation and filtration. In literature that discusses soil stabilization, these two mechanisms are often collectively referred to as separation.

A common practice of state Department of Transportation (DOT) engineers when designing roads on weak subgrade soil has been to include an amount of "sacrificial" aggregate in addition to the amount required by standard design methods (FHWA, 1989). The reason for this practice is that a significant portion of the aggregate may be lost to the weak subgrade through the two previously discussed mechanisms, effectively reducing the ability of the base course to distribute traffic loading stresses. However, as mentioned, virtually all design theories of layered pavement systems assume that the component materials will remain as placed. A study conducted by Joseph Fluett attempted to quantify the amount of aggregate lost in this manner by surveying state DOT engineers to assess their experience with a range of weak subgrade conditions

(FHWA, 1989). The survey was performed to assist in the research and preparation of a FHWA design method that uses geotextiles to eliminate base course aggregate loss. The results of the survey are summarized in Figure 2.4

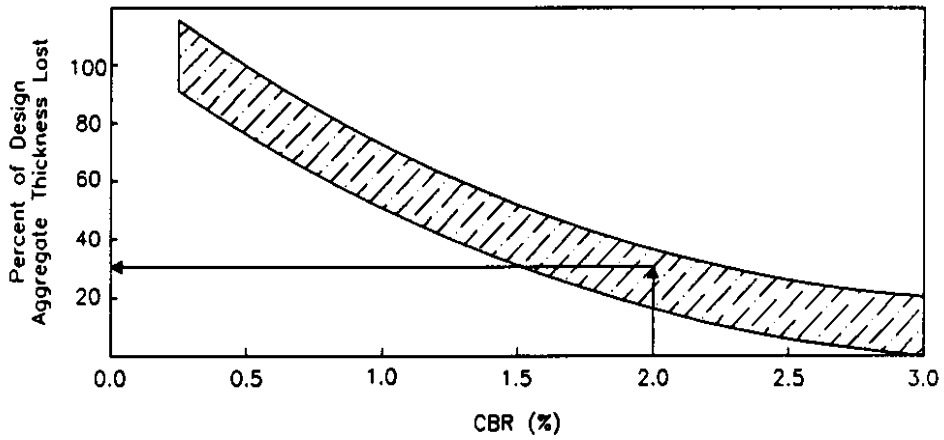


**Figure 2.4 Percent of design aggregate thickness lost as a function of subgrade CBR (after FHWA, 1989).**

According to the survey results, DOT engineers anticipate significant aggregate loss when the strength of the subgrade soil is equivalent to a CBR of 3% or less. The amount of aggregate that the engineers expect to lose corresponds to the amount of sacrificial aggregate that they have found must be added to the base course thickness prescribed by standard design methods. For example, according to Figure 2.3, if a subgrade has a CBR of 2%, and standard design methods require a base course thickness of 250 mm, approximately 30% more aggregate would be added, obtaining a total base course thickness of 330 mm. This addition is based on the anticipation that approximately 80 mm of the base course thickness will be lost. Using the FHWA design method, a geotextile may be used to ensure that the originally prescribed thickness of the base course remains constant.

A geogrid, by virtue of its design, is unable to provide complete separation of base course and subgrade material mainly because of its aperture size. Placement of the geogrid between the base course and subgrade may restrict penetration into the subgrade of aggregate particles that exceed these dimensions. However, much of the aggregate may still penetrate, and the migration of fines can still occur. Contamination

of aggregate base courses in geogrid-stabilized road sections has been documented in field trials (Austin and Coleman, 1993) and large-scale laboratory pavement loading tests (Barksdale *et al.,* 1989; Al-Qadi *et al.,* 1994).

### *2.4.2.2 Reinforcement*

Reinforcement is described by Koerner (1990) as the often synergistic improvement of a total system created by the inclusion of a geosynthetic (that is good in tension) into a soil (that is usually poor in tension). When a geosynthetic is placed within the base course or at the bottom of the base course, it is reported to reinforce a road section by two principal methods: tensioned membrane reinforcement and shear type reinforcement (Koerner, 1990; Christopher and Holtz, 1991). It has also been reported that geosynthetic stiffness is an important characteristic in road reinforcement (Barksdale *et al.,* 1989; Webster, 1991).

Tensioned membrane reinforcement occurs when a vertical load is applied to a deformable soil that is reinforced with a geosynthetic. Koerner (1990) described the horizontal stress that may be induced to a geosynthetic by using an equation from Taylor (1948):

$$\sigma_h = \frac{P}{\pi z^2}\left[3\sin^2\Theta\cos^3\Theta - \frac{(1-2\upsilon)\cos^2\Theta}{1+\cos\Theta}\right] \qquad (2.10)$$

where,

$\sigma_h$ = Horizontal stress at depth z and angle $\Theta$;

P = Applied vertical load;

z = Depth beneath the surface where is $\sigma_h$ being calculated;

$\upsilon$ = Poisson's ratio; and

$\Theta$ = Angle from the vertical beneath the surface load P.

Koerner observes that directly beneath the load, where $\Theta$ = 0 degrees,

$$\sigma_h = \frac{P}{\pi z^2}\left[0.5-\upsilon\right] \qquad (2.11)$$

The Poisson's ratio for soils normally ranges from 0.3 to 0.5. As can be seen from Eq. 2.11, the greater the applied vertical load P, the greater the stress in the geosynthetic. Similarly, the smaller the distance, z, between the load and the fabric, the greater the stress in the geosynthetic.

Tensioned membrane reinforcement is a characteristic of both geotextiles and geogrids, and is a function of the geosynthetic's tensile modulus. Christopher and Holtz (1985) illustrate the effect of tensioned membrane reinforcement by considering wheel load stresses transmitted to a weak subgrade. If the magnitude of the stresses is high enough, plastic deformation of the subgrade will result. If a geosynthetic is placed above the subgrade, it will also deform under loading. If the geosynthetic has a sufficiently high tensile modulus, an appreciable amount of tensile stress resistance may be developed. The vertical resultant of the membrane resisting stress may act to help support vehicular loading. However, it has been suggested (Christopher and Holtz, 1991; Giroud and Bonaparte, 1984; and Holtz and Sivakugan, 1987) that the tensioned membrane effect is negligible unless a rut depth of at least 100-mm is developed. Because of this requirement for a relatively high deformation, tensioned membrane reinforcement is not usually considered to be a significant factor in low deformation road systems, such as flexible and rigid pavements (Christopher and Holtz, 1991; Koerner, 1990, Smith *et al.,* 1995).

Shear type reinforcement occurs as a result of shear stresses and strains at the bottom of the base course under surface loading. As shown in triaxial tests by Broms (1977), a geotextile placed within the triaxial specimen permits the application of higher normal stresses compared to those required for equivalent strains in unreinforced specimens. No large-scale tests of geotextile-stabilized road sections have been reported in which the contribution of shear-type reinforcement was quantified.

The shear type of reinforcement provided by geogrids is purported to laterally confine base course aggregate. This mode of reinforcement is thought to be the principal mechanism by which geogrids work, and is thought to result in an increase of the section's modulus. The restriction of lateral movement is thought to result from the interlock that occurs when aggregate particles are bound within the geogrid apertures (Kennepohl *et al.,* 1985; Hass *et al.,* 1988).

The efficiency with which the underlying geotextile or geogrid can mobilize horizontal shear strength, and thereby restrict the lateral movement of aggregate, may be

quantified by the frictional efficiency between the aggregate and geosynthetic material. The frictional efficiency is often measured by direct shear tests or pullout tests (Koerner, 1990; GRI Test Methods and Standards, 1993) using the candidate geosynthetic and soil, and may be defined as:

$$E_f = \left( \frac{\tan \delta}{\tan \phi} \right) \tag{2.12}$$

where,

$E_f$ = Frictional efficiency;

$\delta$ = Interface friction angle between the geosynthetic and the soil; and

$\phi$ = Angle of internal friction of the soil.

From this equation, it can be seen that the geosynthetic's frictional efficiency is determined by comparing the interface friction angle between the soil and geosynthetic and the internal angle of friction of the soil. Shown in Table 2.3 are the interface friction angles and frictional efficiencies for some woven geotextiles and biaxial geogrids as determined by the use of a direct shear apparatus (Yuan *et al.,* 1993).

**Table 2.3 Frictional efficiencies measured for some Amoco geotextiles and Tensar geogrids (after Yuan *et al.,* 1993).**

| Geosynthetic | Soil[1] | Interface Friction Angle, $\delta$ (°) | Efficiency |
|---|---|---|---|
| Amoco 2002 | Concrete Sand | 25 | 0.56 |
| Amoco 2006 | Concrete Sand | 28 | 0.63 |
| Amoco 2016 | Concrete Sand | 30 | 0.69 |
| Amoco 2044 | Concrete Sand | 32 | 0.74 |
| Tensar BX110 | Concrete Sand | 38 | 0.93 |
| Tensar BX1200 | Concrete Sand | 39 | 0.97 |
| Amoco 2002 | AASHTO No. 57 Stone | 36 | 0.90 |
| Amoco 2006 | AASHTO No. 57 Stone | 36 | 0.93 |
| Amoco 2016 | AASHTO No. 57 Stone | 41 | 0.84 |
| Amoco 2044 | AASHTO No. 57 Stone | 41 | 0.84 |
| Tensar BX110 | AASHTO No. 57 Stone | 40 | 1.0 |
| Tensar BX1200 | AASHTO No. 57 Stone | 41 | 1.0 |

[1] Peak internal angle of friction of sand was $40^o$ and peak internal angle of friction of stone was $41^o$.

According to the data in Table 2.3, under direct shear conditions the geogrid appears to mobilize friction with efficiency between 90 and 100%, whereas the geotextile mobilizes friction with efficiency between 56 and 84%. The maximum theoretical frictional efficiency that a geosynthetic may have with a soil is 1.0 if the failure plane is to develop at the geosynthetic-soil interface. Related to the reinforcement property is tension creep. Tension creep is a property of polymeric materials such as polypropylene geotextiles and geogrids. Creep occurs in non-oriented polypropylene as the molecular chains slip along one another within the crystalline regions (Koerner, 1994). It is a function of time, stress, temperature, and other environmental factors, and is usually regarded as an important design consideration in geosynthetic-reinforced earth structures (AASHTO, 1990; FHWA, 1993). When a geosynthetic is used to reinforce soil in retaining walls and steep slopes, the reinforcement's allowable design strength is obtained by multiplying the geosynthetic's ultimate strength by a creep reduction factor. The creep reduction factor is based on unconfined creep test results (ASTM D 5262). The reduction factor corresponds to a tensile load which induces no more than 10% strain at the end of a specified test period. If, for example, the tensile load equals 30% of a specimen's tensile strength, the corresponding reduction factor is 0.30. For polypropylene geosynthetics, the creep reduction factor typically ranges from 0.15 to 0.3 for a 10,000-hour test period.

A geosynthetic that provides tensioned membrane or shear type support to surface loads experiences both constant and dynamic tensile stress. Therefore, creep of the polymeric material must result. The consequence of geosynthetic creep is stress relaxation. Thus, the reinforcement in a road section initially provided by a polypropylene geotextile and geogrid diminishes over time. However, no data exists on this phenomenon.

## 2.5 Research Programs

Several research programs were initiated over the past two decades to understand the geosynthetic effectiveness in flexible pavements. In the following review, attention is paid to the research related to the use of geosynthetics at the base course-subgrade interface. In late 1980, a research program was initiated to evaluate existing road reinforcing materials, including geogrids (Abdel Halim *et al.,* 1983). It included the design and implementation of an experimental program as a cooperative effort between the Royal Military College (RMC) at Kingston, the Ontario Ministry of Transportation and

Communications, Gulf Canada, Ltd., and the University of Waterloo. After considering candidate materials, a geogrid manufactured by the Tensar Corporation was selected for further study. The main objective of the research was to investigate the mechanical behavior and load-carrying capabilities of flexible pavements when a geogrid is included within the HMA wearing course. This program is relevant, because the same laboratory modeling procedures were used in subsequent research programs conducted by some of the same investigators to evaluate geogrid stabilization of the base course of a road section.

The study was performed using the RMC testing program in which Tensar biaxial geogrid AR-1 was placed within HMA flexible pavement sections of various thicknesses (Abdel Halim *et al.,* 1983). Five pavement sections were constructed directly on a sand subgrade and designated as test loops. Within each test loop, between four to nine tests were conducted.

The test loops were constructed in a concrete pit measuring 4 m x 2.4 m x 2 m deep, and equipped with a sump and water distribution system. The subgrades for each loop were constructed to a thickness of 1.2 m with medium to coarse sand. The sand was placed in lifts of 150 mm at an optimum water content of 11.5%, and then compacted using a plate tamper. No measurements of subgrade soil strength at any water content were reported. Instead, test loops were evaluated for saturated and dry subgrade conditions. The saturated and dry states were achieved using the test pit's sump and water distribution system.

Completion of the sand subgrade was followed by the construction of a HMA layer. An aggregate base course was not included in the pavement cross section. For each test loop, half of the pavement was reinforced with a geogrid, and the other half was left unreinforced. The unreinforced portion of the pavement was intended to function as a test control. Next, the geogrid was installed over half of the HMA surface. This was followed by the placement of an additional 50 mm of HMA compacted using a plate tamper. Additional HMA lifts of 25 mm to 75 mm were placed and compacted to bring the pavement layer to its desired thickness. The total pavement thicknesses ranged from 150 mm to 250 mm.

Each test was performed by loading the pavement surface through a rigid circular plate with a diameter of 300 mm. Loading was controlled by a hydraulic actuator and a computer-linked function generator. To model traffic loading, a sinusoidal pulse was

applied to the pavement surface at a frequency of 10 Hz with a peak load of 40 kN for a total pressure of 550 kPa through a steel plate of 150 mm diameter and 13-mm thickness. At predetermined cycle counts, dynamic loading was discontinued, and a static loading sequence was applied. The static loading sequence was necessary to make it possible to read surface displacement gages, strain gages, and pressure cells.

To monitor test section loading responses, a load cell and linear variable displacement transformer (LVDT) were part of the loading actuator and were used for all five test loops. Dial gages were positioned on the loading plate and two were positioned on the pavement surface. These instruments permitted the recording of surface deflections at their respective locations during static loading periods.

Each test loop also included foil-type strain gages attached to the bottom and top of the geogrid at various locations to permit an evaluation of the magnitude and distribution of elastic and plastic strains induced by pavement loading. Four test loops included the embedment of mastic strain carriers in the HMA directly beneath the loading plate locations, where it was anticipated that maximum tensile strains would occur.

One test loop included the placement of a circular aluminum plate pressure cell beneath the loading plate location at a depth of about 50 mm below the sand-HMA interface. The pressure plate was 155 mm in diameter and 13 mm thick. The authors noted that its presence affected the value of the permanent deformation, because it acted as additional reinforcement. Its purpose was to allow a comparison of stresses at the plate for reinforced and control sections.

After the loading of a test loop was completed, the pavement layer and top 150 mm of subgrade sand were removed. Next, the second 150 mm thick layer of sand was remixed and recompacted. This was followed by the reconstruction of the top 150 mm thick subgrade lift and construction of the pavement layer as required by test loop objectives. After construction of the subgrade for the first test loop, the initial 0.9 m of subgrade sand was never remixed and recompacted.

Each test location was loaded until at least one of following failure criteria was met to compare the performance of reinforced and control sections. The criteria were:

- A permanent vertical surface deformation of 30 mm,
- Extensive cracks developed,

- A steady increase occurred in the measured value of stresses on the subgrade,

The investigators sought to establish several relationships between the number of loading cycles applied and response of the pavement sections by adjusting some of the controllable variables for each loop, including the strength of the subgrade and the thickness of the HMA layer.

By varying HMA layer thickness for both reinforced and control locations, the investigators sought to determine how much additional HMA was required to obtain performance improvement equivalent to that provided by a geogrid. Based on the results of their study, the authors concluded that placement of the geogrid within the HMA pavement could provide substantial savings in HMA thickness. They also stated that the geogrid made it possible to double the number of load repetitions and to prevent or minimize fatigue cracks in the HMA layer. Although the thicker unreinforced section yielded lower elastic rebound, the reinforced section produced lower permanent tensile strain and less fatigue cracking.

This testing program accomplished more than an evaluation of the performance of pavement sections when a geogrid is placed within the HMA pavement layer. It identified difficulties and established some procedures for subsequent laboratory programs which sought to further investigate the effect of geosynthetic stabilization. It served as the basic model for continued geogrid reinforcement research at the University of Waterloo, and for the research conducted at Virginia Tech.

The research also revealed opportunities to improve the laboratory model of the pavement section. For example, testing of sections constructed with subgrades that were either dry or saturated failed to represent quantifiable subgrade strength conditions. A more complete evaluation requires the construction of subgrades with a range of shear strengths, as well as quantification and verification of these values. Also, realistic cross sections are required to effectively assess potential field performance. In the RMC program, the pavement was constructed directly over the subgrade. The margin of improvement implied by the geogrid cannot be directly translated to field conditions, where an aggregate base course is usually used. Further, pure sand subgrades are likely to represent only a fraction of the conditions typically encountered in the field, and can be expected to behave differently than subgrades consisting of fine-grained soil. To properly evaluate the effect of geogrid reinforcement in the HMA layer, cross sections that more effectively model actual roads would be preferable.

A comprehensive investigation of geogrid reinforcement of granular base layers of flexible pavement was carried out at the University of Waterloo by Hass (1986). The program consisted of repeated load tests on varying thicknesses of reinforced and unreinforced granular bases. Other controlled variables included reinforcement location and subgrade strength. The objectives of the program were to develop equivalency factors for the geogrid-reinforced granular base sections and to develop data for structural design guidelines. The program demonstrated that:

- The granular layer coefficient determined from the AASHTO method of design ranged from 1.4 to 1.8.
- Pavement sections incorporating geogrid reinforcement carried three times the number of load applications as conventional unreinforced sections.
- The geogrid reinforcement should be placed at the bottom of relatively thin bases, whereas they should be placed at the midpoint of bases 250 mm thick or greater.

A research program (Laier *et al.,* 1986) inquires the properties of different geotextiles at unpaved or only weakly fixed surfaces with limited thickness by intensive loading. A loading device was constructed which simulates heavy construction traffic, and the loading was applied using a dual wheel and a frame assembly. The dual wheel applies dynamic loading, and observations on deformation were observed with a Benkelman Beam assembly. After loading, the sections were excavated, and geotextile samples were obtained. Changes in effective opening size, permeability, intake of soil material, and strain characteristics were obtained. The test results show fundamental differences in the geotextile types under intensive loading. The authors suggested the need to perform more research in the area of geosynthetic-stabilization behavior of flexible pavements.

The results of the RMC program encouraged researchers to evaluate the effect of a geogrid placed in a granular base course layer. Based on the results of preliminary computer modeling, researchers at the University of Waterloo hypothesized that a geogrid could reduce deformation at the pavement surface by decreasing vertical strains and plastic deformations of the subgrade (Kennepohl *et al.,* 1985). Further, it was suggested that construction of roads with geogrid-reinforced base courses could be accomplished relatively simply and inexpensively. For these reasons, a laboratory test program was initiated at the University of Waterloo to quantify the potential benefits of

geogrid base reinforcement and to produce the data necessary to develop a design procedure.

Three reports of the Waterloo research program have been reviewed: Kennepohl *et al.* (1985), Carroll *et al.* (1987), and Hass *et al.* (1988). In general, the test setup and procedure were planned to simulate the RMC program as closely as possible. Kennepohl *et al.* (1985) reported that three test series were completed, and Hass *et al.* (1988) and Carroll *et al.* (1987) reported that a total of six test series were conducted.

Six “plate-loading” test series were designated as loops one through six by Hass *et al.* (1988) and Carroll *et al.* (1987), but Kennepohl *et al.* (1985) designated the three loops discussed in their report as A, B, and C. Based on a comparison of the descriptions of the loops in these reports, loops A, B, and C appear to correspond to loops 1, 2, and 4, respectively. Within each loop, four plate-loading tests were performed, each at a different location on the pavement surface, to evaluate the effects of different test variables.

The test pit at the University of Waterloo consisted of a large rectangular plywood box reinforced by a steel frame. It measured 4.5 m x 1.8 m x 0.9 m deep. The walls of the box were lined with galvanized steel sheeting and were sealed at the joints with a silicon caulking compound for moisture retention.

The subgrade of each test loop was constructed using fine beach sand classified as poorly graded sand (SP), according to the USCS. It was reported that 60% passed 0.64 mm sieve, 32% passed 0.25 mm sieve, and 4% passed 0.13 mm sieve. Kennepohl *et al.* (1985) reported that CBR tests were performed on the subgrade sand at different moisture contents. However, no information has been provided on the number of CBR tests conducted or on the method of achieving a specified CBR value.

The base course was constructed using a well-graded crushed stone aggregate classified as GW according to the USCS. The HMA was a dense-graded aggregate mix with a maximum particle size of 15 mm and 85/100-penetration grade asphalt cement. The reinforcement was a biaxial polypropylene geogrid manufactured by Tensar and designated as BX1100. It is also referred to as SS1.

The loading system consisted of an MTS function generator and servo-hydraulic controller that drove an actuator assembly mounted to a bolt-down rolling plate on a

reaction frame. The hydraulic actuator was equipped with a 100-kN load cell and an internally-mounted LVDT.

The loading sequence for each test section consisted of a series of dynamic loads followed by a single static load at fixed cycle counts. A dynamic loading force of 40 kN was applied at a rate of 8 Hz through a rigid plate with a diameter of 300 mm, resulting in a pressure of 550 kPa. The static load was applied to permit surface displacement gages, strain gages, and pressure cells to be read and the readings were recorded.

To help establish the pavement surface displacement profile, a total of five dial gages were placed across the 1.8-m-wide axis of the test pit. Two gages were positioned directly on the pavement surface on either side of the loading plate. The other three dial gages were placed directly on the loading plate, one near the center of the plate and the remaining two near opposite edges of the plate. The LVDT mounted inside the hydraulic actuator was also used to monitor pavement displacement beneath the loading plate.

According to Hass *et al.* (1988), pressure cells were installed in the subgrade in test loops one through five to help compare differences in stress distribution between reinforced and unreinforced sections. Strains in the reinforcing geogrid were measured using foil-type strain gages. These instruments were attached to the geogrid at various locations of increasing radial distance from the load center.

It can be seen that target CBR values of 8, 4, and 1% were selected for test loops A, B, and C, respectively. It can also be seen that tests were performed with the geogrid positioned at three different levels within the base course. These subgrade strengths and geogrid locations were evaluated with combinations of different HMA layer and base course thicknesses.

The study concluded that for geogrid reinforced pavements, the most effective location for reinforcement was in the lower half of the base course, and that the reinforced base course was able to withstand 3 times as many load cycles as the control section. In one test section, the geogrid was significantly stressed beyond its range of totally recoverable elastic response, showing the ineffectiveness of pre-tensioning.

A 50% reduction in base course thickness was possible if a geogrid was included in the design. Its optimum location would be at the bottom of the base course with thicknesses of less than 250 mm. For thicker base courses, the geogrid should be placed near the middle of the base course.

Barksdale *et al.* (1989) conducted both an analytical and a large-scale laboratory study. The analytical study involved finite element modeling of pavement sections reinforced with either geotextiles or geogrids. The laboratory study was performed using the University of Nottingham Pavement Test Facility (UNPTF).

The analytical study was performed using a finite element program called GAPPS7 and was designed to predict the response of geosynthetic-reinforced pavement sections. Using a linear cross-anisotropic model (i.e. different elastic material properties in the vertical and horizontal directions), the researchers evaluated reinforced pavement sections with variations in geosynthetic stiffness, pavement geometry, and subgrade strength. Geosynthetic stiffness was defined as the geosynthetic's tensile modulus at 5% strain (secant modulus at 5%). Because most geosynthetics do not have exactly the same tensile properties in the machine and cross-machine directions, the stiffness of the geosynthetic is dependent on its orientation.

The analytical model used by the authors indicated that the effect of the geosynthetic reinforcement was relatively small in terms of the change it caused in tensile strain at the bottom of the HMA layer, the vertical subgrade stress and strain, and vertical deflections throughout the pavement section. However, the model indicated that the presence of the geosynthetic could have a small but significant effect on the radial and tangential stresses and strains developed in the base course and the top of the subgrade during loading.

The laboratory study included four series of experiments using large-scale pavement models, and each series comprised three test sections. In this study, the researchers sought to evaluate the effect of the following variables: geosynthetic type (e.g. geogrid or geotextile), location of geosynthetic within the base course, pre-rutting of reinforced and non-reinforced subgrade, pre-stressing the aggregate base with the geosynthetic, and pavement material quality.

The pavement models were constructed in a concrete test pit with a surface area measuring 4.9 m x 2.4 m. The HMA wearing surface used in the construction of the pavements ranged in thickness from 30 mm to 40 mm. The first section was constructed using a gap-graded HMA prepared in accordance with British Standard 594 (Barksdale *et al.* 1989). The wearing surface for the remaining three series was constructed with HMA prepared using the Marshall design method.

The base course thicknesses ranged from 150 mm to 220 mm. The sections in the first test series were designed to be relatively weak using a sand and gravel mixture with a maximum particle size of 19 mm and classified as a British Type 2 subbase. An aggregate with a higher shear strength, meeting British Standard Type 1 requirements, was used in subsequent sections. The Type 1 aggregate had a maximum particle size of 38 mm and consisted of crushed dolomitic limestone. This material is typical of those used in British highway construction.

The subgrade was constructed using silty clay. It was found to have a plastic limit (PL) of 18%, a liquid limit (LL) of 37%, and an optimum water content of 15.5%. The clay was transported to the test facility in the form of unfired bricks. For each test series, a 450 mm-thick layer of this material was placed over a 1.1 m-thick layer of drier and stiffer silty clay. After each section was tested, the top 450 mm of clay subgrade was excavated and recompacted. The top 460 mm layer was placed at a CBR of 2.6% and a water content of 18%. The material below this layer had a CBR of 8 to 10%.

The geotextile used in the study was a very heavy and strong woven polypropylene material. It was reported to have a wide-width tensile strength of 155 kN/m and a weight of 970 gm/m$^2$. Typical woven and nonwoven polypropylene geotextiles used in road stabilization applications in the United States range in weight from about 130 to 540 gm/m$^2$ and have a wide-width tensile strength that does not usually exceed 70 kN/m (IFAI, 1994).

The geogrid used in the study was a Tensar BX1100 biaxial polypropylene geogrid. It was reported to have a wide-width tensile strength of 21 kN/m and a weight of 204 gm/m$^2$. The stiffness of the geotextile and geogrid at 5% strain was measured to be 750 kN/m and 280 kN/m, respectively.

The load was applied to the pavement surface by a 560 mm-diameter wheel with a width of 150 mm at velocities between 3 and 5 km/hr. The wheel was attached to a support carriage, which enabled control of the wheel's movement and load. Wheel wander was modeled by shifting the wheel path in increments of 75 mm over a total of nine positions during a phase designated as multi-track testing. Following application of these loads, single-path loads were applied in locations where the pavement was not yet rutted in order to further evaluate the test sections. This phase was designated as single-track testing.

The principal measurement of pavement section performance was the amount of vertical deflection induced at the pavement surface by the wheel loads. However, instrumentation and data acquisition were used to continuously record transient stresses near the top and bottom of the base course and near the top of the subgrade. Permanent strain in the base course and subgrade was recorded at intervals of 100 to 200 wheel passes.

In planning their research program, the Barksdale *et al.* (1989) chose to focus on the effect of reinforcement, one of the two principal modes by which geosynthetics are reported to improve pavement performance. Careful consideration was given to the stiffness of the geotextile and geogrid in both the computer and laboratory models of the pavement sections. However, it appears that it was not possible to evaluate reinforcement effects independently of the separation effects provided by the geotextile. The authors observed that no contamination of the base course occurred in sections where the geotextile was installed between the base course and subgrade. However, in the control and geogrid-reinforced test sections, the base course was contaminated 25 mm to 38 mm above the subgrade.

The authors concluded that placement of a geosynthetic in the middle of a thin aggregate base can reduce total permanent deformations, and that this is the optimum location for geosynthetic reinforcement in thin pavement sections constructed with low quality aggregate. In contrast, researchers in the Waterloo study determined that the base course-subgrade interface was the optimum location for a geogrid if the base course has a thickness less than 250 mm (Carroll *et al.,* 1987).

The authors also concluded that for improvement of fatigue performance of the HMA wearing surface, the optimum position for geogrid reinforcement appears to be at the interface of the HMA layer and the aggregate. This conclusion appears reasonable, if the geogrid tensile modulus is considered the most significant property. However, it is interesting to note that the researchers in the Waterloo program found no performance improvement with a geogrid placed at the HMA-base course interface (Carroll *et al.,* l987).

The authors also found that geogrid reinforcement performed better than a much stiffer woven geotextile. Their test results, however do not seem to support this conclusion. The investigation did not compare the performance of these two materials except in test series 4, where the geotextile was located in the middle of the base

course. In this position, the beneficial influence of geotextile separation is considerably reduced. Further, the geotextile significantly improved the performance of the pavement section in both test series 1 and 3.

Jorenby and Hicks (1986) conducted a laboratory study to illustrate the influence of soil fines on the modulus of an aggregate base course. The aggregate meets Unified Soil Classification System (USCS) criteria for classification as well-graded gravel (GW) for base course. The material used as soil fines consisted of a soil meeting USCS criteria for classification as lean clay (CL).

The test procedure included blending the clay with the aggregate to represent specific levels of contamination with soil fines. The% increase in fine content of the aggregate was designated as "S." Levels of S equal to 0, 2, 4, 6, 8, and 19.5% were evaluated. The levels of contamination were chosen, because they represent a range of added fines found in other laboratory tests where geotextile separators were used (Walter, 1982; Hoare, 1982; Bell *et al.,* 1982). Jorenby and Hicks (1986) noted that the level of contamination would be a function of several factors, including geotextile and soil variations.

The blended aggregate was compacted to 95% of its maximum density in a 100 mm-diameter mold. Next, the resilient modulus of the aggregate sample was evaluated with the use of a triaxial cell and an MTS testing machine. The relationship between state of stress and resilient modulus was characterized using bulk stress parameters:

$$\theta = \sigma_1 + \sigma_2 + \sigma_3 \qquad (2.13)$$

where,

$\theta$ = Bulk stress;

$\sigma_1$ = Major principal stress or total vertical stress; and

$\sigma_2$ and $\sigma_3$ = Minor principal stress.

The resilient modulus was determined at four levels of bulk stress: 69, 138, 241, and 655 kPa. The bulk stress of 241 kPa represented the stress state in the base course, and 138 kPa represented the stress state in the subgrade.

In general, it was found that the resilient modulus increased until the added fine content reached 6%. Because the fine content of the original aggregate mixture was

5.5%, an increase of 6% represented a total fine content of 11.5%. An increase in fines beyond that amount was found to result in a sudden and significant decrease in the resilient modulus of the base course. The relationship between resilient modulus, bulk stress, and fine content established by Jorenby and Hicks (1986) is shown in Figure 2.5.

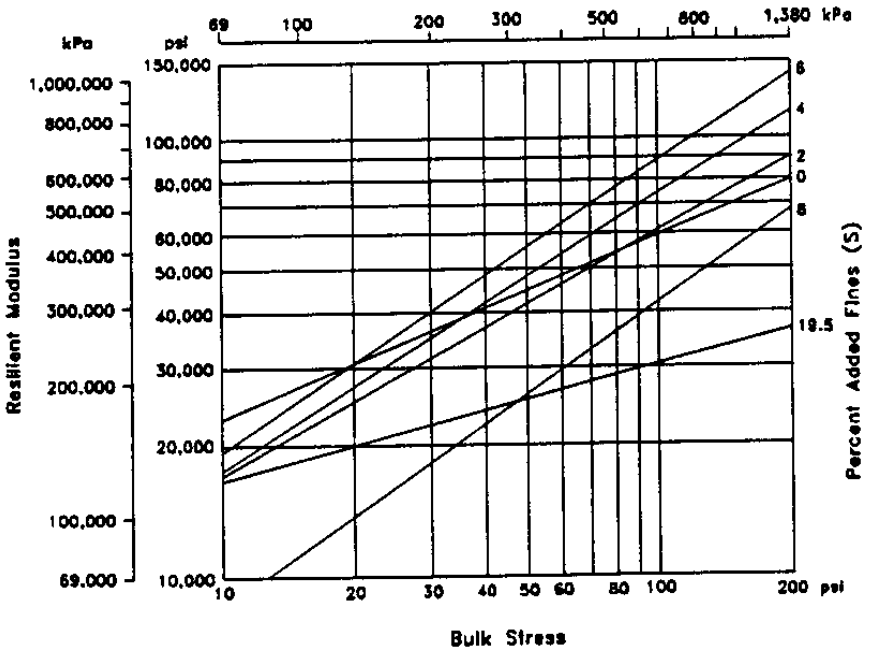


**Figure 2.5 Resilient modulus verses bulk stress for various fine contents (after Jorenby and Hicks, 1986).**

It should be noted that in their experiment the fines were blended directly into the aggregate mix. It is possible that in the base course of a road structure, the same degree of blending may not occur. Rather, the fines may simply migrate into existing voids, but not intercede between aggregate particles. If this occurs, the loss of aggregate shear strength may not be as great as this experiment suggest. The amount by which soil fines reduce the point to-point contact of aggregate particles may depend upon the amount of aggregate movement which occurs under traffic loading.

The relationship between resilient modulus and the fine content of the base course is further illustrated in Figure 2.6. It can be seen that the stiffness of the base course reaches a maximum when S equals 6% for all levels of bulk stress, and that additional added fines lead to a sharp decrease in resilient modulus. Accordingly, these results suggest that designs based on a stiffness criteria should limit the intrusion of soil fines so

that the total fine content of the base course remains below 11%. However, use of this stiffness criterion may not permit adequate drainage through the aggregate. To provide adequate drainage, Jorenby and Hicks (1986) suggest that the total fine content of the base course be limited to 8%, which corresponds to a value of S equal to 2.5% for the aggregate mix used in their study.

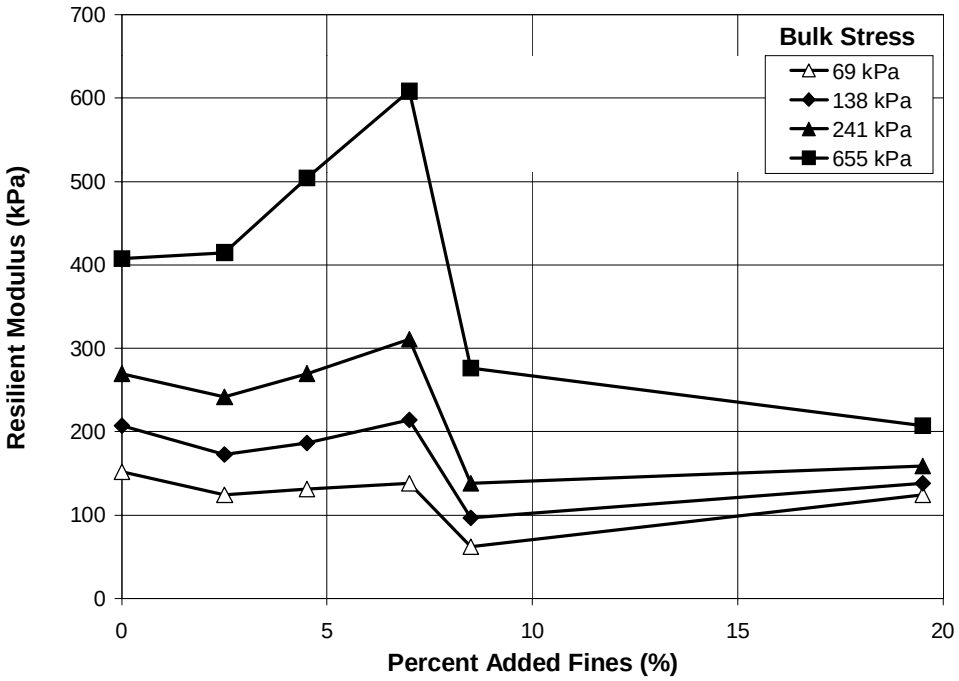


**Figure 2.6 Resilient modulus verses percent added fines (after Jorenby and Hicks, 1986).**

Jorenby and Hicks (1986) evaluated the influence that added fines would have on the service life of a pavement section by employing three analytical models: the US Forest Service method with the AASHTO equation, the Boussinesq method of equivalent thickness, and elastic layer theory (ELSYM5). To facilitate their evaluation, the researchers defined pavement life ratio (PLR) as the allowable number of 80 kN equivalent axle loads for a given percentage of added fines divided by the allowable axle loads when no fines are added. The three models used for PLR analysis yielded different estimates of pavement life, but showed a general trend of decreased service life with increased amounts of added fines.

Yang and Yu (1989) studied the use of geosynthetics to prevent mud pumping under railway lines. Many of their results are applicable to pavement systems. They constructed laboratory test specimens to model a soft subgrade that had the potential to liquefy during the dynamic loads produced by trains. After preliminary laboratory tests were performed, they constructed a full-scale field test. Yang and Yu (1989) concluded that geotextiles are effective in preventing mud-pumping. The separation and drainage characteristics of the geotextiles were found to play a key role in overall mud-pumping prevention.

Miura *et al.* (1990) discussed analytical modeling and field tests for investigating the mechanism of reinforcement by a polymer grid in suppressing non-uniform settlement of pavements constructed on soft clay ground. A series of laboratory tests on reinforced and unreinforced model pavements in a soil tank indicated that the polymer grid is useful for suppressing non-uniform settlement of pavement under cyclic loading. Deformation analyses using the finite element method was carried out to examine the reinforcement effect of a polymer grid in a model pavement. To investigate the performance of a polymer grid in practice, a test road of 300-m-length with six sections of different kinds of pavement was constructed on soft clay ground. The results from this study showed a significant improvement in pavement performance when geogrids are used as reinforcing materials.

Tsai *et al.* (1993) completed a full-scale study on the use of geotextiles as separators on Washington state highway SR-507. The focus of their study was the constructability and durability of geotextiles during the construction process. Strain gages were placed in the soil and on the geotextiles to measure the strain during the placement of the aggregate base course layers. A 350 kN dump truck with a dual rear axle was used to simulate pavement construction traffic. The number of loading cycles varied between sections. The sections were later excavated to determine the mechanisms of reinforcement. Tsai *et al.* (1993) found that the geotextiles prevented intermixing of the aggregate and subgrade if placed properly, and that the use of geotextiles produced a smaller and much more uniform rut depth. A non-woven, needle-punched geotextile provided the most efficient drainage while the woven geotextiles seemed to retard drainage. A needle-punched polypropylene geotextile reduced rut depth and subgrade deformation most efficiently.

Austin and Coleman (1993) conducted a full-scale field study near Greeneville, Mississippi, to evaluate the performance of geogrid and geotextile stabilization of an unpaved road constructed over very soft soil. When the initial investigation of the test site was performed, it was learned that the subgrade soil consisted of a fat clay meeting USCS classification of CH. It had a natural water content between 27 and 40%, a LL of 73 to 85%, and a PL of 23 to 33%. It was also determined that the CBR value of this soil ranged from 3 to 6%, values which were considered too high to satisfy the objectives of that study.

The investigators sought to obtain a subgrade with CBR values less than about 1%. Thus, the test site was flooded for a period of eight months and then drained. This process had the desired effect, reducing the CBR values to between 0.6 and 0.9% in most locations. The in-situ CBR values were measured using two procedures. The first of these was described as a field-bearing ratio test, although details of the test were not provided and no specific test procedure was referenced. The second procedure used a dynamic cone penetrometer device (Webster *et al.* 1991) to measure soil strength within the top 300 mm of the subgrade. The geosynthetics used to stabilize the road section included four types of polypropylene geogrids and geotextiles. The nonwoven polypropylene was used in conjunction with one of the geogrids. The geosynthetics were installed on the test road, overlapping adjacent sections in the direction of fill placement. Each test section was approximately 6 m wide x 6 m long.

The test sections were loaded by a two-axle dump truck with the rear dual-tire axle loaded to approximately 80 kN. The tire pressures were maintained at 550 kPa. The performance of each test section was based on the number of vehicle passes, that induced surface deflections of 50 mm and 75 mm. The number of passes was converted to ESALs using a factor of 1.13 per each actual vehicle pass.

To minimize the influence that adjacent sections had on each other, data collection stations were established at the midpoints of each test section. In addition to deflection measurements, data collection included measurements of in-situ CBR values of the subgrade and base, as well as dry density, moisture, and thickness measurements of the base. After loading of the test road was completed, each test section was carefully excavated and the percent contamination of the base aggregate by subgrade soil was evaluated.

Although some of the results presented were not logical (such as a lower number of passes to failure needed to fail a strong section compared to a weak section), it was clear that the use of geosynthetics significantly improved the performance of each test section compared to the control sections. The research also demonstrated the effectiveness of the geotextile as a separator. The investigators observed that no contamination of the base aggregate occurred at the geotextile-stabilized sections, but that significant contamination occurred at the control sections and the geogrid sections. The test results suggest that the tensile strength of geogrids may not have a significant influence on their ability to stabilize an unpaved road over weak soil.

Webster (199l) conducted a research program that involved full-scale testing of geogrid-reinforced pavement sections used by light aircraft. The pavement was constructed over weak subgrade soil. The testing was performed at the U.S. Army Corps of Engineers Waterways Experiment Station (USACOE-WES) facility in Vicksburg, Mississippi, inside a large hangar. The test section was divided into four traffic lanes, each containing four test configurations, which the researchers referred to as "Lanes" 1 through 4. Lane 1 and lane 2 used a traffic pattern with wheel loads distributed over five wheel widths for a total width of 2.2 m. Lane 3 and lane 4 used a traffic pattern that consisted of a single wheel path that had a width of 1.5 m.

Webster considered the geogrid's secant modulus at 5% to be a good indication of stiffness, and used this property to attempt a correlation with reinforcement potential. Each test lane was surfaced with an HMA layer with a nominal thickness of 50 mm. It contained a maximum aggregate particle size of 12 mm and had a minimum Marshall stability of 6,700 N. The HMA wearing surface was not considered a test variable during this study.

The base course was constructed using a low quality, crushed limestone aggregate which was classified as silty sand to silty clay (SM-SC) according to the USCS. The maximum particle size was 25 mm and 15% passed the No. 200 sieve. Webster observed that based on his literature review, low quality base material offered the highest potential for geogrid reinforcement. The subgrade was constructed using a local soil (clay). It was classified as a fat clay (CH) according to the USCS. It had an LL of 67% and a PL of 23%.

To construct the test section, an area measuring 44 m x 15 m was excavated to a depth of about 1 m. The lean clay material at the bottom of the excavation was

compacted until its CBR value was greater than 10%. The subgrade was then compacted in lifts of 150 mm. The total pavement section thickness was 1 m. The minimum subgrade thickness of 500 mm occurred in lane 2 under a base course of 460 mm.

The traffic loads were applied over a five-month period using a single-wheel-assembly test cart attached to the front half of a four-wheel-drive truck. The test wheel and tire were from the landing gear of a C-130 aircraft. The load was 133 kN and the tire pressure was 470 kPa.

Failure of the test section was defined as 25 mm of surface rutting. Traffic was usually continued until 75 mm of rutting occurred, or until each item in a test lane sustained 25 mm of rutting. Rut depth measurements were recorded at intervals throughout the traffic test period and included both the permanent deformation in the middle and upheaval on both sides.

The test results indicate that some types of geogrids provided significant performance improvement. However, two of the woven polyester geotextiles and one polypropylene geogrid demonstrated insignificant reinforcement benefit.

Results also indicate that placement of the geogrid in the middle of the base course for relatively thick layers is not as effective as placement at the bottom of the base course. This contradicts the findings in both the Waterloo program and the UNPTF program. Based on the results of the testing program, Webster developed a relationship between unreinforced pavement section thickness and equivalent reinforced section thickness, shown in Figure 2.6. Webster concluded that the total pavement design thickness can be reduced by the amounts indicated in this relationship when a geogrid reinforcement product equivalent to Tensar BX1200 (SS2) is used.

This relationship assumes that the HMA layer is 50 mm thick. It also shows that a total equivalent section thickness of 150 mm is the minimum for which geogrid reinforcement may be used. For designs which require section thicknesses to be greater than 150 mm, it can be seen that aggregate thickness can be reduced from 275 mm to 500 mm, if a reinforcement equivalent to BX1200 (SS2) is used. It can also be observed that as the required unreinforced design thickness increases, the aggregate savings diminish.

The decision by a designer to incorporate a geogrid into a pavement section (using this method) is based on the relationship shown in Figure 2.7 and should be based partly on the potential economic advantages. A logical design sequence may involve calculating the required unreinforced design thickness and reinforced design thickness, and evaluating the potential cost savings based on the reduction in aggregate thickness. If the savings provided by the reduction in aggregate is greater than the cost of the reinforcement, then reinforcement of the section may represent a cost-effective design option. According to Webster (1991), the cost of aggregate should be higher than $12/ton to be feasible to use geogrid (prices used from the time of the study).

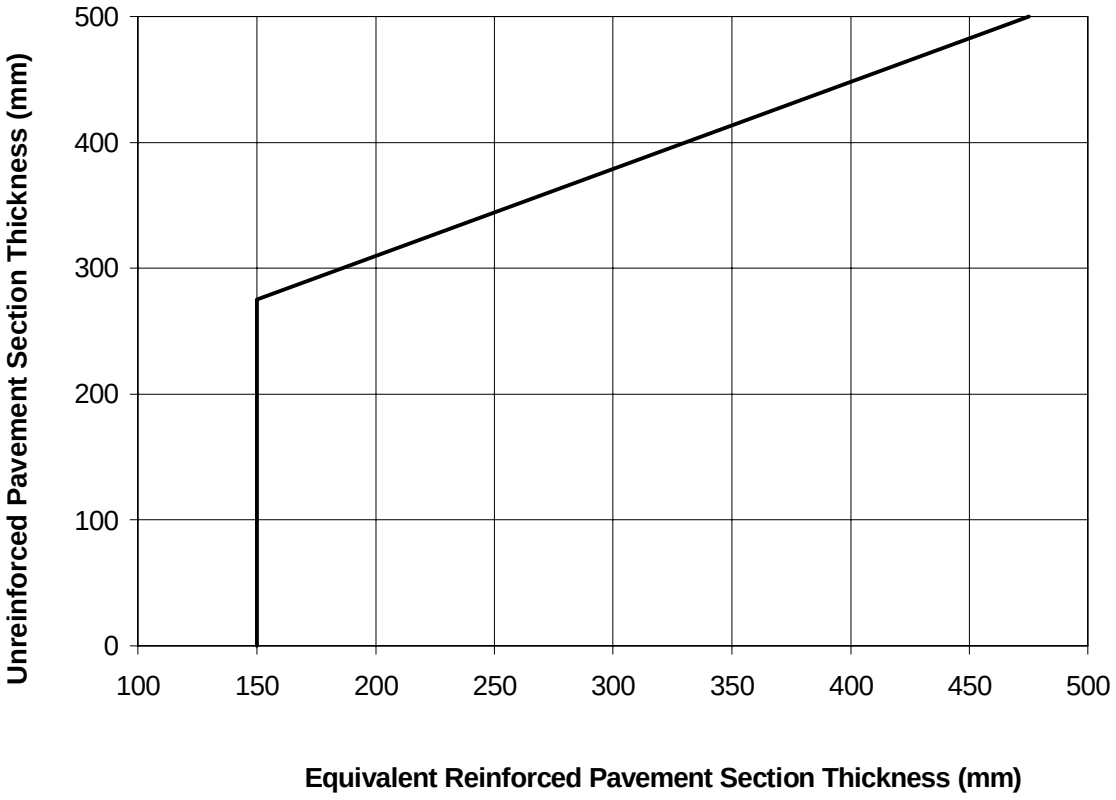


**Figure 2.7 Design criteria for unreinforced pavement section thickness versus equivalent reinforced thickness (after Webster, 1991).**

The results of Webster's study may have important implications for the design of flexible pavements for light aircraft landing fields using geogrid stabilization. Before this can be fully ascertained, the impact of uncontrolled environmental factors must be

evaluated. The subgrade soil used by Webster was fat clay. Based on published reports (Bell *et al.,* 1982; Jorenby and Hicks, 1986), the resilient modulus of the base course decreases as subgrade fines migrate upward. Given the relatively plastic nature of the subgrade soil in Webster's study, migration may be expected to occur as a result of soil softening. For soil softening to take place, excess moisture (e.g., rain or near-surface groundwater flow) is required. By conducting his full-scale research in the protected confines of an aircraft hangar, Webster may have excluded an important environmental factor from his research.

Experimental and analytical investigations were conducted to evaluate the performance of geosynthetic-reinforced flexible pavement sections by Al-Qadi *et al.* (1994). Geosynthetic materials were incorporated in the pavement systems at the bottom of the base layers. Eighteen pavement sections, constructed at a test facility, were tested. The pavement sections were constructed to model a typical secondary road in Virginia which is built over a weak granular (silty sand) subgrade material; the CBR ranged from 2-5.4%. The base material was 21-A (in accordance with Virginia classification) crushed granite used at two different thicknesses, 150 mm and 200 mm. Loading of the pavement sections was accomplished through the use of a computer-controlled pneumatic system that delivered 552 kPa through a 300 mm-diameter rigid plate at a frequency of 0.5 Hz. The resulting displacement of the pavement surface was monitored by an array of linear variable displacement transformers (LVDTs). The study concluded that the geosynthetics can provide substantial improvement to the performance of a pavement section constructed on a low CBR subgrade. The stabilization mechanisms of geogrids and geotextiles are different, with separation mechanism (provided by geotextiles) being an important factor in improving pavement performance. The study also showed quantitative improvement in service life and cost savings when geosynthetics are incorporated in the pavements. In addition, the study provided key information on the contamination potential in pavements not stabilized with geotextiles. A design methodology for pavements stabilized with geosynthetics was provided by the authors (Smith *et al.,* 1995). The laboratory results prompted the authors to test a pavement section under field conditions to determine the effect of geosynthetic stabilization.

## 2.6 Recent Instrumented Pavement Research

Currently, a falling weight deflectometer (FWD) is used to evaluate in-situ moduli of various pavement layers. However, unless a perfect match between calculated and measured deflection basins is achieved (i.e. zero error), multiple sets of moduli may be generated, depending on the assumptions used in the back-calculation analysis. Therefore, the use of instruments to directly measure strains and stresses throughout the pavement system would provide additional information needed to verify the validity of evaluated moduli. Measured responses are also necessary to determine structural distress, to calibrate new design procedures, and to model pavement performance. Because the environment is a major factor in pavement performance, moisture and temperature variations within the pavement system need to be monitored.

Several projects have been undertaken in recent years to evaluate pavement response to mechanical and environmental loading. Such projects are a source of valuable information on pavement response as a system, as well as material characteristic changes over time. The most notable among these projects are: Penn State Test Track; Minnesota Road (MnRoad); Denver Airport Project; Ohio Test Road; WesTrack; and a few LTPP sections.

### *2.6.1 Penn State Test Track*

In the late 1980s, under part of a research project sponsored by the FHWA, Penn State undertook a project to evaluate different pavement instrumentation. The Pennsylvania research program was divided into two phases. In the first phase, an extensive literature search was conducted to identify the existing pavement instrumentation and to select the most promising types of gages for a field testing program. Two sections of flexible pavements 152 and 254 mm-thick-HMA were constructed and instrumented with selected gages. The response of the gages to dynamic loading applied by a tractor-semi-trailer at different levels of axle loading, tire pressure, and speed were investigated. In the second phase, new concepts in pavement instrumentation were investigated. Prototype gages were built and evaluated first in the laboratory and then in the field. The pavement response data, collected in the field testing program, was used to evaluate methods for back-calculating pavement material properties. It was demonstrated that the back-calculated moduli were much more accurate if data from multiple sensors placed throughout the pavement structure

was used in the analysis as compared to a single sensor. Table 2.4 shows the type of instrument used for measurement of a specific variable. Figure 2.8 shows the cross section of the pavement from thin to thick sections. Table 2.5 shows the number of instruments, their location and orientation in the test section.

**Table 2.4 Pavement response and sensor type for the Penn State project.**

| Pavement Response | Sensor Type |
|---|---|
| Stress | •Nottingham diaphragm-type pressure cell |
| Deflection | •Geophones<br>•Single-layer deflectometer<br>•Multi-depth deflectometer |
| Strain | •Dynatest H-gage<br>•Kyowa H-gage<br>•Alberta Research Council (ARC) asphalt carrier block gage<br>•Core gage |
| Temperature | •Thermocouples<br>•Solid state sensors |
| Moisture | •Nuclear dual tube<br>•Moisture/suction-AGWATRONIX |
| Transverse vehicle location | •Ultrasonic sensor |

In summary, the Penn State study contribution was to examine several methods to measure strain, stress, and deflection in flexible pavements, and to evaluate procedures that use this data to determine layer moduli and to validate strains computed by mechanistic techniques. Evaluation of various instruments was the main focus in this study.

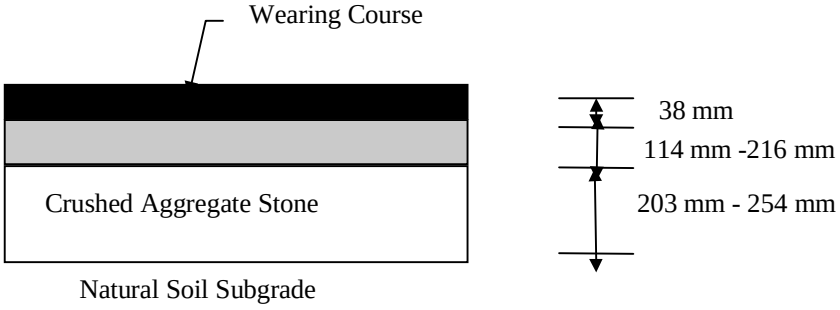


**Figure 2.8 Pavements cross sections.**

**Table 2.5 Summary of gages for field testing.**

| Gage Type | Number of Gages/Section | Orientation | Location |
|---|---|---|---|
| Nottingham pressure cells | 2 / thin | Vertical | At the top of base course |
| Geophones | 3 / thin and thick | Vertical | At the pavement surface |
| Geophones | 3 / thin and thick | Vertical | At the top of base course |
| Geophones | 3 / thin and thick | Vertical | At the top of subgrade |
| Single layer deflectometer | 1 / thick | Vertical | At the top of base course |
| Single layer deflectometer | 1 / thick | Vertical | At the top of subgrade |
| Multi-depth deflectometer | 1 / thin and thick | Vertical | Throughout the depth of pavement |
| Dynatest strain gage (H-Type) | 2 / thin and thick | Longitudinal | At the bottom of HMA |
| Kyowa strain gage (H-Type) | 4 / thin and thick | Longitudinal | At the bottom of HMA |
| Asphalt concrete block gage (ARC) | 1 / thin and thick | Longitudinal | At the bottom of HMA |
| Core gage | 4 / thin and thick | Longitudinal | At the bottom of HMA |
| Core gage | 2 / thin and thick | Vertical | At the lower one third of HMA |
| Core gage | 2 / thin and thick | Transverse | At the bottom of HMA |
| Thermocouples | 8 / thin and thick | N/A | Throughout the depth of the pavement |
| Solid state temperature sensors | 8 / thin and thick | N/A | Throughout the depth of the pavement |

### *2.6.2 MnRoad*

Recently, a pavement research facility was constructed in the state of Minnesota: Minnesota/Road (MnRoad). It consists of approximately 40-160m pavement test sections. Twenty-three of these test sections have been loaded with freeway traffic, and the remainder have been loaded with calibrated trucks. Freeway traffic loading began in June 1994. Embedded in the roadway are 4572 electronic sensors, 1151 of which are used to measure pavement response to dynamic axle loading. The specific brands and models of each type of sensor were selected based on Minnesota Department of Transportation (MnDOT's) recommendations derived from four research contracts for evaluation of pavement sensors, and by consultation with other government agencies

and instrumentation experts worldwide. The main purpose of this facility is to verify and improve existing pavement design models, learn more about the factors that affect pavement response and performance, and develop new pavement models that will allow building and maintaining more economical roadways.

Research and collection of data on the MnRoad project is underway, and the purpose of the project is to enhance the knowledge of pavement response to dynamic loading, and possibly development of new design techniques based upon the data collected.

### *2.6.3 Ohio Test Track*

As part of the Long Term Pavement Performance (LTPP) Specific Pavement Studies (SPS), a project was started in Ohio, called the Ohio Test Track. All the test sections are constructed as part of one project where the climate, soil, and topography are uniform throughout. Since the basic instrumentation plan proposed by SHRP was limited, the Ohio Department of Transportation (ODOT) opted to develop a more comprehensive plan for the test track. The four independent parts of Ohio project are divided into the following categories:

- *SPS-1* (Strategic Study of Structural Factors for Flexible Pavements): Variables studied in this project include HMA thickness, base type and thickness, and the presence or absence of drainage conditions.
- *SPS-2* (Strategic Study of Structural Factors for Rigid Pavements): Variables in this study include Portland cement concrete thickness, base type and thickness, concrete strength, pavement width, and the presence or absence of drainage conditions.
- *SPS-8* (Study of Environmental Effects in the Absence of Heavy Traffic-Asphalt and Concrete): This project includes two instrumented sections, one of asphalt concrete, and the other of Portland cement concrete. These sections are subjected to low volume and light weight traffic.
- *SPS-9* (Asphalt Program Field Verification Studies): The objective in this part of the project is to verify the SHRP asphalt specifications.

The main objective of the Ohio Test Track was to encompass a long-term study of structural factors, maintenance effectiveness, rehabilitation, and environmental factors on the mechanistic response of various pavement sections. Of particular interest is the interaction of load response to environmental parameters.

### *2.6.4 Denver Airport*

In 1992, the Federal Aviation Administration (FAA) initiated a major research effort to study the in-situ response and performance of Portland cement concrete pavements. FAA, in cooperation with the U.S. Army Corps of Engineers and Waterways Experiment Station (CEWES), instrumented several pavement slabs in the take-off area of Runway 34R at the Denver International Airport (DIA), which was under construction at that time. With the support of the DIA airport authority, the City and County of Denver, and the FAA Denver Airport District Office, a total of 460 sensors were installed in the various layers of the pavement structure. A comprehensive data acquisition system was also installed for remote access. Video cameras were installed next to the instrumented pavement section to provide live images of the aircraft landing, and a record of time-based surface deterioration. Since the opening of the airport, the FAA has completed a series of tests to debug the entire system. Data collected in this project include real-time pavement responses to actual aircraft traffic, environmental parameters, and weather conditions. The focus of the test section is to determine the effect of aircraft loading on pavement design and service life, as well as monitor deterioration development due to environmental loading.

### *2.6.5 WesTrack*

The most recent addition to the stock of test track sites is WesTrack, a 2.9 km oval loop in western Nevada. The construction and the two-year truck loading of the track are being funded by the FHWA as part of a significant study of HMA paving materials and construction. Construction of the first pavement test sections on WesTrack was completed in October 1995, and truck loading was initiated in March 1996. The main focus of this project is not on pavement design development, but rather on HMA performance evaluation. The WesTrack program therefore has two major objectives: continued development of performance-related specifications (PRS) for HMA pavement construction by emphasizing how materials and construction variability affect the eventual pavement performance and service life, and to provide an evaluation of SHRP Superpave™ Level III mixture design and performance prediction models. The instrumentation of the 26 sections is primarily environmental. Although HMA strain gages were used, their service life was less than six months.

### *2.6.6 Florida Test Study*

In 1973, a research project on State Route 80 (SR80) South of Belle Glade was initiated to investigate different embankment construction techniques, including cement treatment of embankment material and the use of geotextile as a separator from the organic soil. In 1980, a 20-km section of the SR80 northeast of Belle Glade was realigned and widened to four lanes. The project was constructed in two phases. Phase I consisted of excavating a canal from the south side of the project and using marl material from the canal as embankment and surcharge material for the two roadways. Three different geotextiles (two nonwoven and one woven) were used as separators between the embankment and the organic soil. Phase II consisted of removing the surcharge and completing the construction of embankment after settlement was practically complete. In light of the fact that geosynthetics were incorporated in the pavement system over soft subgrade, a laboratory study was undertaken by Florida Department of Transportation (FDOT) to establish the control parameters for the field application.

In FDOT, the most common uses of geotextiles and geogrid are in drainage, erosion control or as a separator and reinforcement in pavement and embankment construction over soft ground. A 2.4-m x 7.3-m pit was divided into 2.4-m x 2.4-m sections, consisting of an unreinforced (control) section, a geogrid-stabilized section and a geotextile-stabilized section. The sections were dynamically loaded at a frequency of 1.0 Hz using a closed loop hydraulic system. Stresses of 345 kPa and 480 kPa were applied through a 0.3-m diameter rigid plate on top of base material. The water table was varied within the organic soil and marl subgrade below the base material. Surface deflections of the plate were measured with a pair of LVDTs. Test durations varied from one day (30,000 cycles) to one week (over 200,000 cycles). Two extended tests with one million loading cycles were performed on the geogrid and geotextile stabilized sections. Additional series of tests were made with the water table at the bottom of the base course, and also with the water table lowered to the top of the organic soils. Dynamic cone penetrometer, field CBR and Clegg impact tests were performed after the plate tests to determine the strength variation of the base course material in the test pit.

Based on the comparison of plate load deflections of like sections for this soil profile, it was concluded that the control (unreinforced) sections deformed more than the two reinforced sections. As to the performance of the geotextile and geogrid stabilized

sections for the specific soil cross-section in this study, there was no clear-cut advantage of one over the other. In other words, if properly designed, one geosynthetic is as good as the other. Since the geotextile is not as stiff as the geogrid, it is critical during field installation to insure that no slack or wrinkles are built into the geotextile.

## 2.7 Response Monitoring

As indicated earlier, pavement instrumentation is crucial to understanding material performance in the field, as well as pavement system response to loading and environment. Parameters that need to be measured in the field include strains, stresses, deflections, moisture, and temperature. Measuring these parameters in the field allows for the development of an accurate performance model and the calibration of the mechanistic pavement design. The following four sections detail current instrumentation used to measure pavement system response to loads and environment.

### *2.7.1 Strain Gages*

Measurement of traffic-induced pavement strains at specific locations is important to predict the failure mechanisms. Environmental loading is also important, as it can cause excessive expansion/contraction strains in an HMA layer, as well as curl and warping in a concrete slab. It has been documented that mechanical loading may cause strain-based failures at the bottom of HMA (fatigue), or at the top of the subgrade (rutting). The viscoelastic nature of HMA may also cause plastic flow rutting in the HMA layers. As the critical locations in any pavement system can be identified, it becomes possible to choose appropriate instrumentation to measure the relative strains at these locations.

Different strain gages have been tested over the years. Denver Airport used H-bar strain gages, which operate in a dynamic mode, to measure strains induced at the top and bottom of concrete layers. Penn State Test Track, MnRoad, WesTrack, Ohio SPS, and the researchers in Virginia also used H-Type strain gages. This type of embedment gage consists of an electrical resistance strain gage embedded within a strip of glass-fiber-reinforced epoxy, which is surrounded by several protective layers of various materials. These strain gages are installed in the longitudinal and the transverse directions in Ohio and MnRoad. The performance of these gages has been very successful in the field, and their survivability rate is the highest in their category. The major manufacturers of this type of gage are Dynatest, Tokyo Sokki, and Kyowa.

Researchers from Alberta Research Council in Canada (ARC) embedded strain gages in thin sheets of asphalt (50 mm x 150 mm x 13 mm) to measure the longitudinal strain at the bottom of HMA. The procedure allows asphalt on the surface of the carrier block (which will soften when it comes in contact with the hot HMA) to bond monolithically with the HMA layer. This type of gage is used in MnRoad and WesTrack.

In addition, there is another type of gage called the foil strain gage. These gages are attached to full-depth cores extracted from an actual pavement, and the instrumented core is replaced into the pavement section. The main concern with this approach is whether effective bonding is achieved between the instrumented core and the surrounding pavement. If the bonding agent, which is epoxy, is too stiff compared to the surrounding pavement, then stress concentrations will occur and inaccurate measurements of strain will be recorded. Field experience with this approach has shown that there are some epoxies commercially available that work well, but high failure rates are still normally encountered.

Strain gages are also used in concrete slabs to measure strains induced by slab deflection, dynamic mechanical impact on joints, and curl and warp conditions. MnRoad and Ohio SPS used Dynatest Past-II-PCC embedment strain gages which consist of electrical resistance strain gages embedded within strips of glass-fiber reinforced epoxy, with transverse steel anchors at each end to form an H-shape. Tokyo Sokki TML-60 strain gages were also used in both projects, as well as TML KM-100B used in Ohio. These standard wire gages are designed for the measurement of internal strains in concrete under dynamic loading. The gage is coated with a coarse grit to help bond the gage to the concrete. Measurement Group LWK-06-W250B-350 and Geokon VCE 4200 Vibrating Wire strain gages are also used in the field to measure compression and tension in dowel bars, and to measure warp and curl in concrete slab. The strains measured by Geokon may be affected by temperature, moisture, creep, and shrinkage. A thermistor is built into the vibrating wire gage so that accompanying temperature measurements can be made. Carlson A-8 strain meters were used in the Ohio SPS sections to measure strains resulting from thermal variations. These gages are elastic wire strain meters containing two coils of highly elastic steel wire, one of which increases in length and electrical resistance with change in strain.

Soil Strains were measured in the Penn State Test Track using Transportation and Road Research Laboratory (TRRL) soil strain gages using Carlson strain gages. The

gages used at Penn State were placed after the construction of the base course by excavating to the subgrade and backfilling. It is important to monitor this type of gage performance during backfilling and compaction.

### *2.7.2 Stress/Pressure Cells*

Although measurement of strain is clearly important in determining certain major failure modes, the relative importance of stress/pressure measurement cannot be overlooked. Stresses can be calculated from measured strains if material properties, loading, and layer thicknesses are known. However, because some of these parameters are not known (in the field), stress measurements will be essential to back-calculate material properties under field "construction" conditions. In addition, there are certain factors in the field that are practically impossible to simulate accurately numerically (e.g. geosynthetics and drainage effect). Attempts have been made to model these conditions numerically, but the absence of meaningful data from field tests has made stress measurement a necessity. This section details the pressure cells that have been used in the field in various projects, the advantages/disadvantages of these instruments, and their working principles.

The primary function of pressure cells is to monitor the change in the stress-state of the overlying layers and to measure the increase in vertical pressure due to dynamic traffic loading. The Kulite type 0234 earth pressure cells are designed to operate within a vertical pressure range of 0 to 690 kPa, and are 54 mm in diameter, with a thickness of 14.3 mm. The Kulite 0234 contains a diaphragm that excites a silicon strain gage upon diaphragm deformation. The Carlson-type TP-101 earth pressure cells are also designed to operate within a vertical pressure range of 0 to 690 kPa. The TP-101's stainless steel pressure head is 114 mm in diameter and 6.4 mm thick, and is welded to a 16 mm outside diameter stainless steel tube that is attached to a silicon strain gage transducer. Geokon 3500 is a large diameter soil stress cell consisting of two circular steel plates welded together around their rims to create a composite assembly 13 mm thick with a diameter of 150 mm. The space between the plates is filled with liquid. A steel tube connects the liquid to an electrical pressure transducer mounted several centimeters from the cell. The pressure transducer responds to changes in total stress applied to the cell.

Geokon 3410S is a pore water pressure cell normally used in subsurface applications. It is similar in operation to the Geokon 3500, but is specifically designed to operate under intense static load conditions. In addition to the dynamic pore water pressure cells, static condition earth pressure cells like Geokon 4800E and 4500Sl can be used in the subsurface layers, both in vertical and horizontal conditions, to measure the static development of pressure caused by pavement deformation and initial settlement under natural and mechanical loading.

MnRoad and Ohio SPS used Geokon 3500 pressure cells. Kulite 0234 has been used successfully in MnRoad. Penn State Test Track used Nottingham pressure cells at the interface of the base course and the HMA layer. Their performance was also satisfactory.

### *2.7.3 LVDT's and Deflectometer*

Pavements may fail because of excessive deformation in the subgrade. There are several ways to measure deformation in a pavement section. The most common is to place linear variable deformation transformers (LVDTs) in the pavement after construction. The usual placement procedure is to excavate a hole and place an anchor and guiding rods vertically through several layers. Devices such as Multi-depth Deflectometer (MDD) and Single Depth Deflectometer (SDD) are commonly used to measure subsurface deformation of various layers (Denver Airport and Penn State). Ohio SPS used Schaevitz GPD 121-500DC, an LVDT similar in function to MDD. Disturbance of pavement layers during installation of these instruments may affect the quality of the collected data.

In the WesTrack, a Forest Service liquid level gage was used to measure subsurface deformation. This is a relatively simple and cheap instrument, but it is more labor-intensive to collect the data. The performance of this technique has been excellent and reasonably accurate.

Accelerometers (Kistler 8628 B50) are the devices that measure slab acceleration at MnRoad. They give a direct measure of horizontal and vertical movement that occurs at the slab joints in terms of acceleration. The double integral of the acceleration can be correlated to displacement, and therefore displacements at joints can be predicted.

### *2.7.4 Environmental Measurements*

The two most important environmental factors that influence the service life of pavements are temperature and moisture. Excessive temperature changes may cause flow and contraction in HMA, and curl and warp in concrete. Although temperature is one of the most important failure modes in pavements, until recently, it has not been included in any design procedure. Moisture also causes major problems ranging from pumping to subgrade weakness. Therefore, temperature and moisture monitoring is important to develop a database that will be used to calibrate any pavement design models. Instruments used to measure temperature are thermocouples and thermistors. Moisture levels are measured by either gypsum blocks or Time Domain Reflectometry (TDR's).

Denver Airport uses thermistors to measure hourly temperature profiles in the concrete slabs. In Ohio SPS sections, thermistors are also used to monitor the temperature profiles in the HMA, base course, and subgrade. WesTrack uses thermocouples because of their excellent performance history and relatively low cost.

Moisture measurements were taken in the past using gypsum blocks that provided a qualitative measurement. However, Time Domain Reflectometry (TDR) is a highly efficient technique and performs well under adverse conditions. The precision of the measurements performed by TDR is very close to actual moisture levels inside a pavement section, if accurate dielectric properties of the soil can be determined. Projects like MnRoad and Ohio SPS use TDR. LTPP also recommends TDR as a standard moisture measurement device.

CRREL Resistivity Probe can provide information regarding the depth of frost penetration. This probe is an important part of the MnRoad and Ohio SPS and also complements resistivity probes with isolated piezoelectric water wells.

# 3. SITE CHARACTERIZATION AND PAVEMENT CONSTRUCTION

Nine heavily instrumented flexible pavement sections were constructed in Bedford County, Virginia. This chapter presents the site characterization, the construction process, and the material properties.

## 3.1 Site Characterization

The site chosen for construction of the full-scale field test sections was selected through a cooperative effort between Virginia Tech personnel and representatives of the Virginia Department of Transportation (VDOT). Selection of the research site was based on the following factors:

- A secondary road section over 150 m in length, because this length would allow each of the nine individual test sections to be at least 15 m long.
- Low volume traffic with an annual average daily traffic (AADT) of less than 800 vehicles per day.
- Proximity to the Virginia Tech campus to facilitate active monitoring.
- A low subgrade California Bearing Ratio (CBR) value.
- Subgrade consisting of natural soils, as opposed to compacted fills.
- Cooperation from the contractor to allow for down-time to install the instrumentation.
- Ability to redirect traffic during instrument installation

Representatives from the VDOT reviewed preliminary road construction plans within the region and eventually identified a road planned for construction that met the above criteria and was acceptable to the Virginia Tech personnel. The site is located approximately 100 km from the Virginia Tech campus at the intersection of Routes 757 and 616 in Bedford County, Virginia. Records showed that the road has an estimated AADT of approximately 550 vehicles per day (1988) with 5% trucks. The alignment had a constant 4% grade and a constant radius of curvature. The loading conditions along this roadway are nearly identical between test sections, with the exception of the area located at the intersection of routes 757 and 616 (section 5).

The road was constructed on approximately 3 m of cut in the middle and on the existing subgrade at the end of the testing sections. The subgrade consisted of a virgin residual soil. The pre-construction average CBR (soaked) of the subgrade soil was measured to be about 2-3%, while CBR values after construction were measured up to 8%. Site investigation and a limited preliminary laboratory-testing program were completed before construction of the new road began. Figure 3.1 shows the original road, the new alignment, and the full width of the sections instrumented. The new alignment required approximately 3 to 4.6 m of cut at the cross section to obtain the correct subgrade elevation.

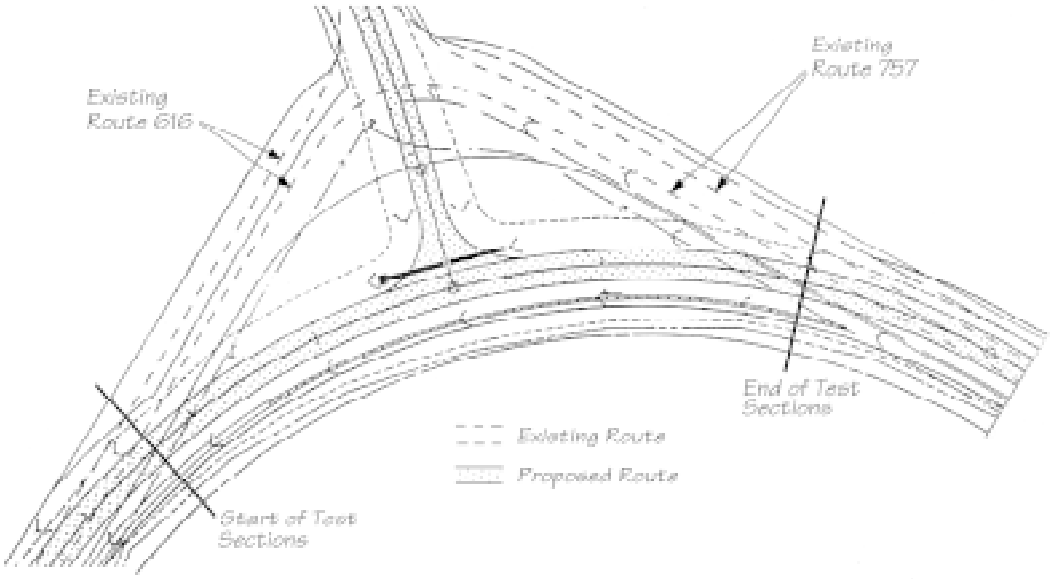


**Figure 3.1 Original road alignment and new alignment.**

Figure 3.2 gives a detailed view of the test sections and the support structures. This figure shows a plan view of the individual test sections, and the instrument cable routing path for each section. At the midpoint of each section, wires from the instruments were run through flexible PVC pipes up the hillside into plastic junction boxes. All junction boxes were interconnected with PVC pipe to the middle of section 5. At the middle of section 5, a large reinforced concrete “bunker” was installed to house the data acquisition system and other ancillary equipment.

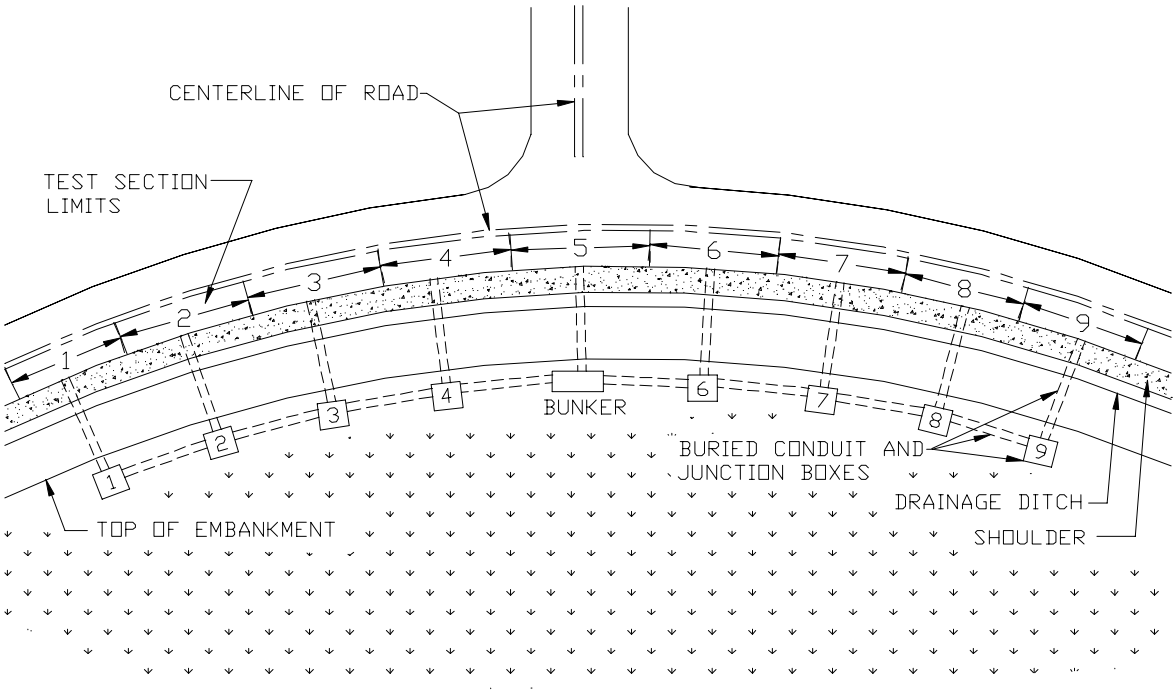


**Figure 3.2 Layout of the test sections and support structures.**

The nine test sections differed in the type of geosynthetic stabilization used and thickness of the base course layers. Table 3.1 presents the initial design of each of the instrumented test sections. The design thickness of the HMA wearing surface was 70 mm. However, during construction, the thickness of the HMA wearing surface was increased to an average of 89 mm (including a chip seal layer).

**Table 3.1 Initial design of instrumented sections.**

| Section No. | Stabilization | Base Course Thickness (mm) |
|---|---|---|
| 1 | Control | 100 |
| 2 | Geotextile | 100 |
| 3 | Geogrid | 100 |
| 4 | Control | 150 |
| 5 | Geotextile | 150 |
| 6 | Geogrid | 150 |
| 7 | Control | 200 |
| 8 | Geotextile | 200 |
| 9 | Geogrid | 200 |

## 3.2 Construction Materials

This section details the materials used in the construction of the instrumented test sections. It also includes properties of the subgrade, base course, geosynthetic stabilization, and hot-mix asphalt (HMA) layers, as well as index testing results on the materials. These results have been compiled from laboratory and field tests performed by the Virginia Tech research team.

### *3.2.1. Subgrade Soil*

Samples of the residual subgrade soil were taken at several locations along the proposed road before test section construction. Auger samples were taken at 45 m intervals, at depths of 1, 2, and 3 m at each sampling location. The auger samples were taken in accordance with test method ASTM D 1452-80, and were used for subgrade soil classification purposes and for performing the initial soaked CBR tests on reconstituted specimens. The locations of the auger samples taken are shown in Appendix A, Figure A 1.

Further subgrade soil samples were taken in accordance with test method ASTM D 1587-94 for use in index testing and resilient modulus testing. Thin-walled sampling tubes with 76 mm outside diameter were used to obtain the soil samples. Three tube samples were taken from each boring location. Sampling was performed at depths of 0.15 to 0.76 m, 0.8 to 1.4 m, and 1.4 to 2.0 m from the existing ground surface. A schematic of the boring locations relative to the test sections is shown in Appendix A, Figure A 1.

Additional soil samples, taken from the shoulders of the test sections after construction, were used for index testing, soaked CBR testing, and verification of the results obtained from the preliminary site investigation. The locations of the samples taken are shown in Appendix A, Figure A 1.

Index and physical property tests performed on the subgrade soil to determine its material properties include:

- Standard test method for classification of soils for engineering purposes (ASTM D 2487-93).
- Standard test method for particle-size analysis of soils (ASTM D 422-63).

- Standard test method for liquid limit, plastic limit, and plasticity index of soils (ASTM D 4318-95a).
- Standard test method for specific gravity of soils (ASTM D 854-92e1).
- Standard test method for moisture-density relations of soils and soil aggregate mixtures using 2.49 kg rammer and 305 mm drop (ASTM D 69-96).
- Standard test method for moisture-density relations of soils and soil-aggregate mixtures using 4.54 kg rammer and 457 mm drop (ASTM D 1557-91).
- Standard test method for water content of soil and rock in place by nuclear methods (shallow depths) (ASTM D 3017-96e1).

Soil Classification: The subgrade is primarily composed of two different residual soil types across the length of the road test sections, as reported by Brandon *et al.* (1996). They are a reddish-brown material found throughout the majority of the test sections, and a yellowish-brown material found mostly in test sections 4 and 5. The reddish-brown material that classified as a CH using ASTM D 2487-93, and predominantly as an A-7-6 by AASHTO classification methods. The subgrade in test sections 4 and 5 is a yellowish-brown silt and classifies as an ML using ASTM D 2487-93, and predominantly as an A-5 by AASHTO classification methods.

Soil Gradation: The results of the gradation analyses on the subgrade soil types as well as those for the base course are shown in Appendix A, Figure A 2. The CH subgrade material in the majority of the test sections has approximately 76% of its soil particles finer (by weight) than the 75µm (number 200) sieve. The ML material found predominantly in sections 4 and 5 has approximately 73% of its soil particles finer (by weight) than the 75µm (number 200) sieve.

Atterberg Limits: The results of the Atterberg Limits tests performed on samples of the CH subgrade material indicated liquid limits (LL) of 56% to 68%, and plasticity indices (PI) of 28% to 37%. The ML subgrade material in sections 4 and 5 was found to have an LL of approximately 41%, and a PI in the range of 4% to 6%. The results of the Atterberg Limits tests are given in Appendix A, Table A 1.

Specific Gravity: The CH material has a specific gravity of 2.77, and the ML material has a specific gravity of approximately 2.74. The results of the specific gravity test are given in Appendix A, Table A 2.

Laboratory Compaction Characteristics: ASTM D 3017-88 with a compaction effort of 2700 kN-m/m$^3$ was applied to laboratory specimens to determine the characteristics of the subgrade soil. A maximum dry density of 17.1 kN/m$^3$ at an optimum water content of 17% was obtained for the ML soil, and 15.8 kN/m$^3$ maximum dry density at 24.4% optimum moisture content was obtained for the CH soil. The results of the compaction tests are shown in Appendix A, Figure A 3. In the field, a nuclear gauge was used to determine the dry densities and the moisture contents of the subgrade soil before placement of the base course layer. The results are shown in Appendix A, Table A 3.

Resilient Modulus: The resilient modulus of the subgrade soil along the test section was determined in the lab using an MTS machine and in the field using a Falling Weight Deflectometer (FWD). The laboratory resilient modulus tests were performed on undisturbed field samples taken in accordance with ASTM D 1587-92e1. The samples were tested at confining stresses of 21 and 41 kPa.

The deviator stresses used in determining the resilient moduli were based on the responses of the pressure cells within the subgrade of the test sections. These responses were recorded during instrument calibrations performed at the project site. The resilient moduli obtained from the laboratory tests are shown in Appendix A, Tables A 4 and A 5. The measured vertical stress ($\sigma_V$) was multiplied by the at-rest state coefficient of earth pressure ($K_o$ = 0.36) to obtain the horizontal stresses $\sigma_H$. The confining pressures of 21 and 41 kPa were selected because the calculated horizontal stress ($\sigma_H$) is around that range. Equations for the resilient modulus as a function of deviator stress were developed and used to determine the resilient modulus for the three different base course thicknesses. Appendix A, Figures A 4 through A 13 show laboratory results for the resilient modulus as a function of deviator stress ($\sigma_d$). Field instrument response for the calibration run of 80 kN axle load, 560 kPa tire pressure and 56 km/hr speed were used for calculation of resilient modulus. The 560 kPa tire pressure was selected because it represents the largest portion of truck traffic on secondary roads. Figure A 14 (Appendix A) shows a test ready sample in the MTS machine.

Soaked CBR: California Bearing Ratio (CBR) tests were performed on soaked subgrade soil samples. The tests were performed in accordance with ASTM D 1883-94. The objective of the testing was to determine the soaked subgrade CBR values expected in the constructed field test sections. Different compaction efforts were used on samples

compacted at the same moisture content. A plot of soaked CBR as a function of molded dry density for the subgrade material is shown in Appendix A, Figure A 15. The relationship to estimate the resilient modulus of the subgrade from the CBR value is given by (Huang, 1993).

$$M_r = 1500 \times CBR \quad (3.1)$$

Where, $M_r$ = Resilient modulus of the subgrade in psi.

### *3.2.2 Base Course Material*

Samples of the base course material were taken at 30 m intervals during placement of the material and tested to find their properties. The base course material used in construction of the test sections is type 21-B in accordance with Virginia Department of Transportation specifications.

Index and physical property tests were performed on the base course aggregate to determine its material properties. These tests include:

- Standard test method for classification of soils for engineering purposes (ASTM D 2487-93).
- Standard test method for sieve analysis of fine and coarse aggregate (ASTM C136-96a)
- Standard test method for moisture-density relations of soils and soil-aggregate mixtures using 4.54 kg rammer and 457 mm drop. (ASTM D 1557-91).
- Standard test method for water content of soil and rock in place by nuclear methods (shallow depths) (ASTM D 3017-96e1).

Base Course Classification: The base course material is composed of limestone aggregate quarried by W. W. Boxley in Roanoke, Virginia. It was found to be a GW by the USCS, and is classified as 21-B by VDOT.

Base Course Gradation: The base course aggregate was found to have approximately 50% by weight of its coarse fraction retained on the 4.75 mm (No. 4) sieve, with a coefficient of uniformity (Cu) of 16, and a coefficient of curvature (Cz or Cc) of 1.5. The results of the gradation analysis on the base course material is shown in Appendix A, Figure A 16.

Specific Gravity: The base course samples taken from the project site were combined in the laboratory for specific gravity testing. The specific gravity of the base course aggregate was found to be 2.78. The results of the specific gravity tests on the base course material are given in Appendix A, Table A 2.

Compaction Characteristics: ASTM D 2922-96e1 were performed on the base coarse aggregate specimens to determine the compaction characteristics of the base course. The optimum moisture content of 6.1% corresponds to a maximum dry density of 22.4 $kN/m^3$. Figure A 17 (Appendix A) shows these results along with values obtained from nuclear gauge measurements made in the field. A nuclear gauge was used to determine the dry densities and the moisture contents of the base course before placement of the HMA layers.

Resilient Modulus Tests: The resilient modulus of the base course aggregate sampled from the test sections was determined in the laboratory for remolded specimens. Specimens were tested in accordance with interim test method AASHTO T 294-92-I. The samples were tested at confining stresses of 21, 35, 69, 103, and 138 kPa.

The vertical stresses used in determining the resilient moduli were the responses of pressure cells within the base course of the test sections (same procedure as detailed earlier for subgrade resilient modulus). These responses were recorded during instrument calibrations performed at the project site. The base resilient modulus was determined using the appropriate laboratory-developed relationship for the wet condition. Representative graphs for wet- and dry-condition resilient modulus as a function of bulk stress are shown in Appendix A, Figures A 18 and A 19. A field moisture content of 5.5% (wet condition, Appendix A, Figure A 18) was used for calculation of base course resilient modulus. Table A 6 (Appendix A) shows the final resilient modulus value as determined based on field instrumentation response. Field instrument response for the calibration run of 80 kN axle load, 560 kPa tire pressure, and 56 km/hr speed was used for calculation of resilient modulus.

### *3.2.3. Geosynthetic Layer*

The geosynthetic stabilization layers of polypropylene-based polymer materials used in construction of the test sections are the same types used in the construction and testing of previous laboratory test sections at Virginia Tech. A woven geotextile was used in test sections 2, 5, and 8 and a geogrid was used in test sections 3, 6, and 9.

The material properties for the geosynthetics are shown in Appendix A, Tables A 7 and A 8.

### *3.2.4. Hot-Mix Asphalt Layer*

The properties of the hot-mix asphalt (HMA) layer were determined from samples taken at approximately 30-m intervals during construction of the field test sections. Specimens were also taken by core sampling of the HMA along the length of the test section by VDOT personnel after construction. The index and physical property tests performed on the HMA layer are as follows:

- Bulk specific gravity test, paraffin film method (ASTM D 1188-96).
- Bulk specific gravity test, saturated surface dry method and height measurement method (ASTM D 2726-96ae1).
- Theoretical maximum specific gravity of the laboratory specimens (ASTM D 70-82).
- Average HMA content, ashing method (ASTM D 2172-95).
- Volumetric properties of the HMA.
- Bulk specific gravity of the core specimens (ASTM D 2726-96ae1).
- Creep compliance for the laboratory and field specimens.
- Resilient modulus of field specimens (ASTM D 4123-82)

HMA Gradation: HMA gradation was performed on the samples collected form the test section. The samples were taken from the wheel path, and the middle of the lane. Two samples were taken from section one through three. Figures A 20 through A 22 (Appendix A) show the HMA gradation curves.

Laboratory Test Specimens: Thirty-six Marshall specimens were compacted from the HMA samples taken during placement of the HMA layer in the field. These specimens were used to define the various properties of the HMA described in this section. A total of ten core specimens were taken from the inside wheel path along the road test section by VDOT personnel six months after the construction of the road. These samples were used to determine material properties of the HMA properties such as bulk specific gravity, resilient modulus, and creep compliance.

Ten core specimens were taken from the approximate vicinity of the previous field samples in November 1996. Also, Eighteen specimens were taken from the first three sections (six samples per section) as recently as October 1997. These samples were used to determine the effect of mechanical and thermal loading on the HMA properties (i.e. air voids, creep compliance, and resilient modulus) after being in service.

Bulk and Theoretical Maximum Specific Gravity: For the specimens collected during construction, the bulk specific gravity of the HMA specimens prepared in the laboratory was determined using three methods: paraffin film method (D 1188-89), saturated surface method (D 2726-90), and height measurement method. The results from these methods are given in Appendix A, Tables A 9 through A 11. The theoretical maximum specific gravity was determined in accordance with standard test method ASTM D 70-82. The results are shown in Appendix A, Table A 12.

For the specimens collected in November 1996, the bulk specific gravity (ASTM D 2726-90) and maximum theoretical specific gravity (ASTM D 70-82) are shown in Appendix A, Table A 13 and A 14, respectively.

Asphalt Content: Asphalt content was determined using the ashing method (ASTM D 2172-92). The results of the tests are shown in Appendix A, Tables A 15 through A 17.

Bulk Specific Gravity of the Core Specimens: The bulk specific gravity of the core specimens was determined in accordance with ASTM D 2726-90. The average value of bulk specific gravity for the asphalt was determined to be 2.25 in October 1994, and 2.33 in November 1996. The test results are shown in Appendix A, Tables A 10 and A 13, respectively.

VMA, VFA, VTM, Stability and Flow: Voids in the total mix (VTM), voids in the mineral aggregate (VMA), and voids filled with asphalt (VFA), as well as the HMA density, were determined (Appendix A, Table A 18) for October, 1994 and November, 1996. The stability and flow of six Marshall specimens were also determined and the results for October 1994 are shown in Appendix A, Table A 19.

Creep Compliance: As explained earlier, three sets of specimens were collected from the Bedford project between 1993 and 1997. The first set consisted of nine specimens cored in October, 1994 the second of 10 specimens cored in November, 1996 and the third of 18 specimens cored in October, 1997. The October 1994 specimens were tested using an MTS machine under a creep load of 365 kN for 100 sec, with an

immediate relaxation of 100 sec. The tests were performed at a temperature of 25 °C for the October 1994 specimens. The creep compliance obtained from these tests for the aforementioned specimens are shown in Appendix A, Figures A 23 through A 31. The extreme closeness of various creep results allow for the average creep curve to be used for the entire section. Figure A 32 (Appendix A) shows the average of all the tests (Appendix A, Figures A 23 through A 31).

Appendix A, Figures A 33 through A 41 show the creep compliance for specimens collected in November, 1996. The test procedure for November, 1996 specimens differed from the October, 1994 specimens in two ways:

- A creep load of 365 kN was applied to the specimens for 1000 sec rather than 100 seconds, with a corresponding relaxation of 300 sec, as compared to 100 seconds
- The tests were performed at reference temperatures of 40, 25, and 5 ºC.

The sequence of temperature variation adopted during testing was 40, 25, and 5 ºC. This change of temperature from high to low may excessively damage the specimen at high temperature (40 ºC) ranges, causing false creep behavior due to internal damage at lower temperature ranges (25 ºC and 5 ºC). To check the temperature effect on the results, a new specimen was tested using the 5, 25, and 40 ºC temperature variation. The existence of a small difference in both the creep behaviors was observed (see Appendix A, Figure A 42).

Because the creep curves for November, 1996 showed minimum variation between sections, an averaged creep curve for the whole test section was drawn. Appendix A, Figure A 43 shows one creep curve for the entire test section at the three reference temperatures for November, 1996.

Creep compliance was also determined for the specimens collected from the site in October, 1997. The test procedure was the same as that performed on the November 1996 specimens. Results are presented in Appendix A, Figures A 44 through A 61.

Resilient Modulus of HMA Samples: Resilient modulus tests of HMA were performed in accordance with ASTM D 4123-82 on specimens fabricated in the laboratory and on core samples taken from the test sections (for October, 1994, November, 1996 and October 1997). Core specimens were trimmed to a thickness of 62.5 mm for resilient modulus testing. Thicknesses of the core specimens before trimming are presented in Appendix A, Table A 20. A cyclic dynamic load of 2 kN was applied to the specimens.

Specimens were tested at temperatures of 40 ºC, 25 ºC, and 5 ºC, using an environmental chamber in which liquid nitrogen was used to achieve the required test temperature of 5 °C. Three different sweeps of 3, 2, and 1 sec of dynamic loading (0.1 sec loading and 2.9, 1.9, and 0.9 sec relaxation, respectively) were performed on each Marshall specimen. Each loading and unloading sweep consists of 200 cycles; measurements were averaged from the last five cycles. Each individual test consisting of the three loading sweeps took 1200 sec. Specimens were conditioned for at least one hour before testing at desired temperature.

The same procedure was repeated for samples collected in November, 1996 and October 1997. Appendix A, Tables A 21 show the resilient modulus calculated from the various specimens in October 1994, November 1996, and October, 1997. It is noted that November 1996 and October 1997 resilient modulus is higher than the October 1994 values, showing the effect of mechanical loading and aging, which causes the stiffness of the material to increase. It is also noted that at 5 ºC there exists a smaller increase in resilient modulus during the span of three years as compared to 40 ºC. This can be explained by a much stiffer behavior of HMA at lower temperature, as compared to the higher ranges. During laboratory testing, it was observed that the MTS machine performs poorly when determining the Poisson's ratio. ASTM D 4123-82 suggests reference values of Poisson's ratio when such a situation arises. The values of Poisson's ratio and resilient moduli at reference temperatures are shown in Appendix A, Table A 21. Appendix A, Figures A 62 and A 63 show the Poisson's ratio, and the resilient modulus for October 1994, November 1996, and October 1997 as determined from laboratory tests.

## 3.3 Construction Procedure

The Coffee Construction Company of Bedford, Virginia was the primary contractor for the construction of Route 757. Construction activities at the site started in early June, 1994 and ended in mid-August, 1994.

Initial excavation of the site took place from early June to early July, 1994. During this construction phase, much of the infrastructure of the project was installed. This included installing a pole for the phone and electric power, burying the PVC conduit for channeling of the instrumentation wire, and installing the data acquisition bunker.

### *3.3.1 Service Pole*

The service pole was the first item to be installed at the site. It houses the phone and electric services and is located near the bunker. The plans for the service pole, shown in Figure 3.3, were based on specifications supplied by Southside Electric Cooperative (SEC), the local electric company. Prior to bunker installation, the service pole was equipped with a circuit breaker panel and outdoor outlets (not shown) to provide power, thus eliminating the need for generators. The panel and outlets were later incorporated into the data acquisition housing system.

The 16 mm eyelet at the top of the pole provides an anchor point for the power lines brought in by SEC. All wire on the pole above ground is enclosed in metal conduit or in locked service boxes to deter vandalism. Below the ground surface, wires run through Schedule 40 PVC conduit directly to the bunker.

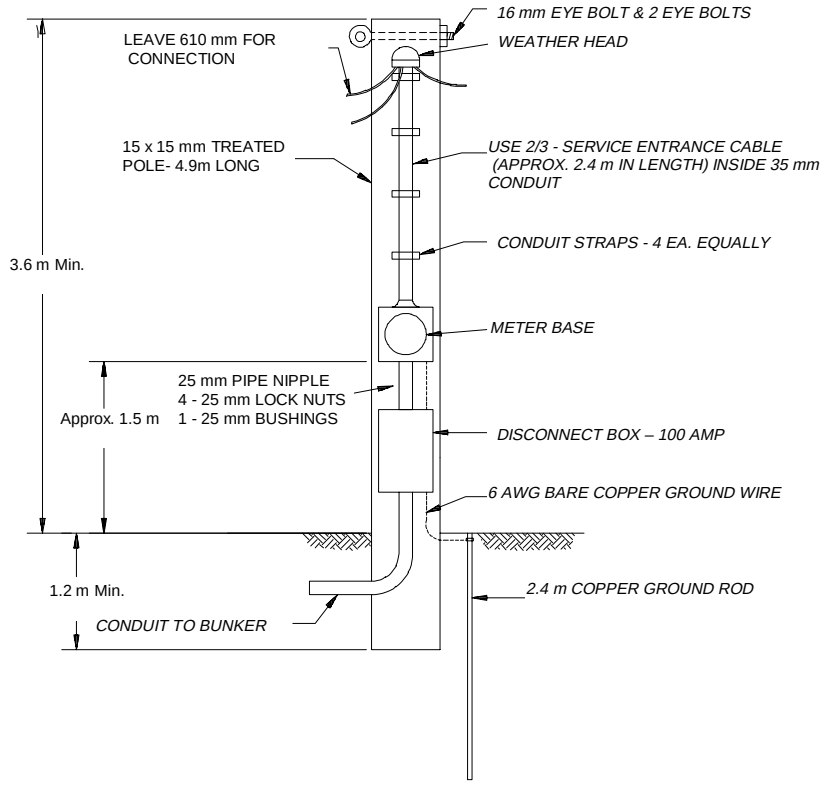


**Figure 3.3 Plans for service pole.**

### *3.3.2 Data Acquisition Bunker, Design and Installation*

Since the project is located in Bedford County, a rural part of Virginia and approximately 100 km from Virginia Tech, there was concern about theft and vandalism of project property. Since the instruments and conduits were all buried and all connections were either buried or locked in junction boxes, the only item left to be protected was the data acquisition system. A reinforced concrete bunker was designed to conceal and protect the data acquisition equipment from theft, vandalism, and adverse weather conditions. The two types of bunker designs considered were pre-cast concrete box and cinder block on concrete slab. The pre-cast concrete box was chosen because of its overall strength with respect to lateral earth pressures, its ability to resist moisture penetration, and its adaptability over cinder blocks with respect to the forming of inlets for the conduit.

The bunker is a modified 3.8 $m^3$ concrete septic tank consisting of two identically shaped halves reinforced with 6.4 mm rebar. It has a wall thickness of 64 mm and a ceiling and floor thickness of 89 mm. The circular inlets in the bunker were created by casting.

PVC coupling joints were cemented directly into the structure to insure a snug fit between the bunker and the conduit. The circular inlets on the top of the bunker, as shown in Figure 3.4, are the locations of the ventilation fans, and the large square inlet is the entrance to the bunker. The left, front, and right views show the circular inlets for the instrumentation wire conduits. Sections 1-4 enter on the left, section 5 on the front, and sections 6-9 on the right. Power and phone lines enter through the back wall. In the bottom half, a drain was cast into the front left corner (not shown) in case seepage into the bunker occurred.

Ventilation fans were adapted to modified pieces of 102 mm PVC conduit and later cemented inside the bunker to the ventilation inlets. Screens secured to the exhaust hoods prevent insects from entering the bunker. Wooden 51 mm x 102 mm studs were bolted to the bunker walls and ceiling to provide a means for attaching lights, outlets, the circuit breaker panel, and the section control board used for wiring.

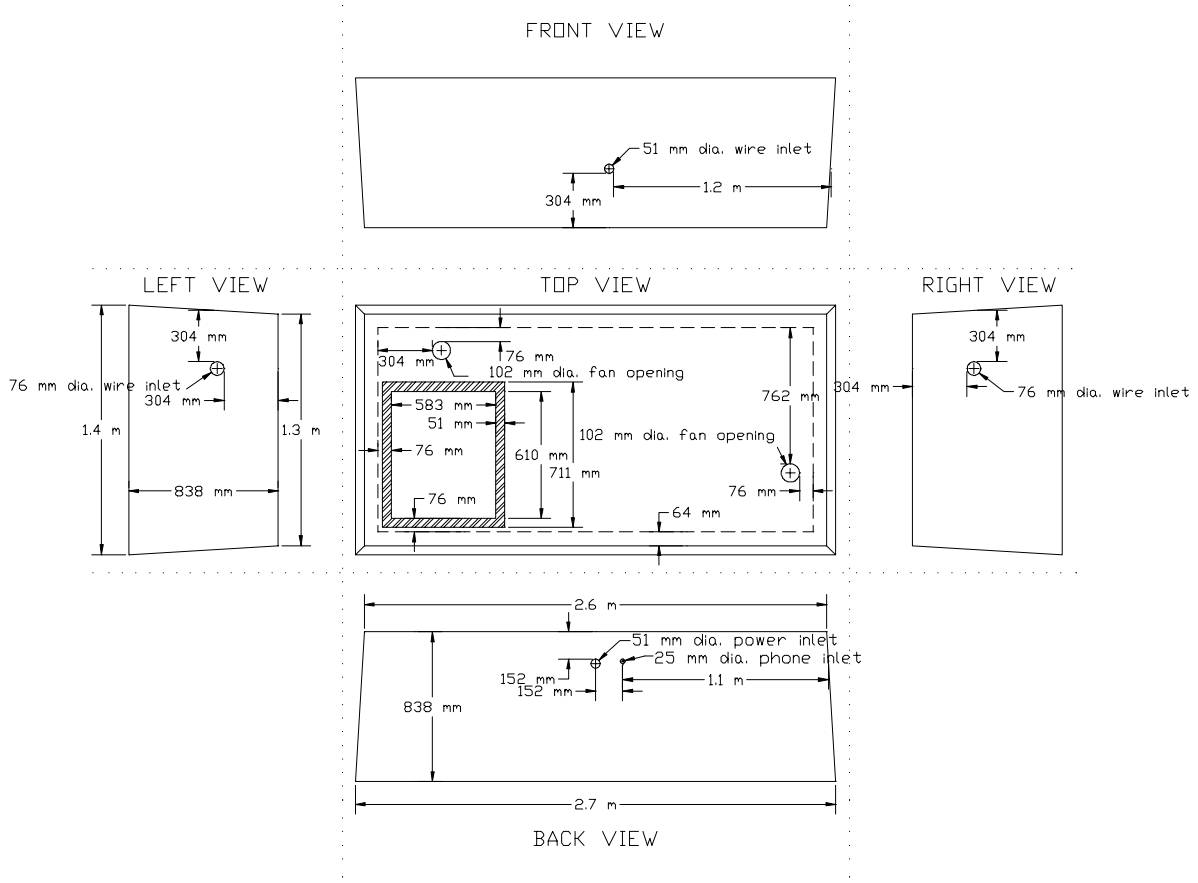


**Figure 3.4 Plans for top half of bunker - exploded view.**

Using a Bob Cat model 643 with a model 907 backhoe attachment, a 3.7 x 2.1 x 2.1 m-deep pit was excavated to bury the bunker on the top of the slope above section 5, as shown in Figure 3.5. A hand augured drainage line installed from the corner of the pit emerges 0.6 m above the roadway drainage ditch. The drainage line prevents build-up of water around the bunker.

After the pit was lined with filter fabric, it was backfilled with 0.6 m of #57 (in accordance with AASHTO) crushed stone. The lower half of the bunker was tarred on the bottom and lowered into place. To create a watertight seal between the halves, a tar-putty gasket was applied to the seam before lowering the top half of the bunker. After connection of the instrumentation wire conduit, tarring was completed on the top portion of the bunker that was below the ground surface, and Thompsons' Water Seal was applied to the portion above. The remaining portion of the pit was backfilled with

the crushed stone and the filter fabric was wrapped back towards the bunker to prevent migration of fines into the drainage area around the bunker (Figure 3.5).

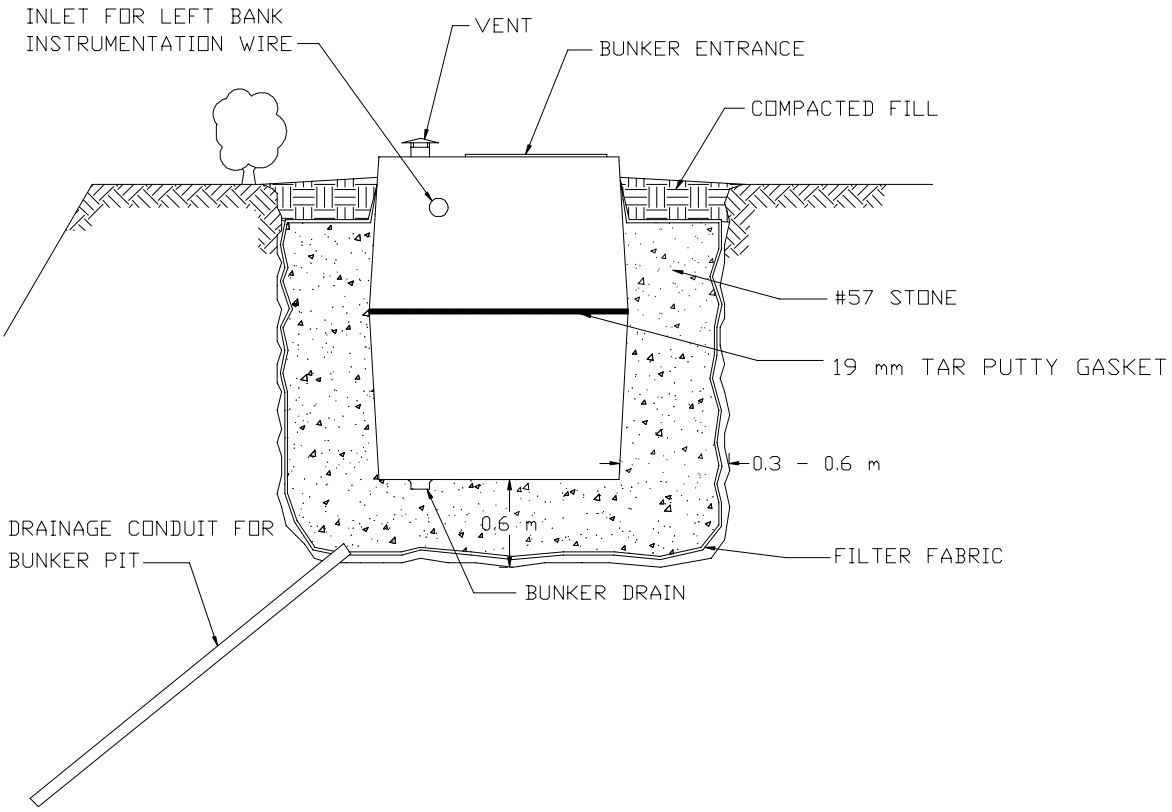


**Figure 3.5 Cross-section of bunker placement.**

Using some of the excavated material from the pit, the perimeter of the bunker was filled in and compacted. A metal frame was bolted to the bunker entrance to provide a means of securing the 6.4 mm-thick metal plate cover. Tar-putty was placed between the frame and the bunker, and a rubber gasket was fitted to the top of the frame to prevent rainwater from entering the bunker. To conceal the 300 mm of bunker exposed above the ground from passersby, several small bushes were planted along the front face.

### *3.3.3 Instrumentation of Subgrade*

After the native soil was excavated to the proper elevation, the subgrade instrumentation (details on instrumentation may be found in Chapter 4) was installed. All

instruments were placed in the inner lane, with most under the outside wheel path. On July 19, 1994, the Virginia Tech crew began installing the subgrade instrumentation for sections 1 through 9, starting at section 9. Instruments in sections 5-9 were installed on July 19, and sections 2-4 were installed on July 20. Section 1 was not completed until July 21 because of continuing construction on section 1 by the contractor. Instruments located in the subgrade were Kulite earth pressure cells, Carlson earth pressure cells, soil strain gages, thermocouples, and gypsum blocks.

The subgrade was excavated using small garden shovels and spoons to place the pressure cells. The pressure cells were installed with their top surface lying about 25 mm below the subgrade surface. A small trench was also excavated to accommodate the wires from the pressure cells to the conduit pipes. The pressure cells and the wires were then covered with a layer of fine sand to protect them from damage.

Thermocouples were installed in the pavement subgrade layer at a depth of 152 mm below the layer surface. Excavation of the subgrade material was accomplished using a 89 mm outside diameter hand auger with a depth marking on the tool shaft. The thermocouple was placed in the hole, and subgrade material was backfilled and compacted over it using the handle of a shovel. A trench for the exposed wire length was excavated using hand tools, and the cable was covered using compacted subgrade material.

The gypsum blocks were installed in a similar manner as the thermocouples. The gypsum blocks were installed in the subgrade layer at depths of 0.15 m and 0.6 m below the ground surface. The subgrade soil was excavated with a hand auger to the desired depth of installation. The gypsum blocks were placed in the hole, and subgrade material was gently recompacted in the hole using the handle of a shovel.

The soil strain gages were installed with their upper surface lying 51 mm below the surface of the control sections' subgrade. The cables from the strain gages were placed and covered with a thin layer of sand backfill to protect them from damage. The instrument and cable were then covered with the compacted native soil and evened to the existing subgrade surface using a flat-bladed shovel.

Concurrent with the installation of the instrumentation, nuclear density tests were conducted on the subgrade soil. Two density tests for each section were performed on the subgrade by the Virginia Tech crew using a Troxler nuclear density gauge Model No.

3440. One test used the backscatter procedure (no penetration) and the other used direct transmission, with the source located 152 mm below the ground surface. Results of these tests are shown in Table 3.2. Moisture contents using backscatter ranged from 29%-36%, with an average moisture content of 32%. Moisture contents measured using direct transmission were lower than the backscatter values. They ranged from 24%-31%, with an average of 28%. Dry densities measured using the backscatter procedure ranged from 11.24-13.9 kN/m$^3$, while dry densities using direct transmission ranged from 13.4-14.4 kN/m$^3$. Their average dry densities were 12.3 and 14.0 kN/m$^3$, respectively.

**Table 3.2 Results of nuclear density tests on subgrade.**

| Section | Backscatter | | Direct Transmission (150 mm) | |
|---|---|---|---|---|
| | Moisture (%) | Dry Density (kN/m$^3$) | Moisture (%) | Dry Density (kN/m$^3$) |
| 1 | 31.6 | 12.6 | 28.6 | 14.1 |
| 2 | 31.6 | 13.5 | 30.2 | 13.8 |
| 3 | 33.0 | 11.7 | 24.0 | 14.4 |
| 4 | 30.7 | 12.6 | 28.3 | 13.4 |
| 5 | 29.4 | 12.7 | 23.8 | 13.9 |
| 6 | 30.5 | 11.2 | 26.3 | 14.1 |
| 7 | 35.6 | 11.4 | 29.8 | 14.3 |
| 8 | 29.6 | 13.9 | 28.9 | 14.6 |
| 9 | 36.2 | 11.4 | 31.1 | 13.5 |

### *3.3.4 Installation of Geosynthetics*

After the subgrade instrumentation was installed, the subgrade surface was rolled smooth and swept clean of debris prior to the installation of the geogrid and geotextile on July 24 and 25, 1994. The geosynthetics had been cut to the proper size and instrumented at Virginia Tech prior to being transported to the site. The strain gages were attached as described in Chapter 4 of this report and were adequately protected during transportation. Sections 1, 4, and 7 were control sections with no geosynthetics. Geotextile was placed on sections 2, 5, and 8. Sections 3, 6, and 9 were stabilized with the geogrid. The strain gages on the bottom of the geotextile and geogrid were protected from heavy equipment by constructing a pad beneath each strain gage. The pad was constructed by digging a hole in the subgrade 13 mm deep and approximately

twice the size of the gage and then filling it with sand. The pad was used to reduce the risk of damage to the gages by angular aggregate that may exist in the subgrade.

### *3.3.5 Placement of the Base Course Layer*

In July, 1994 the contractor put down the base course layer of VDOT class 21-B aggregate. The aggregate was first end-dumped on the side of the test section that did not have any instrumentation, the aggregate was then carefully bladed to the other lane with a motor-grader to avoid damage to the instruments. Each layer was compacted with a vibratory roller. A 100 mm layer of compacted aggregate was placed over sections 1-3; 150 mm and 200 mm of compacted aggregate were placed over sections 4-6 and sections 7-9, respectively. The site had to be re-rolled on August 2 due to damage from heavy rain. Density tests were performed on the base course on August 4 and 6. Table 3.3 shows the results of the nuclear density tests on the base course. Moisture contents ranged from 2.0%-3.2%, with an average moisture content of 2.6%. The average dry density of the base course layer was 22.4 kN/m$^3$.

**Table 3.3 Results of nuclear density tests on base course.**

| Section | Backscatter | |
|---|---|---|
| | Moisture (%) | Dry Density (kN/m$^3$) |
| 1 | 3.11 | 23.4 |
| 2 | 3.17 | 23.3 |
| 3 | 2.49 | 23.3 |
| 4 | 1.99 | 23.7 |
| 5 | 2.07 | 24.1 |
| 6 | 2.33 | 20.7 |
| 7 | 2.42 | 21.2 |
| 8 | 2.38 | 21.1 |
| 9 | 3.18 | 21.2 |

### *3.3.6 Instrumentation of the Base Course Layer*

The base course layer was instrumented in the same manner as the subgrade. Pressure cells, gypsum blocks, and thermocouples were installed below the compacted surface of the base course. After the instrument locations were marked using surveying instruments, the base course was excavated using garden shovels and hand tools to

accommodate the instruments and wiring. The thermocouples used for the base course and HMA layers were installed at the same time. The thermocouples and gypsum block locations for the base course were excavated to approximately mid-depth of the layer for each section, while the pressure cells were installed at 25 mm from the base course surface. The thermocouples were installed in the same manner as the subgrade layer with the exception that poorly-graded sand and fine aggregate were used to surround and backfill each thermocouple to avoid instrument damage from large angular aggregate. The cable trenches to the shoulder were constructed in the same manner. The base course was then re-rolled by the contractor to ensure surface uniformity. The locations of the instruments were surveyed.

### *3.3.7 Construction and Instrumentation of HMA Wearing Surface*

Prior to the HMA layer construction, the HMA layer thermocouples were installed and exposed 25 mm above the surface of the base course. AC-30-based emulsion (CRS-2) mixed with a poorly-graded sand at a ratio of approximately 1 to 1 was used to coat the exposed thermocouple length prior to placement of the chip seal and HMA wearing surface. The HMA strain gages were also placed prior to the chip seal and the two-38-mm class SM-2A HMA layers. The gages were coated with an emulsion mixture to protect them during paving. The HMA wearing surface was constructed on August 13, 1994. The first layer, a chip seal, was compacted with a vibratory roller. The maximum aggregate size in the chip seal was 9.5 mm. Since heavy equipment had the potential to cause severe damage to the HMA strain gages, extreme caution was taken to keep equipment from rolling directly over them. The roadway was later surveyed by the Virginia Tech crew to determine the thickness of the HMA layer and accurately define the location of the instruments. Also, tell-tale metal plates were placed underneath the base course and HMA layers to measure layer thickness nondestructively.

Four piezoelectric traffic sensors were installed in the HMA wearing surface along the length of the pavement test sections. Two sensors act as triggers for the data acquisition system, and the other two are used as weigh-in-motion sensors. The average traffic speeds and driving habits on the test pavement section determined the physical position for each of the sensors. The primary data acquisition trigger sensor, installed approximately before the instruments in test section 1, acts as a trigger for the data acquisition for all nine test sections. The first of the two weigh-in-motion sensors was installed between test sections 3 and 4. The second of the two weigh-in-motion

sensors was installed before section 7. The secondary data acquisition trigger was installed between sections 5 and 6, acts as a trigger for the data acquisition for sections 6 through 9.

Oversized channels were cut into the surface of the flexible pavement wearing surface. E Bond G-100 type, two-part epoxy was used to secure the sensors within the cut channels. The epoxy is quite durable and is approved for this type of application by many state agencies. Two layers of bituthane tape were applied to the surface of the sensors to protect them during snow removal. The first layer is a 51 mm-wide covering, the second is a 152 mm-wide covering. Both layers of tape overlay the entire length of the sensors and extend to the road shoulder.

# 4 INSTRUMENTATION AND INSTRUMENT CALIBRATION

## 4.1 Instrumentation Types

Five basic types of instruments were used in this research: earth pressure cells, strain gages, temperature sensors, soil moisture sensors, and piezoelectric polymer traffic sensors. The following sections will briefly describe the instruments and any laboratory modifications made to them.

### *4.1.1 Carlson TP-101 & Kulite Type 0234 Vertical Earth Pressure Cells*

The earth pressure cells installed in the test pavement sections included the Kulite type 0234 and Carlson type TP-101. The primary functions of these cells are to monitor the change in the stress state of the overlying layers and to measure the increase in vertical pressure due to dynamic traffic loading. The Kulite type 0234 earth pressure cells are designed to operate within a vertical pressure range of 0 to 690 kPa, and are 54-mm in diameter with a thickness of 14.3 mm. The Kulite 0234 contains a diaphragm that excites a silicon strain gage upon diaphragm deformation. A schematic of this type of pressure cell is shown in Figure 4.1. The Carlson type TP-101 earth pressure cells are also designed to operate within a vertical pressure range of 0 to 690 kPa. The TP-101's stainless steel pressure head is 114-mm in diameter and 6.4 mm thick, and is welded to a 16 mm outside diameter stainless steel tube that is attached to a silicon strain gage transducer. A schematic of a Carlson cell is shown in Figure 4.2.

Before installation, each pressure cell was checked for sensor integrity by applying a 10-volt direct current to the excitation leads of the instrument. Its zero value and load response were then recorded. These values would be used for field calibrations. Care was taken not to overload the pressure cell while checking its particular load response. Kulite type 0234 required no physical modifications before instrument installation. However, the Carlson TP-101 was modified from its as-manufactured condition to accommodate the large pressure transducer housing. Since the housing would lie too close to the surface of the installation pavement layer, the stainless steel tube was bent to accommodate the proposed installation provisions. Once the tubing was bent on all the pressure cells, new zero values and load responses were recorded for each cell.

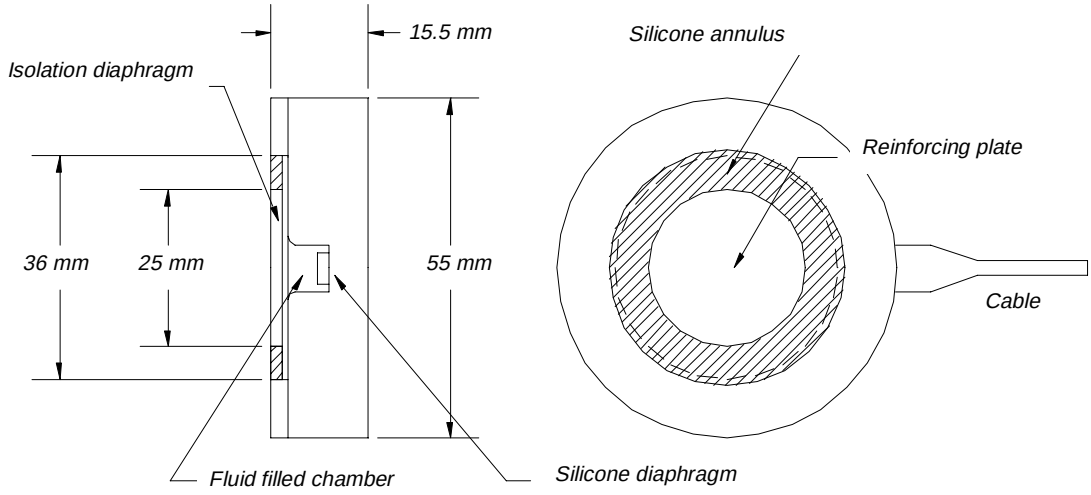


**Figure 4.1 A schematic of the Kulite type 0234 earth pressure cell.**

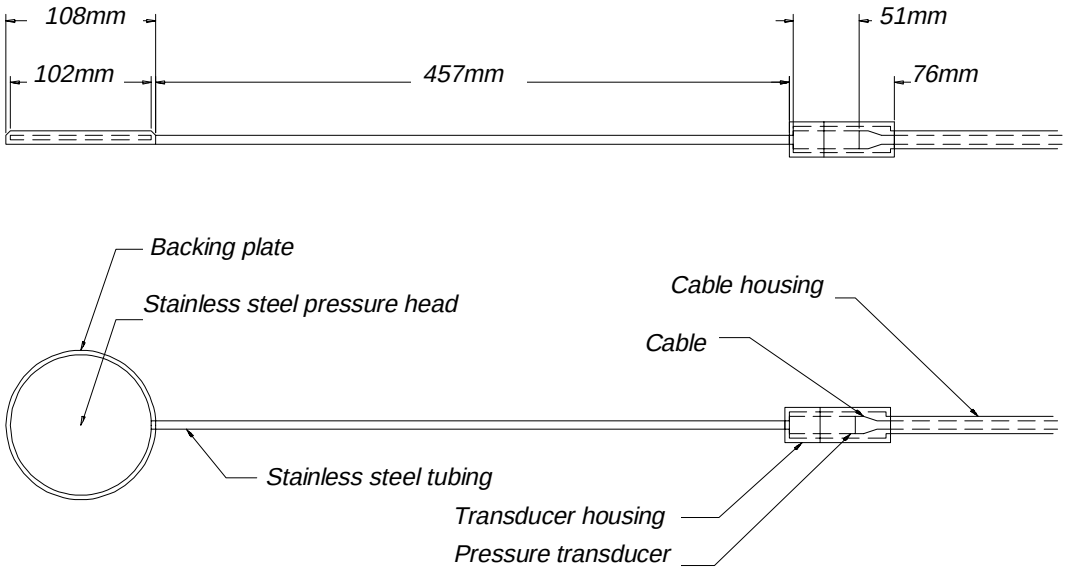


**Figure 4.2 A schematic of the Carlson type TP-101 earth pressure cell.**

Two types of 4-conductor cable were used as lead wires for the pressure cells. The first was a Belden shielded multi-conductor plenum control cable and the second a

Dearborn shielded multi-conductor plenum control cable. Both cable types were composed of 22-gauge tinned copper lead wires and polyethelene or PVC jacketing with an overall wrapped shield. The resistance of all lead wires was measured.

All wire connections were first fluxed and then soldered according to standard guidelines. The solder connections, except for the shield splices, were then individually insulated with 3M FP-type heat shrink tubing or its equivalent. The wire connections were wrapped with a rubber butyl tape to act as a moisture barrier, and the connection was covered with 3M MW-type epoxy lined heat-shrink tubing or its equivalent. The MW-type tubing extended 12.7 to 25.4 mm onto the bodies of the attached cables. The attachment was completed by wrapping the connection with two layers of 3M type 33+ electrical tape for further protection. The attached lead wire connections were then checked for circuit integrity. The new instrument zero values and load responses were recorded for each cell.

### *4.1.2 Carlson JO-1 Soil Horizontal Strain Gages*

Carlson JO-1 concrete joint meters were used to measure the strain in the top of the subgrade layer of the non-stabilized sections. The JO-1 is a displacement-type transducer, measuring the ratio of resistance between two coils of steel wire. The JO-1 was modified by the manufacturer, RST Instruments, to include 76 mm diameter end plates (increased from 38 mm) to accommodate the larger displacements that may be realized in soil.

The Carlson JO-1 gages were checked in the laboratory for instrument integrity by measuring the ratio of the resistance of the triple pairs of lead wire. The measured resistance was then checked against the supplied factory calibration sheets. The laboratory zero values were then recorded for instrument calibration in the field. No physical modifications were performed on the soil strain gages in the laboratory. The JO-1 gages were equipped with three paired wires for a total of six individual wires. A Belden 6-conductor shielded plenum control cable was used to accomplish lead wire extension. All wire connections proceeded in the same manner as that of the earth pressure cells. The soil strain gages were then checked for circuit integrity, and their resistance ratios were recorded.

### *4.1.3 T-Type Thermocouple Temperature Gages*

Temperature gage construction consisted of a twisted, welded pair of T-type thermocouple wires. T-type thermocouples are composed of a constantan and copper wire pair. After the wire pair was welded, the exposed end was surrounded by 6.4 mm inside diameter copper tubing. The tubing was then attached to the cable insulation by 3M MW-type heat-shrink tubing. This was done to insulate the tubing from the exposed wire pair and provide a reservoir for epoxy. 3M DP-270 electrical grade epoxy was used to surround the thermocouple and to serve as a barrier to environmental effects. The thermocouples were then checked for their response to temperature change. Each instrument's response in the laboratory was recorded. No lead wire splicing was performed on the thermocouples as they were manufactured to full length.

### *4.1.4 Gypsum Block Moisture Sensors*

Boyoucous gypsum blocks were used for moisture measurement in the subgrade and base course layers. The soil moisture block is equipped with two stainless steel electrodes surrounded by nylon-impregnated gypsum. As the gypsum is exposed to moisture, the resistance between the two electrodes decreases, indicating an increase in the moisture content of the soil.

The soil moisture cells were manufactured with a pair of 18-gauge lead wires, with a cable length of 1.5 m. The factory cable was cut off 38 to 51 mm from the body of the cell, and lead wires were attached. A Belden 2-conductor shielded plenum control cable was used for lead wire extension. All wire connections proceeded in the same manner as that of the earth pressure cells. The soil moisture blocks were then checked for circuit integrity, and their resistance was recorded.

### *4.1.5 Kyowa KM HMA Horizontal Strain Gages*

Kyowa KM-type embedded HMA strain gages were used to monitor the changes in strain at the bottom of the HMA wearing surface layer. Gage construction consisted of a foil-type strain gage, 102-mm in length, sandwiched between two sheets of composite fiberglass with a 3-conductor lead cable, as shown in Figure 4.3

The Kyowa strain gages were checked for sensor integrity before they were allocated for installation. A strain gage indicator was used to check the initial gage response using the supplied factory gage factors. The gage zero value and strain response were

recorded. These values would be used for laboratory calibration.

The Kyowa HMA strain gages were modified from their original condition to include aluminum end bars. The gages were fastened in an aluminum mold that centered the gage and aligned the end bars, which were fabricated from 76-mm-long aluminum bar stocks with a 10 x 10 mm cross-section. One of the end bars was also machined to allow the lead wires to extend from the new gage assembly. The end bars were fastened to the Kyowa gage using 3M DP-190 duo-pack epoxy adhesive. The DP-190 was chosen for its heat resistance and relatively short curing time.

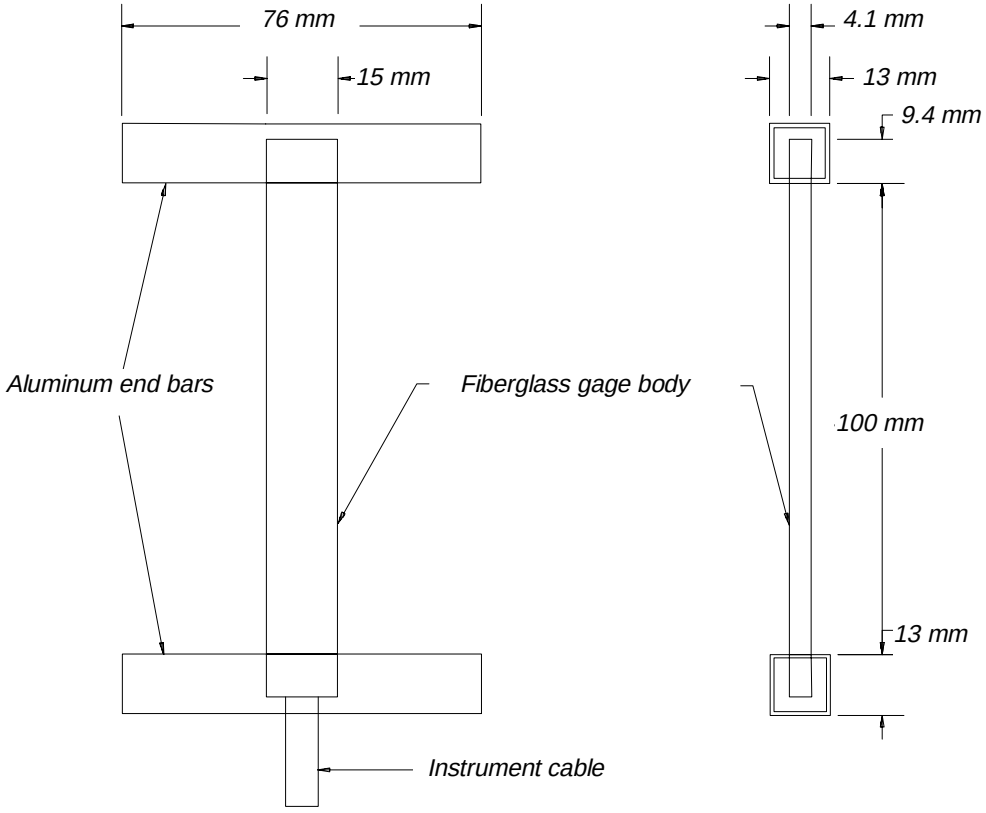


**Figure 4.3 A schematic of the Kyowa type embedded HMA strain gage.**

The final gage length was determined to be 100 mm, reduced from an initial length of 119 mm. A new gage factor was determined for the manufactured gages, based on the new gage length. The new gage factor would be used for field instrument calibration.

The Kyowa strain gages were equipped with three 22-gauge wires with a cable length of 305 mm. The factory cable was cut off 38 to 51 mm from the body of the new gage construction and lead wires were attached. A Belden 3-conductor shielded plenum control cable was used for lead wire extension. All wire connections were done in the same manner as that of the earth pressure cells. The hot-mix asphalt (HMA) strain gages were then checked for circuit integrity, and their zero values were recorded for later use in field instrument calibration.

### *4.1.6 Measurements Group Foil-Type Horizontal Geotextile Strain Gages*

Measurements Group N2A 06 40 CBY 120 foil-type strain gages were used to monitor the changes in horizontal strain at the bottom of the geotextile. The fabric strain gages were checked for sensor integrity before they were allocated for installation. A strain gage indicator was used to check the initial gage response using the supplied factory gage factors. The gage zero values were recorded. These values would be used later for calibration after gage installation.

The 102-mm-long foil strain gages were attached to the underside of the geotextile using Measurements Group M-Bond epoxy-type adhesive. A layer of Teflon tape was placed over the gage and secured only at the ends of the gages. The gages were then coated with Measurements Group J-Bond adhesive over the Teflon tape, followed by a layer of wrinkled aluminum foil and a layer of RTV silicone to protect the gage assembly from environmental effects.

The geotextile strain gages were equipped with three 28-gauge lead wires with a wire length of 20 mm. A Belden 3-conductor shielded plenum control cable was used to complete the lead wire extension. The solder connections between the gage lead wires and the extension cables were accomplished in the same manner as the pressure cell connections. The connections were then secured to the geotextile (which was cut to the required size in the field) by lacing chord. The lead cables were secured to the geotextile from the gage locations to the edge of the geotextile, using the same method used for the connections, to prevent damage to the wire connections and gage assemblies. The strain gage assemblies were then checked for circuit integrity, and their zero values were recorded for later use in field instrument calibration.

### *4.1.7 Texas Measurements Foil-Type Horizontal Geogrid Strain Gages*

Texas Measurements FLK-6-1L foil-type strain gages were used to monitor the changes in horizontal strain at the bottom of the geogrid. These strain gages, consisting of a 25-mm-long foil-type strain gage with three lead wires, were checked for sensor integrity before installation. A strain gage indicator was used to check the initial gage response using the supplied factory gage factors. The gage zero values were recorded to be used for calibration after gage installation. The foil strain gages were attached to the underside of the geogrid in the same manner as the geotextile strain gages. The strain gages were protected in the same manner as those used on the geotextile.

The geogrid strain gages were equipped with three 28-gauge lead wires with a wire length of 20 mm. A Belden 3-conductor shielded plenum control cable was used for lead wire extension. The solder connections and lead wire attachment were accomplished in the same manner as those for the geotextile gage assemblies. The strain gage assemblies were then checked for circuit integrity, and their zero values were recorded for later use in field instrument calibration.

### *4.1.8 Piezoelectric Polymer Traffic Sensors*

AMP Sensors, Inc.'s Roadtrax Series P Traffic Sensor is a permanent, in-the-road, class II traffic sensor used for vehicle classification and counting. The sensor consists of an aluminum channel, the sensor element, and a polyurethane elastomer to protect the sensor and converts mechanical energy into an electrical charge when a stress is imparted on it. Each sensor is 1.8 m long, 25 mm wide, and approximately 25 mm thick. The voltage output signal (millivolt range) from the instrument is conveyed through a 30.5-m-long factory-installed coaxial cable. The piezoelectric sensors were checked for sensor integrity before considering them for installation. An oscilloscope was used to check the initial sensor response as a stress was applied to the polyurethane surface of each sensor. No other calibrations or modifications were performed on the sensors in the laboratory.

Table B 1, (Appendix B) lists all the instruments embedded in the test section. Each instrument has a unique identification number is used to identify the type, location and the direction of the instrument in the test section.

## 4.2 Wiring and Data Acquisition System

The wiring from the instruments in the road to the data acquisition system in the bunker was accomplished in two stages. The wires were transported through buried conduit to junction boxes where connections were made to terminal strips that were connected to wires leading to a control board in the bunker. This two-stage approach eliminated the need for sharp bends in the wire and reduced the risk of damage to the wire. A description of the construction of all of the wire connections is included in the following sections.

### *4.2.1 Conduit and Junction Box Installation*

Schedule 40 PVC, which is rated for direct burial, houses the instrumentation wire from the road to the junction boxes. PVC was chosen because the tight seals between joints eliminate moisture penetration and rodent damage.

A 300-mm-deep trench on top of the embankment was constructed to bury the PVC. The trench covered a 122-m length of the roadway section and is 0.6 to 0.7 m from the edge. Beginning at the end of the trench, eight 0.6 x 0.6 x 0.3-m-deep holes were excavated at 15.2-m intervals that correspond to the center of each test section, with the exception of section five. A 305 x 305 x 152 mm PVC junction box with a removable cover and a rubber gasket seal (to prevent moisture penetration) was placed in each excavation. Instrumentation wire from section 5 ran directly into the bunker so no junction box was needed.

Between each of the junction boxes, five 3-m sections of conduit were joined using standard PVC cleaner and cement. The conduit was connected to the junction box through pre-drilled holes using a threaded PVC couple and metal lock nut. The connection was then sealed with a silicone caulk.

Figure 4.4 shows the 51 mm flexible PVC conduit used to direct the instrument wire under the drainage ditch and up the steep embankment from the road to the junction boxes. The required conduit diameter was determined to be three times the cross-sectional area of the wire it protected. The diameter of the conduits increased from 50 to 76 mm from the ends of the test sections to the bunker.

Lead wires were attached in the field for the piezoelectric strip sensors. Once the sensors were installed in the pavement, trenches for the lead wires for each sensor were

excavated using a hand-operated Ditch Witch and hand tools. The lead wires were then placed in the trenches and run to the data collection system bunker. Lead wires that were too short to reach the bunker were extended using a Belden 18-gauge, 2-conductor, shielded plenum control cable. All lead wire connections were performed in the same manner as those for the other instruments. The instrument cables were then placed in the trenches, which were backfilled with the excavated soil. The integrity of the lead wire extensions was checked both before and after compaction of the trench material.

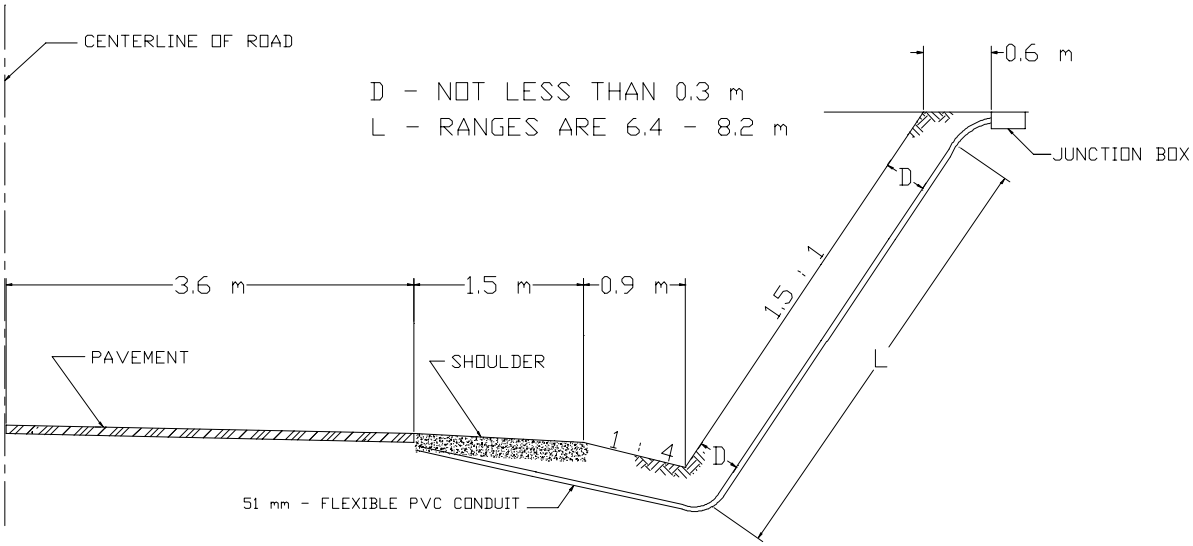


**Figure 4.4 A typical cross-section of PVC conduit from junction box to road.**

### *4.2.2 Junction Box Connections*

All instrument lead wire connections were accomplished through the use of terminal strips, except for the moisture cell connections. The moisture cell lead wires terminate within the junction boxes for the sections being measured. This was done because the gypsum block readings are extremely sensitive to resistance, and an increased cable length would increase resistance.

All wire ends leading into and away from the junction boxes were fluxed and tinned. Additionally, AMP or Thomas and Betts #6 spade tongue terminals were crimped onto the exposed tinned wire ends. The spade connectors were then fastened to Vbeau or

Realistic #6 terminal strips. The exception was the temperature sensors, which were fastened to terminal strips constructed of either constantan or copper (supplied by Omega Engineering, Inc). The temperature sensor cable wires were also completed with either constantan or copper spade tongue connectors that were crimped onto the exposed wire ends.

The earth pressure cell leads have two signal excitation wires and two signal output wires per instrument cable. A 12-gauge Belden 2-conductor shielded plenum control cable was used to supply the 10-volt direct current power bus to each junction box for the pressure cells. Each pressure cell was powered by the bus, and the signal voltage was sent to the control board in the data collection system bunker. Since only two leads per instrument were required to read the output signal, the signals were conducted through a 4-conductor, 22-gauge Belden conductor shielded plenum control cable that controlled two instruments per cable. Three 4-conductor cables were used for each control section, and two 4-conductor cables were used for each stabilized section. The cabling scheme allowed for an extra pair of wires per section to be used in case of wire damage.

The soil strain gage lead cables contain three pairs of 22-gauge lead wires conducted through a 6-conductor Belden shielded control cable. The leads were paired off in the junction boxes, connected to the terminal strips, and then carried to the control board in the data collection system bunker. The temperature gauges were fabricated from T-type thermocouple wire. The completed wire ends were fastened to terminal strips of the same metal composition within the junction boxes. Thermocouple cabling was used to carry the output signal to the control board in the data collection system bunker.

The HMA layer H-type strain gage cables consisted of a 3-conductor Belden shielded control cable. Only two of the three lead wires were used for instrument readings. Since only two leads per instrument were required to measure the instrument resistance, they were directed through a 4-conductor, 22-gauge Belden shielded plenum control cable. The cable handled two instruments per cable, hence two 4-conductor cables were used for each section.

The strain gage cables for both types of geosynthetics contained a 3-conductor Belden shielded control cable. Only two leads per instrument were required to measure the resistance of the gages; thus, they were completed in the same manner as the HMA strain gages. Three 4-conductor cables were used per stabilized section to carry the

instrument readings to the control board in the data collection system bunker

### *4.2.3 Instrument Cable Connection Control Board*

All of the instrument cables for all of the test sections were run through Schedule 40 PVC conduit into the data collection system bunker. The instrument cables were grouped by test section number and instrument type, and were routed to the control board. The control board a 1.2 x 0.9-m plywood sheet mounted to the interior road-side wall of the bunker, is divided into nine sections of equal dimension, one for each test section's instrument cables. Terminal strips are mounted on the board in order to complete instrumentation circuitry and data acquisition system connections. A 50 mm hole was made at the center of each divided section to accommodate cable routing to the terminal strips.

The exposed wire ends of each instrument cable were fluxed and tinned. AMP or Thomas and Betts #6 spade tongue terminals were crimped onto the exposed tinned wire ends to allow lead wire connection to the terminal strips. The spade connectors were then fastened to Vbeau or Realistic #6 terminal strips. The temperature sensors were fastened to terminal strips constructed of constantan and copper supplied by Omega Engineering Inc., as in the junction box connections.

The instrument circuitry for the vertical earth pressure cells was completed in the junction boxes by supplying the excitation voltage to the instruments. The pressure transducer within the body of each type of pressure cell is a full Wheatstone bridge. The output signal of each gage was the only circuitry received in the bunker.

The instrument circuitry for the soil horizontal strain gages was completed within the Keithley Metrabyte data acquisition system. The circuit for an instrument was analyzed as a half bridge. Each pair of paired wires of an instrument was considered a resistor, and the bridge was completed on the data acquisition card with two 120-ohm resistors. The data acquisition card for the soil strain gages supplied an excitation voltage of 5 volts direct current to the half bridge, and interpreted the resulting output voltage from the half bridge as a measurement of strain.

The instrument circuitry for the temperature sensors was also completed within the data acquisition system. The T-type thermocouple wires were connected to a thermal isolation block on a temperature gage card. The Keithley Metrabyte data acquisition software converts the output voltage from a thermocouple to temperature in degrees

Celsius. No other circuitry was used for temperature measurement.

The instrument circuitry for the soil moisture cells was completed through the use of an impedance bridge. Each soil moisture cell is a resistance device. The resistance of a cell is a function of the moisture within the body of the gypsum block. As moisture within the block increases, the resistance of the cell decreases. Ambient soil temperature and soil type also affect the resistance of moisture cells. An alternating current excitation voltage at a given frequency is applied to the instrument leads, and the impedance of the LCR (Inductance-Resistance-Capacitance) circuit is determined from the impedance bridge. The impedance measured is given in ohms. Laboratory analyses of the soil moisture cells for each soil type were performed to calibrate the gauges. Impedance values at differing soil moisture contents were used for the gauge calibrations.

The instrument circuitry for the HMA layer and geosynthetics strain gages was completed on the control board. The resistance of each strain gage was approximately 120 ohms. Initial variances from the resistance datum were from increased resistance due to instrument lead cable length. The instrument circuits were completed as a full Wheatstone bridge using three 120-ohm precision resistors. An excitation voltage of 10 volts direct current was applied to each full bridge, and the resulting output voltage was interpreted by the data acquisition system. The full bridges were completed on the cable control board using terminal strips to accommodate the additional legs of the circuits. The instrumented pavement sections are detailed in Appendix B, Figures B 1 through B 9.

### *4.2.4 Data Acquisition Hardware*

The data acquisition hardware was manufactured by Keithley Instruments Inc. There are several components to the data acquisition hardware. The main component is a data acquisition backplane board. To connect the backplane board to a computer, there is an interface card that plugs into an IBM PC expansion slot. Finally, there are modules that plug into the backplane board to read signals from the instruments.

The backplane board used on this project is a Keithley Instruments, Inc. Model 500A. There are ten slots on the backplane board that can hold input modules. For analog input, the first slot holds a master analog measurement module.

For the backplane board to communicate with the PC, there must be an interface

card. The interface card used with this system is an IBIN-A card. It is plugged into an expansion slot in an IBM-compatible 486 computer. The address of the IBIN-A is set with hardware switches and specified with the software during the installation procedure. A 25-pin cable connects the IBIN-A to the 500 A backplane board. In addition to serving as an interface, the IBIN-A generates interrupts at specified intervals during data acquisition to control the timing of readings. To complete the installation, the installation program, which sets the address and controls the IBIN-A-generated interrupts was run.

Four types of input modules were installed on the 500A: a master analog measurement module, an analog input module, a thermocouple input module, and a strain gage and DC amplifier module.

The master analog measurement module (AMM2) is installed in the first slot on the 500 A. This module selects and conditions signals from all of the cards installed on the 500 A. It can apply a global gain of 2, 5, and 10 to a signal obtained from any of the cards. It also has a 16-bit A/D converter for all of the cards, and can accept eight differential, or 16 single-ended analog inputs. These signals can have a local gain of 10. The signals can have a full range of (10V. Because of the low net gains on this card, there were no instruments connected to it.

The analog input module (AIM3A) is used for most of the instruments. All of the earth pressure cells, HMA strain gages, foil strain gages, and Roadtrax® sensors are connected to this type of module. The AIM3A can accept 16 differential or 32 single ended analog inputs. It is capable of local gains of 10 and 100. All of the modules installed in the 500 A are set for differential inputs.

The thermocouple input module (AIM7) is used to connect the T-type thermocouples. This module has a reference junction on the card to aid in the conversion of a signal to its corresponding temperature. In addition, the reference junction and all of the inputs terminate on an isothermal block to eliminate any temperature variation between the inputs and the reference junction. The local gain is not selectable, and is automatically set to 100. The global gain for T-type thermocouples is set to 5. The AIM7 module can have up to 16 thermocouples connected to it.

The strain gage and DC amplifier module (AIM8) is used to obtain signals from the soil strain gages. It is capable of local gains of 10, 100, and 1000. It also has on-board excitation that can be set between 0 and 10 V. There are sockets on the module to

install bridge completion resistors. Since the soil strain gages are read as half-bridges, two completion resistors are installed on each channel. There are a total of four channels on this card. Each channel has positive and negative excitation, as well as a positive and negative input. Readings taken from this card are relatively slow, so the strain gages connected to this card do not read dynamically while vehicles are passing. For all modules, most settings are software-controlled. A file was created that has all channel and instrument information.

### *4.2.5 Data Acquisition Software*

The software was created using Microsoft QuickBASIC 4.5 and software from Keithley Instruments, Inc. (KDAC500/M), which is a compiler version of their data acquisition software. It contains subroutines that control the data acquisition hardware when called from a QuickBASIC program. The data acquisition software runs from a program that handles the switching from the data acquisition program to the communications software in order to download the data files. It begins by running the data acquisition program. When the data acquisition program ends, the data files are compressed into one file. A communication program is then started in host mode and waits for a phone call. During a session, the user is prompted for a name and password, and then is allowed to download the data file. After the session is complete, the communication program automatically terminates. The compressed data files are saved for four days in case there should be a problem with downloading; all files then are deleted.

The data acquisition program performs all of the actual data acquisition functions. It waits for a signal from the Roadtrax( sensors, and then begins to take a series of readings in the sections according to which sensor was triggered. First, a set of readings is taken from the thermocouples and saved in a data file as temperatures in degrees Celsius. As soon as the program finishes taking the thermocouple readings, another subroutine is executed that takes a single sweep of readings from the soil strain gages and stores it in another file. The goal is to find long-term soil strain behavior; therefore, the file is appended with strain values of the soil every time the program returns back to the triggering stage.

Next, it reads data from groups of sections depending on where the trigger occurred. The program is set up to take readings every five msec. If section 1 is triggered, the

program would successively read sections 1-2, 2-4, 3-6, 4-8, and 5-9 for 1.365 sec each, followed by successive readings of sections 7-9, 8-9, and 9 for 1.135 sec each. This set of readings would obtain signals from a vehicle traveling between 48 and 80 km/hr. If section 5 is triggered, readings will be taken in sections 6 through 9 for 5.5 sec. After completing a series of readings, the program appends all of the data to a data file. The data are saved as voltages and no conversion factors are applied to the data. It then returns to the beginning of the program to wait for another signal. At 9:00 p.m. daily, the data program exits and returns control to the data acquisition program. A listing of the computer program used to collect the data from the instruments is provided in Appendix C.

# 5 DATA ANALYSIS AND EXCAVATION

## 5.1 Traffic

A K-Hill Signals, Inc. traffic counter was employed on the instrumented lane of the test section to record the traffic volume. During installation and initial calibration, this counter was determined to increment by 3 for every 2 axle passes. The cumulative counter reading was recorded on each visit to the site; an example of recorded data is given in Table 5.1. Since the full-scale reading of the instrument is 99,999, it was assumed that when a subsequent reading was of lesser magnitude than the preceding reading, the count had exceeded the maximum count, and a value of 100,000 counts was added to the second reading. Thus, for example, on the dates 9/19/95 and 10/30/95, the following readings were recorded: 85,476 and 20,736, respectively. Since the second reading is less than the first, it was assumed that between these events, the counter had re-started and the readings were actually 85,476 and 120,736, respectively.

**Table 5.1 Data from traffic counter.**

| Date | Volume Counter Reading | Vehicles per Day |
|---|---|---|
| 9/19/95 | 85476 | 250 |
| 10/30/95 | 20736 | 287 |
| 11/14/95 | 32586 | 263 |
| 1/17/96 | 76811 | 230 |
| 3/15/96 | 29821 | 305 |
| 4/17/96 | 58461 | 289 |
| 5/9/96 | 81781 | 353 |
| 6/20/96 | 30776 | 389 |
| 7/20/96 | 75416 | 496 |
| 8/19/96 | 28516 | 590 |

As a first approximation, it was further assumed that there were two axles per vehicle. Thus, the initial count difference was mapped to an estimated vehicle count as follows:

$$\frac{\text{Vehicles}}{\text{Day}} = \frac{(A - B)}{3C} \tag{5.1}$$

where,

A = count on date number 2;

B = count on date number 1; and

C = number of day between dates 1 and 2.

The calculated vehicle count for various periods is given in Table 5.1. It can be seen that the daily vehicle count increases over the period 9/19/95 through 8/19/96 from about 250 vehicles per day (vpd) to 590 vpd. This is due to the proximity of the test section to Smith Mountain Lake, which results in an increase in volume of traffic during the summer.

The traffic counter registers only the passage of axles regardless of whether each axle comprises part of a two-axle or multi-axle vehicle. In addition to the volume counter, four piezoelectric sensors were installed in the pavement surface for triggering the data acquisition system and measuring vehicle speeds. These sensors were also used to count the number of vehicles passing. Based on this initial onsite experimentation and calibration, it was observed that a vehicle with a piezoelectric response above 500 mV may be characterized as a truck. Based on this observation, the threshold level for the triggers was set as 500 mV, to provide an accurate count of the number of trucks passing the test section per day. Thus, the percentage of trucks on the test section was found to range between 8%-10%.

Due to the high frequency sampling rate of the data acquisition, one axle load can be deleted several times. Typical piezoelectric sensor recorded data is shown in Table 5.2. Therefore, a correction factor must be used. Using the sampling rate, the speed of the vehicle and the triggered length (the piezoelectric sensor width = 25 mm), an average correction factor was obtained. The procedure is best explained by the following example. If the average speed of a vehicle passing the piezoelectric sensor in a day is 20 m/s, and the width of the piezoelectric strip is 25.4 mm, the duration of the influence of the tire on the piezoelectric sensor may be calculated using the following equation (Huang, 1993).

$$d = \frac{12a}{s} \tag{5.2}$$

**Table 5.2 Data from piezoelectric sensors.**

| Date | Piezoelectric Sensor Reading | Vehicles per Day |
|---|---|---|
| 4/1/95 | 3623 | 580 |
| 4/2/95 | 2686 | 430 |
| 4/3/95 | 2917 | 467 |
| 4/4/95 | 3141 | 503 |
| 4/5/95 | 1129 | 181 |
| 4/6/95 | 3042 | 487 |
| 4/7/95 | 1681 | 269 |
| 4/8/95 | 4205 | 673 |
| 4/9/95 | 3508 | 561 |
| 4/10/95 | 3706 | 593 |
| 4/11/95 | 2308 | 369 |
| 4/12/95 | 2904 | 465 |
| 4/13/95 | 3558 | 569 |
| 10/19/95 | 1423 | 228 |
| 10/20/95 | 1622 | 260 |
| 10/21/95 | 1204 | 193 |
| 10/22/95 | 1132 | 181 |
| 10/23/95 | 1400 | 224 |
| 10/24/95 | 1306 | 209 |
| 10/25/95 | 1676 | 268 |
| 5/12/96 | 2507 | 401 |
| 5/13/96 | 2681 | 429 |
| 5/14/96 | 2194 | 351 |
| 5/15/96 | 2017 | 323 |
| 5/16/96 | 1974 | 316 |
| 5/17/96 | 2623 | 420 |
| 5/18/96 | 2413 | 386 |
| 6/2/96 | 3013 | 482 |
| 6/3/96 | 2762 | 442 |
| 6/4/96 | 2327 | 372 |
| 6/5/96 | 2321 | 371 |
| 6/6/96 | 3229 | 517 |
| 6/7/96 | 2281 | 365 |
| 6/8/96 | 2832 | 453 |

Assuming 5% of the vehicles have 3 axles.

where,

d = Duration of influence on the piezoelectric sensor (sec);

a = Width of the piezoelectric sensor (m); and

s = Speed of the vehicle (m/s)

For the above example, a duration of influence on the piezoelectric sensor of 0.015 sec (65.5 Hz) results. This yields the number of counts recorded per axle by the data acquisition (sampling rate = 200 Hz) to be 3 (200/65.5). Assuming that 95% of the vehicles passing the piezoelectric strip have 2 axles and 5% have 3 axles, this yields a conversion factor of 6.25 per vehicle. This factor is used to convert the piezoelectric sensor data to corresponding vpd (see Table 5.2). The calculated number of vpd from the piezoelectric sensors is approximately the same range as that calculated from the volume counter.

## 5.2 Pavement Temperature Data

Low temperature cracking is a major cause of pavement failure. The thermal gradient plays a very important role in the development of undue stresses in pavements. In addition, knowledge of the temperature and the mechanical loading applied to pavements is of extreme importance to model the behavior of the pavement system and its response to coupled external mechanical and thermal loading. To monitor the temperature profile of the different pavement layers, a total of 15 thermocouples were placed at different depths (HMA, base course, and subgrade) in the test pavement section. The thermocouples in the HMA layer were placed 25 mm from the bottom of the HMA. For the base course and subgrade, the thermocouples were placed at the mid layer and at 150 mm depth, respectively.

Thermocouples in the HMA layer were placed in sections 2, 3, 4, 7, 8, and 9, while thermocouples in the base course and subgrade were placed in sections 1, 4, and 7. The thermocouples were attached to an AIM-7 thermocouple card that recorded directly the thermocouple reading in Celsius (°C) every time the pavement instrumentation was triggered. Thus, the pavement system temperature profile was recorded multiple times a day. Thermocouple readings were recorded in a separate data file that was downloaded every night. The data file was processed at Virginia Tech, and the data was assembled

in appropriate format for temperature history and profile.

The temperature profiles from December, 1994 through April, 1996 are presented in Appendix D, Figures D 1 through D 15. The figures depict the maximum, minimum, and average temperatures per day for the span of 18 months. All the figures show that a relatively large temperature spike occurred in June-July, 1995. In general, the HMA showed the highest difference in temperature between different seasons in the pavement system, followed by the base course layer and the subgrade.

A maximum temperature of 40 °C was recorded in the HMA (see Appendix D, Figures D 4 and D 5). In January-February, 1996, the temperature dropped to approximately 0 °C (Appendix D, Figure D 4). It was also found that surface temperature usually varied by 5 °C from the measured HMA temperature.

In general, the temperature profile (over 18 months) indicates that the temperature drops after November, 1995 and then starts to rise rapidly from March, 1996 onwards. This rise in temperature would cause thawing conditions in the subgrade, resulting in a lower subgrade resilient modulus. This is confirmed by the FWD back-calculation of the subgrade resilient modulus in April and June, 1996.

In order to characterize the diurnal temperature pattern, several sample days were selected. Appendix D, Figures D 16 through D 30 show the various temperatures recorded in the different layers at different times of the day. The time span covers approximately one year. Appendix D, Figure D 16 shows the day-based reading for the subgrade thermocouples in sections 1, 4, and 7. Section 1 subgrade thermocouple recorded the greatest temperature variation, with a minimum of approximately 9 °C at 6:00 AM and a maximum of 25 °C at 4:00 PM. The subgrade showed a relatively small range of temperature change of approximately 7 °C for section 4 and 3 °C for section 7. The reason for the high variation in temperature for section 1 is its lowest total pavement thickness.

Appendix D, Figure D 17 shows the temperature pattern of base course for sections 1, 4, and 7. The shift in temperature observed between these sections is mainly attributed to the different depths of the thermocouple location (mid-depth of the base layer).

Appendix D, Figure D 18 shows the HMA temperature for various sections on March 22, 1995. The maximum temperature was observed around 4:00 PM. Appendix D,

Figures D 19 through D 30 show the diurnal temperature patterns for selected days during the year. It is clear that in winter the subgrade is warmer than the HMA, while in the summer this pattern is reversed.

In addition to the pavement temperature profiles, weather station data for air temperatures in Bedford County were obtained from the National Climatic Data Center (NCDC) for correlation purposes. Appendix D, Figure D 31 shows the average monthly temperatures covering a period from April, 1994 to November, 1996. These data represent averages calculated from daily measurements recorded by NCDC. It is observed that the maximum air temperature for 1995 recorded by the local weather station correspond to those measured by the thermocouples. The maximum average monthly air temperature in 1995 was approximately 30 °C (June-July, 1995). The minimum, however, was observed in January-February, 1995, and the temperature dropped to approximately -3 °C. This also supports the observation that the HMA temperature is higher than the ambient air temperature in the summer. HMA absorbs the heat and attains a temperature level greater than its boundary conditions, and then slowly transmits the thermal gradient by thermal diffusion throughout the various underlying layers. The same was also observed during periods of low temperature, but to a lesser extent.

## 5.3. Pavement Moisture and Precipitation Data

Gypsum blocks were installed in sections 1, 2, 3, 7, 8 and 9. In each of these sections, three gypsum blocks were placed in the subgrade and the base course layer. The gypsum blocks are located at the mid-point of the base course layer and at 150 mm and 610 mm deep in the subgrade. General Radio Company's Impedance Bridge model 1650-B was used to measure the resistance that is correlated to the field moisture content. The Impedance Bridge uses the principle of applying approximately an alternating current of 98 Hz to the gypsum block and measuring the resistance in ohms. The measured resistance is then converted to moisture content using the calibration curves derived from laboratory tests performed on the base course and subgrade samples selected from the site. As indicated earlier, sections 1 through 3 and 6 through 9 consist of CH soil, while sections 4 and 5 are composed of ML subgrade. Since all the gypsum blocks are located in the sections with CH soil, the calibration curve developed for CH materials was selected for conversion of Impedance Bridge reading of resistance

into moisture content.

Gypsum block resistance was recorded from March, 1995 to March, 1997. The resistance readings obtained from the base course and two different depths of the subgrade were recorded and converted into moisture contents using the laboratory-developed calibration curve. Appendix E, Figure E 1 shows the moisture content variations over the monitoring period. It can be seen that the moisture content at a depth of 150 mm in the subgrade is above or close to 35%. This indicates that the subgrade at this location is saturated. This leads to two conclusions: either the gypsum blocks are saturated (steady state of equilibrium), or the field density levels are different than those for which the Proctor density-moisture content curves were established. Since strict quality control of construction and field nuclear gauge readings confirm that the compaction level in the field was within tolerable limits, the nature of mechanism of gypsum blocks is the major factor influencing the measurements.

Laboratory evaluation at Virginia Tech during calibration procedures for gypsum blocks indicated that the gypsum block acts like a sponge and absorbs moisture from its surroundings until it reaches a state of equilibrium. After this state of equilibrium with the surroundings is reached the base level readings of a gypsum block attains a level, where a shift factor is introduced into the calibration equation. To determine the shift factor, field samples at 150 mm and 610 mm deep in the subgrade were taken, and the actual, impedance bridge readings taken at that time were correlated with the field soil sample moisture contents.

In November, 1996, 18 samples were taken from the subgrade (2 from each section), at 150 mm and 610 mm. Impedance bridge readings were also taken from the gypsum blocks at the same time. The soil samples were tested in the laboratory and their respective moisture contents were determined. The shift factor was established as the average difference between the measured moisture content and the estimated moisture content (using gypsum blocks). Appendix E, Table E 1 presents the data used in determining the shift factor. A greater correction factor for gypsum blocks located at 150 mm (2.5%) in the subgrade is established than at 610 mm (0.4%), respectively.

Appendix E, Table E 2 shows the average moisture contents before and after the correction factors are applied. This approach is considered valid due to insignificant variability in moisture contents between the different sections (see Appendix E, Table E 1 and Figure E 2).

Appendix E, Figure E 3 shows the average corrected moisture content levels in the pavement section. Results show that moisture contents rise to approximately 36% during the months of May through July, 1995 (conformed by NOAA; see Appendix E, Figure E 4, where the precipitation levels reach 350 mm) and then drop steadily to approximately 27% in November, 1996. The base course moisture content was steady (5% ± 1%) over the evaluation period.

## 5.4. Rut depth measurement

Rut depths have been recorded since the opening of the test section to traffic. The rut depth measurements were taken monthly to bimonthly in the instrumented inner lane. The procedure adopted to measure the rut depth involves a straight edge aluminum bar of 53.2 mm thickness and a scale. The straight edge has an approximate length of 1.8 m. The scaled ruler has a flat horizontal plate which can slide across the entire linear dimensions embedded on the scale. To minimize errors, the rut depths in each section were taken approximately 1 m before and after the instrumented areas. Thus the influence of embedded instruments on the rut depth is minimized. The maximum rut depth in each section was then determined based on the average of the two measurements for each wheel path.

Appendix F, Figure F 1 shows the rut development from August, 1994 through November, 1996 for sections 1, 2, and 3. The initial rut depth at the start of the traffic on the pavement section in August, 1994 is considered the reference. During the first three months, excessive deformation in all sections was noted, which is consistent with normal pavement behavior. Section 1 had a maximum rut depth of 10 mm and slowly progressed to 12.5 mm in June 1995. During July to August 1995 there is a sudden increase in rut depth due to summer traffic, as it approached the 15 mm mark. From October, 1995 through July, 1996, a steady rise in the rut depth is noted until it reached 17.5 mm. From August through November, 1996, there was a rapid rise in the rut depth, and during September, 1996, the rut depth increased rapidly to 23 mm. There has been a further increase in the rut depth, and in January 1998, the rut depth was in excess of 30 mm, which is considered severe rutting.

Section 2, which is geotextile-stabilized section, started at 8 mm rut depth in the first three months. The rut depth gradient remained fairly low until May, 1996. During the months of June through November, 1996, the geotextile-stabilized section developed a

steep rut gradient, and stabilized at a rut depth of 17 mm. Section 3 was stabilized with a geogrid, and started at an initial rut depth the same as that of the control section. The rut depth showed approximately the same trend as that of the geotextile-stabilized section until April, 1996. The gradient rose in May-June, 1996 and then flattened out. A sudden increase in rut depth was observed in September, 1996 for section 3 due to extreme mechanical loading. The rut depth in section 3 was approximately 20 mm in January 1998.

During the month of September 1996, extra traffic loading was applied to the pavement section using a truck with a 134 kN axle load and a tire pressure of 700 kPa. The truck applied approximately 117 passes per day on the pavement section for 2 weeks (see Table 5.3). This accelerated loading was performed to fail the test sections. The rapid increase in rut depth observed after August, 1996 is mainly due to the accelerated loading applied to the test section.

**Table 5.3 Extra vehicular loading during August, 1996.**

| Date | No of Passes | Average Speed (km/hr) |
|---|---|---|
| 8/13/96 | 63 | 38 |
| 8/14/96 | 110 | 38 |
| 8/15/96 | 110 | 42 |
| 8/16/96 | 130 | 47 |
| 8/19/96 | 118 | 29 |
| 8/20/96 | 136 | 32 |
| 8/21/96 | 105 | 32 |
| 8/22/96 | 162 | 32 |
| 8/23/96 | 120 | 32 |
| **Total** | **1054** | **36** |

**Vehicle properties:**
Front axle tire pressure = 630 kPa
Rear axle tire pressure = 700 kPa
Axle load = 134 kN

The rut depths as reported in Appendix F, Figure F 1 show a definite contribution from the section stabilized with geotextile. Section 2 shows the smallest amount of rutting in the 100 mm base course category.

Appendix F, Figure F 2 shows the rut development in sections 4 through 6 over a

span of approximately 28 months. Section 4 shows a small amount of rutting as compared to sections 5 and 6 until August, 1996. It should be noted that sections 4, 5, and 6 lie in the vicinity of the intersection junction on the test section. Intersection traffic traveling in section 4 starts to slow down towards the end of section 4, and comes to approximately a complete halt condition in section 5. This slow rate of vehicle motion causes larger stresses and strains on this section. The vehicles entering from the intersection have two options available: either turn left (entering the non-instrumented outside lane), or traverse section 6 and onward (in the instrumented lane). By moving into the instrumented lane, the vehicle enters section 6 at a very slow speed and then slowly accelerates in order to traverse the test section. This also causes undue low vehicle speed-related stresses and strains in section 6. Due to this unequal loading condition among sections 4, 5, and 6, a direct comparison of their rut depths cannot be made. Sections 5 and 6 show a closer resemblance to each other than to section 4 in terms of the traffic condition. The rut depth in section 4 started at 5.5 mm and progressed slowly until May, 1996, when it reached approximately 9 mm. During June-July, 1996, there was a steep rut gradient visible in section 4, which raised the rut depth to 11 mm (where it remained constant all throughout the month of September, 1996). Since January 1997, the rut depth in section 4 has stabilized at approximately 14.5 mm.

Sections 5 and 6 start at a rut depth of 8 mm in October, 1994, and their rut gradients were almost the same until May 1995. There was a small rise in the rut gradient for both sections in June, 1996, when the individual rut depth rose to approximately 13 mm for section 6 and 12 mm for section 5. By September 1996, the rut depth leveled in both sections and attained steady-state levels. Sections 4, 5 and 6 show the same amount of final rut gradient. The rapid increase in rut depth in sections 4, 5, and 6 correlates directly with the reduction in resilient modulus of the subgrade (FWD back-calculation) of these sections during April through July, 1996. The effect of the extra vehicular loading is also evident from the sharp rise in the rut depth gradient during August, 1996. Since January, 1996, the rut depths in sections 5 and 6 are approximately 13 mm and 12 mm, respectively.

Section 8 started at a rut depth of approximately 7 mm and progressed slowly until September, 1996 to a rut depth of 8.3 mm. From September, 1996 onwards, the rut depth gradient picked up very fast, possibly due to the extra truck loading applied to this section. The current rut depth in section 8 is 13 mm. Section 7 started at a rut depth of

approximately 9.5 mm in contrast to section 8, which showed a more steady gradient until September, 1996. The maximum rut depth of approximately 14 mm was measured in January 1998. Section 9 was in the intermediate range between sections 7 and 8. The initial rut depth in 1994 for section 9 was 8 mm and it steadily rose to 9.2 mm by April, 1996. There was a sporadic jump in rut depth following April, 1996. From September 1996 onwards, there was a rapid increase in rut depth (see Appendix F, Figure F 3) until the 13.5 mm-mark was reached.

## 5.5 Falling Weight Deflectometer (FWD)

The Virginia Department of Transportation (VDOT) FWD was chosen to perform seasonal structural evaluations of the test sections. This device, which drops a calibrated mass onto a circular plate (radius 150 mm) in contact with the pavement surface, records the magnitude of the applied load, the vertical deformation response of the pavement surface at the center of the loaded plate, and a six locations offset from the loaded axis.

Two types of analysis may be performed on FWD data. The simplest and most direct analysis relies on computing a Surface Modulus, E0, defined as the applied load divided by the measured axial deformation. This value is analogous to a spring constant (kN/mm) and provides a gross measure of the overall structural value of the pavement system, including the subgrade. A more sophisticated analysis is possible using various techniques of "back-calculation," which seek to match the observed pavement response to that returned by a mathematical model of a layered linear elastic half-space. This technique generally relies upon varying the linear elastic moduli of the component material layers until a satisfactory match to the observed surface deflection is achieved.

The surface modulus of each section was computed for each of the seasonal site visits. This technique is simple, because it requires that no assumptions be made relative to the thickness or elastic response of component layer materials. However, it is subject to modification in HMA surfaced pavement due to the effects of temperature upon the viscoelasticity of the asphalt bound materials, and can be further influenced by the presence of an effective rigid layer underlying the pavement at some depth. The results of these analyses are shown in Figure 5.1.

It can be seen from Figure 5.1 that the overall pavement responses of sections 1, 2, 3, and 9 stand out as being distinct from those in sections 4, 5, 6, 7, and 8 which are

remarkably consistent. This apparent difference is ascribed to the details of the design of this road section, which was relocated to transform an intersection into a curve. Consequently, in spite of a significant excavation (mainly in sections 4 through 8), the sections at each end of the new construction are somewhat influenced at some depth by the presence of previously undisturbed and compacted subgrade materials. This will also explain the increased surface moduli observed in these sections; the authors believe that this is due not to stronger pavement sections, but to residual pre-compacted subgrade.

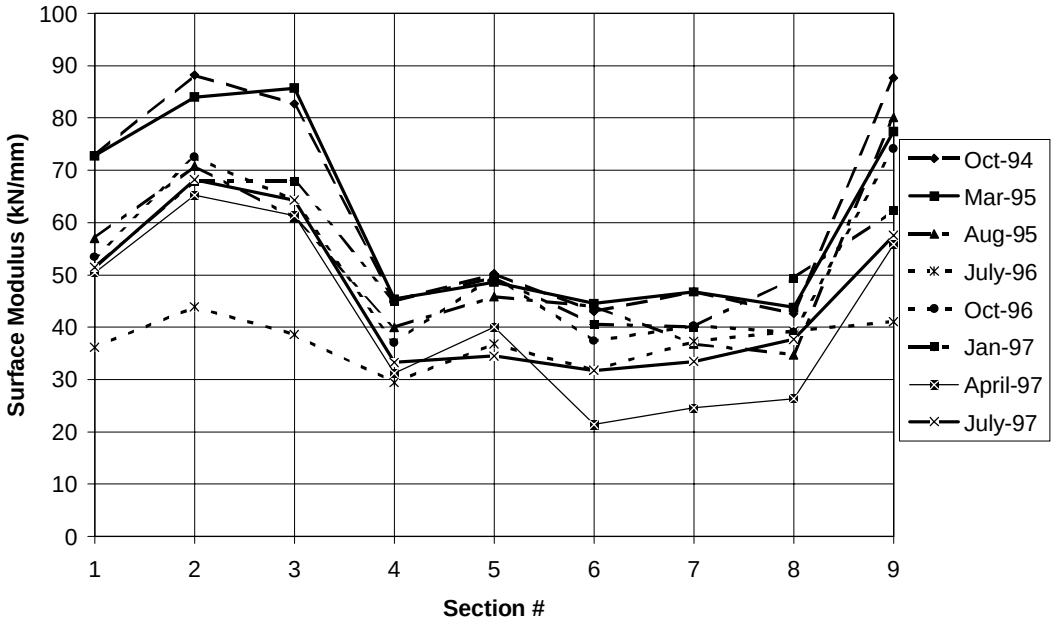


**Figure 5.1 FWD-derived surface moduli.**

Nonetheless, if the surface moduli for sections 1, 2 and 3 are closely examined, it will be seen that for all FWD tests, the surface modulus of section 2 (geotextile) exceeds that of section 3 (geogrid), which in turn exceeds that of section 1 (control). This pattern, also observed in sections 4, 5, and 6 (150 mm base) and in sections 7 and 8 (200 mm base), tends to indicate that the geotextile may contribute more to the structure than other sections (Al-Qadi *et al.,* 1997).

FWD measured deflection profiles were plotted for different periods to define any inconsistency that might occur in the measurements taken by the geophones. Appendix

G, Figures G1 through G 72 show the deflection basin profile for different load levels from October, 1994 through July, 1997.

Two methods of analysis were used in an attempt to quantify the development of a transition layer before a more simplified method yielded more realistic results. Both methods yielded quantitatively the same pattern of results: however, it became clear that each method had different sensitivities to variability in the field data. Both methods are described below in brief and then followed by a more detailed description of the method finally adopted.

### *5.5.1 ELSYM5 Analysis*

The ELSYM5 program is a linear elastic program that treats up to five layers. In this program, the pavement may be loaded with one or more identical uniform circular loads applied vertically to the pavement surface. The program superimposes the effects of the various loads and computes the orthogonal stresses, strains, and displacements, along with the principal stresses and strains, at locations within the pavement specified by the user.

Input values required to run the program are the layer thicknesses, resilient moduli, and Poisson's ratios of all layers in the system. A load of 40 kN was used with the corresponding tire pressure of 552 kPa. This is representative of the largest portion of truck traffic on secondary roads, and of the FWD test loading at 40 kN. The resilient moduli of the HMA and base course layers were determined in the Civil Engineering Materials Laboratory at Virginia Tech. It should be stated that the base course resilient modulus was found to be a function of its thickness. The subgrade resilient modulus used was the one back-calculated for corresponding sections with geotextiles. The pavements without geotextiles were modeled as four-layer systems, comprising a HMA layer, the base course, the transition layer (formed as a result of base contamination), and an infinite subgrade layer. For the months that FWD data was recorded, the relevant input data was used for the ELSYM5 analysis, i.e., the layer thickness, Poisson's ratio and resilient modulus of all the layers. The thickness and resilient modulus of the transition layer was varied for each period in the control and geogrid sections to try to match the stress values obtained from the ELSYM5 program to the measured stress values in the pavement layers during the calibration runs. The deflection results from the ELSYM5 analysis were also matched to the surface deflection

results from the FWD. In this way, the thickness of the transition layer was estimated for the seven occasions on which FWD data was taken (Appea *et al.,* 1998).

### *5.5.2 KENLAYER Analysis*

The KENLAYER program developed by Huang (1993) is a layered analysis program that takes into account the viscoelastic nature of the HMA layer and its response to dynamic loads. It has the advantage of allowing different material parameters for each seasonal period. The backbone of the layered program is the solution for a multi-layer elastic system under a circular loaded area. The solutions are superimposed for multiple wheels, and collocated at various loading times for viscoelastic layers. With the exception of the HMA layer, all the other layers were assumed to be linearly elastic.

The use of the KENLAYER program for the analysis of viscoelastic layered systems under a moving load involves several steps. Similarly, an axle-load of 40 kN and tire pressures of 552 kPa were used as input values in the analysis. Laboratory-determined creep compliance results were provided as input. In KENLAYER, solutions because of either moving or stationary loads can be obtained. Since the load–time pulse imparted by the FWD is similar to that of a truck wheel moving at 56 km/h, this speed was used in the viscoelastic analysis.

As in the ELSYM5 program, the thickness, Poisson's ratio, and resilient modulus of the four-layer model are used as input data in the program. By varying the thickness and elastic moduli of the transition layer, the deflection and stress at any specified depth in the subgrade for each section (control and geogrid) were obtained. This was done for all seven periods that deflection results were obtained from the FWD.

The stress values and deflection values so obtained were compared and the trial transition layer was adjusted to match the deflection and stress values measured to corresponding to the calibration runs and FWD deflection basin data. In this way, the thickness for the transition layer (extent of base contamination) was estimated. The deflections and stresses predicted by ELSYM5 (linear elastic analysis) and the measured values by the embedded instruments did not match all the times. Stresses and deflections calculated by ELSYM5 were less than the measured responses. KENLAYER, on the other hand, gave higher deflections than measured values, while stresses were lower. The higher predicted deflection may be attributed to the viscoelastic treatment of the HMA layer in the analysis, which also results in less

predicted stress at the base course-subgrade interface.

### *5.5.3. Detailed FWD Analysis*

The back-calculation of subgrade resilient moduli was determined using MODULUS ver. 5.0 computer program. MODULUS uses a linear elastic procedure to determine the layer moduli, and any other unknown that can be derived from the FWD data files. Modulus also predicts the depth to rigid bottom layer below the top of the subgrade based upon the measured deflection of the last sensor in the geophone array. Using this predicted depth to the rigid layer, the back-calculated results from MODULS can be refined to reduce the mean square error of the predicted deflection basin. In this project, MODULUS did indeed detect an effective rigid bottom layer at a varying depth of 0.5-7.5 m (mostly above 2.0 m) below the pavement surface. Further data analysis indicates that the variation in depth to rigid bottom layer did not have any significant effect on the result pattern.

Due to the relatively thin HMA surfacing layer, the elastic properties of this layer were fixed based upon appropriate measured pavement temperatures and the laboratory resilient modulus characterization of specimens obtained form the field. The nominal elastic parameters of the granular base layer were also fixed based upon laboratory measurements (Al-Qadi *et al.,* 1996). The only parameter returned by MODULUS, therefore, was the subgrade modulus (Figure 5.2). This analysis confirms the differential response between the different treatments. For most of the FWD results, the subgrade resilient moduli of the geotextile sections are greater than their corresponding control or geogrid sections. This may be attributed to a weaker base course layer in the control and geogrid sections than in the corresponding geotextile sections, which is consistent with the “pumping of subgrade fines into the base course layer” hypothesis. It was also observed that the difference in the apparent subgrade modulus between different stabilization methods increases with time (see Figure 5.2).

### *5.5.4 Base-layer Contamination Model*

One of the important functions of geosynthetics in pavements is stabilization, which results from their ability to isolate and provide a barrier against the base course-subgrade intermixing (Joreny and Hicks, 1986; Laer and Brau, 1986; Koerner 1994; Koerner and Koerner 1994; Al-Qadi *et al.,* 1994). The extent of contamination and the material properties of the intermixing layer are of critical importance in determining the

performance of pavements. Although the concept of base course contamination has been recognized for sometime (Yoder and Witczak, 1975), an estimate of its contribution to the reduction in pavement service life is still not quantified. The following section details the approach adopted to determine the extent of contamination in this project.

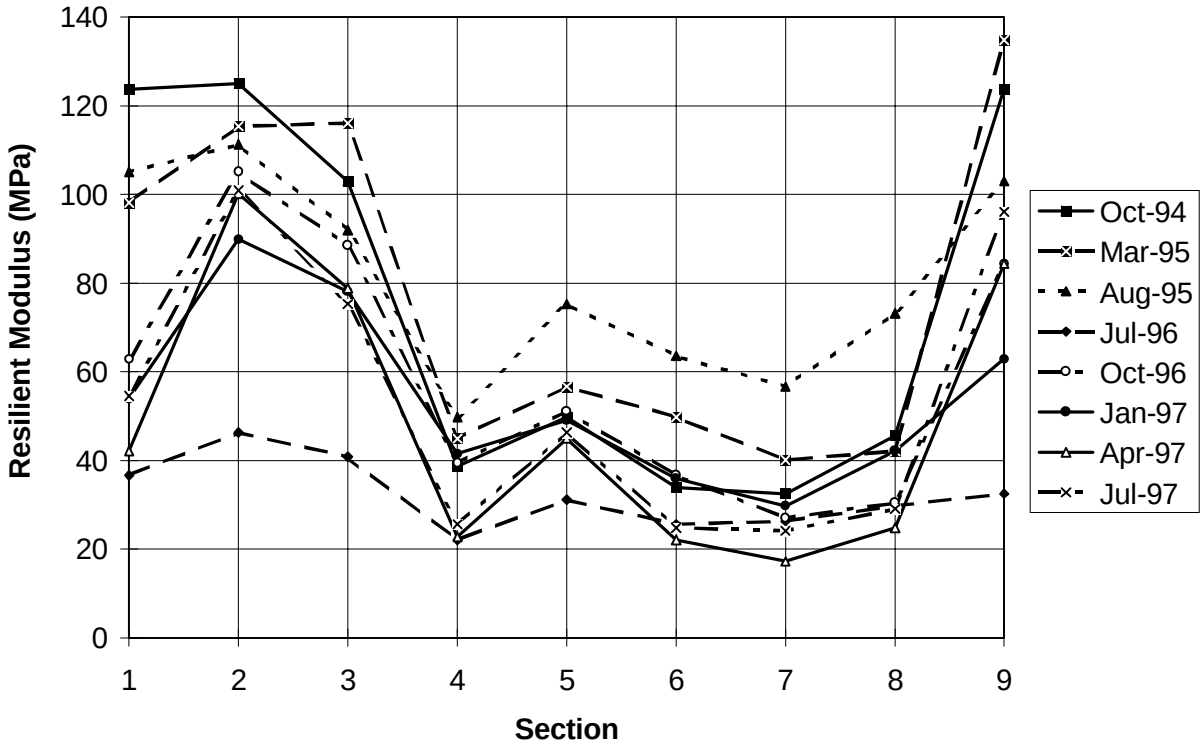


**Figure 5.2 Apparent subgrade resilient modulus variation over time.**

The hypothesis put forth in this study is the development of a transition layer between the subgrade and base layer in the absence of a geotextile. To determine the transition layer thickness developed in control and geogrid-stabilized sections, an independent layer of resilient modulus value between the base and subgrade was added, and the "geotextile subgrade resilient modulus" was considered in the calculations as reference. After adding the transition layer with known properties to the control pavement system, a back-calculation procedure was adopted to determine the subgrade resilient modulus. This is an iterative process where the thickness of the transition layer is changed gradually to yield a subgrade resilient modulus approximately equal to that of the geotextile-stabilized section. The stepwise process is illustrated in a flowchart in Figure

5.3.

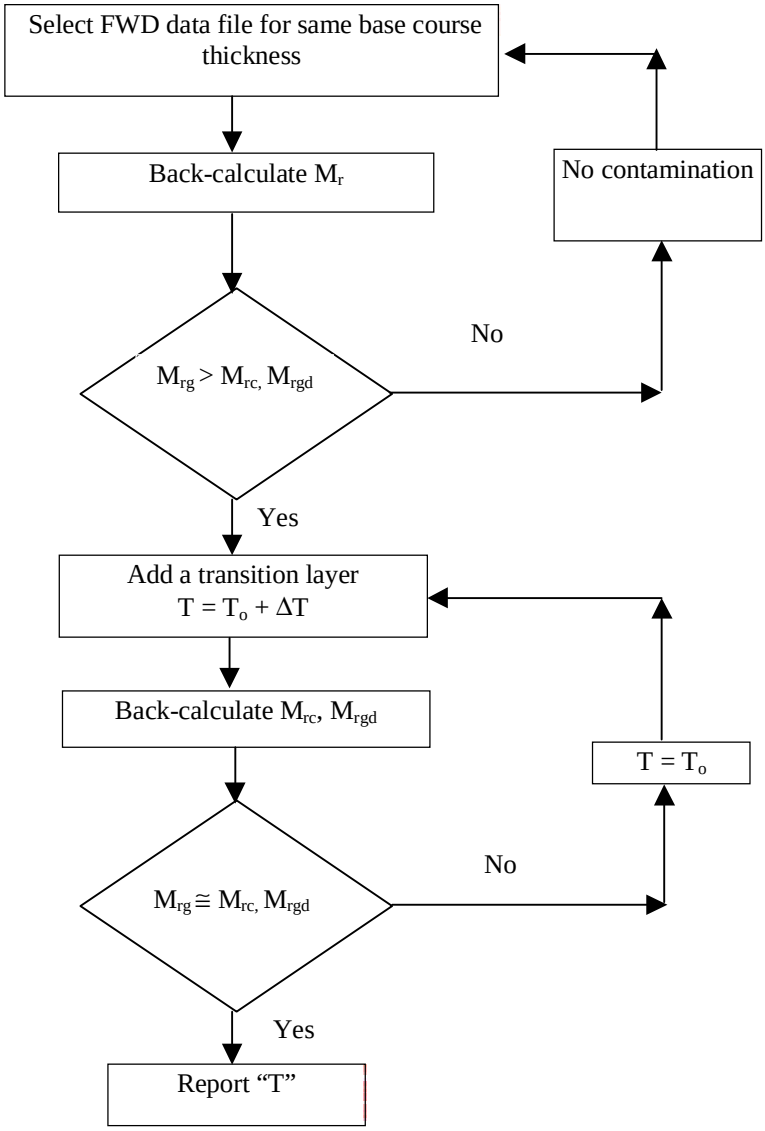


T = Thickness of the transition layer;
$T_o$ = Initial Transition Layer Thickness = 0;
$\Delta T$ = 5 mm;
$M_{rg}$ =Subgrade resilient modulus of geotextile-stabilized section;
$M_{rc}$ = Subgrade resilient modulus of control section; and
$M_{rgd}$ = Subgrade resilient modulus of geogrid-stabilized section.

**Figure 5.3 Flowchart of the iterative procedure of transition layer thickness determination.**

For example, the subgrade resilient modulus from the data collected in August, 1995

for section one (100 mm control section) was 105 MPa, whereas the geotextile-stabilized section had a subgrade resilient modulus of 110 MPa. A transition layer thickness of 13 mm at a resilient modulus of 138 MPa was needed to increase the subgrade resilient modulus to 110 MPa. Over the next 8 months, the transition layer increased to 64 mm. The thickness further increased to 69 mm in October, 1996, indicating asymptotic stabilization of contamination layer versus time (see Figure 5.4). Further tests show insensitivity to greater contamination for the 100 mm test section.

For the thicker base course sections (150 mm and 200 mm), the MODULUS program becomes insensitive to changes in transition layer thickness. This implied that the FWD back-calculation procedure could not estimate the contamination layer thickness accurately in the thicker base course sections (150 mm and 200 mm) at this time.

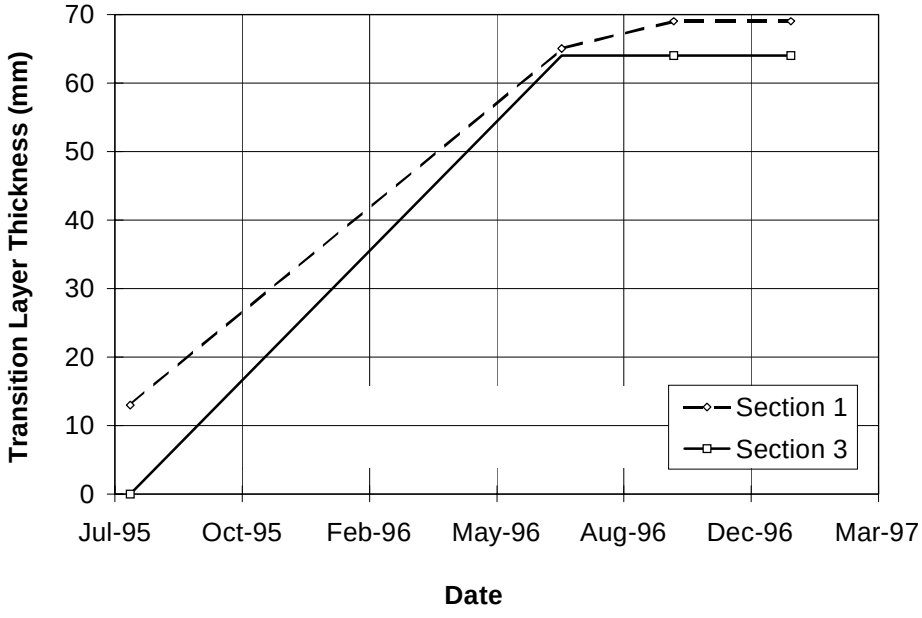


**Figure 5.4 Development of transition layer.**

In summary, the results of this field experiment and analysis of the data derived from nondestructive monitoring (rut depth measurements and FWD) suggest a clear difference in performance when geosynthetic is included in the pavement system, especially in the thinner base sections (1 through 3). Simple analysis of FWD data indicates that the degree of contamination of the granular base by the subgrade material

is a function of the geosynthetic used, no contamination in the geotextile section, and delayed or reduced contamination in the geogrid section. The short duration of the project prevents clear distinctions from being made in the thicker base sections (4 through 9) at this time. It may be concluded that in the 100 mm base course sections, the geotextiles provide adequate protection against subgrade intrusion, while geogrid provides partial protection. This fact is also reinforced by the rutting behavior of those sections (see Section 5.4).

## 5.6 Ground Penetrating Radar (GPR)

Ground penetrating radar (GPR) systems, can be classified as air-coupled systems and ground-coupled systems on the basis of the antennas used. In air-coupled systems, the “horn” antennas are typically 150 to 500 mm above the surface. In ground-coupled systems, a transceiver (a device that transmits and receives electromagnetic [EM] signals) is in full contact with the ground. There are five radar system types that have been used to evaluate constructed facilities: frequency modulation, synthetic-pulse, stepped frequency, synthetic aperture, and pulsed (impulse). The pulsed systems are the most commonly used devices. An impulse GPR system has been used in this study.

Impulse GPR systems transmit short pulses of EM energy that penetrate an assessed structure and reflect back from interfaces where a dielectric contrast exists. The amplitude and arrival time of the reflected signals are analyzed to predict properties not seen from the surface. The GPR technology has been used in civil engineering applications for many years. Some of these applications are: locating reinforcement bars in reinforced concrete structures, detecting deterioration in bridge decks, evaluating the thickness of different layers in a pavement structure, locating buried pipes and cables, and quantifying bridge scour. In this study, GPR has been used to detect interlayer mixing between subgrade and base course layers in flexible pavements.

The following equation gives the principle of the working mechanism of GPR:

$$V = \frac{C}{\sqrt{\varepsilon_r}} \tag{5.3}$$

where,

c = Speed of light in free space = 0 3 x 108 m/s; and

$\varepsilon_r$ = Relative permittivity or dielectric constant.

Permittivity is a property that shows how well a material is capable of storing a charge when an electric field is applied. The permittivity of free space, which is considered as a reference material, is equal to $\varepsilon_r = 8.854 \times 10^{-9}$ F/m. Permittivity of different materials is expressed as a ratio to $\varepsilon_r$ and is called the dielectric constant. Using equation 5.3, knowing the measured dielectric constant of an assessed material and the measured return signal time, the depth of a reflective interface can be easily found. Another important concept is the signal attenuation. This factor is mainly a function of the GPR system frequency and the material electrical conductivity, which is a material's ability to conduct an electric current. In fact, the lower the frequency, the deeper the signal can penetrate; however, the resolution decreases. Also, the higher the conductivity, the lower the signal penetration. Thus, the amplitude of the reflected signal depends on the dielectric contrast between the two materials. The reflection coefficient in low-loss materials is approximated by:

$$r = \frac{\sqrt{\varepsilon_{r1}} - \sqrt{\varepsilon_{r2}}}{\sqrt{\varepsilon_{r1}} + \sqrt{\varepsilon_{r2}}} \tag{5.4}$$

where,

$\varepsilon_1$ = Dielectric constant of layer 1; and

$\varepsilon_2$ = Dielectric constant of layer 2.

This means that if the two materials have significant difference in their dielectric constants, the reflected signal will be strong and the interface could be easily identified.

### *5.6.1 Data Collection*

The GPR system used in this study generates trigger pulses in the control unit at about a repetition rate of 50 KHz. These trigger pulses are sent to the transducer (through a control cable) where they are transformed into bipolar pulses and then radiated into the subsurface. The small (290 mm x 270 mm x 140 mm), light (6 kg) control unit for this system operates on 12 V DC battery and is hooked, through a cable, to an antenna that has a 900 MHz center frequency, a 1.1 ns pulse width, and dimensions of 80x180x330 mm. This antenna is designed for high resolution at shallow penetration depths, which is suitable for the objective of this investigation.

The system was used on the test section in April, 1996, August, 1996, January, 1997, April, 1997, June, 1997, and October, 1997. This was done to monitor any changes with time in the different layers of the pavement structure. A total of fifteen passes was taken each time over the pavement (with exception of the evaluation in October 1997, which was limited). Figure 5.5 shows the location of these passes on the different sections of the pavement.

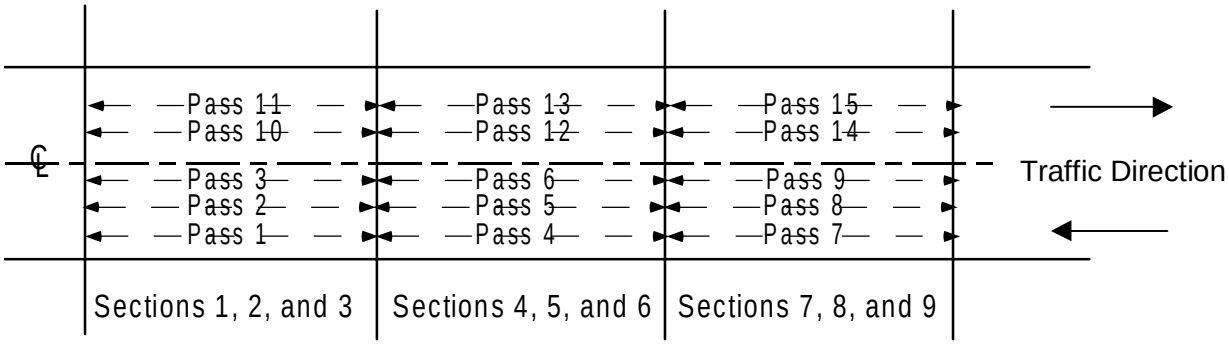


**Figure 5.5 Location of GPR passes.**

### *5.6.2 Data Interpretation*

After taking the field data, the files were transferred to a personal computer where they were analyzed using RADAN (Radar Data Analyses) software. The criterion used to evaluate the performance of the geosynthetics is the time it takes the wave to reach the base/subgrade interface and the amplitude of this reflected wave. The color code presented in all figures represents the intensity of the reflected signal. This means that different colors are assigned to different ranges of the reflected wave amplitude. A weak reflection is represented by green (homogeneity in the scanned material, which leads to no wave reflection); red and dark blue represent great changes in the dielectric properties.

Figures 5.6 through 5.8 represent the scans taken over sections 1, 2, and 3, respectively, in June, 1997. By comparing these figures, it was observed that the EM wave takes more time to reach and reflect back from the base/subgrade interface in sections 1 and 3 than it does in section 2. This means that the dielectric constant of the base course in sections 1 and 3 is higher than that in section 2. Since the base material

used in the three sections prior to construction is the same, it is concluded that contamination of the base layer with fines pumping from the subgrade has occurred in sections 1 and 3. This is also confirmed from the amplitude of the reflected wave which is higher in sections 1 and 3 than in section 2. The migration of the fines into the base course increased the dielectric constant of the layer because of the moisture content of these fines. Appendix H, Figures H 1 to H 15 contain figures for the rest of the six sections for June, 1997 and all the sections for August, 1996. The same conclusion was reached for all the sections in Appendix H.

## 5.7. Field Calibrations

Initial calibrations of the instruments were performed in the laboratory before construction of the field test sections. Additional calibrations were performed on some instruments after the road sections were constructed and in service. Instrument calibrations are used to convert the collected field data to meaningful pressure, strain, temperature, and moisture measurements in the pavement system layers. Unless otherwise stated, the instrument conversions used for data analysis are those supplied by the instrument manufacturer.

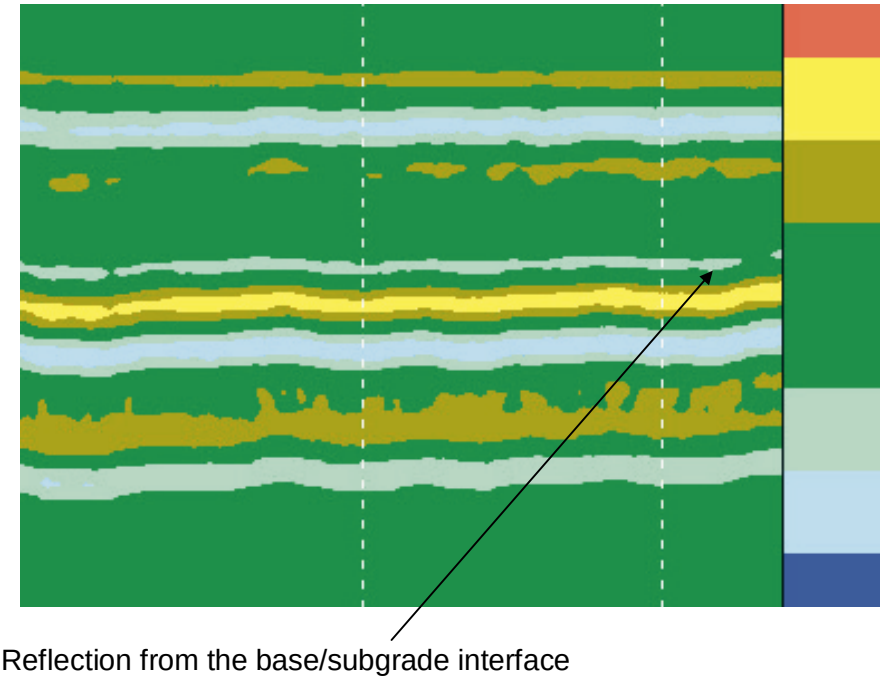


**Figure 5.6 GPR scans over section 1 (June, 1997).**

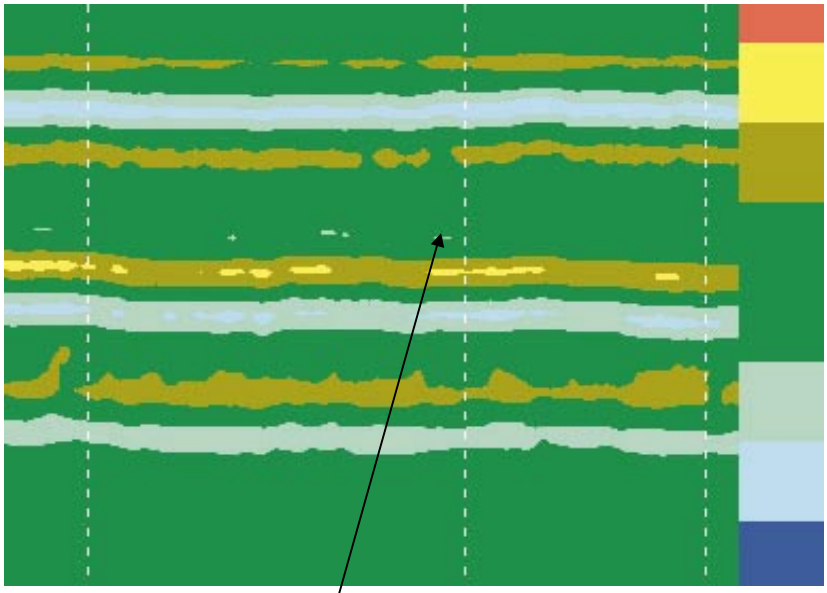


**Figure 5.7 GPR scans over section 2 (June, 1997).**

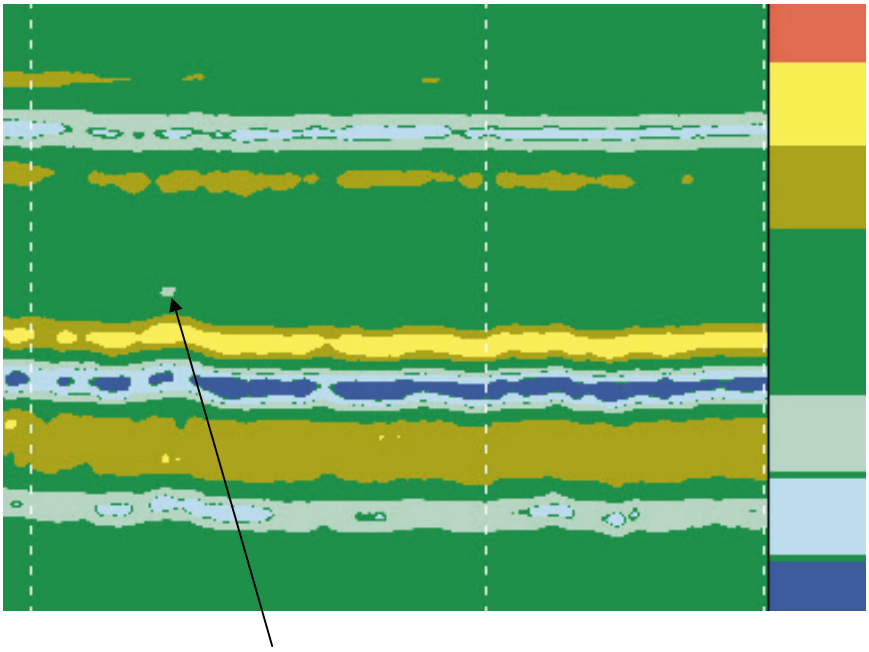


**Figure 5.8 GPR scans over section 3 (June, 1997).**

The goal of field calibrations is to qualify the class of vehicle triggering the data acquisition system and calibrate the instrument readings in each test section to known vehicle properties. A single-axle, dual-wheeled, flatbed truck with specified load configurations, tire pressures, and speeds was used to calibrate the test section instrumentation.

Three calibration operations have been performed. The first calibration was performed in April, 1995, the second in August, 1995, and the third in April, 1996. The calibration data is of vital importance as it simulates to a large extent a controlled environment-testing situation. The calibrations allow the creation of reference tables and figures to estimate and correlate the response of the pavement system to unclassified field vehicles. Each calibration is comprised of a combination of five different tire pressures, three different speeds, and four axle loads. This generates a total of 60 different categories in each calibration. The wide range of conditions covered by the calibration runs accounts for a variety of possible vehicular load and speed combinations encountered in the field. The speed of the calibration truck was determined using the speedometer and a radar gun.

Single axle loads of 22, 53, 80, and 102 kN, tire pressures of 420, 490, 560, 630, and 700 kPa, and vehicle speeds of 40, 56, and 64 km/hr were used for field calibrations. The data acquisition system was triggered manually during the calibration process to exclude any normal traffic interference.

Once the collected data was analyzed, tables were generated for pressure cells and strain gage measurement. Plots were grouped based on base course thickness. Appendix I, Figure I 1 shows a representative response of an earth pressure cell installed in the base course of a control section. The decrease in pressure with increasing vehicle speed is expected. As the vehicle's speed increases, the pressure and damage to the pavement system decrease. Additionally, as the tire pressures and wheel loads increase, the damage to the pavement system increases.

The procedure adopted for development of plots for the subgrade pressure involved selecting a particular location from the shoulder at 0.5 m in the X-Y plane. This allowed for corrections to be applied in a more consistent and accurate manner. It also allowed comparing same location pressure and strains under nearly similar boundary influences.

It should be mentioned that not all the instruments responded in the same manner under the wheel load, and therefore sometimes there existed an inaccurate response from a strain gauge, which did not correspond to the surrounding gauges. ELSYM 5 was used to develop the appropriate master curves for the pressure distribution across the cross-section of the pavement under a dual load for different temperatures. This would allow using these analytical results to determine the exact wheel paths of the travelling vehicles, since instruments are distributed in the expected wander area. The developed master curves were thus used to correct the measured inaccurate response in accordance with the surrounding gauge measurements. A typical master curve for the 80 kN is shown in Figure 5.9.

Plots of 80 and 102 kN axle load categories for a tire pressure of 560 kPa are presented (for calibration one) in Appendix I, Figures I 2 to I 11. A smaller pressure response was measured in the geotextile-stabilized sections compared to the other sections. Appendix I, Figures I 12 through I 21 show the same results for the 22 and 53 kN axle load categories.

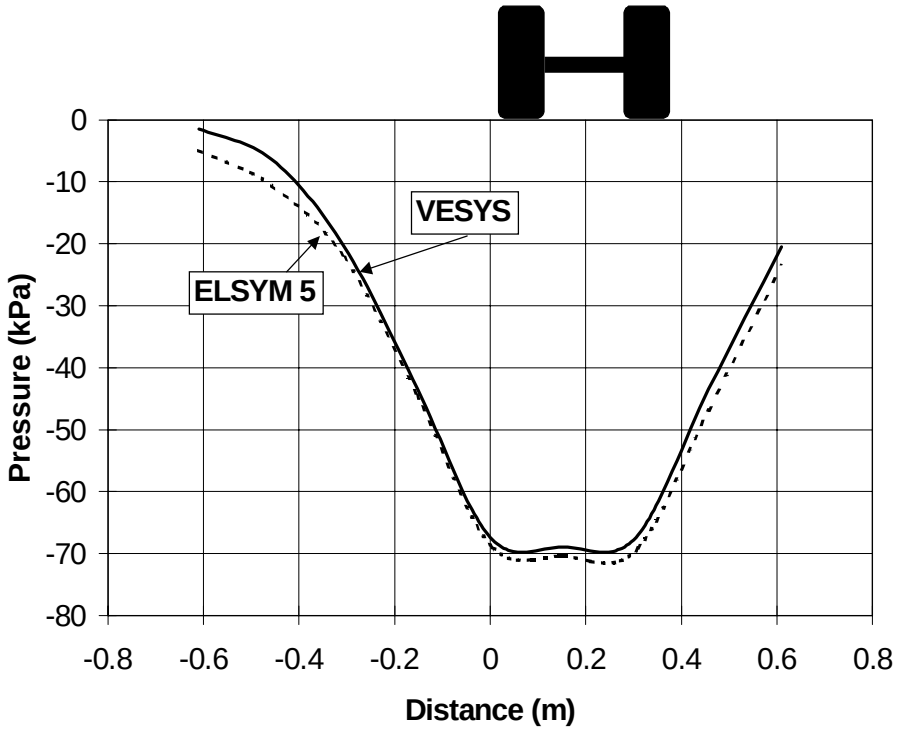


**Figure 5.9 Pressure at the top of the subgrade for 80 kN axle load and 560 kPa tire pressure with HMA temperature of 25 °C.**

The results for calibration two show the same trends in measured stresses and strains as calibration one. Appendix I, Figures I 22 through I 41 show the measured stresses and strains from calibration number two. Due to the fact that calibration two was conducted in the summer, greater pressure and strain values were measured at different layers, as the resilient modulus of HMA is lower than that in calibration one. The trends in the 53 kN and 23 kN axle load categories conform to that observed in the 80 kN and 102 kN ranges.

Calibration three was performed in April, 1996. The temperature levels measured by the thermocouples inside the pavement lie in an intermediate range when compared to calibrations one and two. Appendix I, Figures I 42 through I 50 show the responses from various surviving instruments at that time. It is noticed that the developed pressures at the base course-subgrade interface lie in an intermediate range when compared to calibrations one and two (see Appendix I, Figure I 42).

For a particular calibration, the lower pressure response from the geotextile-stabilized sections may be attributed to the fact that intermixing of base and subgrade material reduces the strength of individual layers and the overall stiffness of the pavement system as a whole.

A verification of the stress and strain master curves in terms of variances between pressure and strain distributions was also performed using a viscoelastic pavement analysis program (VESYS). A minimal difference in magnitudes was observed, but was not sufficient enough to cause any significant change in the correction of field responses (see Figure 5.9).

The four piezoelectric sensors placed in the pavement section act as triggers as well as weigh-in-motion devices. During calibrations, responses from all the piezoelectric sensors were used to develop master curves for the determination of the approximate weight and tire pressure range. Appendix I, Figures I 51 through I 53 represent the set of calibration curves derived from piezoelectric sensor response versus the calibration truck speed, with each curve representing a different tire pressure and the same axle loads for calibrations one through three.

The unknown vehicle speed was found by dividing the known distance between two piezoelectric sensors (triggers) by the time taken for the vehicle to strike sensors (measured by the data acquisition system). Then the unknown vehicle's weight and tire

pressure could be interpolated from the calibration curves. For example, if a vehicle traveling at 60 km/h gives a response of 1800 mV, then using the set of figures shown in Appendix I, Figure I 51, the vehicle can be placed in an approximate 630-700 kPa tire pressure category, with 102-134 kN axle-load range. Although the same vehicle can be placed in tire pressure categories less than 630 kPa that would raise the relative axle load to such a high level that it becomes unrealistic for a secondary road.

## 5.8 Data Analysis

### *5.8.1 Static Data*

During the first three months, static data was collected from all the instruments. Most of the initial loss in instrumentation was in the area of geotextile strain gages and occurred within the first three weeks. This led to the conclusion that instrumenting geotextiles would not provide significant information due to the material's nature.

Appendix J, Figures J 1 through J 5 show the strain-time response of the HMA and geosynthetic strain gages. The development of strain in the geotextile was rapid due to the fabric's nature to stretch under small loading under applied loading (cloth-like). The development of strain within the geogrid was smaller as compared to the geotextile. This is attributed to the geogrid being a much stiffer medium. This type of behavior is observed in both directions (parallel and perpendicular to traffic).

Appendix J, Figures J 1, J 2 and J 3 represent a strain comparison of geotextile, geogrid, and HMA over a span of three months in the direction perpendicular to traffic. The maximum developed strain in the geotextile was approximately 0.70%, where the geogrid achieved 0.18%, and the HMA was approximately 0.21%. The strain gages on the geotextile failed at a much earlier stage than the rest of the gages, because the developed strain in geotextile rose more rapidly than that of the geogrid-stabilized section after the first month. The 100 mm section, being structurally weaker, deforms more under mechanical loading, resulting in a higher deformation at the HMA level than at the base course-subgrade interface (geogrid, see Appendix J, Figure J 1). In the 150 mm, section the HMA strain rose more rapidly in the first two months, but later on is surpassed by the geogrid strain (see Appendix J, Figure J 2). The 200 mm section shows the HMA strain to be much lower than the geogrid strain (see Appendix J, Figure J 3). In general, one would expect the strain in the HMA to be higher considering the location of geogrid and its higher stiffness.

Dynamic strain data at the bottom of HMA was also collected over the span of 24 months. Initially, the performance of the strain gages and survivability was satisfactory, but over the span of the project a large number of the gages failed. A discussion of the dynamic behavior of these gages can be seen in section 5.8.2 of this report.

A static "base level" bottom of the HMA strain was also recorded by the data acquisition system. This “base strain” provides the accumulation of strain at the bottom of HMA over the span of the entire project. Appendix J, Figures J 6 through J 14 provide the accumulated strain plots at the bottom of HMA over 25 months in various sections. These plots indicate no set pattern for the strain accumulation based upon stabilization in various sections. For example, strain levels in section 1 are lower than those observed in section 2; however, in section 4, the strain levels are higher than those observed over a period of time in section 5 (Appendix J, Figures J 6 through J 11). The strains in the geogrid-stabilized section 3 also were erratic when compared to the accumulated strains in sections 2 and 3 (Appendix J, Figures J 7, J8, J10, and J 11).

The conclusion drawn from the static strain gage measurements is that there exists no set pattern for the HMA strain gages. The performance of each section cannot be judged from these strains, because several factors can influence the gage performance, such as miss-orientation, gage sensitivity, and interaction of the surrounding material with the gage. These factors make the strain measurements not reliable.

### *5.8.2 Dynamic Data*

Data was collected from the field project during the past three years. The accumulated size of the raw data is approximately 1.2 GB. After the data was downloaded from the site, a series of data reduction programs was run on the raw data file to extract the loading responses. The credible responses were recorded manually in an Excel® spreadsheet format. From there, a series of steps was followed to achieve the final dynamic response of the strain and stress levels in the test section.

The main objective behind the evaluation of credible responses was to determine the stress or strain response as a direct result of mechanical and thermal loading. The procedure adopted is similar to that used in the reduction of calibration data. A gauge position was fixed in the XY plane, and the response of the various sections to traffic was evaluated. As stated earlier, the field data is more complicated than the calibration data because of the driver’s tendency to wander in the wheel path. This effect causes

more uncertainty in measured responses and sometimes causes complete absence or a very mild response from a certain gauge compared to the surrounding gauges.

The first step in evaluating field data was the development of the master curves using a linear elastic program ELSYM5. Figure 5.10 shows the master curve for the subgrade and base course. This master curve is drawn for an HMA layer of thickness 100 mm and a dual axle load of 80 kN at a HMA temperature of 12 °C. Similarly, master curves were developed for other HMA temperature ranges by effectively varying the resilient modulus of the HMA.

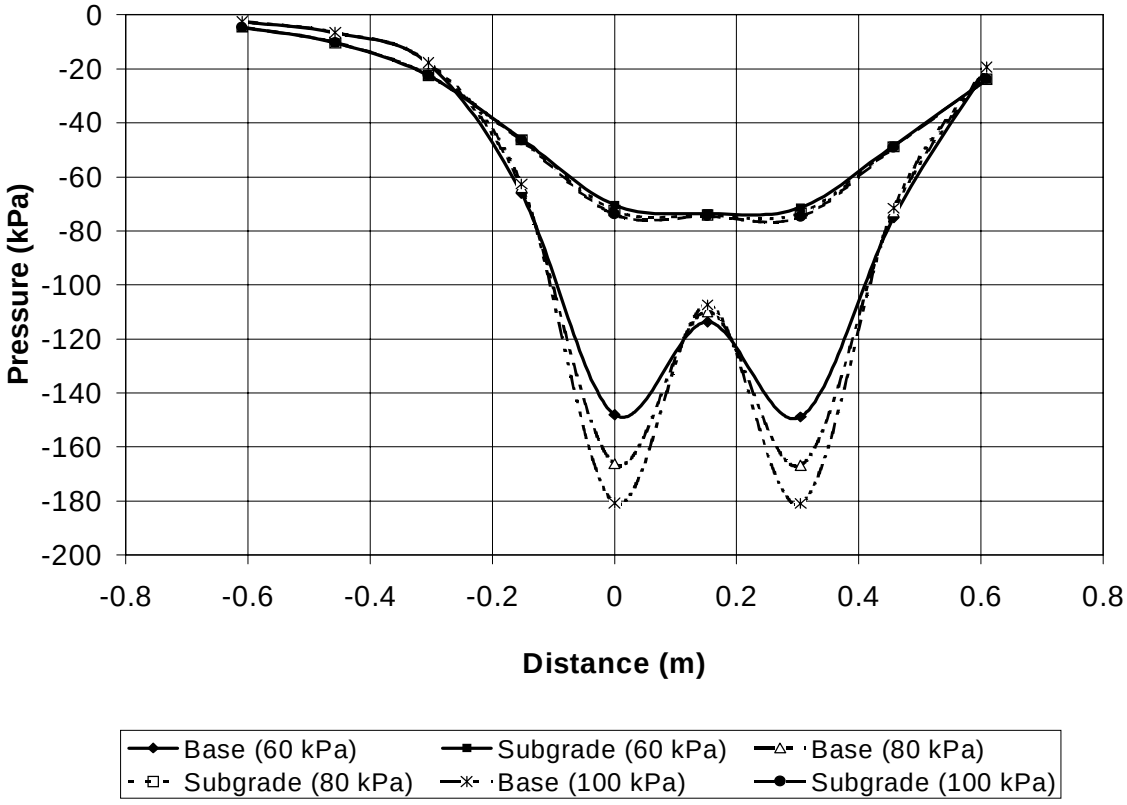


**Figure 5.10 ELSYM 5 master curve for 80 kN axle load, 560 kPa tire pressure at 12 °C.**

Different plots were obtained for various axle loads, base course thicknesses, tire pressures, and temperatures. These master curves indicate that the differences between the pressure developed at the top of the subgrade is negligible (less than 2% variation) across the domain of the pressure cells in a particular section. The reconstruction of missing subgrade responses was performed using the appropriate

master curve. It should also be noted that the distance between the pressure cells is approximately 100 mm in the direction transverse to the flow of traffic.

Appendix K, Figures K1 through K 29 show the responses from subgrade pressure cells. The speed of the vehicle, weight, and tire pressure range was determined using the calibration weight classification figures (see Appendix I, Figures I 51 to I 53). The three calibrations performed cover the entire range of trigger responses and field conditions encountered in the field over the working span of the project. The speed of the vehicle was determined using the time taken by the vehicle to cover the distance between triggers 1 and 2. The temperature of the HMA was determined from the recorded thermocouple readings. This temperature, as described earlier, was essential to estimate the appropriate value of the HMA resilient modulus.

The data collected from the field show a trend of lower pressure development in the sections stabilized with geotextiles. Appendix K, Figure K 4 shows a sample output from the pressure cells in the subgrade for a vehicle travelling at 60 km/hr with a weight range of 80-102 kN, and a tire pressure range of 630-700 kPa; the HMA temperature was 6 °C. The figure shows that the pressure develops at the top of the subgrade as a particular vehicle traverses the test section. A drop in pressure as the vehicle moves from section 3 (100 mm) to 4 (150 mm) is also evident. There is a further drop in pressure as the vehicle moves from section 6 (150 mm) to section 7 (200 mm). This drop in pressure results from an increase in the base course thickness. Few vehicle responses did not correspond to the predominant behavior of the subgrade pressure cells as shown in Appendix K, Figure K 29. Such occurrences were uncommon, and did not influence the final conclusion that “the geotextile-stabilized sections develop a lower pressure in the subgrade, as compared to the control and geogrid-stabilized sections”. The superior performance of geotextile-stabilized sections may be due to the barrier provided by the geotextile at the base course-subgrade interface to the migration of fines from the subgrade to the base course, and aggregate penetration from the base course to the subgrade. Geogrid-stabilized and control sections, on the other hand, fail to completely isolate and separate the two layers where intermixing of the materials does take place, resulting in the formation of a transition layer. Geotextile-stabilized sections, while effectively separating the base course and subgrade, still allows the moisture to travel, thus avoiding moisture buildup at the interface. As an average, section 2 (geotextile-stabilized) develops 10% less pressure than section 1 (control).

Before the development of the master curves for the base course pressure cells, the master curves developed using ELSYM5 were revisited. It was observed that the ELSYM5 master curves for base course pressure show a very high range of variation in 100 mm distance between the pressure cells. However, the data collected from the field clearly showed that the variance between the two adjacent pressure cells is minimal. A possible reason for such analytical effect may be due to ELSYM 5 converting a point load into a uniformly distributed load (see Figure 5.10). In order to confirm that measured responses from various locations in the base course layer, a finite element model for pressure loading was developed. The model was linear elastic and was used to check the extrapolation accuracy. ABAQUS ver 5.6 was used to run a reference analysis for 100 mm, 150 mm, and 200 mm base course thickness. Contour plots for stresses, deformations, and strains for a section with 100 mm of HMA layer, 100 mm thick base course and 1.6 m of subgrade are shown in Figures 5.11 through 5.13. The contour plots clearly show that the areas of interest where the pressure cells lie in the base course are practically under the same pressure contour (see Figure 5.11).

Based on this analogue, no adjustment was done to the measured base course pressure cell responses in the base course. Appendix K, Figures K 30 through K 38 show the pressure cell responses from the base course pressure cells, which are located in sections 1, 4, and 7. The plots are grouped in months for easy interpretation. There is a clear trend among the base course pressure cells as the pressure increases with the increase in base course thickness. The response from the pressure cells is very consistent. The increase in pressure indicates that as the sections get structurally stronger, the instrument response increases. However, stabilization performances cannot be judged, because all the base course pressure cells lie in the control sections.

Strains were also measured in the wheel path in a similar manner pressure cells. The strain gauges lie in the direction perpendicular (short) and longitudinal (long) to the vehicle motion. Finite element based-strain contour plots were used to develop the master contour plots. At the bottom of HMA, the strain contours are very consistent and do not show appreciable variation. The displacement contours from which the strain and the stress contours are developed in the finite element procedure show the same trend (see Figure 5.13). Appendix K, Figures K 39 through K 41 show the behavior of the short direction HMA strain gauges under dynamic loading. No clear distinction can be made about the sectional performance based upon the measured strain levels. Similar

behavior is observed in the short direction strain gauges (Appendix K, Figure K42 through K 44).

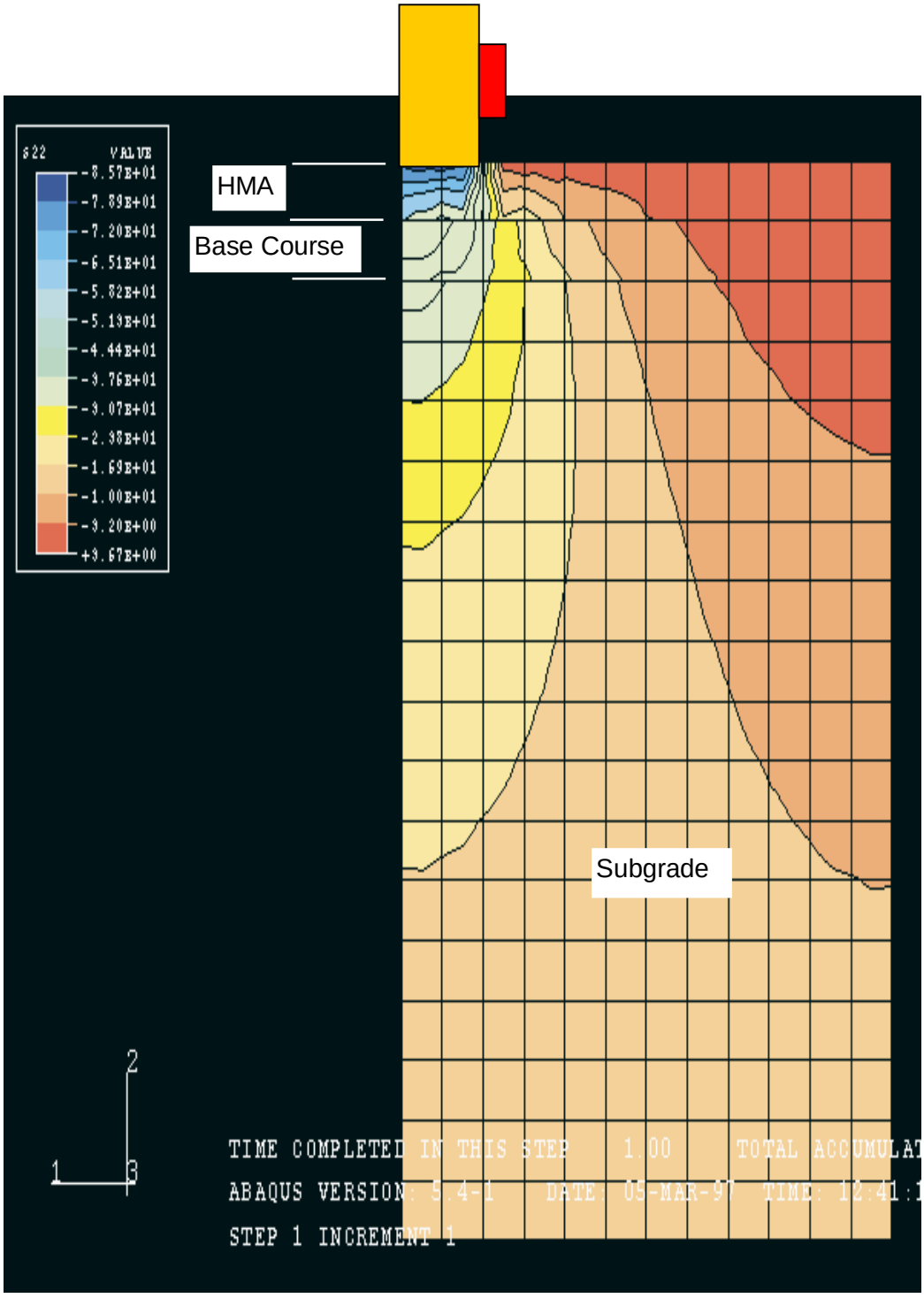


**Figure 5.11 Contour plot for vertical stress.**

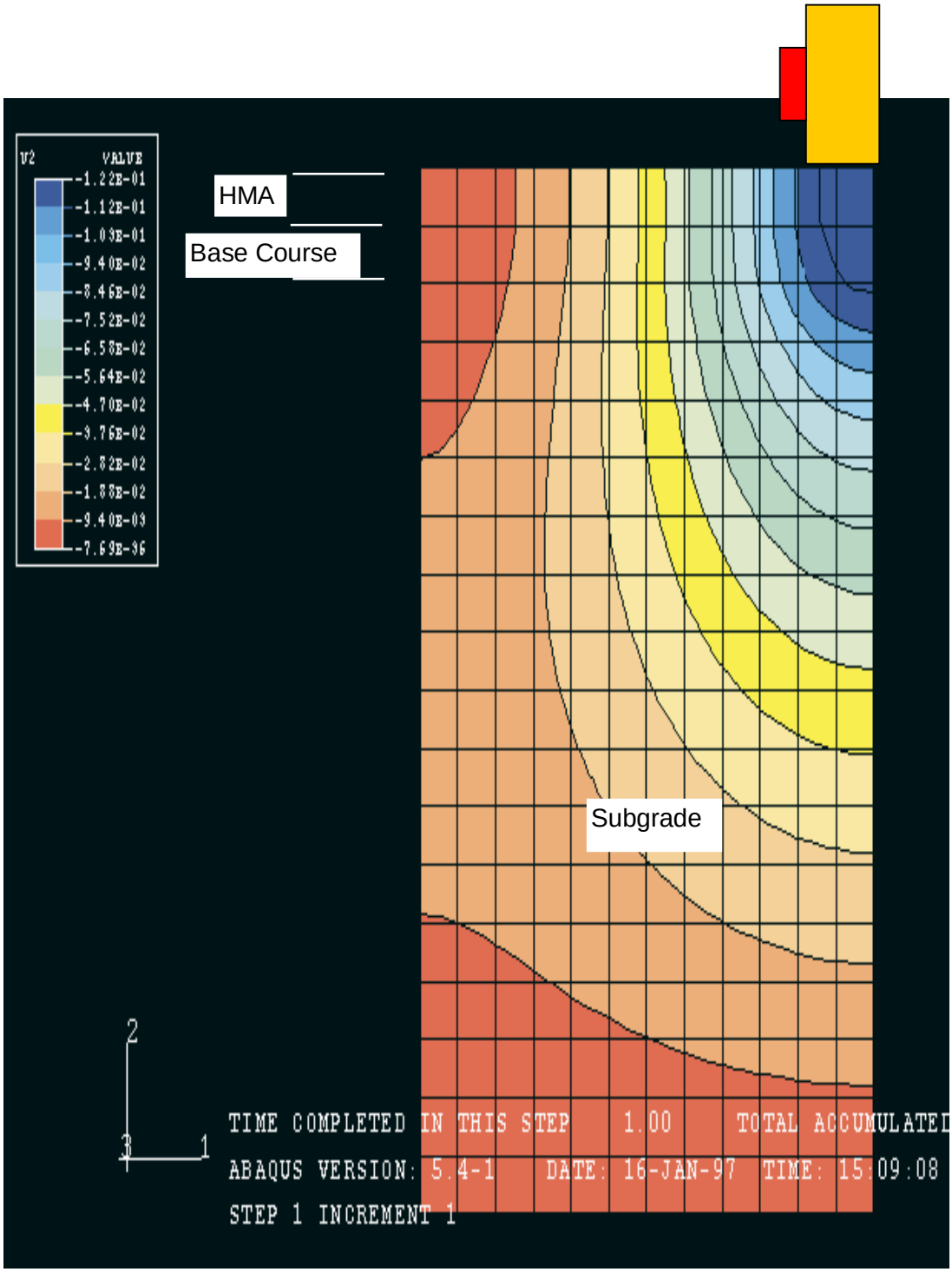


**Figure 5.12 Contour plot for vertical deformation.**

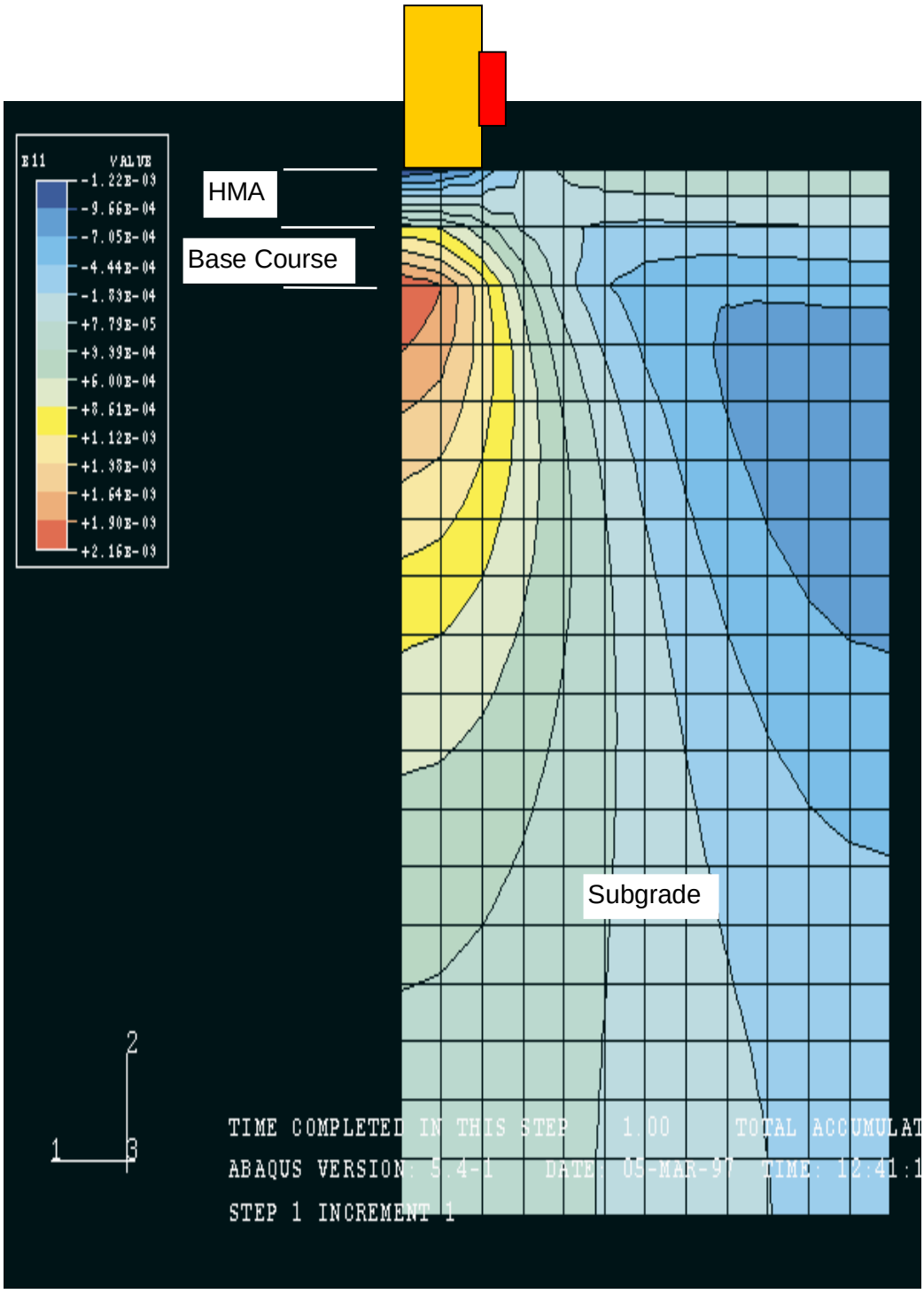


**Figure 5.13 Contour plot for horizontal strain.**

In order to evaluate further the geotextile-stabilized section performance, results from calibrations one and two were also plotted in the same manner. The objective was to clearly identify the predominant trends in section performances and correlate them with the dynamic data collected from the field. Excellent correlation was seen in the subgrade pressure cells (see Appendix K, Figures K 45 through K 49 for calibration one, and Appendix K, Figures K 60 through K 64 for calibration two). The strain response from various gages is plotted in Appendix K, Figures K 50 through K 59 for calibration one and Appendix K, Figures K 65 through K 74 for calibration two.

### *5.8.3 Statistical trend Analysis*

A clear trend was observed in the dynamic data collected from the random vehicle responses. It was observed that the control sections had a higher subgrade pressure response at the base course-subgrade interface than the geotextile and geogrid-stabilized sections when vehicles pass. It was also observed that the geogrid-stabilized sections had a greater pressure development at the top of the subgrade than the geotextile-stabilized section when vehicular loading was applied. To prove it statistically a t-test with hypothesis testing was conducted. The test hypothesis is presented in Table 5.4.

**Table 5.4 Hypothesis testing for the dynamic data.**

| Groups (Group 1 – Group 2) | Null Hypothesis $H_o$ | Alternate Hypothesis $H_a$ | Level of Significance | Decision |
|---|---|---|---|---|
| Section 1 – Section 2 | The mean of Group 1 is equal to or less than the mean of Group 2 | The mean of Group 1 is greater than the mean of Group 2 | 0.00005 | Reject $H_o$ |
| Section 3 – Section 2 | | | 0.0292 | Reject $H_o$ |
| Section 1 – Section 3 | | | 0.01005 | Reject $H_o$ |
| Section 4 – Section 5 | | | 0.00005 | Reject $H_o$ |
| Section 6 – Section 5 | | | 0.1579 | Accept $H_o$ |
| Section 4 – Section 6 | | | 0.0339 | Reject $H_o$ |
| Section 7 – Section 8 | | | 0.00005 | Reject $H_o$ |
| Section 9 – Section 8 | | | 0.0023 | Reject $H_o$ |
| Section 7 – Section 9 | | | 0.0899 | Accept $H_o$ |

To characterize the significance of the trend for the measured pressures at the top of the subgrade the measured dynamic pressure cell responses were normalized for all the

sections in the same base course thickness group. The groups that were used for statistical analysis are shown in Table 5.4. It is determined from the level of significance that the geotextile-stabilized sections have a lower subgrade pressure development than the control section, indicating lower distress. Comparing the geogrid-stabilized sections with the geotextile-stabilized sections, it is observed that the geotextile-stabilized sections have a lower distress compared to the geogrid-stabilized sections. Results from sections 1, 2 and 3 show that the geotextile-stabilized sections have a lower distress than the geogrid-stabilized and control sections.

Table 5.4 also shows the test results for the 150-mm and 200-mm base course thicknesses. Comparing section 5 and 6, the level of significance indicates that there is not enough evidence to reject the null hypothesis. The same is true for section 7 and section 9. Similar results were also noted in the determination of the transition layer, where the back-calculation procedure was not able to quantify the thickness of the transition layer.

## 5.9 Excavation and Gradation Analysis

In October, 1997 the first three sections of the test project were excavated in an effort to determine the extent of contamination in the base course layer. In collaboration with VDOT, two feet wide strips of the HMA layer were carefully excavated from the first three sections (sections 1 through 3). After the HMA layer in the respective sections had been removed, prefabricated forms were placed on top of the cleaned base course in the instrumented lane in the outer instrumented wheel path, the inner wheel path, and the middle of the lane. Figure 5.14 (a) and 5.14 (b) show the excavated pit and the location of the forms. All excavations were at least five feet from instrument locations.

The prefabricated forms were made out of wood, and had four rectangular openings with inside dimensions of 0.23 m x 0.23 m each. Careful excavation of the base course was performed in locations 1, 2, 3 and 4, as shown in Figure 5.14 (a), for each form for each of the these locations. The excavations were performed in 50-mm increments in the base course, and the depth of the excavation was checked with a tape measure for accuracy. A total of four samples from each depth increment were taken per location.

A total of 72 samples were collected from the three excavated test sections. All samples were properly labeled, placed in moisture proof bags, and brought from the site to the laboratory for further testing. Once the base course in the two feet wide section

was cleared, the geotextile and the geogrid samples were carefully collected from the excavated area. With the base course cleared and the geosynthetics removed, samples from the subgrade were taken from all the excavated sections. Samples were taken in 50-mm-deep increments. A total of 18 samples were collected from the subgrade of the three excavated sections. The excavated samples from the subgrade were also properly labeled and placed in moisture proof bags to avoid any change in moisture contents.

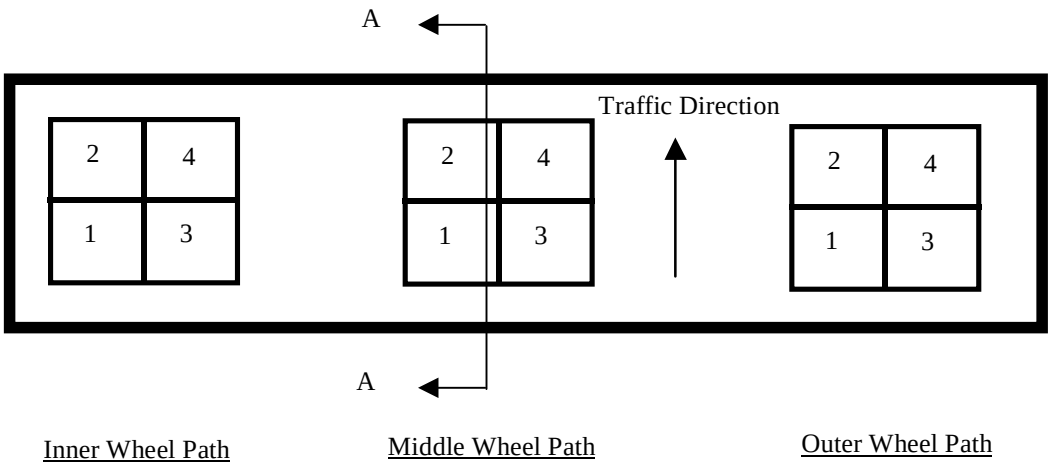


**Figure 5.14 (a) Excavated section with location of forms.**

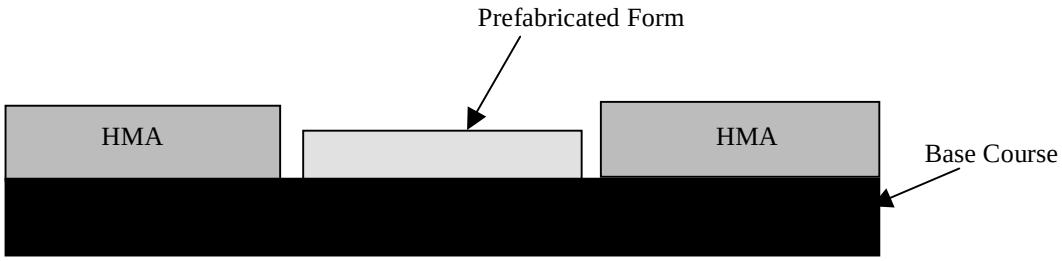


**Figure 5.14 (b) Cross-sectional view of the excavated section.**

### *5.9.1 Base Course Samples*

Two different types of tests were performed on the base course samples collected from the field, namely:

- Standard test method for total moisture content of aggregate by drying (ASTM C 566-89)
- Standard test method for sieve analysis of fine and coarse aggregate (ASTM C 136-95a)

*Moisture content* of the samples was determined using the ASTM C 566-89 standard. The samples were transported from the site in plastic Ziplock® bags to avoid loss of moisture. All the samples were tested and it was found that the moisture contents of the tested samples varied between 5.8% and 6.3%. These measurements were in the same range as observed by the moisture blocks in the field (see section 5.3).

*Base course gradations* were performed on the samples collected from the field in accordance with ASTM C 136-95a standard. Because the total number of samples collected from the field was quite large (72 samples), samples 1 and 2, and samples 3 and 4 were combined for each location to reduce the number of the samples. This mixing reduced the final number of gradations performed to 36. These 36 gradations were performed by washing the aggregate through sieve number 200 and then drying it in the oven at 110 °C for 24 hrs. This step was incorporated in the ASTM C 136-95a to break-up the conglomerated fines in the sample. The resultant gradations of the samples were plotted along side the original gradation of the base course obtained June 1994, when the base course was placed (see Appendix L, Figures L 1 through L 18). These Figures show that percent fines have increased over the three years of service. The increase in fines is probably due to disintegration of the aggregate and the pumping of fines from the subgrade. However, a comparison of Appendix L, Figures L 4, L 10 and L 16 shows that differences are present between the three sections. The percentage of fines in control section is approximately 17%, in the geogrid-stabilized section 15% and in the geotextile-stabilized section 11%. Appendix L, Figure L 19 through L 30 show the three gradations of section 1 (control), section 2 (geotextile-stabilized), and section 3 (geogrid-stabilized) for the layer 1 (top 50-mm) and layer 2 (bottom 50-mm) of the base course. The relative difference between the fines in the three sections was also supported by the visual observations made in the field. In all gradations, a lower percentage of fines was observed in the geotextile-stabilized section than in the control and geogrid-stabilized sections. This is a very significant finding of this study that is supported by the back-calculation and decreased structural capacity of the geogrid-stabilized and control sections, when they are compared to geotextile-

stabilized sections. It is important to note that a significant increase in base course fines (above 12%) can significantly reduce the resilient modulus of the base course layer.

### *5.9.2 Geosynthetic Materiel*

The geosynthetic samples collected from the field were tested for ultimate strength and the ultimate elongation. Table 5.5 shows the test results for the geosynthetics before the start of the test project in July, 1994, and after three years of in-field testing in October, 1997. There is considerable reduction in ultimate strength of the geotextile in the warp direction (33%) during the three years of field-testing, whereas in the fill direction, the ultimate strength of the material remains intact during that time (three years). The geogrid, on the other hand, did not encounter any change in ultimate strength after three years of testing. There was considerable strain development in the geotextile in the warp direction (38%) compared to the fill direction (21%). The geogrid, on the other hand, developed 29% strain in the machine direction compared to the cross-machine direction of 34%, indicating higher strain in the geogrid-stabilized sections than in the geotextile-stabilized section. This strain development is a direct result of the distress encountered by the section. Even though it is expected that the geotextile-stabilized section should develop a higher strain because of the cloth-like nature of the stabilization material, the lower level of developed strain indicates lower structural distress, possibly because of the absence of transition layer.

**Table 5.5 Characteristics and properties of geosynthetics used (before and after testing).**

| Material | Direction | Ultimate/Before Testing | | Ultimate/After Testing | |
|---|---|---|---|---|---|
| | | Strength (kN/m) | Elongation (%) | Strength (kN/m) | Elongation (%) |
| Geotextile | Warp | 27 | 23.6 | 18 | 14.8 |
| | Fill | 25 | 9.9 | 25 | 12.5 |
| Geogrid | Machine | 19 | 8.9 | 19 | 12.4 |
| | X-Mach | 33 | 9.3 | 32 | 14.1 |

### *5.9.3 Subgrade Samples*

The subgrade samples were taken in increments of 50 mm each. A total of three samples were taken from 50 mm, 100 mm and 150 mm deep. Two different types of tests were performed on the base course samples collected from the field:

- Standard test method for laboratory determination of water (moisture) content of soil and rock (ASTM D 2216-92).
- Standard test method for particle-size analysis of soils (ASTM D 422-63).

*Moisture content* of the samples was determined using the ASTM D 2216-92 standard. The samples were transported from the site in plastic Ziplock® bags to avoid loss of moisture. All the samples were tested and it was found that the moisture contents of the tested samples varied between 25% and 31%. These measurements were within the range as observed by the moisture sensors in the field (see section 5.3).

*Subgrade Gradations* were performed on all the samples collected from the site. These gradations included the hydrometer analysis for the subgrade material passing No. 200. The gradations for various sections are shown in Appendix L, Figures L 31 through L 39. There are negligible differences between the three sections in terms of the subgrade gradation, indicating that the subgrade fines present in the base course may be pumped from a depth greater than 150 mm inside the subgrade. Since the presence of large quantities of fines is evident in the base course, the possible development of pressure gradients at depths greater than 150 mm is the probable cause of subgrade fines migration (Perkins, 1998). A much larger study to determine exactly the depth at which these fines are pumped from is currently underway at Virginia Tech (Perkins, 1998).

The presence of fines in the base course material is a clear indication of the contamination that occurs in the control and geogrid-stabilized sections. This contamination of the base course is very significant considering the small base course thickness sections (below 100 mm). Long term testing will yield more conclusive results on the pavement sections having thicker base course sections. Although measured pressures at the top of the subgrade indicate similar performance characteristics in both thick and thin base course sections, indicating similar performance characteristics, a quantitative assessment of the transition layer would require long-term testing.

### *5.9.4 Layer Thicknesses*

Once the debris had been cleared from the excavated test section, thickness of the HMA and the base course were measured. Table 5.6 represents the thicknesses of the HMA and the base course determined using two procedures. The first procedure was direct measurement of the thickness of the HMA layer and the thickness of the base

course in the field. The second method was determination of the thickness of the base course by subtracting the thickness of the HMA samples cored from the respective section from the field measured thickness of the base course and HMA. From Table 5.6, differences can be seen in the two methods of measurements. However, the second method appears to be more accurate.

**Table 5.6 Thicknesses of various layers and core specimens from the field.**

| Section | Location | Average HMA* | Average HMA and Base Course* | Average HMA** | Base Thickness Field* | Base Thickness Field** |
|---|---|---|---|---|---|---|
| | | (mm) | (mm) | (mm) | (mm) | (mm) |
| | Inner | 89 | 178 | 65 | 89 | 113 |
| 1 | Middle | 93 | 199 | 75 | 106 | 124 |
| | Outer | 89 | 203 | 83 | 114 | 121 |
| | Inner | 97 | 210 | 82 | 112 | 128 |
| 2 | Middle | 95 | 212 | 95 | 116 | 117 |
| | Outer | 100 | 222 | 99 | 122 | 124 |
| | Inner | 95 | 218 | 86 | 123 | 132 |
| 3 | Middle | 97 | 216 | 95 | 119 | 121 |
| | Outer | 99 | 222 | 110 | 123 | 113 |

* Field measured
** Core measurement

# 6 DEVELOPMENT OF EMPIRICAL-MECHANISTIC PAVEMENT DESIGN

At the start of the 1920's, design and construction of pavements were entirely empirical. Some efforts were made after World War I to design pavements as a function of loading, but it was not until World War II that the explosion of traffic and air travel generated the need for a mechanistic pavement design procedure (Huang, 1993). During World War II the aircraft load on runways increased dramatically, causing the United States Corps of Engineers to develop charts for thickness design of airfield pavements. This pavement design methodology was modified to make it suitable for highway design, where the applications of mechanical loads are more and their intensity less (Yoder and Witczak, 1975).

Methods of flexible pavement design can be grouped into five categories: empirical methods (with or without soil strength tests), limiting shear failure methods, limiting deflection methods, regression methods based on pavement performance and road tests, and mechanistic-empirical methods. A review of the literature makes it clear that pavement design procedures, although changing through extensive development in the past half century, still lack completeness and real life modeling capabilities.

During the past three decades attempts were made to enhance pavement analysis and design by calculating the stresses and strain at critical locations inside a pavement system (namely at the bottom of HMA and at the top of subgrade) and compare them to calculated strain levels at critical locations in the pavement system for determination of failure strains (Ku *et al.,* 1967; Battiato *et al.,* 1977). Various probabilistic equations and regression models were developed, which included in their formulation critical strains and/or the resilient moduli of the pavement layers, resulting in the development of models which have different parameters. Some attention was also given to temperature related failure, including linear elastic fracture mechanics characterization of HMA properties under the influence of temperature (Paris *et al.,* 1963; Majidzadeh *et al.,* 1976; Lytton, 1986; Lytton *et al.,* 1993).

One of the goals of this project was the development of a mechanistic-empirical design procedure for analysis and design of flexible pavements using rutting, fatigue, and temperature as the three main failure modes.

The approach to the problem is to design the pavement for transient thermal and mechanical loading. Viscoelasto-plastic material characterization is the best possible

way to approach the problem. Once the goal is identified, the mechanics of the problem at hand have to be characterized. To develop a flexible pavement design, the field results from a project in Bedford County, Virginia were used to calibrate and compare the final developed design procedure. The concept of transition layer formed at the interface of base course and subgrade (Appea *et al.,* 1998) is also incorporated into the design approach, thereby realizing the importance of geosynthetics. Powerful axisymmetric linear elastic analysis is used to solve the system of equations for mechanical and thermal loading on the pavement structure (van Cauwelaert, 1986; Jones, 1975). Elasto-viscoelastic correspondence principle (EVCP) and Boltzman superposition integral (BSI) are used to convert the elastic solution to its viscoelastic counterpart and also to introduce the dynamic nature of vehicular loading. Pseudo elastoplasticity is introduced into the problem by determining the extent of plastic strain using laboratory experimentation results, and estimating the failure mechanisms, based on accumulated displacements and strains as opposed to the total displacements and strains (recoverable and non-recoverable).

The pavement design approach developed in this design procedure is based on existing techniques as well as some new ones developed to address visco-plasticity and elasto-plasticity. All materials are initially considered linear elastic, but as time progresses, the visco-elasticity, and then visco-plasticity are introduced into the system using various mechanical principles and laboratory results. Base course and subgrade materials are considered as linear elastic (Zaghloul *et al.,* 1993; Barksdale *et al.,* 1989). Also, throughout the design procedure, laboratory results for plastic stains and displacements from the subgrade samples collected from the Bedford project are used to evaluate the accumulated deformations and strains in the subgrade. An attempt is made to eliminate the concept of Equivalent Single Axle Load (ESAL), and replace it with measurable variables, i.e. tire pressure and contact area. The number of passes of specific tire pressures and contact areas in dual, dual tandem or dual tridem manner characterize the dynamic mechanical load intensity applied to the pavement. The developed design approach consists of the following steps:

1. Identification of the input parameters.
2. Calculation of the elastic solution under mechanical loading.
3. Calculation of elastic solution under thermal loading.

4. Conversion of the mechanical and thermal elastic solutions to their viscoelastic counterpart using Elastic viscoelastic correspondence principle (EVCP).
5. Introduction of the dynamic loading for mechanical and thermal loading using Boltzman Superposition Integral (BSI).
6. Combining the effect of mechanical and thermal loading.
7. Accumulation of deformations and plastic strains.
8. Introduce the effect of geotextile-stabilization.
9. Determination of failure mechanisms: rutting, fatigue, and temperature cracking.

## 6.1 Step 1 - Charactarization of the Input Parameters

The design procedure requires the creep curve of HMA or the mechanical viscoelastic model for the determination of the creep curve. These values are fitted to a regression curve using a Dirichlet series. A minimum of seven points (Huang, 1993) is required for a satisfactory fit to the creep data. The evaluation of linear viscoelastic collocation constants is performed in this step. The input variables required for the pavement system are listed as follows:

1. Number of seasons in a year.
2. Global latitude of the project.
3. Trial thickness of various layers.
4. Base temperature in a season.
5. Average dynamic temperature variation in a season.
6. Average speed of the vehicle in a season
7. Number of trucks per season.
8. Number of tires, and their respective locations.
9. Creep compliance, Poisson's ratio of the HMA.
10. Resilient modulus and Poisson's ratio of the base course and subgrade.
11. Interface conditions.
12. Radius of the tires, tire pressure, and global XY coordinates of the center of the tires.

13. Global XY locations of interest.
14. Designation of HMA layer and the last base course layer.
15. Maximum plastic strain magnitudes (%) for HMA layer at different temperatures (5 °C, 25 °C and 40 °C were chosen).
16. Maximum plastic strain magnitude (%) for the subgrade for different confining pressures (35 kPa and 105 kPa).
17. Number of years for analysis.
18. Compounded percentage increase in traffic per year.

## 6.2 Step 2 - Elastic Solution for Mechanical Loading

A linear elastic approach is adopted to solve the problem for evaluation of stresses strains, and displacement under mechanical loading. The HMA layer is considered as visco-elastoplastic, where the base course and the subgrade are considered as linear elastic. Later on in the modeling the subgrade is transformed into a elasto-plastic material, where the level of deformation is determined based on the applied load and the confining pressure. Burmister (1943) first proposed the classical solution to a layered system. The concept of purely elastic solution revolves around the Airy stress function, which defines a contour of unknown quantity, in the vertical and transverse direction of a particular layer, and is given by the following equation.

$$\nabla^4 \varnothing = 0 \tag{6.1}$$

where,

$$\varnothing = \left( \frac{\partial^2}{\partial r^2} + \frac{1}{r}\frac{\partial}{\partial r} + \frac{\partial^2}{\partial z^2} \right)\left( \frac{\partial^2}{\partial r^2} + \frac{1}{r}\frac{\partial}{\partial r} + \frac{\partial^2}{\partial z^2} \right) \tag{6.2}$$

Where, r and z are defined for the axisymmetric coordinate system. In terms of the coefficients A, B, C, D, the function $\phi$ is given by:

$$\varnothing_i = \frac{z^3 J_0(m\rho)}{m^2}\left[A_i e^{-m(k_i - k)} + B_i e^{-m(k - k_{i-1})} + C_i mke^{-m(k_i - k)} + D_i mke^{-m(k - k_{i-1})}\right] \tag{6.3}$$

where,

$\varnothing_i$ = Airy Stress Function for the $i^{th}$ layer;

z = Distance from the top of the HMA to the top of the subgrade;

m = Convergence parameter;

A, B, C, D = Constants of integration matrices, dependent upon the thickness of the layer and the boundary conditions on top and bottom of the layer;

$J_0$ = Bessel function of the first kind and order 0;

ρ = r/z;

r = location of the applied load in the XY plane;

k = h/z; and

h = depth of the point under consideration.

Evaluation of stresses in terms of the Airy stress function is performed using the following equations of elasticity:

$$(\sigma_z)_i = \frac{\partial}{\partial z}\left[(2-v)\nabla^2 \varnothing_i - \frac{\partial^2 \varnothing_i}{\partial z^2}\right] \tag{6.4}$$

$$(\sigma_r)_i = \frac{\partial}{\partial z}\left[v\nabla^2 \varnothing_i - \frac{\partial^2 \varnothing_i}{\partial r^2}\right] \tag{6.5}$$

$$(\sigma_t)_i = \frac{\partial}{\partial z}\left[v\nabla^2 \varnothing_i - \frac{1}{r}\frac{\partial \varnothing_i}{\partial r}\right] \tag{6.6}$$

$$(\tau_{rz})_i = \frac{\partial}{\partial z}\left[(1-v)\nabla^2 \varnothing_i - \frac{\partial^2 \varnothing_i}{\partial z^2}\right] \tag{6.7}$$

$$w_i = \frac{(1+v)}{E}\left[(1-2v)\nabla^2 \varnothing_i + \frac{\partial^2 \varnothing_i}{\partial r^2} + \frac{1}{r}\frac{\partial \varnothing_i}{\partial r}\right] \tag{6.8}$$

$$u_i = -\frac{(1+v)}{E}\left[\frac{\partial^2 \varnothing_i}{\partial r \partial z}\right] \tag{6.9}$$

where,

$(\sigma_z)_i$ = vertical stress in the $i^{th}$ layer;

$(\sigma_r)_i$ = radial stress in the $i^{th}$ layer;

$(\sigma_t)_i$ = tangential stress in the $i^{th}$ layer;

$(\tau_{rz})_i$ = shear stress in the $i^{th}$ layer;

$w_i$ = vertical deformation in the $i^{th}$ layer; and

$u_i$ = horizontal deformation in the $i^{th}$ layer.

This approach of elastic solution was selected because the accuracy of results obtained from Airy stress function approach is comparable in accuracy to the finite element solution (van Cauwelaert, 1986).

The problem as stated above is solved under axisymmetric conditions in 2-D space. This is a close approximation to the 3-D analysis, which requires excessively large amount of time. Due to the complexity of the problem and the need for successive iterations, only methods like finite elements can solve such problems with acceptable accuracy (Zienkiewicz and Taylor, 1994). Airy stress function has an advantage over the finite element approach under axisymmetric conditions, which is the ability to handle multiple axle configurations. Due to the complexity of the problem and the need for repetitive analysis with changing material, as well as mechanical and environmental conditions, the need for a computer based elastic solution becomes more necessary. The problem of solving for stresses, strains and displacements is performed using public domain software called BISAR developed by van Cauwelaert (1986), which can accommodate five layers.

## 6.3 Step 3 - Elastic Solution for thermal Loading

The thermal loading problem was solved using Classical Lamination Theory (CLT). This theory has been in use for fiber reinforced composite materials for decades, but its use in pavements and civil engineering is practically non-existent. The idea behind the analysis in CLT is to divide a structure into several thin sheets called laminas, and then apply the in-plane loading in the form of normal and shear forces, and/or normal or shear moments. If this theory is to be applied in the analysis of the thermal problem for pavements, the applied moments are considered zero, and the applied thermal load in terms of a thermal gradient is applied. This produces normal and shear forces in the laminate. The material properties of the laminate are used to calculate a sixth order square stiffness matrix and is a direct result of the resilient modulus, Poisson ratio, and the material dimensions. Although the problem of solving the laminate is complicated in

fiber reinforced composite materials because of the orthotropic nature of the material, it is relatively easy to simulate an isotropic condition, thus reducing the complexity of the calculation. The resultant forces and moments acting on a laminate are obtained by integration of the stresses in each layer or lamina through the laminate thickness, as in Eq. 6.10 and 6.11.

$$N_x = \int_{-\frac{t}{2}}^{\frac{t}{2}} \sigma_x dz \tag{6.10}$$

$$M_x = \int_{-\frac{t}{2}}^{\frac{t}{2}} \sigma_x z dz \tag{6.11}$$

Actually, $N_i$ (where, i = x, y, xy) is the force per unit length (width) of the cross-section of the laminate and $M_i$ (where, i = x, y, xy) is the moment per unit length. The entire collection of force for an N-layered (see Figure 6.1) system is defined as:

$$\begin{bmatrix} N_x \\ N_y \\ N_{xy} \end{bmatrix} = \int_{-\frac{t}{2}}^{\frac{t}{2}} \begin{Bmatrix} \sigma_x \\ \sigma_y \\ \tau_{xy} \end{Bmatrix} dz = \sum_{k=1}^{N} \int_{z_{k-1}}^{z_k} \begin{Bmatrix} \sigma_x \\ \sigma_y \\ \tau_{xy} \end{Bmatrix}_k dz \tag{6.12}$$

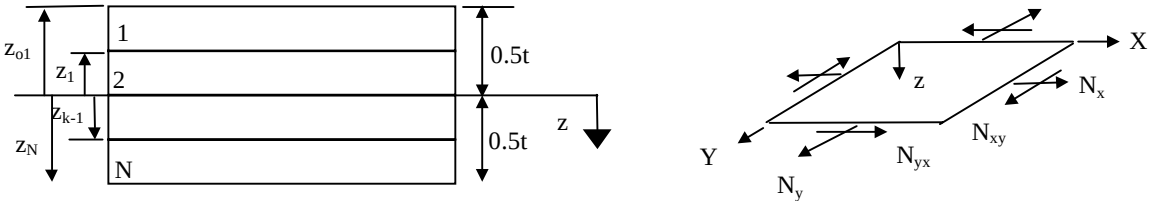


(a) Geometry of an N-layered laminate (b) In-plane forces on a flat laminate

**Figure 6.1 Laminate Geometry and In-plane forces.**

Where, $z_k$ and $z_{k-1}$ are defined in Figure 6.1. The integration in Eq. 6.12 can be rearranged to take advantage of the constant stiffness matrix for a lamina.

$$\begin{Bmatrix}\sigma_x\\ \sigma_y\\ \tau_{xy}\end{Bmatrix}=\begin{bmatrix}Q'_{11} & Q'_{12} & Q'_{16}\\ Q'_{21} & Q'_{22} & Q'_{26}\\ Q'_{16} & Q'_{26} & Q'_{66}\end{bmatrix}_k\left\{\begin{Bmatrix}\varepsilon_x^0\\ \varepsilon_y^0\\ \gamma_{xy}^0\end{Bmatrix}+z\begin{Bmatrix}k_x^0\\ k_y^0\\ k_{xy}^0\end{Bmatrix}\right\} \tag{6.13}$$

The lamina stress strain equations are substituted (Eq. 6.13 into Eq.6.12) to obtain a solvable form for force and moment resultants (see Eq 6.14 and 6.15). Where, $\varepsilon_x^0$, $\varepsilon_y^0$, $\varepsilon_{xy}^0$ are the mid axis strains and the $k_x^0$, $k_y^0$, $k_{xy}^0$ are the mid axis curvatures.

$$\begin{Bmatrix}N_x\\ N_y\\ N_{xy}\end{Bmatrix}=\sum_{k=1}^{N}\begin{bmatrix}Q'_{11} & Q'_{12} & Q'_{16}\\ Q'_{21} & Q'_{22} & Q'_{26}\\ Q'_{16} & Q'_{26} & Q'_{66}\end{bmatrix}_k\left\{\int_{z_{k-1}}^{z_k}\begin{Bmatrix}\varepsilon_x^0\\ \varepsilon_y^0\\ \gamma_{xy}^0\end{Bmatrix}dz+\int_{z_{k-1}}^{z_k}\begin{Bmatrix}k_x^0\\ k_y^0\\ k_{xy}^0\end{Bmatrix}zdz\right\} \tag{6.14}$$

$$\begin{Bmatrix}M_x\\ M_y\\ M_{xy}\end{Bmatrix}=\sum_{k=1}^{N}\begin{bmatrix}Q'_{11} & Q'_{12} & Q'_{16}\\ Q'_{21} & Q'_{22} & Q'_{26}\\ Q'_{16} & Q'_{26} & Q'_{66}\end{bmatrix}_k\left\{\int_{z_{k-1}}^{z_k}\begin{Bmatrix}\varepsilon_x^0\\ \varepsilon_y^0\\ \gamma_{xy}^0\end{Bmatrix}zdz+\int_{z_{k-1}}^{z_k}\begin{Bmatrix}k_x^0\\ k_y^0\\ k_{xy}^0\end{Bmatrix}z^2dz\right\} \tag{6.15}$$

The mid axis strains and curvatures are not functions of depth z and therefore can be removed from Eqs 6.14 and 6.15, thus yielding Eqs 6.16 and 6.17.

$$\begin{Bmatrix}N_x\\ N_y\\ N_{xy}\end{Bmatrix}=\begin{bmatrix}A_{11} & A_{12} & A_{16}\\ A_{12} & A_{22} & A_{26}\\ A_{16} & A_{26} & A_{66}\end{bmatrix}\begin{Bmatrix}\varepsilon_x^0\\ \varepsilon_y^0\\ \gamma_{xy}^0\end{Bmatrix}+\begin{bmatrix}B_{11} & B_{12} & B_{16}\\ B_{12} & B_{22} & B_{26}\\ B_{16} & B_{26} & B_{66}\end{bmatrix}\begin{Bmatrix}k_x^0\\ k_y^0\\ k_{xy}^0\end{Bmatrix} \tag{6.16}$$

$$\begin{Bmatrix}M_x\\ M_y\\ M_{xy}\end{Bmatrix}=\begin{bmatrix}B_{11} & B_{12} & B_{16}\\ B_{12} & B_{22} & B_{26}\\ B_{16} & B_{26} & B_{66}\end{bmatrix}\begin{Bmatrix}\varepsilon_x^0\\ \varepsilon_y^0\\ \gamma_{xy}^0\end{Bmatrix}+\begin{bmatrix}D_{11} & D_{12} & D_{16}\\ D_{12} & D_{22} & D_{26}\\ D_{16} & D_{26} & D_{66}\end{bmatrix}\begin{Bmatrix}k_x^0\\ k_y^0\\ k_{xy}^0\end{Bmatrix} \tag{6.17}$$

where,

$$A_{ij}=\sum_{k=1}^{N}(Q'_{ij})(z_k-z_{k-1}) \tag{6.18}$$

$$B_{ij}=\frac{1}{2}\sum_{k=1}^{N}(Q'_{ij})(z_k^2-z_{k-1}^2) \tag{6.19}$$

$$D_{ij}=\frac{1}{3}\sum_{k=1}^{N}(Q'_{ij})(z_k^3-z_{k-1}^3) \tag{6.20}$$

In Eqs. 6.18 through 6.20, $A_{ij}$ is called the extensional stiffness, $B_{ij}$ is called coupling

stiffness, and $D_{ij}$ is called the bending stiffness. The presence of $B_{ij}$ implies coupling between bending and extension of the laminates. However, if applied moments are equal to zero, then the $B_{ij}$ matrix components are zero, thus simplifying the problem.

In application of these equations to pavements to solve the thermal problem, the same approach as that used in the mechanical load application problem is used. The problem is treated in a visco-elastoplastic manner similar to that discussed earlier for the mechanical loading. If the total unit forces and moments applied to a laminate are the sum of the mechanical and thermal forces and moments, then:

$$N^{Tot} = N^{Mech} + N^{Ther} \tag{6.21}$$

$$M^{Tot} = M^{Mech} + M^{Ther} \tag{6.22}$$

where,

$N^{Tot}$ = Total forces applied;

$N^{Mech}$ = Total mechanical load related forces;

$N^{Ther}$ = Total thermal load related forces;

$M^{Tot}$ = Total moments applied;

$M^{Mech}$ = Total mechanical load related moments; and

$M^{Ther}$ = Total thermal load related moments.

For this particular problem, the mechanical loading related functions are all zero, and the only remnants of Eqs. 6.21 and 6.22 are those related to thermal gradient. Thus, the following expression is used to calculate the forces and moments applied on the body due to thermal gradients:

$$\begin{Bmatrix} N_x \\ N_y \\ N_{xy} \end{Bmatrix}^{Ther} = \sum_{k=1}^{N} \begin{bmatrix} Q'_{11} & Q'_{12} & Q'_{16} \\ Q'_{21} & Q'_{22} & Q'_{26} \\ Q'_{16} & Q'_{26} & Q'_{66} \end{bmatrix}_k \alpha(z_k - z_{k-1})(T_2 - T_1) \tag{6.23}$$

$$\begin{Bmatrix} M_x \\ M_y \\ M_{xy} \end{Bmatrix}^{Ther} = \frac{1}{2} \sum_{k=1}^{N} \begin{bmatrix} Q'_{11} & Q'_{12} & Q'_{16} \\ Q'_{21} & Q'_{22} & Q'_{26} \\ Q'_{16} & Q'_{26} & Q'_{66} \end{bmatrix}_k \alpha(z_k^2 - z_{k-1}^2)(T_2 - T_1) \tag{6.24}$$

where,

$Q_{ij}^{/}$ = Transformed reduced stiffness matrix;

$T_2$-$T_1$ = Applied thermal gradient;

$z_k$-$z_{k-1}$ = Thickness of the lamina; and

$\alpha$ = Coefficient of thermal expansion of HMA.

As, $[N]^{Tot} = [N]^{Ther}$, and $[M]^{Tot} = [M]^{Ther}$, the final equation that has to be solved takes the following form:

$$\begin{bmatrix} A_{11} & A_{12} & A_{16} & B_{11} & B_{12} & B_{16} \\ A_{12} & A_{22} & A_{26} & B_{12} & B_{22} & B_{26} \\ A_{16} & A_{26} & A_{66} & B_{16} & B_{26} & B_{66} \\ B_{11} & B_{12} & B_{16} & D_{11} & D_{12} & D_{16} \\ B_{12} & B_{22} & B_{26} & D_{12} & D_{22} & D_{26} \\ B_{16} & B_{26} & B_{66} & D_{16} & D_{26} & D_{66} \end{bmatrix} \begin{Bmatrix} \varepsilon_x^0 \\ \varepsilon_y^0 \\ \gamma_{xy}^0 \\ k_x^0 \\ k_y^0 \\ k_{xy}^0 \end{Bmatrix} = \begin{Bmatrix} N_x \\ N_y \\ N_{xy} \\ M_x \\ M_y \\ M_{xy} \end{Bmatrix}^{Ther} \quad (6.25)$$

With the mid axis strains and curvatures calculated from Eq. 6.25, the magnitudes of top and bottom of HMA strains can be directly calculated using the following relationships:

$$\varepsilon_x^{\text{top HMA}} = \varepsilon_x^0 + (\text{z coordinate of the top of HMA}) \bullet k_x^0 \quad (6.26)$$

$$\varepsilon_y^{\text{top HMA}} = \varepsilon_x^0 + (\text{z coordinate of the top of HMA}) \bullet k_y^0 \quad (6.27)$$

$$\gamma_{xy}^{\text{top HMA}} = \varepsilon_x^0 + (\text{z coordinate of the top of HMA}) \bullet k_{xy}^0 \quad (6.28)$$

Similarly, the strain at the bottom of HMA layer can be calculated. In order to solve the HMA layer thermal problem the above mentioned technique is used. Before the problem can be solved numerically, it must be noted that HMA is a highly thermally susceptible material, with material properties dependent upon the time and temperature of the surroundings. At high temperature, the surface temperature of HMA is usually above the air temperature, necessitating the need for estimation of the actual thermal gradient at the top of HMA. The following equation is used to evaluate the maximum HMA temperature, as function the air temperature and latitude (SuperPave, 1996).

$$T_{top} = (T_{air} - 0.00618(\text{Latitude})^2 + 0.22891(\text{Latitude}) + 42.2)0.9594 - 17.78 \quad (6.29)$$

where,

Latitude = Latitude in degrees;

$T_{air}$ = Maximum air temperature; and

$T_{top}$ = Temperature 20 mm below the top of the pavement, and considered as maximum.

The first step in the calculation of strains due to thermal loading is to calculate the reduced stiffness and the transformed reduced stiffness matrix (see Eqs 6.30 and 6.31).

$$Q_{11} = \frac{E}{(1-v^2)},\ Q_{12} = \frac{vE}{(1-v^2)},\ Q_{22} = \frac{E}{(1-v^2)},\ Q_{66} = \frac{E}{2(1+v)} \tag{6.30}$$

$$\begin{aligned}
Q'_{11} &= Q_{11}\cos^4\theta + 2(Q_{12}+2Q_{66})\sin^2\theta\cos^2\theta + Q_{22}\sin^4\theta \\
Q'_{12} &= (Q_{11}+Q_{22}-4Q_{66})\sin^2\theta\cos^2\theta + Q_{12}(\sin^4\theta+\cos^4\theta) \\
Q'_{22} &= Q_{11}\sin^4\theta + 2(Q_{12}+2Q_{66})\sin^2\theta\cos^2\theta + Q_{22}\cos^4\theta \\
Q'_{16} &= (Q_{11}-Q_{12}-2Q_{66})\sin\theta\cos^3\theta + (Q_{12}-Q_{22}+2Q_{66})\sin^3\theta\cos\theta \\
Q'_{26} &= (Q_{11}-Q_{12}-2Q_{66})\sin^3\theta\cos\theta + (Q_{12}-Q_{22}+2Q_{66})\sin\theta\cos^3\theta \\
Q'_{66} &= (Q_{11}+Q_{22}-2Q_{12}-2Q_{66})\sin^2\theta\cos^2\theta + Q_{66}(\sin^4\theta+\cos^4\theta)
\end{aligned} \tag{6.31}$$

Where, $Q_{ij}$ are the individual components of the reduced stiffness matrix (3 x 3), and the $Q_{ij}^{/}$ are the individual components of the transformed reduced stiffness matrix (3 x 3). Theta ($\theta$) is the orientation of fibers with respect to the X-axis for fiber reinforced polymers, and in the case of isotropic materials is equal to zero.

## 6.4 Step 4 - Elastic Visoelastic Correspondence Principle (EVCP)

The first step in this process is the Dirichlet fit of the given creep compliance. The given creep compliance is fitted to the following equation:

$$\text{Creep} = G_i \sum_{i=1}^{7} e^{(-\frac{t}{T_i})} \tag{6.32}$$

where,

$G_i$ = Dirichlet Constants;

t = Time in seconds; and

$T_i$ = Relaxation times in seconds.

In order to calculate the Dirichlet constants, the following equation has to be solved

$$[Amat][Amat]^T[Gmat]=[Amat][Dmat] \tag{6.33}$$

where,

$$Amat = \begin{bmatrix} e^{-\left(\frac{0.01}{0.01}\right)} & e^{-\left(\frac{0.01}{0.03}\right)} & e^{-\left(\frac{0.01}{0.1}\right)} & e^{-\left(\frac{0.01}{1}\right)} & e^{-\left(\frac{0.01}{10}\right)} & e^{-\left(\frac{0.01}{30}\right)} & e^{-\left(\frac{0.01}{100}\right)} \\ e^{-\left(\frac{0.03}{0.01}\right)} & e^{-\left(\frac{0.03}{0.03}\right)} & e^{-\left(\frac{0.03}{0.1}\right)} & e^{-\left(\frac{0.03}{1}\right)} & e^{-\left(\frac{0.03}{10}\right)} & e^{-\left(\frac{0.03}{30}\right)} & e^{-\left(\frac{0.03}{100}\right)} \\ e^{-\left(\frac{0.1}{0.01}\right)} & e^{-\left(\frac{0.1}{0.03}\right)} & e^{-\left(\frac{0.1}{0.1}\right)} & e^{-\left(\frac{0.1}{1}\right)} & e^{-\left(\frac{0.1}{10}\right)} & e^{-\left(\frac{0.1}{30}\right)} & e^{-\left(\frac{0.1}{100}\right)} \\ e^{-\left(\frac{1}{0.01}\right)} & e^{-\left(\frac{1}{0.03}\right)} & e^{-\left(\frac{1}{0.1}\right)} & e^{-\left(\frac{1}{1}\right)} & e^{-\left(\frac{1}{10}\right)} & e^{-\left(\frac{1}{30}\right)} & e^{-\left(\frac{1}{100}\right)} \\ e^{-\left(\frac{10}{0.01}\right)} & e^{-\left(\frac{10}{0.03}\right)} & e^{-\left(\frac{10}{0.1}\right)} & e^{-\left(\frac{10}{1}\right)} & e^{-\left(\frac{10}{10}\right)} & e^{-\left(\frac{10}{30}\right)} & e^{-\left(\frac{10}{100}\right)} \\ e^{-\left(\frac{30}{0.01}\right)} & e^{-\left(\frac{30}{0.03}\right)} & e^{-\left(\frac{30}{0.1}\right)} & e^{-\left(\frac{30}{1}\right)} & e^{-\left(\frac{30}{10}\right)} & e^{-\left(\frac{30}{30}\right)} & e^{-\left(\frac{301}{100}\right)} \\ 1 & 1 & 1 & 1 & 1 & 1 & 1 \end{bmatrix};$$

Gmat = Dirichlet constants (7 x 1); and

Dmat = Matrix of Given creep compliance's (7 x 1).

Once the given creep compliance is fitted to the time series, the time temperature shift principle is used to move the creep compliance to the required base temperature. This procedure incorporates low and high seasonal temperature effect into the equation by introducing it into the stiffness matrix. In order to approach reality a greater number of seasons is needed (example 24). The shift factors (time-temperature shift) at 5 °C and 40 °C are required as input, where the 25 °C is considered as reference. The shift factors are fitted to a straight line between 5 °C and 25 °C, and 25 °C and 40 °C, thus providing an interpolating range. The following equation is used to transfer the given creep compliance to another perspective seasonal base temperature.

$$[Dmat]_c = 10^{(Log_{10}[Dmat]_g + A_{TG})} \quad (6.34)$$

where,

$A_{TG}$ = Shift factor at the required temperature;

$[Dmat]_g$ = Creep compliance matrix at given temperature (7 x 1); and

$[Dmat]_c$ = Calculated creep compliance at the required temperature (7 x 1).

Once the given creep compliance has been shifted to the base temperature, the applicable portion of the creep compliance curve covering the seasons is selected in order to be used in the elastic analysis. Figure 6.2 shows a sample creep compliance shift factor curve as a function of the temperature derived for the HMA in the Bedford project.

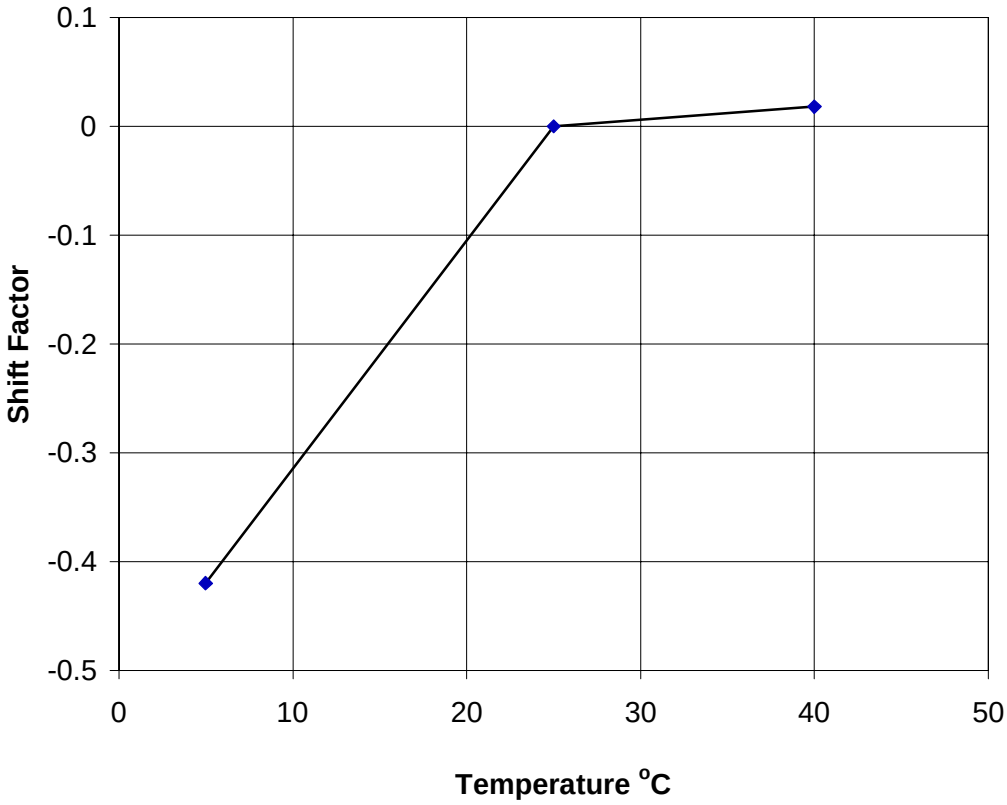


**Figure 6.2 Shift factors for the HMA samples collected from the test section.**

Using the inverse of creep compliance at the base temperature for the season as the current creep modulus, the elastic solution is performed 7 times (the same number of times as the rows of the creep compliance matrix) to obtain seven solutions of vertical stress, tensile strains and displacements at the top of HMA, bottom of HMA, and the top of subgrade. Another important consideration considered at this point is the Poisson's ratio relationship to the temperature in HMA. For this purpose Poisson's ratios for the three temperature ranges of 5 °C, 25 °C and 40 °C are used. Once the solutions for the respective stresses, strains, and displacements is obtained, the process of conversion of the elastic solution to the viscoelastic solution using the Elastic Viscoelastic Correspondence Principle (EVCP) is performed.

The seven solutions now represent the variation of viscoelastic media modulus, Poisson's ratio, and temperature as a function of time and season. The solution at this point in time is strictly linear viscoelastic. The representative solution for Dirichlet constants using the strains and displacements is given by the following equation:

$$\begin{bmatrix} e^{-\left(\frac{0.01}{0.01}\right)} & e^{-\left(\frac{0.01}{0.03}\right)} & e^{-\left(\frac{0.01}{0.1}\right)} & e^{-\left(\frac{0.01}{1}\right)} & e^{-\left(\frac{0.01}{10}\right)} & e^{-\left(\frac{0.01}{30}\right)} & 1 \\ e^{-\left(\frac{0.03}{0.01}\right)} & e^{-\left(\frac{0.03}{0.03}\right)} & e^{-\left(\frac{0.03}{0.1}\right)} & e^{-\left(\frac{0.03}{1}\right)} & e^{-\left(\frac{0.03}{10}\right)} & e^{-\left(\frac{0.03}{30}\right)} & 1 \\ e^{-\left(\frac{0.1}{0.01}\right)} & e^{-\left(\frac{0.1}{0.03}\right)} & e^{-\left(\frac{0.1}{0.1}\right)} & e^{-\left(\frac{0.1}{1}\right)} & e^{-\left(\frac{0.1}{10}\right)} & e^{-\left(\frac{0.1}{30}\right)} & 1 \\ e^{-\left(\frac{1}{0.01}\right)} & e^{-\left(\frac{1}{0.03}\right)} & e^{-\left(\frac{1}{0.1}\right)} & e^{-\left(\frac{1}{1}\right)} & e^{-\left(\frac{1}{10}\right)} & e^{-\left(\frac{1}{30}\right)} & 1 \\ e^{-\left(\frac{10}{0.01}\right)} & e^{-\left(\frac{10}{0.03}\right)} & e^{-\left(\frac{10}{0.1}\right)} & e^{-\left(\frac{10}{1}\right)} & e^{-\left(\frac{10}{10}\right)} & e^{-\left(\frac{10}{30}\right)} & 1 \\ e^{-\left(\frac{30}{0.01}\right)} & e^{-\left(\frac{30}{0.03}\right)} & e^{-\left(\frac{30}{0.1}\right)} & e^{-\left(\frac{30}{1}\right)} & e^{-\left(\frac{30}{10}\right)} & e^{-\left(\frac{30}{30}\right)} & 1 \\ 1 & 1 & 1 & 1 & 1 & 1 & 1 \end{bmatrix} \begin{Bmatrix} G_1 \\ G_2 \\ G_3 \\ G_4 \\ G_5 \\ G_6 \\ G_7 \end{Bmatrix} = \begin{Bmatrix} (R)_1 \\ (R)_2 \\ (R)_3 \\ (R)_4 \\ (R)_5 \\ (R)_6 \\ (R)_7 \end{Bmatrix} \quad (6.35)$$

where,

$R_i$ = Elastic solutions for stresses, strains or displacements for seven creep compliance locations; and

$G_i$ = The seven Dirichlet constants for the particular function (stress, strain or displacement).

With the Dirichlet constants calculated the next step is to use the same formulation as that for creep to calculate the equation for the fitted curve as shown in Eq. 6.36.

$$\text{Response} = G_i \sum_{i=1}^{7} e^{\left(-\frac{t}{T_i}\right)} \quad (6.36)$$

where,

Response = Stress, strain or displacement;

$G_i$ = Dirichlet constants for the particular function;

t = Time in sec; and

$T_i$ = Relaxation time in seconds.

## 6.5 Step 5 - Boltzman Superposition Integral (BSI)

It is noted that the responses calculated in Eq. 6.36 are all under static load, and have to be modified to incorporate the dynamic behavior of the mechanical and thermal loading. In order to convert the static responses into their dynamic counterparts, use of Boltzman superposition integral (BSI) is employed. BSI uses the static magnitude of the response function and multiplies it with the dynamic spikes shape function to obtain the

dynamic response. The shape function is a function of the speed of the vehicle and tire contact radius, and has the following haversine behavior characterized by Eq. 6.37 and shown in Figure 6.3.

$$\text{Dynamic function} = q\sin^2\left[\frac{\pi}{2}+\frac{\pi t}{d}\right] \tag{6.37}$$

where,

q = Maximum intensity of the applied pressure or vertical stress; and

d = Width of the dynamic spread and is a function of speed of the vehicle, and contact radius.

The dynamic spread "d" is calculated by the following simple formulation:

$$S = V.t \tag{6.38}$$

where,

S = Distance of influence of the tire as a function of radius of the tire;

V = velocity of the vehicle; and

t = Spread of the dynamic spike = d.

The duration of the load depends upon the vehicle speed "V" and tire contact radius "a". Since it is reasonable to assume that the load has practically no effect when it is a distance of '6a' from point of origin (Huang, 1993), Eq. 6.38 is modified to the following form:

$$d = \frac{12a}{V} \tag{6.39}$$

Figure 6.3 shows the feedback from Eq. 6.37 when the applied tire pressure is 550 kPa, and the tire radius is 150 mm.

The dynamic application of load is obtained by calculating the area under the curve (see Figure 6.3), and multiplying it with the magnitude of the static response. Eq. 6.40 shows the mathematical representation of application of BSI to evaluate the dynamic response.

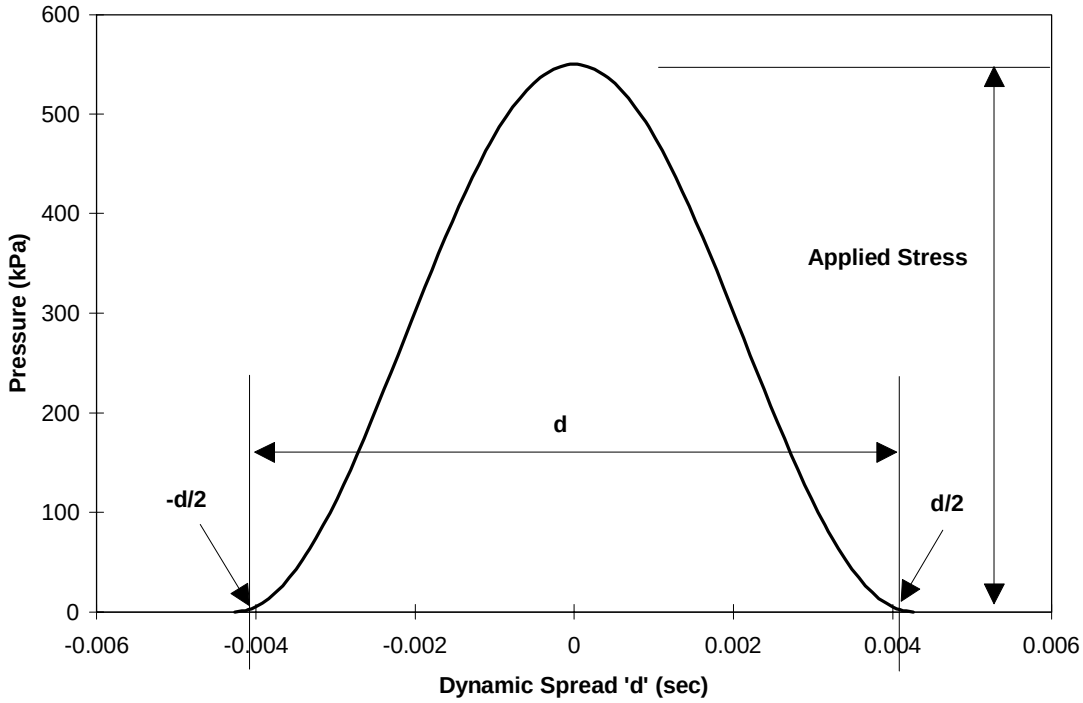


**Figure 6.3 Moving Load variation as a function of time for 550 kPa applied pressure and 150 mm tire radius.**

Figure 6.4 shows the physical meaning of Eq. 6.40. Assuming that the magnitude of the static response is represented by a rectangle, the conversion to the dynamic response is obtained by multiplying the area under the curve of the applied dynamic load, which is a function of tire radius, and speed (Eq. 6.39).

$$\text{Dynamic Response} = \text{Area} \bullet \text{Static Response} \tag{6.40}$$

## 6.6 Step 6 - Superimposing Mechanical and Thermal Loading

The rule of superposition of functions is used to combine the stresses, strains, and displacements due to mechanical and thermal loading. Eq 6.41 through 6.43 show the final states of the calculated functions:

$$\varepsilon_{Total} = \varepsilon_{mechanical} + \varepsilon_{Thermal} \tag{6.41}$$

$$\sigma_{Total} = \sigma_{mechanical} + \sigma_{Thermal} \tag{6.42}$$

$$d_{Total} = d_{mechanical} + d_{Thermal} \tag{6.43}$$

where,

$\varepsilon_{Thermal}$ = Strain due to thermal loading;

$\varepsilon_{Mechanical}$ = Strain due to mechanical loading;

$\sigma_{Thermal}$ = Stress due to thermal loading;

$\sigma_{Mechanical}$ = Stress due to mechanical loading;

$d_{Thermal}$ = Displacement due to thermal loading;

$d_{Mechanical}$ = Displacement due to mechanical loading;

$\varepsilon_{Total}$ = Final strain due to mechanical and thermal loading;

$\sigma_{Total}$ = Final stress due to mechanical and thermal loading; and

$d_{Total}$ = Final displacement due to mechanical and thermal loading.

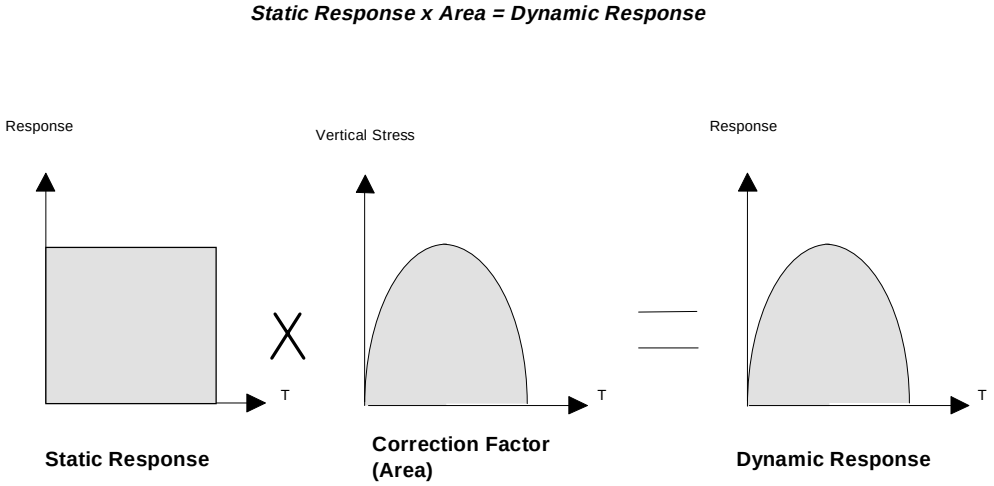


**Figure 6.4 Physical representation of conversion of static response to dynamic response.**

These stresses and strains are evaluated at all the critical locations (i.e. top of HMA, Bottom of HMA, and top of subgrade). Figure 6.5, show the critical locations for evaluations of stresses, strains, and displacements.

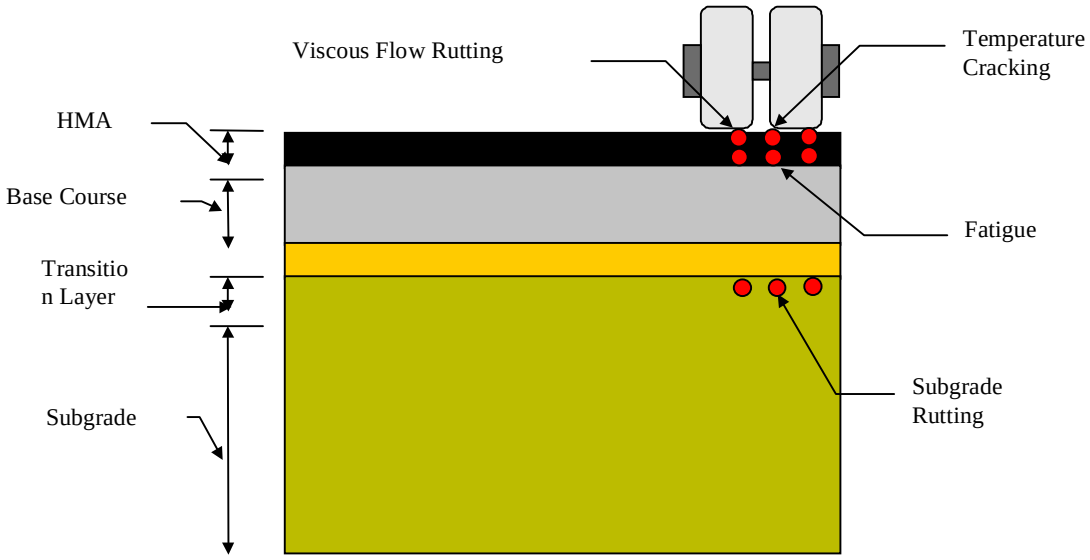


**Figure 6.5 A schematic pavement cross-section with critical locations.**

With these functions (stresses, strains, and displacements) evaluated, the next logical step is to accumulate displacements and strains to determine the mode of rutting and fatigue. Effects of thermal loading are composited into the results, and therefore, the final strain levels must also be checked for the low temperature cracking, which is critical at the top of the HMA layer.

## 6.7 Step 7 - Accumulation of Deformations and Plastic Strains

The failure modes considered in flexible pavements are rutting, fatigue, low temperature cracking, and aggregate contamination. Deformations at the top of HMA are cumulative, are based on the additive viscous and plastic deformation of the entire structure, and are a function of the applied dynamic loading.

The final stresses, strains, and displacements at the end of step 6 are dynamic visco-elastic in nature, and there is no plastic deformation incorporated in the system. Laboratory tests were performed on HMA and the subgrade samples collected from the field project in Bedford, Virginia are used to determine the extent of cumulative deformations and strains in both materials. The test setups employed to determine these values are described in the following sections.

### *6.7.1 HMA Testing*

Marshall size specimens were collected from the field on three separate occasions over the entire span of the project. Some of these specimens were tested for determination of resilient modulus and some were used for determination of creep compliance. In order to determine the magnitudes of visco-plastic deformations, HMA samples that had not been tested before for creep compliance and resilient modulus were placed in the Materials Testing Systems (MTS) machine under a preload of 9 N. Such a low level of preload is necessary not to introduce initial permanent deformation in the specimen and, at the same time, to avoid rocking of HMA sample under dynamic loading. A dynamic load of 440 kPa was applied to the specimen, with a 0.1-sec loading spike and 0.9-sec relaxation spectrum. This dynamic load was applied to the specimen for 1000 seconds and the vertical and horizontal deformation data were measured. The collected data were analyzed and plots for cumulative deformations as a function of time were generated. As HMA is temperature susceptible, three temperatures of 5 °C, 25 °C and 40 °C were selected to perform the tests. Figure 6.6 shows the average accumulated strain (plastic strain) for six specimens (averaged) as a function of time for the three different temperature levels. These accumulated strain levels are used to determine the percentage of plastic strain as a function of time and temperature and to determine the level of plastic strain in the HMA.

### *6.7.2 Subgrade Testing*

Tests using an MTS machine under varying dynamic loads and confining pressures were also performed on the subgrade samples collected from the Bedford project. Analysis of the dynamic data from the field showed that the vertical pressure at the top of the subgrade is between 35 kPa and 105 kPa and the confining pressures ranged between 35 kPa and 140 kPa. Using a preload of 14 kPa, the subgrade samples were tested under dynamic loads of 35 kPa and 105 kPa, and confining pressures of 35 kPa, 70 kPa and 140 kPa for 7000 sec. The resultant plots for percentage accumulated strain as a function of time can be seen in Figures 6.7 and 6.8. These data are essential to determine the contribution of subgrade deformation to the overall rutting in the system.

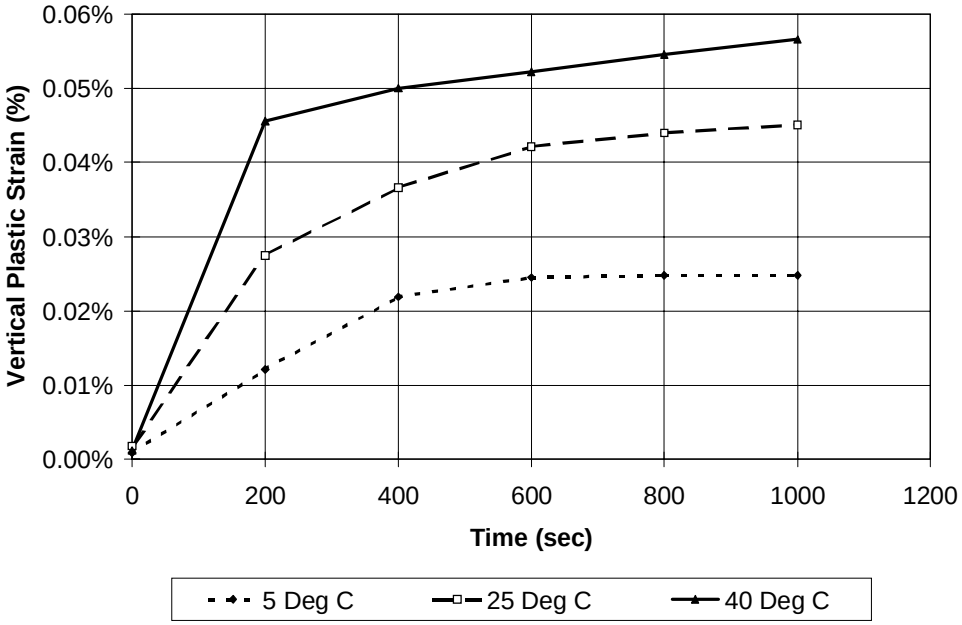


**Figure 6.6 Extent of vertical plastic strain accumulation for HMA samples over time.**

## 6.8 Step 8 – Introduce the Effect of Geotextile Stabilization

The structural contribution of geotextiles is that it separates the base course layer and the subgrade. The base course-subgrade interface in sections without geotextile stabilization has a transition layer formed in the base course. Chapter 5, section 5.5.4 details the transition layer thickness in the section with 100 mm base course thickness. The difference in analysis technique is that pavements without geosynthetics would develop a transition layer, thereby jeopardizing the structural capacity of the system. This impacts the overall performance of the pavement system. The transition layer formed at the interface of the base course and the subgrade possesses a resilient modulus and Poisson's ratio that lies between that of the base course and the subgrade, which can be estimated by standard back-calculation procedure.

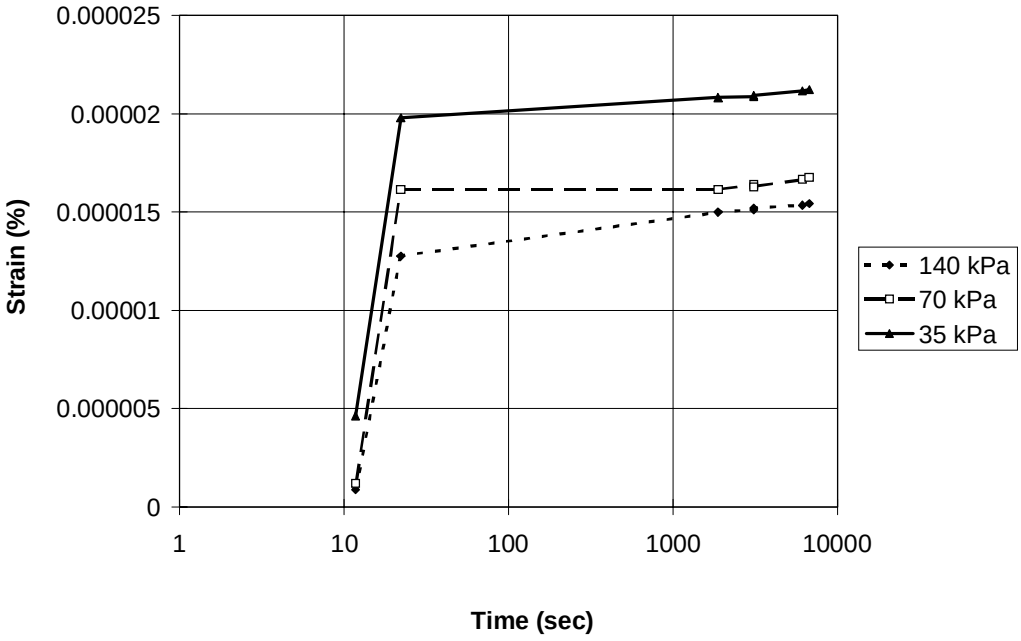


**Figure 6.7 Percentage plastic strain over time (35 kPa).**

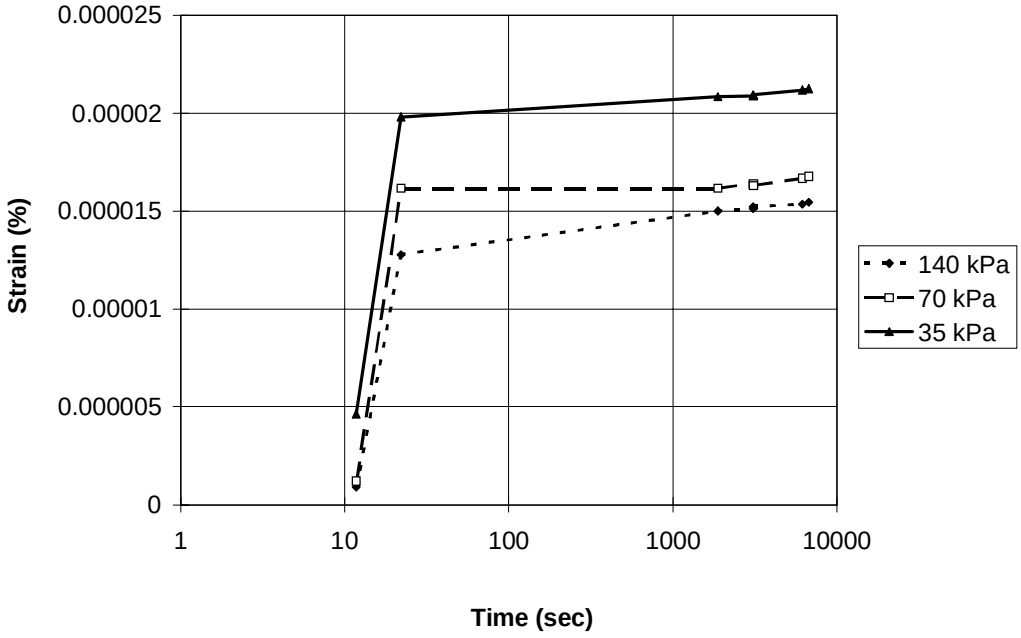


**Figure 6.8 Percentage plastic strain over time (105 kPa).**

## 6.9 Step 9 - Determination of Failure Mechanisms

The aforementioned steps give the final levels of accumulated strains and displacements. Based upon the temperature levels in HMA and the level of confining and applied pressure at the top of the subgrade, the percentage of accumulated plastic strain, and accumulated deformation is calculated from the total strains. Rutting, fatigue and low temperature failure modes are evaluated using comparative analysis of failure strains and displacements to calculated strains and displacements at the end of every season. Each failure case is handled in a different manner, and a brief discussion of the three modes and the evaluation techniques to estimate the life of the pavement based on these functions are described below.

### *6.9.1 Rut Depth*

A realistic estimate of the rut depth (accumulated deformation) is obtained by repeating the procedure described above in steps 1 through 5 at the end of every season. Thus, a final plot of rut depth with time can be obtained, and with a preset cut-off limit, an estimate of the service life of the pavement in terms of rutting can be obtained. At the same time, the contribution of the subgrade rutting to the overall rutting in the entire system can also be determined.

### *6.9.2 Fatigue Life*

It is known that fatigue is a function of frequency of applied loading (Lytton *et al.,* 1988). There are two stages to fatigue cracking in a pavement structure:

- Initiation of crack at the bottom of HMA layer
- Progression of crack through the HMA layer

During the first stage of cracking, the bottom of the HMA layer, which is under tensile loading, develops small micro-cracks. Due to continued loading, these cracks progress to the top of HMA layer. Once the cracks reach the top of the HMA, there is a catastrophic failure in the flexible pavements usually evident on the surface in the form of “alligator cracking.” The determination of the initiation of the crack at the bottom of HMA is a function of the strain level the pavement has achieved at that location. The theory of fatigue failure follows the procedure where the strains are accumulated at the bottom, until the fracture strain in tension is reached. On the time scale, this point is

called crack initiation time. At this point, a micro-fracture develops at the bottom of the HMA layer. In real life, the pavement undergoes healing and crack progression phases, but in almost all cases the time taken by the micro-cracks to progress through the thickness of the HMA layer is fairly small (Lytton *et al.,* 1986). The plastic strain levels are derived directly from the total strain which when reach a preset level, initiate fatigue cracking. This plastic strain level is a unique number for different asphalts, and can be estimated experimentally using the indirect tensile test. Time taken by the crack growth through the thickness of the HMA layer is evaluated using Paris Law for linear elastic fracture mechanics (Lytton *et al.,* 1986; 1988). Paris Law gives crack propagation in terms of cycles of applied loading, stress intensity factor, and material properties. Equation 6.42 gives the numerical representation of Paris Law,

$$\frac{da}{dN} = C(dK)^m \tag{6.42}$$

where,

a = Crack length;

N = Number of cycles;

$m = \frac{2}{f}$;

f = Slope of the log of the creep compliance verses log of time

$C = 10^{\frac{-(m+1.558)}{0.401}}$

K = Stress intensity factor = $(S_{max} - S_{min})\left[ w\text{Tan.}\left( \frac{\pi a}{w} \right) \right]^{0.5}$;

($S_{max}$-$S_{min}$) = Applied load in “psi”; and

w = Twice the thickness of the HMA layer.

Figure 6.9 provides the life of the pavement as a function of “m” for HMA samples collected from the field project. This figure is developed using the Paris law and the creep compliance for the HMA specimens collected from the field. It is evident that the service lives of the pavements lie between three to fifteen years, and the corresponding range of “m” is 0.75 to 1. Once C and m values are obtained, Eq. 6.42 can be solved

numerically with small increments, and the corresponding “N” is obtained.

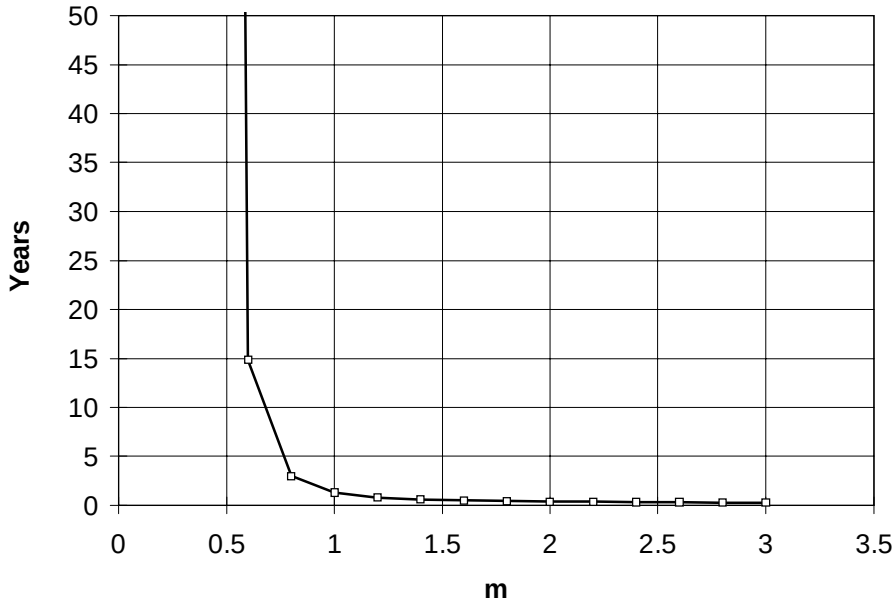


**Figure 6.9 Pavement life as a function of material constant “m”.**

### *6.9.3 Thermal Cracking*

Since HMA is the top most layer in the pavement structure, it receives the maximum amount of thermal gradient, and therefore is most susceptible to cracking due to temperature effects. Thermal cracking is a combined effect of the regular daily thermal gradient and the brittleness caused in the HMA due to the low base temperature. The low base temperature effect is incorporated into the stiffness matrix of the regular problem, where the additional tensile strain caused by the dynamic thermal loading is superimposed onto the plastic strain in the lateral direction caused by the mechanical loading. The procedure is similar to the mechanical problem, where the cumulative compressive strain at the top of HMA is calculated at the end of each season. The cut-off cumulative strain for this mode of failure is also the same as that for fatigue, as both the failure modes are in tension.

The steps described above detail the individual mechanics of the problem. To link these individual steps in a organized sequence can be most efficiently done in the form of a computer program. Figure 6.10 details the link between each step and the

organization of the calculation procedure in a flow chart. The step-wise procedure shown in Figure 6.10 was developed into a computer program that is attached in Appendix M. Appendix M also contains a sample input file and explanation of the input variables in the input file.

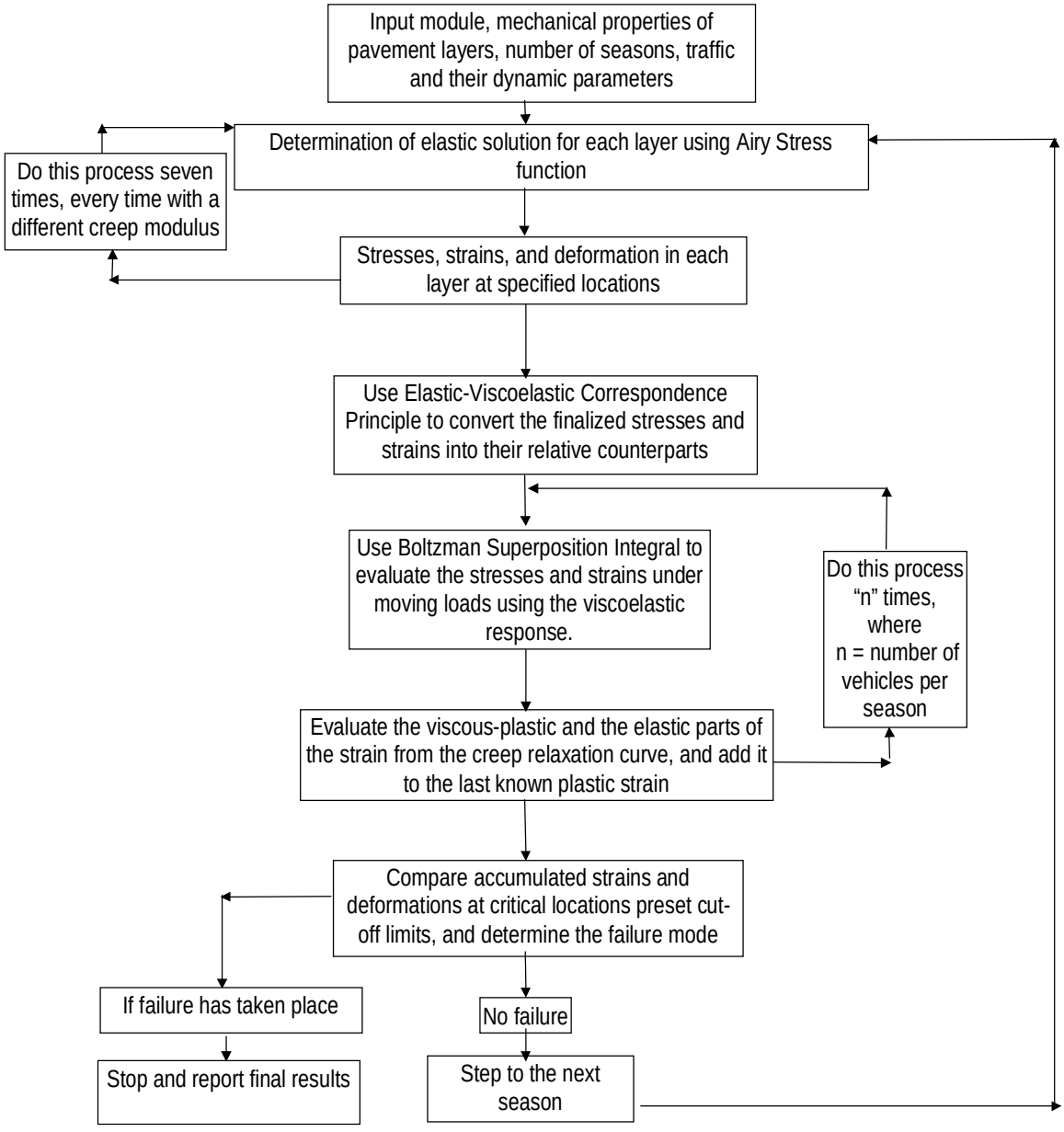


**Figure 6.10 Proposed mechanistic pavement design approach**

## 6.10 Test Problems

Two test problems were evaluated using the analysis and design technique discussed above. Problem 1 consists of a secondary test road, and problem 2 is a typical interstate pavement. Figure 6.11 shows the structural layout of the two test pavement problems. Tables 6.1 and 6.2 provide the trial thicknesses and the material properties of the various layers used in the analysis of the two pavement types.

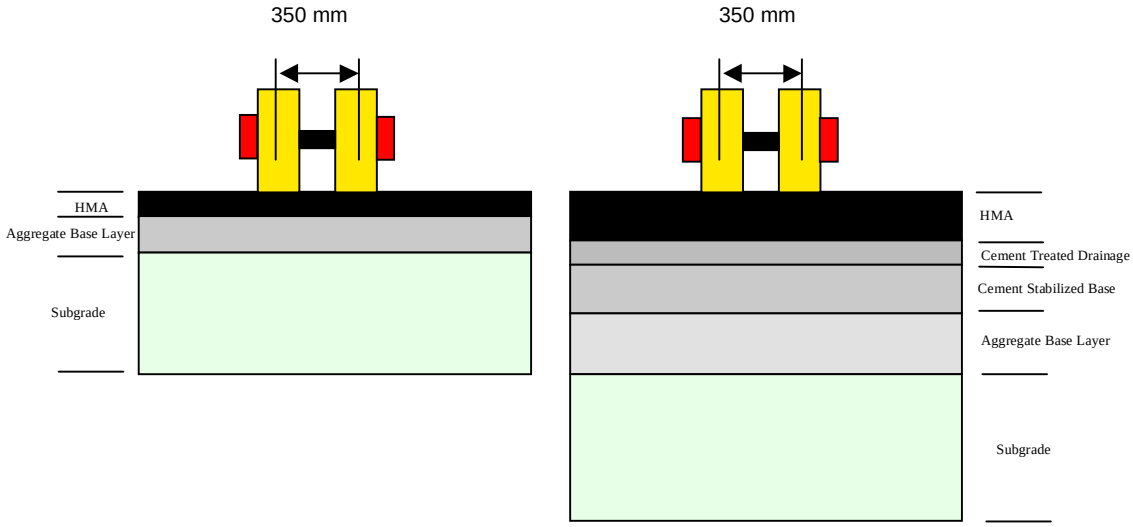


a) Typical Secondary Pavement b) Typical Interstate Pavement

**Figure 6.11 Secondary and interstate pavement systems with mechanical loading.**

**Table 6.1 Trial thicknesses and material properties for the test problems (base layer and subgrade).**

| Layer | Secondary Road | | | Interstate | | |
|---|---|---|---|---|---|---|
| | h (mm) | $M_r$ (MPa) | $v$ | h (mm) | $M_r$+ (MPa) | $v$ |
| **HMA** | 89 | * | 0.32 | 254 | * | 0.32 |
| **Cement Treated Drainage layer** | * | * | * | 76 | 1728 | 0.19 |
| **Cement Stabilized Base Layer** | * | * | * | 230 | 1520 | 0.22 |
| **Aggregate Base Layer** | 100 | 242 | 0.35 | 305 | 276 | 0.35 |
| **Transition Layer** | 50 | 145 | 0.37 | 76 | 172 | 0.35 |
| **Subgrade** | Infinity | 55 | 0.40 | Infinity | 104 | 0.35 |

* Not used in this analysis
\+ Based on typical AASHTO, 1993 coefficients

Figure 6.12 shows the thermal gradient and the lowest base temperatures encountered per season for both the test problems in various seasons. Figure 6.13 shows the number of trucks per season for both the secondary and interstate test sections. Figure 6.14 shows the average speed of the trucks traveling on the two sections over the span of twelve seasons (1 year). The information presented in these Tables and Figures is derived from the data collected over the last three years.

**Table 6.2 Creep compliance for the secondary road and the interstate.**

| Location | Time (sec) | Creep Compliance Secondary Road ($m^2$/kN) | Creep Compliance Interstate ($m^2$/kN) |
|---|---|---|---|
| 1 | 0.01 | 0.000007041 | 0.000000667 |
| 2 | 0.03 | 0.000007600 | 0.000000769 |
| 3 | 0.1 | 0.000008310 | 0.000000909 |
| 4 | 1 | 0.000009538 | 0.000001110 |
| 5 | 10 | 0.000012917 | 0.000001250 |
| 6 | 30 | 0.000031034 | 0.000001430 |
| 7 | 100 | 0.000050483 | 0.000000250 |

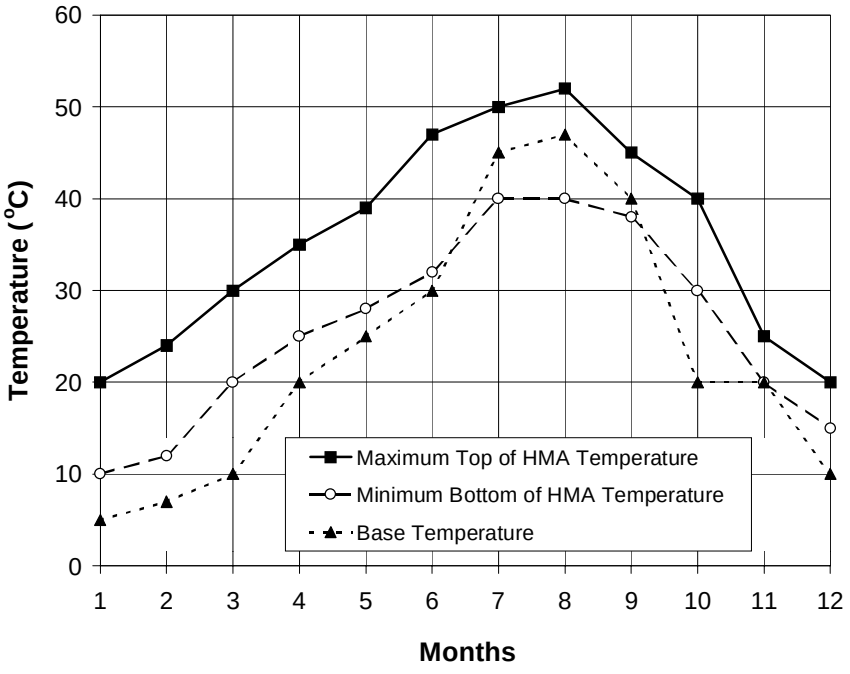


**Figure 6.12 Maximum, minimum and base temperature over the span of 12 seasons (months).**

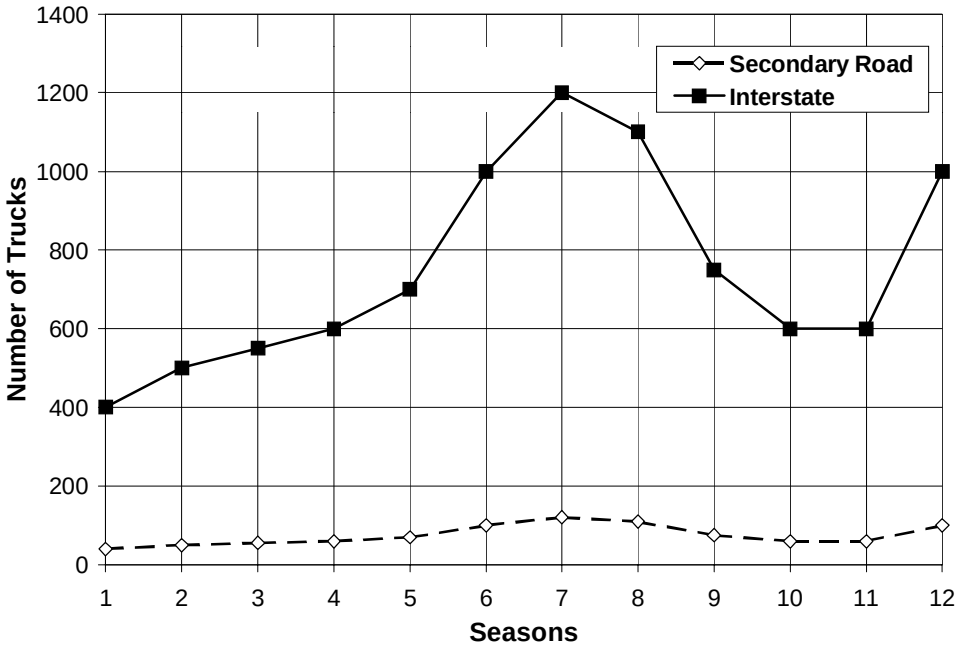


**Figure 6.13 Number of trucks per day passing over the interstate and the secondary road.**

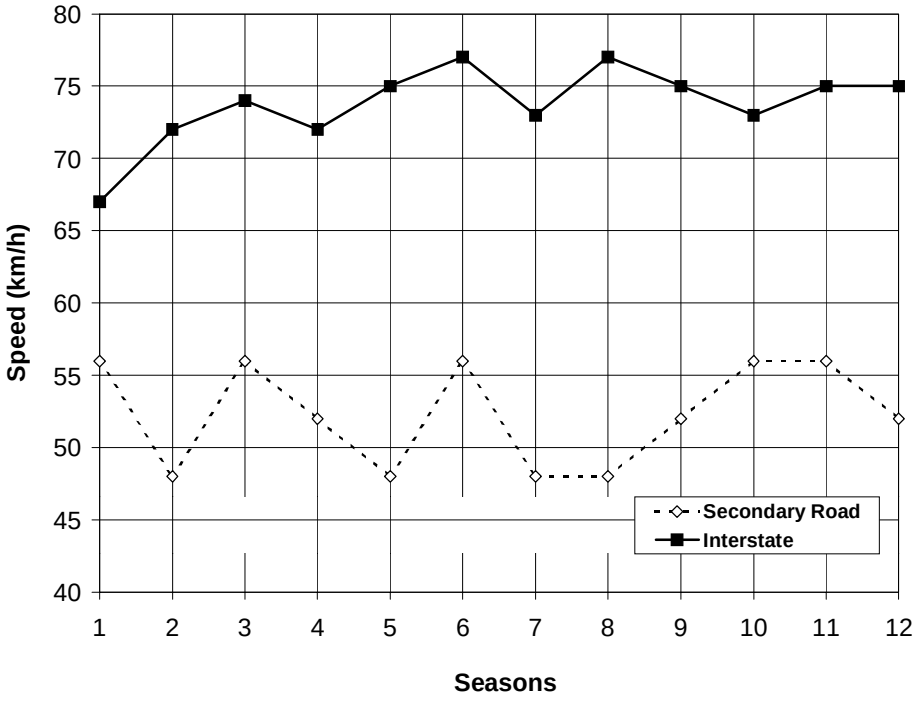


**Figure 6.14 Average speed of the vehicles over the span of 12 seasons for the test problem.**

Table 6.3 details the tire pressures and the contact radius of the trucks, and also the interface slip conditions for the various layers.

**Table 6.3 Tire pressure, contact radius, and interface conditions for the given problem.**

| **Number of Tires** | | 2 | | | |
|---|---|---|---|---|---|
| **Number of XY Locations for Analysis/Design** | | 2 (Fixed) | | | |
| **Coordinates for the XY Locations** | | **Location 1** | | **Location 2** | |
| | | **X** | **Y** | **X** | **Y** |
| | | 0 | 0 | 175 mm | 0 |
| **Number of Depths for XY Locations** | | At Interfaces | | | |
| **Interface Condition (1 = No Slip, 0 = Full Slip)** | | 1 (For All Interfaces) | | | |
| **Tire Pressure** | **Contact Radius** | **X-Coordinate*** | | **Y-Coordinate*** | |
| 550 kPa | 150 mm | 0 | | 0 | |
| 550 kPa | 150 mm | 350 mm | | 0 | |

* Also see Figure 6.11

The latitude and the coefficient of thermal expansion for the HMA layer used in the thermal problem are 57.32° and 3.75 x $10^{-4}$ /°C.

### *6.10.1 Secondary Road*

The problem was run under two conditions:

- With transition layer (control)
- Without transition layer (geotextile stabilized)

The results of the test problem for the two cases are shown in Figures 6.15 through 6.17. Figure 6.15 shows the rut depth for the control and geotextile stabilized sections over the span of 10 years. Setting a cut-off limit of 20-mm for the rut depth, it is seen that the control section achieves the limit in 2.3 years, whereas the geotextile stabilized section achieves the cut-off limit in 3.8 years. There is an increase in service life of the pavement of approximately 1.5 years when stabilization is incorporated into the system. When comparing the calculated rut depths with those measured in the field from the test section in Bedford, Virginia, strong agreement is obtained (see Appendix F, Figure F 1) for the rut depth over the period of time.

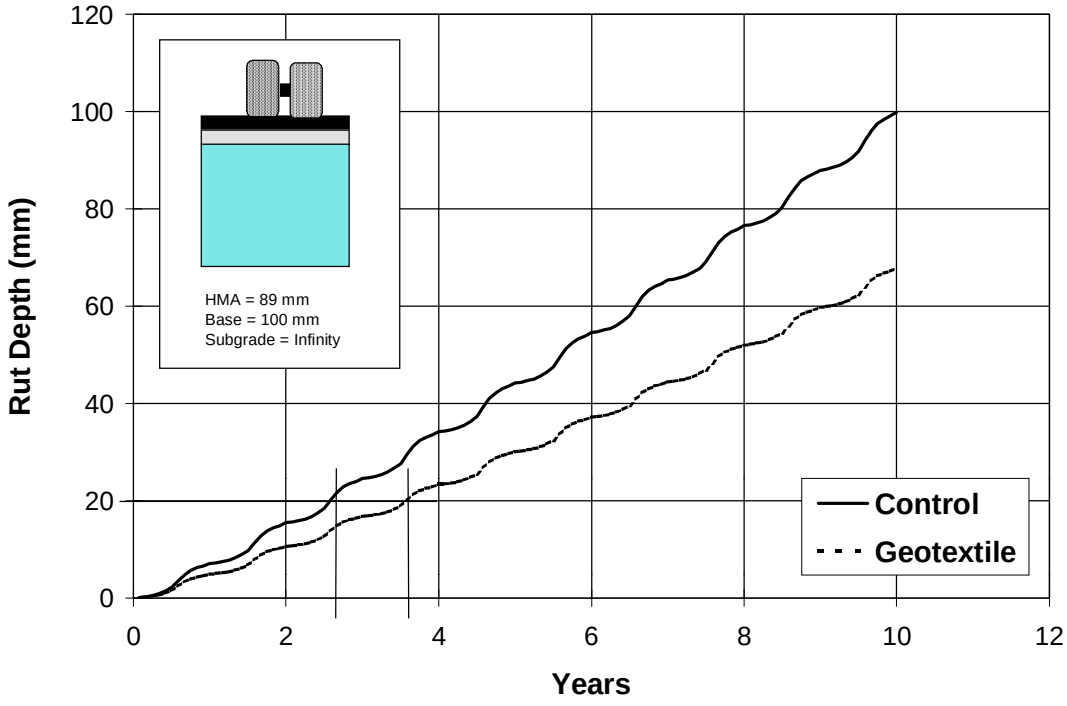


**Figure 6.15 Rut depth for the secondary road.**

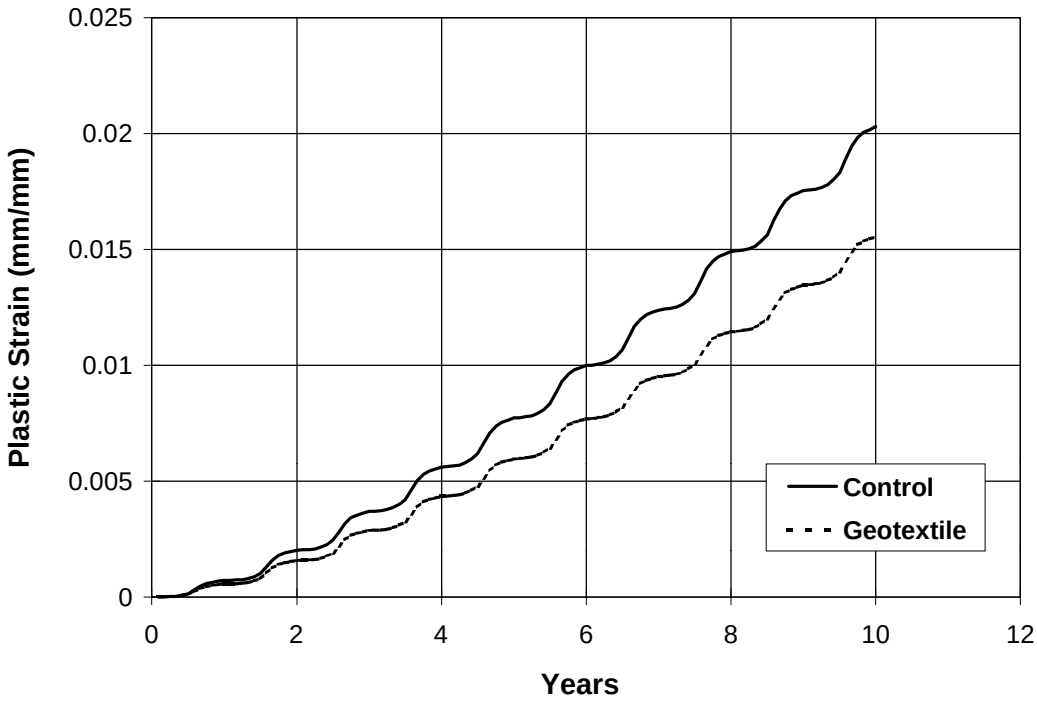


**Figure 6.16 Plastic strain at the top of the HMA layer.**

Figure 6.16 shows the development of plastic strain at the top of the HMA layer due to temperature and mechanical loading. There is some formation of tensile strain at the top of the HMA layer in the first few months, but under the influence of mechanical loading, the state of plastic strain becomes compressive and supersedes the tensile plastic strain before it can be of any damage to the pavement, thereby retarding the formation of any cracks at the top of HMA layer. However, if the thermal loading cycles have much higher gradients, and the stiffness of the HMA is low, then there is a strong possibility of low temperature cracking in pavements. Differences are also seen in the geotextile-stabilized and the control section in terms of the temperature susceptibility. The difference is caused because of the compressive strain induced by the mechanical loading superseding the thermal loading, and the geotextile-stabilized section being structurally stronger.

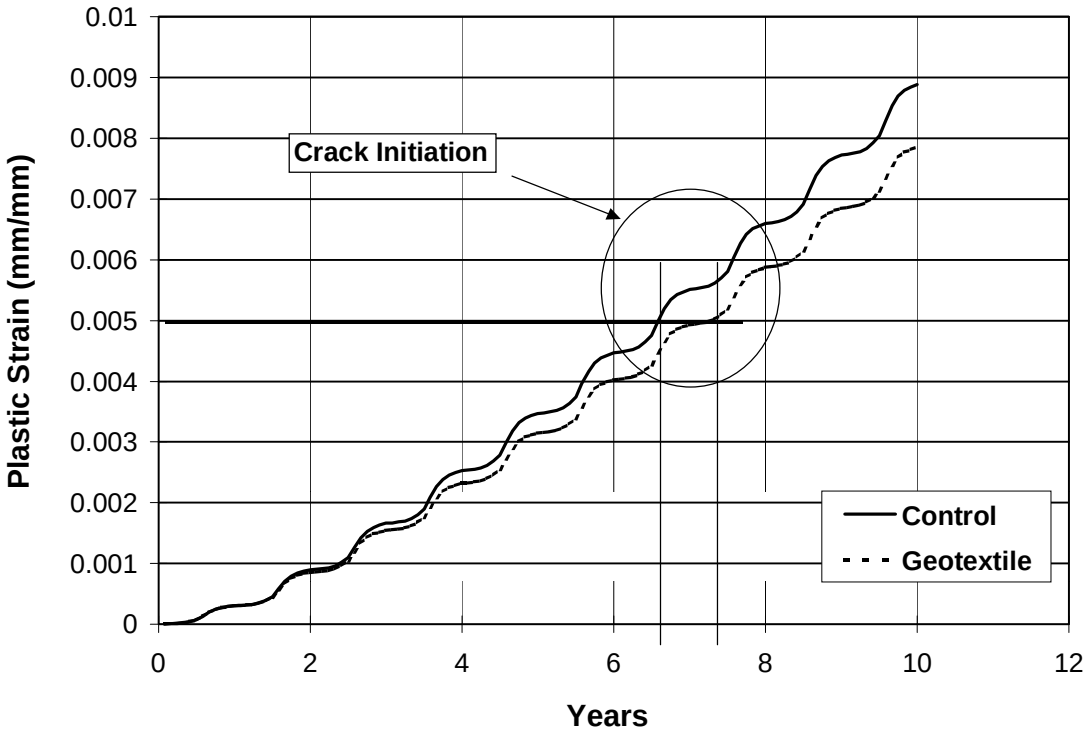


**Figure 6.17 Plastic strain at the bottom of HMA layer.**

Figure 6.17 shows the bottom of the HMA tensile plastic strain as a function of time. This strain is responsible for fatigue cracking in flexible pavements and is used to

determine the initiation of the crack in the HMA layer. Assuming a 0.5% plastic strain as the cut-off limit at which cracking begins, the time taken by the pavement to initiate the first crack is 6.8 years for the control section and 7.2 years for the geotextile-stabilized section. The almost negligible difference in crack initiation times between the two sections indicates that the location of stabilization does not have a strong impact on crack initiation. Using Paris Law, the time needed for the crack to reach the top of the HMA layer is 7 months. Finally, the time for the fatigue cracking to initiate and reach the top of the HMA layer for the control section is 7.2 years for the control section and 7.8 years for the geotextile-stabilized section.

### *6.10.2 Interstate*

The setup of the interstate problem has been defined in Tables 6.1 through 6.3, and Figures 6.11 through 6.14. The test problem for the interstate is composed of significantly large thicknesses compared to the secondary road problem. The difference between the two problems lies in the layer properties, especially creep compliance, plastic strain potential (see Table 6.4), traffic intensity, and vehicle speeds. Figure 6.18 shows the rut depth as a function of time for the interstate section. Due to the stronger structural nature of the interstate section, lower potential of permanent deformation (higher compaction levels), and high speeds of the traveling vehicles, the interstate section develops a 20-mm rut depth at around 8.4 years for both the control and geotextile-stabilized sections. In terms of long term performance, the interstate section does not show any influence from the geotextile-stabilization at the base course subgrade interface. Important reasons for this effect are the large thicknesses of the individual layers and the low influence of mechanical loading on the subgrade. Comparing the contribution of subgrade rutting to the overall rutting behavior of the system, it is found that 99.8% rutting is produced in the HMA (flow and volumetric), whereas the subgrade only contributes 0.2% of the entire rut depth in the system.

**Table 6.4 Maximum percentage of plastic strain for secondary and interstate road.**

| Temperature | 5 °C (%) | 25 °C (%) | 40 °C (%) |
|---|---|---|---|
| **Secondary Road** | 0.025 | 0.045 | 0.057 |
| **Interstate** | 0.014 | 0.021 | 0.0255 |

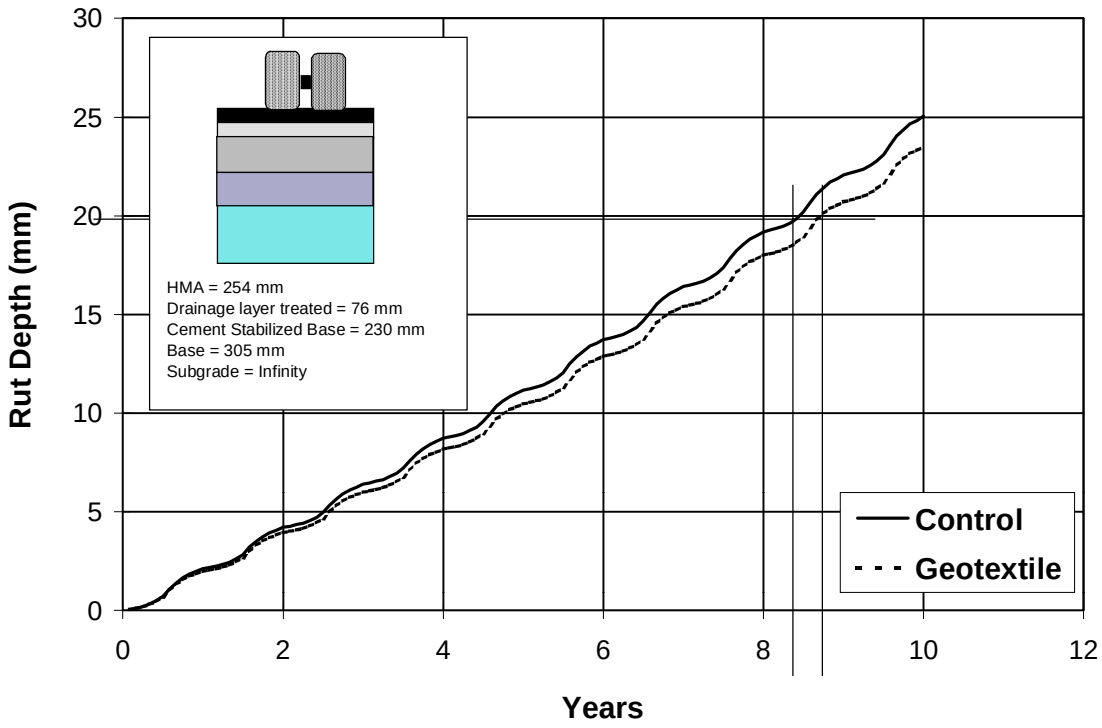


**Figure 6.18 Rut depth for the Interstate road.**

When looking at the thermally induced strain at the top of the HMA layer, it is seen that during the first four months there is a tensile strain accumulation at the top of the HMA layer, but it is superseded by the compressive plastic strain induced by the large intensity of mechanical loading (see Figure 6.19). The maximum compressive strain developed at the top of the HMA layer is 0.2% over the span of 10 years.

Interms of fatigue cracking at the bottom of HMA, the maximum tensile cumulative strain as developed over a period of 10 years, is 0.08% (see Figure 6.20). This intensity is not enough to initiate a crack at the bottom of the HMA layer, and therefore, the pavement will not develop fatigue based cracking in 10 years. Interms of the difference between the geotextile stabilized and non-geotextile stabilized pavements, there is no difference in pavement performance when considering fatigue life.

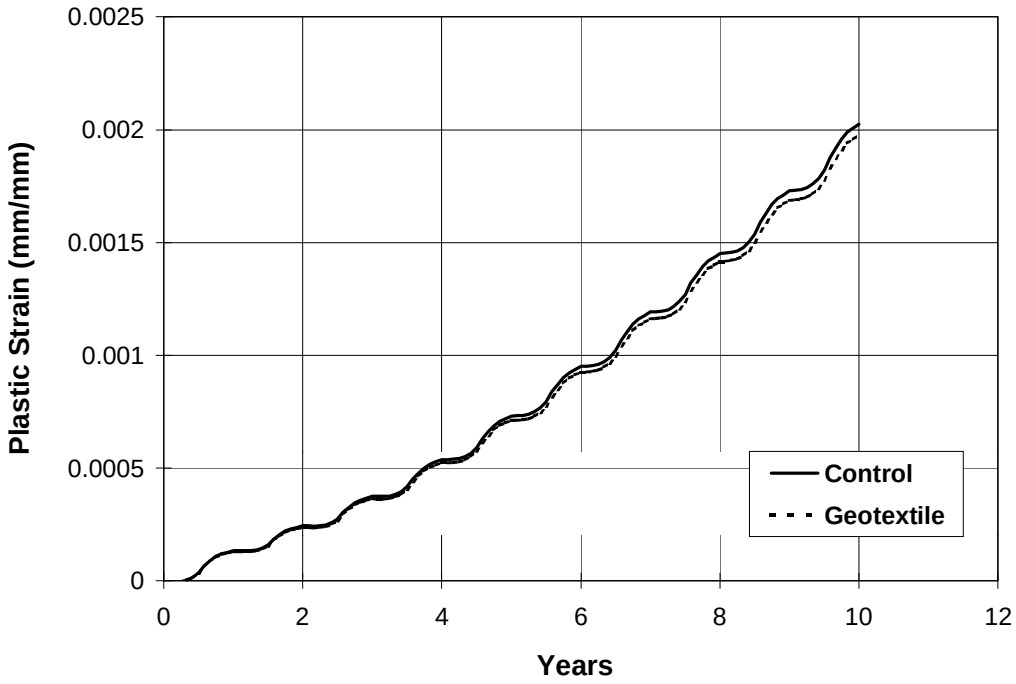


**Figure 6.19 Plastic strain at the top of the HMA layer.**

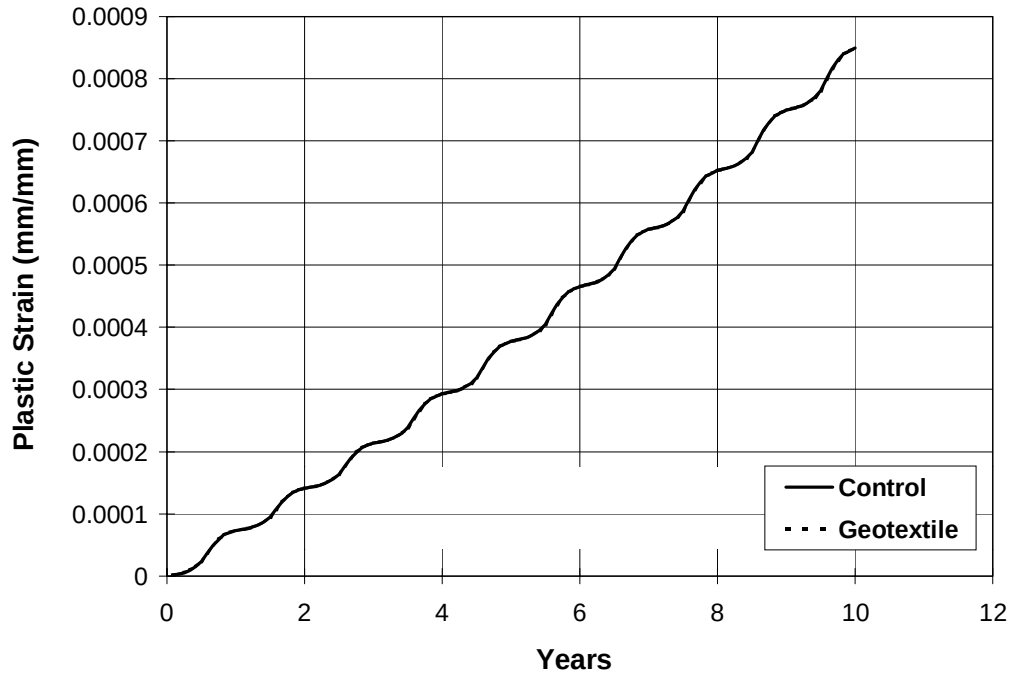


**Figure 6.20 Plastic strain at the bottom of HMA layer.**

# 7 FINDINGS, CONCLUSIONS, AND RECOMMENDATIONS

In June 1994, a 150-m-long secondary road pavement section in Bedford County, Virginia was instrumented. This pavement section was divided into nine individual sections each approximately 15 m long. Sections one through three have a 100-mm-thick limestone base course (VDOT 21-B), sections four through six, have a 150-mm-thick base course, and sections seven through nine have a 200-mm-thick base course. Three sections were stabilized with geotextiles and three with geogrids at the base course-subgrade interface; and the other three were kept as control sections. One of each stabilization category was included in each base course thickness group. The outside wheel path of the inner lane was instrumented with strain gages, pressure cells, piezoelectric sensors, thermocouples, and moisture sensors. A data acquisition system was used to collect instrument responses on site. Section performances, based on the instrumentation response to control and normal vehicular loading, indicated that geosynthetic stabilization provided significant improvement in pavement performance. This finding agreed with other measurements, such as rut depth, ground penetration radar survey and falling weight deflectometer survey.

Falling weight deflectometer testing was performed on all nine sections from October 1994 through July 1997. The measured deflections were analyzed using the MODULUS back-calculation program and further analyzed using other linear elastic and viscoelastic programs to determine the extent of base course contamination by subgrade fines (transition layer). It was determined that the thickness of the transition layer (in the 100-mm-thick base course group) was greater in the control and geogrid-stabilized sections than in the geotextile-stabilized section. This conclusion was also supported by excavation and gradation analysis performed on subgrade and base course samples collected from the 100-mm thick sections in October, 1997.

Finally, a new mechanistic-empirical flexible pavement design method for pavements with and without geosynthetics has been developed. Elasto-viscoelastic material characterization is used to characterize the HMA layer. The field results from Bedford County, Virginia project have been used to calibrate and validate the final developed design procedure. The concept of transition layer formed at the interface of base course and subgrade is also incorporated into the design approach. Powerful axisymmetric linear elastic analysis is used to solve the system of equations for mechanical and thermal loading on the pavement structure. Elasto-viscoelastic correspondence principle

(EVCP) and Boltzman superposition integral (BSI) are used to convert the elastic solution to its viscoelastic counterpart and also to introduce the dynamic nature of vehicular loading. Pseudo-elastoplasticity is introduced into the problem by determining the extent of plastic strain using laboratory experimentation results and estimating the failure mechanisms, based on accumulated strains as opposed to the total strain (recoverable and non-recoverable). The pavement design approach presented in this dissertation is a hybrid of already existing techniques, as well as new techniques developed to address the visco-plastic nature of HMA.

## 7.1 Findings

This project resulted in several findings. These findings are:

1. Master curves can be developed from the piezoelectric sensor responses to determine the approximate vehicle axle load and tire pressure classes.
2. The measured pressure at the base course-subgrade interface for the geotextile-stabilized sections was lower than the geogrid-stabilized and control sections, within a specific base course thickness group.
3. As expected, strain gages at the bottom of HMA did not provide any conclusive evidence of improved sectional performance due to the presence of geosynthetics.
4. Due to the woven nature of the geotextile, strain measurements do not reflect the tensile strain developed in the material.
5. Rutting in the control section (100-mm-thick base course) was more severe than rutting in the geosynthetically stabilized sections.
6. Falling weight deflectometer back-calculation revealed weaker subgrade strength for the geogrid-stabilized and control sections than for the geotextile-stabilized sections over the three-year evaluation period.
7. Hot-mix asphalt (HMA) showed aging over three years as indicated by resilient modulus testing.
8. Ground penetrating radar survey revealed the development of an intermixing layer (transition layer) in control and geogrid-stabilized sections.
9. Excavation of the 100-mm-base course group showed significant contamination (fine intrusion) in the control and geogrid-stabilized sections.

## 7.2 Conclusions

In addition to the aforementioned findings, four main conclusions were drawn from this project (for flexible secondary roads built on a subgrade with a CBR less than 8%) after three and a half years of in-situ and laboratory testing:

1. Geotextile-stabilized sections develop lower distress levels in terms of subgrade pressures and rut depths than geogrid-stabilized and control sections because of their separation capability. Thus, the resilient modulus of the base layer remains intact. This leads to the conclusion that the subgrade fine movement into the base layer when a separator is absent jeopardizes its strength.
2. Field performance, excavation, and gradation of materials at the base course-subgrade interface support the hypothesis regarding the separation function of geotextiles.
3. Based on the results of this study, geotextile-stabilization increases the service life of secondary road pavements by 1.5 to 2 times.
4. A mechanistic-empirical pavement design approach for pavements with and without geosynthetics has been developed.

## 7.3 Recommendations

Based on the findings and conclusions of this study, the following recommendations are made:

1. Long-term monitoring of the pavement performance of the test section is needed.
2. A database of the performance of geosynthetically-stabilized/reinforced flexible pavements will enhance the understanding of geosynthetic effectiveness.
3. The performance of interstate highway pavements with geosynthetics needs to be investigated.
4. Similar research is needed for nonwoven geotextiles and other types of geosynthetic reinforcements and separators.

# 8 REFERENCES


Appea, A. K., Al-Qadi, I. L., Bhutta, S. A., and Coree, B. J., "Quantitative Assessment of Transmission Layer in Flexible Pavements," 77th Transportation Research Board, Paper No. 980994, Washington, DC, 1998.

Abdel Halim, A. O., Haas, R. and Phang, W. A., "Geogrid Reinforcement of Asphalt Pavements and Verification of Elastic Theory," Transportation Research Record 949, Transportation Research Board, Washington DC. 1983.

Abdulshafi, A., and Majidzadeh, K., "Combo Viscoelastic-Plastic Modeling And Rutting Of Asphaltic Mixtures," Transportation Research Record 968, Washington DC. 1984, pp. 19-31.

Al-Qadi, I. L., Brandon, T. L., Valentine, R.J., and Smith, T. E., "Laboratory Evaluation of Geosynthetic Reinforced Pavement Sections," Transportation Research Record 1439, Transportation Research Board, Washington DC. 1994, pp. 25-31.

Al-Qadi, I. L., Brandon, T. L., Smith, T., and Lacina, B. A., "How Do Geosynthetics Improve Pavement's Performance," Proceedings of Material Engineering Conference, San Diego, CA. 1996, pp. 606-616.

Al-Qadi, I. L., Brandon, T. L., Bhutta, S. A., Appea, A. and Lacina, B. L., Field Testing of Geosynthetically Stabilized Pavement Sections, Draft, Second Progress Report Submitted to Amoco Fabrics and Fibers Company and The Virginia Center for Innovative Technology, Virginia Tech, Blacksburg, VA. 1996.

American Association of State Highway and Transportation Officials, "In Situ Soil Improvement Techniques," Task Force 27 Report, Washington, DC. 1990.

American Association of State Highway and Transportation Officials, ASHTO Guidelines for Design of Pavement Structures, Washington, DC. 1993.

Asphalt Institute, Research and Development of the Asphalt Institute Thickness Design Manual, 9th Ed., Research Report 82-2, Lexington, KY. 1982.

Asphalt Institute, Thickness Design: Asphalt Pavements for Highways and Streets, Lexington, KY. 1991.

Austin, D. N., and Coleman, D. M., "A Field Evaluation of Geosynthetic-Reinforced Haul Roads over Soft Foundation Soils," Proceedings of Geosynthetic Conference, Vancouver, BC, Canada. March 30- April 1, 1993, pp. 65-80.

Baker, H. B., Buth, M. R., and Van Deusen, D. A., Minnesota Road Research Project: Load Response Instrumentation Installation and Testing Procedures, Final Report. 1992-94, Minnesota Dept. of Transportation, Maplewood. Physical Research Section. Report No. MN/PR-94/01, Mar. 1994.

Barksdale, R. D., Brown, S. F., and Francis, C., “Potential Benefits of Geosynthetics in Flexible Pavement Systems," National Cooperative Highway Research Program, Report No. 315, Transportation Research Board, Washington, D. C. 1989.

Barksdale, R. D., “Compressive Stress Pulse Times In Flexible Pavements For Use In Dynamic Testing,” Transportation Research Board, Washington DC. Transportation Research Record 345, 1971, pp. 32-44.

Barksdale, R. D., “ Nonlinear Theory For Predicting The Performance Of Flexible Highway Pavements,” Transportation Research Board, Transportation Research Record 337, Washington DC. 1970, pp. 22-39.

Battiato, G., Verga, C., and Ronca, G., “Viscoelastic Deformations In A Two-Layered Paving System Predicted From Laboratory Creep Results,” Transportation Research Record 640, 1977, pp. 34-38.

Battiato, G., and Verga, C., “The AGIP Viscoelastic Method For Asphalt Pavement Design,” Proceedings Of The Fifth International Conference On The Structural Design Of Asphalt Pavements , Ba Arnhem; Netherlands, August 23-26 1982, pp. 59-66.

Bell, L., McCullough, L. M., and Snaith, M. S., "An Experimental Investigation of Base Protection Using Geotextiles," Proceedings, Second International Conference on Geotextiles, Las Vegas, NV. 1982.

Blanchard, A. H., American Highway Engineers Handbook, John Wiley & Sons, NY. 1919.

Bonnaure, F., Gest, G., Gravois, A., and Ugé, P., “A New Method of Predicting the Stiffness Modulus of Asphalt Paving Mixtures," AAPT, 1977.

Bradbury, R. D., Reinforced Concrete Pavements, Wire Reinforcement Institute, Washington, DC, 1938.

Brandon, T. L., Al-Qadi, I. L., Hoffman, S. E., Lacina, B. A., Scarlet, M. J., Weisz, D. E., and Bhutta, S. A., Field Testing of Geosynthetically Stabilized Pavement Sections, Draft, Progress Report Submitted to Amoco Fabrics and Fibers Company and The Virginia Center for Innovative Technology, Virginia Tech, Blacksburg, VA. 1996.

Button, J. W, Epps, J. A., and Lytton, R. L., "Laboratory Evaluation of Fabrics for Reducing Reflection Cracking," Report No. RF 3424-3, Texas Transportation Institute, Texas A&M University,1983.

Broms, B. B., "Triaxial Tests with Fabric-Reinforced Soil," C.R.R.L Int. Soils Text, Paris, Vol. 3, 1977, pp. 129-133.

Carroll, R. G. Jr., Walls, J. C., and Haas, R., "Granular Base Reinforcement of Flexible Pavements Using Geogrids," Geosynthetic Conference '87, New Orleans, LA. 1987, pp.46-57.

Carpenter, S. H., and Lytton, R. L., "Procedure For Predicting Occurrence And Spacing Of Thermal-Susceptibility Cracking In Flexible Pavements," Transportation Research Board, Washington DC. Transportation Research Record 671, 1978, pp. 39-46.

Caesar, J., De Bello Gallico, Oxford University Press. 1996

Cedergren, H. R, Seepage, Drainage, and Flow Nets, 3rd Ed., John Wiley and Sons, Inc., New York NY. 1989.

Cedergren, H. R, "The World's Longest Bathtubs," Civil Engineering, American Society of Civil Engineers, New York NY, September, 1994

Chan, F., Barksdale, R. D., and Brown, S. F., "Aggregate Base Reinforcement of Surfaced pavements" Geotextiles and Geomembranes, Vol. 8, No. 3, Elsevier Science Publishers, 1989, pp. 165-189.

Cheung, Y. K. and Zienkiewicz, O. C., "Plates and Tanks on Elastic Foundations - An Application of Finite Element Method," International Journal of Solids and Structures, Vol. 1, 1965, pp. 451-461.

Chou, Y. T. and Huang, Y .H., "A Computer Program for Slabs with Discontinuities," Proceedings, International Air Transportation Conference Vol. 1 1979, pp. 121-136.

Chou, Y. T. and Huang, Y. H., "A Computer Program for Slabs with Discontinuities on Layered Elastic Solids," Proceedings, 2nd International Conference on Concrete Pavement Design, Purdue University. 1981, pp. 78-85.

Chou, Y. T. and Huang, Y. H., “A Finite Element Method for Concrete Pavements," Proceedings, International Conference on Finite Element Methods, Shanghai, China. 1982, pp. 348-353.

Christopher B. R and Holtz, R. D., Geotextile Engineering Manual, Federal Highway Administration, Washington, DC. 1985.

Christopher, B. R, and Holtz, R. D., "Geotextiles for Subgrade Stabilization in Permanent Roads and Highways," Proceedings, Geosynthetics '9I Conference, IFAI, St. Paul MN. 1991.

Collop, A. C., Cebon, D., and Hardy, M. S. A., “ Viscoelastic approach to rutting in flexible pavements ,” Journal of Transportation Engineering Vol. 121 No. 1, Jan-Feb. 1995, pp. 82-93.

Cowell, M.J. and Sprague, C. J., "Comparison of Pullout Performance of Geogrids and Geotextiles," Proceedings, Geosynthetics '93 Conference, IFAL St. Paul MN. 1993.

Darter, M. I., Hall, K. T. and Kuo, C. M., “Support under Portland Cement Concrete Pavements,” NCHRP Report 372, TRB, 1995.

Dass, W. C. Geosynthetics and Fiber-Reinforced Materials for Airfield Pavements: A Literature Review, Air Force Engineering & Services Center, 1991.

De Jong, D. L., Peutz, M. G. F. and Korswagen, A. R., “Computer Program BISAR. Layered Systems under Normal and Tangential Surface Loads,” Koninlijke/Shell-Laboratorium, External Report AMSR.0006.73, Amsterdam 1973.

DeBerardino, S. J., and Hawkins W. M., “Durability Study of type 3401 Twenty Years After Installation: The Smyrna Road Project,” Transportation Research Record 1439, Washington DC. 1994.

Dewar, S., "The Oldest Roads in Britain," The Countryman, Vol. 59, No. 3, 1962.

Der-Wen, C., Jose, M., and Kenneth, H., “Nondestructive Structural Evaluation of Pavements, ” Transportation Research Record 1355, Transportation Research Board, Washington DC. 1992.

Dondi, G., “Three Dimensional Finite Element Analysis of a Reinforced Paved Road,” Fifth International Conference on Geotextiles, Geomembranes and Related Products, Singapore, September 5-9, pp. 95-100, 1994.

Edwards, J. M. and Valkering, C. P., “Structural Design of Asphalt Pavements for Road Vehicles - The Influence of High Temperatures," Highways and Road Construction., 1974.

Espinoza, R. D., “Soil-Geotextile Interaction: Evaluation of Membrane Support,” Geotextiles and Geomembranes, Elsevier Science Limited, Vol 13. pp. 281-293, 1994.

FHWA, Geotextile Design Examples, Geoservices, Inc. Report to the Federal Highway Administration, Contract No. DTFH-86-R-102, Washington, DC, 1989.

FHWA, Guidelines for Design, Specification, and Contracting of Geosynthetic Mechanically Stabilized Earth Slopes on Firm Foundations, US DOT, FHWA-SA-93025, Washington, D.C, 1993.

“Flexible Pavement Design Guide for Primary and Interstate Roads in Virginia," VDOT, 1969, revised 1995.

Forsyth, R.A., “Synthesis of Highway Practice 189: Pavement Structural Design Practices," NCHRP, TRB, 1993.

Giroud, J. P., and Bonaparte, R, "Design of Unpaved Roads in Trafficked Areas with Geogrids," Proceedings of the Symposium on Polymer Grid Reinforcement, ICE, London, 1984

Giroud, J. P., and Noiray, L., "Geotextile-Reinforced Unpaved Road Design," Journal of the Geotechnical Engineering Division, ASCE, Vol. 107, No. GT 9, pp. 12331254. Discussion: Vol. 108, No. GT12, 1981, pp. 1654-1670.

Gilbert, P. A., Oldham, J. C., and Coffing Jr., L.R, Laboratory Measurement of Pullout Resistance of Geotextiles Against Cohesive Soils, Technical Report GL-92-6, USACOE-WES, Vicksburg, MS, 1992.

Glynn, D. T., and Cochrane, S. R., “Behavior of Geotextiles as Separating Membranes on Glacial Till Soil,” Geosynthetic ‘87 Conference, New Orleans, LA. 1987, pp. 26-37.

Goldbeck, A. T., “Thickness of Concrete Slabs," Public Roads, 1919, pp. 34-38.

Gomez-Achecar, M., and Thompson, M. R., “ILLI-PAVE-Based Response Algorithms For Full-Depth Asphalt Concrete Flexible Pavements,” Transportation Research Record 1095, 1986, Transportation Research Board, Washington DC. pp. 11-18.

GRI Test Methods and Standards, Geosynthetics Research Institute, Philadelphia, PA, 1993.

Gurum, D., Marienfeld, M. and Hayes, C., “Evaluation of a Nonwoven Geotextile versus a Lime-Treated Subgrade in Atoka County, Oklahoma,” Transportation Research Record 1439, Transportation Research Board, Washington, DC. 1994, pp. 7-11.

Guram, D., Marienfeld, M., and Hayes Curtis., “Evaluation of Nonwoven Geotextile Verses Lime-Treated Subgrade in Atoka county, Oklahoma,” Transportation Research Record, No. 1439, Transportation Research Board, Washington DC., 1994.

Hass, R., “Granular Base Reinforcement of Flexible Pavements using Tensar Geogrids, Test Program Results and Development of Design Guidelines,” Tensar Technical Notes, March, 1986.

Hass, R.., Walls, J. and Carroll, R.G., “Geogrid Reinforcement of Granular Bases in Flexible Pavements,” Transportation Research Record 1188, Transportation Research Board, Washington, D.C, 1988.

Harichandran, R. S., Baladi, G, Y., and Yeh, M., “Development of a Computer Program for Design of Pavement Systems Consisting of Bound and Unbound Materials," Department of Civil and Environmental Engineering, Michigan State University, 1989.

Hewes, L. I., American Highway Practice, Vols. 1&2, J. Wiley & Sons, NY, 1942.

Hicks, L. D., “Current Base Design Practices in North Carolina," Proceedings, Highway Research Board, Vol. 26, 1946.

Hoare, D. J., "A Laboratory Study Into the Pumping of Clay Through Geotextiles Under Dynamic Loading," Proceedings, Second International Conference on Geotextiles, Las Vegas, NV. 1982.

Holtz, R D., Christopher, B. R, and Berg, R. R, Geosynthetic Design and Construction Guidelines, National Highway Institute, Publication No. FHWA Hl-95-038, Washington, DC. 1995.

Holtz, R. D. and Sivakugan, "Design Charts for Roads with Geotextiles," Geotextiles and Geomembranes Vol. 5, No. 3, 1987, pp. 191-199.

Huang, Y. H., Pavement Analysis and Design , Prentice Hall, Englewood Cliffs, New Jersey. 1993.

Huang, Y. H. and Wang, S. T., “Finite Element Analysis of Concrete Slabs and Its Implications for Rigid Pavement Design," Highway Research Record 466, HRB, 1973, pp. 55-69.

Huang, Y. H. and Wang, S. T., “Finite Element Analysis of Rigid Pavements with Partial Subgrade Contact," Transportation Research Record 485, TRB, 1974, pp. 1-48.

Huang, Y. H., “Finite Element Analysis of Slabs on Elastic Solids," Transportation Engineering Journal Vol. 100, ASCE, No. TE2, 1974, pp. 403-416.

Heukelom, W. and Klomp, A. J., "Dynamic Testing as a Means of Controlling Pavements During and After Construction," Proceedings of International Conference on the Structural Design of Asphalt Pavements, Ann Arbor, MI. 1962.

Hudson, W. R. and Matlock, H., “Analysis of Discontinuous Orthotropic Pavement Slabs Subjected to Combined Loads," Highway Research Record 131, HRB, 1966, pp. 1-48.

Industrial Fabrics Association International, 1993 Specifier's Guide, Geotechnical Fabrics Report, St. Paul, MN. 1992.

Industrial Fabrics Association International, 1995 Specifier's Guide, Geotechnical Fabrics Report, St. Paul, MN. 1994.

Industrial Fabrics Association International, Geosynthetics Market Report for the United States and Canada, St. Paul, MN. 1994.

Ingold, T. S., Reinforced Earth, Thomas Telford Ltd., London, England. 1982.

Ingold, T. S., and Miler, K. S., Geotextile Handbook, Thomas Telford, London, England. 1988.

Ismail, I., and Raymond, G. P., “Influence of Geosynthetic Reinforcement on Granular Soils,” Transportation Research Record 1474, Washington DC. 1995.

Jorenby, B. N. and Hicks, R G., "Base Course Contamination Limits," Transportation Research Record 1095, Washington, DC. 1986.

Jones, A., and Peattie, K. R., “Surface Deflection on Road Structures,” Symposium on Road Tests for Pavement Design, Lisbon, 1962.

Jones, R, M., Mechanics of Composite Materials, Hemisphere Publishing Corporation, 1975.

Kaplan, E. W., “Effects of Geosynthetics on Soil Properties and of Environment on Pavement Systems,” Transportation Research Record 1188, Washington, DC. 1988.

Kelley, E. F., “Applications of the Results of Research to the Structural Design of Concrete Pavements," Public Roads, 1939, pp. 96-98.

Kennepohl, G., Kamel N., Walls, J., and Hass, R, "Geogrid Reinforcement of Flexible Pavements: Design Basis and Field Trials," Proceedings, Annual Meeting of the Association of Asphalt Paving Technologists, Vol. 54, San Antonio, TX, 1985.

Koerner, G. R., Koerner, R. M. and Martin, J. P., “Design of Landfill-Leachate Collection Filters," Journal of Geotechnical Engineering Vol. 120, No. 10, 1994, pp. 1792-1803.

Koerner, R. M., and Koerner, G. R., “Separation: Perhaps the most underestimated geotextile function,” Geotechnical Fabrics Report, Industrial Fabrics Association International, St. Paul, MN. 1994, pp. 4 - 10.

Koerner, R. M., Designing With Geosynthetics, Third Edition, Prentice-Hall Inc. NJ. 1990.

Ku, A. B., “Stress-Strain Law For Viscoelastic Flexible Pavement Under Temperature Variations,” International Conference of Structural Design of Asphalt Pavements,” 1967, pp. 198-200.

Laier, H., and Brau, G., “The Use of Geotextiles in Road Construction under Intensive Dynamic Loading," Proceedings, 3rd International Conference on Geotextiles Vol. 4, 1986, pp. 995-1000.

Lacina, B. A., “A Study of the Response of Geosynthetic Reinforced Flexible Pavement Test Sections to Dynamic Loading,” Thesis submitted in partial fulfillment for the degree of MS: Virginia Tech, Blacksburg, VA, 1995.

Lawson, C. R., "Some Examples of Separation Geotextiles under Road Pavements," Proceedings of the Institute of Civil Engineers: Transportation, 1992, pp. 197-202.

Li, N, Haas, R, and Kennepohl, G., “Geosynthetics In Asphalt Pavements: Structural, Materials, Design And Performance Considerations,” Proceedings Of The Thirty-Seventh Annual Conference Of Canadian Technical Asphalt Association, Victoria, British Columbia, Nov. 1992, pp. 224-242

Lytton, R. L., Uzan, J., Fernando, G., Roque, R., and Hiltunen, D., “Development and Validation of Performance Prediction Models and Specifications for Asphalt Binders

and Paving Mixes," Strategic Highway Research Program Report No. SHRP A-357, 1993.

Lytton, R. L., and Jayawickrama, P. W., "Reinforcing Fiber Glass for Asphalt Overlays," Texas Transportation Institute, May, 1986

Maag, R. G, Thissen J. A., and Heinen, R. F., "Petromat Performance on Flexible and Composite Pavements," Kansas Department of Transportation, 1986.

Majidzadeh, K., Ilves, G. J. and Sklyut, H., Mechanistic Design of Rigid Pavements, Development of the Design Procedure, Vol. 1, Report No. FHWA-RD-86-124, Vol. 2, Design and Implementation Manual, Federal Highway Administration, 1984.

Majidzadeh, K. C., Ramasamooj, C., and Karakouzian, M., "Application of Fracture Mechanics for Improved Design of Bituminous Concrete," Report No. FHWA-RD-76-91, Vol. 1, June, 1976.

Marchionna, A., Cesarini, M., Fornaci, M. C., and Malgarini, M., "Pavement Elastic Characteristics Measured By Means Of Tests Conducted With The Falling Weight Deflectometer," Transportation Research Record 1007,Transportation Research Board, Washington DC. 1985, pp. 46-53.

May, R. W., Witczak, M. W., and Moossazadeh, J., Brown, S. F., Pappin, J. W., "Layered Pavement Systems," Transportation Research Record 810, Transportation Research Board, Washington, DC. 1981.

McCullough, B. F., Van Til, C. J., and Hicks, R. G., "Evaluation of AASHO Interim Guides for Design of Pavement Structures," NCHRP Report 128, 1972.

McDowell, C., Triaxial tests in Analysis of Flexible Pavements," Highway Research Board, Research 16-B, 1954.

Miura, N., Sakai, A., Taesiri, Y., Yamanouchi, T. and Yasuhura, K., "Polymer Grid Reinforced Pavement on Soft Clay Grounds" Geotextiles and Geomembranes, Vol. 9, pp. 99-123, 1990.

Mukhtar, M. T., and Dampsey, B. J., "Interlayer Stress Absorbing Composite for Mitigating Reflection Cracking in Asphalt-Concrete Overlays," Report No. UILU-ENG-96-2006, Illinois Department of Transportation, 1996.

Ningyuan, L., Hass, R., and Kennepohl, G., “Geosynthetics in Asphalt Pavements: Structural, Materials, Design and Performance Considerations,” Proceedings of the Annual Conference of Canadian Technical Asphalt Association, 1992, pp. 224-242.

Older, C., “Highway Research in Illinois," Transactions, ASCE, Vol. 87, 1924, pp. 1180-1222.

Paris, P. C., and Erdogan, F., “A Critical Analysis of Crack Propagation Laws,” Transactions of the ASME, Journal of Basic Engineering, Series D 85, No 3, 1963.

Palmer, L. A., and Barber, E. S., “Soil Displacement under a Circular Loaded Area," Proceedings, Highway Research Board, Vol. 20, 1940, pp. 279-286.

Perkins, K. E., and Brandon, T. L., “Performance Of Soil-Geotextile Systems In Dynamic Laboratory Tests,” Presented at the 77th Annual Meeting of The Transportation Research Board, Washington DC, January 11-15, 1998.

Petit, C., Caperaa, S., and Michaut, J-P "Influence of Modulus Ratio on Crack Propagation in Multi-layered Pavements," E & FN Spon, London,1996, pp.220-227.

Pickett, G., and Ray, G. K., Transactions, ASCE, Vol. 116, 1951, pp. 49.

Portland Cement Association, Concrete Pavement Design, 1951, 1966 and 1984.

Powel, B., and Mohney, J., “Durability of Geotextiles Used in the Reinforcement of Walls and Road Subgrade,” Transportation Research Record, No. 1439, Washington DC., 1994.

Proceedings, 3rd International Road Congress, New York, 1913.

Predoehl, N. H, "Evaluation of Paving Fabric Test Installation in California-Final Report," Draft, California Department of Transportation, Translab. 1989.

Rao, C. S., “Finite Element Method for Structural Design of Heavy Duty Granular Pavements,” Journal of Computers and Structures, Vol. 40, No. 5, 1991, pp. 1223-1233.

Rowe, G. M., Brown, S. F., Sharrock, M. J., and Bouldin, M. G., “Visco-Elastic Analysis of Hot Mix Asphalt Pavement Structures,” 74th Annual Transportation Research Board Meeting, Washington DC. Jan 22-28, 1995.

Saxena, S. K., “Pavement Slabs Resting on Elastic Foundation," Highway Research Record 466, HRB, 1973, pp. 163-178

Sebealy, P., Tabatabaie, N., Kulakowski, B., and Scullion, T., Instrumentation of Flexible Pavements-Field Performance of Selected Sensors, Final Report No. FHWARD-91-094, Pennsylvania State University, State College, PA, 1991.

Sehn, A L. and Duncan, J.M., "Experimental Study of Earth Pressures on Retaining Structure," Geotechnical Engineering Division, Dept. of Civil Engineering, Virginia Polytechnic Institute and State University, Blacksburg, VA, 1990.

Shaler, N. S., American Highways, The Century Book Co., NY, 1896.

Sharma, M. G., Kenis, W. J., and Mirdamadi, M., "Evaluation Of Mechanical Parameters Of In-service Pavements From Field Data," Proceedings Of Sixth International Conference, Structural Design Of Asphalt Pavements, Volume I, University Of Michigan, July 13-17, 1987, Ann Arbor, MI. pp. 710-724.

"Shell Design Charts for Flexible Pavements," Koninklijke/Shell-Laboratorium, Amsterdam, Netherlands. 1963.

Siel, B. D., Tzong, W. H., and Chou, N. N. S., "In-Soil Stress-Strain Behavior of Geotextile," Geosynthetic '87 Conference, New Orleans, LA. 1987, pp. 260-265.

Smith, T. E.,, Laboratory Behavior of Geogrid and Geotextile Reinforced Flexible Pavement, Thesis submitted in partial fulfillment for the degree of MS: Virginia Tech, Blacksburg, VA, 1994.

Tabatabaie, A. M. and Barenberg, E. J., Longitudinal Joint Systems in Slip-Formed Rigid Pavements, Vol. 3; Users Manual, Report FAA-RD-79-4, III, U.S. Department of Transportation, 1979.

Tabatabaie, A. M. and Barenberg, E. J., "Structural Analysis of Concrete Pavement Systems," Transportation Engineering Journal, ASCE, Vol. 106, TE6, 1980, pp. 493-506.

Taylor, D. W., Fundamentals of Soil Mechanics, John Wiley and Sons, Inc., New York NY, 1948.

Teller, L. W., and Sutherland, E. C., The Structural Design of Concrete Pavements," Reprints from Public Roads, Vols. 16, 17 and 23. 1935-1943.

"Thickness Design, Flexible Pavements for Streets and Highways," The Asphalt Institute, Manual Series No. 1, 1954 - 1969, 1981, 1991.

Tsai, W. S., Savage, B. M., Holtz, R. D., Christopher, B. R., and Allen, T. M., "Evaluation of Geotextiles as Separators in a Full-Scale Road Test," Proceedings of Geosynthetic Conference, Vancouver, BC, Canada. March 30-April 1, 1993, pp.35-48.

Tayabji, S. D. and Colley, B. E., Analysis of Jointed Concrete Pavement, Report No. FHWA-RD-86-041, Federal Highway Administration, 1986.

Ullidtz, P., and Busch, C., “Laboratory Testing Of a Full-Scale Pavement: The Danish Road Testing Machine”, Transportation Research Board, Transportation Research Record, Issue No. 715, 1979.

van Zanten, R. V., Geotextiles and Geomembranes in Civil Engineering, A. A. Balkema, Rottingham, Netherlands. 1986.

Verga, C, Battiato, G, and Ronca, G., “Deformability Of Flexible Pavements Subjected To Repeated Moving Loads,” Transportation Research Board, Washington DC. Transportation Research Record, Issue No. 572, 1976, pp. 97-110.

Vitruvius, “De Architecture," Dover Publications, 1914, 1960.

Vokac, R., “Thickness of Surface and Base Courses for Flexible Pavements," Proceedings, Highway Research Board, Vol. 23, 1943.

Walter, J., Fabrics as a Separation Layer, Oregon State University, Corvallis, OR, 1982.

Webster, S. L., Geogrid Reinforced Base Courses for Flexible Pavements for Light Aircraft, Report No. GL-93-6, Report for US Department of Transportation / Federal Aviation Administration / Department of the Army, US Army Corps of Engineers Waterways Experiment Station, Vicksburg, MS, 1991.

Westergaard, H. M., “Analysis of Stresses in Concrete Pavement due to Variations in Temperature," Proceedings, Highway Research Board, Vol. 6, 1926, pp. 201-215.

Westergaard, H. M., “Stresses in Concrete Pavements Computed by Theoretical Analysis," Public Roads, Vol. 7., 1926, pp. 25-35.

Westergaard, H. M., “Theory of Concrete Pavement Design," Proceedings, Highway Research Board, Part I, 1927, pp. 175-181.

Westergaard, H. M., “Analytical Tools for Judging Results of Structural Tests of Concrete Pavements," Public Roads, Vol. 14, 1933, pp. 185-188.

Westergaard, H. M., “Stresses in Concrete Runways of Airports," Proceedings, Highway Research Board, Vol. 19, 1939, pp. 197-202.

Westergaard, H. M., “Stress Concentrations in Plates Loaded over Small Areas," Transactions, ASCE, Vol. 108, 1943, pp. 831-856.

Westergaard, H. M., “New Formulas for Stresses in Concrete Pavements of Airfields," Transactions, ASCE, Vol. 113, 1948, pp. 425-444.

Wise, W. A., “Flexible pavement design with Cone Device," Highway Research Board, Bulletin 114, 1955.

Witzcak, M. W., “Design of Full-depth Asphalt Airfield Pavements," Asphalt Institute Research Report 72-2, 1972.

Yang, C., and Yu, X., "Mud-Pumping Prevention of Railway Subgrade by Using Geotextiles," Proceedings of the Twelfth International Conference on Soil Mechanics and Foundation Engineering, Rio de Janeiro, Brazil, 3, 1989, pp. 1693-1696.

Yoder, E. J., Witczak, M. W., Principles Of Pavement Design, Second Edition, John Wiley and Sons, Inc. New York, 1975.

Zaghloul, S., White, T., “Use of Three-Dimensional, Dynamic Finite Element Program For Analysis Of Flexible Pavements,” Transportation Research Board, Washington DC., Transportation Research Record, Issue No. 1388, 1993, pp. 60-79.

Zienkiewicz, O. J., and Taylor, R. L., The Finite Element Method, Fourth Edition, Volume II, MacGraw Hill International (UK) Limited, 1994.

# APPENDIX A

# MATERIAL CHARACTERIZATION

**Table A 1 Results of Atterberg limits tests on subgrade soil.**

| Sample No. | Color | LL | PL | PI | USCS |
|---|---|---|---|---|---|
| T1 B3 | Yell. - Brn. | 40.3 | 36.7 | 3.6 | ML |
| T3 B1 | Yell. - Brn. | 41 | 37 | 4 | ML |
| T3 B3 | Yell. - Brn. | 41.6 | 36 | 5.6 | ML |
| T2 B1 | Red - Brn. | 68.3 | 31 | 37.3 | CH |
| T1 B2 | Red - Brn. | 55.8 | 28.3 | 27.5 | CH |
| T1B1 | Red - Brn. | 58.4 | 29.1 | 29.3 | CH |

**Table A 2 Specific gravity test results.**

| Material | Sample No. | Gs | Average Gs |
|---|---|---|---|
| Base Course (GW) | All | 2.78 | 2.78 |
| Subgrade, ML | T1 B1 | 2.75 | |
| Subgrade, ML | T3 B3 | 2.74 | 2.74 |
| Subgrade, ML | T3 B2 | 2.74 | |
| Subgrade, CH | T1 B2 | 2.78 | |
| Subgrade, CH | T1 B1 | 2.78 | 2.77 |
| Subgrade, CH | T2 B2 | 2.76 | |

**Table A 3 Average field dry densities and water contents of subgrade soil by nuclear methods (ASTM D 3017 – 96e1).**

| Section No. | Wet Density (kN/m3) | Dry Density (kN/m3) | Water Content (%) |
|---|---|---|---|
| 1 | 18.1 | 14.1 | 28.7 |
| 2 | 18 | 13.8 | 30.3 |
| 3 | 17.9 | 14.4 | 24 |
| 4 | 17.2 | 13.4 | 28.4 |
| 5 | 17.2 | 13.9 | 23.8 |
| 6 | 17.9 | 14.1 | 26.3 |
| 7 | 18.6 | 14.3 | 29.9 |
| 8 | 18.9 | 14.6 | 29 |
| 9 | 17.7 | 13.5 | 31.1 |

## Table A 4 Subgrade resilient modulus calibration one (laboratory results).

**Bulk stress calculation**

| Base Thickness (mm) | Measured Vertical Stress $\sigma_V$ (kPa) | Horizontal Stress $\sigma_H$ (kPa) | Deviator Stress (kPa) |
|---|---|---|---|
| 100 | 129.9 | 46.8 | 83.1 |
| 150 | 94.0 | 33.9 | 60.2 |
| 200 | 80.8 | 29.1 | 51.7 |

**Resilient modulus from various laboratory tests (kPa)**

| Reference Figure | Figure A 4 | | Figure A 5 | | Figure A 6 | |
|---|---|---|---|---|---|---|
| Confinig Pressure | 41 kPa | 21 kPa | 41 kPa | 21 kPa | 41 kPa | 21 kPa |
| Base Thickness-100 mm | 30 | 21 | 36 | 30 | 40 | 39 |
| Base Thickness-150 mm | 36 | 27 | 39 | 34 | 50 | 45 |
| Base Thickness-200 mm | 40 | 30 | 40 | 36 | 56 | 48 |

| Reference Figure | Figure A 7 | | Figure A 8 | | Figure A 9 | |
|---|---|---|---|---|---|---|
| Confinig Pressure | 41 kPa | 21 kPa | 41 kPa | 21 kPa | 41 kPa | 21 kPa |
| Base Thickness-100 mm | 38 | 30 | 43 | 33 | 93 | 81 |
| Base Thickness-150 mm | 43 | 33 | 46 | 36 | 99 | 84 |
| Base Thickness-200 mm | 45 | 35 | 48 | 37 | 101 | 85 |

| Reference Figure | Figure A 10 | | Figure A 11 | | Figure A 12 | |
|---|---|---|---|---|---|---|
| Confinig Pressure | 41 kPa | 21 kPa | 41 kPa | 21 kPa | 41 kPa | 21 kPa |
| Base Thickness-100 mm | 92 | 74 | 74 | 62 | 63 | 45 |
| Base Thickness-150 mm | 99 | 78 | 79 | 67 | 68 | 52 |
| Base Thickness-200 mm | 103 | 80 | 81 | 69 | 71 | 55 |

## Table A 5 Subgrade resilient modulus calibration two (laboratory results).

**Bulk stress calculation**

| Base Thickness (mm) | Measured Vertical Stress $\sigma_V$ (kPa) | Horizontal Stress $\sigma_H$ (kPa) | Deviator Stress (kPa) |
|---|---|---|---|
| 100 | 152.3 | 54.8 | 97.5 |
| 150 | 142.2 | 51.2 | 91.0 |
| 200 | 134.2 | 48.3 | 85.9 |

**Resilient modulus from various laboratory tests (kPa)**

| Reference Figure | Figure A 4 | | Figure A 5 | | Figure A 6 | |
|---|---|---|---|---|---|---|
| Confinig Pressure | 41 kPa | 21 kPa | 41 kPa | 21 kPa | 41 kPa | 21 kPa |
| Base Thickness-100 mm | 28 | 19 | 34 | 29 | 36 | 36 |
| Base Thickness-150 mm | 29 | 20 | 35 | 29 | 38 | 37 |
| Base Thickness-200 mm | 30 | 21 | 35 | 30 | 39 | 38 |

| Reference Figure | Figure A 7 | | Figure A 8 | | Figure A 9 | |
|---|---|---|---|---|---|---|
| Confinig Pressure | 41 kPa | 21 kPa | 41 kPa | 21 kPa | 41 kPa | 21 kPa |
| Base Thickness-100 mm | 36 | 29 | 41 | 32 | 90 | 80 |
| Base Thickness-150 mm | 37 | 30 | 42 | 33 | 91 | 81 |
| Base Thickness-200 mm | 38 | 30 | 42 | 33 | 92 | 81 |

| Reference Figure | Figure A 10 | | Figure A 11 | | Figure A 12 | |
|---|---|---|---|---|---|---|
| Confinig Pressure | 41 kPa | 21 kPa | 41 kPa | 21 kPa | 41 kPa | 21 kPa |
| Base Thickness-100 mm | 89 | 72 | 71 | 60 | 60 | 42 |
| Base Thickness-150 mm | 90 | 73 | 72 | 61 | 61 | 43 |
| Base Thickness-200 mm | 92 | 74 | 73 | 62 | 62 | 44 |

**Table A 6 Base course resilient modulus (laboratory tests).**

## Calibration Number 1

| Base Thickness (mm) | Measured Vertical Stress $\sigma_V$ (kPa) | Horizontal Stress $\sigma_H$ (kPa) | Bulk Stress (kPa) | Resilient Modulus (kPa) |
|---|---|---|---|---|
| 100 | 144.3 | 51.9 | 248.2 | 276 |
| 150 | 138.3 | 49.8 | 237.8 | 268 |
| 200 | 126.6 | 45.6 | 217.7 | 253 |

## Calibration Number 2

| Base Thickness (mm) | Measured Vertical Stress $\sigma_V$ (kPa) | Horizontal Stress $\sigma_H$ (kPa) | Bulk Stress (kPa) | Resilient Modulus (kPa) |
|---|---|---|---|---|
| 100 | 152.3 | 54.8 | 262.0 | 286 |
| 150 | 142.2 | 51.2 | 244.6 | 273 |
| 200 | 134.2 | 48.3 | 230.9 | 263 |

**Table A 7 Geotextile properties (after Amoco Fabrics and Fibers Company)**

| Property | Grab Tensile (N) | Grab Elongation (%) | Mullen Burst (MPa) | Puncture (N) | Trapezoidal Tear (N) | UV Resistance (%)** | Apparent Openinig Size US Sieve No. |
|---|---|---|---|---|---|---|---|
| ASTM Test No. | D 4632 | D 4632 | D 3786 | D 4833 | D 4533 | D 4355* | D 4751 |
| 2002 | 889.6 | 15 | 2.8 | 400.32 | 333.6 | 70 | 30/70 |

* Fabrics conditioned as per ASTM D 4355
** Percent of minimum grab tensile after conditioning

**Table A 8 Geogrid properties (after Industrial Fabrics Association International)**

| Property | Mass/Unit Area $kg/m^3$ | Aperture Size MD/XD mm | Thickness at Rib/Junction mm | Wide Width Strip Tensile Test kg/m | | |
|---|---|---|---|---|---|---|
| | | | | 2% Strain | 5% Strain | Ultimate |
| ASTM Test No. | D 3776-84 | | D 1777-64 | D 4595-86 | | |
| BX1200 | 34.8 | 25/33 | 1.0/3.8 | 369 | 697 | 1169 |

**Table A 9 Bulk specific gravity (parafin film method).**

| Sample number | | 1-9 | 1-10 | 2-9 | 2-10 | 3-9 | 3-10 |
|---|---|---|---|---|---|---|---|
| Dry wt in air, g | A | 1183.5 | 1215.4 | 1191.6 | 1165.9 | 1172.3 | 1202.2 |
| Submerged wt, g | B | 664.6 | 682.1 | 634.3 | 618.7 | 624.2 | 663 |
| Wt in air, g | C | 1197.1 | 1230.4 | 1206.4 | 1184.6 | 1188.4 | 1221.8 |
| Bulk specific gravity, $G_{mb}$ | A/(C-B-(C-A)/0.89) | 2.288 | 2.287 | 2.214 | 2.14 | 2.147 | 2.24 |

**Table A 10 Bulk specific gravity (saturated surface dry method).**

| Sample number | | 1-9 | 1-10 | 2-9 | 2-10 | 3-9 | 3-10 |
|---|---|---|---|---|---|---|---|
| Dry wt in air, g | A | 1183.5 | 1215.4 | 1191.6 | 1165.9 | 1172.3 | 1202.2 |
| Submerged wt, g | B | 685.5 | 7.4.6 | 674.7 | 662 | 670.5 | 694.1 |
| SSD wt, g | C | 1184.3 | 1215.9 | 1202.8 | 1180.8 | 1185.4 | 1204.1 |
| Bulk specific gravity, $G_{mb}$ | A/(C-B) | 2.373 | 2.377 | 2.256 | 2.247 | 2.277 | 2.357 |

## Table A 11 Bulk specific gravity (height measurement method).

| Specimen No | wt. in Air (g) | Height Measurements (mm) | | | Average Height (mm) | Specific Gravity |
|---|---|---|---|---|---|---|
| | | 1 | 2 | 3 | | |
| 1-9 | 1183.5 | 62.1 | 62.3 | 62.7 | 62.4 | 2.416 |
| 1-10 | 1215.4 | 63.9 | 64.7 | 67.5 | 65.4 | 2.367 |
| 2-9 | 1191.6 | 67.8 | 67.1 | 67.3 | 67.4 | 2.252 |
| 2-10 | 1165.9 | 66 | 66.4 | 66.1 | 66.2 | 2.244 |
| 3-9 | 1172.3 | 65.5 | 64.7 | 65.7 | 65.3 | 2.287 |
| 3-10 | 1202.2 | 64.9 | 64.4 | 64.4 | 64.6 | 2.371 |

## Table A 12 Theoretical maximum specific gravity (lab specimens).

| Sample number | | 2-10 | 1-10 | 1-9 | 3-9 | 2-9 | 3-10 |
|---|---|---|---|---|---|---|---|
| Pycnometer number | | #1 | #2 | #3 | #1 | #2 | #3 |
| Wt submerged in water, g | A | 155.2 | 142.9 | 154 | 155.2 | 142.9 | 154 |
| Wt of Pycnometer in air, g | B | 309.7 | 298.7 | 308.5 | 309.7 | 298.7 | 308.5 |
| Wt of pycnometer and sample in air, g | C | 1242 | 1154.4 | 1074.9 | 1163 | 1158.3 | 1113.7 |
| Wt and sample in water, g | D | 696.6 | 642.8 | 603.4 | 647.3 | 642.7 | 619.9 |
| Wt of sample, g | E=C-B | 932.3 | 855.7 | 766.4 | 853.3 | 859.6 | 805.2 |
| Theoretical maximum specific gravity, g | F=E/(E+A-D) | 2.385 | 2.405 | 2.418 | 2.362 | 2.389 | 2.373 |

## Table A 13 Bulk specific gravity (saturated surface dry method, November, 1996).

| Sample Number | Identifier | 1 | 2 | 3 | 4 | 5 | 6 |
|---|---|---|---|---|---|---|---|
| Dry wt in air, g | A | 1191.3 | 1162.2 | 1136.9 | 1092.3 | 1209.1 | 1096.5 |
| Submerged wt, g | B | 685.8 | 658.9 | 658.2 | 637.6 | 690.8 | 626.8 |
| SSD wt, $G_{mb}$ | C | 1193.5 | 1164 | 1139.4 | 1104 | 1210.2 | 1098.2 |
| Bulk specific gravity, $G_{mb}$ | A/(C-B) | 2.35 | 2.30 | 2.36 | 2.34 | 2.33 | 2.33 |
| Density ($kN/m^3$) | 9.8*A/(C-B) | 23.00 | 22.55 | 23.16 | 22.96 | 22.82 | 22.80 |

## Table A 14 Theoretical maximum specific gravity (November, 1996).

| Sample Number | Identifier | 1 | 4 | 8 |
|---|---|---|---|---|
| Weight of beaker (g) | $W_1$ | 396.5 | 396.5 | 396.5 |
| Weight of beaker + sample (g) | $W_2$ | 1014.9 | 959.7 | 1004.3 |
| Weight of sample (g) | $A = W_2-W_1$ | 618.4 | 563.2 | 607.8 |
| Weight of beaker + sample + water (g) | D | 1731.5 | 1530.3 | 1534.9 |
| Weight of beaker + water (g) | E | 1368.25 | 1200.7 | 1177.7 |
| Theoretical maximum specific gravity | A/(A+E-D) | 2.42 | 2.41 | 2.43 |

**Table A 15 Asphalt content lot No. 1 (ashing method).**

| LINE | ITEM | | SAMPLE 1 (1-1) | SAMPLE 2 (1-2) |
|---|---|---|---|---|
| A | Wt of original sample and cone and filter, g | | 1839.3 | 1844.7 |
| B | Wt of cone, g | | 469.9 | 468.1 |
| C | Wt of original sample, g | A-B-G | 1361.2 | 1368.3 |
| D | Wt of clean aggregate and container, g | | 1438.6 | 1445.7 |
| E | Wt of container, g | | 168 | 168.4 |
| F | Wt of clean aggregate, g | D-E | 1270.6 | 1277.3 |
| G | Initial wt of filter paper, g | | 8.2 | 8.3 |
| H | Final wt of filter paper, g | | 8.6 | 8.6 |
| I | Wt of filler in filter paper. g | H-G | 0.4 | 0.3 |
| J | Total volume of solvent, cubic-cm | | 880 | 860 |
| K | Wt of solvent, g | | 1148.2 | 1123.2 |
| L | Final wt of AC and fines in solvent, g | C-F | 90.6 | 91 |
| M | Volume of AC and fines in solvent, cubic-cm | J-(K-L)/1.329 | 84.2 | 83.3 |
| O | Amount of filler in total solvent, g | 1.656(L-1.03M) | 6.4 | 8.6 |
| P | Total wt of aggregate in sample, g | F+I+O | 1277.4 | 1286.2 |
| Q | Percentage of asphalt, % | (C-F-O)100/C | 6.20% | 6.00% |
| | | | | |
| | Average Asphalt Content = 6.1% | | | |

**Table A 16 Asphalt content lot No. 2 (ashing method).**

| LINE | ITEM | | SAMPLE 1 (2-1) | SAMPLE 2 (2-2) |
|---|---|---|---|---|
| A | Wt of original sample and cone and filter, g | | 1867.4 | 1702.3 |
| B | Wt of cone, g | | 468 | 468.1 |
| C | Wt of original sample, g | A-B-G | 1391.1 | 1226 |
| D | Wt of clean aggregate and container, g | | 1568.3 | 1426.3 |
| E | Wt of container, g | | 275.2 | 276.9 |
| F | Wt of clean aggregate, g | D-E | 1293.1 | 1149.4 |
| G | Initial wt of filter paper, g | | 8.3 | 8.2 |
| H | Final wt of filter paper, g | | 8.7 | 8.4 |
| I | Wt of filler in filter paper. g | H-G | 0.4 | 0.2 |
| J | Total volume of solvent, cubic-cm | | 1475 | 940 |
| K | Wt of solvent, g | | 1937.7 | 1228.9 |
| L | Final wt of AC and fines in solvent, g | C-F | 98 | 76.6 |
| M | Volume of AC and fines in solvent, cubic-cm | J-(K-L)/1.329 | 90.7 | 73 |
| O | Amount of filler in total solvent, g | 1.656(L-1.03M) | 7.6 | 2.3 |
| P | Total wt of aggregate in sample, g | F+I+O | 1301.1 | 1151.9 |
| Q | Percentage of asphalt, % | (C-F-O)100/C | 6.50% | 6.10% |
| | | | | |
| | Average Asphalt Content = 6.3% | | | |

**Table A 17 Asphalt content lot No. 3 (ashing method).**

| LINE | ITEM | | SAMPLE 1 (3-1) | SAMPLE 2 (3-2) |
|---|---|---|---|---|
| A | Wt of original sample and cone and filter, g | | 1766.9 | 1662.8 |
| B | Wt of cone, g | | 470.1 | 467.6 |
| C | Wt of original sample, g | A-B-G | 1288.2 | 1186.6 |
| D | Wt of clean aggregate and container, g | | 1375.8 | 1276.1 |
| E | Wt of container, g | | 168.7 | 167.5 |
| F | Wt of clean aggregate, g | D-E | 1207.1 | 1108.6 |
| G | Initial wt of filter paper, g | | 8.6 | 8.5 |
| H | Final wt of filter paper, g | | 9.2 | 8.9 |
| I | Wt of filler in filter paper. g | H-G | 0.6 | 0.4 |
| J | Total volume of solvent, cubic-cm | | 890 | 885.6 |
| K | Wt of solvent, g | | 1161.3 | 1156.7 |
| L | Final wt of AC and fines in solvent, g | C-F | 81.1 | 78 |
| M | Volume of AC and fines in solvent, cubic-cm | J-(K-L)/1.329 | 77.2 | 73.9 |
| O | Amount of filler in total solvent, g | 1.656(L-1.03M) | 2.6 | 3.1 |
| P | Total wt of aggregate in sample, g | F+I+O | 1210.3 | 1112.1 |
| Q | Percentage of asphalt, % | (C-F-O)100/C | 6.10% | 6.30% |
| | | | | |
| | Average Asphalt Content = 6.2% | | | |

**Table A 18 VMA, VFA, VTM for the laboratory specimens (October, 1994 and November, 1996).**

| Specimen No. | October, 1994 | | | |
|---|---|---|---|---|
| | VTM (%) | VMA (%) | VFA (%) | Density (kN/m$^3$) |
| **Lot 1** | 3.38 | 14.70 | 77.00 | 22.83 |
| **Lot 2** | 5.74 | 19.70 | 70.66 | 21.69 |
| **Lot 3** | 4.75 | 19.27 | 75.33 | 22.09 |

| Specimen No. | November, 1994 | | | |
|---|---|---|---|---|
| | VTM (%) | VMA (%) | VFA (%) | Density (kN/m$^3$) |
| **1** | 2.89 | 18.35 | 84.23 | 23.02 |
| **4** | 2.90 | 18.68 | 84.45 | 22.92 |
| **8** | 3.70 | 18.01 | 79.43 | 22.92 |

**Table A 19 Marshall test results for laboratory specimens.**

| Specimen Number | Stability (kN) | Flow (mm) |
|---|---|---|
| Section 9 (A) | 13 | 356 |
| Section 9 (B) | 13 | 279 |
| Section 2 (A) | 12 | 203 |
| Section 2 (B) | 11 | 229 |
| Section 5 (A) | 11 | 203 |
| Section 5 (B) | 14 | 305 |

**Table A 20 Thickness of the core specimens.**

| Specimens | Total Thickness (mm) |
|---|---|
| Section 1 | 78.6 |
| Section 2 | 76.7 |
| Section 3 | 98.8 |
| Section 4 | 95.9 |
| Section 5 | 90.6 |
| Section 6 | 88.9 |
| Section 7 | 86.9 |
| Section 8 | 84.4 |
| Section 9 | 85.6 |

**Table A 21 Poisson's ratio, and average resilient modulus as a function of temperature.**

| Temperature ($^{o}$C) | Poisson's Ratio | October, 1994 | November, 1996 | October, 1997 |
|---|---|---|---|---|
| 5 | 0.25 | 3168 | 3232 | 3267 |
| 25 | 0.35 | 2765 | 2976 | 2989 |
| 40 | 0.4 | 2619 | 2852 | 2861 |

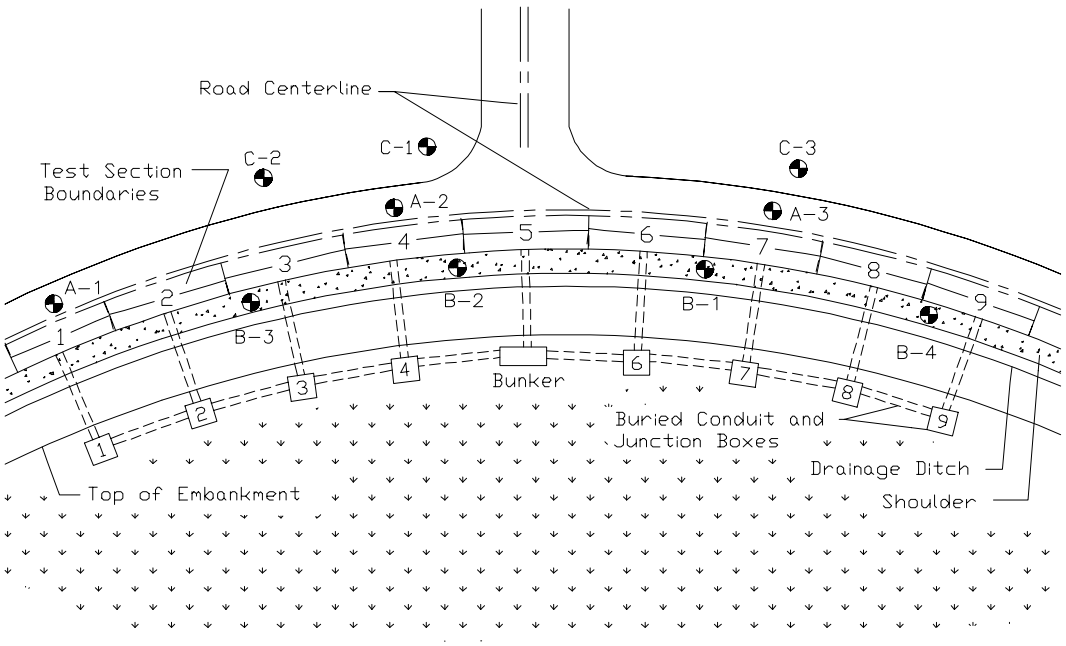


**Figure A 1 Sample locations across the test sections.**

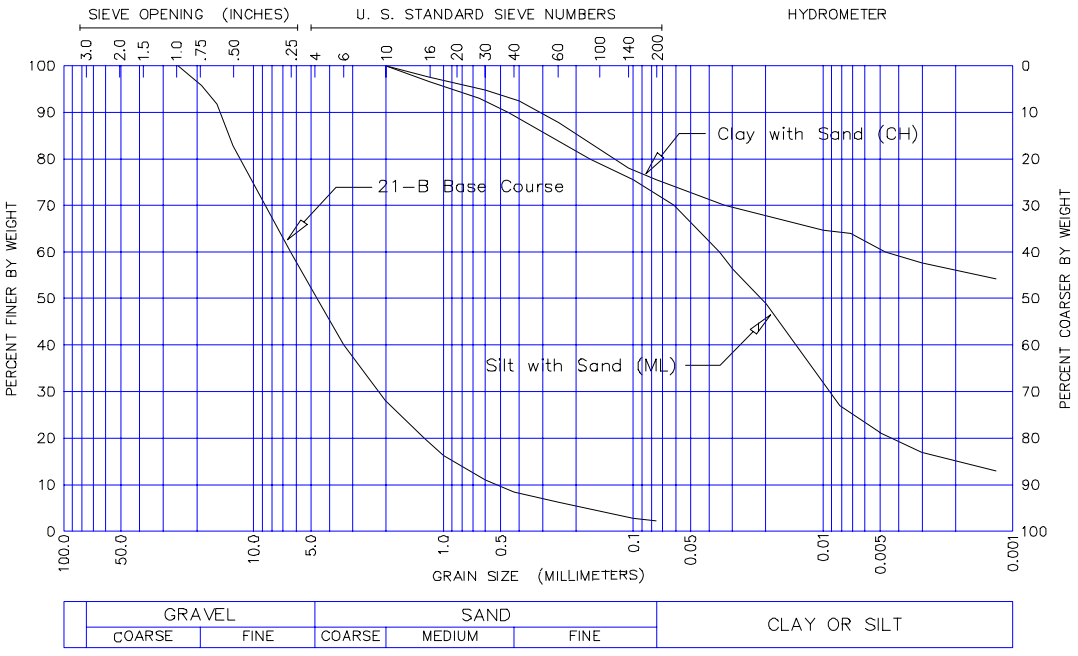


**Figure A 2 Gradation curves for the subgrade and base course materials.**

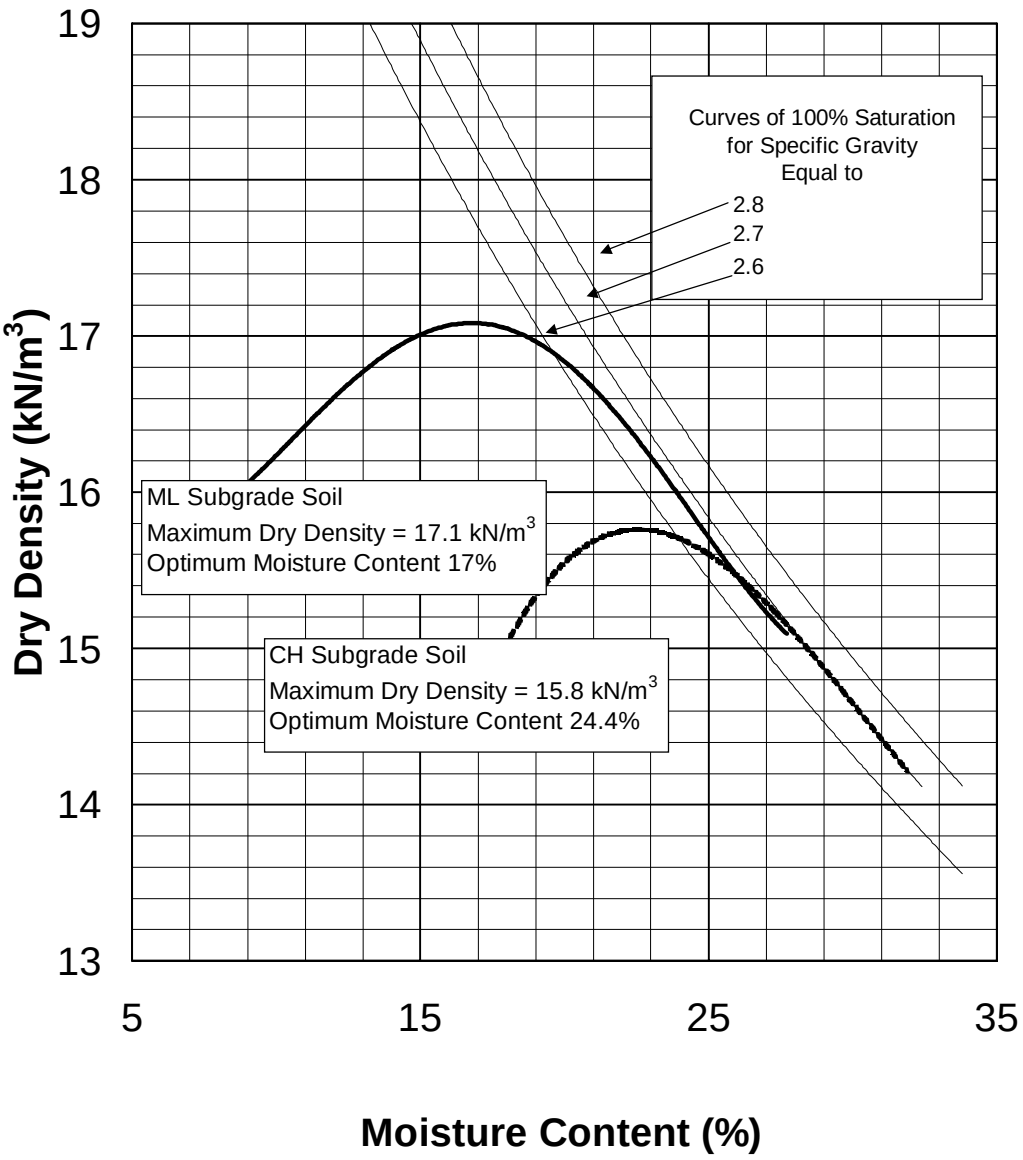


**Figure A 3 Dry density versus water content for subgrade soil at a Modified Proctor effort of 2700 kN-m/m3.**

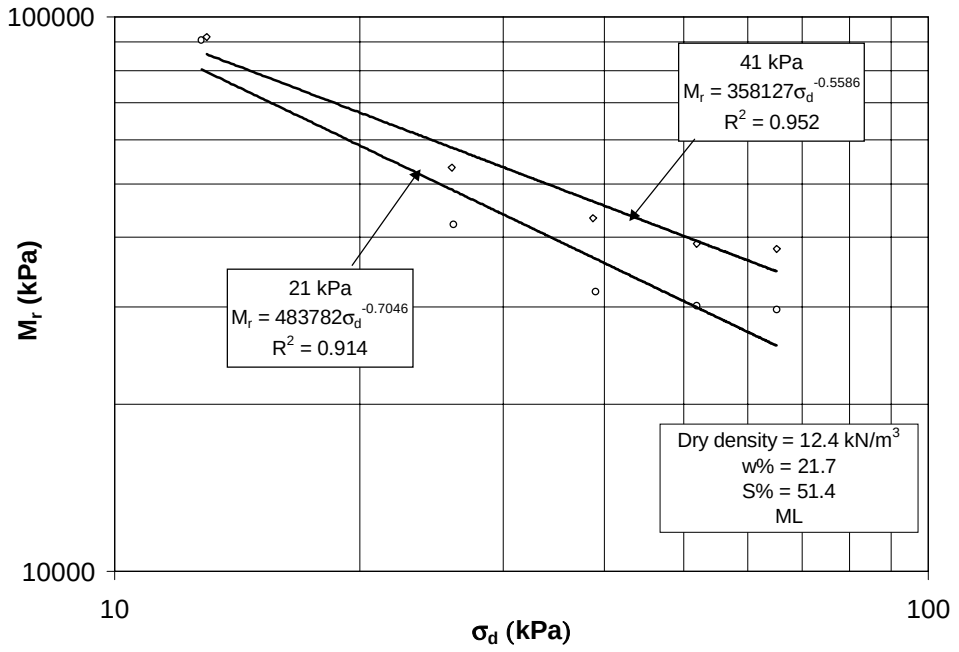


**Figure A 4 Subgrade resilient modulus as a function of deviator stress for ML specimen at 21.7% moisture content.**

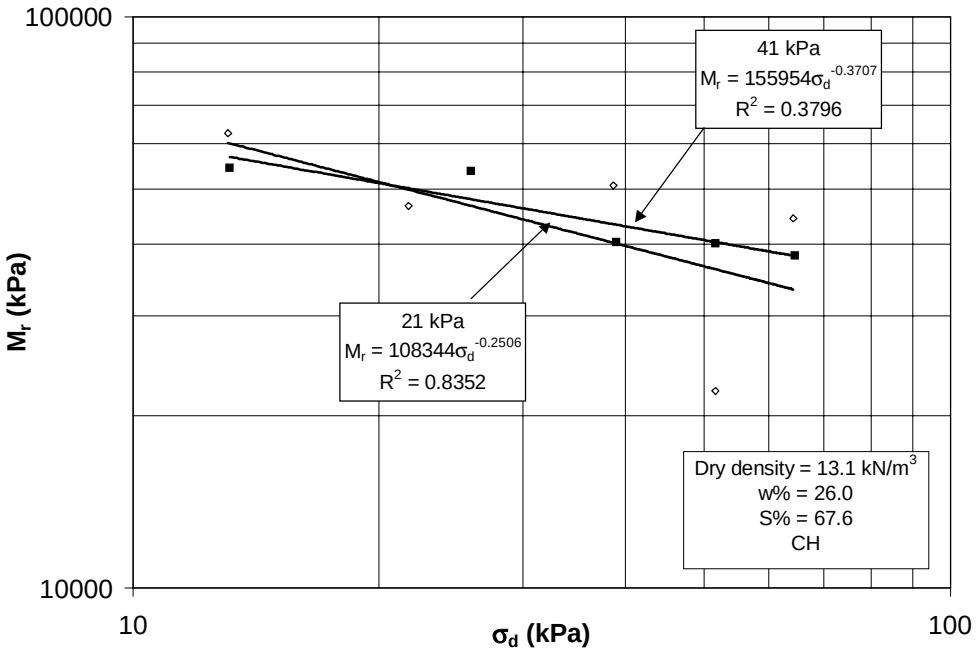


**Figure A 5 Subgrade resilient modulus as a function of deviator stress for CH specimen at 26% moisture content.**

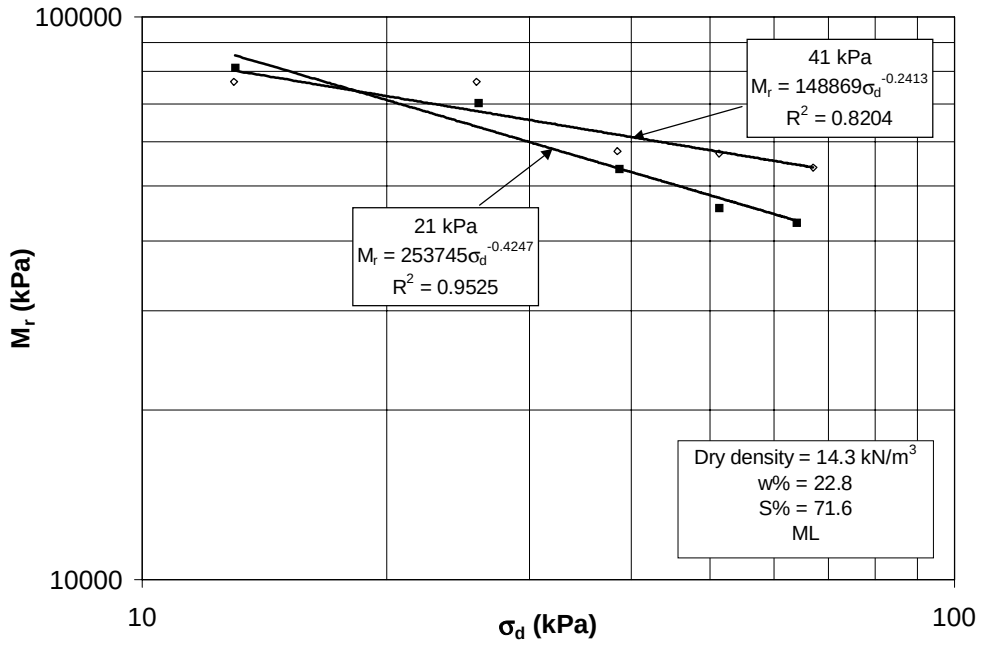


**Figure A 6 Subgrade resilient modulus as a function of deviator stress for ML specimen at 22.8% moisture content.**

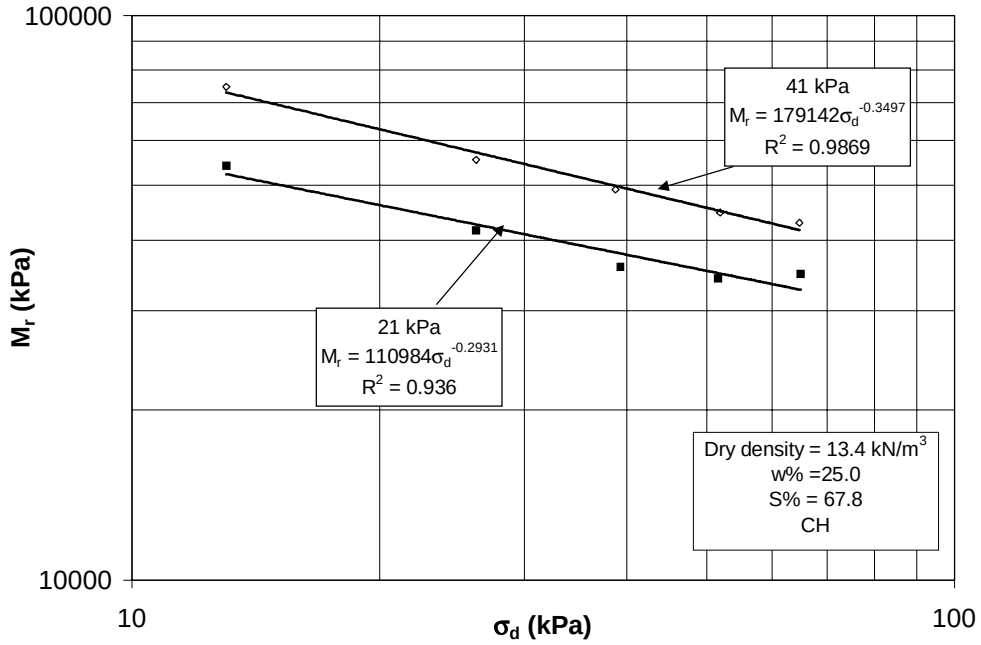


**Figure A 7 Subgrade resilient modulus as a function of deviator stress for CH specimen at 25% moisture content.**

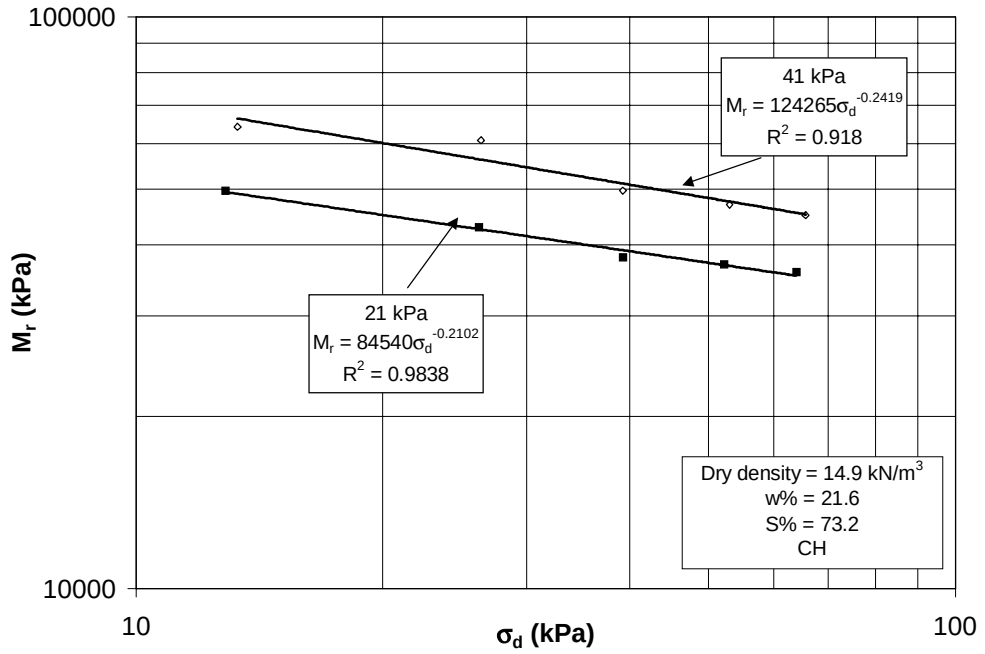


**Figure A 8 Subgrade resilient modulus as a function of deviator stress for CH specimen at 21.6% moisture content.**

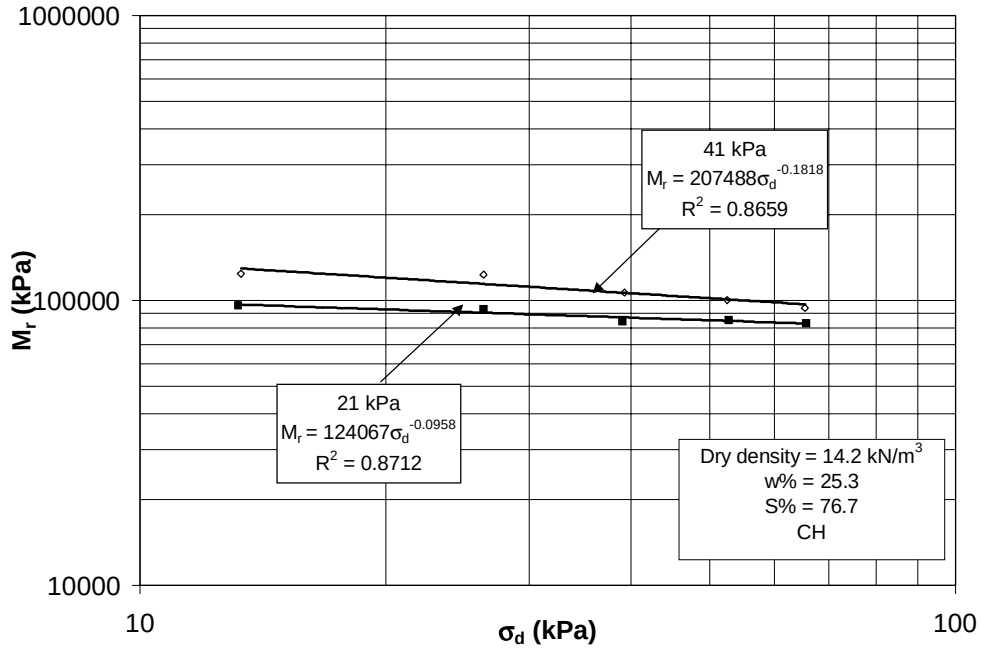


**Figure A 9 Subgrade resilient modulus as a function of deviator stress for CH specimen at 25.3% moisture content.**

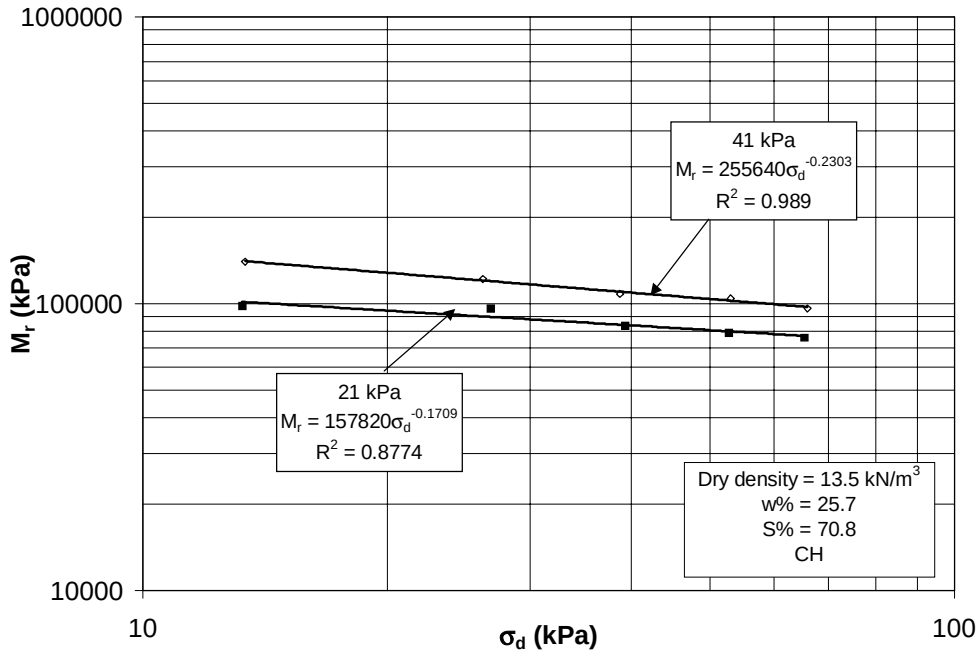


**Figure A 10 Subgrade resilient modulus as a function of deviator stress for CH specimen at 25.7% moisture content.**

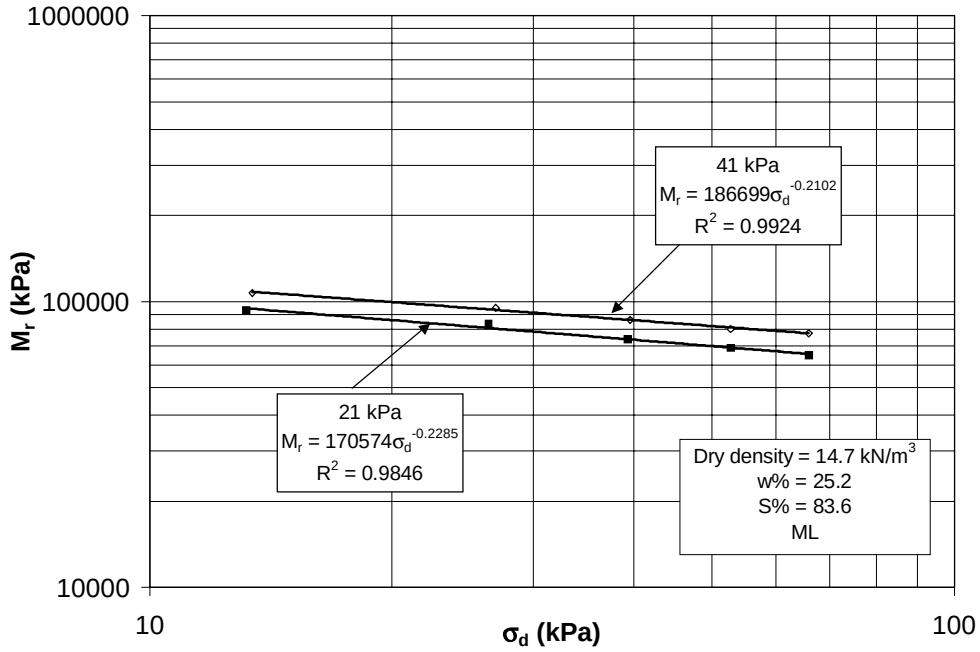


**Figure A 11 Subgrade resilient modulus as a function of deviator stress for ML specimen at 25.2% moisture content.**

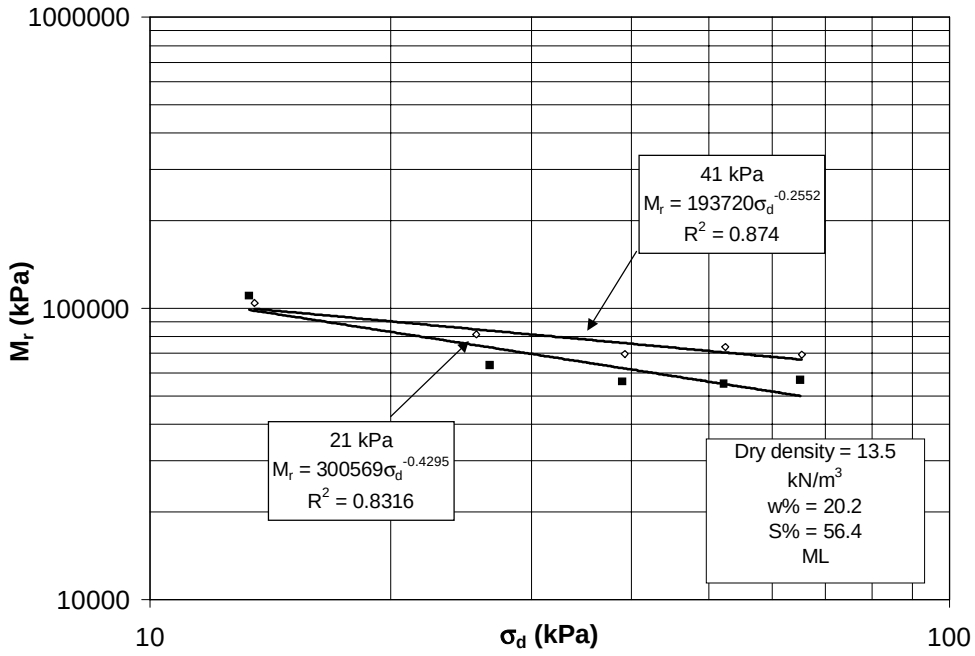


**Figure A 12 Subgrade resilient modulus as a function of deviator stress for ML specimen at 20.2% moisture content.**

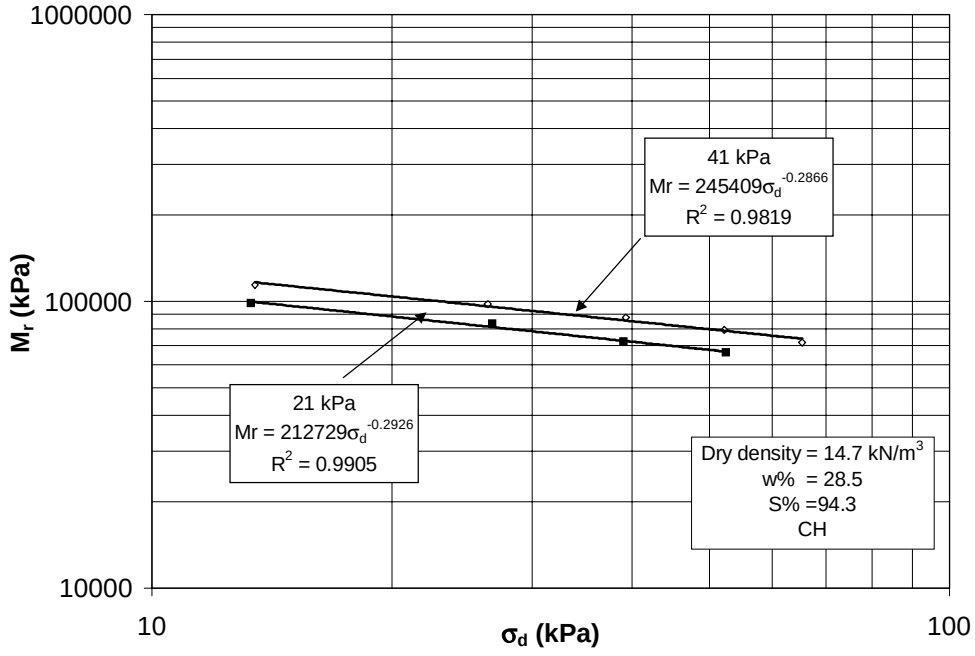


**Figure A 13 Subgrade resilient modulus as a function of deviator stress for CH specimen at 28.5% moisture content.**

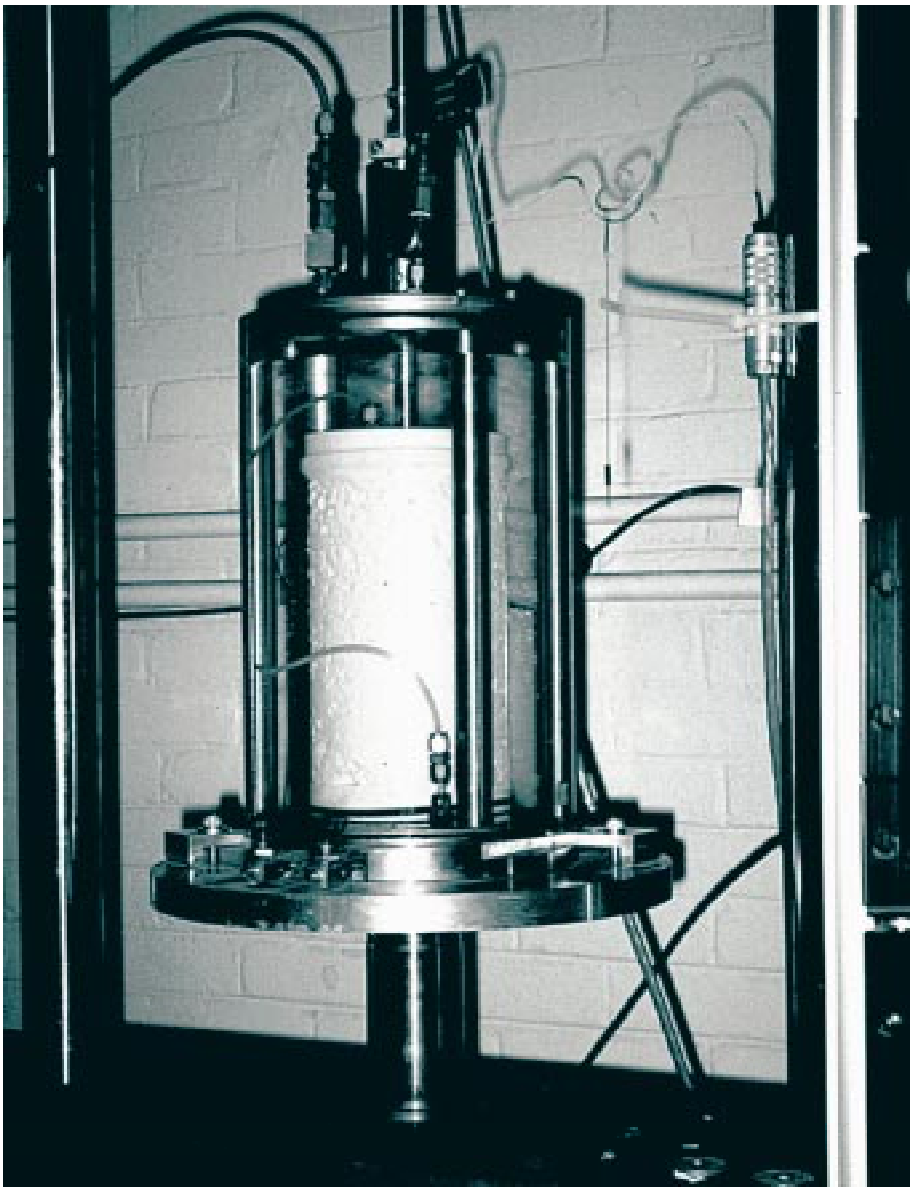

**Figure A 14 A subgrade sample in a triaxial cell ready for testing in an MTS machine.**

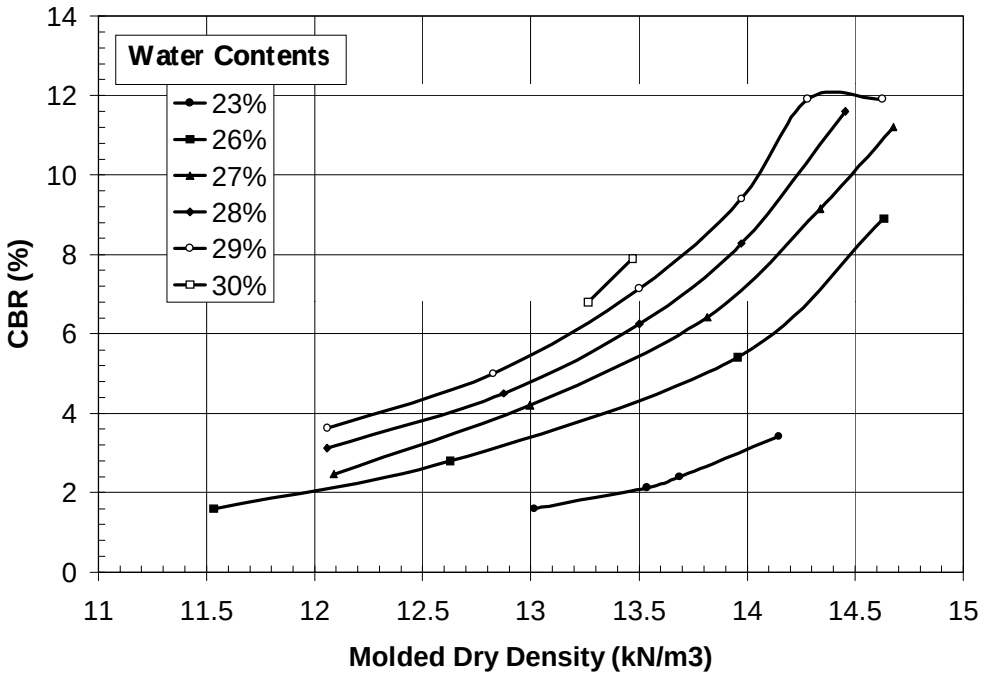


**Figure A 15: CBR test results for subgrade soil as a function of compacted dry density and water content.**

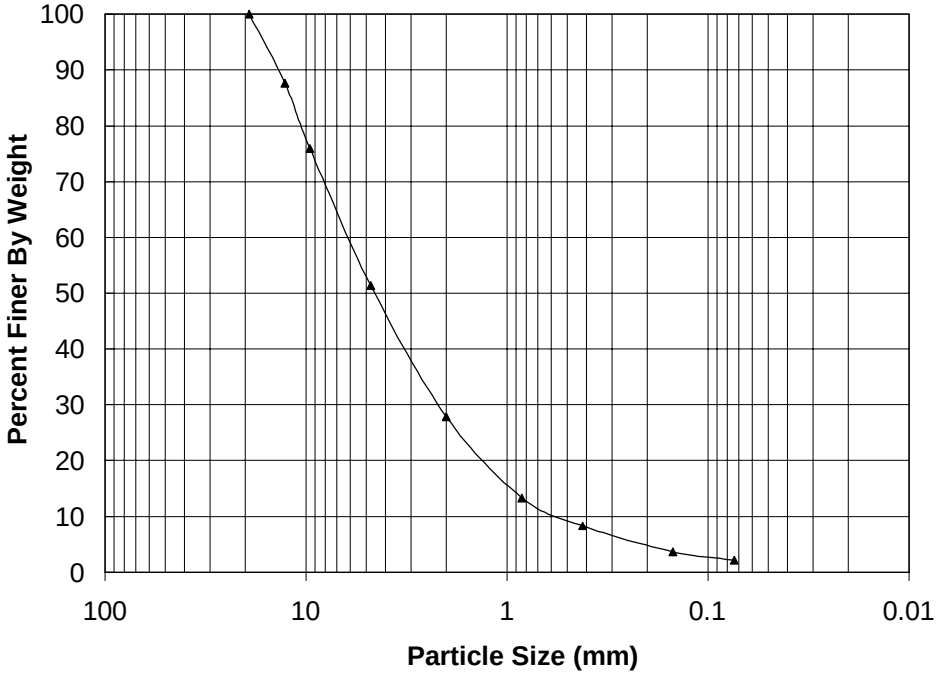


**Figure A 16: Gradation Curve for base course.**

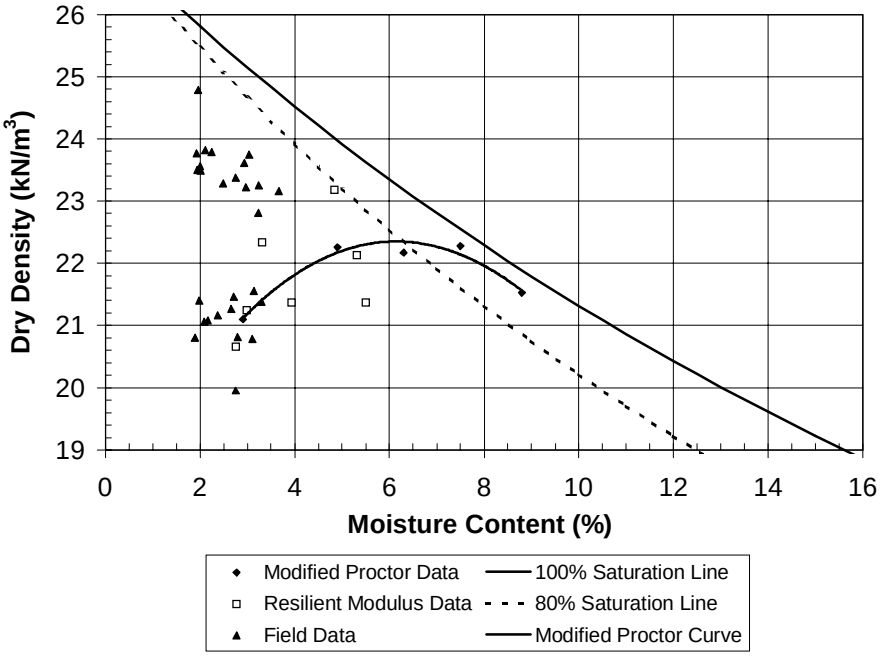


**Figure A 17: Dry density vs. water content for the base course material.**

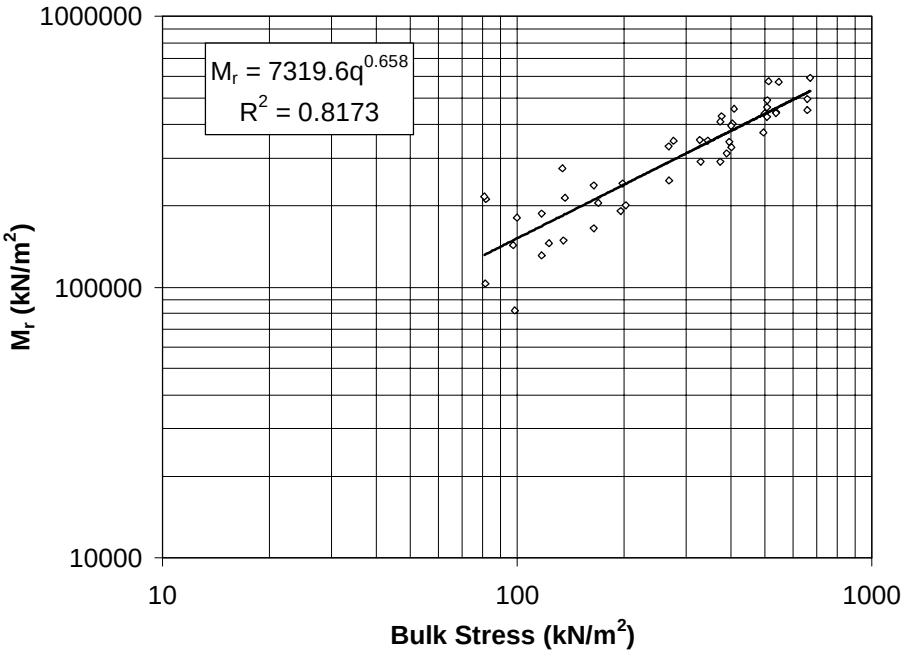


**Figure A 18 Resilient modulus for base course under wet condition.**

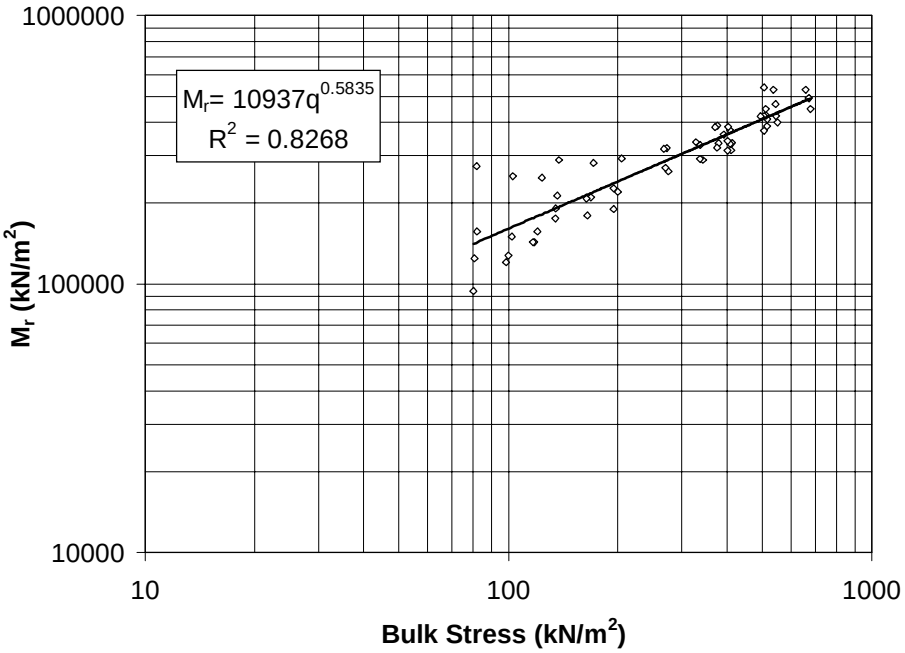


**Figure A 19 Resilient modulus for base course under dry condition.**

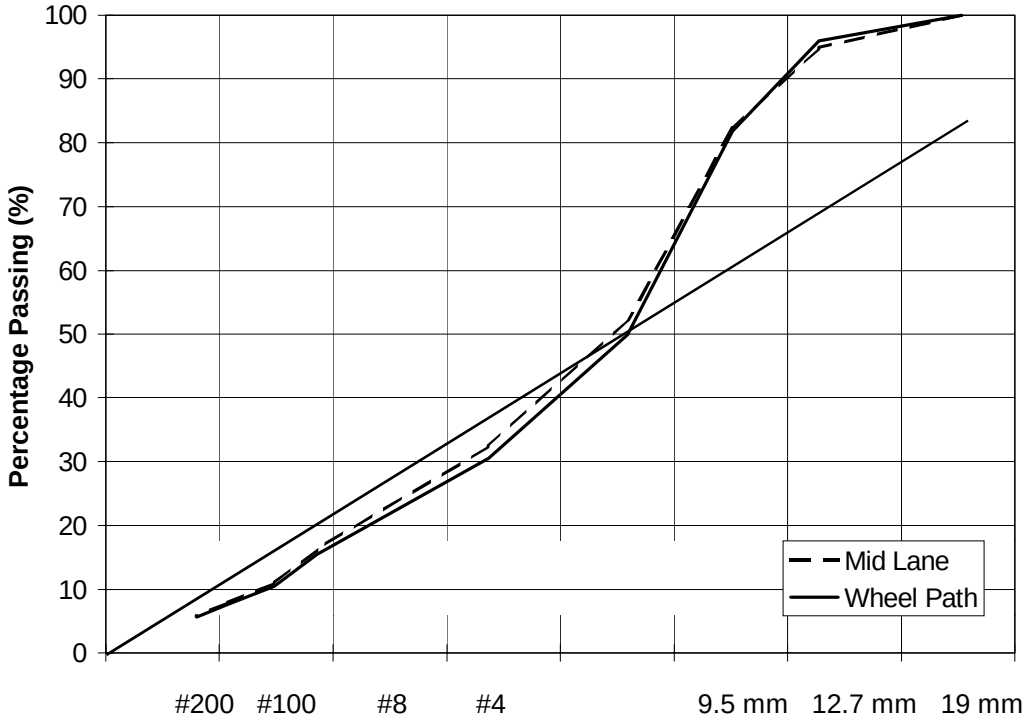


**Figure A 20 HMA gradation for section 1.**

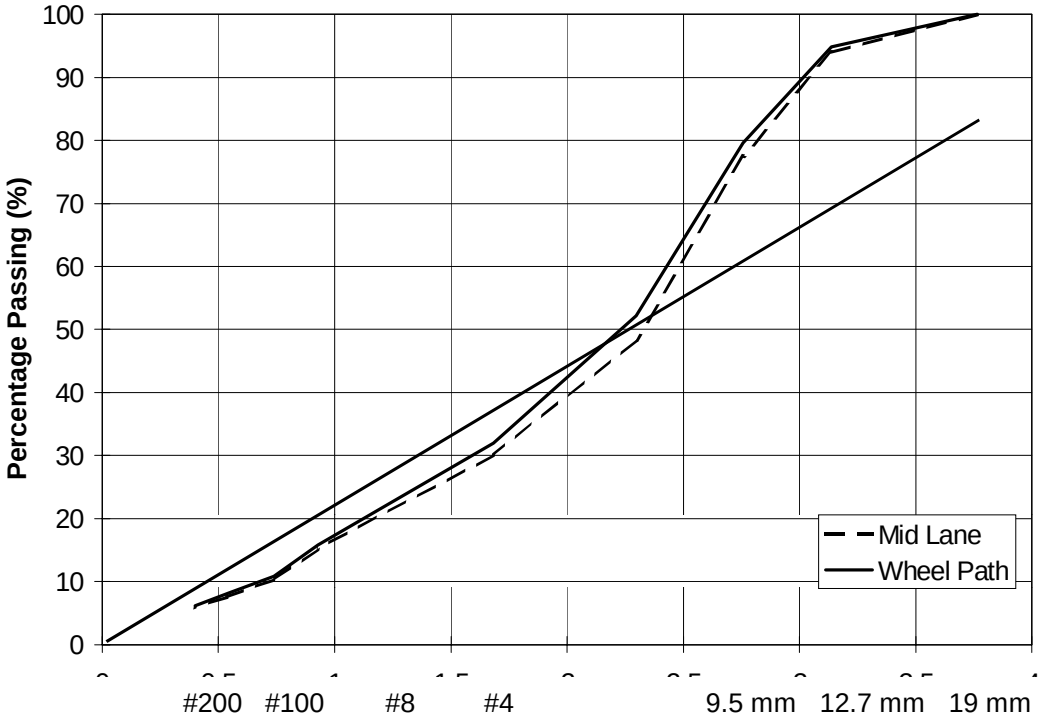


**Figure A 21 HMA gradation for section 2.**

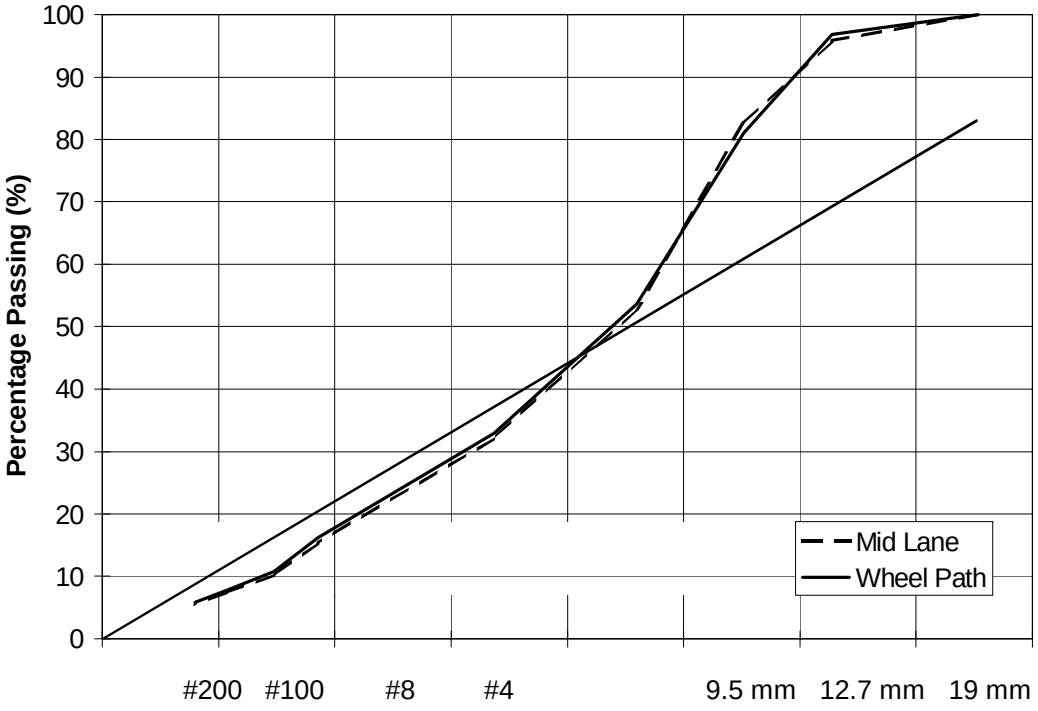


**Figure A 22 HMA gradation for section 3.**

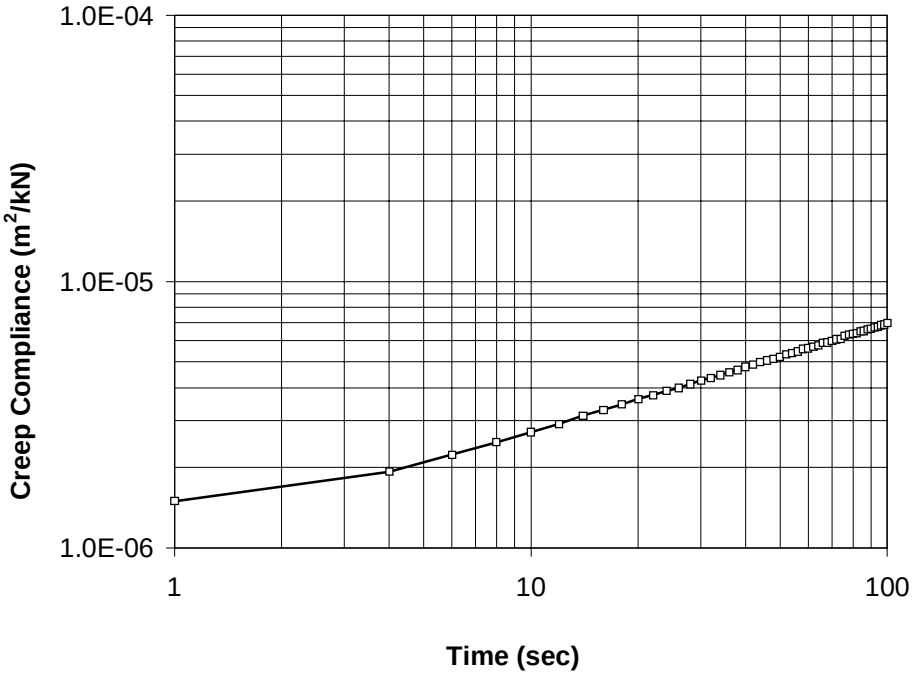


**Figure A 23 Creep compliance, section 1-a (25 °C).**

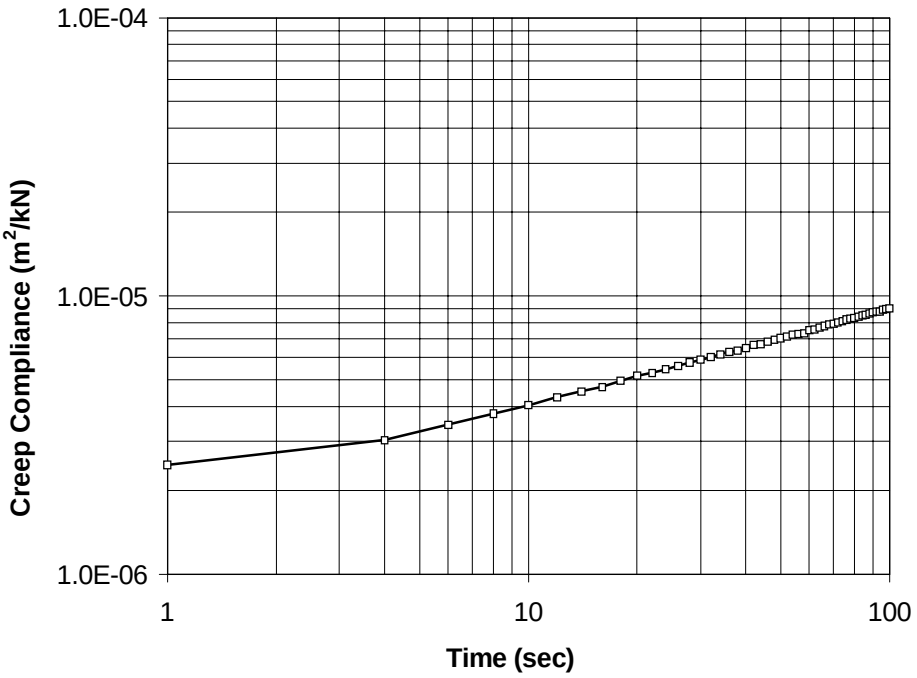


**Figure A 24 Creep compliance, section 1-b (25 °C).**

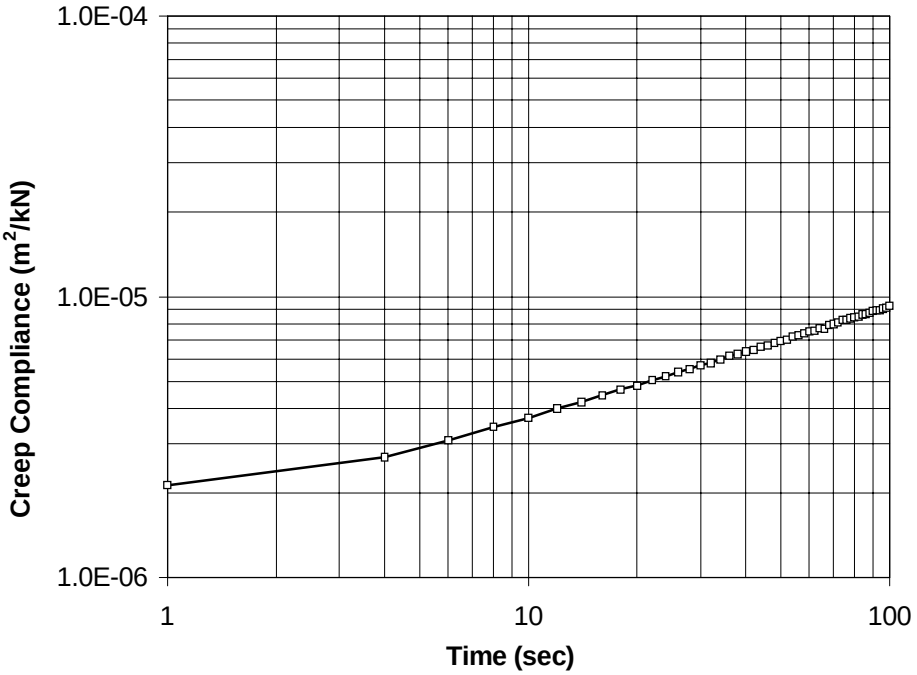


**Figure A 25 Creep compliance, section 3 (25 °C).**

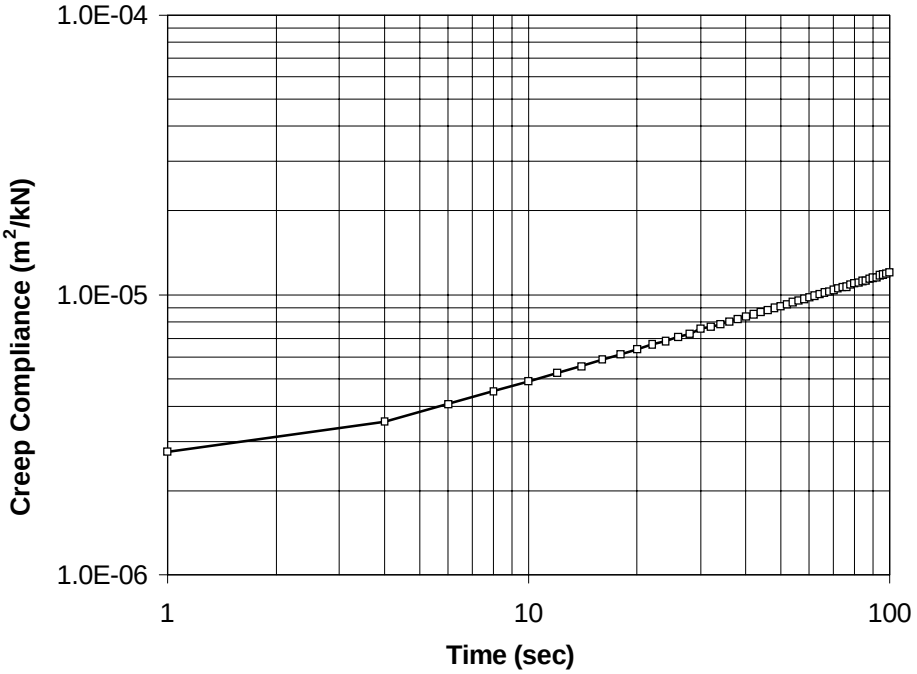


**Figure A 26 Creep compliance, section 4-a (25 °C).**

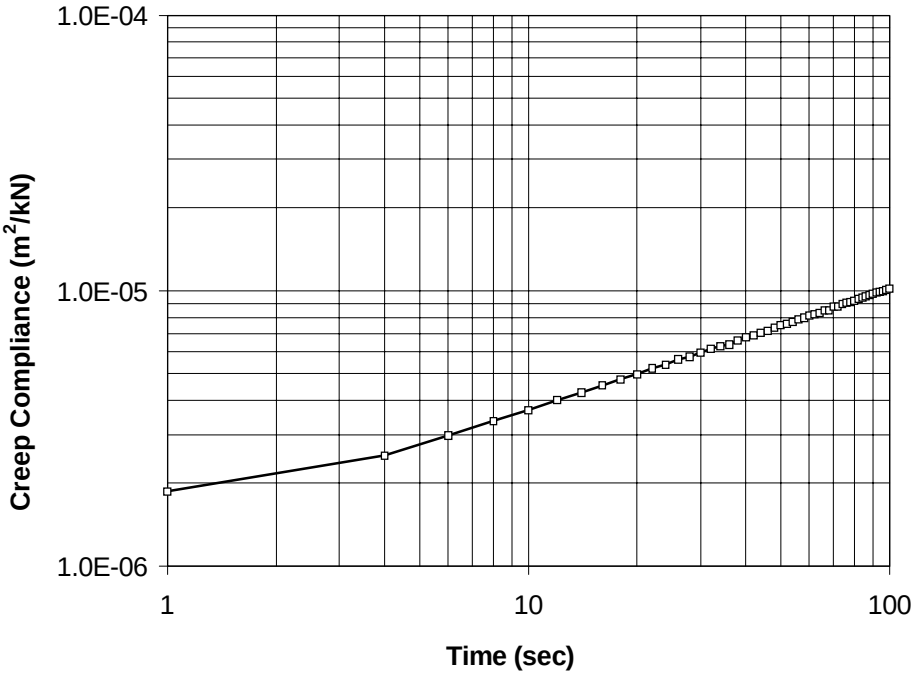


**Figure A 27 Creep compliance, section 4-b (25 °C).**

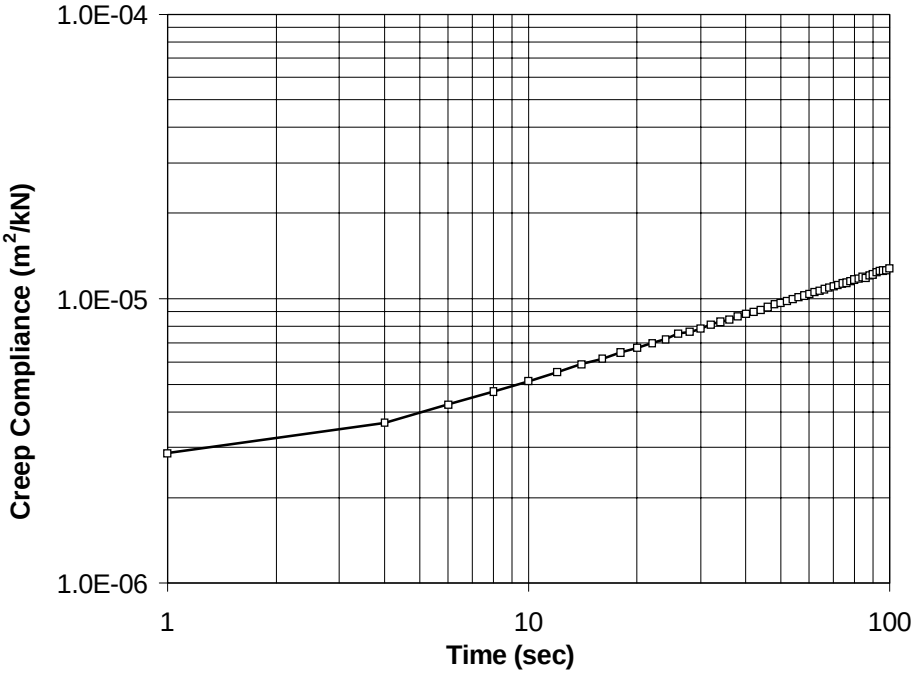


**Figure A 28 Creep compliance, section 5 (25 °C).**

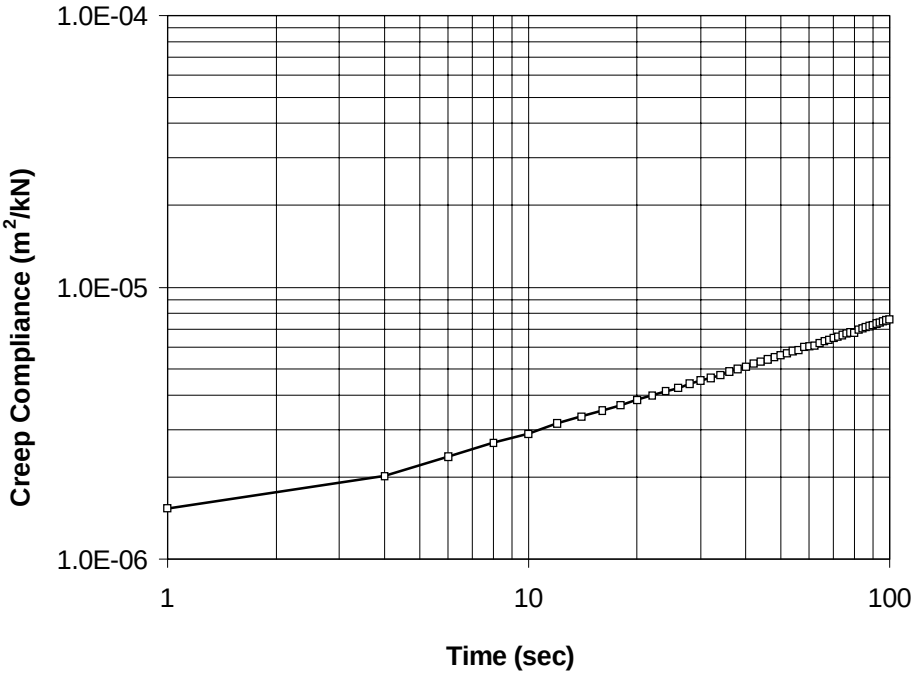


**Figure A 29 Creep compliance, section 7 (25 °C).**

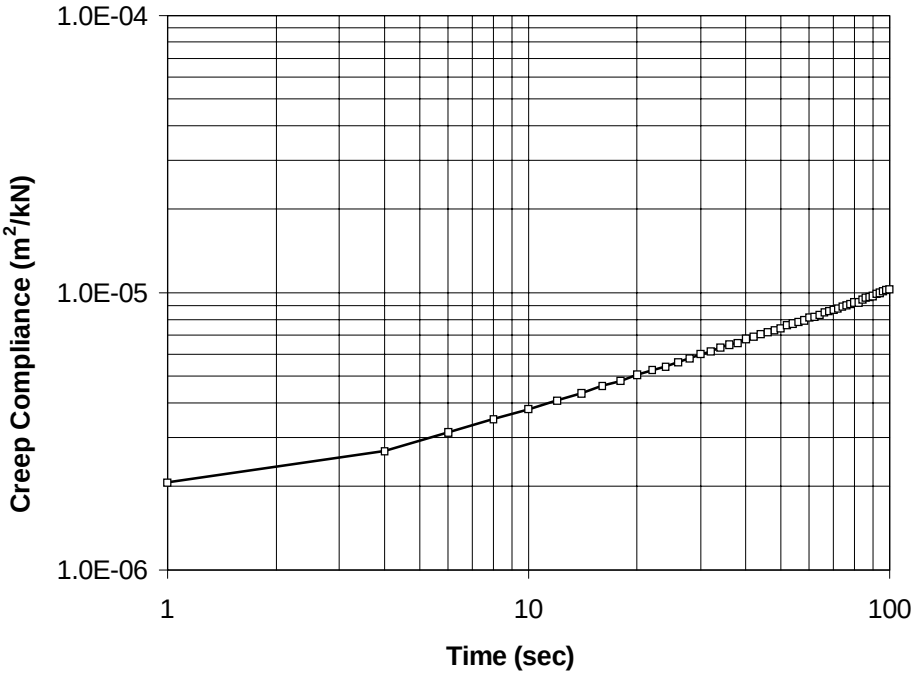


**Figure A 30 Creep compliance, section 9-a (25 °C).**

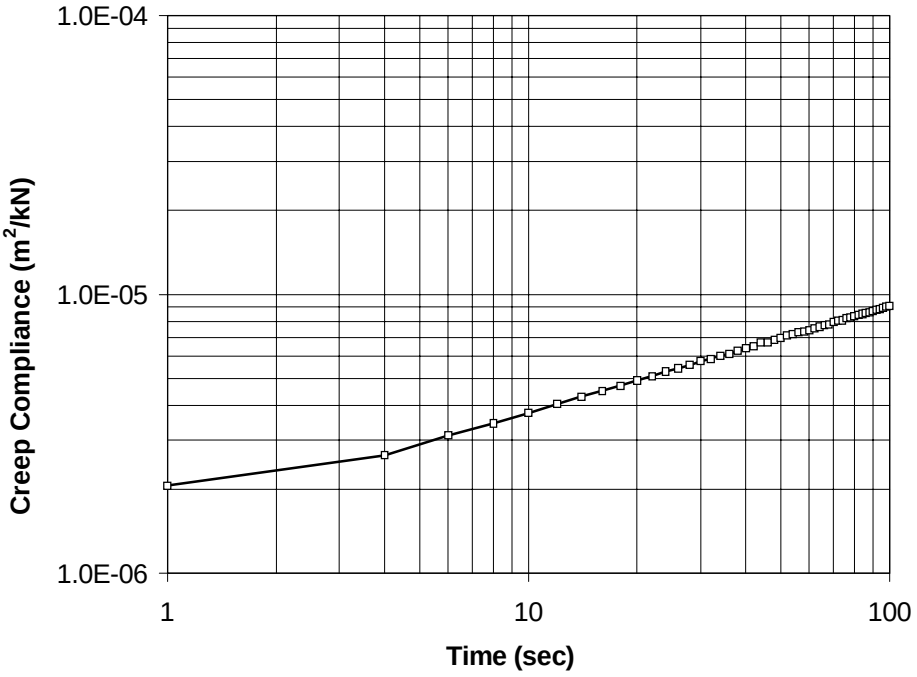


**Figure A 31 Creep compliance, section 9-b (25 °C).**

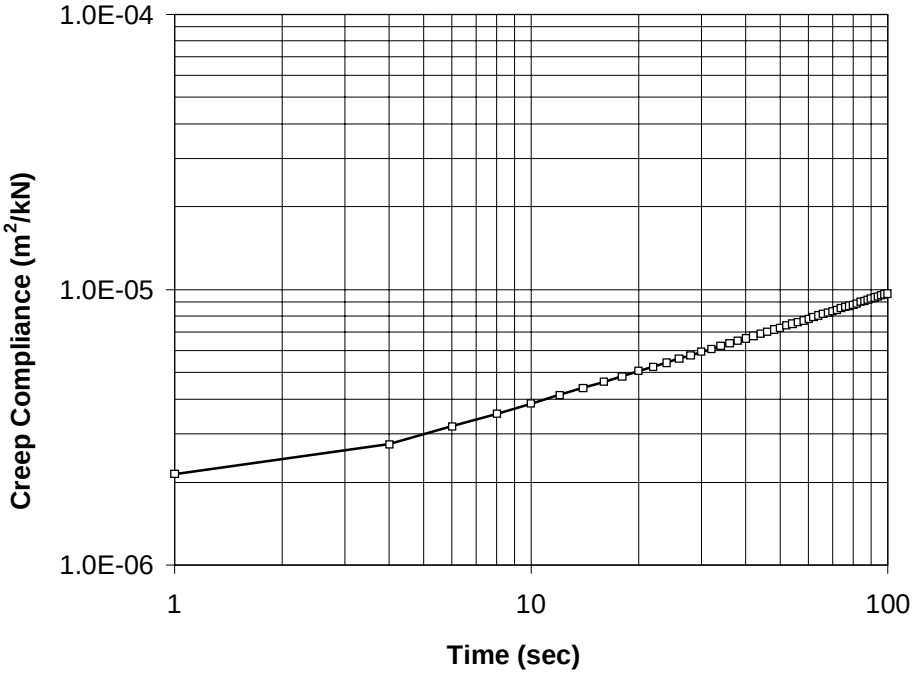


**Figure A 32 Average creep compliance (25 °C).**

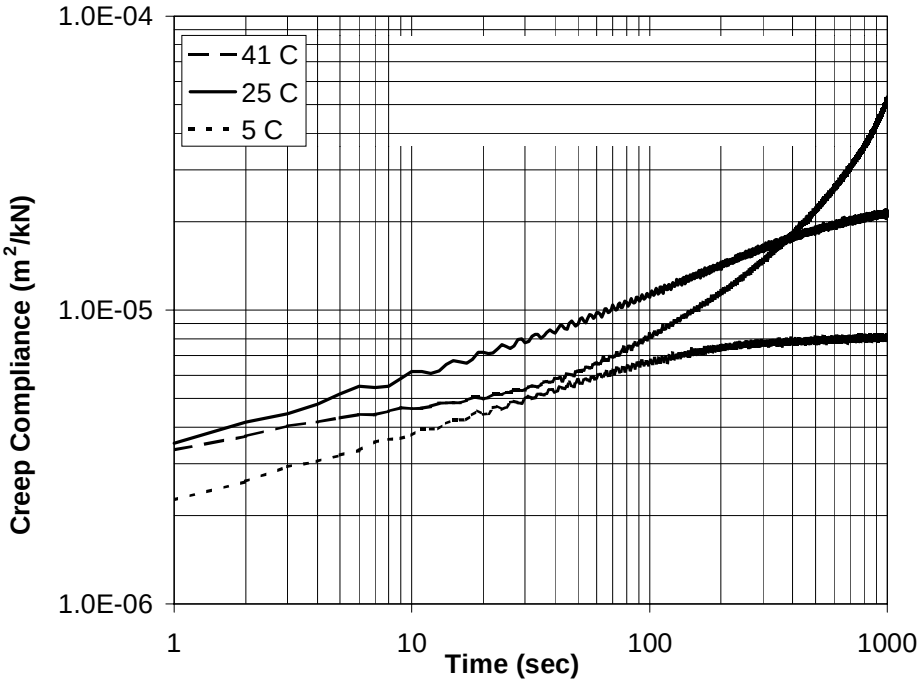


**Figure A 33 Creep Compliance, section 1.**

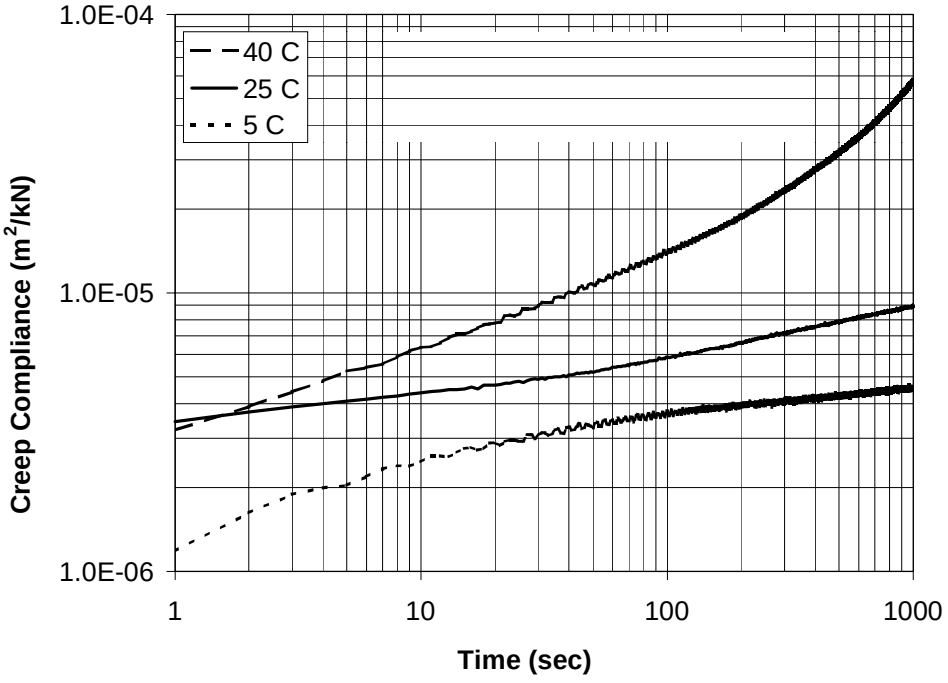


**Figure A 34 Creep Compliance, section 2.**

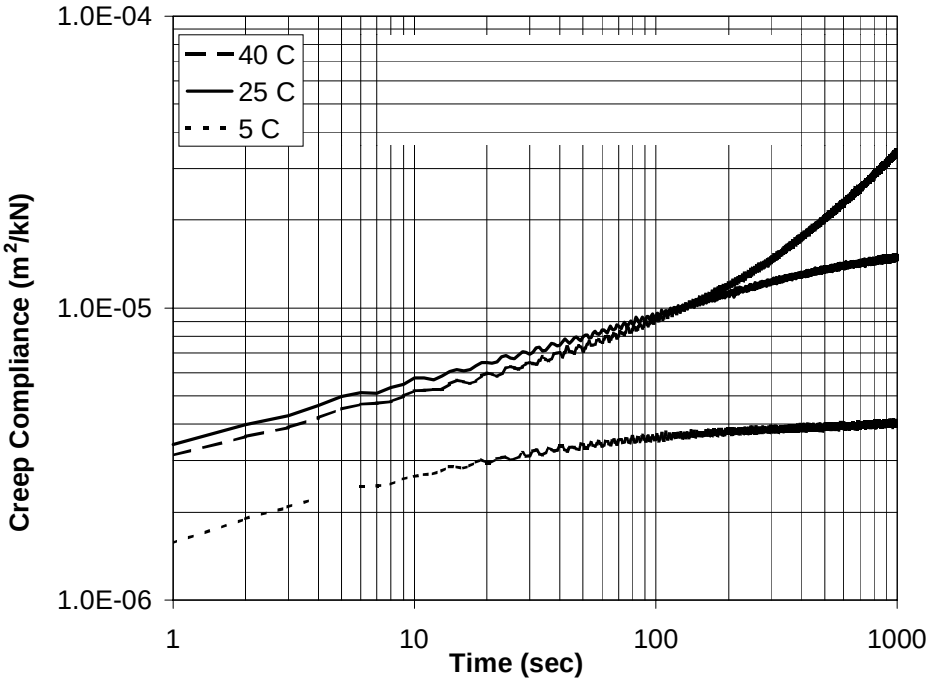


**Figure A 35 Creep Compliance, section 3.**

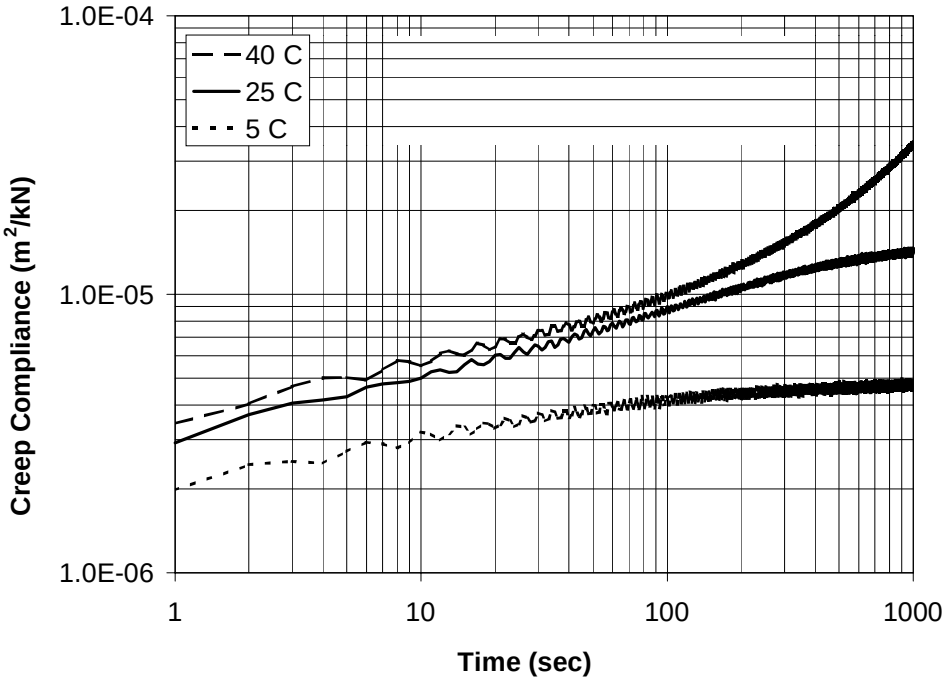


**Figure A 36 Creep Compliance, section 4.**

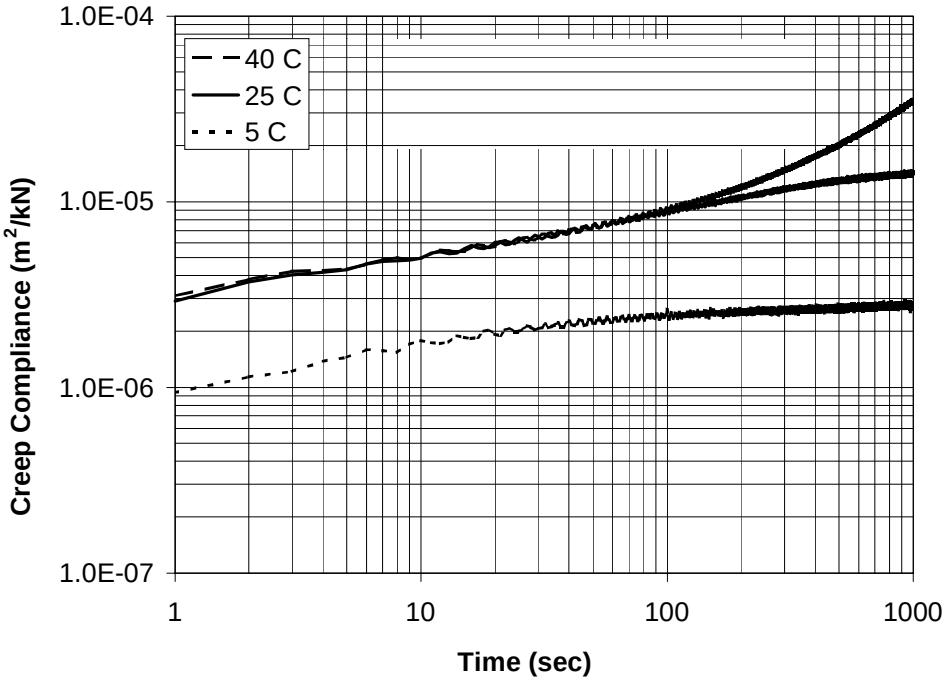


**Figure A 37 Creep Compliance, section 5.**

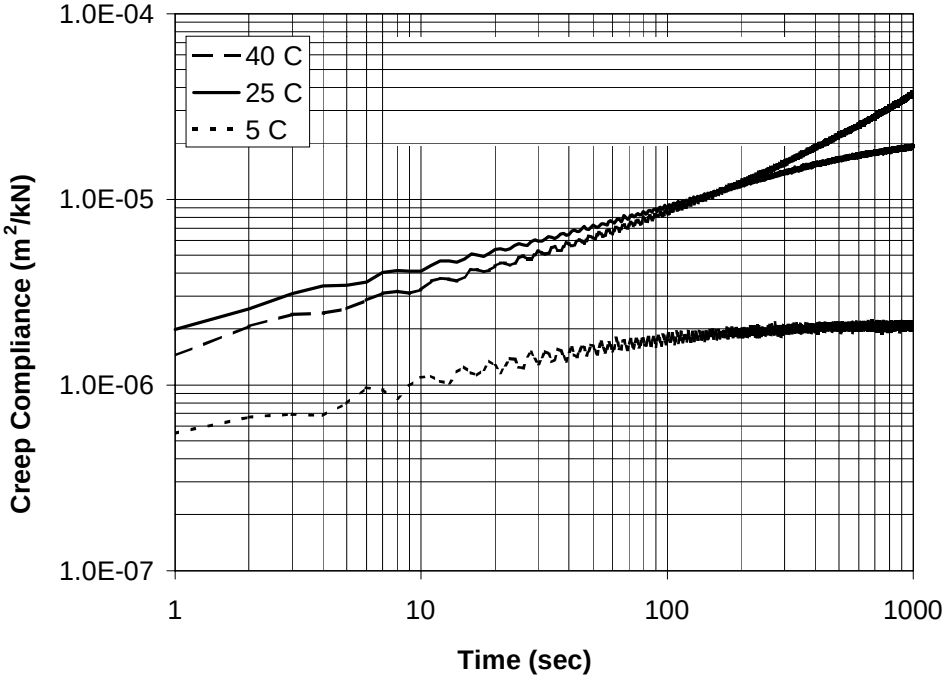


**Figure A 38 Creep Compliance, section 6.**

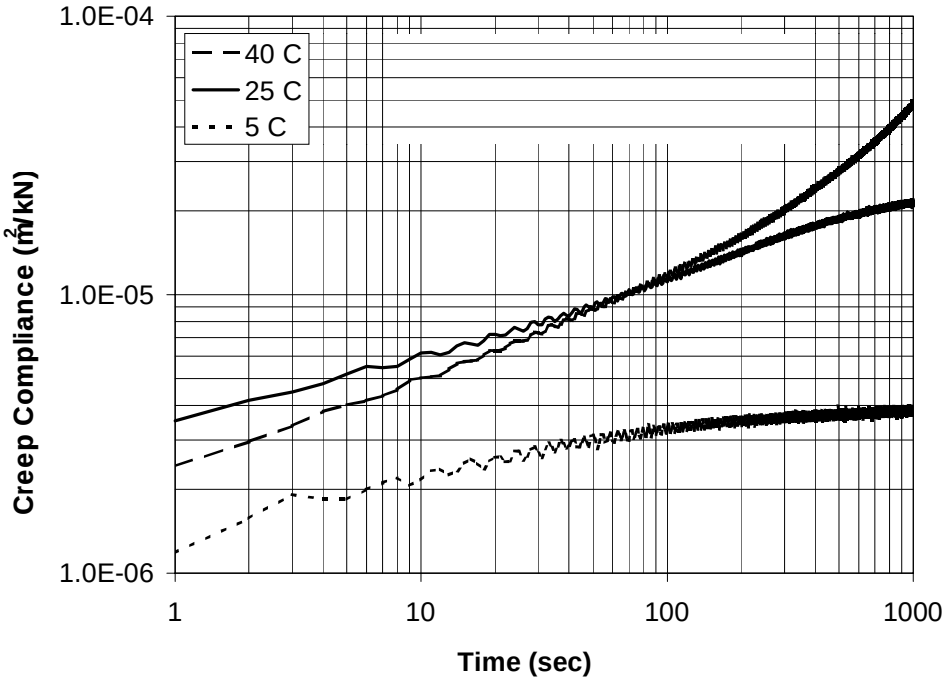


**Figure A 39 Creep Compliance, section 7.**

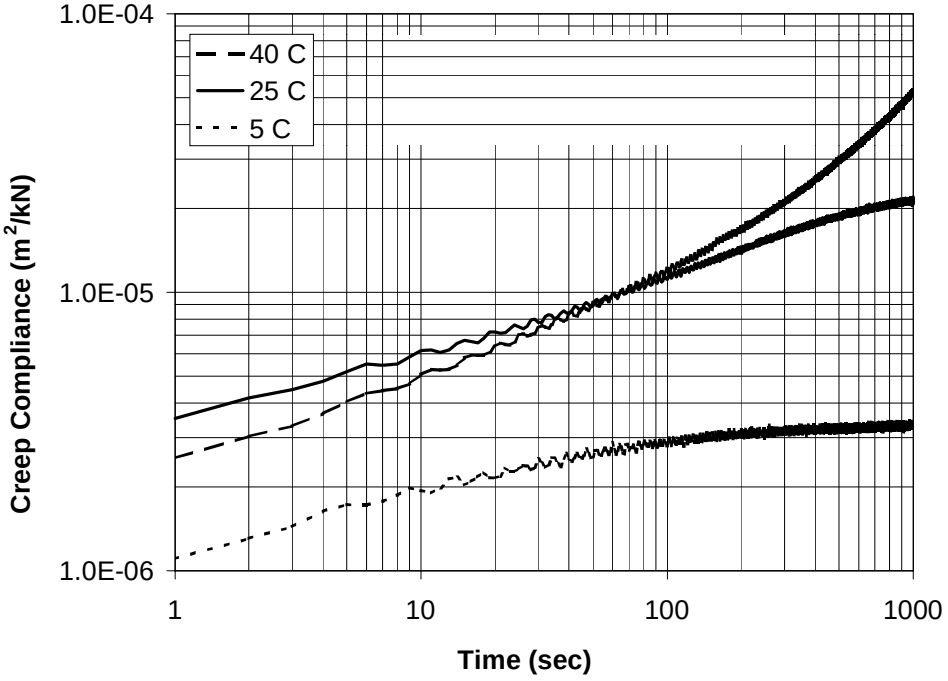


**Figure A 40 Creep Compliance, section 8.**

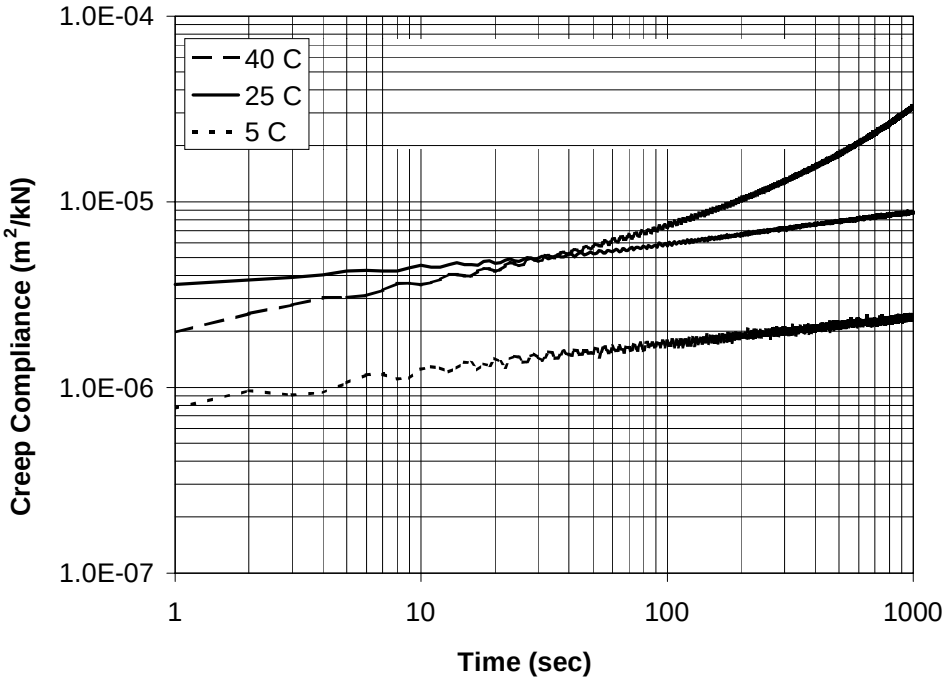


**Figure A 41 Creep Compliance, section 9.**

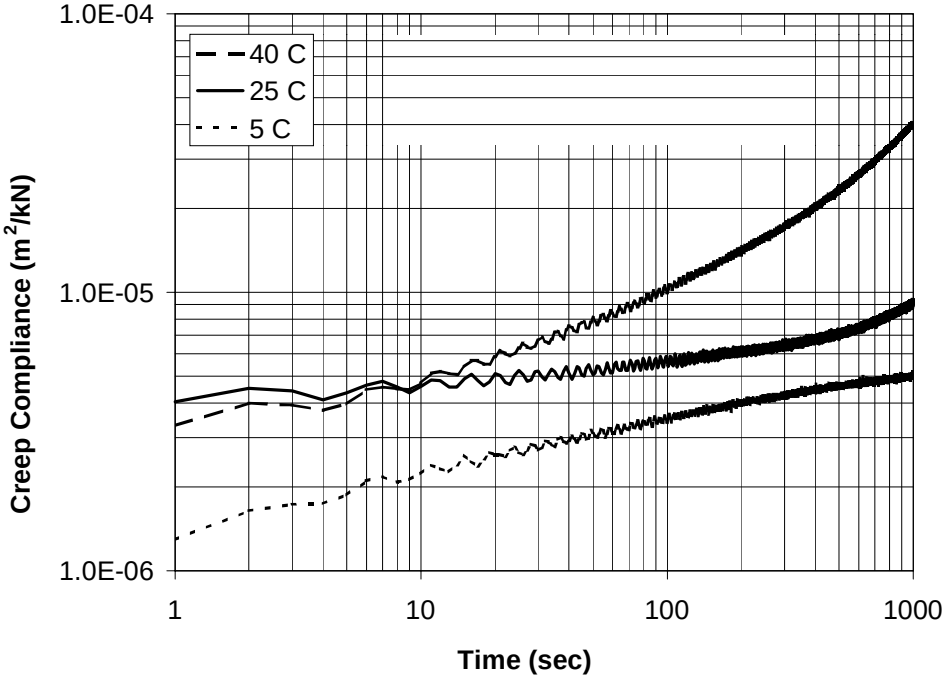


**Figure A 42 Creep Compliance, section 1 for temperature effects.**

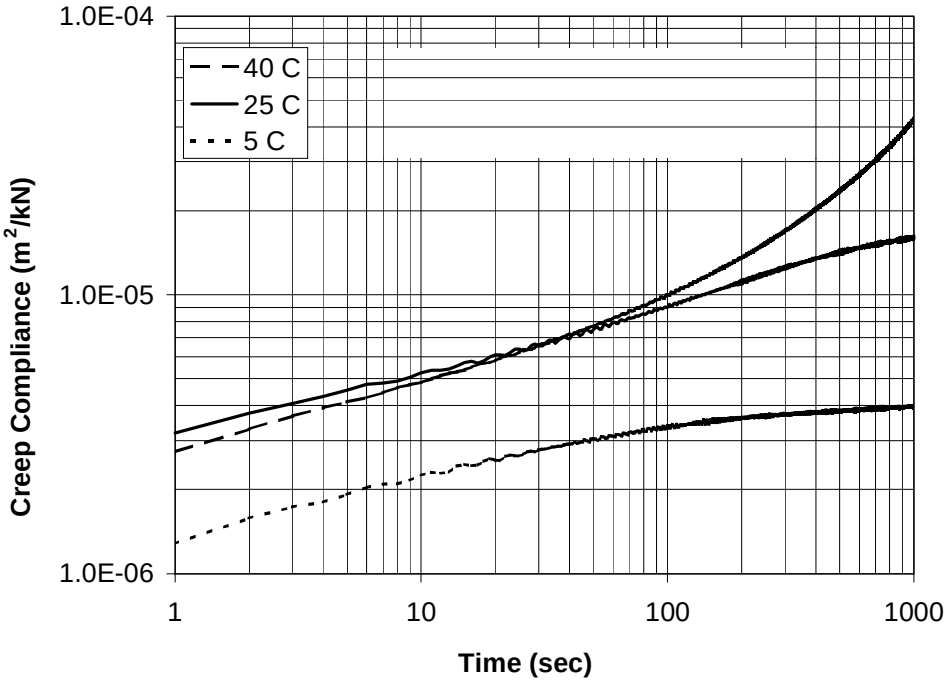


**Figure A 43 Average Creep Compliance, sections 1 through 9.**

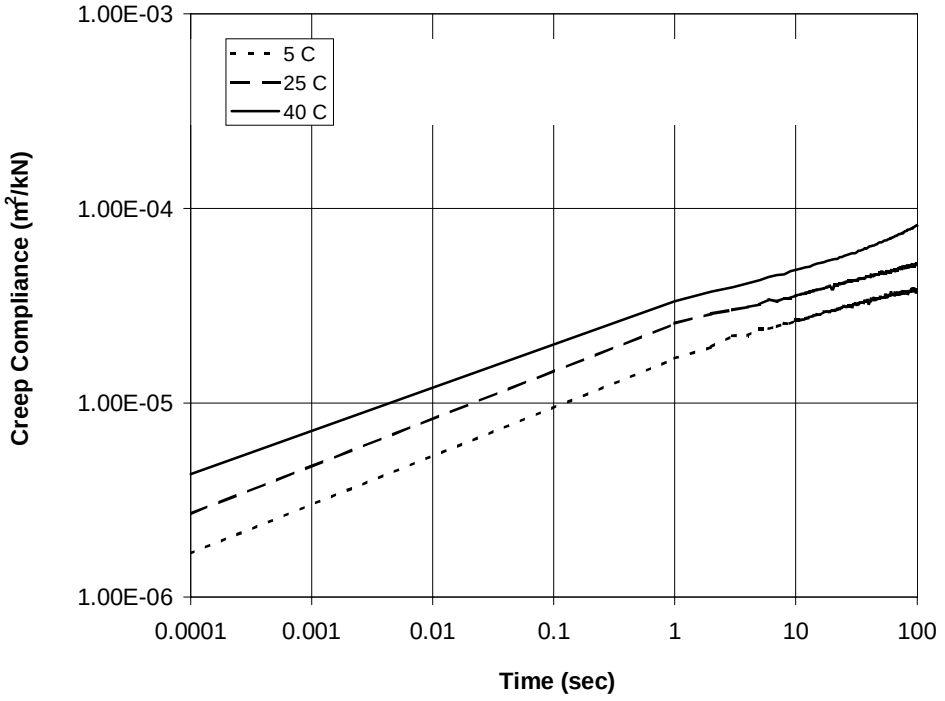


**Figure A 44 Creep compliance for specimen 1-1.**

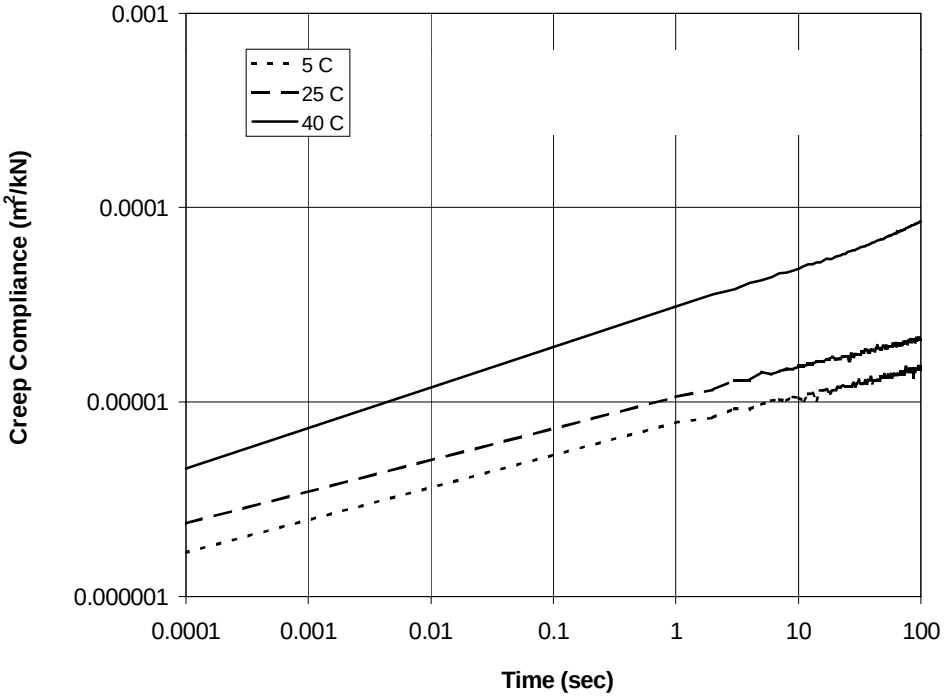


**Figure A 45 Creep compliance for specimen 1-2.**

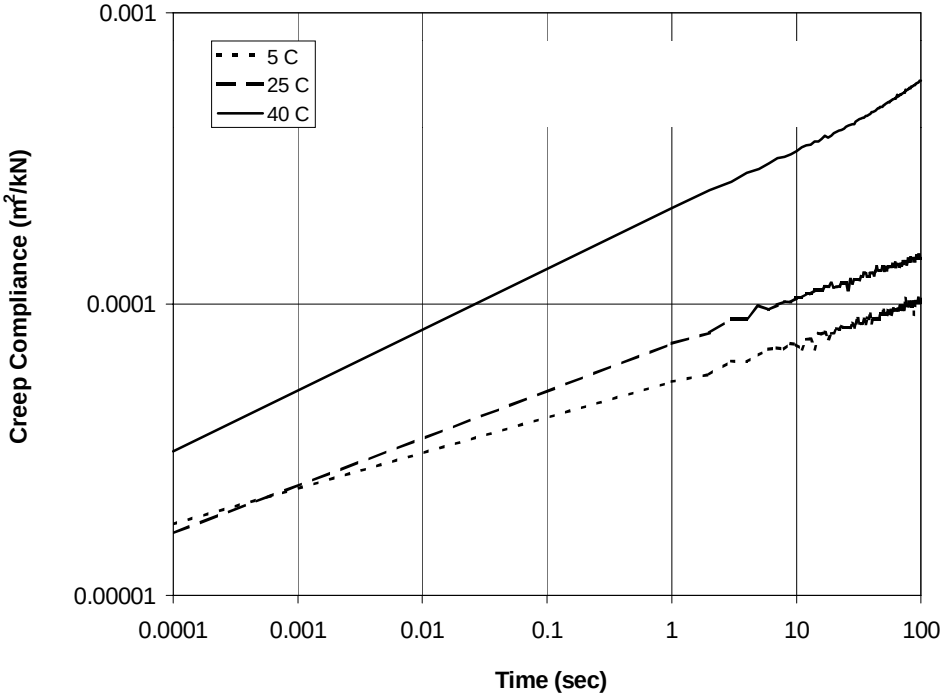


**Figure A 46 Creep compliance for specimen 1-3.**

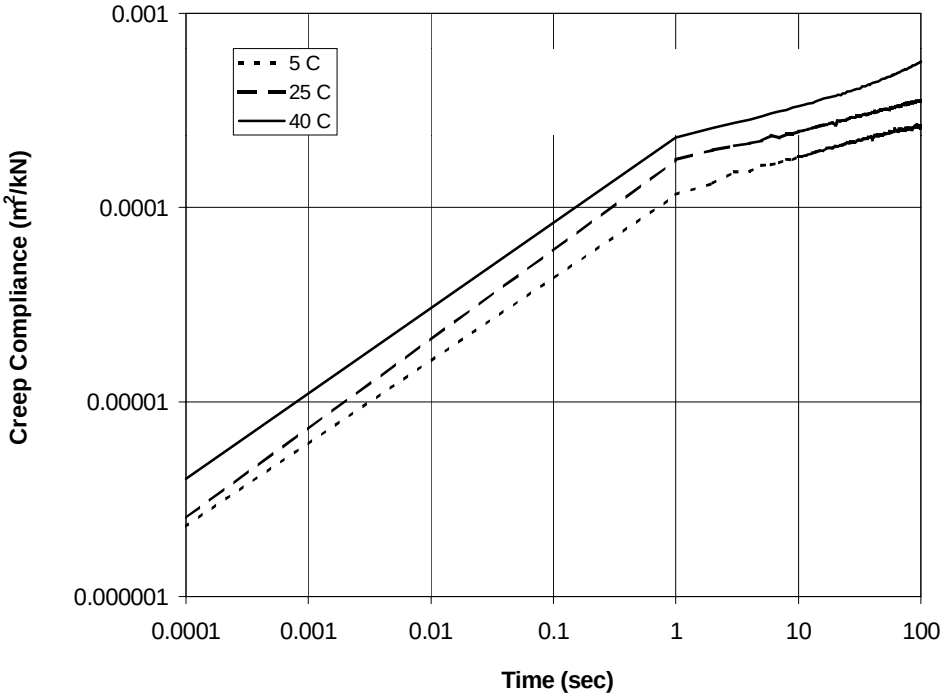


**Figure A 47 Creep compliance for specimen 1-4.**

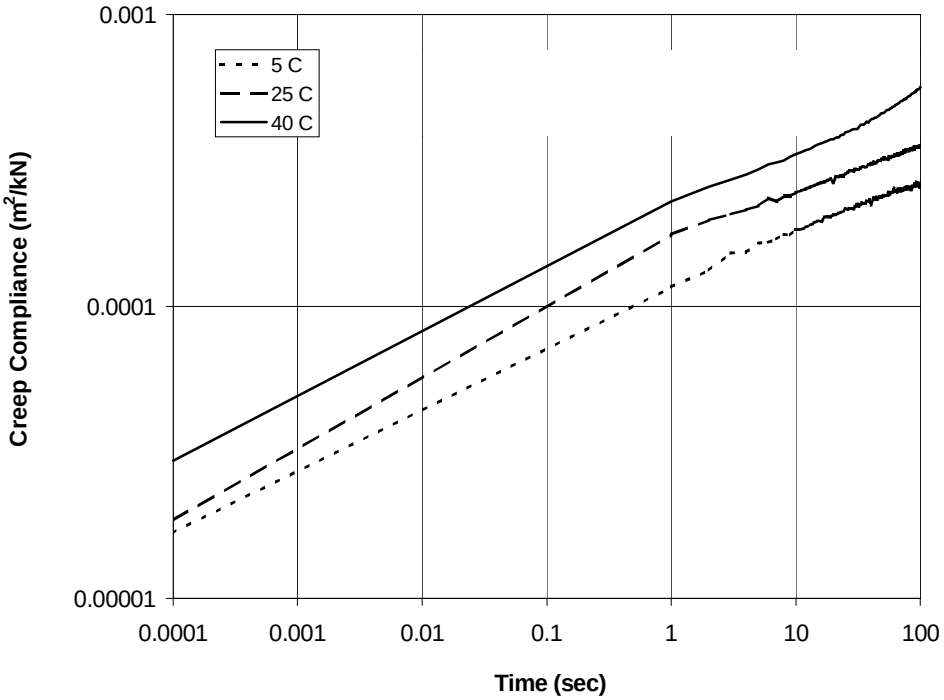


**Figure A 48 Creep compliance for specimen 1-5.**

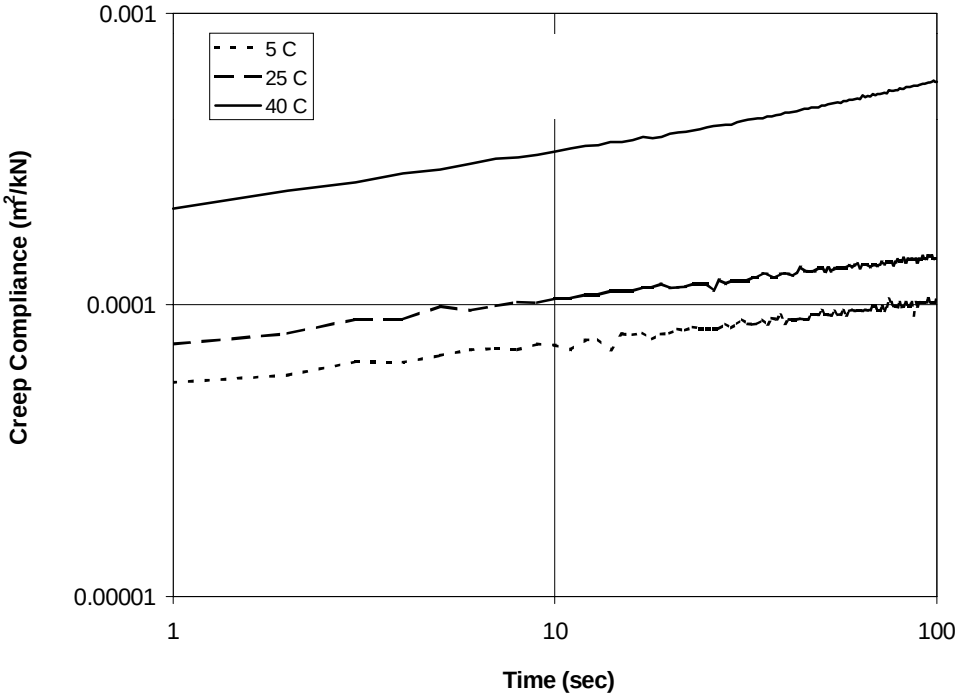


**Figure A 49 Creep compliance for specimen 1-6.**

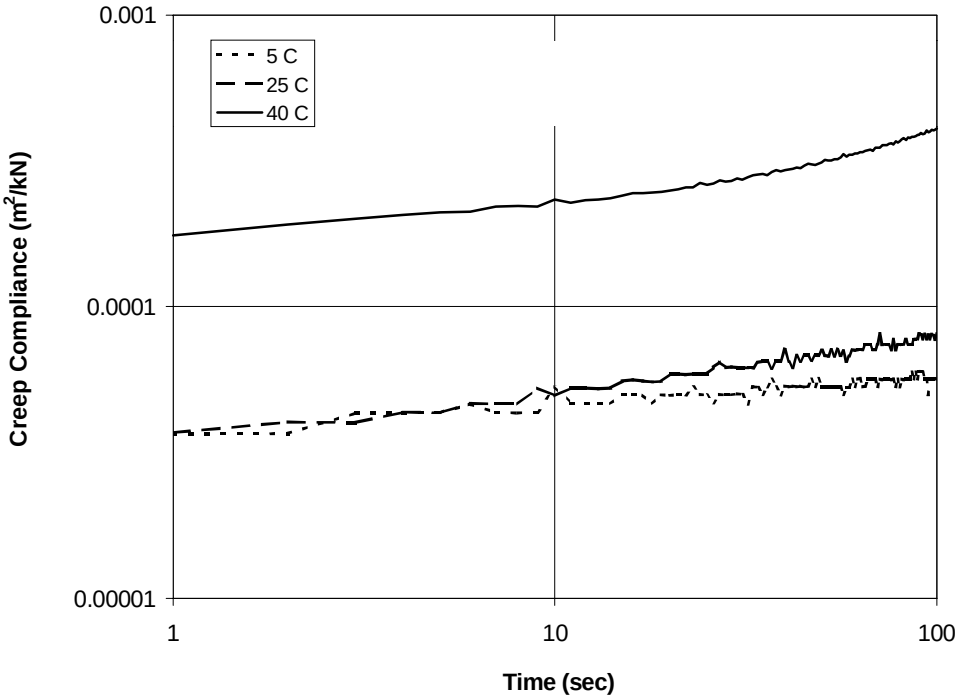


**Figure A 50 Creep compliance for specimen 2-1.**

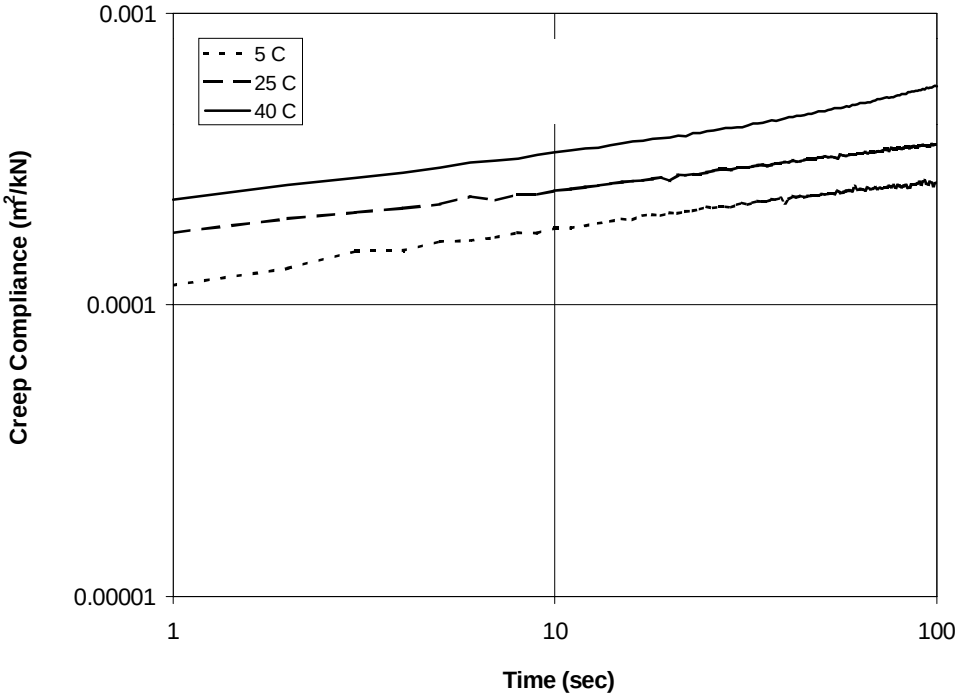


**Figure A 51 Creep compliance for specimen 2-2.**

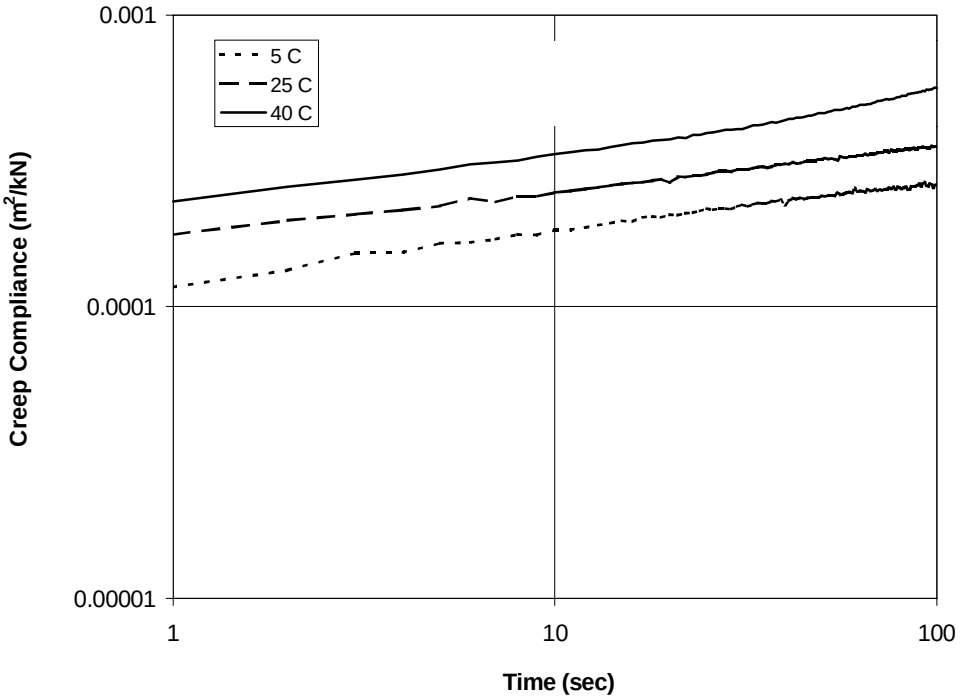


**Figure A 52 Creep compliance for specimen 2-3.**

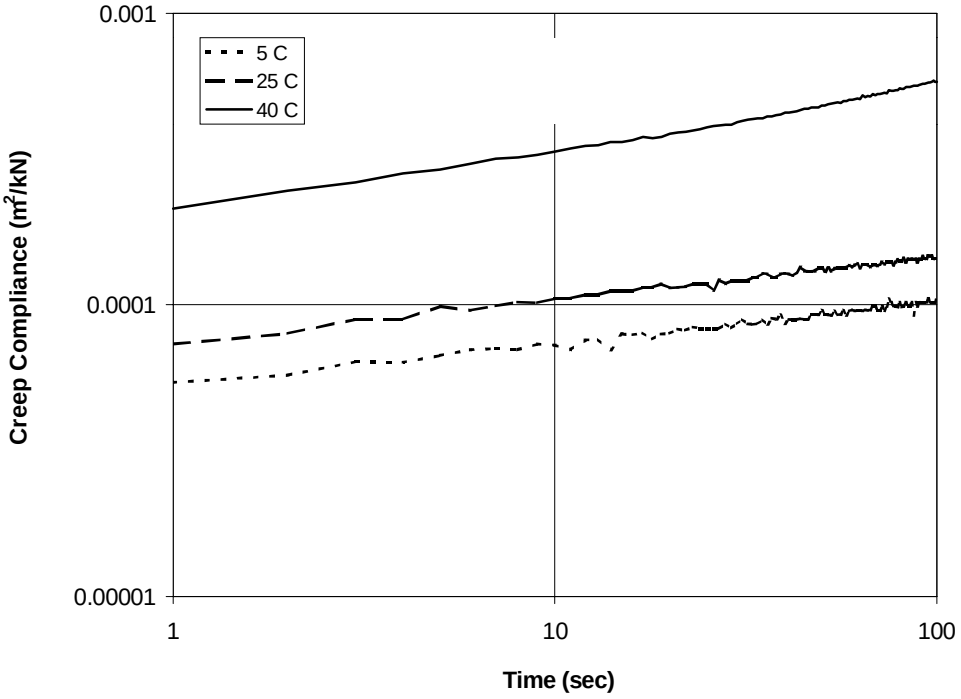


**Figure A 53 Creep compliance for specimen 2-4.**

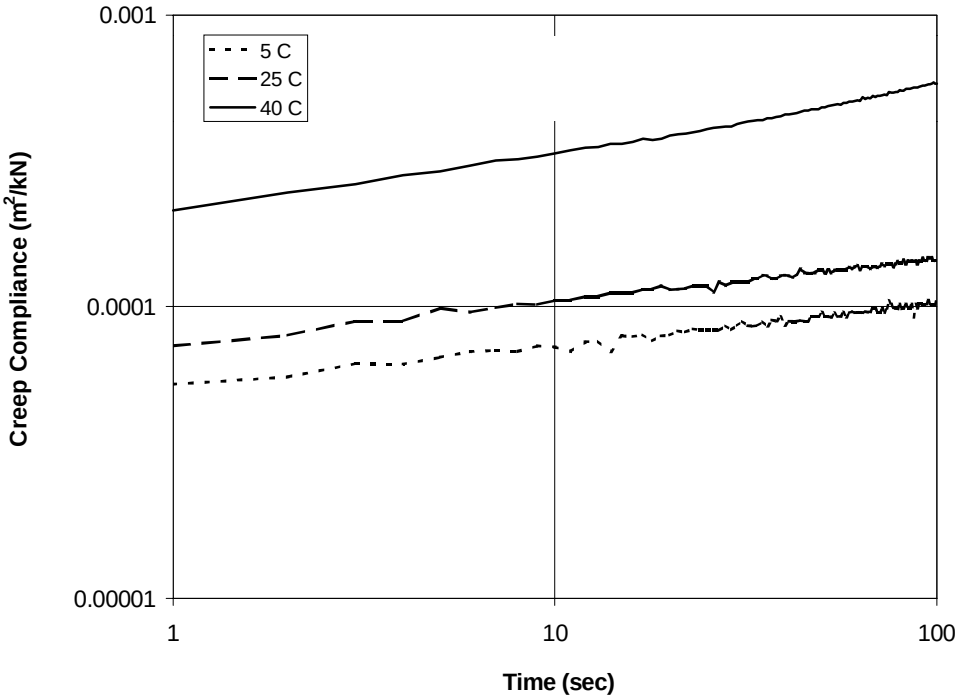


**Figure A 54 Creep compliance for specimen 2-5.**

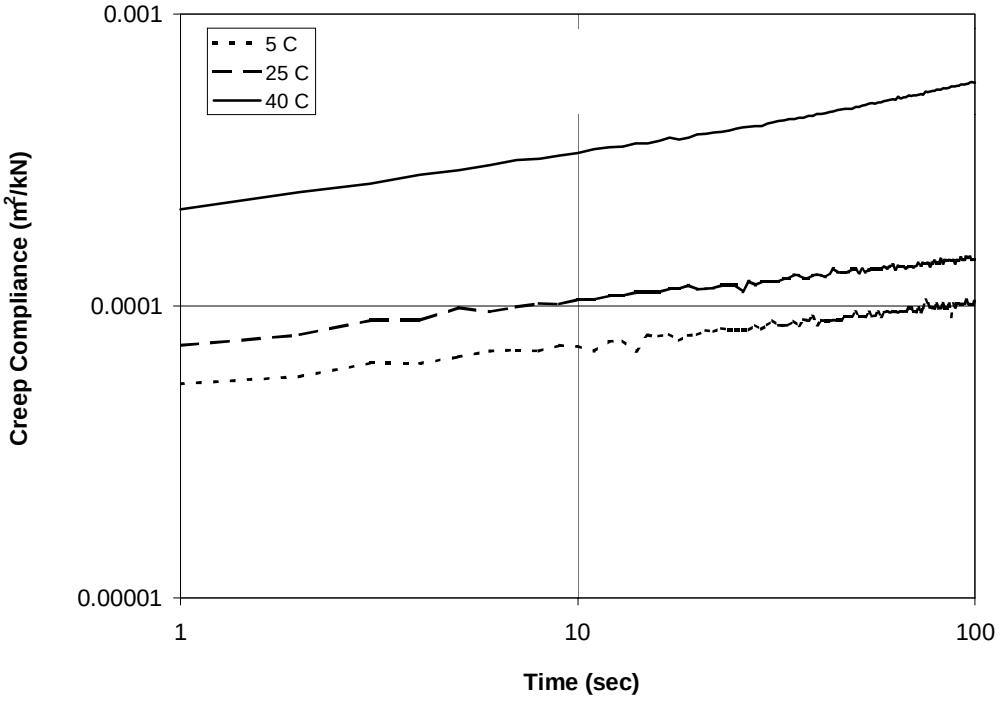


**Figure A 55 Creep compliance for specimen 2-6.**

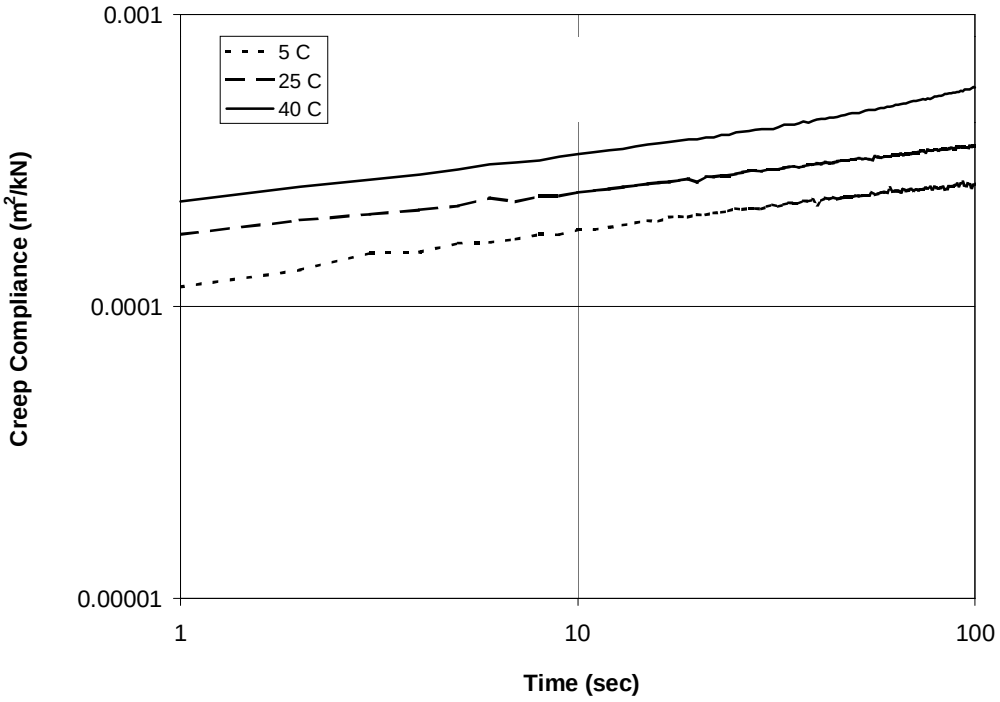


**Figure A 56 Creep compliance for specimen 3-1.**

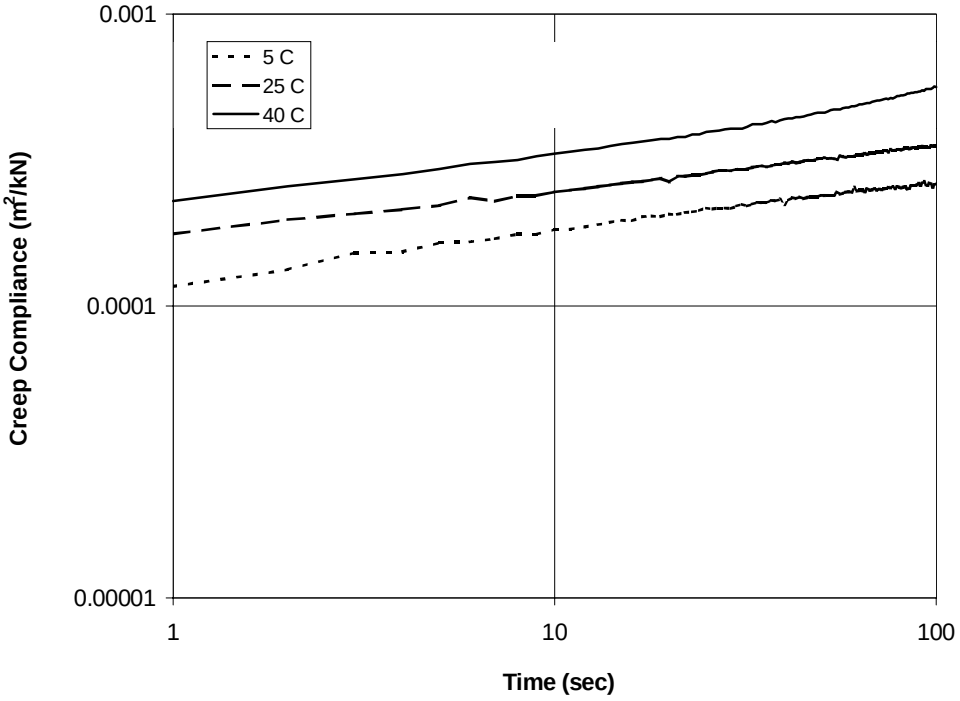


**Figure A 57 Creep compliance for specimen 3-2.**

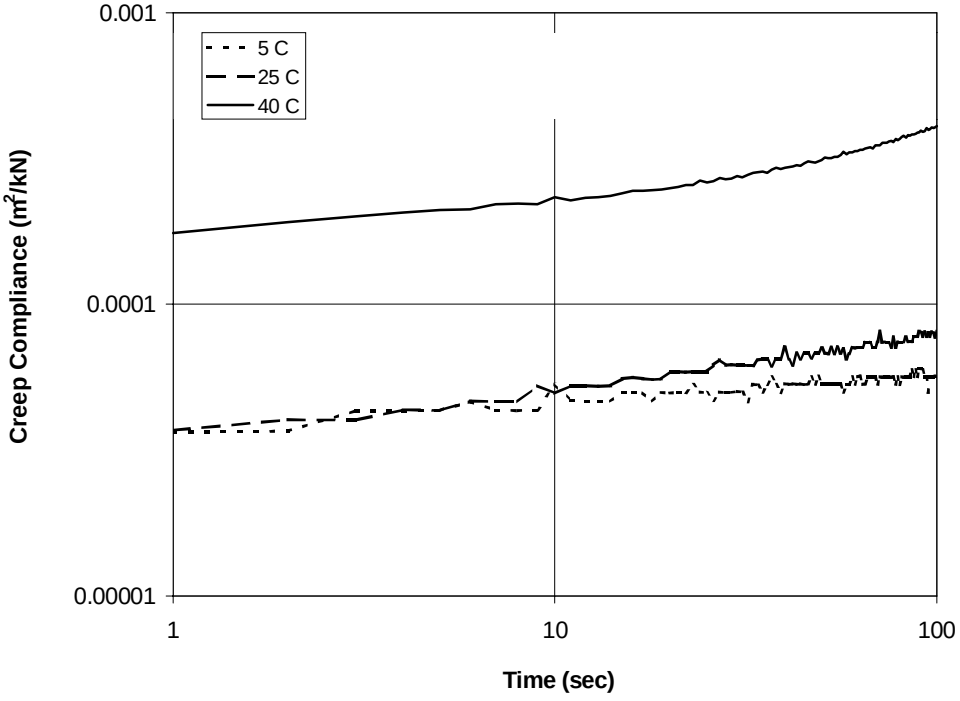


**Figure A 58 Creep compliance for specimen 3-3.**

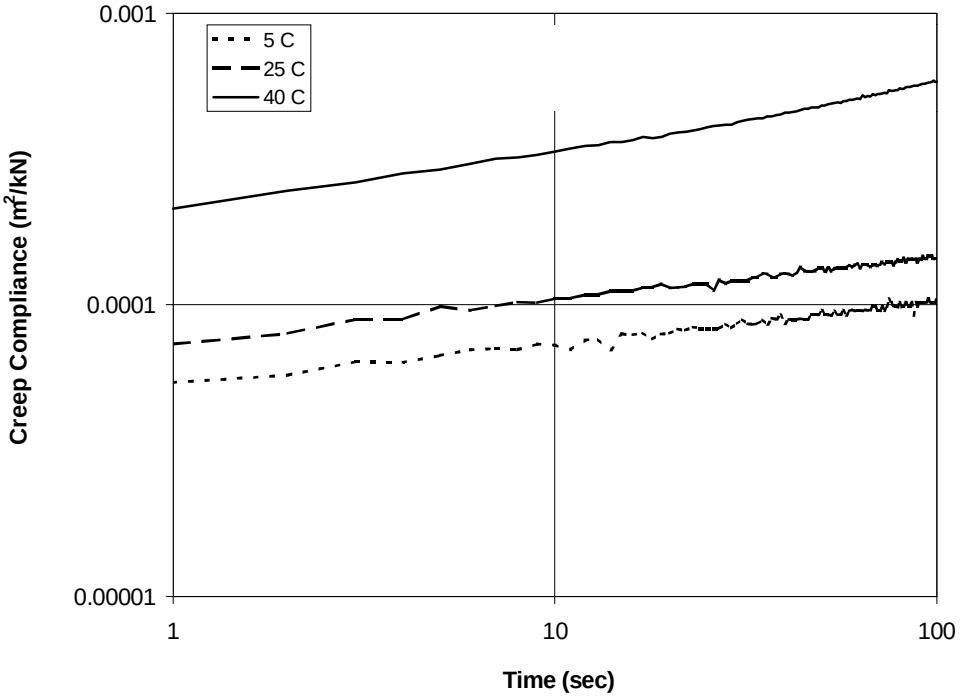


**Figure A 59 Creep compliance for specimen 3-4.**

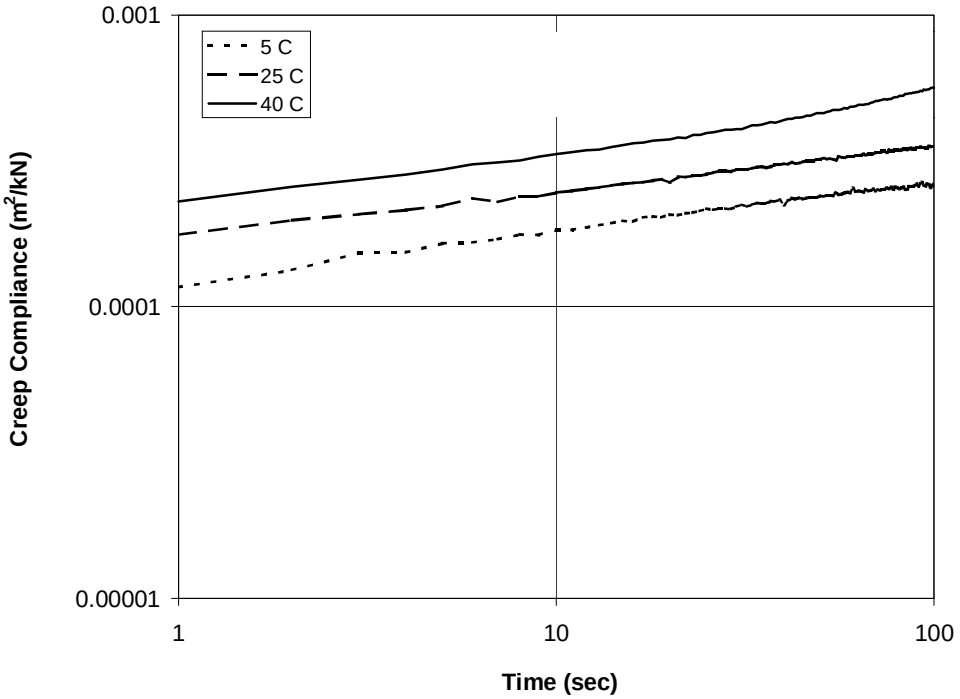


**Figure A 60 Creep compliance for specimen 3-5.**

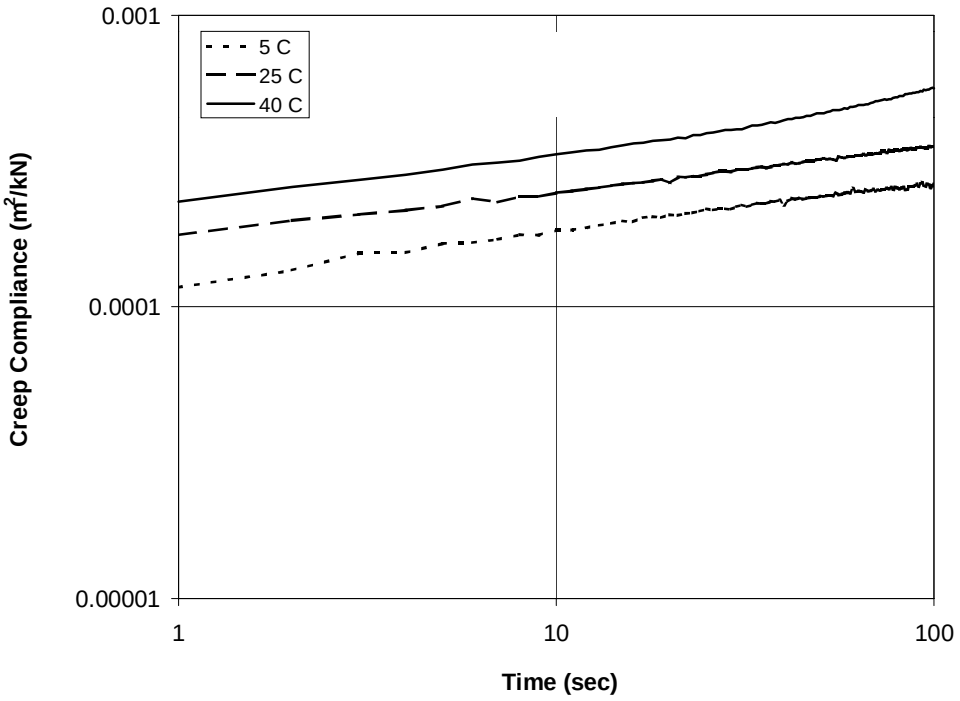


**Figure A 61 Creep compliance for specimen 3-6.**

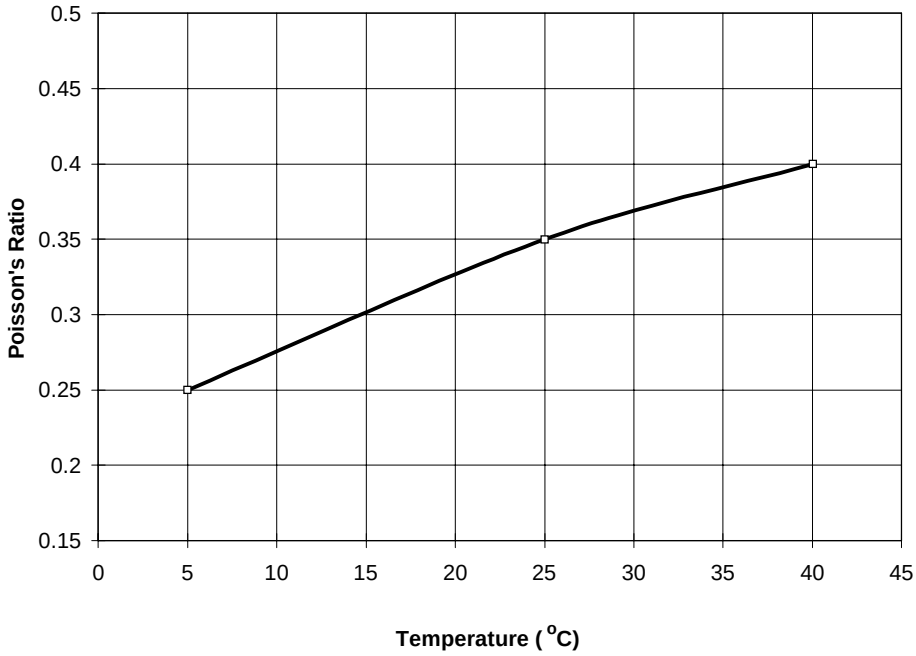


**Figure A 62 Poisson's ratio as a function of temperature.**

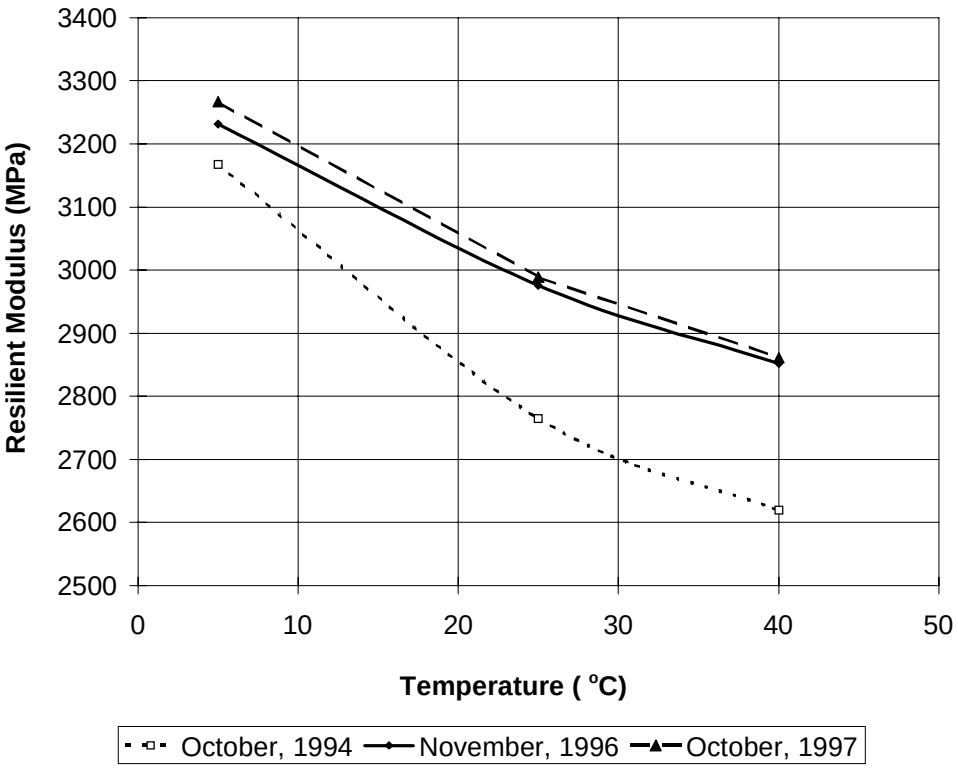


**Figure A 63 Resilient modulus of field specimens as a function of time and temperature.**

# APPENDIX B

# SITE INSTRUMENTATION

## Table B 1 List of all the instruments in the test section.

| Pressure Cells | | Triggers | Strain Gauges | | | | | Thermocouples | Gypsum Blocks |
|---|---|---|---|---|---|---|---|---|---|
| Subgrade | Base Course | | Asphalt | Asphalt | Geotextile | Geogrid | Soil | | |
| 1-KEP-1-SG | 1-CEP-1-BC | 1 TRIG 1 | 1-KST-1-S | 5-KST-18-L | 2-FST-1-S | 3-GST-1-S | 1-CST-1-S | 1-TC-1-SG/-6" | 1-GB-1-SG-2' |
| 1-KEP-2-SG | 1-CEP-2-BC | 4 TRIG 2 | 1-KST-2-L | 5-KST-19-S | 2-FST-2-L | 3-GST-2-L | 1-CST-2-L | 1-TC-2-BC/MID | 1-GB-2-SG-6" |
| 2-CEP-4-SG | 1-CEP-3-BC | 5 TRIG 3 | 1-KST-3-S | 5-KST-20-L | 2-FST-3-S | 3-GST-3-S | 4-CST-3-S | 1-TC-3-AS | 1-GB-3-BC-MID |
| 2-CEP-5-SG | 4-CEP-8-BC | 6 TRIG 4 | 1-KST-4-L | 6-KST-21-S | 2-FST-4-L | 3-GST-4-L | 4-CST-4-L | 2-TC-4-AS | 2-GB-1-SG-2' |
| 3-CEP-6-SG | 4-CEP-9-BC | | 2-KST-5-S | 6-KST-22-L | 2-FST-5-S | 3-GST-5-S | 7-CST-5-S | 2-TC-5-AS | 2-GB-2-SG-6" |
| 3-CEP-7-SG | 4-CEP-10-BC | | 2-KST-6-L | 6-KST-23-S | 2-FST-6-S | 3-GST-6-S | 7-CST-6-L | 3-TC-6-AS | 2-GB-3-BC-MID |
| 4-KEP-3-SG | 7-CEP-15-BC | | 2-KST-7-S | 6-KST-24-L | 5-FST-7-S | 6-GST-7-S | | 3-TC-7-AS | 3-GB-1-SG-2' |
| 4-KEP-4-SG | 7-CEP-16-BC | | 2-KST-8-L | 7-KST-25-S | 5-FST-8-L | 6-GST-8-L | | 4-TC-8-SG/-6" | 3-GB-2-SG-6" |
| 5-CEP-11-SG | 7-CEP-17-BC | | 3-KST-9-S | 7-KST-26-L | 5-FST-9-S | 6-GST-9-S | | 4-TC-9-BC/MID | 3-GB-3-BC-MID |
| 5-CEP-12-SG | | | 3-KST-10-L | 7-KST-27-S | 5-FST-10-L | 6-GST-10-L | | 4-TC-10-AS | 7-GB-1-SG-2' |
| 6-CEP-13-SG | | | 3-KST-11-S | 7-KST-28-L | 5-FST-11-S | 6-GST-11-S | | 7-TC-11-SG/-6" | 7-GB-2-SG-6" |
| 6-CEP-14-SG | | | 3-KST-12-L | 8-KST-29-S | 5-FST-12-S | 6-GST-12-S | | 7-TC-12-BC/MID | 7-GB-3-BC-MID |
| 7-KEP-5-SG | | | 4-KST-13-S | 8-KST-30-L | 8-FST-13-S | 9-GST-13-S | | 7-TC-13-AS | 8-GB-1-SG-2' |
| 7-KEP-6-SG | | | 4-KST-14-L | 8-KST-31-S | 8-FST-14-L | 9-GST-14-L | | 8-TC-14-AS | 8-GB-2-SG-6" |
| 8-CEP-18-SG | | | 4-KST-15-S | 8-KST-32-L | 8-FST-15-S | 9-GST-15-S | | 8-TC-15-AS | 8-GB-3-BC-MID |
| 8-CEP-19-SG | | | 4-KST-16-L | 9-KST-33-S | 8-FST-16-L | 9-GST-16-L | | 9-TC-16-AS | 9-GB-1-SG-2' |
| 9-CEP-20-SG | | | 5-KST-17-S | 9-KST-34-L | 8-FST-17-S | 9-GST-17-S | | 9-TC-17-AS | 9-GB-2-SG-6" |
| 9-CEP-21-SG | | | | 9-KST-35-S | 8-FST-18-S | 9-GST-18-S | | | 9-GB-3-BC-MID |

**Note:**

***Pressure cells, strain gages, triggers***

*First letter of the instrument designates the section number*
*Three letter alphabet describes the type of instrument*
*Two numbers describe the instrument number in the pavement section*

- *CST Soil Strain Gauge*
- *KST Asphalt Strain Gauge*
- *CEP Carlson Earth Pressure cell*
- *KEP Keulite Earth Pressure Cell*
- *TRIG Trigger*
- *SG Subgrade*
- *BC Base course*
- *S Short Direction*
- *L long Direction*

***Pressure cells, strain gages, triggers***

*First letter of the instrument designates the section number*
*Two letter alphabet describes the type of instrument*
*Two numbers describe the instrument number in the pavement section*
*Next numbers designate the layer and the location*

- *TC Thermocouple*
- *GB Gypsum Block*
- *AC HMA*
- *BC Base Course*
- *SG Subgrade*
- *MID Middle of Layer*

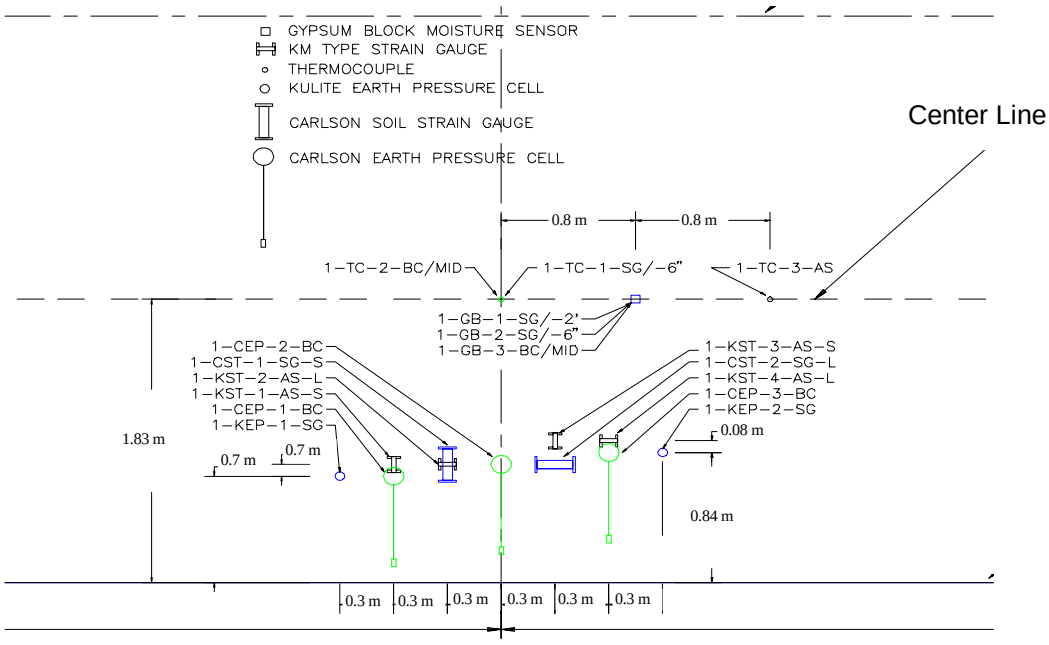


**Figure B 1 Instrumentation layout of section 1.**

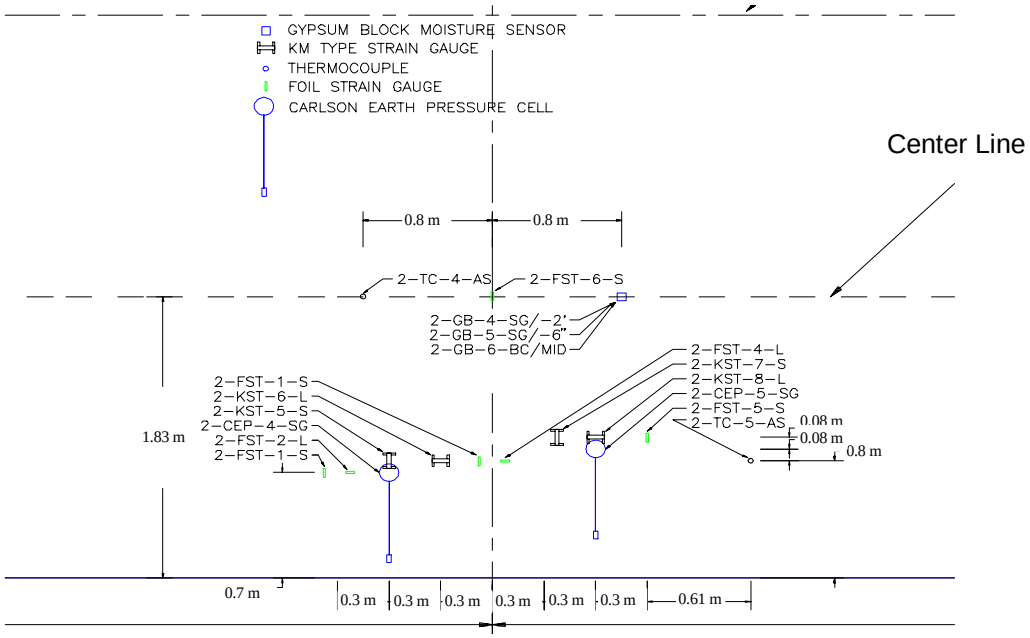


**Figure B 2 Instrumentation layout of section 2.**

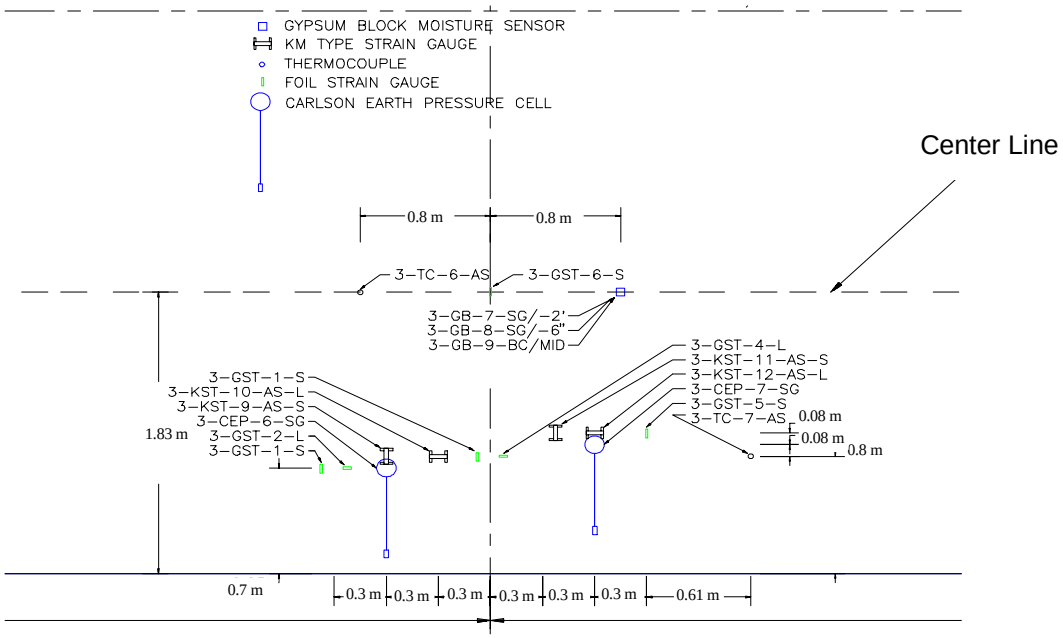


**Figure B 3 Instrumentation layout of section 3.**

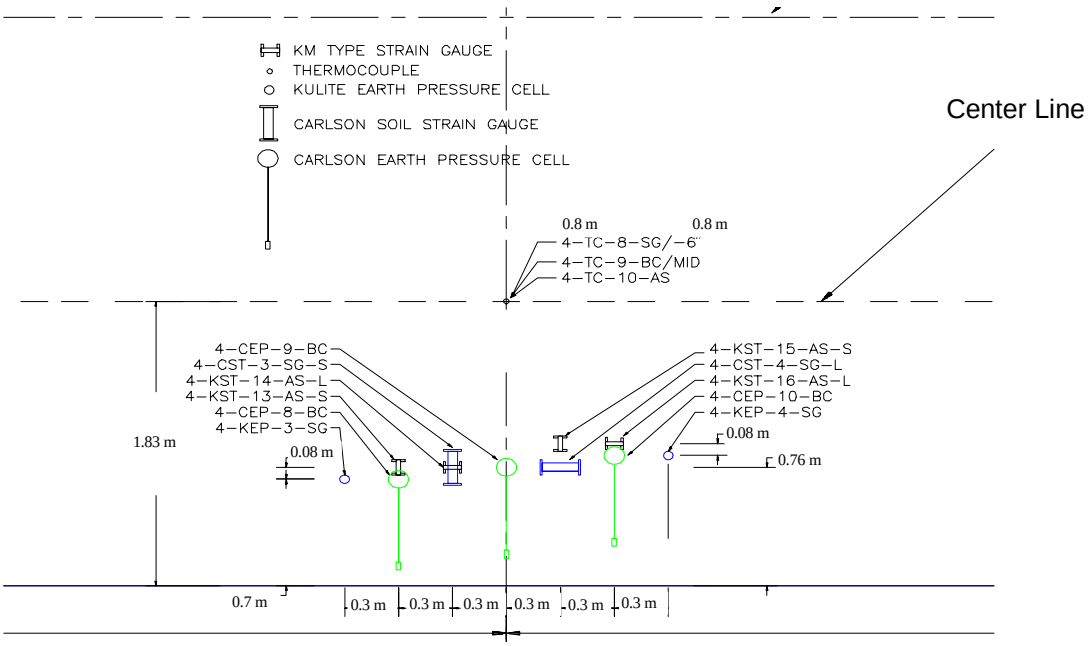


**Figure B 4 Instrumentation layout of section 4.**

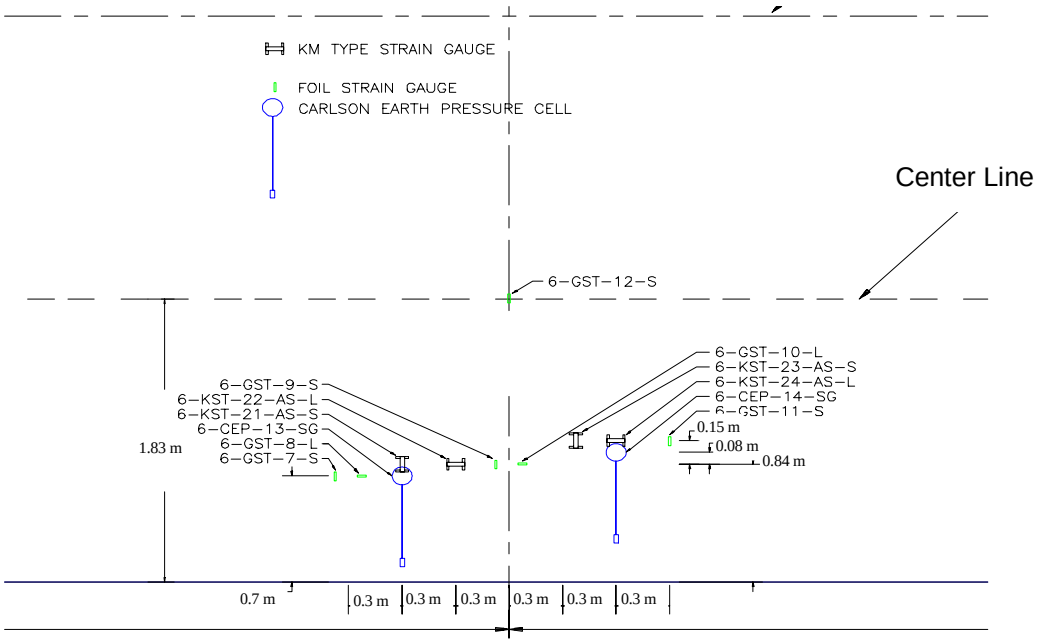


**Figure B 5 Instrumentation layout of section 5.**

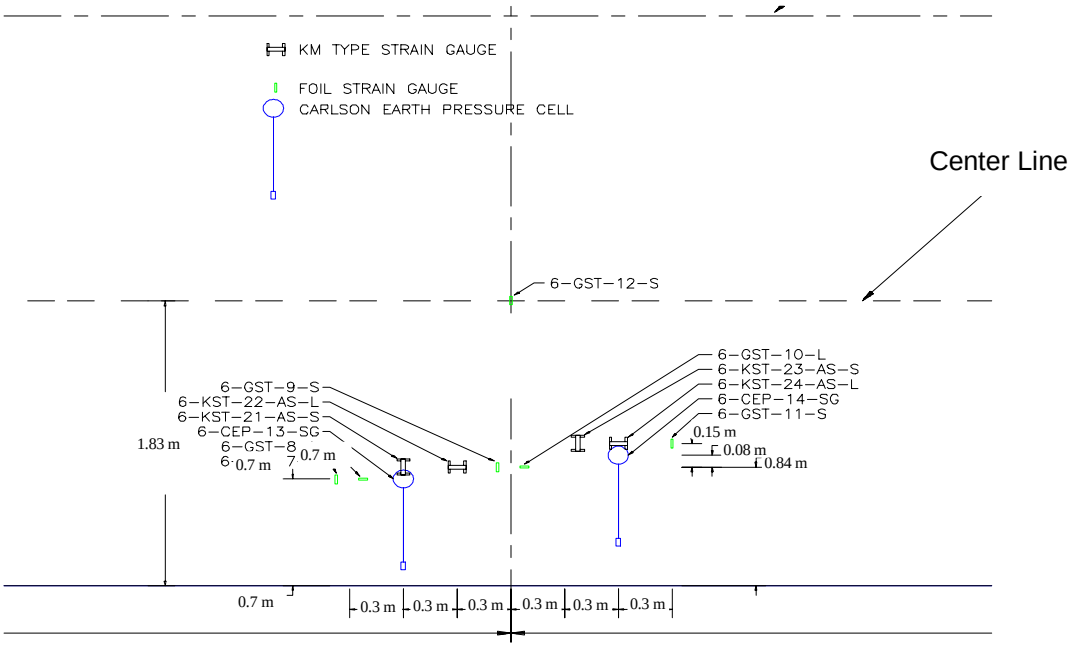


**Figure B 6 Instrumentation layout of section 6.**

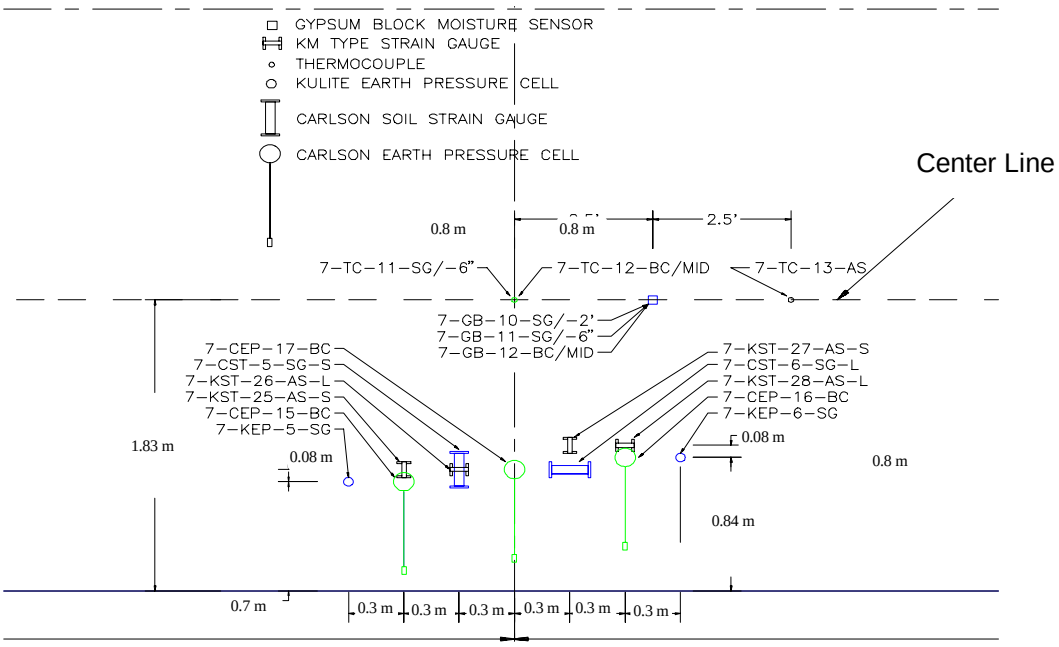


**Figure B 7 Instrumentation layout of section 7.**

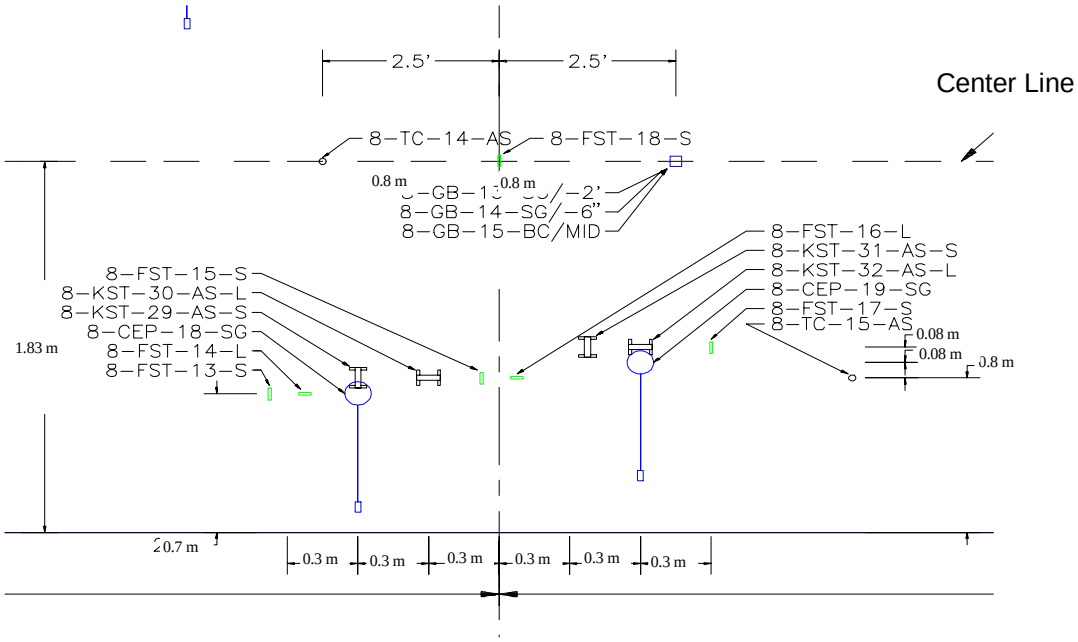


**Figure B 8 Instrumentation layout of section 8.**

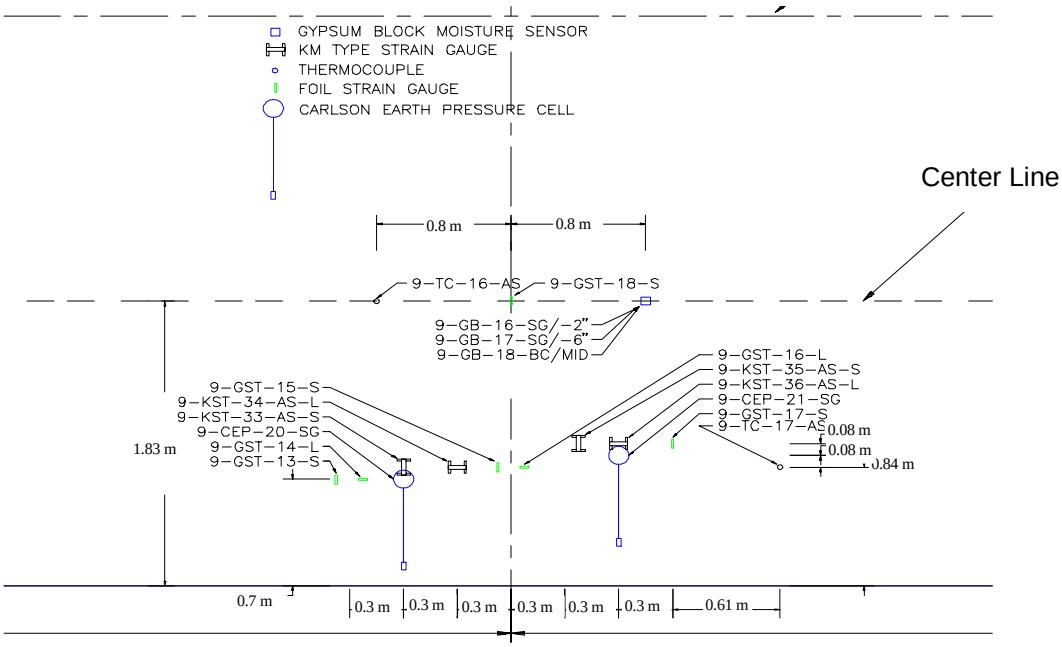


**Figure B 9 Instrumentation layout of section 9.**

# APPENDIX C

# DATA ACQUISITION PROGRAM

**Declaration of various subroutines in the data acquisition program**

```
DECLARE SUB manual (readsect%)
DECLARE SUB soil (channels$)
DECLARE SUB thermo (channels$, tcarsf%)
DECLARE SUB getdata (channels$, variable$, depth%)
DECLARE SUB triggers (readsect%, tcarsf%)
DECLARE SUB adconv (channels$, variable$, depth%, process$)
'$INCLUDE: 'KDAC500.BI'
DIM voltage!(273)
DIM SHARED temp!(20)
DIM SHARED sstr!(15)
```

**Calling intrinsic initialization subroutines**

```
CALL kdinit(BASIC.)
CALL softinit(BASIC.)
CLS
tcarsf% = 0
ON KEY(1) GOSUB outtahere
KEY(1) ON
```

**Assign all the channel names to each section**
**The soil strain gages are currently being read in the triggers subroutine**

```
s1$ = "S3.0,S3.5,S3.6,S3.7,S4.2"
s2$ = "S2.0,S2.1,S4.4,S4.5"
s3$ = "S2.2,S3.4,S4.6,S4.7"
s4$ = "S3.1,S2.3,S6.0,S2.4,S6.1,S5.0,S5.1,S5.3,smeter1"
s5$ = "S3.2,S2.5,S6.2"
s6$ = "S2.6,S2.7,S5.6"
s7$ = "S3.3,S6.3,S2.9,S2.10,S5.12,S5.13,smeter2,smeter3"
s8$ = "S3.9"
s9$ = "S3.8"
```

**mainroutine:**

**Check triggers to wait for car, and determine if it is starting from section 1 or 5 for manual triggering**

```
CALL manual(readsect%)
```

**For automatic triggering (based upon the piezoelectric sensors)**

```
CALL triggers(readsect%, tcarsf%)
IF readsect% = 1 THEN GOTO section1
IF readsect% = 5 THEN GOTO section5
```

**Variable numread = number of readings at 200 Hz**

```
section1:
CLS
LOCATE 10, 15
PRINT "Full Section ...."
```

**Read all the channels, section by section and save in different KEITHLEY variables sections 1 through 9**

```
channels2$ = s1$ + "," + s2$ + "," + s3$ + "," + s4$ + "," + s5$
channels1$ = s6$ + "," + s7$ + "," + s8$ + "," + s9$
channels$ = channels2$ + "," + channels1$
variable$ = "dat1"
process$ = "read"
depth% = 2000
CALL adconv(channels$, variable$, depth%, process$)
```

**Retrieve all the data from KEITHLEY variables, and save in a DOS file**

```
OPEN "c:\keithley\data.dat" FOR APPEND AS #1
PRINT #1, "All Sections"
PRINT #1, DATE$; TIME$;
CLOSE #1
channels2$ = s1$ + "," + s2$ + "," + s3$ + "," + s4$ + "," + s5$
channels1$ = s6$ + "," + s7$ + "," + s8$ + "," + s9$
channels$ = channels2$ + "," + channels1$
variable$ = "dat1"
process$ = "read"
depth% = 2000
CALL getdata(channels$, variable$, depth%)
OPEN "c:\keithley\data.dat" FOR APPEND AS #1
PRINT #1, "New Car"; DATE$; TIME$
CLOSE #1
GOTO mainroutine
```

**section5:**

```
CLS
LOCATE 10, 15
PRINT "Section 6 - 9 ...."
```

**Read all the channels, section by section and save in different KEITHLEY variables sections 6 through 9**

```
channels$ = s7$ + "," + s8$ + "," + s9$
variable$ = "dat"
process$ = "read"
depth% = 1100
CALL adconv(channels$, variable$, depth%, process$)
```

**Retrieve all the data from KEITHLEY variables, and save in a DOS file**

```
OPEN "c:\keithley\data.dat" FOR APPEND AS #1
PRINT #1, "Section 6 To 9 Intersection Car"
```

```
PRINT #1, DATE$; TIME$;
CLOSE #1
CALL getdata(channels$, variable$, depth%)
OPEN "c:\keithley\data.dat" FOR APPEND AS #1
PRINT #1, "New Car"; DATE$; TIME$
CLOSE #1
GOTO mainroutine
```

**outtahere:**

```
END
```

**SUB adconv (channels$, variable$, depth%, process$)**

**Setup background reading, Setup interrupts to determine sampling rate Interrupt set at 5 milliseconds**

```
CALL bgread(variable$, depth%, channels$, 1, NONE, 1, NT, process$)
CALL inton(5, MIL)
```

**Check background process, and wait until it is done to continue**

```
stat% = -1
WHILE stat% <> ST.DONE
  CALL bgstatus(process$, stat%)
WEND
CALL intoff
END SUB
```

**SUB getdata (channels$, variable$, depth%)**

```
DIM voltage!(depth%)

arnm$ = variable$
ioname$ = SPACE$(10)
length% = LEN(channels$)
```

**Determine the number of channels that were read for set of readings**

```
p% = 0
numchannels% = 1
DO
  p% = p% + 1
  IF (MID$(channels$, p%, 1) = ",") THEN numchannels% = numchannels% + 1
LOOP UNTIL p% = length%
P1% = 1
P2% = P1%
OPEN "c:\keithley\data.dat" FOR APPEND AS #1
```

**Determine the name of each channel in the channels$ variable**

```
FOR i% = 1 TO numchannels%

  DO WHILE ((MID$(channels$, P2%, 1) <> ",") AND (P2% < length%))
  P2% = P2% + 1
  LOOP
  IF P2% = length% THEN P2% = P2% + 1
  iolength% = P2% - P1%
  ioname$ = MID$(channels$, P1%, iolength%)
  P1% = P2% + 1
  P2% = P1%
```

**Get all of the data from the channel that was just determined**

```
CALL arget(arnm$, 1, depth%, ioname$, 1, VARSEG(voltage!(0)), VARPTR
            (voltage!(0)), C.MILVLT)
```

**Save the data to an ASCII file**

```
          PRINT #1, ioname$
          FOR j% = 0 TO (depth% - 1)
            PRINT #1, voltage!(j%)
          NEXT j%
NEXT i%
CLOSE #1
CALL ardel(arnm$)

END SUB
```

**SUB manual (readsect%)**

```
10     CLS
          LOCATE 10, 10
          PRINT "1.   Section 1 - 9"
          LOCATE 11, 10
          PRINT "2.   Section 6 - 9"
          LOCATE 12, 10
          PRINT "3.   END"
          LOCATE 20, 10
          INPUT "Enter Selection (1-3)    "; se
          IF se = 1 THEN 20
          IF se = 2 THEN 20
          IF se = 3 THEN END
          GOTO 10
```

```
20  IF se = 1 THEN readsect% = 1
    IF se = 2 THEN readsect% = 5

channels$ = "TC0,TC1,TC2,TC3,TC4,TC5,TC6,TC7,TC8,TC9,TC10,TC12,TC13,
                TC14,TC15"
CALL thermo(channels$, tcarsf%)
END SUB
```

**SUB soil (channels$)**

**Read all Soil strain channels**

```
CALL fgread(channels$, NONE, VARSEG(sstr!(0)), VARPTR(sstr!(0)), C.MILVLT, NT)
OPEN "c:\keithley\soil.dat" FOR APPEND AS #1
PRINT #1, DATE$; TIME$;
FOR i% = 0 TO 10
PRINT #1, sstr!(i%); ",";
NEXT i%
CLOSE
END SUB
```

**SUB thermo (channels$, tcarsf%)**

**Read all thermocouple channels**

```
CALL fgread(channels$, NONE, VARSEG(temp!(0)), VARPTR(temp!(0)),
                C.THCU.T, NT)

OPEN "c:\keithley\temp.dat" FOR APPEND AS #1
PRINT #1, DATE$; TIME$; tcarsf%;
FOR i% = 0 TO 15
PRINT #1, temp!(i%); ",";
NEXT i%
CLOSE
END SUB
```

**SUB triggers (readsect%, tcarsf%)**

```
readsect% = 0
DIM trig!(4)
trig!(0) = 0
trig!(1) = 0
trig!(2) = 0
trig!(3) = 0

trigchan$ = "S3.0,S3.1,S3.2,S3.3"
```

```
'channels$ = "smeter0, smeter1, smeter2, smeter3"
'CALL soil(channels$)
```

**Read trigger channels until they exceed the threshold voltages. Threshold voltages are defined in the WHILE statement**

```
WHILE trig!(0) < 500
```

**Check to see if it is time to quit and upload data**

```
 IF TIME$ = "21:00:00" THEN END

CALL fgread(trigchan$, NONE, VARSEG(trig!(0)), VARPTR(trig!(0)), C.MILVLT, NT)

        IF trig!(0) > 20 THEN tcarsf% = tcarsf% + 1
        LOCATE 10, 10
        PRINT "Waiting For a Car....."
```

**All of these statements are just to check voltages during setup**

```
        PRINT USING "Trigger 1 S3.0 ###.## "; trig!(0)
        PRINT USING "Weigh in Motion S3.1  ###.##"; trig!(1)
        PRINT USING "Weigh in Motion S3.2  ###.##"; trig!(2)
        PRINT USING "Trigger 2 S3.3 ###.## "; trig!(3)
WEND
```

**Determine if the trigger in section 1 or section 5 triggered the system, and pass the value back to the main routine**

```
IF trig!(0) > 500 THEN readsect% = 1
IF trig!(3) > 500 THEN readsect% = 5
```

**tc:**

```
channels$ = "TC0,TC1,TC2,TC3,TC4,TC5,TC6,TC7,TC8,TC9,TC10,TC12,TC13,
             TC14,TC15"
CALL thermo(channels$, tcarsf%)

END SUB
```

# APPENDIX D

# TEMPERATURE AND WEATHER DATA

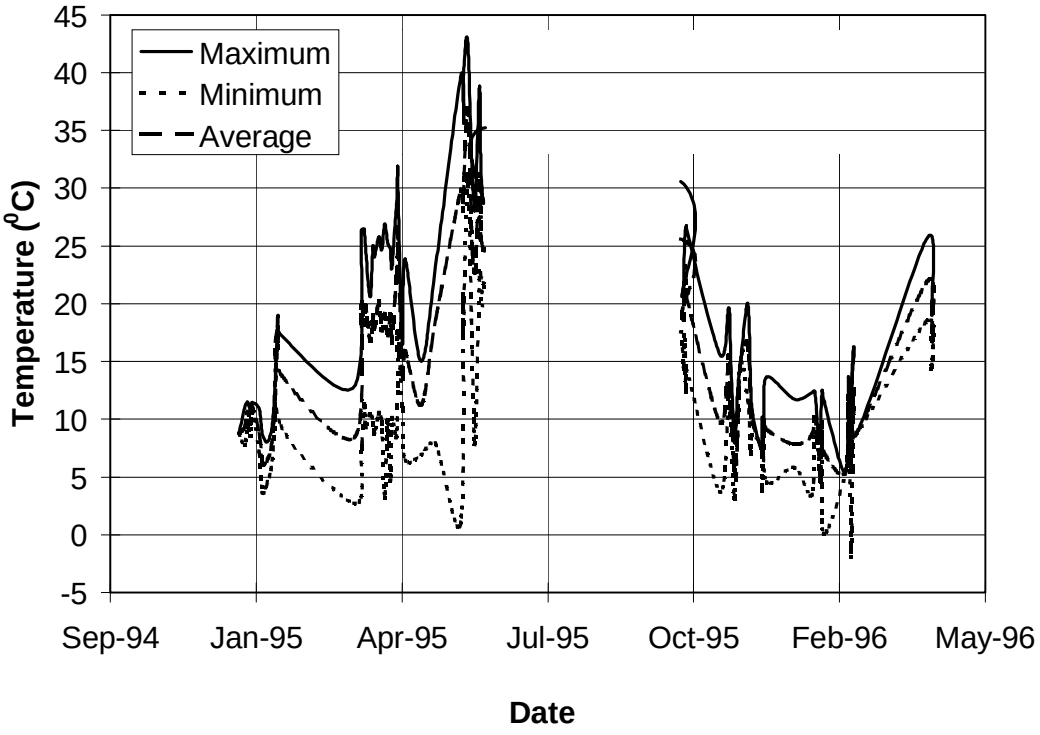


**Figure D 1 Temperature variation measured by thermocouple 1-TC-1-SG-15.**

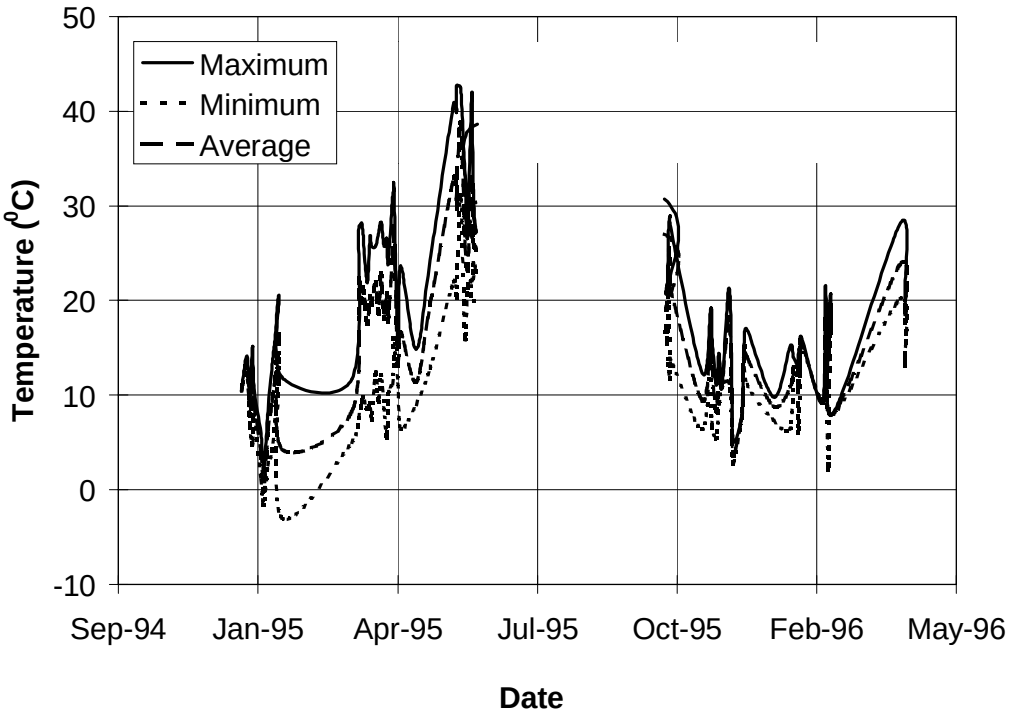


**Figure D 2 Temperature variation measured by thermocouple 1-TC-2-BC-MID.**

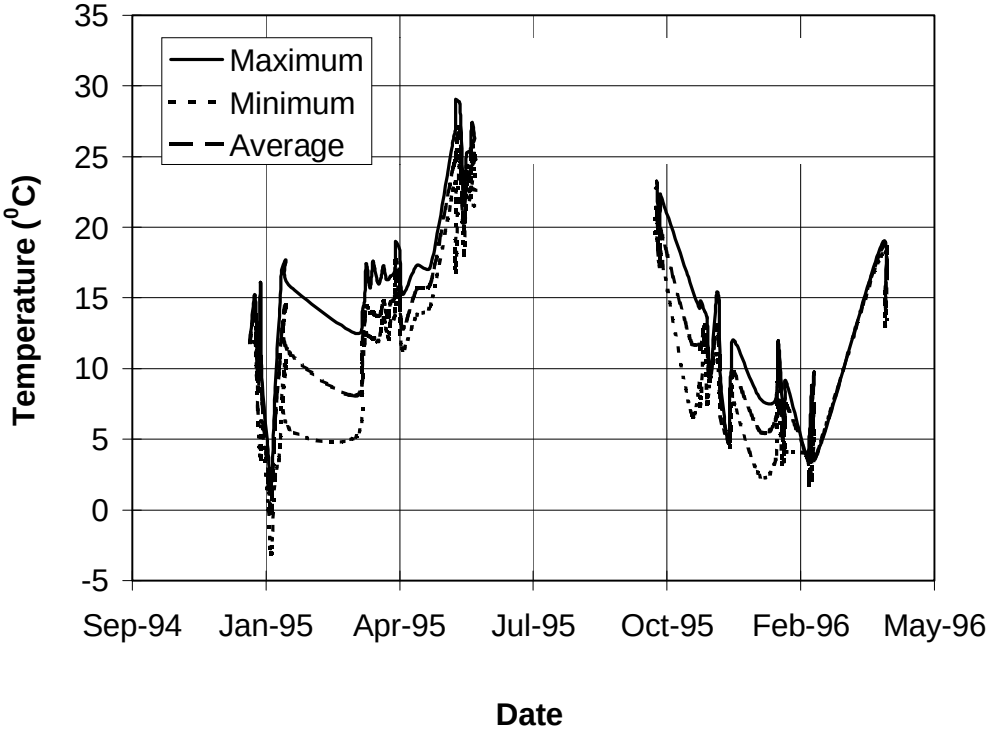


**Figure D 3 Temperature variation measured by thermocouple 2-TC-4-AS.**

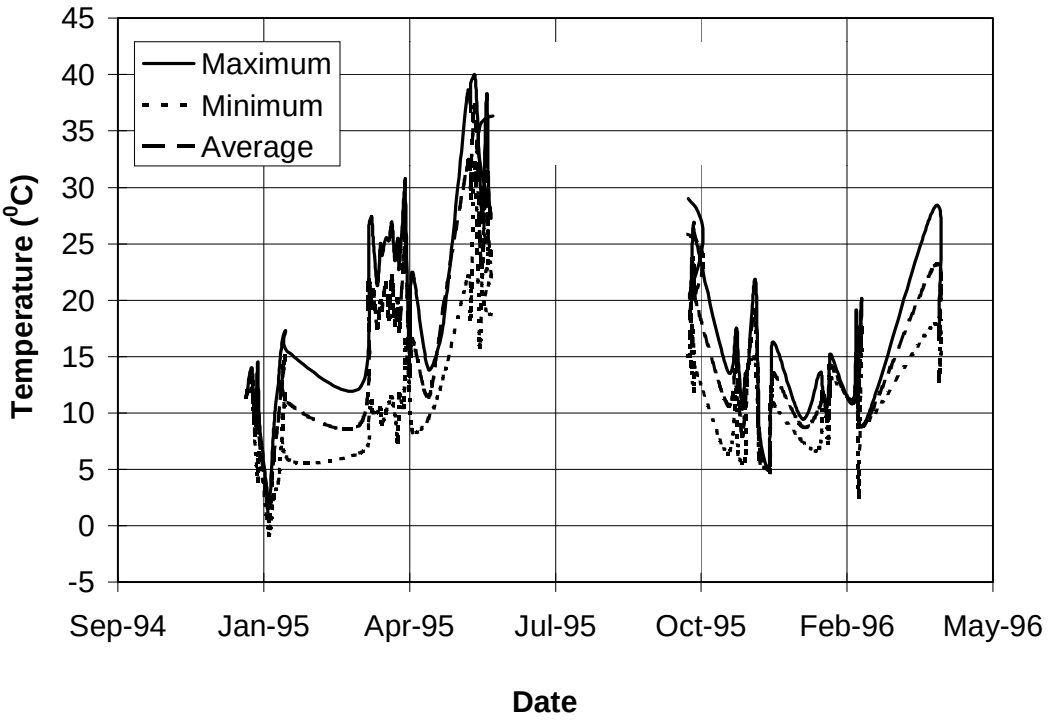


**Figure D 4 Temperature variation measured by thermocouple 2-TC-5-AS.**

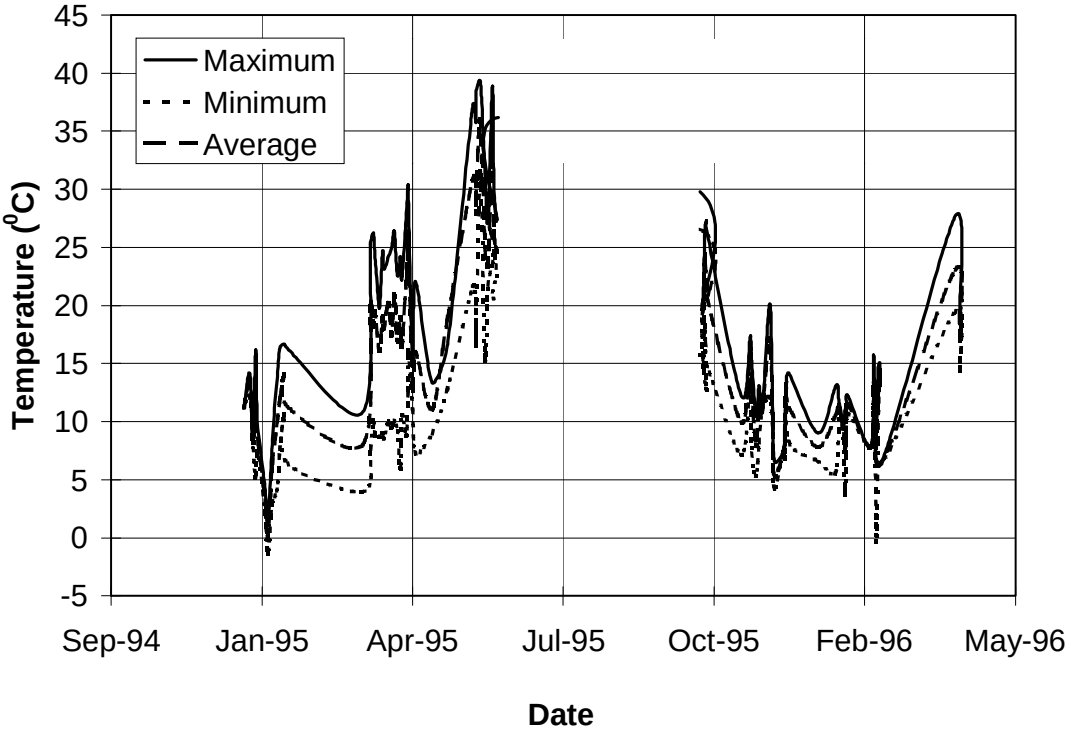


**Figure D 5 Temperature variation measured by thermocouple 3-TC-6-AS.**

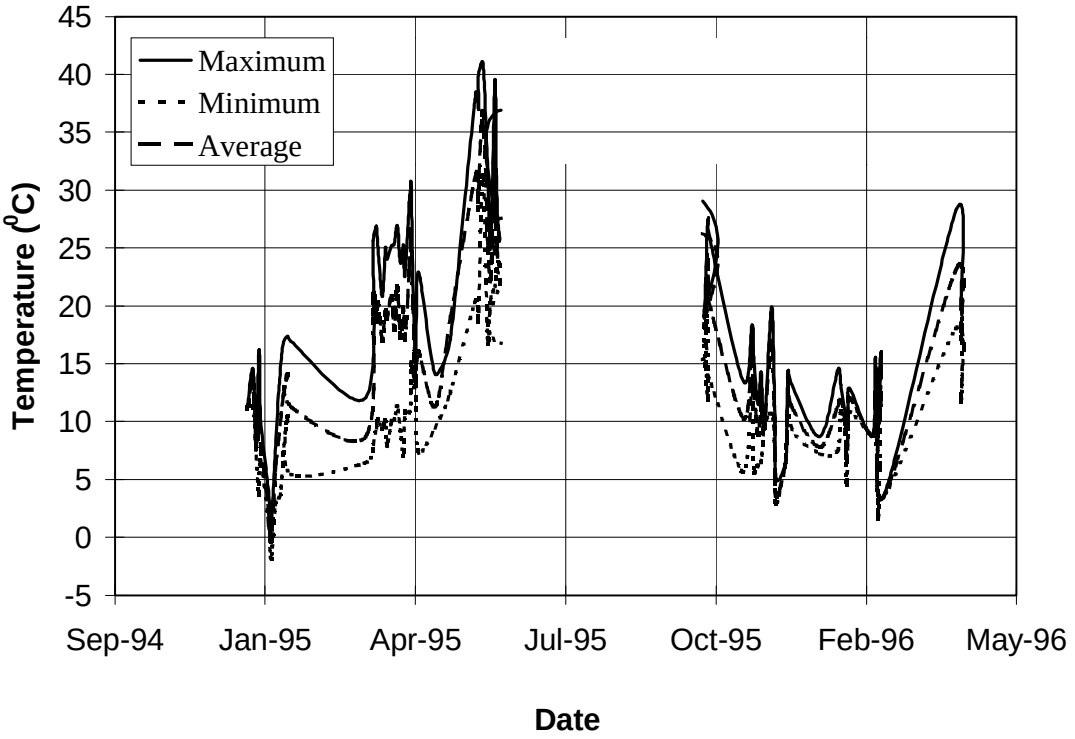


**Figure D 6 Temperature variation measured by thermocouple 3-TC-7-AS.**

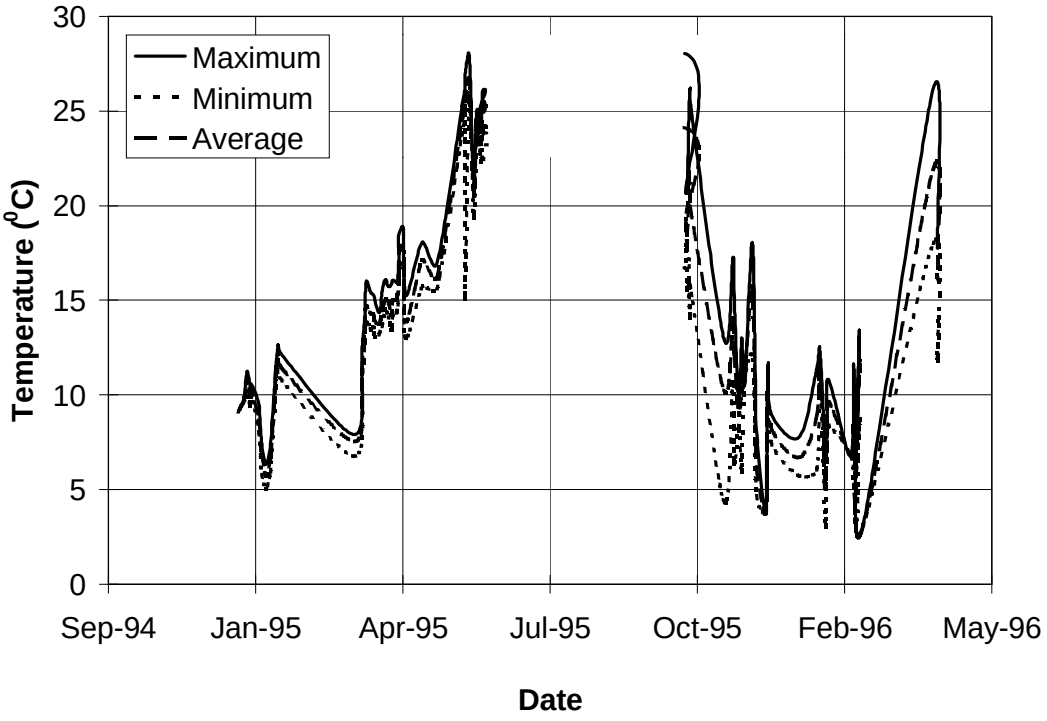


**Figure D 7 Temperature variation measured by thermocouple 4-TC-8-SG-15.**

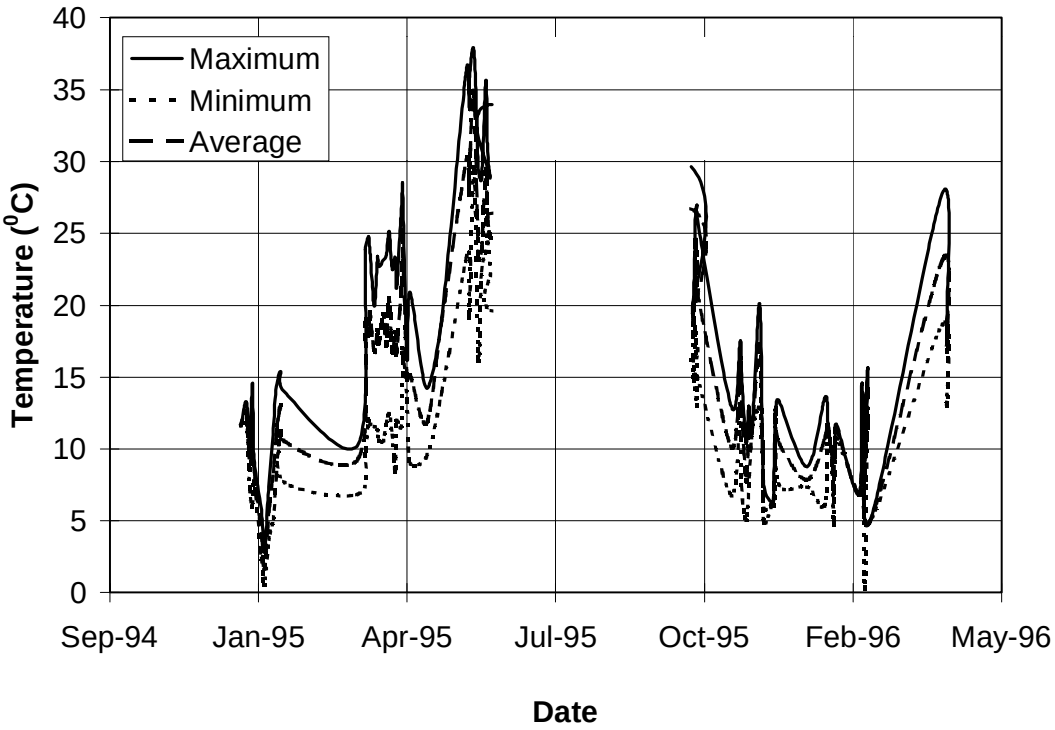


**Figure D 8 Temperature variation measured by thermocouple 4-TC-9-BC-MID.**

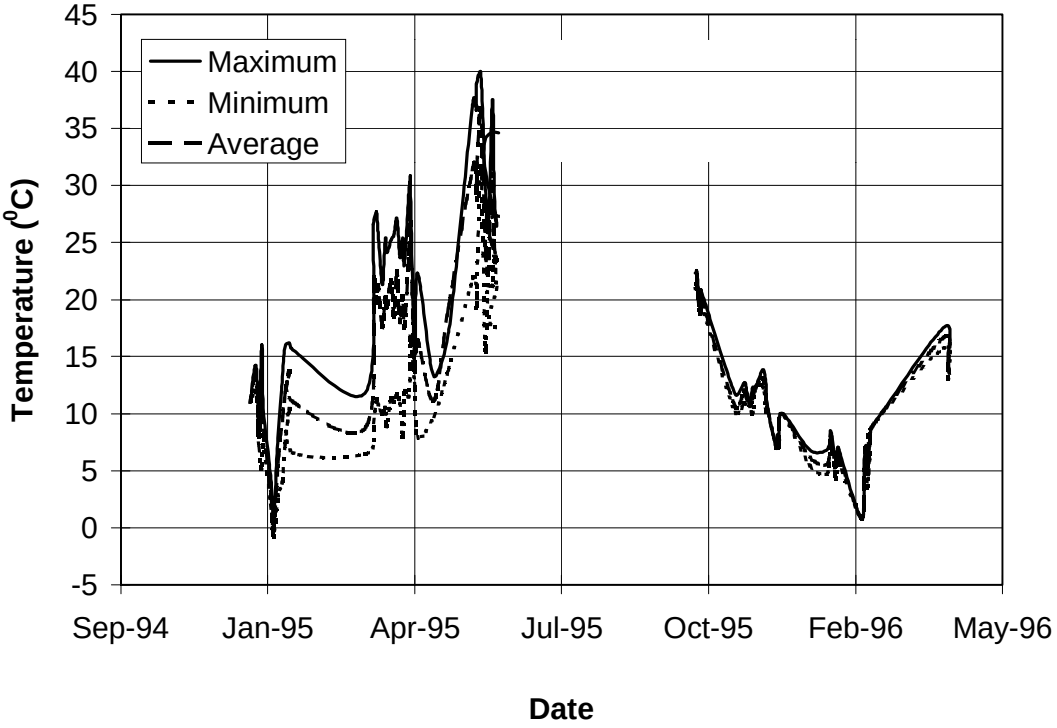


**Figure D 9 Temperature variation measured by thermocouple 4-TC-10-AS.**

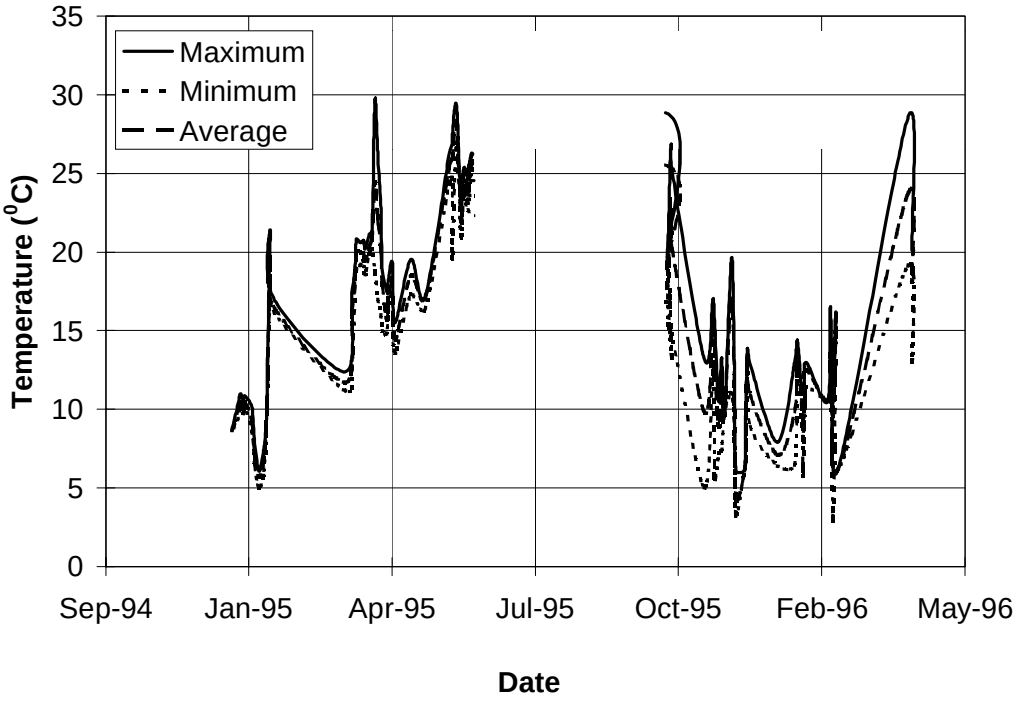


**Figure D 10 Temperature variation measured by thermocouple 7-TC-11-SG-15.**

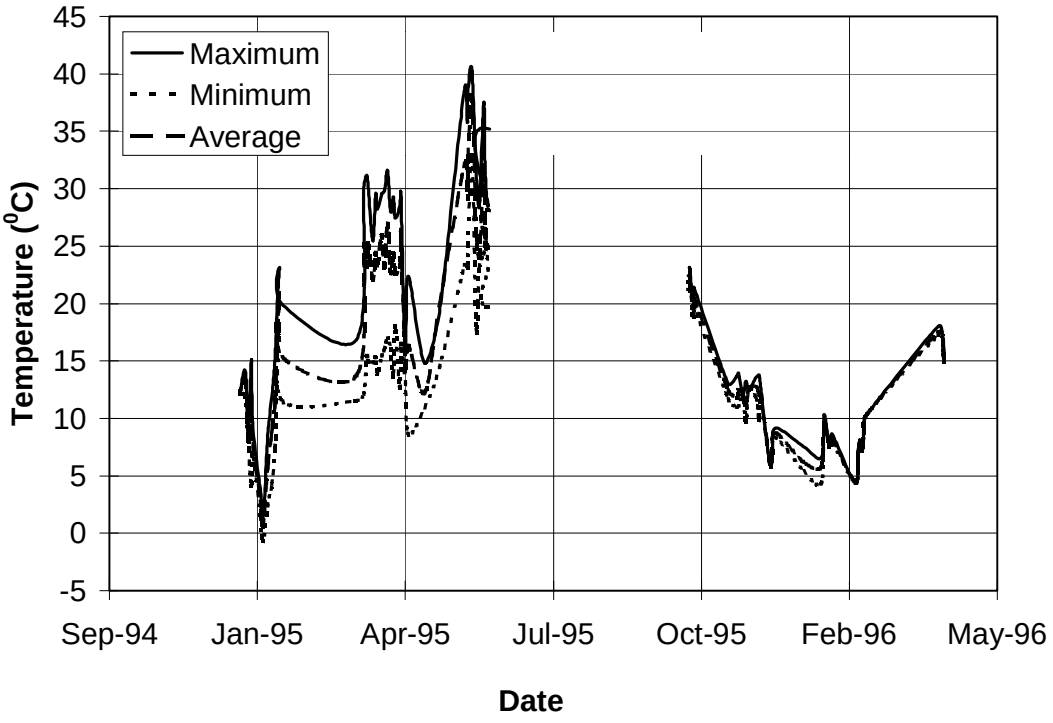


**Figure D 11 Temperature variation measured by thermocouple 7-TC-12-BC-MID.**

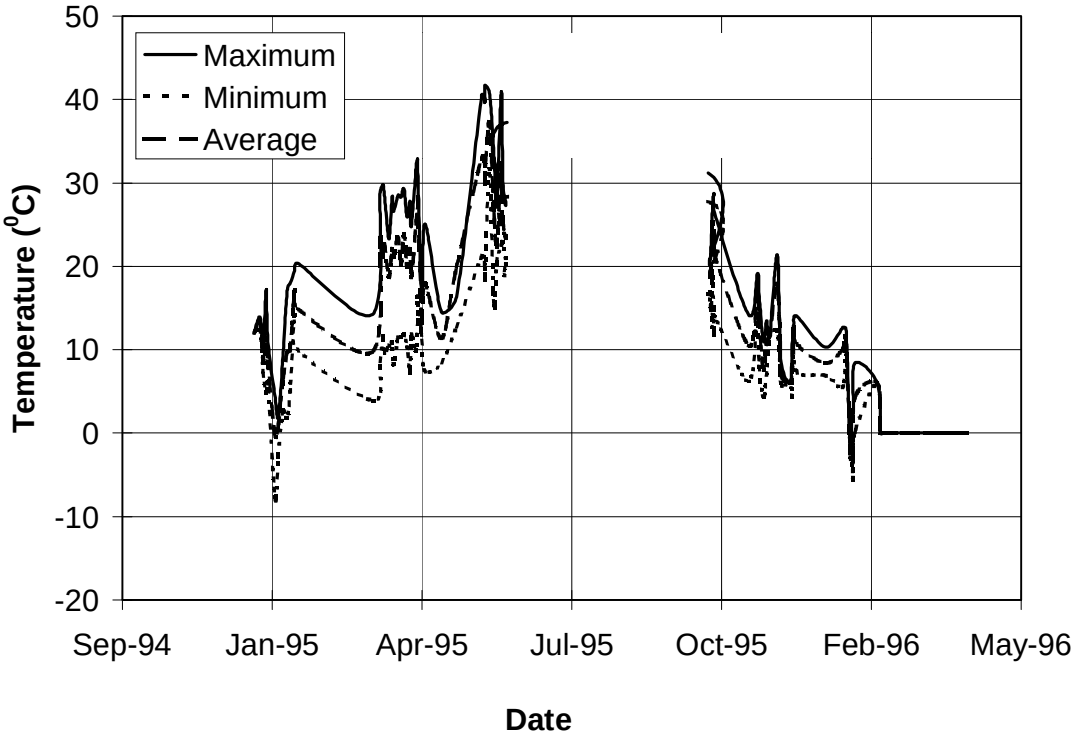


**Figure D 12 Temperature variation measured by thermocouple 7-TC-13-AS.**

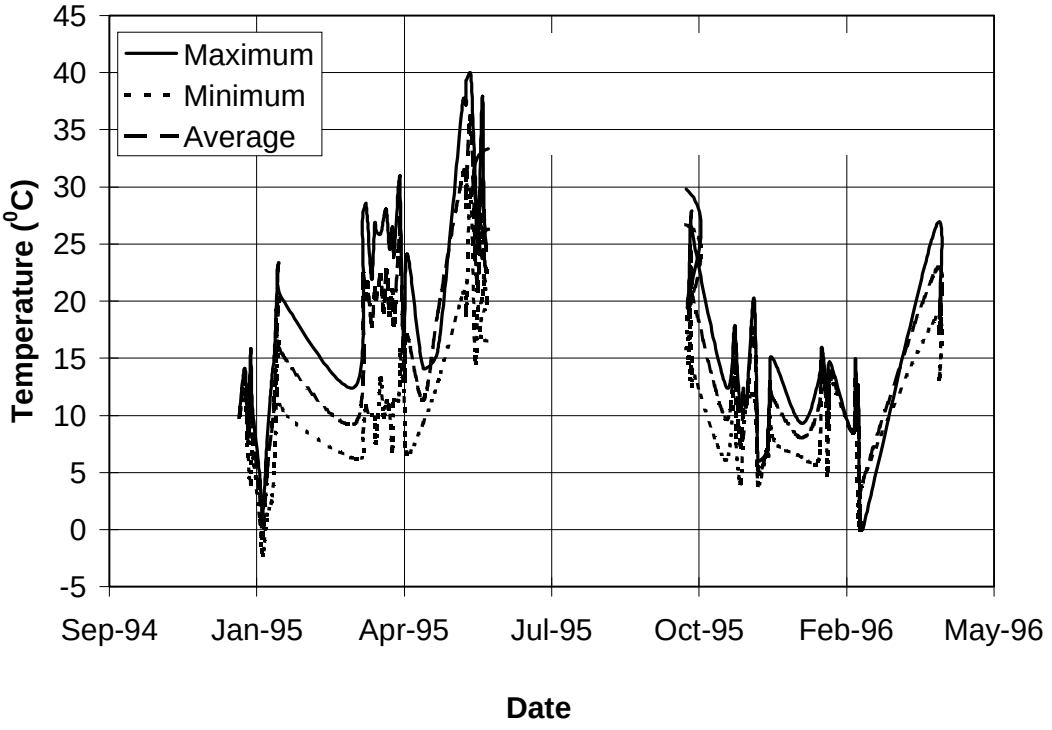


**Figure D 13 Temperature variation measured by thermocouple 8-TC-14-AS.**

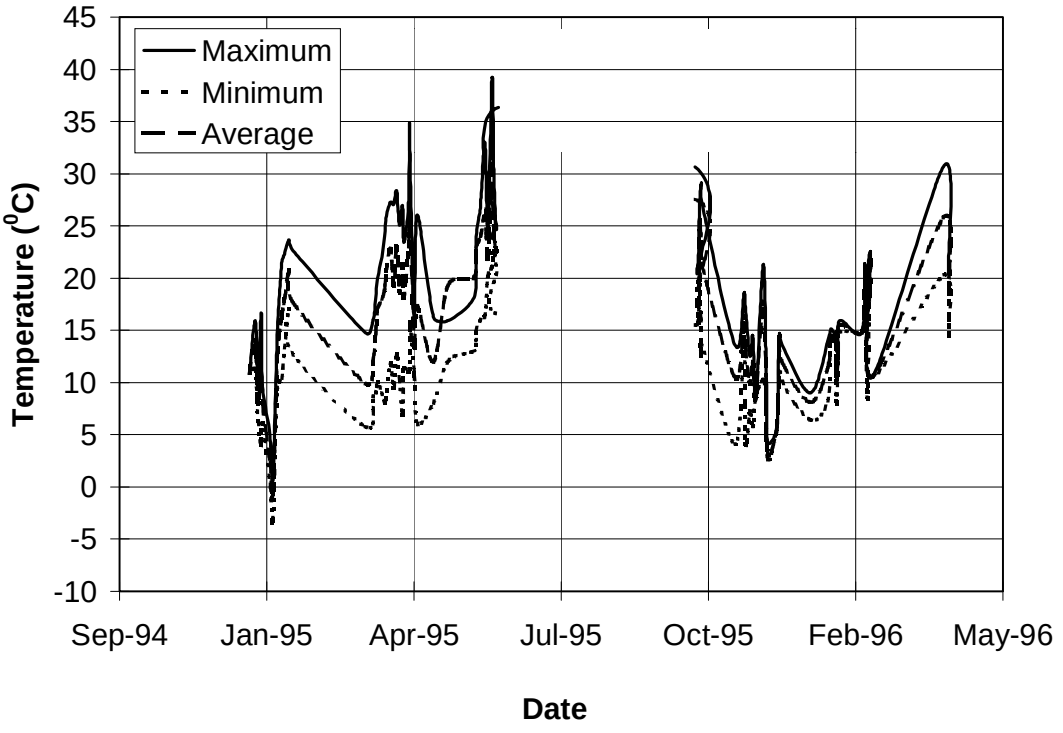


**Figure D 14 Temperature variation measured by thermocouple 8-TC-15-AS.**

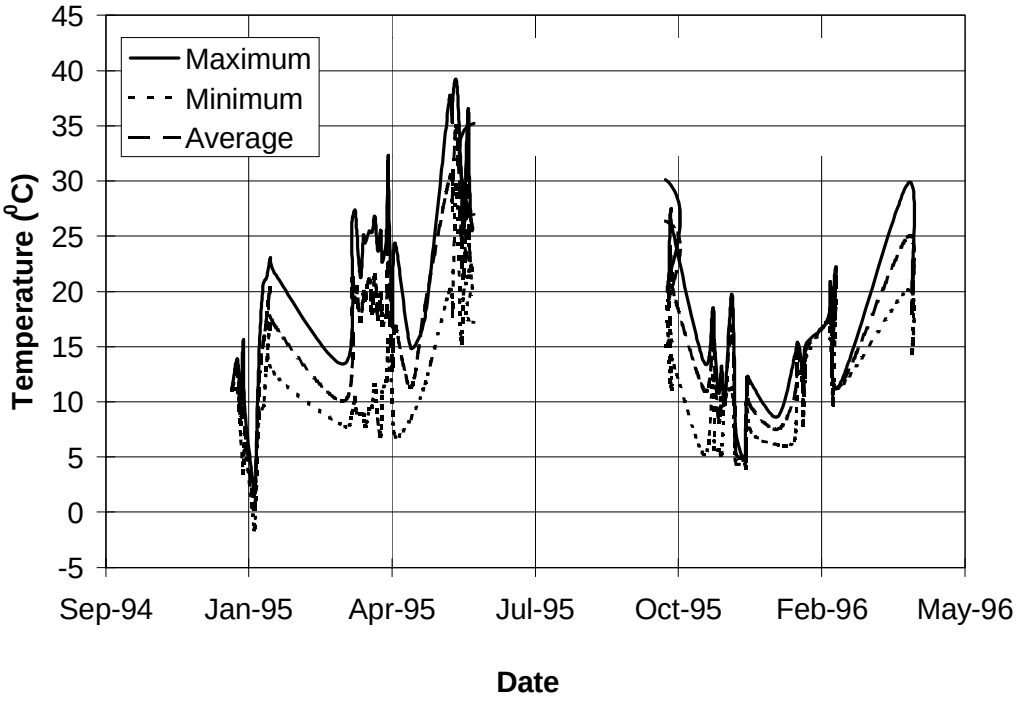


**Figure D 15 Temperature variation measured by thermocouple 9-TC-16-AS.**

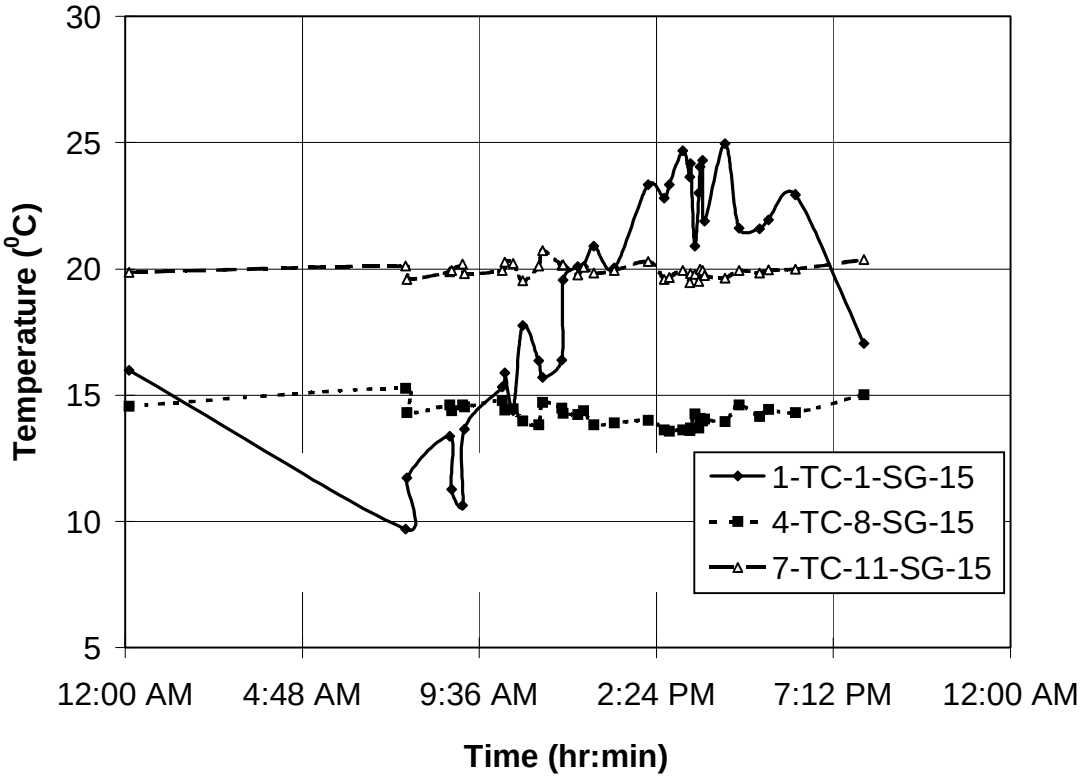


**Figure D 16 Temperature vs. time on March 22, 1995.**

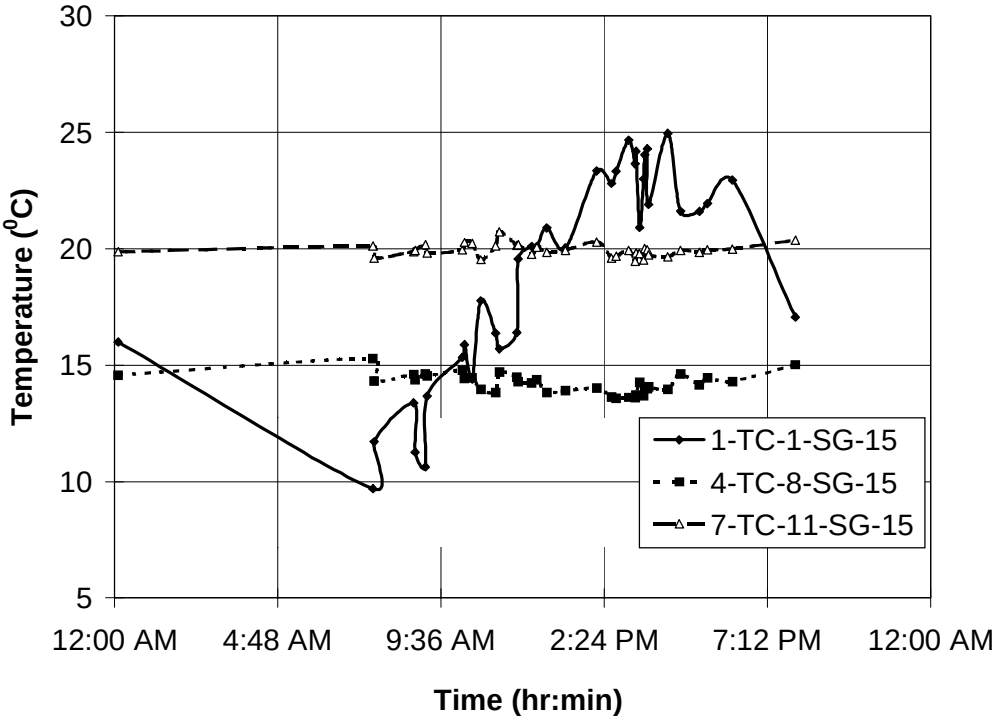


**Figure D 16 Temperature vs. time on March 22, 1995..**

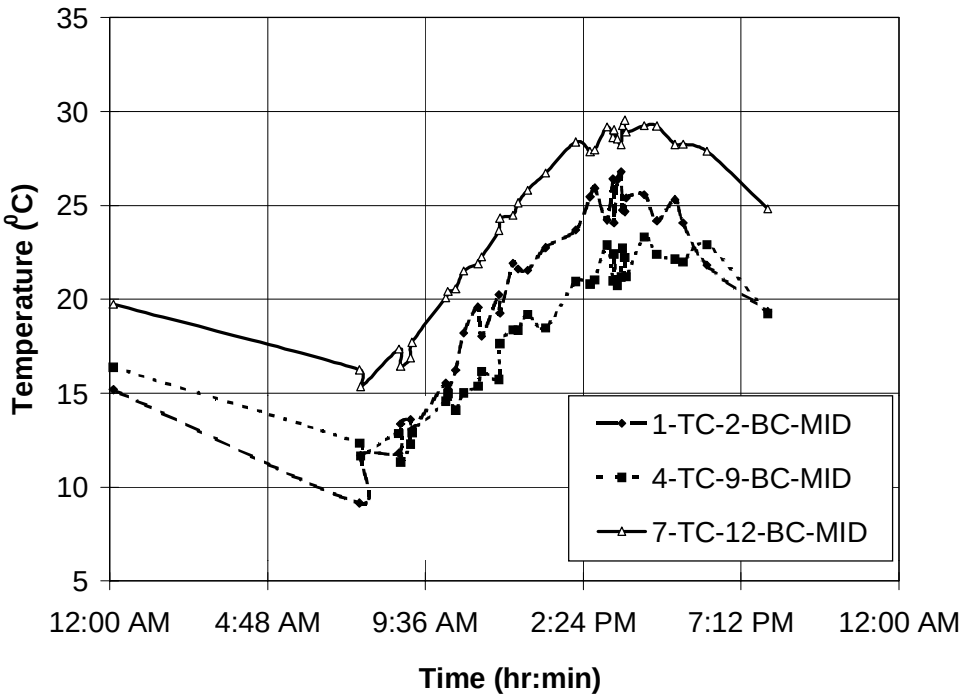


**Figure D 17 Temperature vs. time on March 22, 1995..**

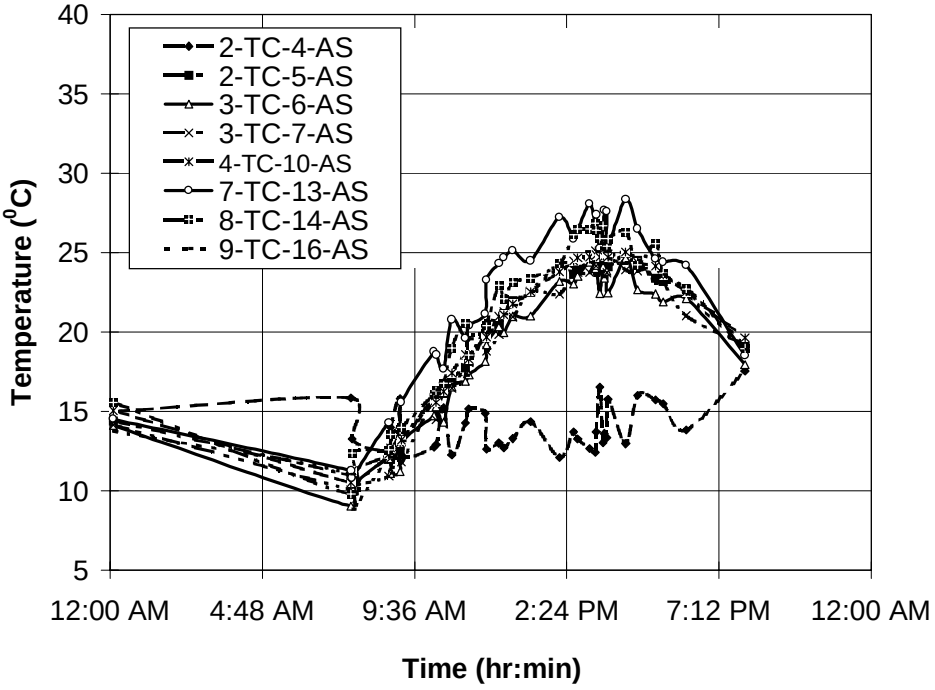


**Figure D 18 Temperature vs. time on March 22, 1995..**

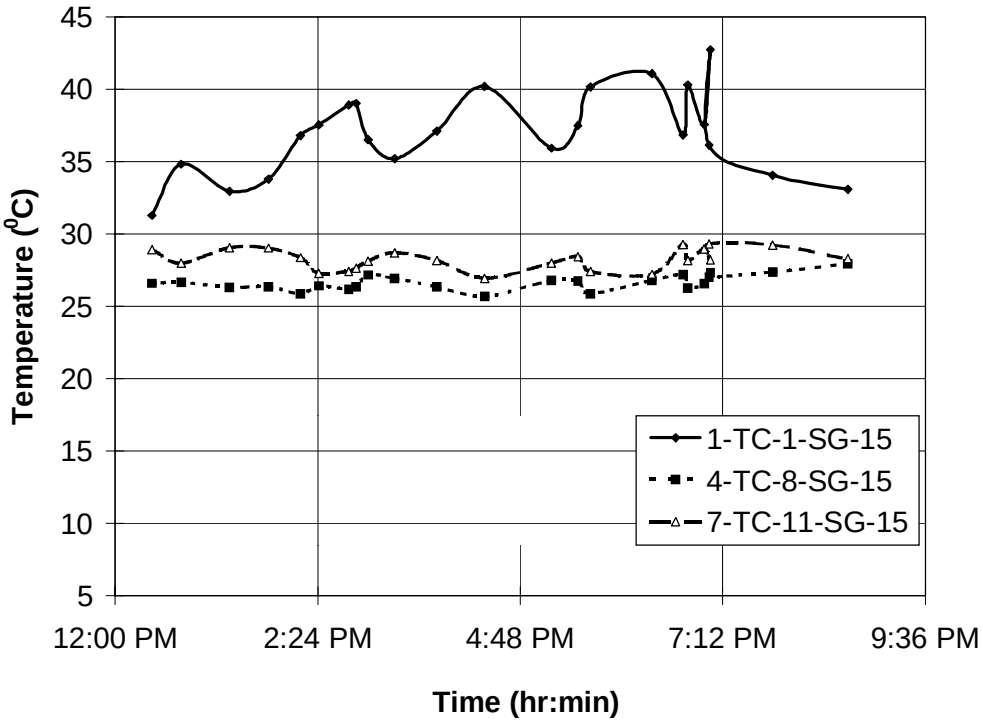


**Figure D 19 Temperature vs. time on May 26, 1995.**

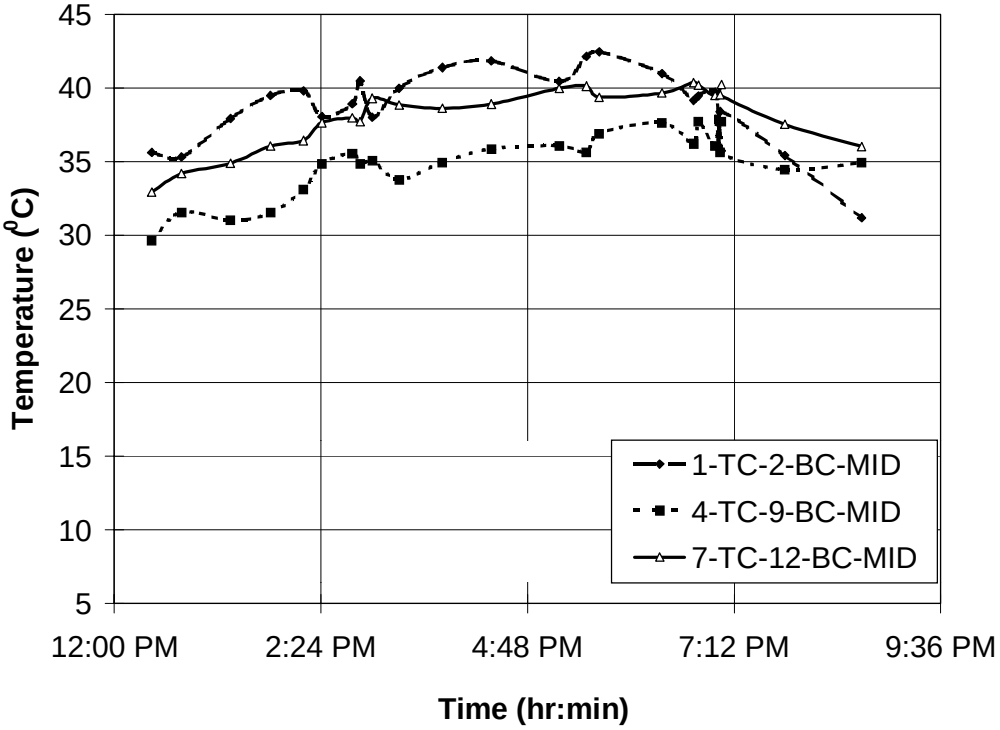


**Figure D 20 Temperature vs. time on May 26, 1995.**

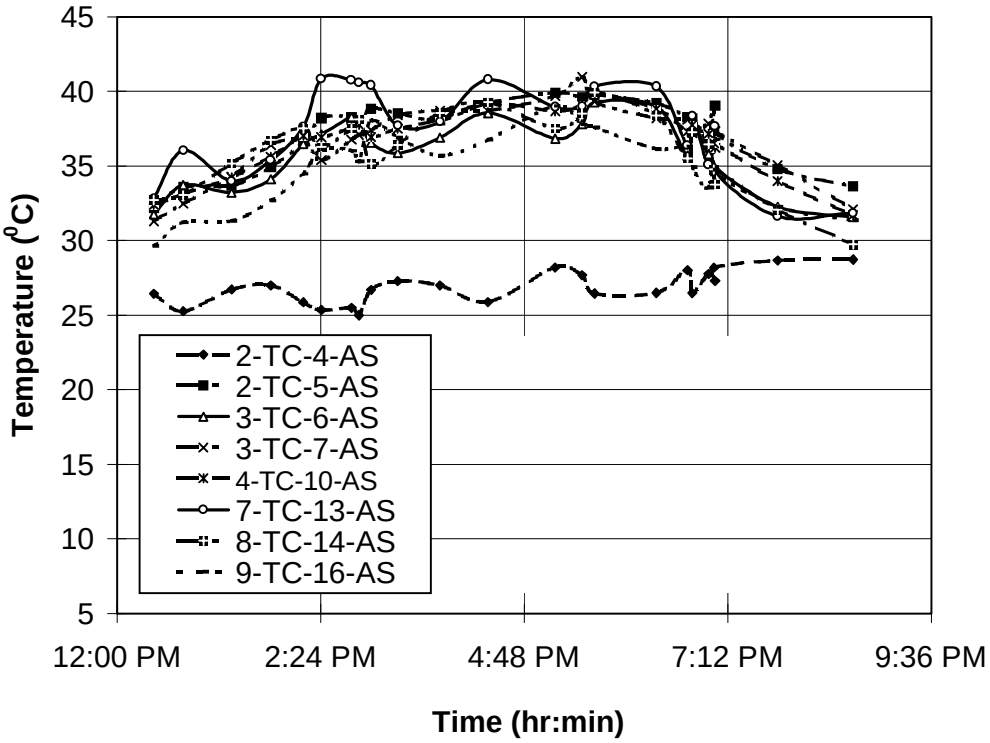


**Figure D 21 Temperature vs. time on May 26, 1995.**

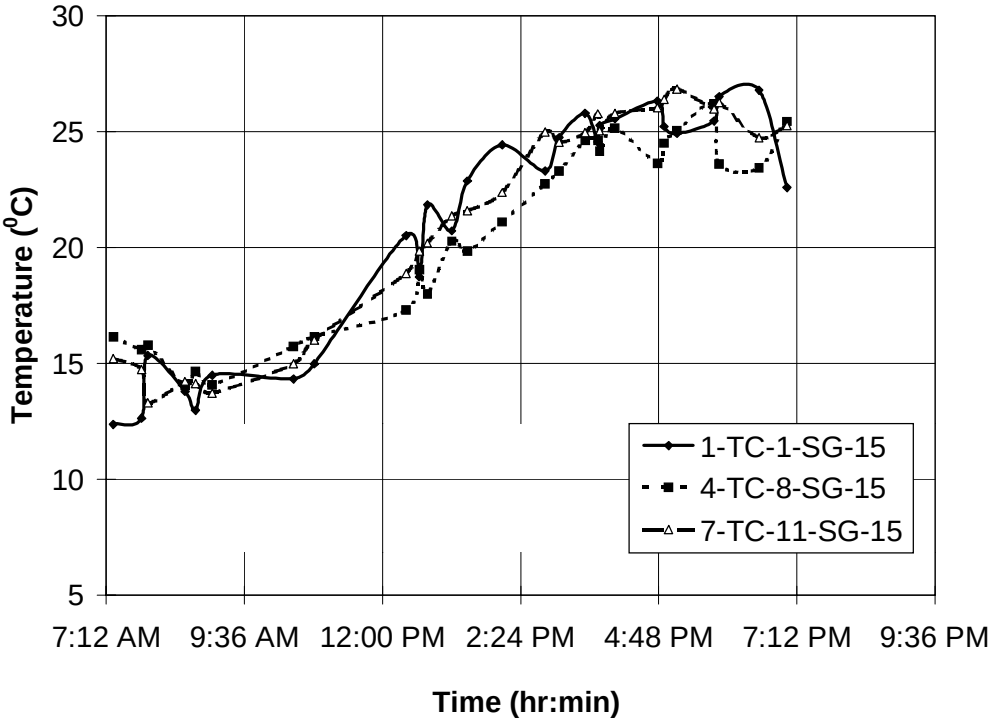


**Figure D 22 Temperature vs. time on October 10, 1995.**

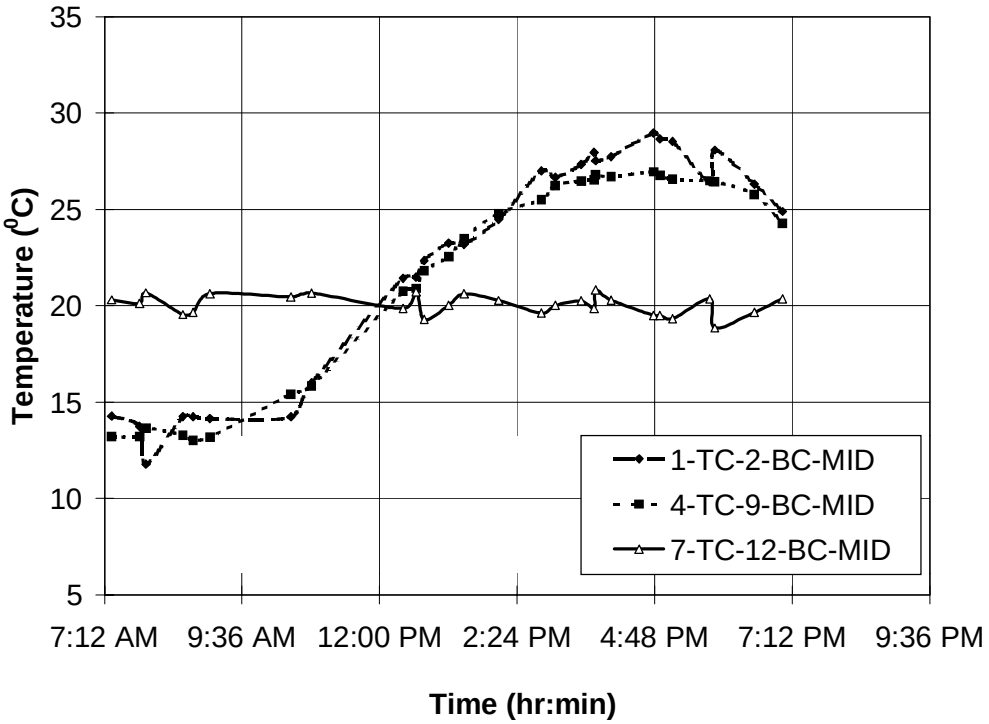


**Figure D 23 Temperature vs. time on October 10, 1995.**

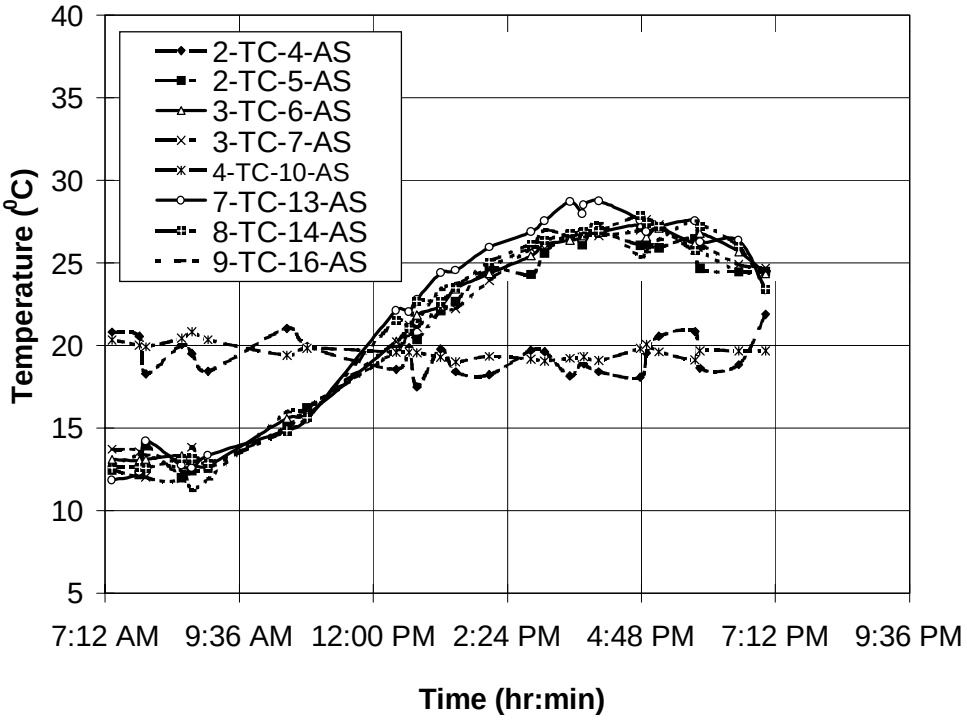


**Figure D 24 Temperature vs. time on October 10, 1995.**

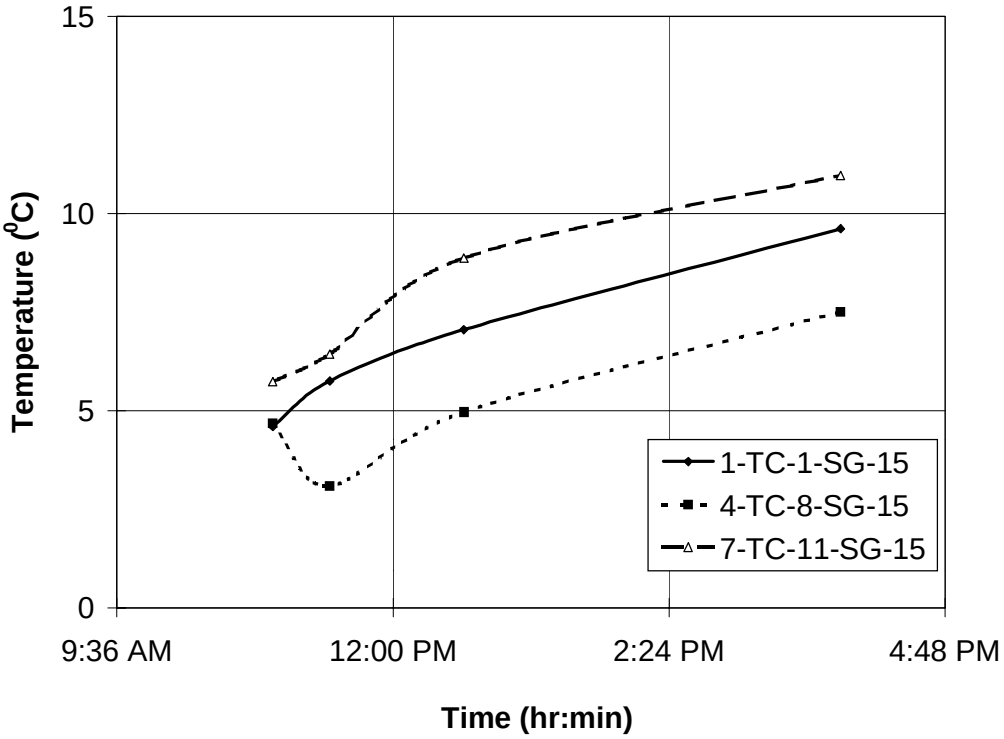


**Figure D 25 Temperature vs. time on January 23, 1995.**

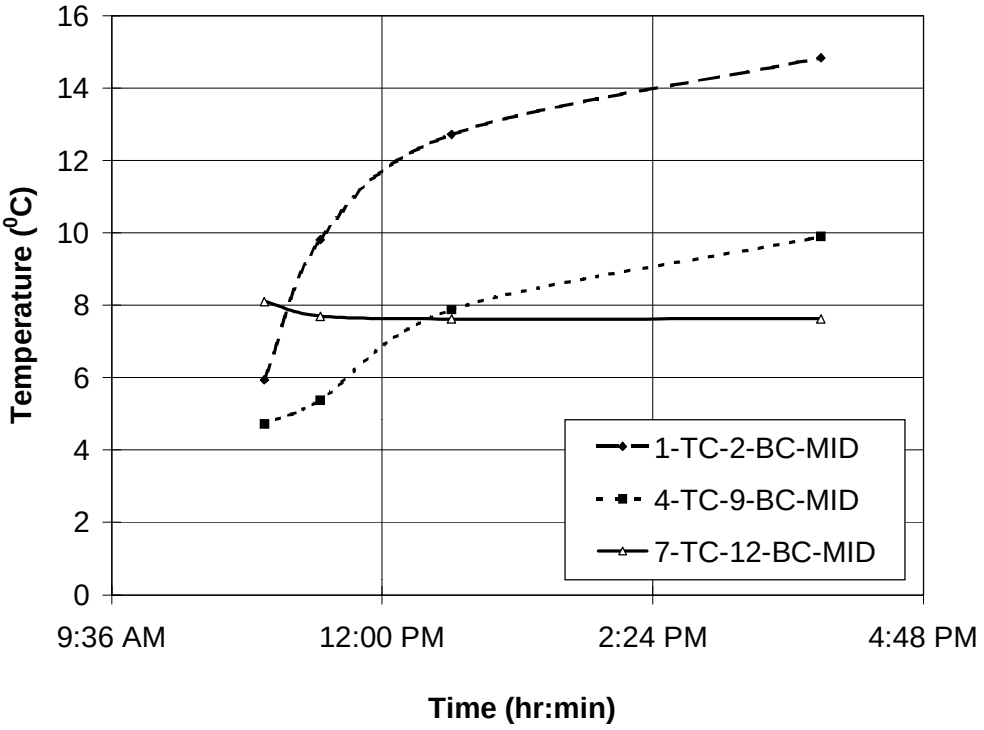


**Figure D 26 Temperature vs. time on January 23, 1995.**

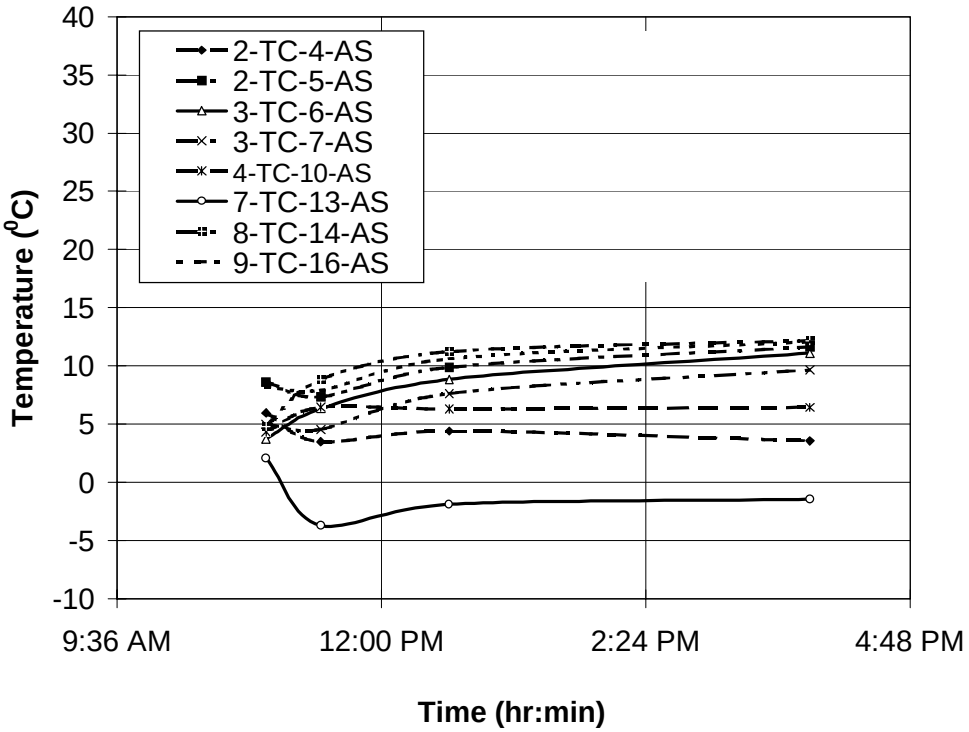


**Figure D 27 Temperature vs. time on January 23, 1995.**

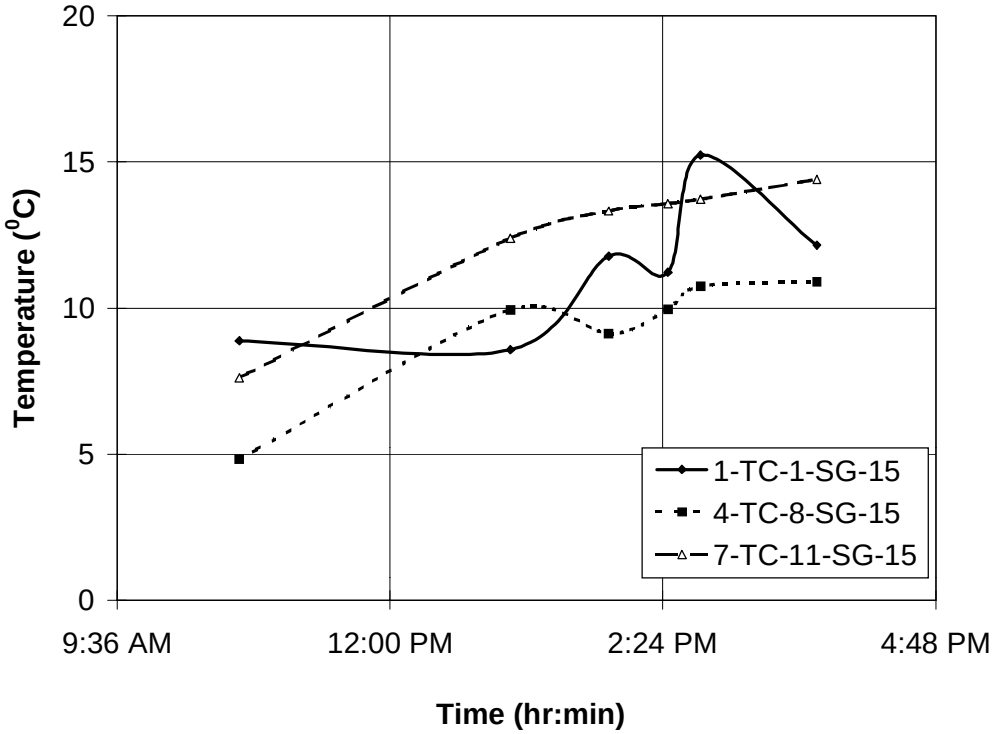


**Figure D 28 Temperature vs. time on February 14, 1995.**

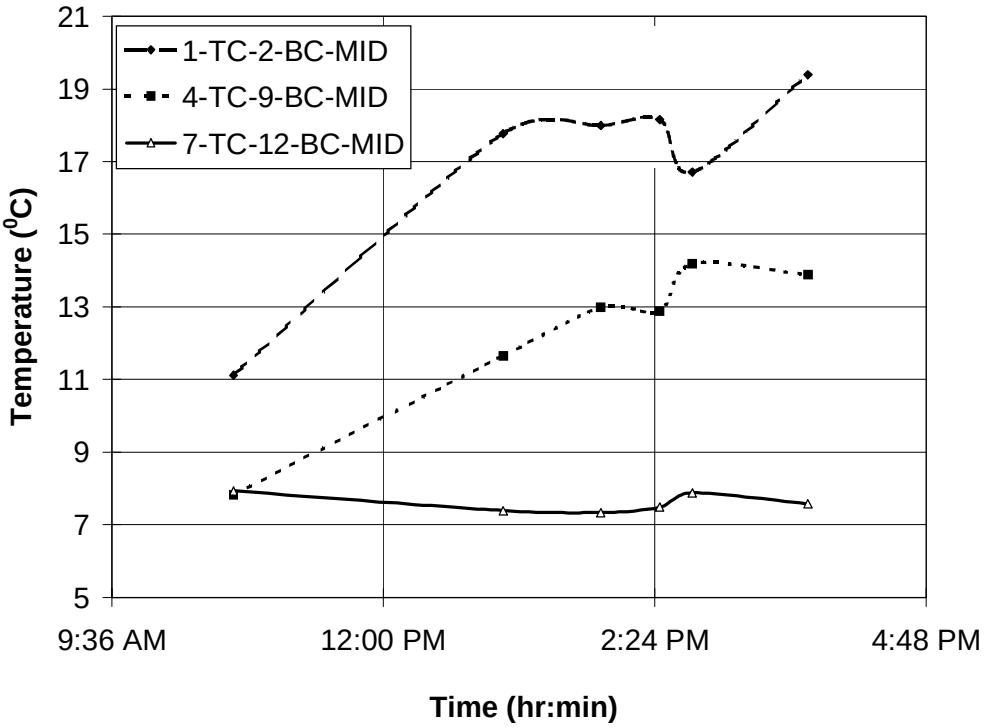


**Figure D 29 Temperature vs. time on February 14, 1995.**

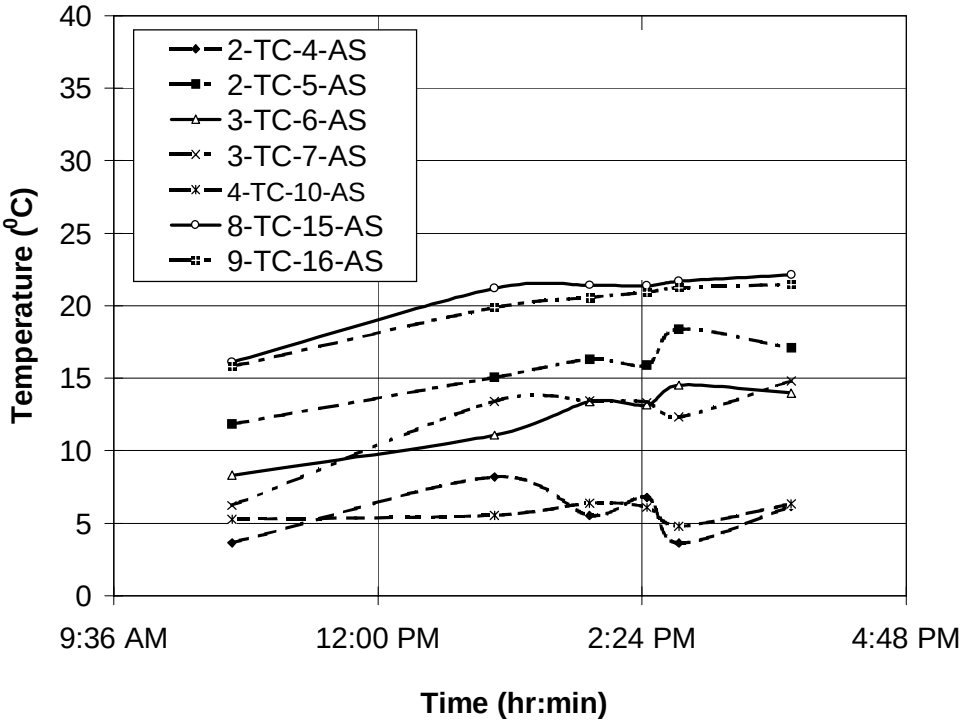


**Figure D 30 Temperature vs. time on February 14, 1995.**

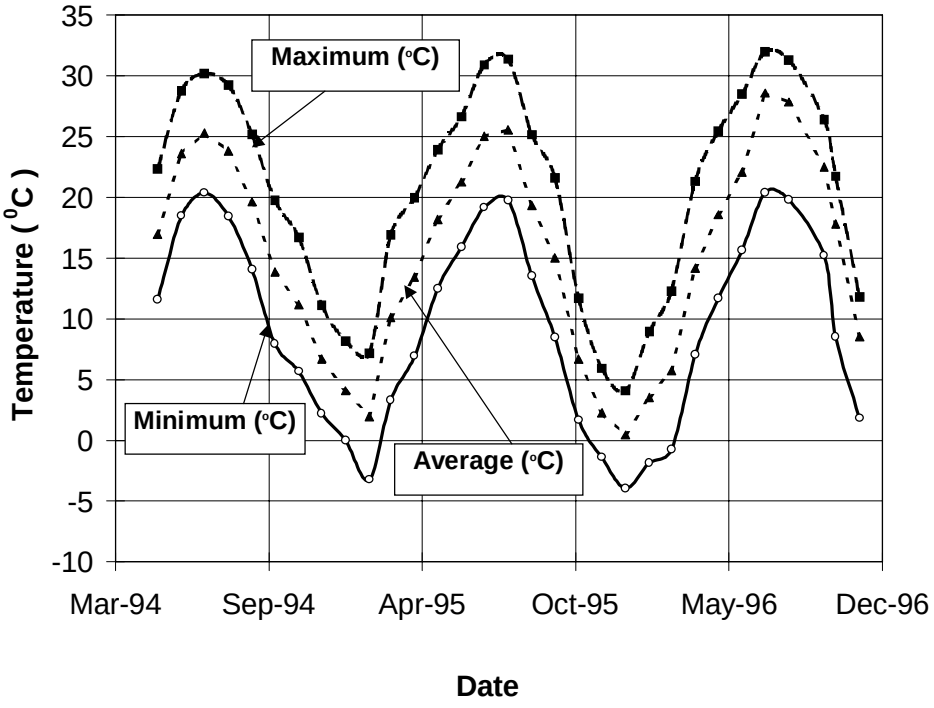


**Figure D 31: Maximum, average, and minimum air temperature data for Bedford County, VA (from weather station).**

# APPENDIX E

# MOISTURE DATA

**Table E 1 Difference between subgrade moisture contents obtained using an Impedance Bridge and oven procedure.**

| *Section No.* | *150 mm deep* | | | *610 mm deep* | | |
|---|---|---|---|---|---|---|
| | *Gypsum Block* | *Oven Procedure* | *Difference* | *Gypsum Block* | *Oven Procedure* | *Difference* |
| 1 | 25.0 | 26.6 | 1.6 | 28.4 | * | * |
| 2 | 32.0 | 32.5 | 0.5 | 24.3 | 26.4 | -2.1 |
| 3 | 30.8 | 31.9 | 1.1 | 29.8 | 24.4 | 5.3 |
| 4 | ------- | 25.1 | * | 24.1 | * | * |
| 5 | ------- | 27.7 | * | 28.3 | * | * |
| 6 | ------- | 28.4 | * | 27.7 | * | * |
| 7 | 30.6 | 24.8 | -5.8 | 29.8 | 30.9 | -1.1 |
| 8 | 31.5 | 22.0 | -9.4 | 25.7 | 28.2 | -2.5 |
| 9 | 30.2 | 27.3 | -2.9 | 25.5 | 27.2 | -1.8 |
| **Average** | **30.0** | **27.4** | **2.5** | **27.1** | **27.4** | **0.4** |

**Table E 2 Field moisture contents in different layers.**

| Date | Avg. Water Cont. (%) | | | Correcterd (%) | | |
|---|---|---|---|---|---|---|
| | ***SG @ - 610 mm*** | ***SG @ - 150 mm*** | ***BC @ Mid Layer*** | ***SG @ - 610 mm*** | ***SG @ - 150 mm*** | ***BC @ Mid Layer*** |
| 24-Mar-95 | 29.7 | 35.9 | 5.0 | 29.2 | 33.4 | 5.0 |
| 31-Mar-95 | 32.3 | 35.5 | 5.2 | 31.8 | 33.0 | 5.2 |
| 06-Apr-95 | 32.6 | 35.8 | 5.2 | 32.1 | 33.3 | 5.2 |
| 26-May-95 | 35.9 | 39.1 | 5.5 | 35.4 | 36.7 | 5.5 |
| 05-Jun-95 | 35.8 | 38.6 | 5.6 | 35.3 | 36.1 | 5.6 |
| 27-Jun-95 | 32.5 | 37.3 | 5.2 | 32.0 | 34.8 | 5.2 |
| 10-Jul-95 | 33.0 | 37.7 | 5.3 | 32.5 | 35.2 | 5.3 |
| 18-Aug-95 | 32.9 | 36.5 | 5.0 | 32.5 | 34.1 | 5.0 |
| 04-Sep-95 | 33.6 | 37.0 | 5.0 | 33.1 | 34.5 | 5.0 |
| 10-Oct-95 | 32.6 | 36.2 | 5.1 | 32.1 | 33.7 | 5.1 |
| 21-Dec-95 | 30.2 | 34.5 | 4.4 | 29.8 | 32.0 | 4.4 |
| 25-Jan-96 | 30.5 | 34.7 | 4.5 | 30.1 | 32.3 | 4.5 |
| 22-Feb-96 | 29.5 | 35.2 | 4.6 | 29.1 | 32.7 | 4.6 |
| 04-Apr-96 | 29.7 | 35.1 | 4.7 | 29.3 | 32.6 | 4.7 |
| 15-May-96 | 29.0 | 35.2 | 4.8 | 28.6 | 32.7 | 4.8 |
| 04-Aug-96 | 29.5 | 34.4 | 4.8 | 29.0 | 31.9 | 4.8 |
| 19-Aug-96 | 30.4 | 34.4 | 4.9 | 29.9 | 31.9 | 4.9 |
| 28-Aug-96 | 31.0 | 34.2 | 4.8 | 30.6 | 31.7 | 4.8 |
| 23-Sep-96 | 29.3 | 33.5 | 4.4 | 28.8 | 31.0 | 4.4 |
| 04-Nov-96 | 27.4 | 30.0 | 4.3 | 27.0 | 27.5 | 4.3 |
| 08-Jan-97 | 29.0 | 32.8 | 4.6 | 28.5 | 30.3 | 4.6 |
| 21-Mar-97 | 25.3 | 34.8 | 3.8 | 24.9 | 32.3 | 3.8 |
| 10-Jun-97 | 28.6 | 33.3 | 4.6 | 28.2 | 30.8 | 4.6 |
| 15-Aug-97 | 28.0 | 32.1 | 4.3 | 27.6 | 29.6 | 4.3 |
| 17-Oct-97 | 29.1 | 33.5 | 4.5 | 28.7 | 31.0 | 4.5 |

*Comments:*

Subgrade at 610 mm correction factor = 0.4 %

Subgrade at 150 mm correction factor = 2.5 %

Base course mid layer = no correction factor

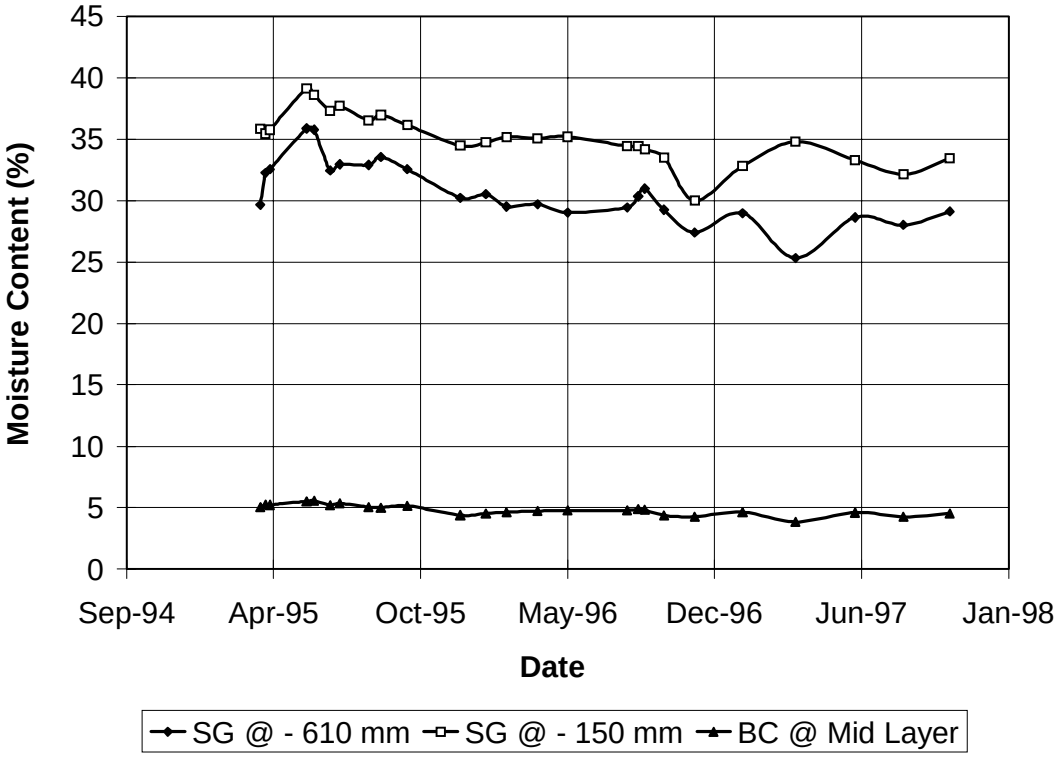


**Figure E 1 Original field moisture content variation.**

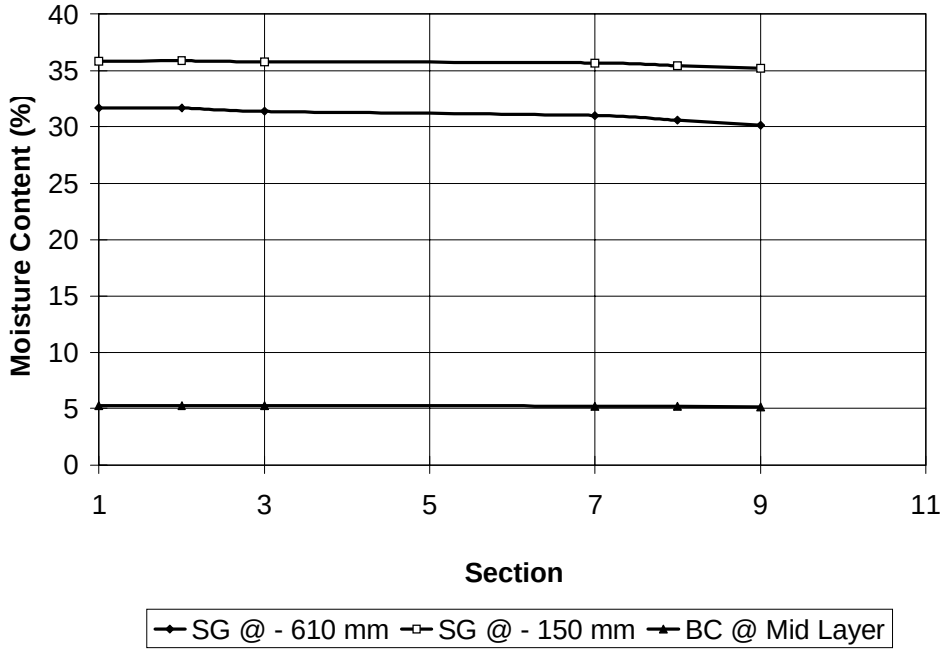


**Figure E 2 Moisture content variation across sections.**

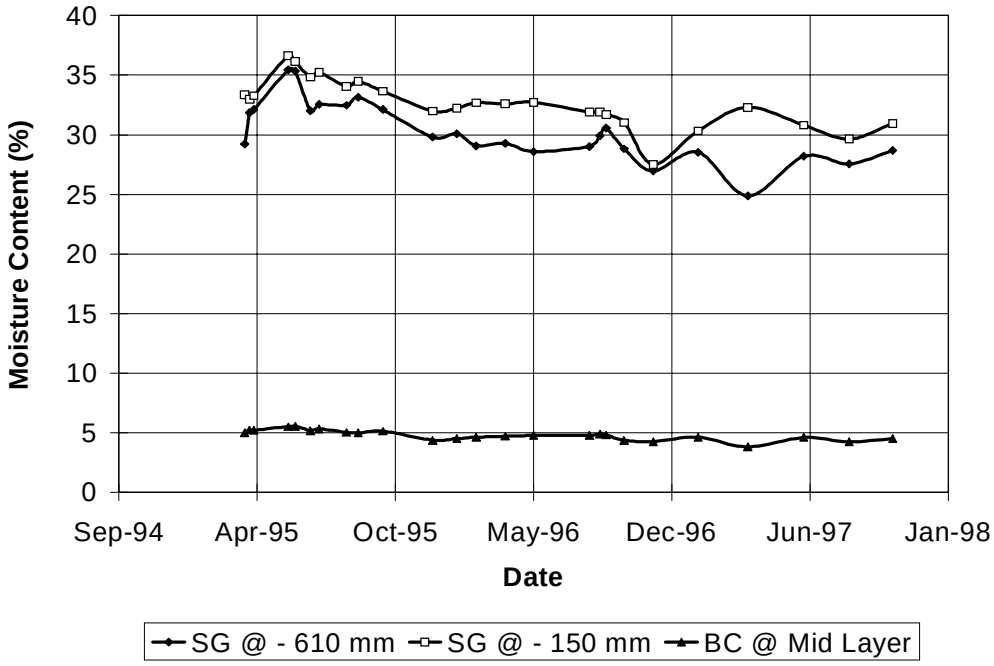


**Figure E 3 Corrected field moisture content variation.**

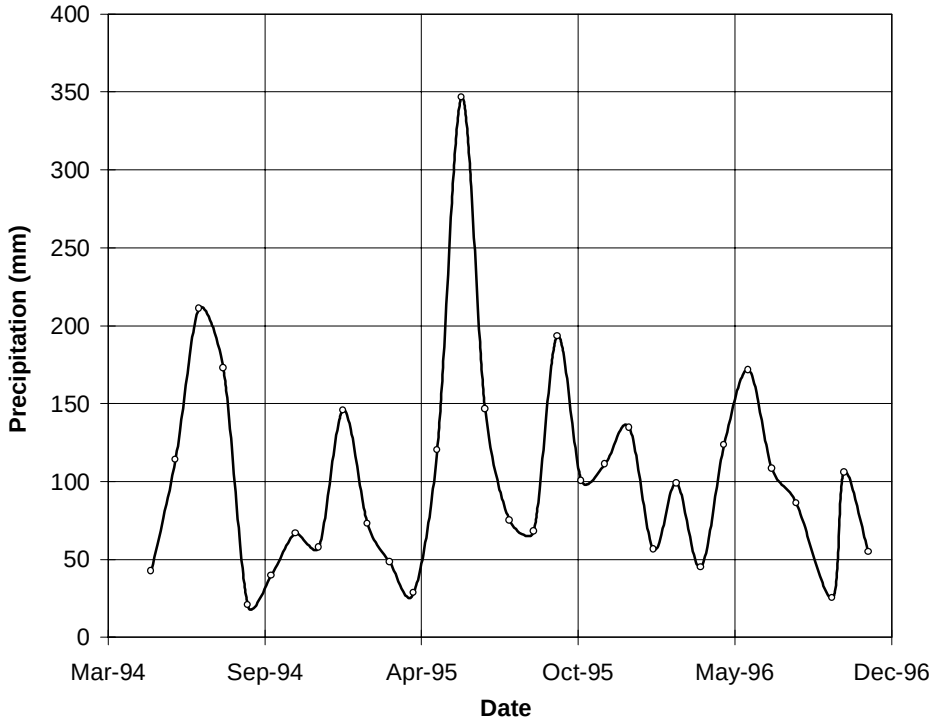


**Figure E 4 Precipitation variation over two years.**

# APPENDIX F

# RUT DEPTH

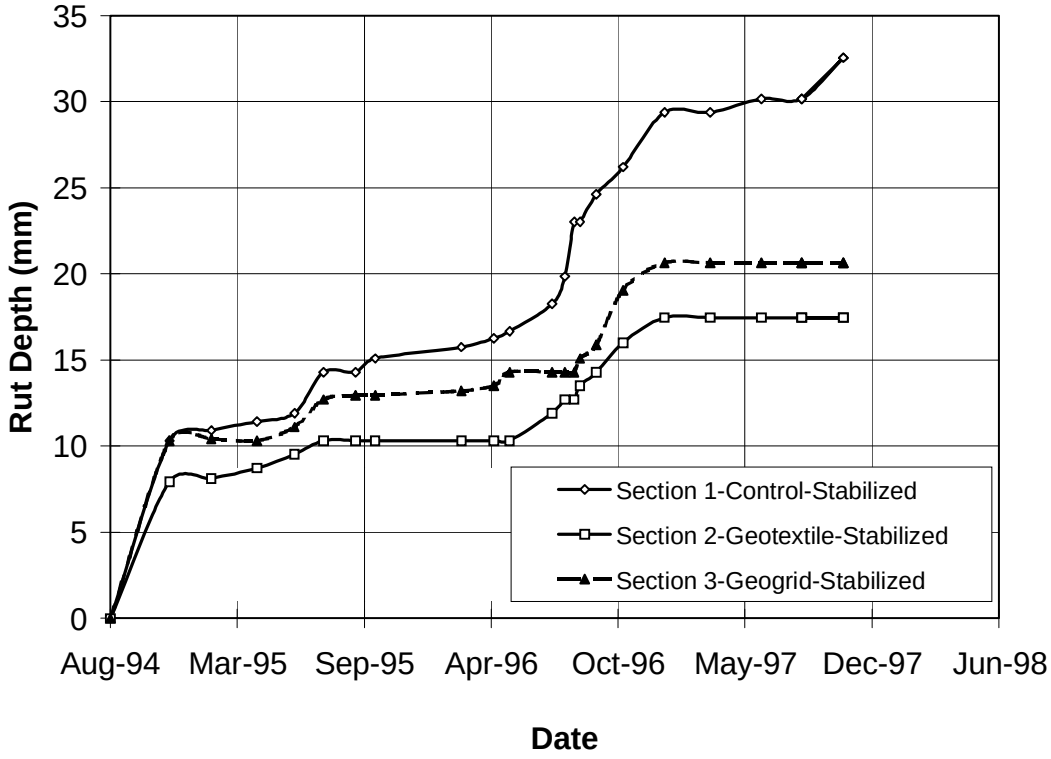


**Figure F 1 Rut depths in sections 1 through 3.**

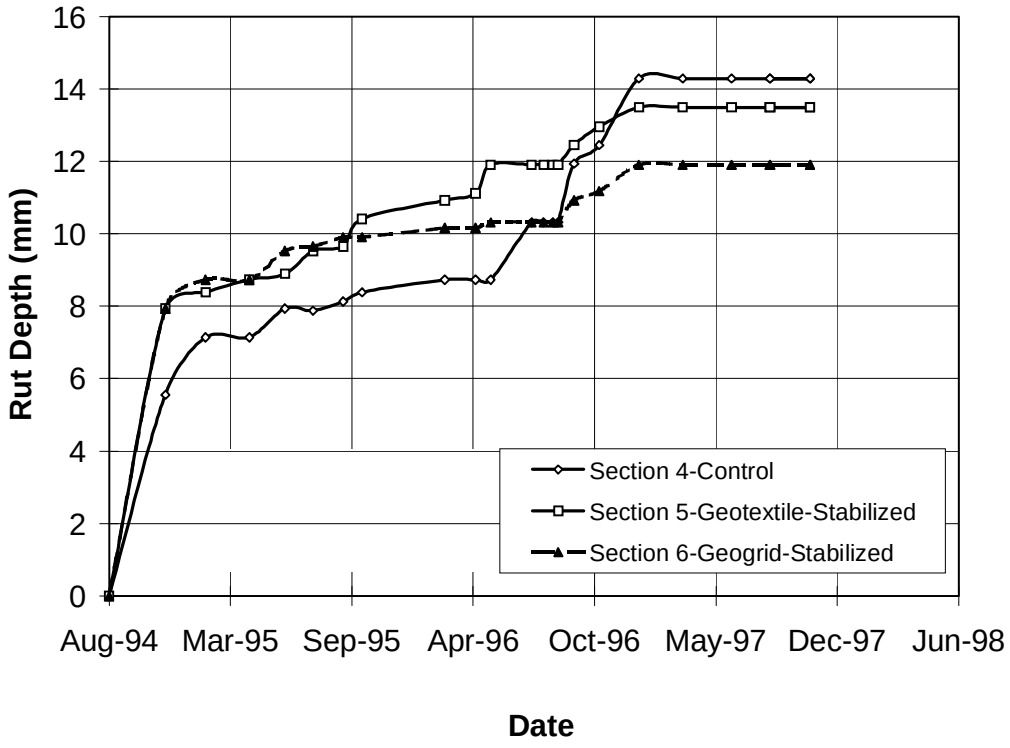


**Figure F 2 Rut depths in sections 4 through 6.**

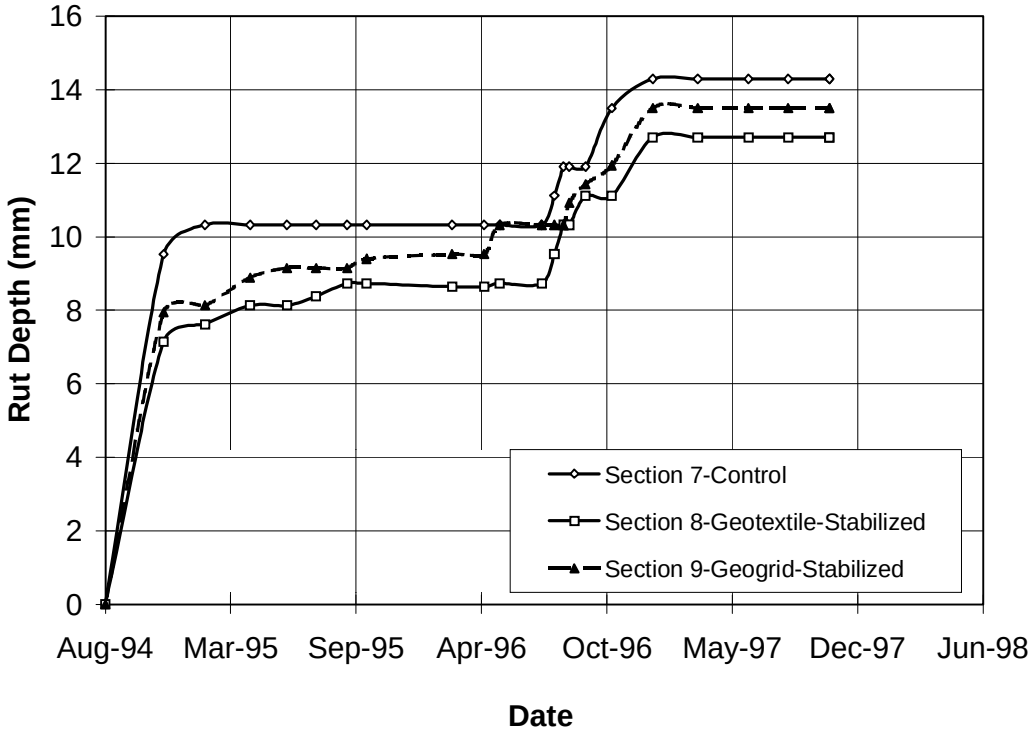


**Figure F 3 Rut depths in sections 7 through 9.**

# APPENDIX G

# FALLING WEIGHT DEFLECTOMETER

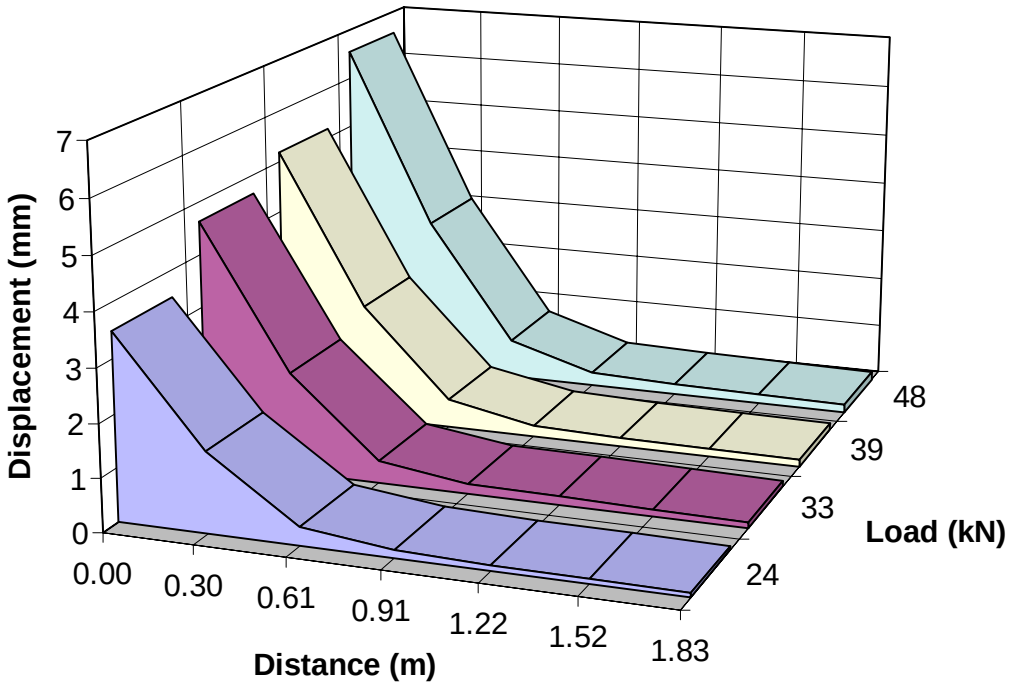


**Figure G 1 Displacement as a function of distance for different FWD load levels (October 1994, section 1).**

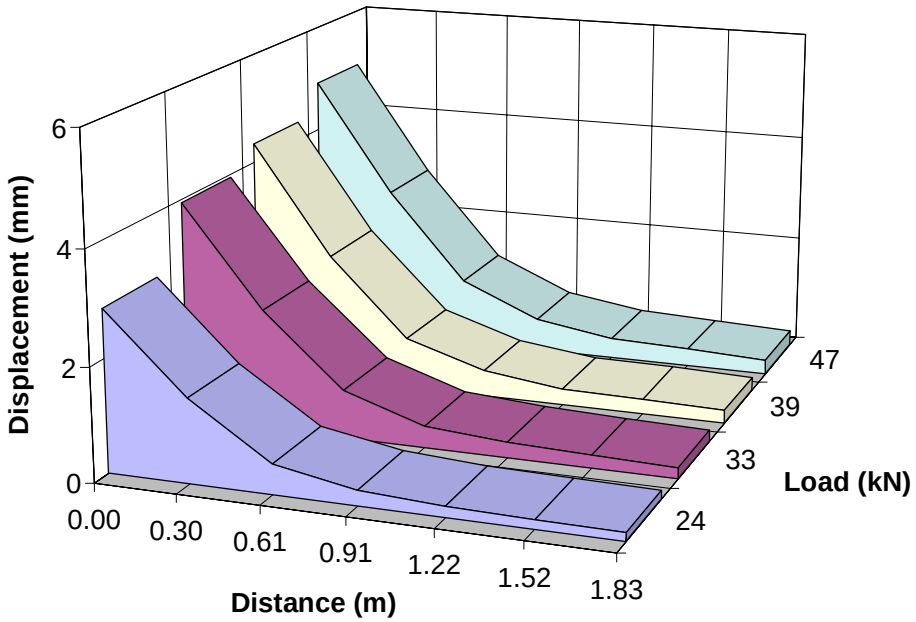


**Figure G 2 Displacement as a function of distance for different FWD load levels (October 1994, section 2).**

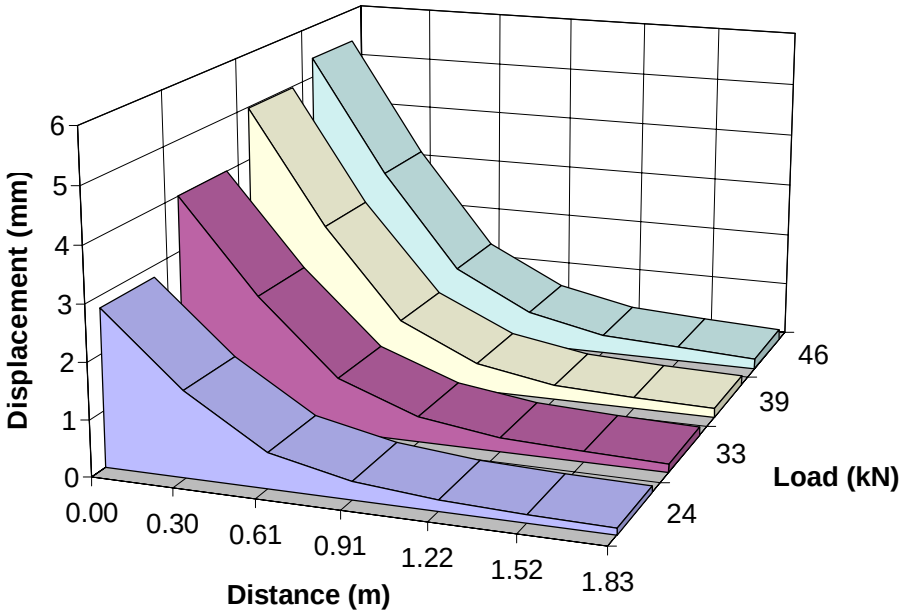


**Figure G 3 Displacement as a function of distance for different FWD load levels (October 1994, section 3).**

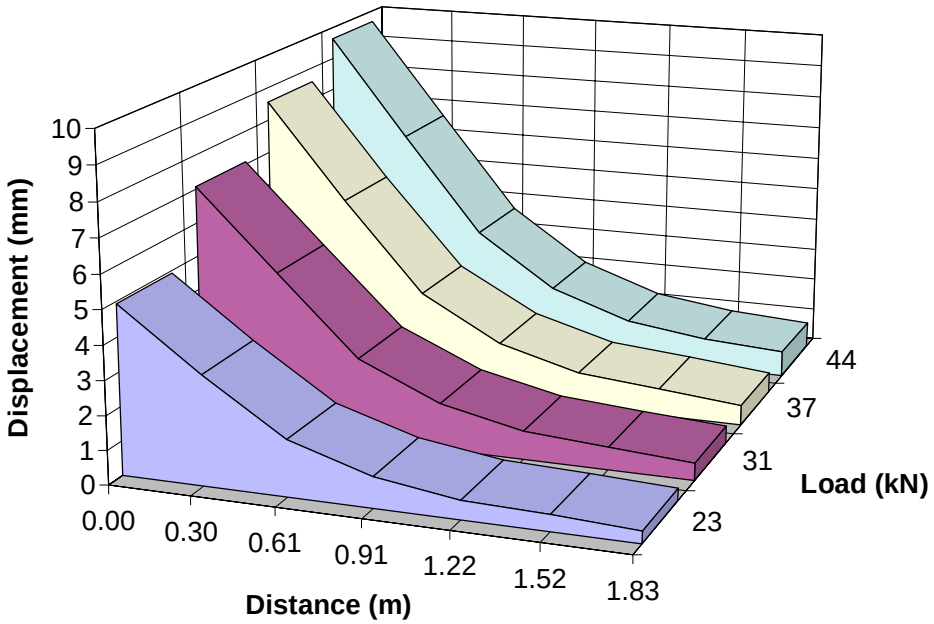


**Figure G 4 Displacement as a function of distance for different FWD load levels (October 1994, section 4).**

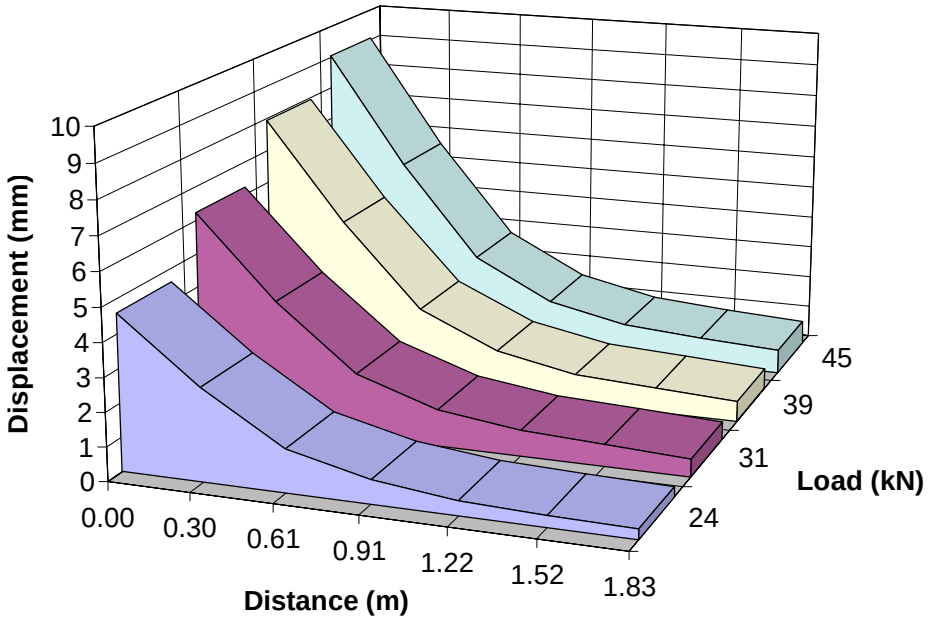


**Figure G 5 Displacement as a function of distance for different FWD load levels (October 1994, section 5).**

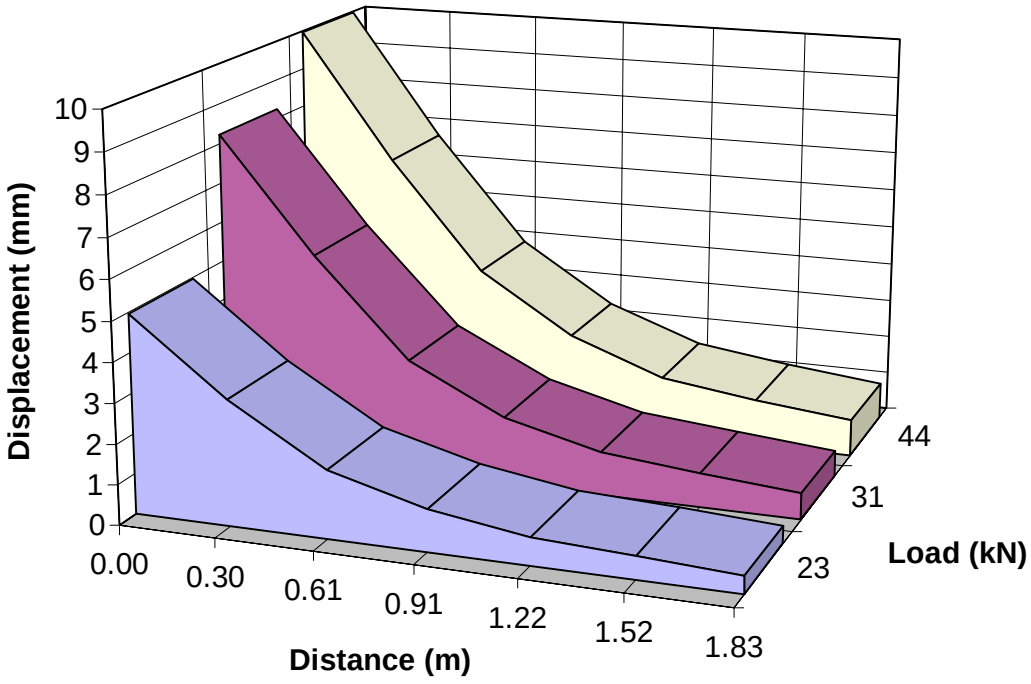


**Figure G 6 Displacement as a function of distance for different FWD load levels (October 1994, section 6).**

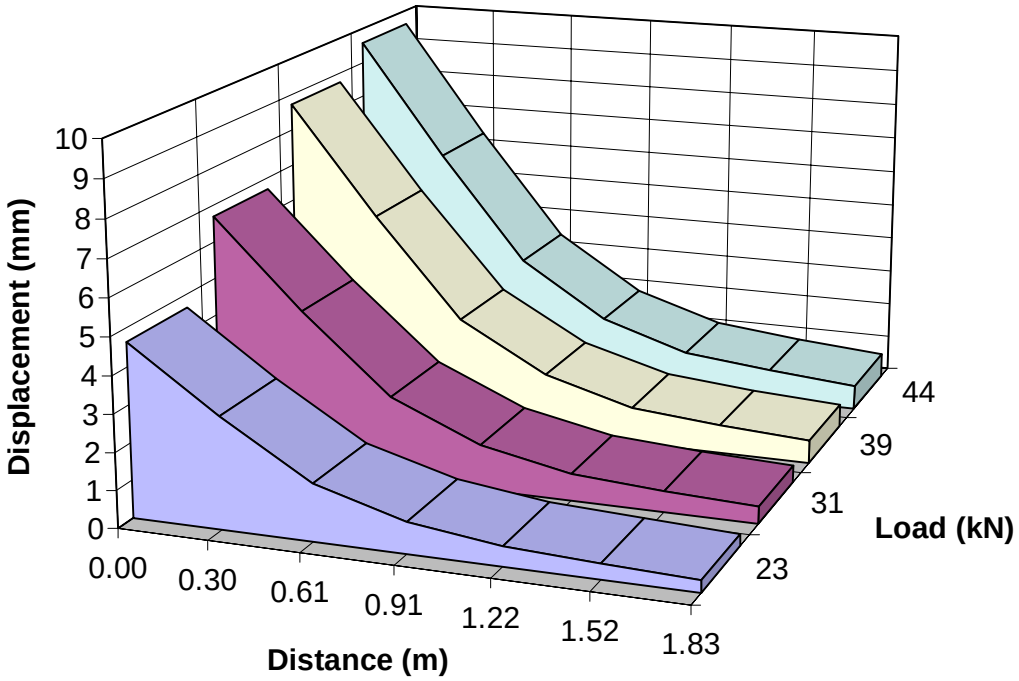


**Figure G 7 Displacement as a function of distance for different FWD load levels (October 1994, section 7).**

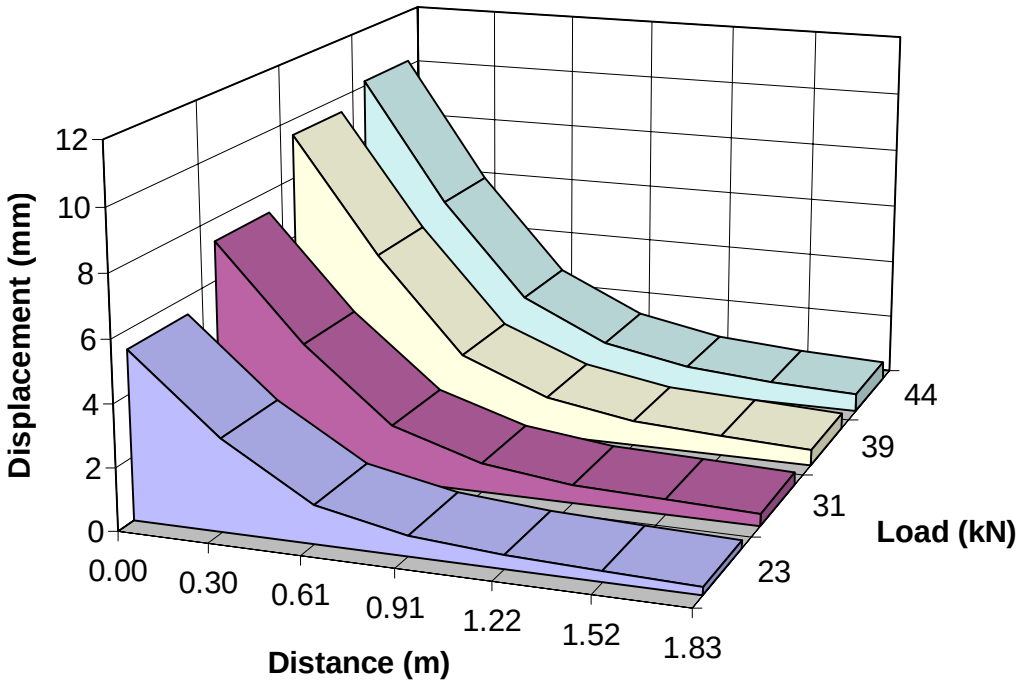


**Figure G 8 Displacement as a function of distance for different FWD load levels (October 1994, section 8).**

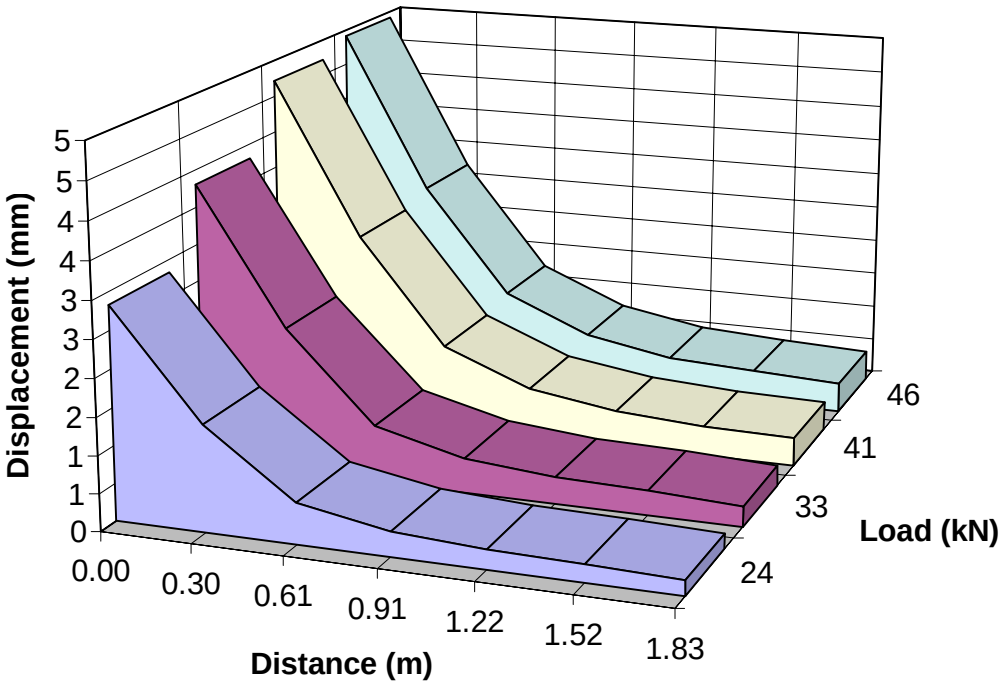


**Figure G 9 Displacement as a function of distance for different FWD load levels (October 1994, section 9).**

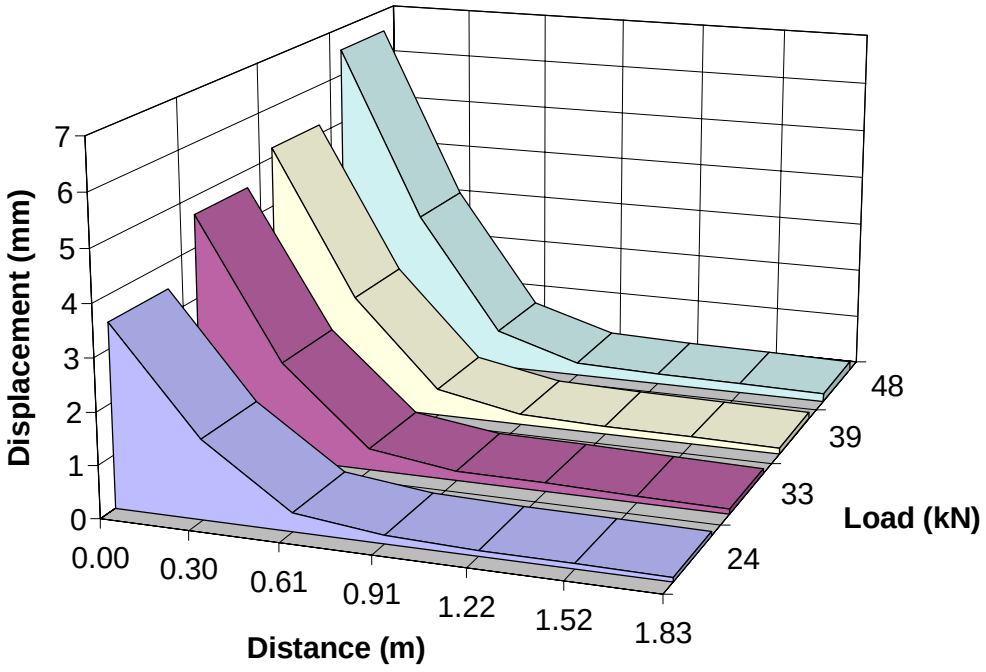


**Figure G 10 Displacement as a function of distance for different FWD load levels (March 1995, section 1).**

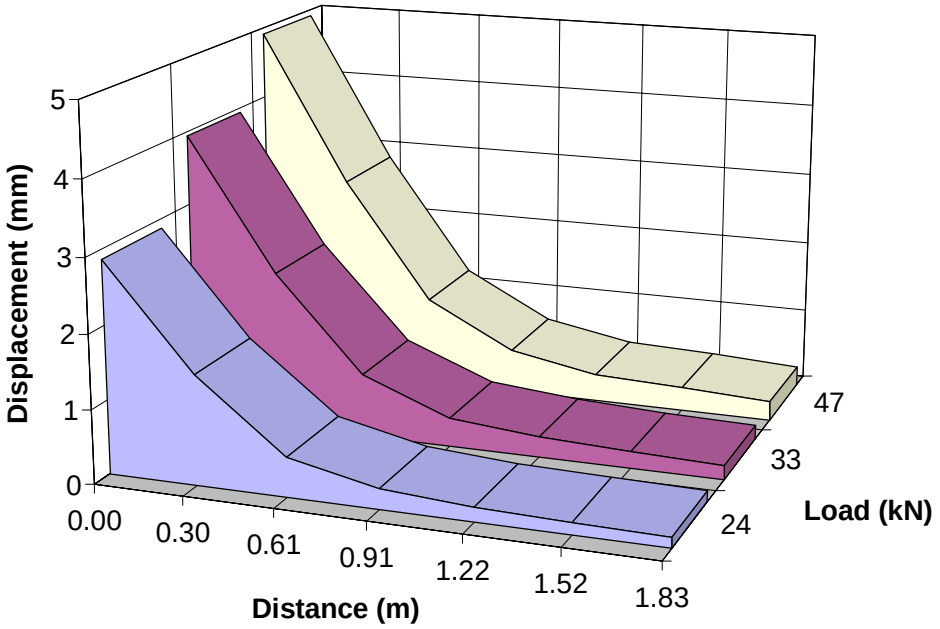


**Figure G 11 Displacement as a function of distance for different FWD load levels (March 1995, section 2).**

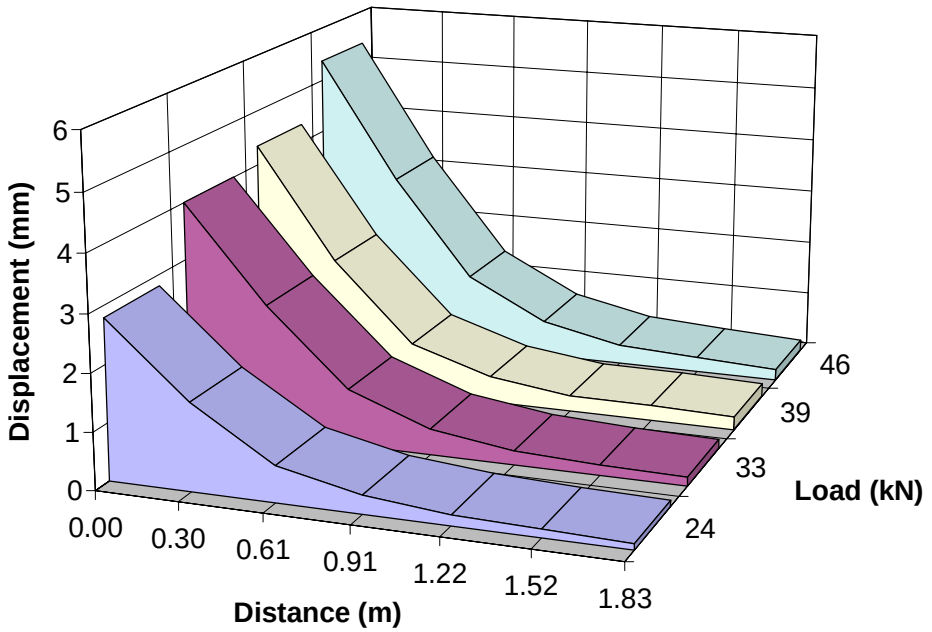


**Figure G 12 Displacement as a function of distance for different FWD load levels (March 1995, section 3).**

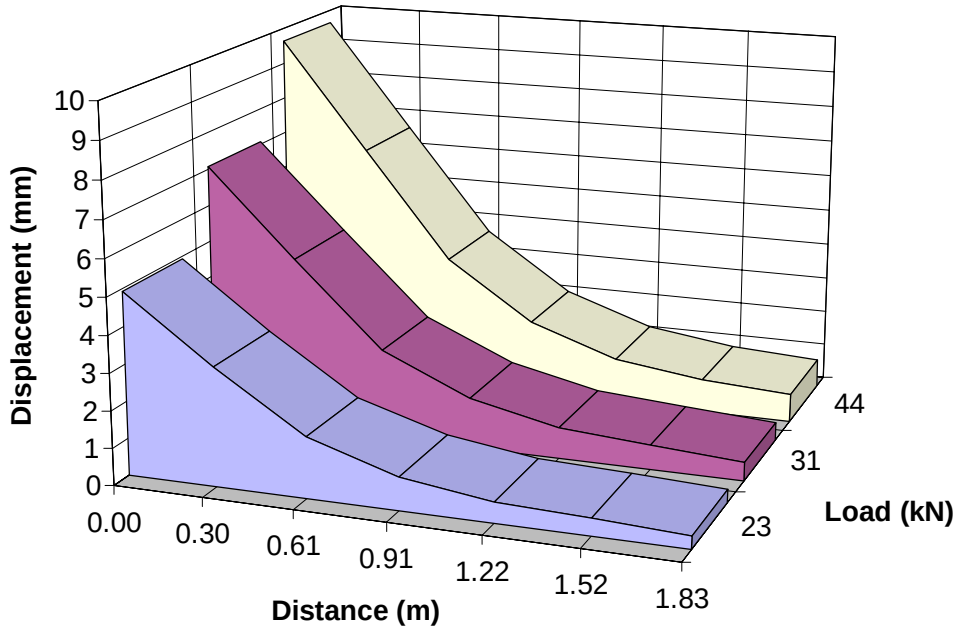


**Figure G 13 Displacement as a function of distance for different FWD load levels (March 1995, section 4).**

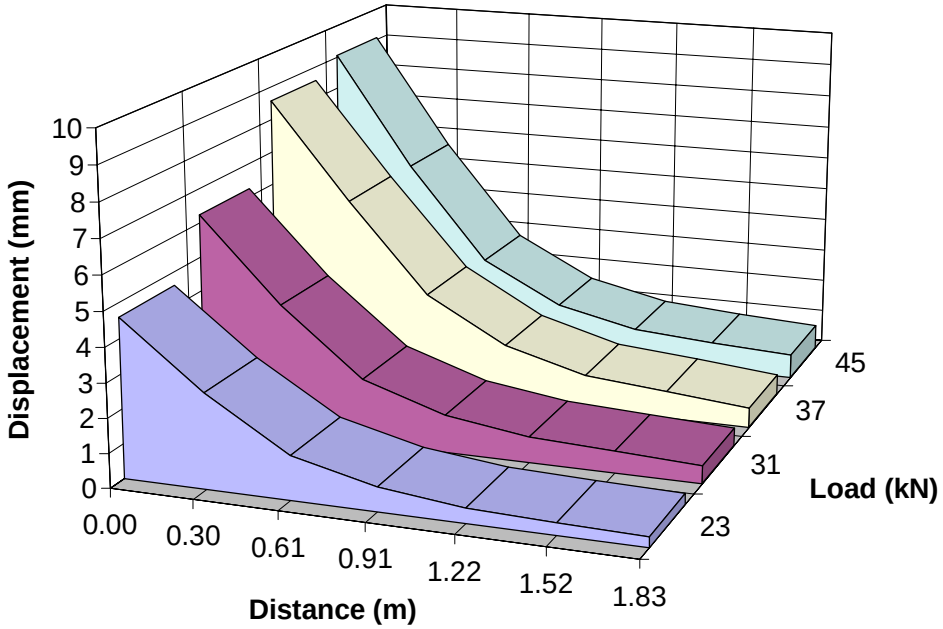


**Figure G 14 Displacement as a function of distance for different FWD load levels (March 1995, section 5).**

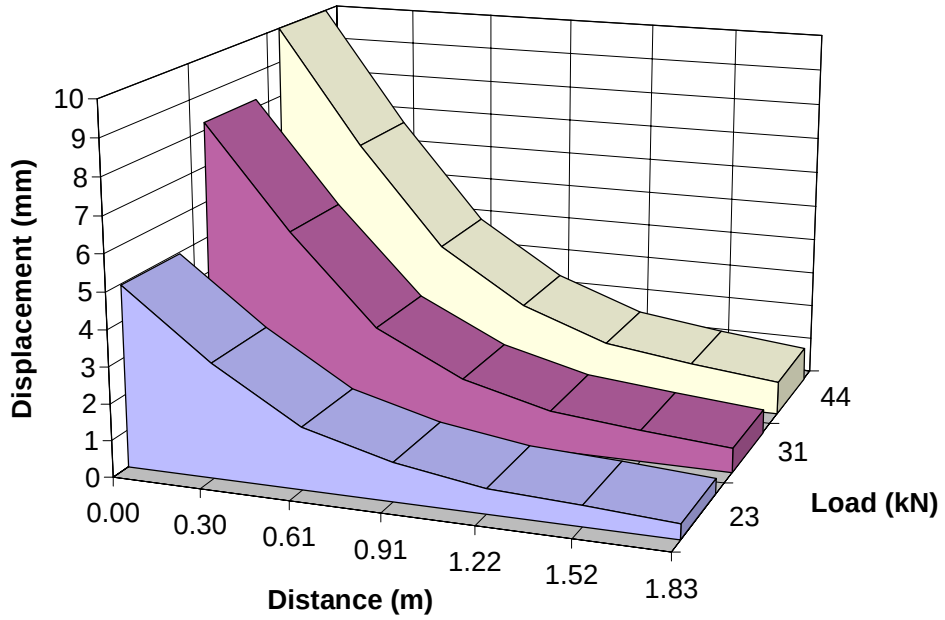


**Figure G 15 Displacement as a function of distance for different FWD load levels (March 1995, section 6).**

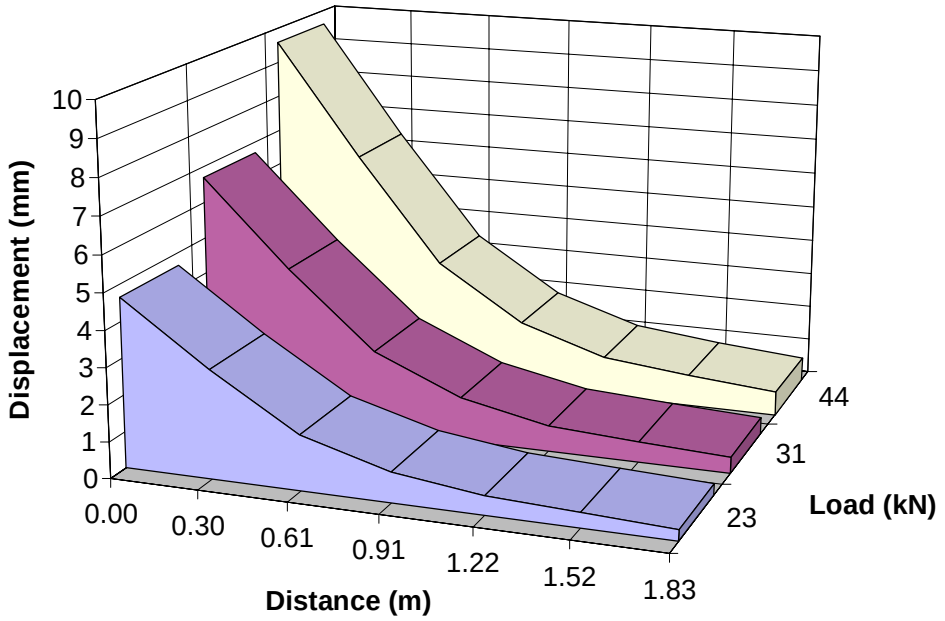


**Figure G 16 Displacement as a function of distance for different FWD load levels (March 1995, section 7).**

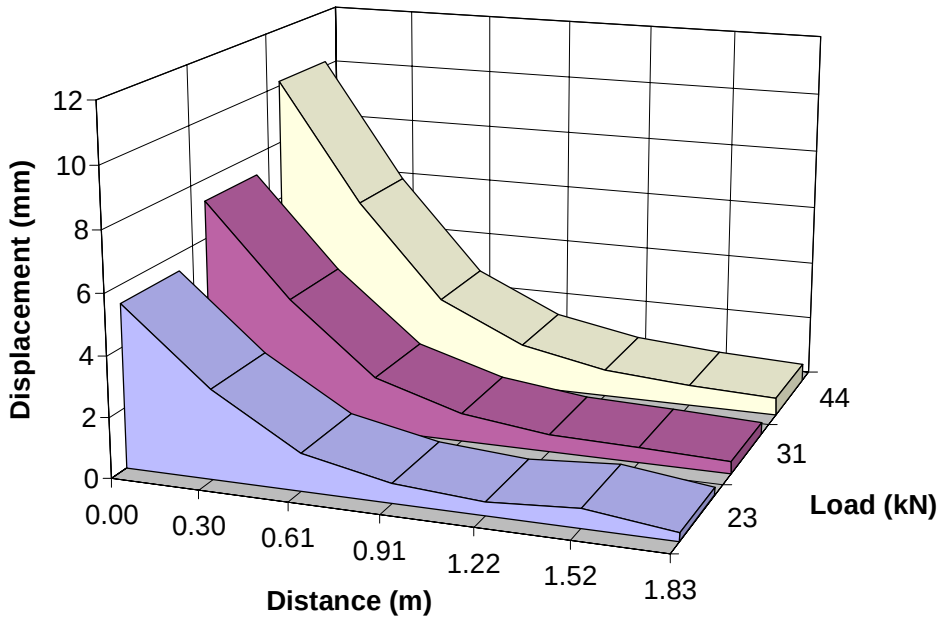


**Figure G 17 Displacement as a function of distance for different FWD load levels (March 1995, section 8).**

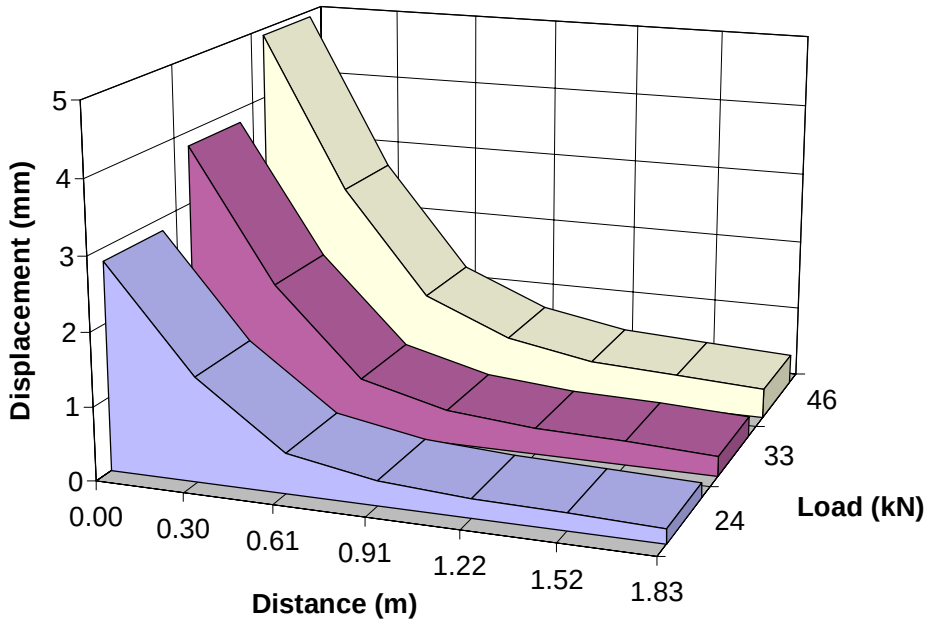


**Figure G 18 Displacement as a function of distance for different FWD load levels (March 1995, section 9).**

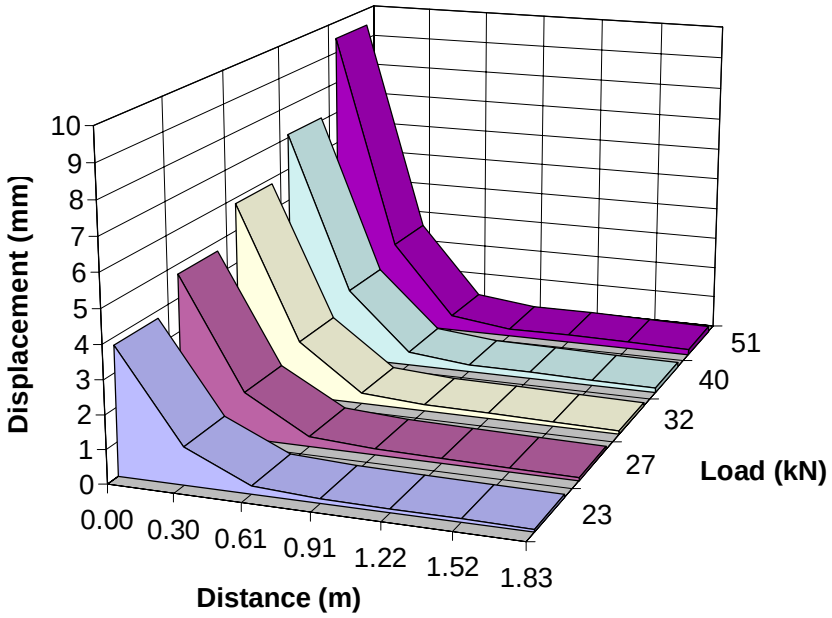


**Figure G 19 Displacement as a function of distance for different FWD load levels (August 1995, section 1).**

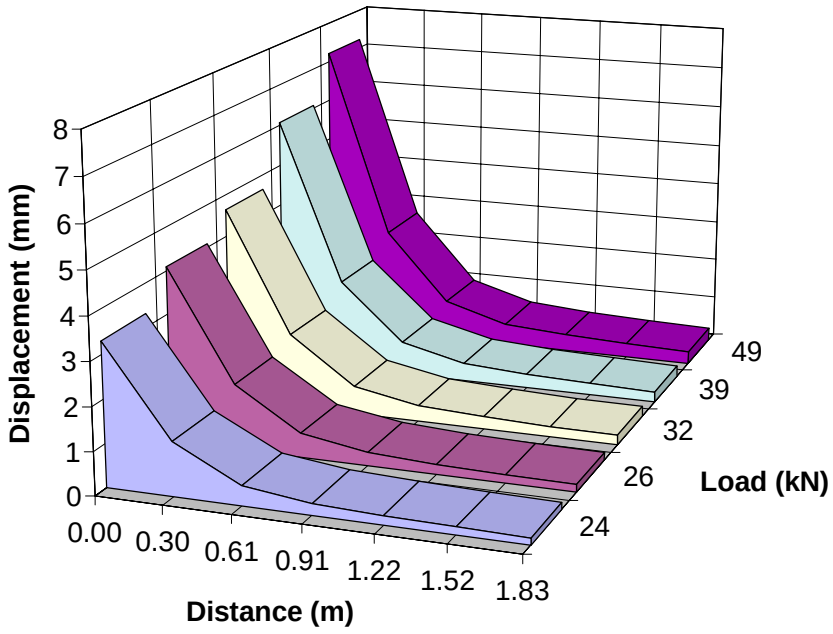


**Figure G 20 Displacement as a function of distance for different FWD load levels (August 1995, section 2).**

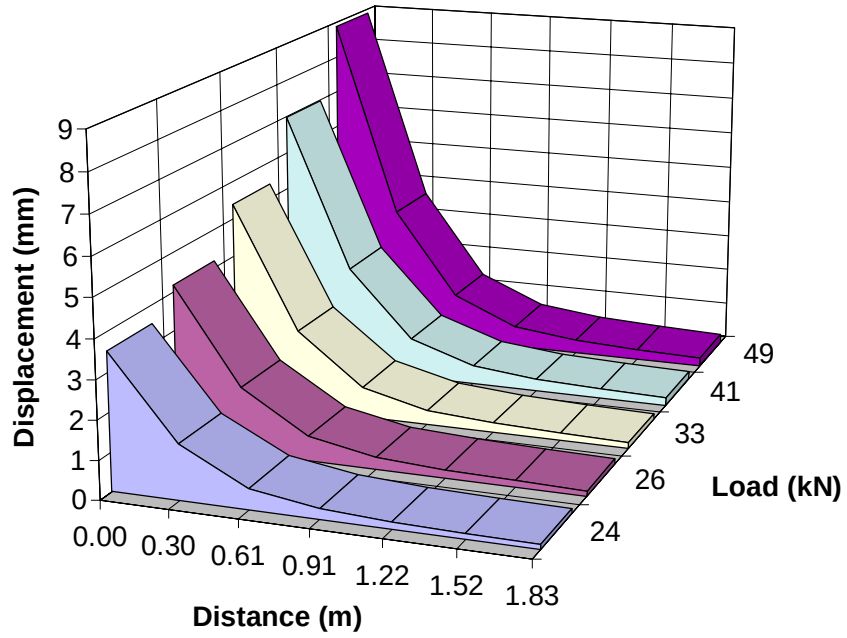


**Figure G 21 Displacement as a function of distance for different FWD load levels (August 1995, section 3).**

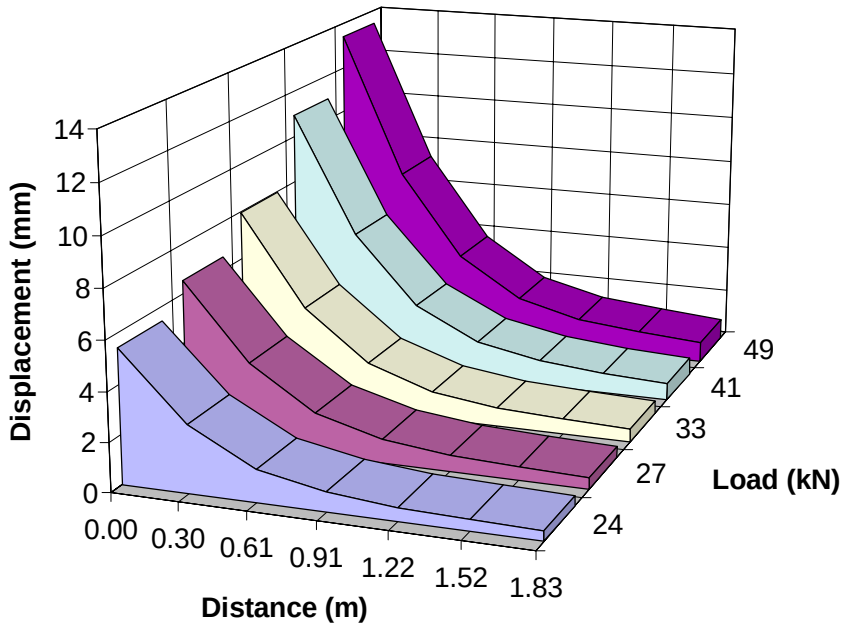


**Figure G 22 Displacement as a function of distance for different FWD load levels (August 1995, section 4).**

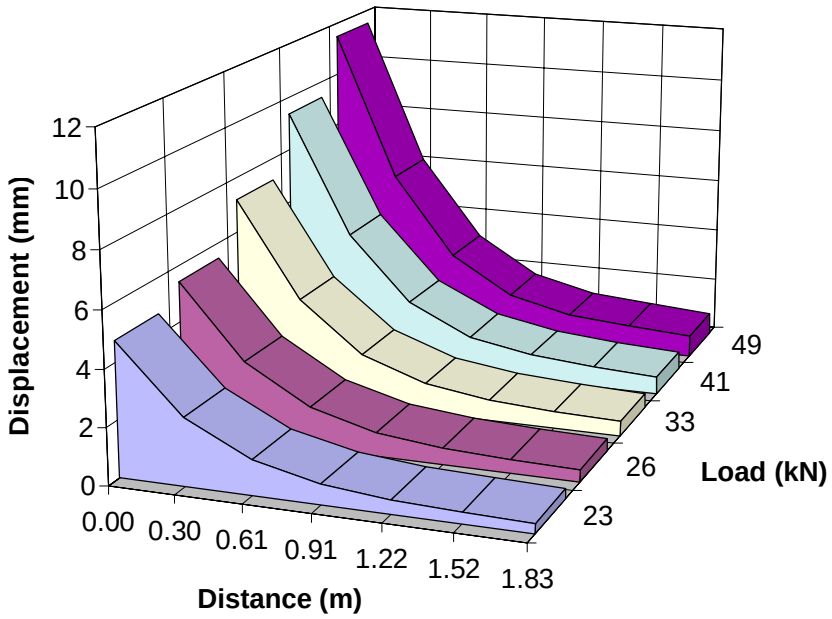


**Figure G 23 Displacement as a function of distance for different FWD load levels (August 1995, section 5).**

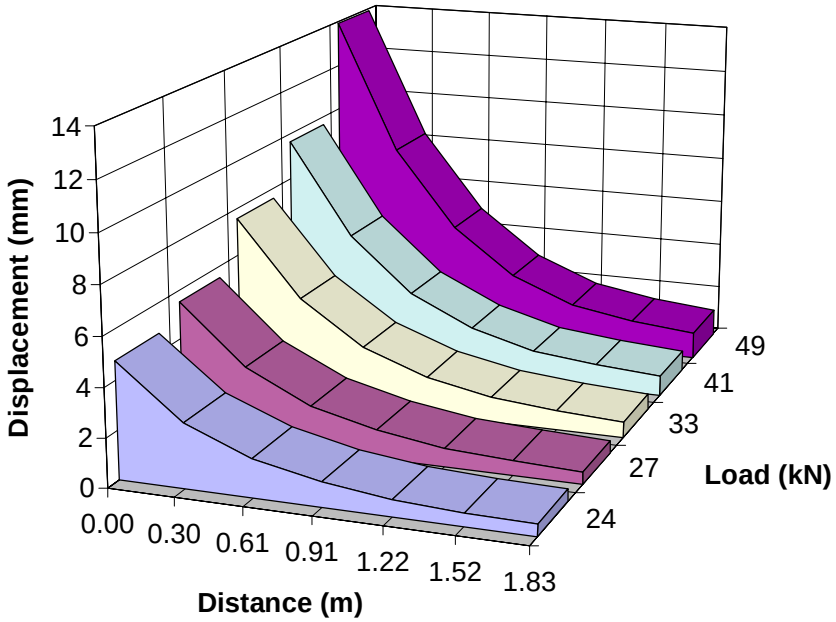


**Figure G 24 Displacement as a function of distance for different FWD load levels (August 1995, section 6).**

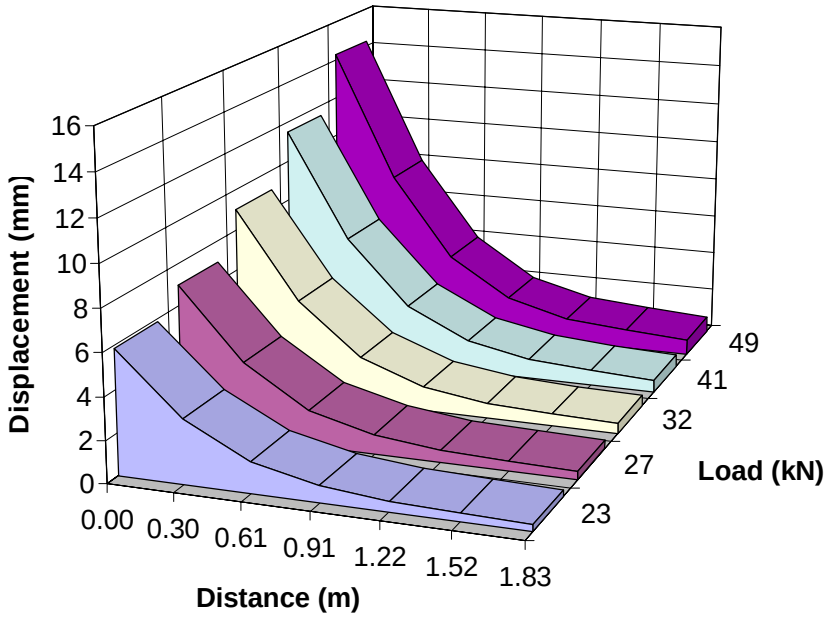


**Figure G 25 Displacement as a function of distance for different FWD load levels (August 1995, section 7).**

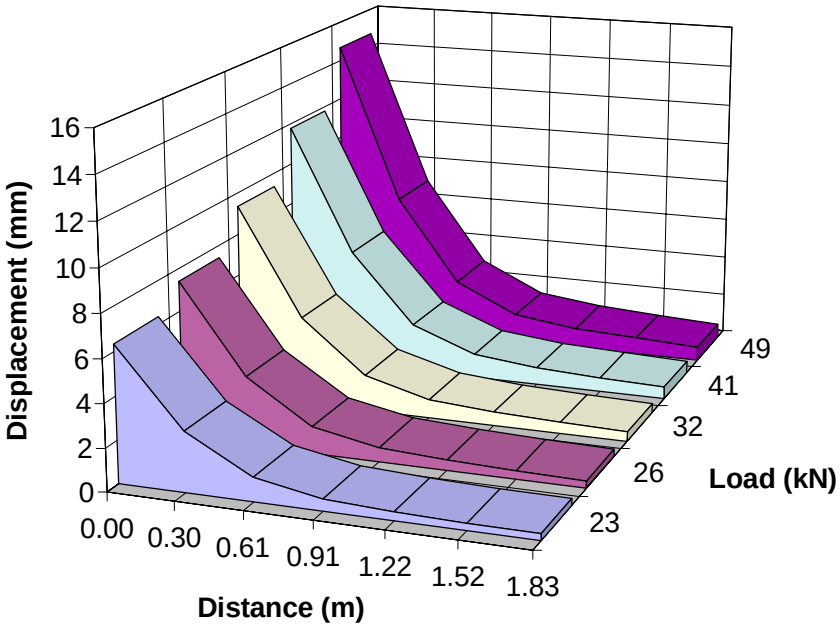


**Figure G 26 Displacement as a function of distance for different FWD load levels (August 1995, section 8).**

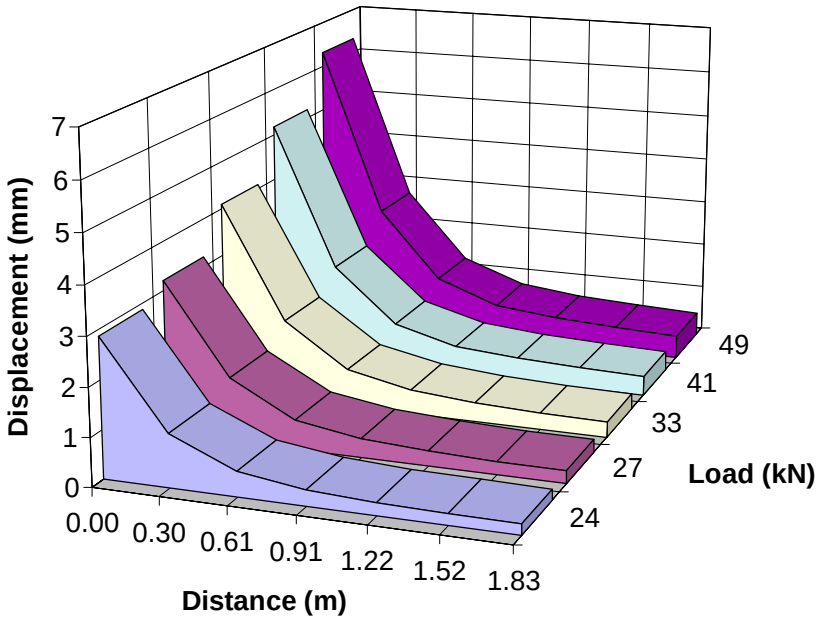


**Figure G 27 Displacement as a function of distance for different FWD load levels (August 1995, section 9).**

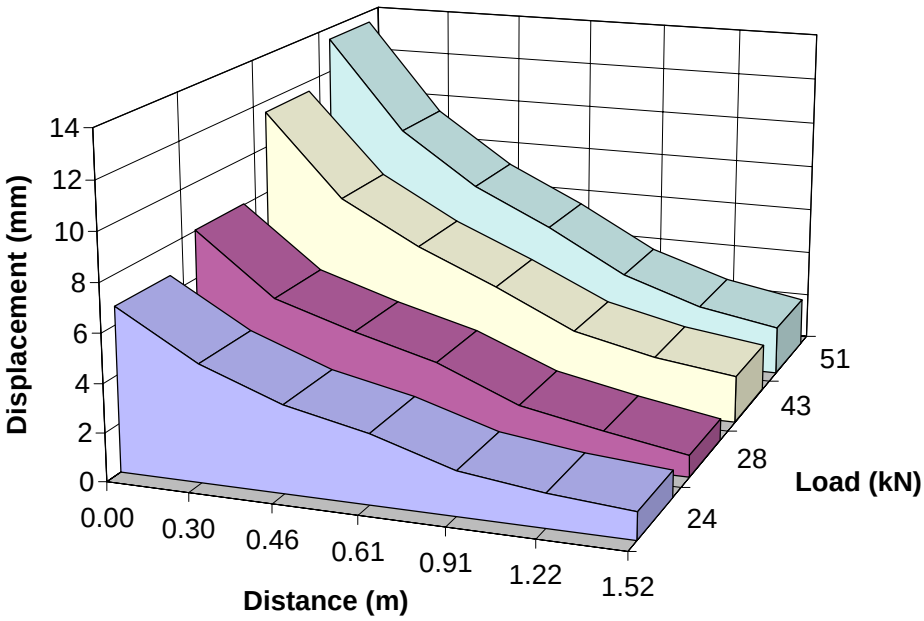


**Figure G 28 Displacement as a function of distance for different FWD load levels (July 1996, section 1).**

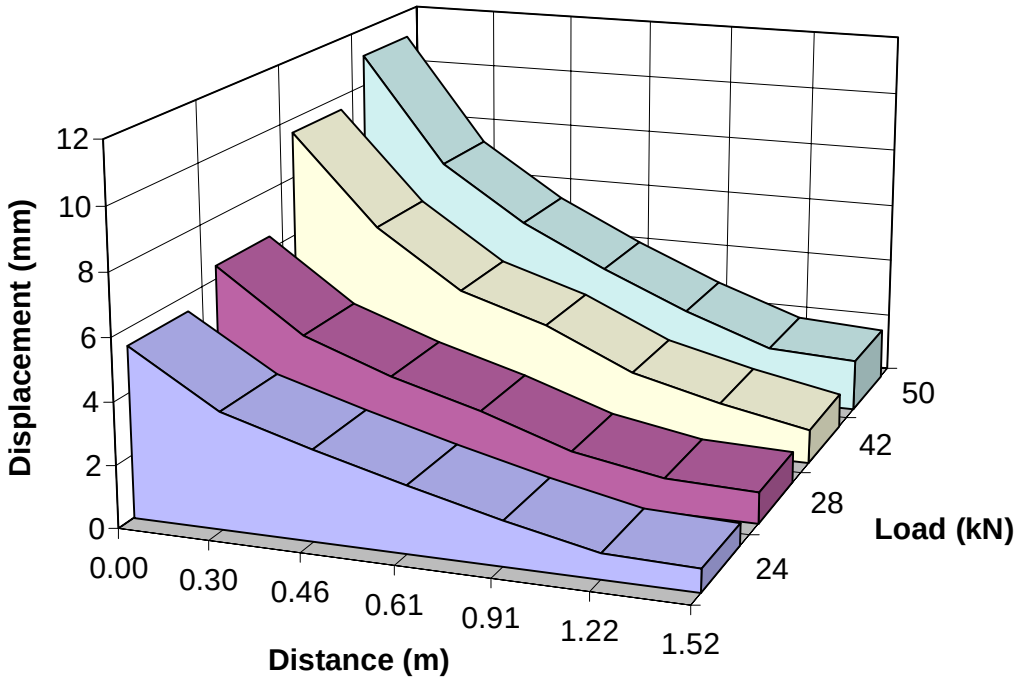


**Figure G 29 Displacement as a function of distance for different FWD load levels (July 1996, section 2).**

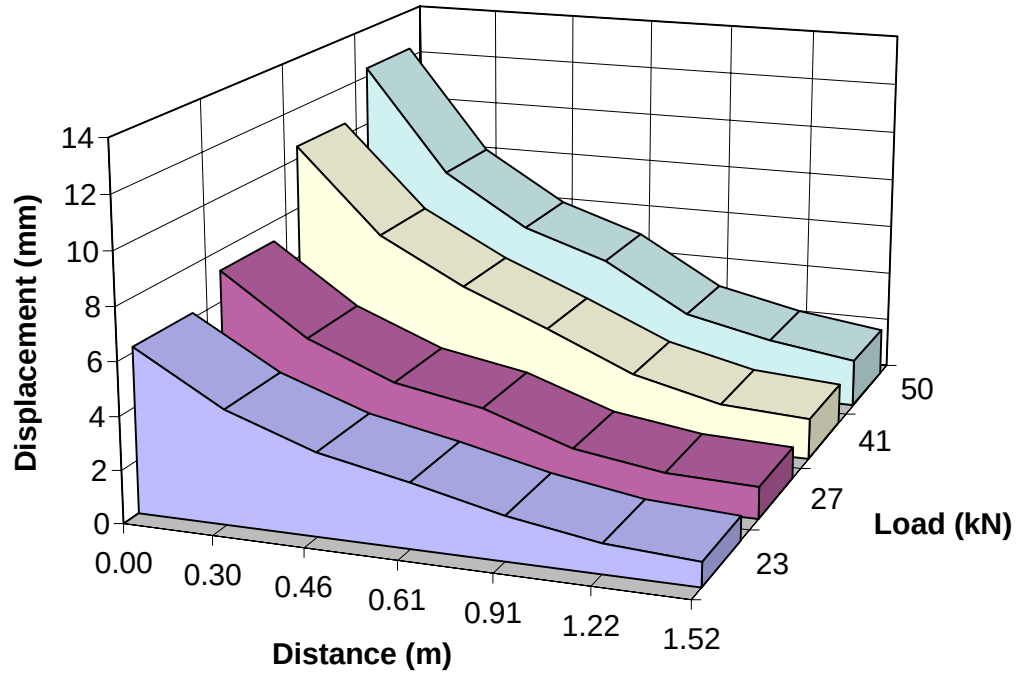


**Figure G 30 Displacement as a function of distance for different FWD load levels (July 1996, section 3).**

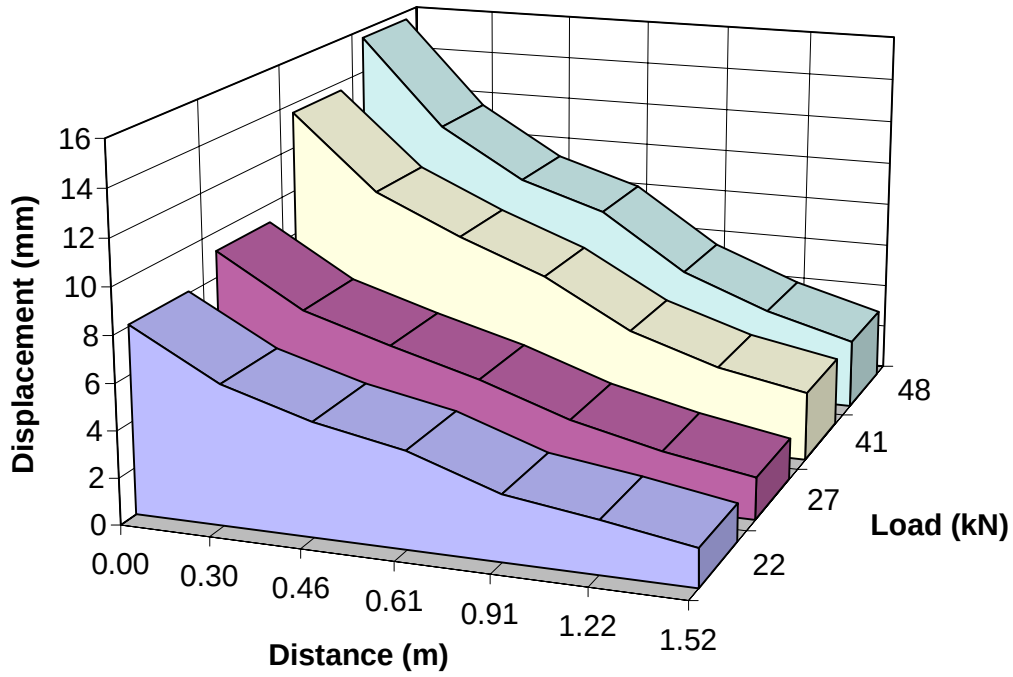


**Figure G 31 Displacement as a function of distance for different FWD load levels (July 1996, section 4).**

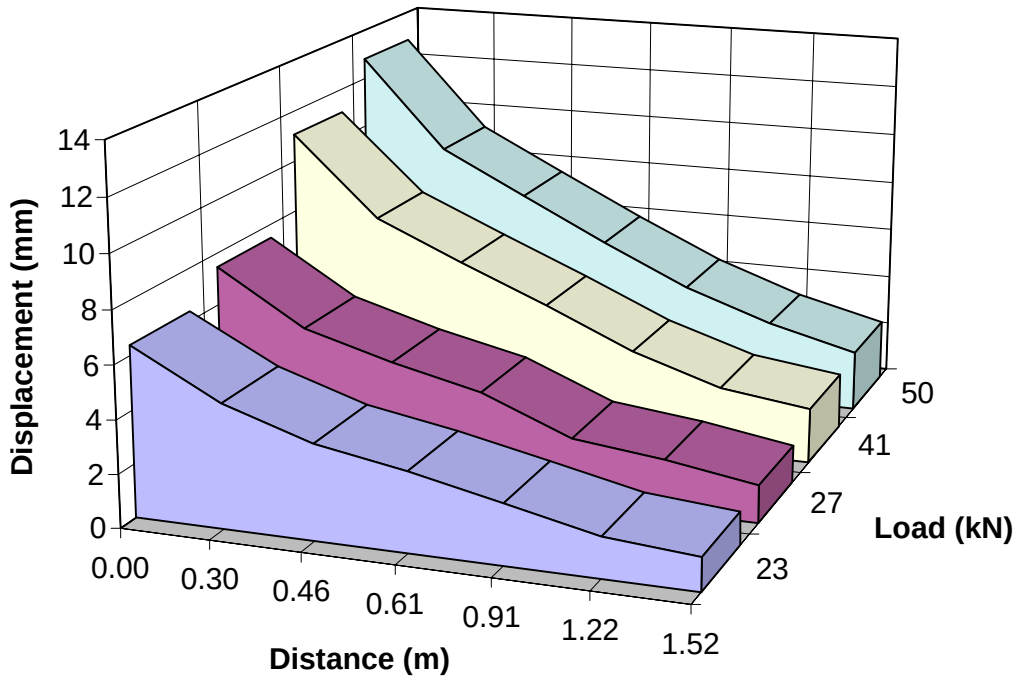


**Figure G 32 Displacement as a function of distance for different FWD load levels (July 1996, section 5).**

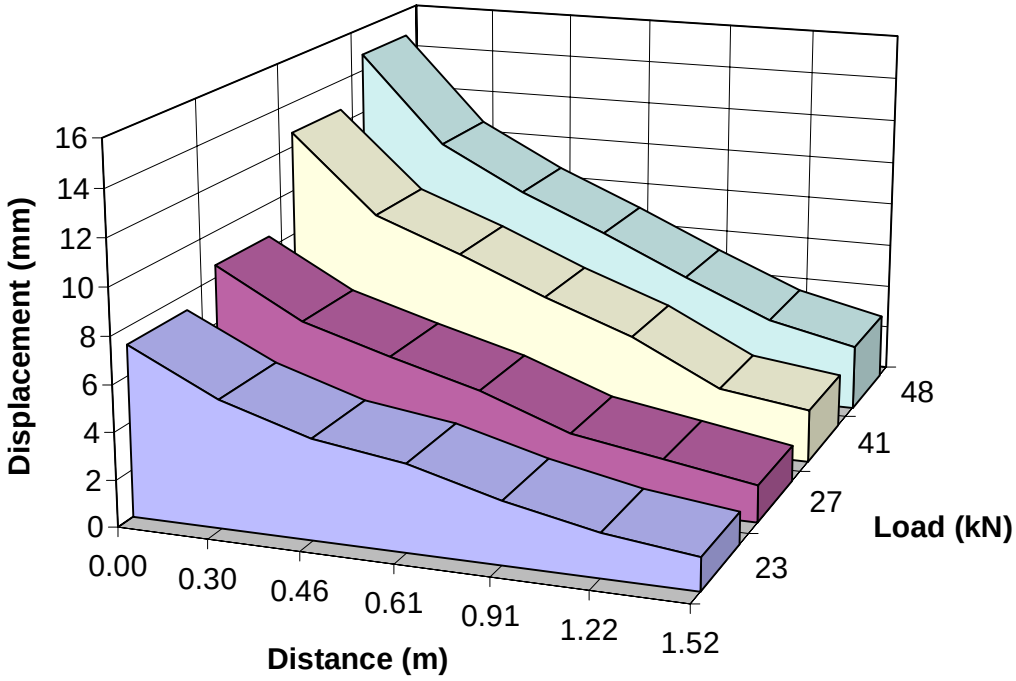


**Figure G 33 Displacement as a function of distance for different FWD load levels (July 1996, section 6).**

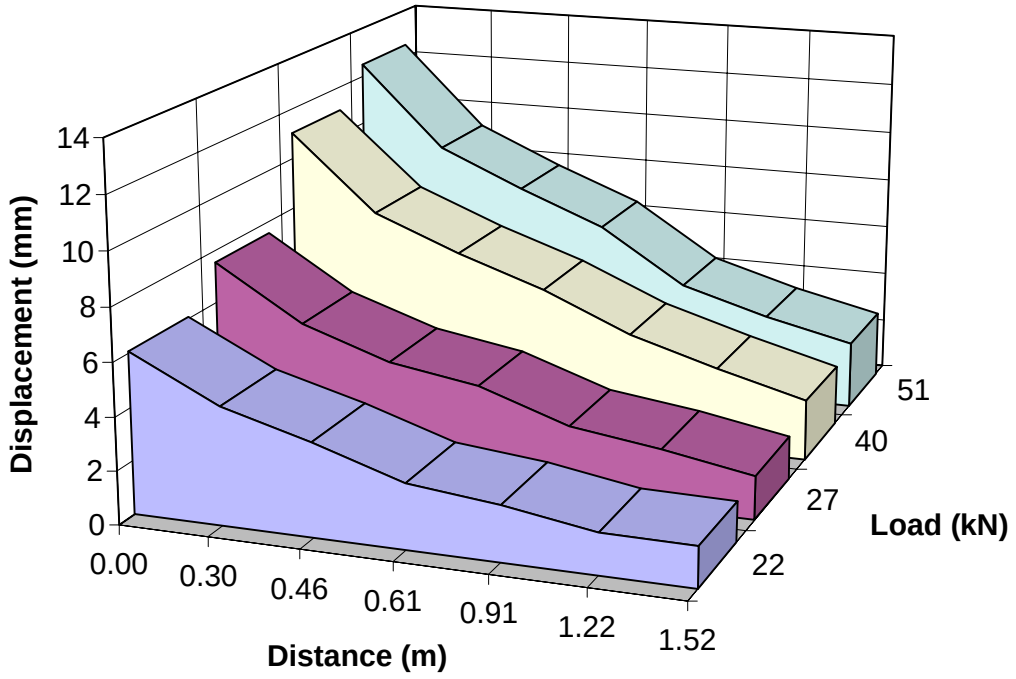


**Figure G 34 Displacement as a function of distance for different FWD load levels (July 1996, section 7).**

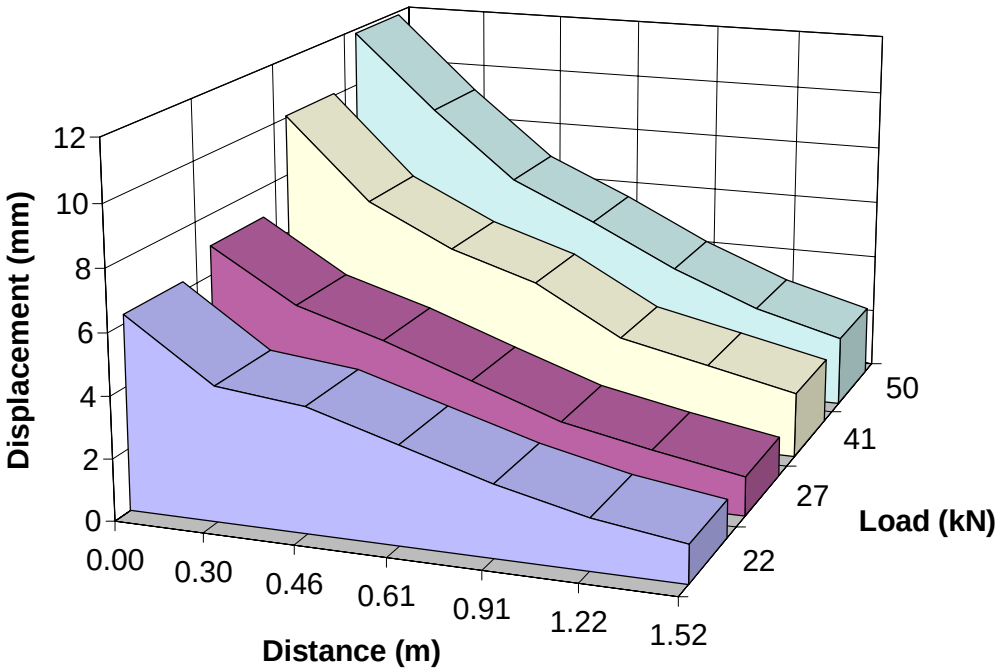


**Figure G 35 Displacement as a function of distance for different FWD load levels (July 1996, section 8).**

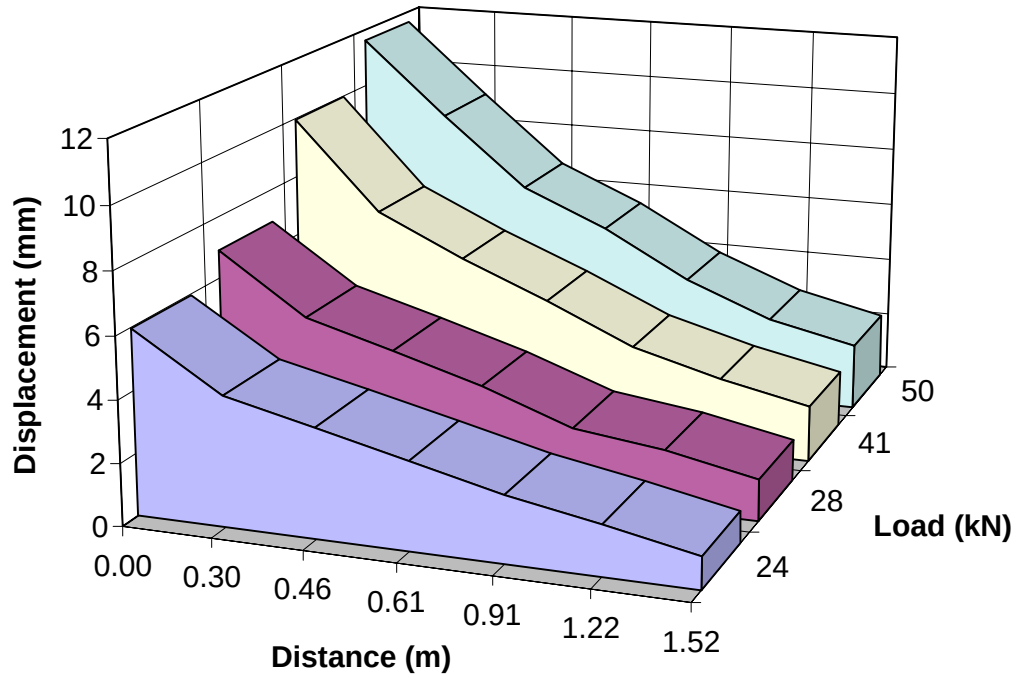


**Figure G 36 Displacement as a function of distance for different FWD load levels (July 1996, section 9).**

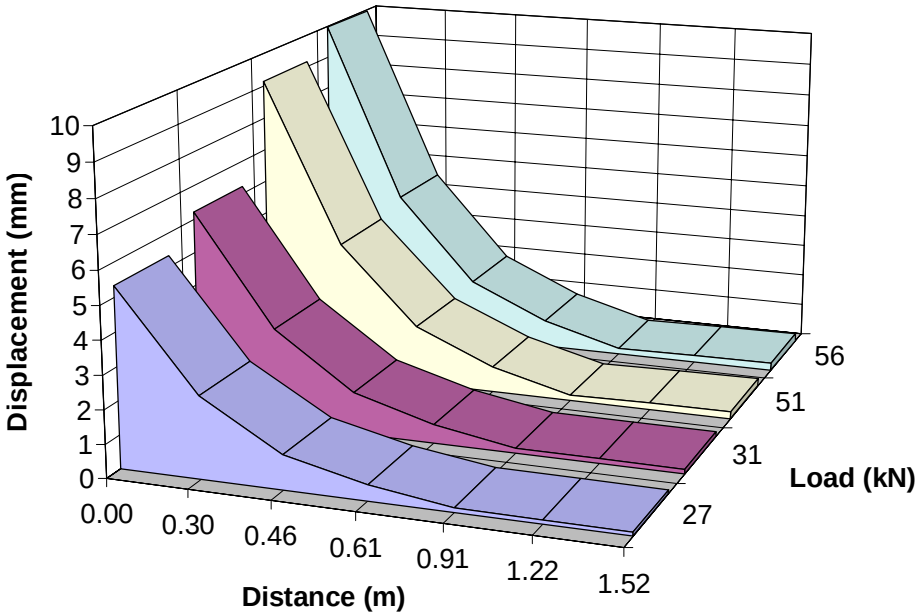


**Figure G 37 Displacement as a function of distance for different FWD load levels (October 1996, section 1).**

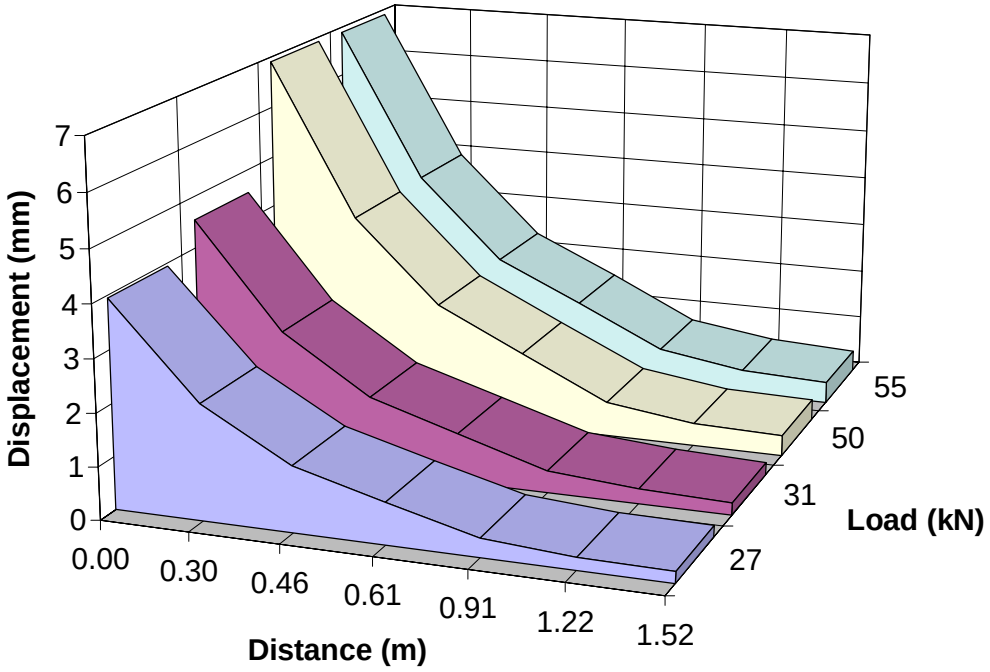


**Figure G 38 Displacement as a function of distance for different FWD load levels (October 1996, section 2).**

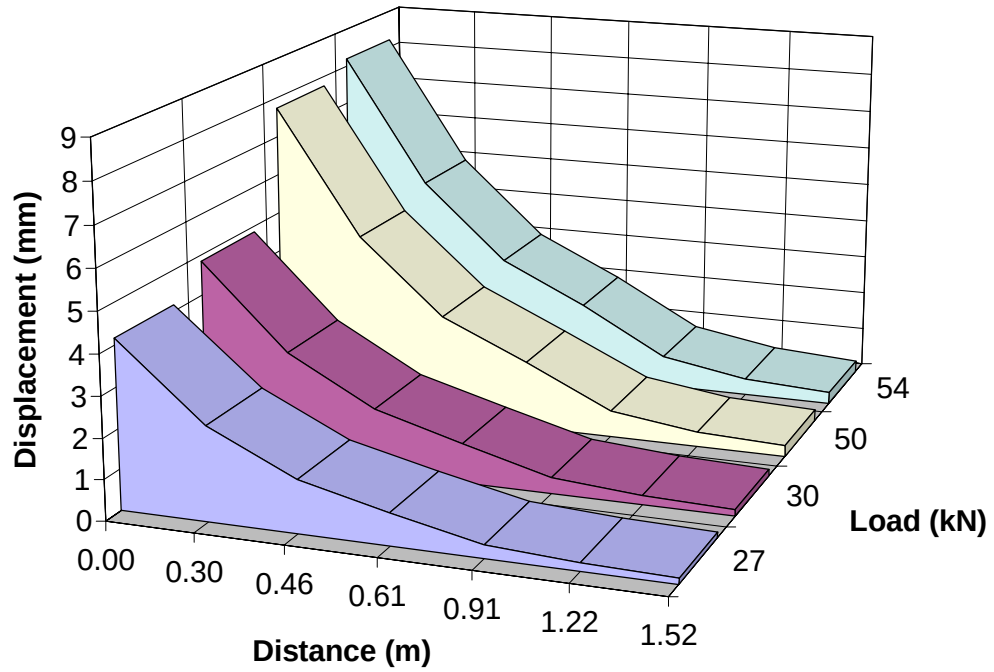


**Figure G 39 Displacement as a function of distance for different FWD load levels (October 1996, section 3).**

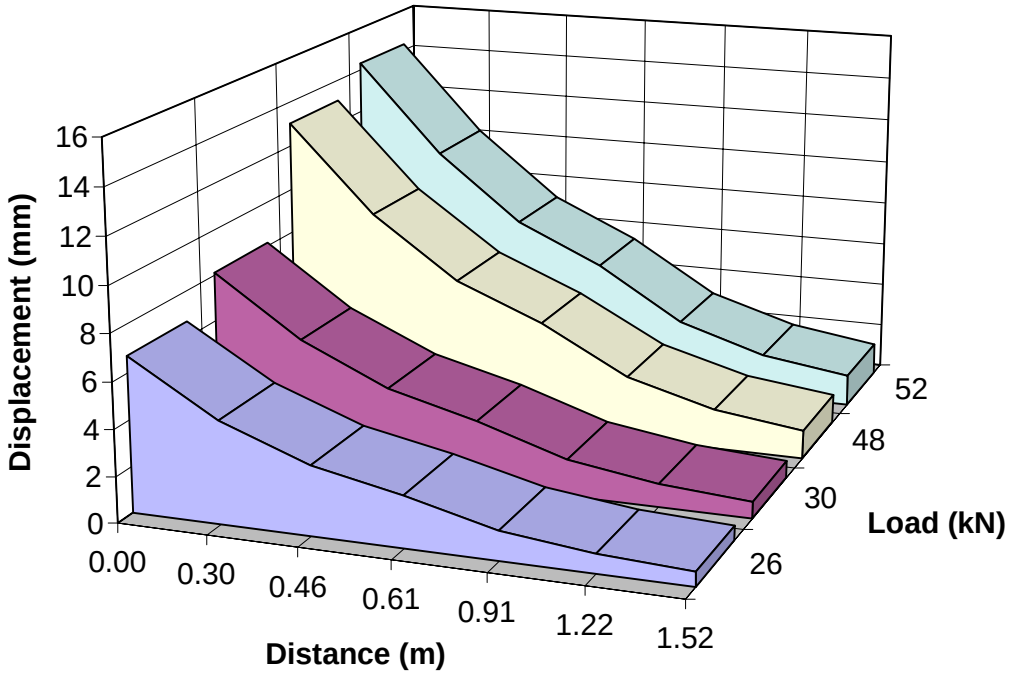


**Figure G 40 Displacement as a function of distance for different FWD load levels (October 1996, section 4).**

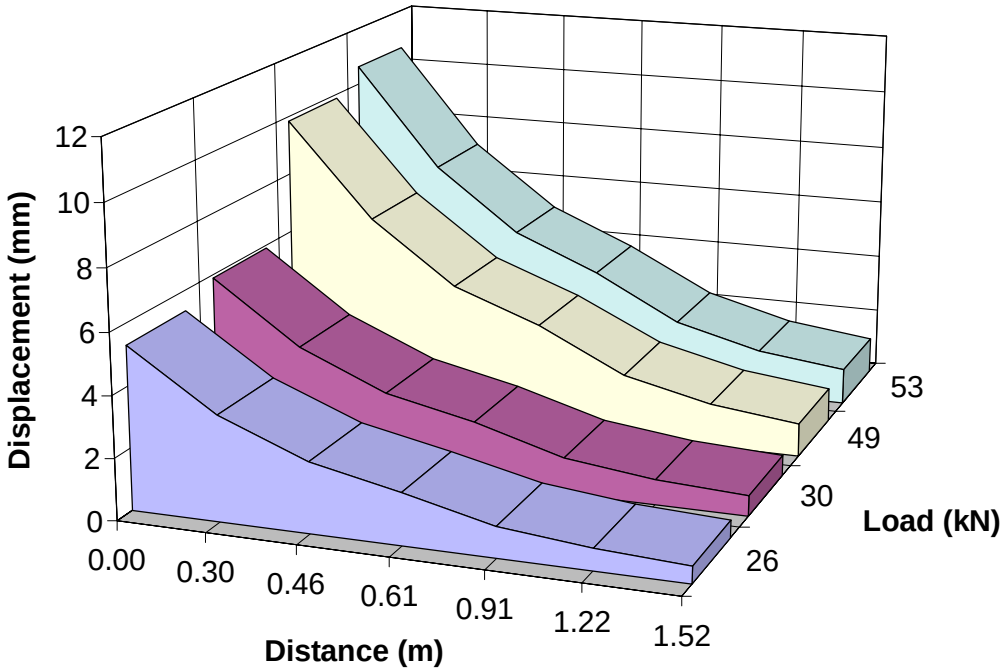


**Figure G 41 Displacement as a function of distance for different FWD load levels (October 1996, section 5).**

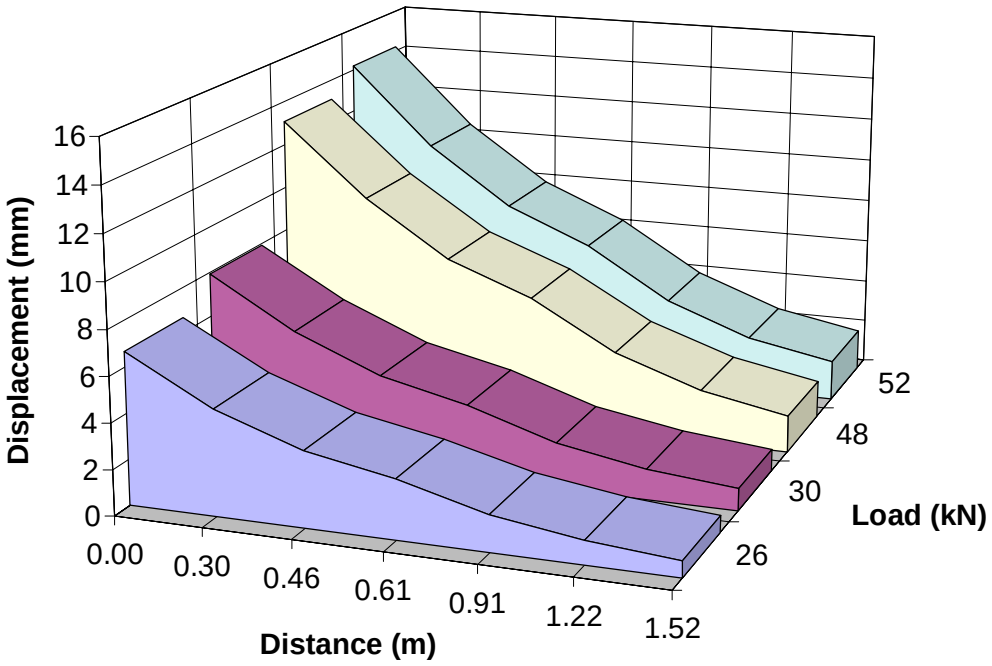


**Figure G 42 Displacement as a function of distance for different FWD load levels (October 1996, section 6).**

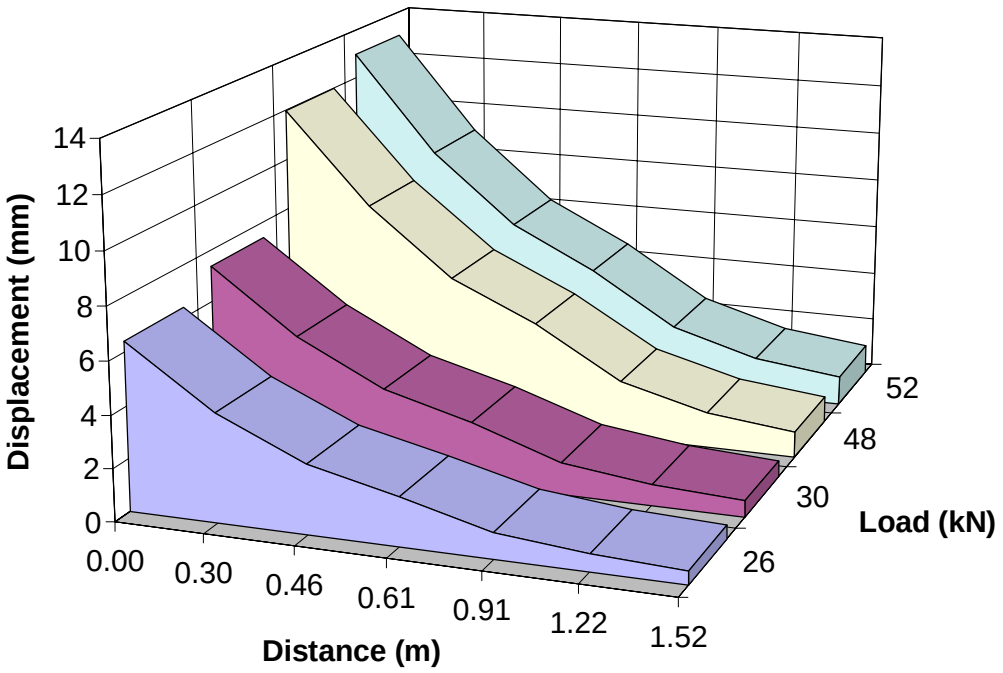


**Figure G 43 Displacement as a function of distance for different FWD load levels (October 1996, section 7).**

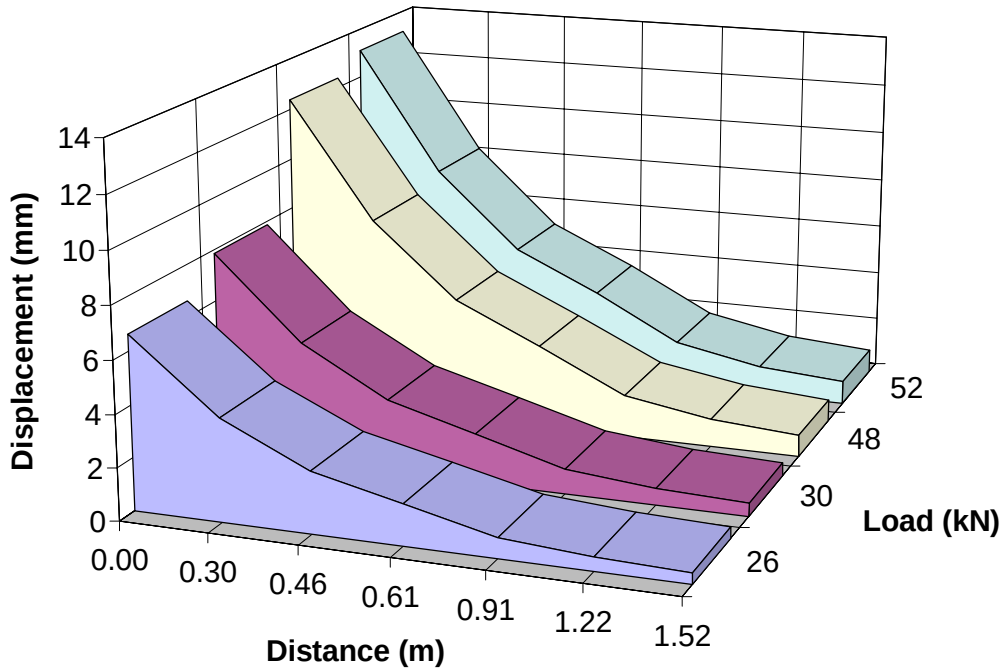


**Figure G 44 Displacement as a function of distance for different FWD load levels (October 1996, section 8).**

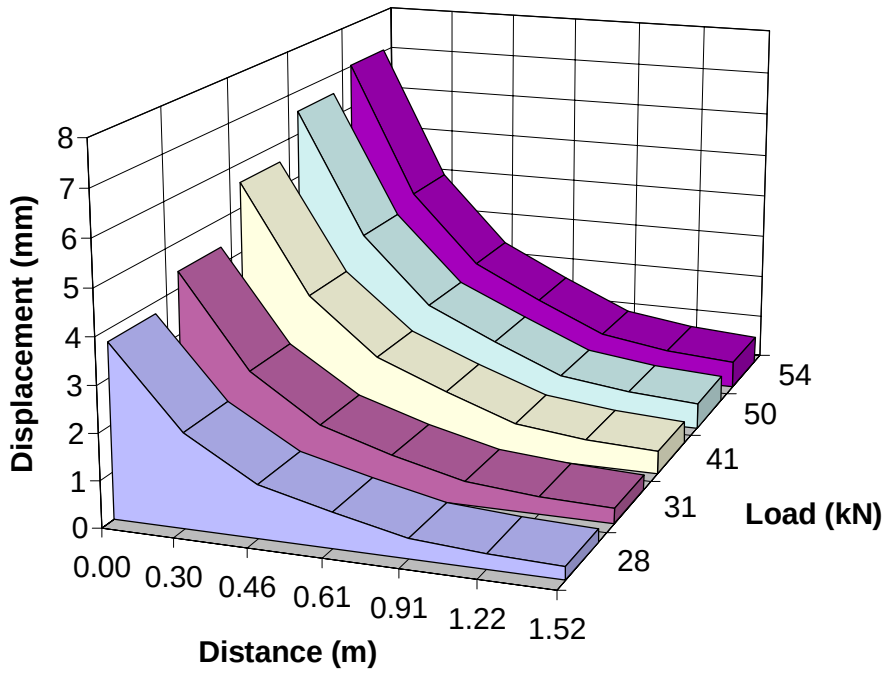


**Figure G 45 Displacement as a function of distance for different FWD load levels (October 1996, section 9).**

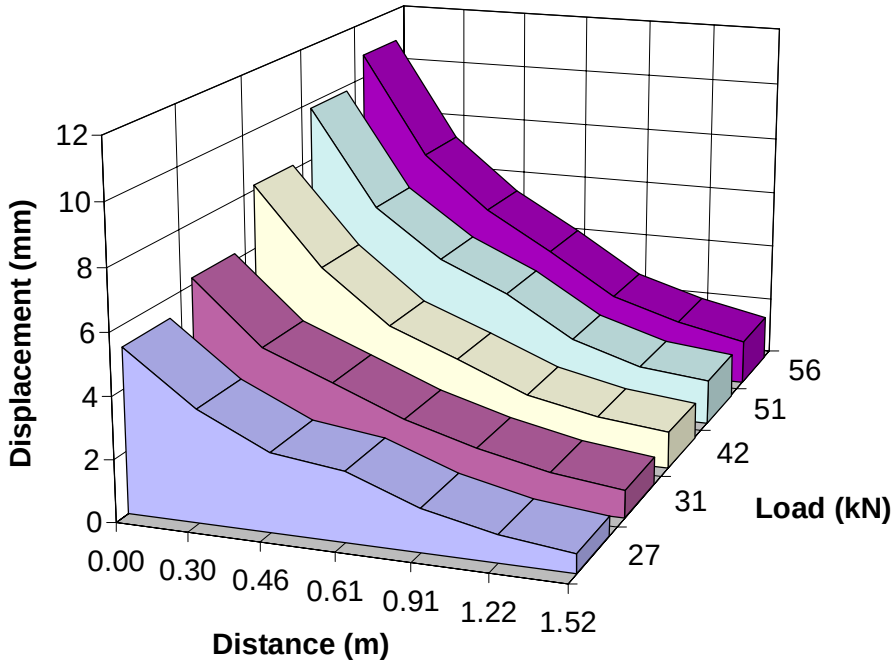


**Figure G 46 Displacement as a function of distance for different FWD load levels (January 1997, section 1).**

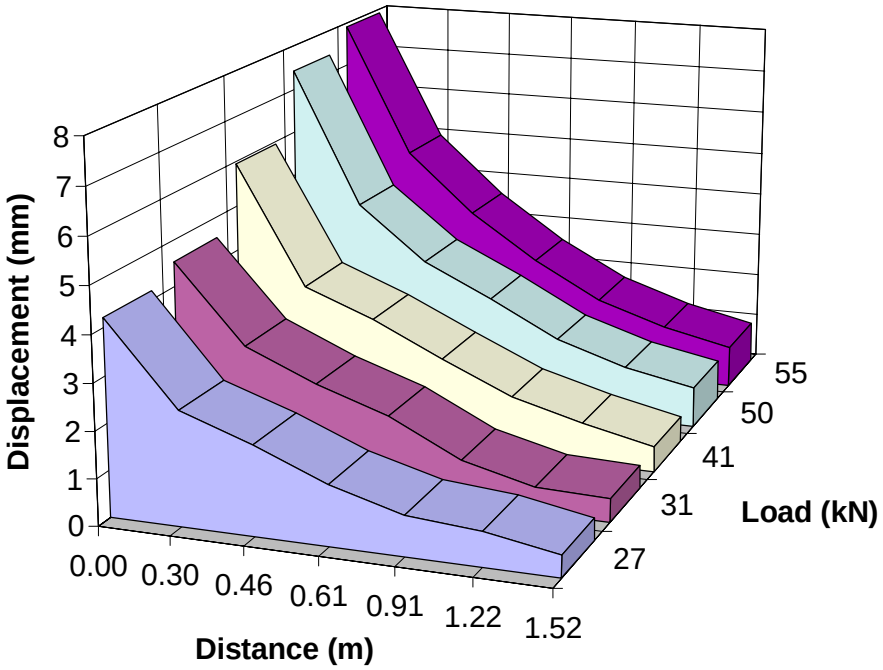


**Figure G 47 Displacement as a function of distance for different FWD load levels (January 1997, section 2).**

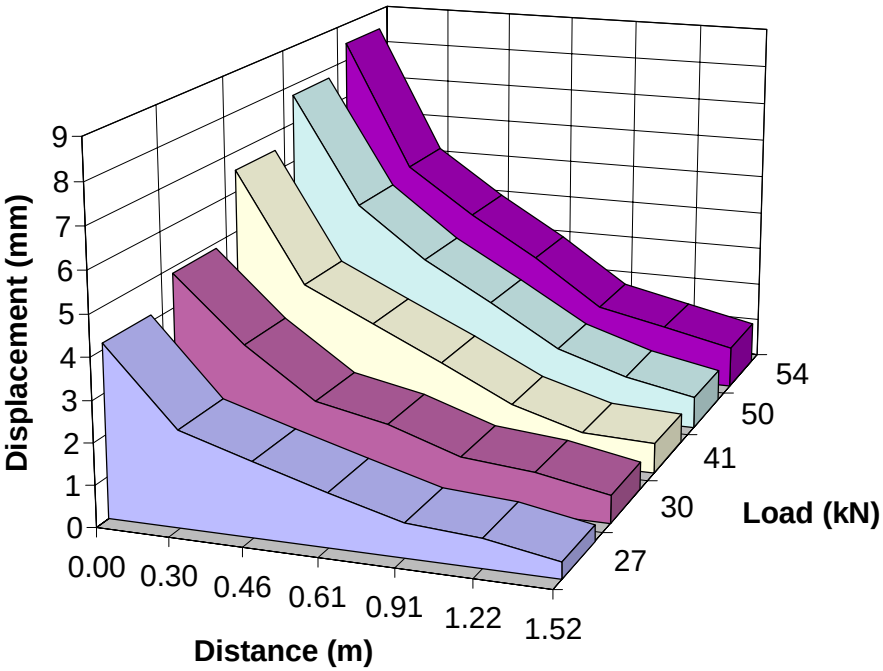


**Figure G 48 Displacement as a function of distance for different FWD load levels (January 1997, section 3).**

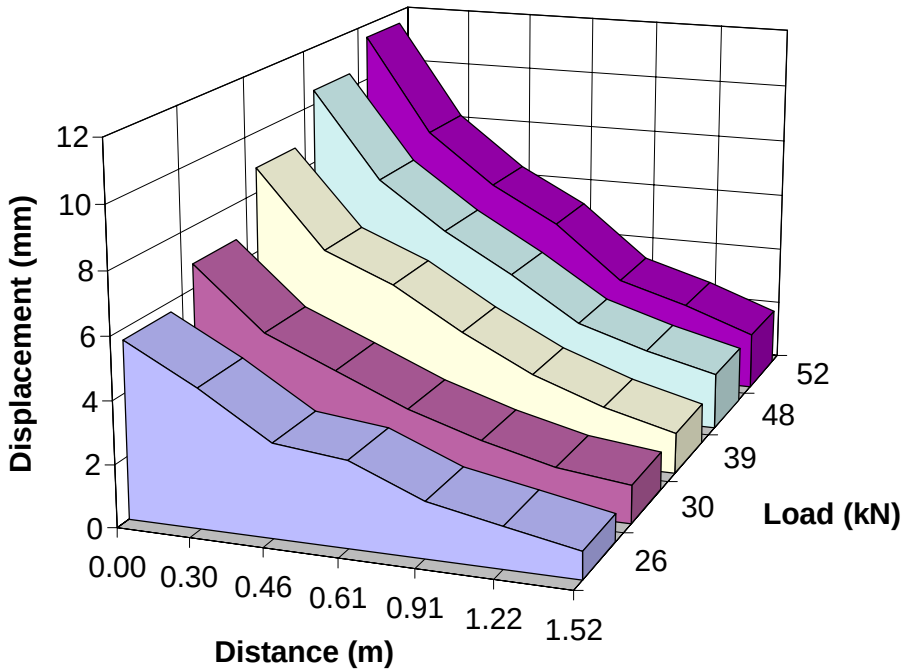


**Figure G 49 Displacement as a function of distance for different FWD load levels (January 1997, section 4).**

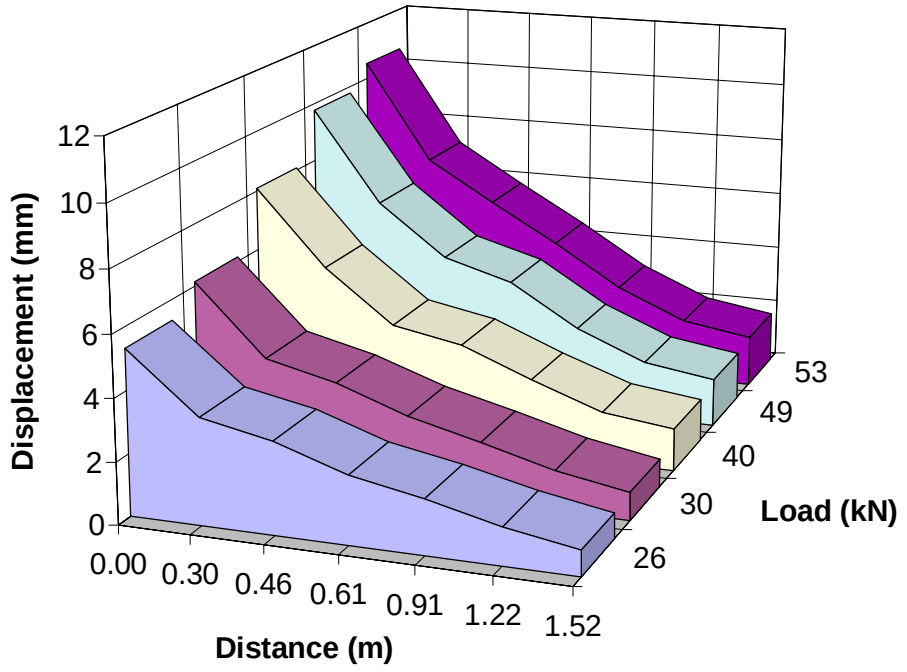


**Figure G 50 Displacement as a function of distance for different FWD load levels (January 1997, section 5).**

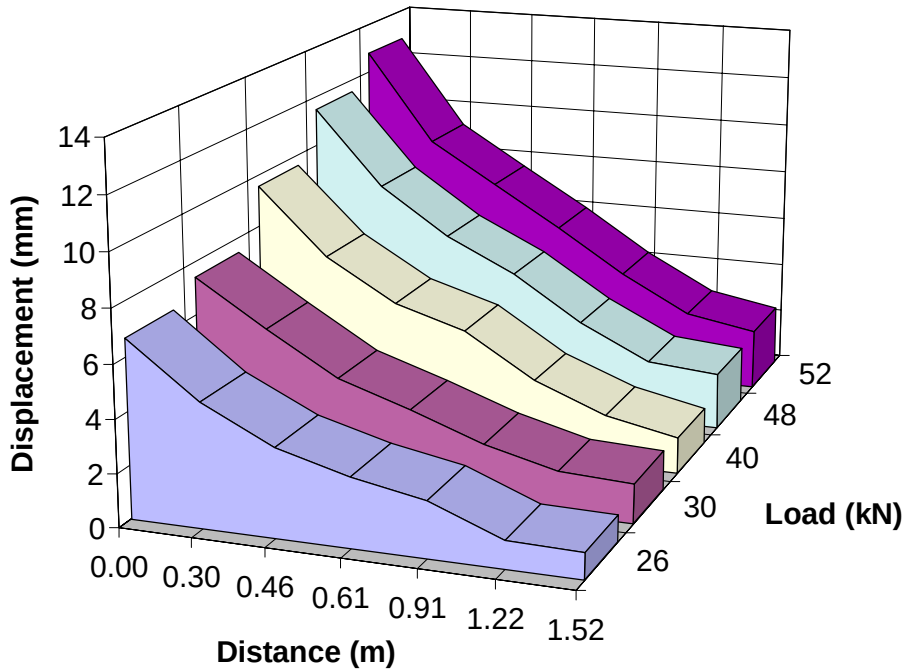


**Figure G 51 Displacement as a function of distance for different FWD load levels (January 1997, section 6).**

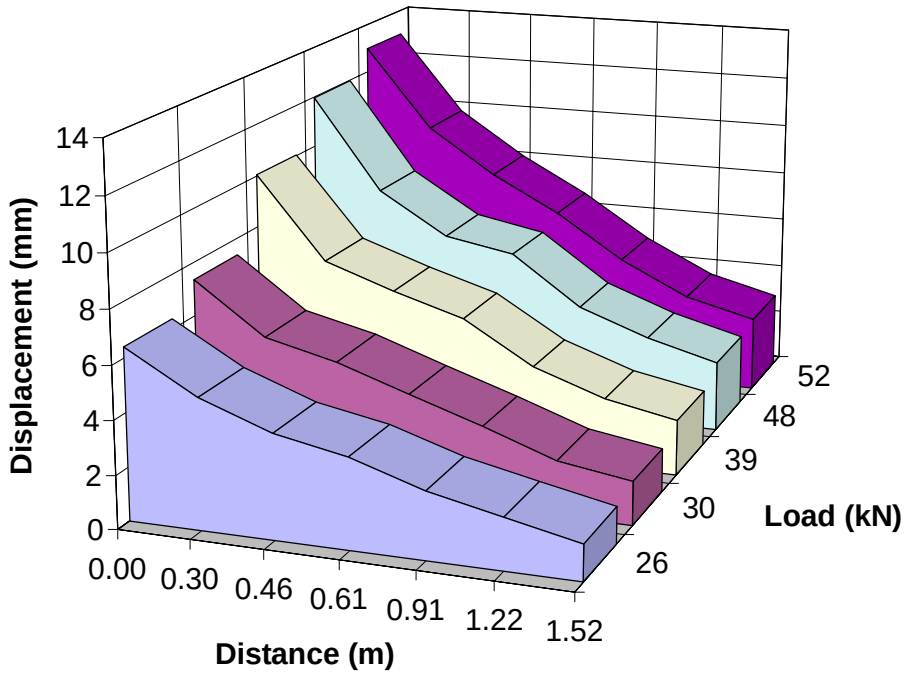


**Figure G 52 Displacement as a function of distance for different FWD load levels (January 1997, section 7).**

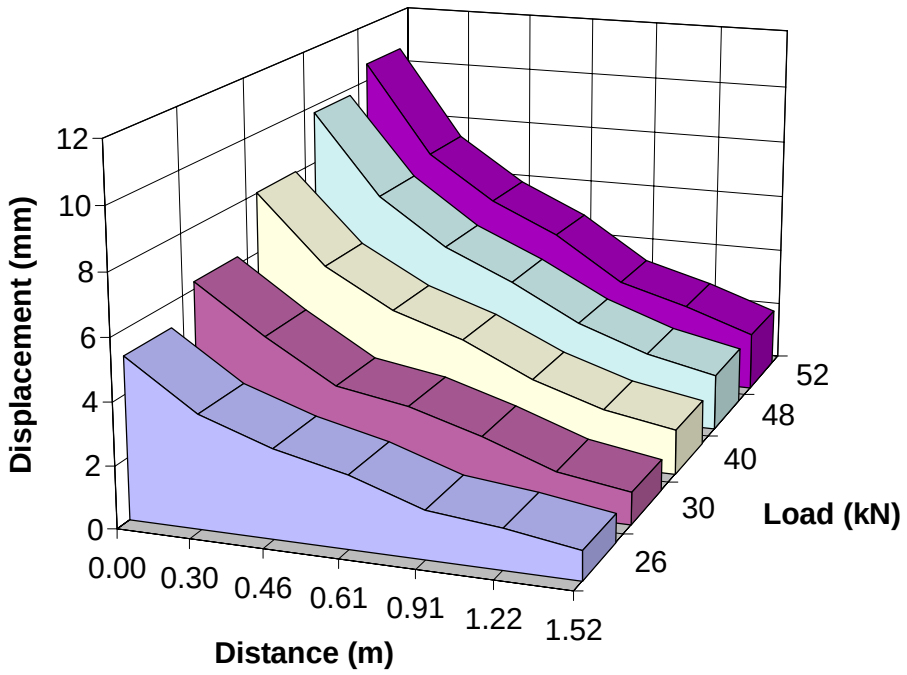


**Figure G 53 Displacement as a function of distance for different FWD load levels (January 1997, section 8).**

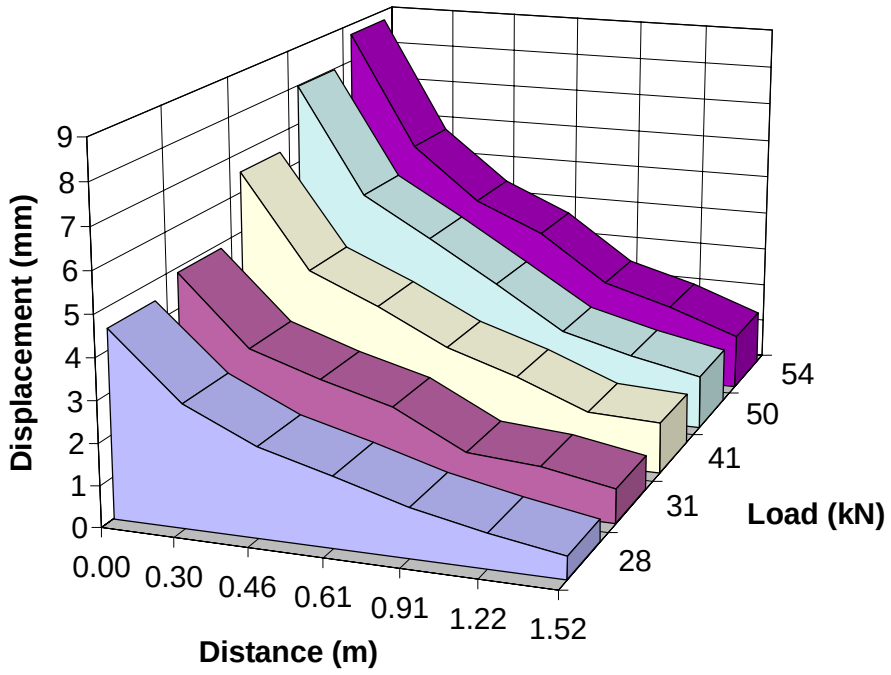


**Figure G 54 Displacement as a function of distance for different FWD load levels (January 1997, section 9).**

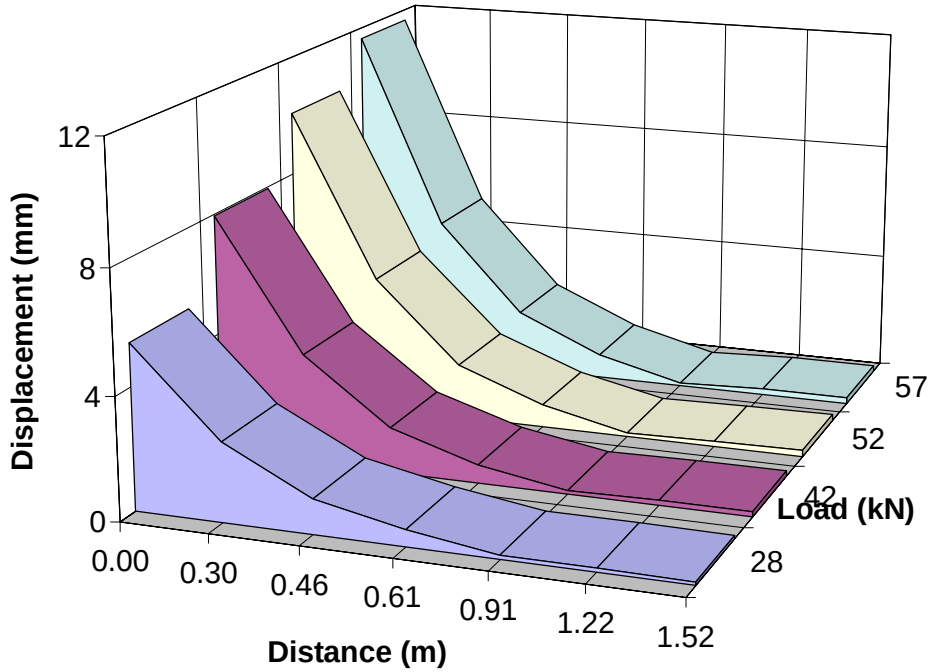


**Figure G 55 Displacement as a function of distance for different FWD load levels (April 1997, section 1).**

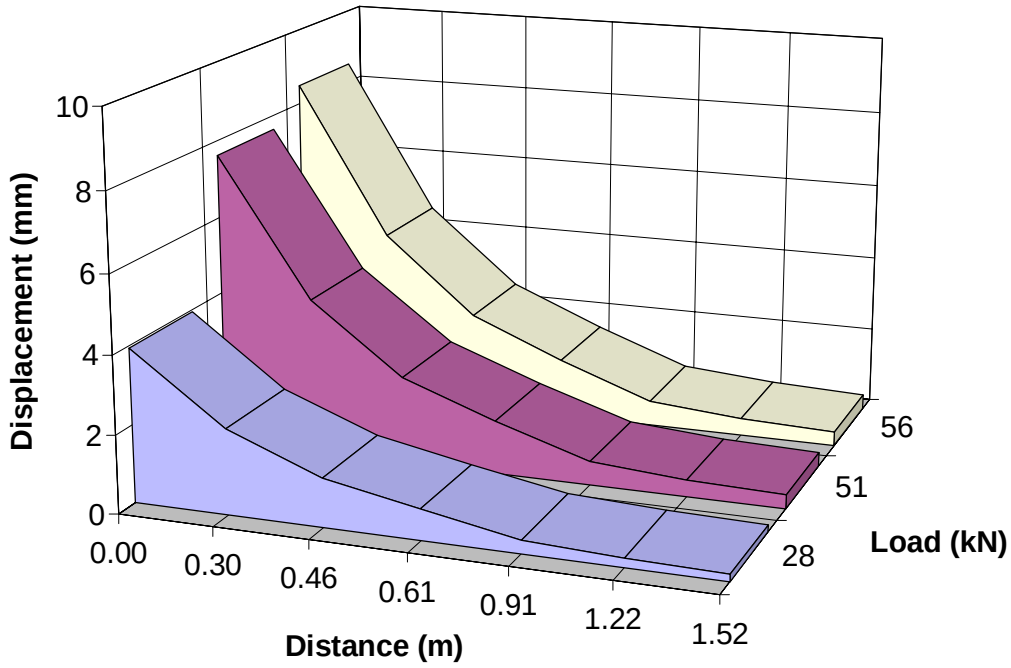


**Figure G 56 Displacement as a function of distance for different FWD load levels (April 1997, section 2).**

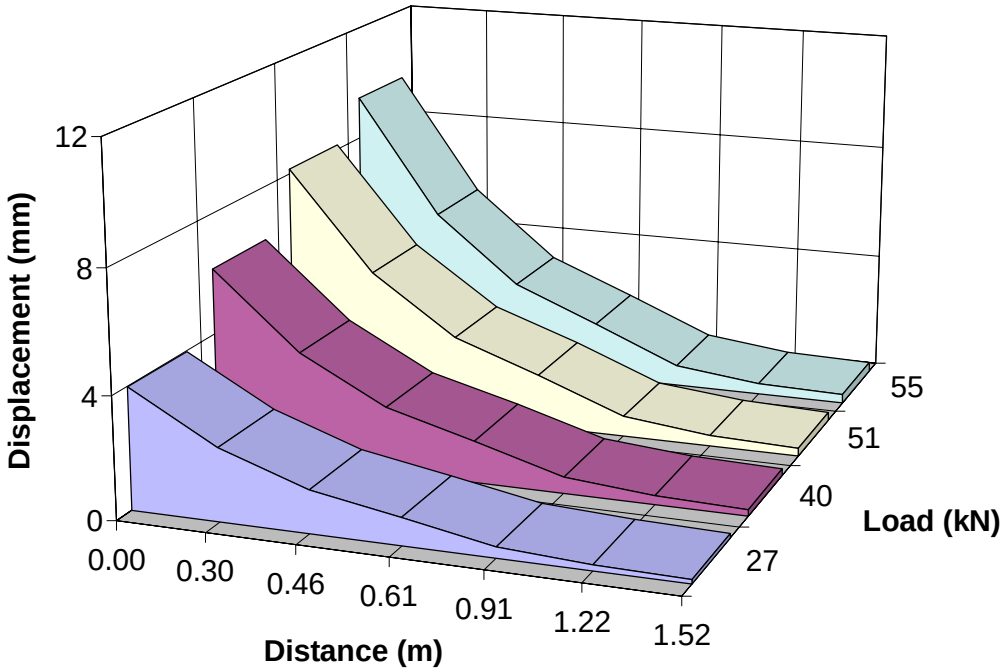


**Figure G 57 Displacement as a function of distance for different FWD load levels (April 1997, section 3).**

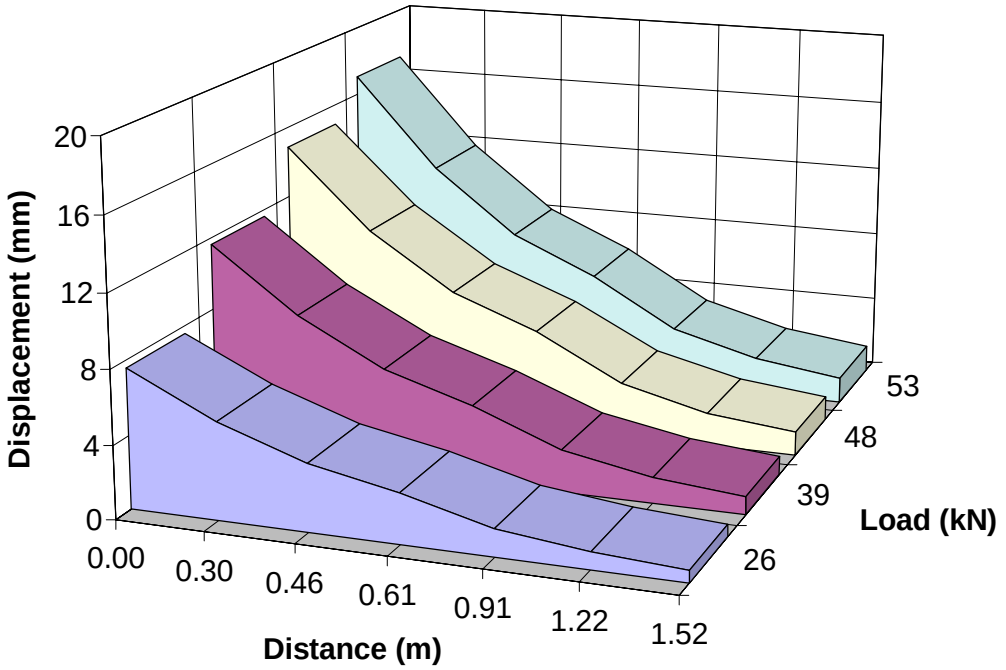


**Figure G 58 Displacement as a function of distance for different FWD load levels (April 1997, section 4).**

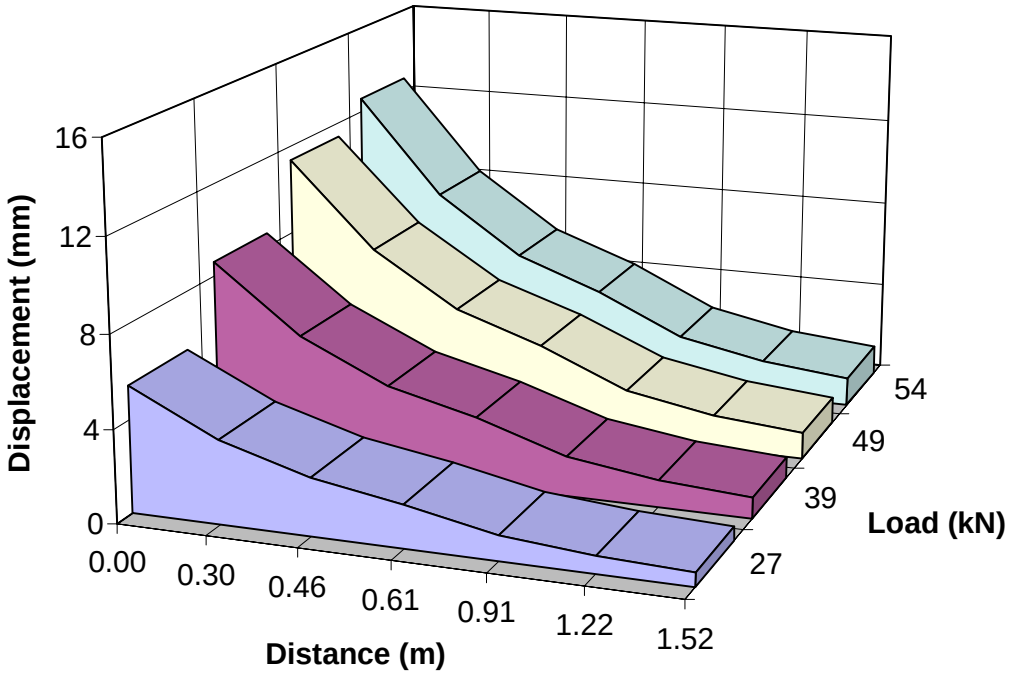


**Figure G 59 Displacement as a function of distance for different FWD load levels (April 1997, section 5).**

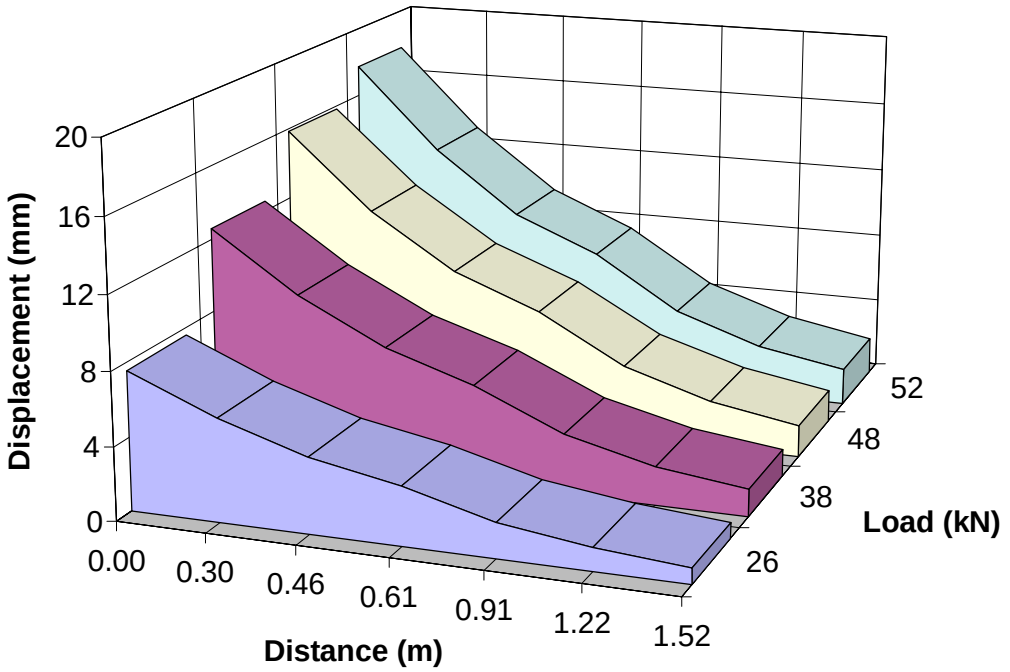


**Figure G 60 Displacement as a function of distance for different FWD load levels (April 1997, section 6).**

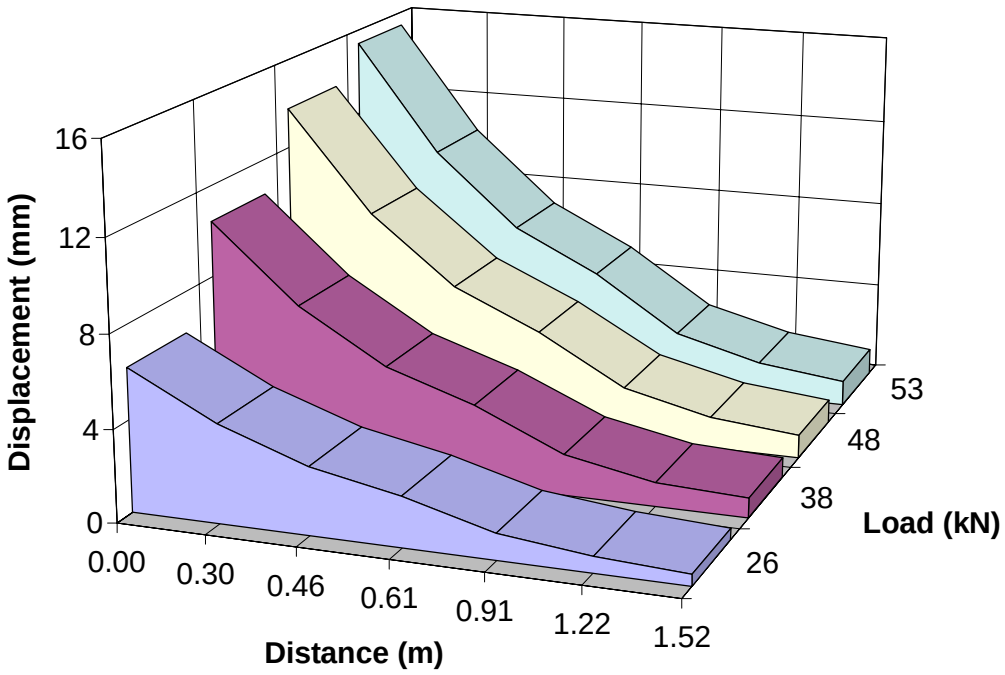


**Figure G 61 Displacement as a function of distance for different FWD load levels (April 1997, section 7).**

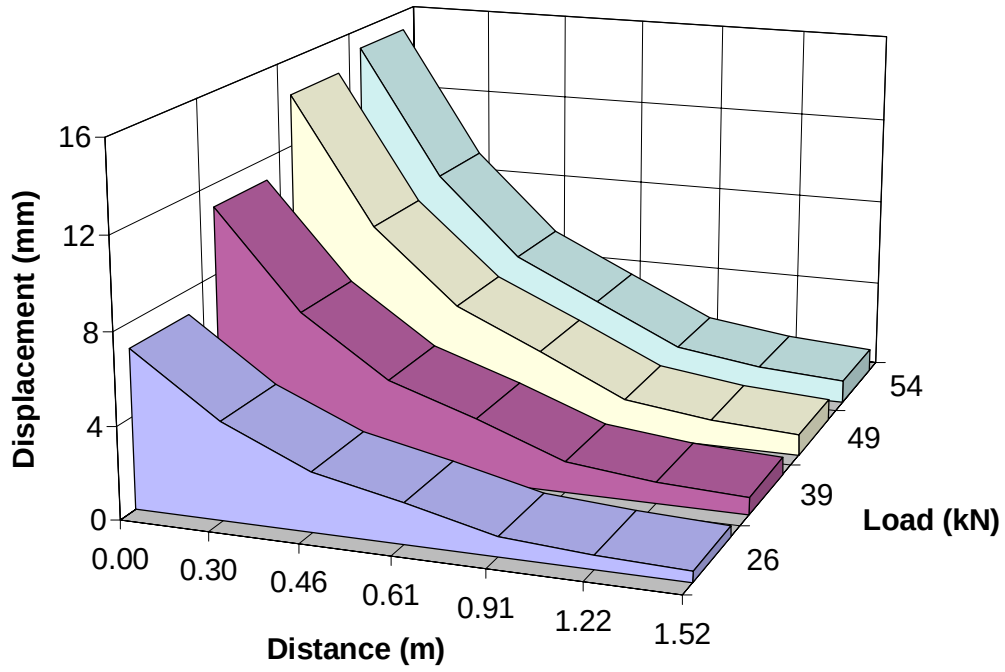


**Figure G 62 Displacement as a function of distance for different FWD load levels (April 1997, section 8).**

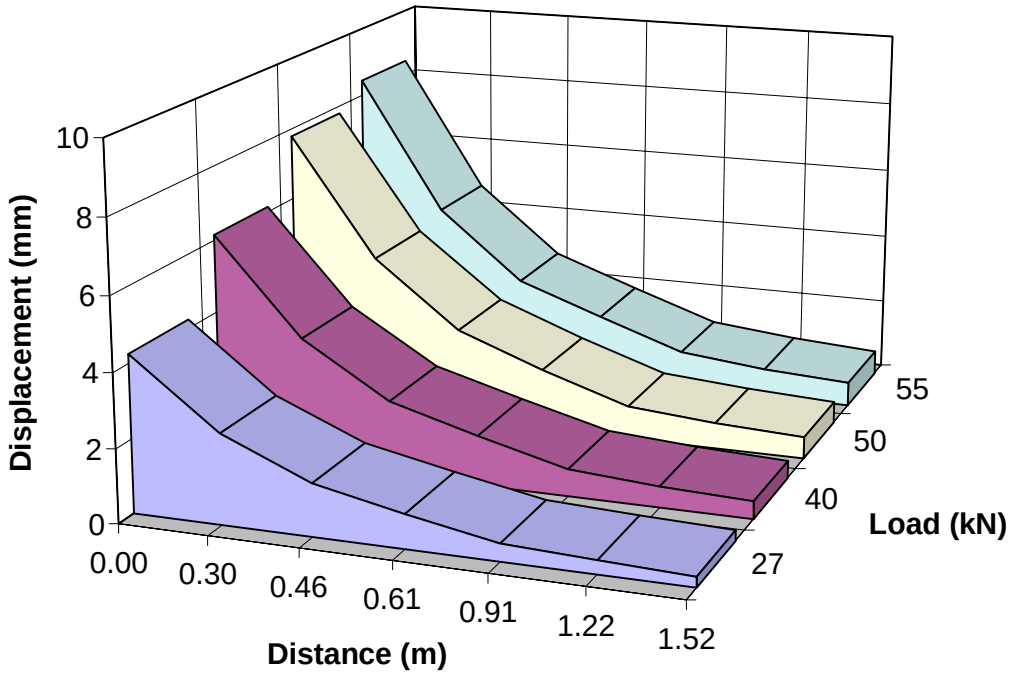


**Figure G 63 Displacement as a function of distance for different FWD load levels (April 1997, section 9).**

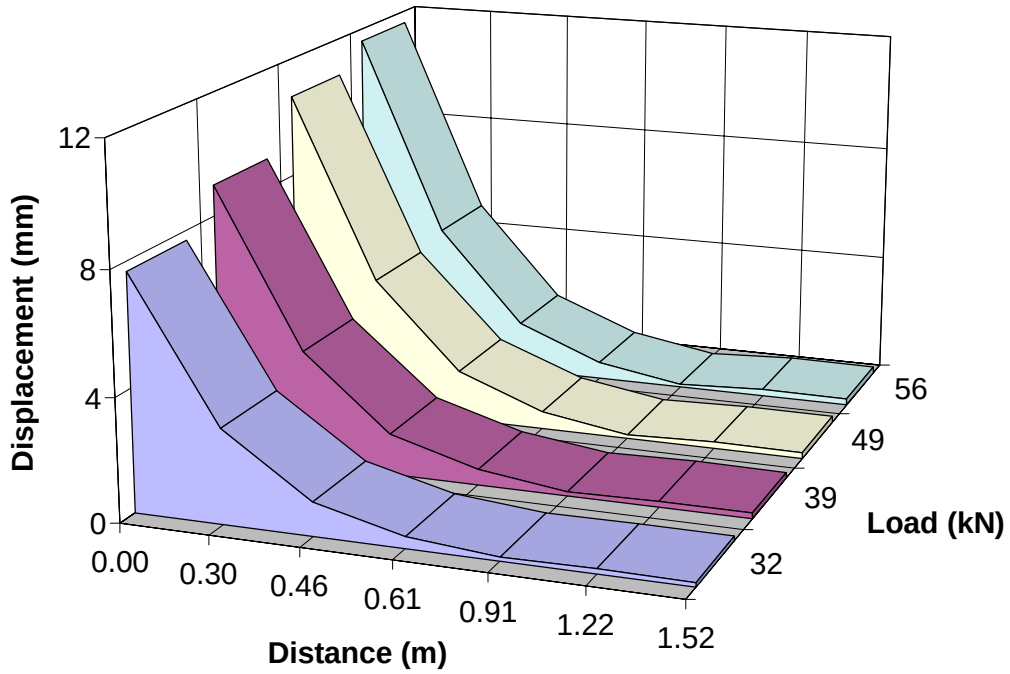


**Figure G 64 Displacement as a function of distance for different FWD load levels (July 1997, section 1).**

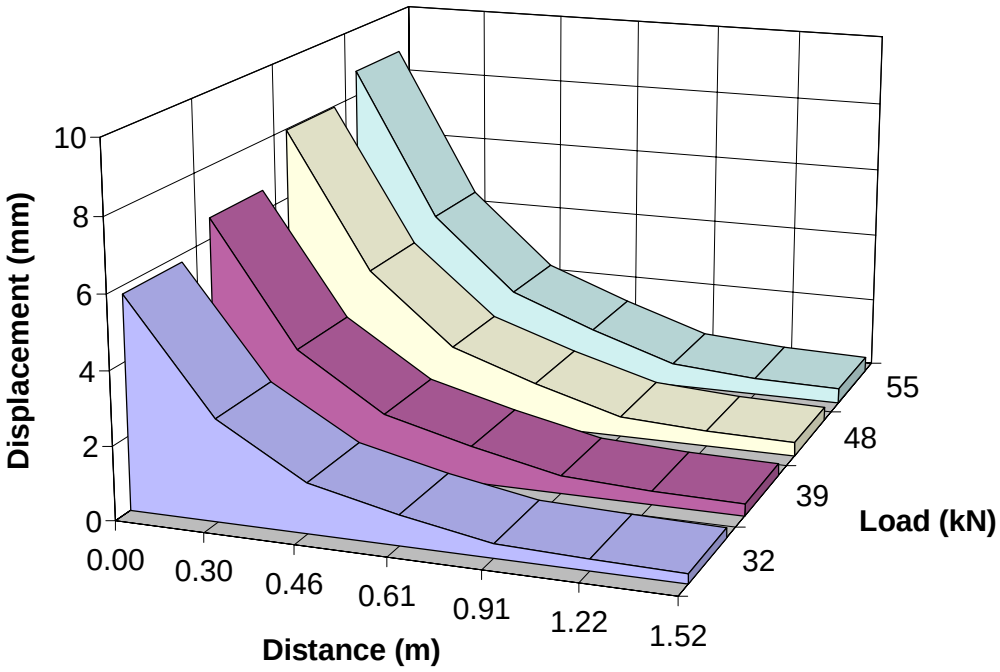


**Figure G 65 Displacement as a function of distance for different FWD load levels (July 1997, section 2).**

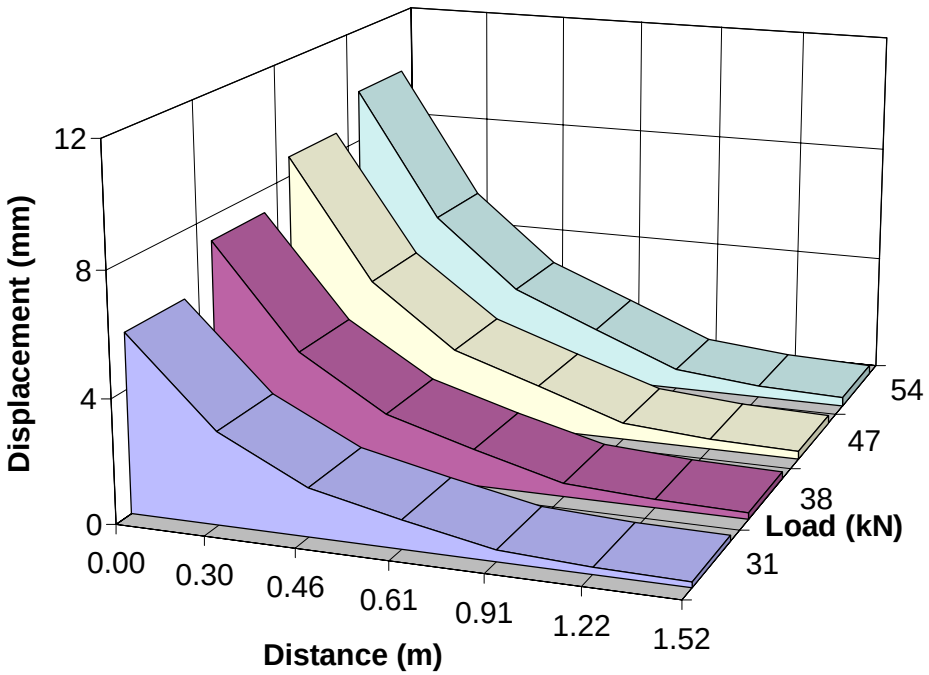


**Figure G 66 Displacement as a function of distance for different FWD load levels (July 1997, section 3).**

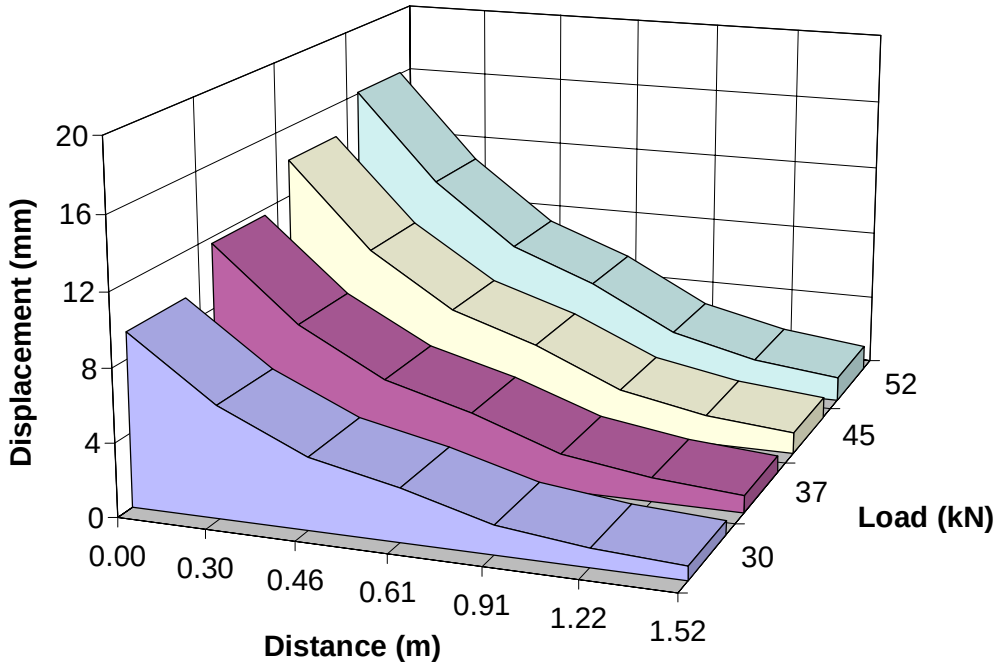


**Figure G 67 Displacement as a function of distance for different FWD load levels (July 1997, section 4).**

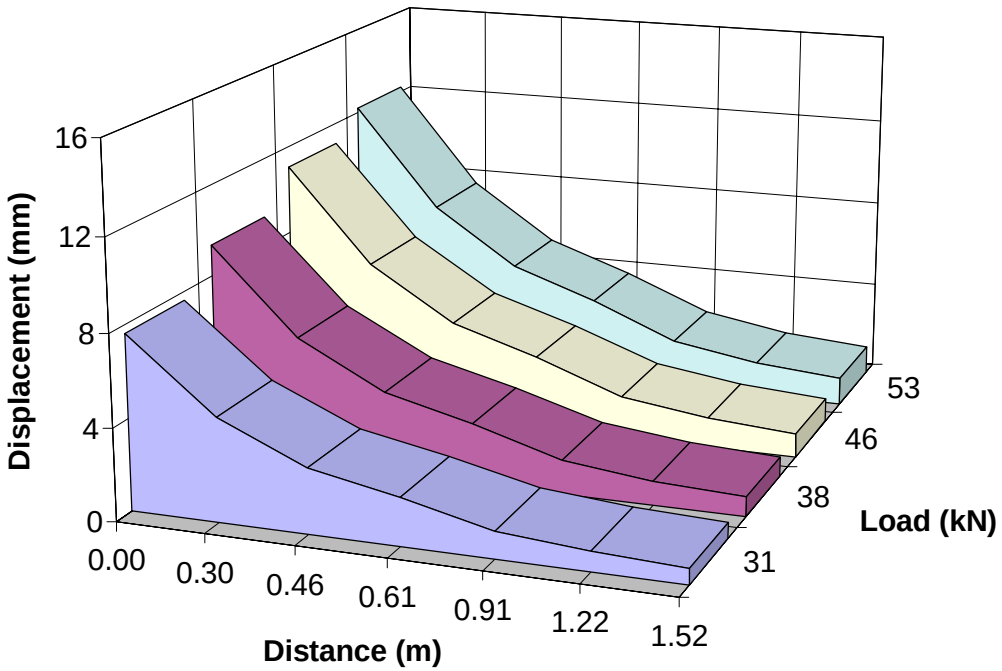


**Figure G 68 Displacement as a function of distance for different FWD load levels (July 1997, section 5).**

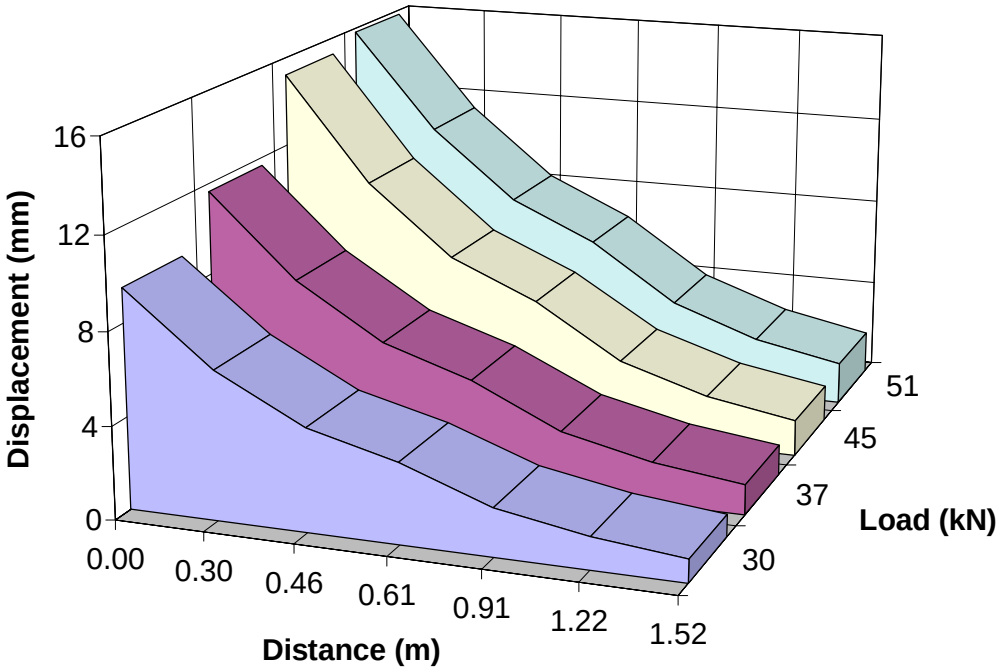


**Figure G 69 Displacement as a function of distance for different FWD load levels (July 1997, section 6).**

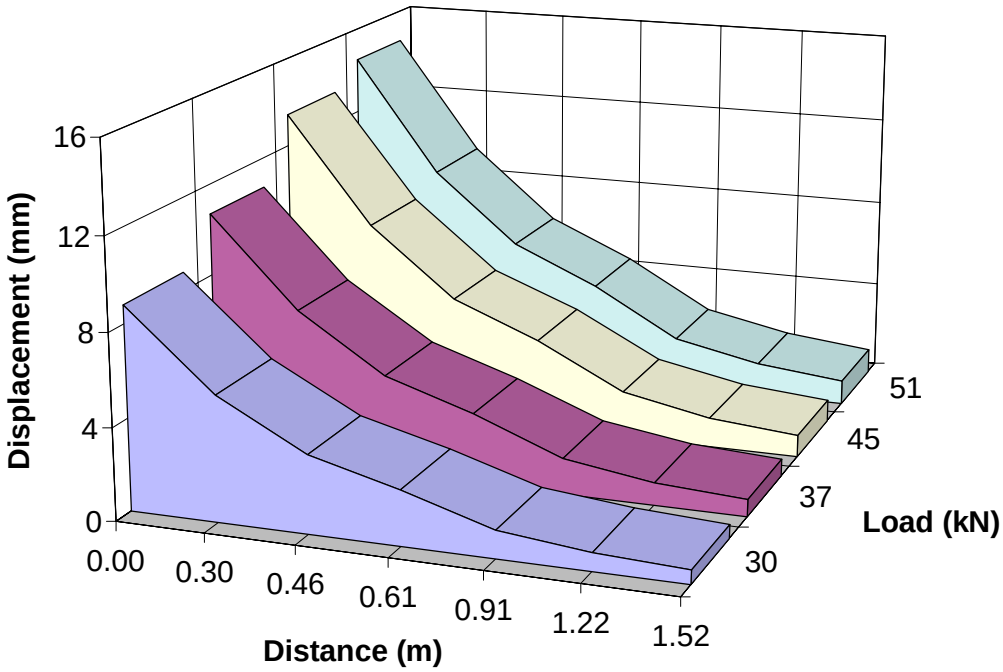


**Figure G 70 Displacement as a function of distance for different FWD load levels (July 1997, section 7).**

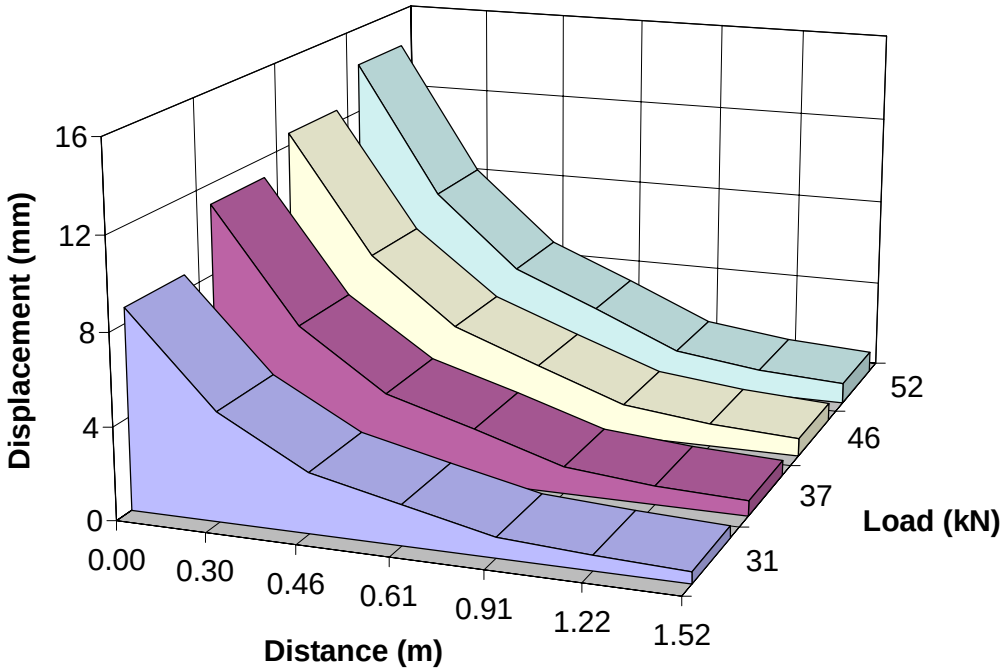


**Figure G 71 Displacement as a function of distance for different FWD load levels (July 1997, section 8).**

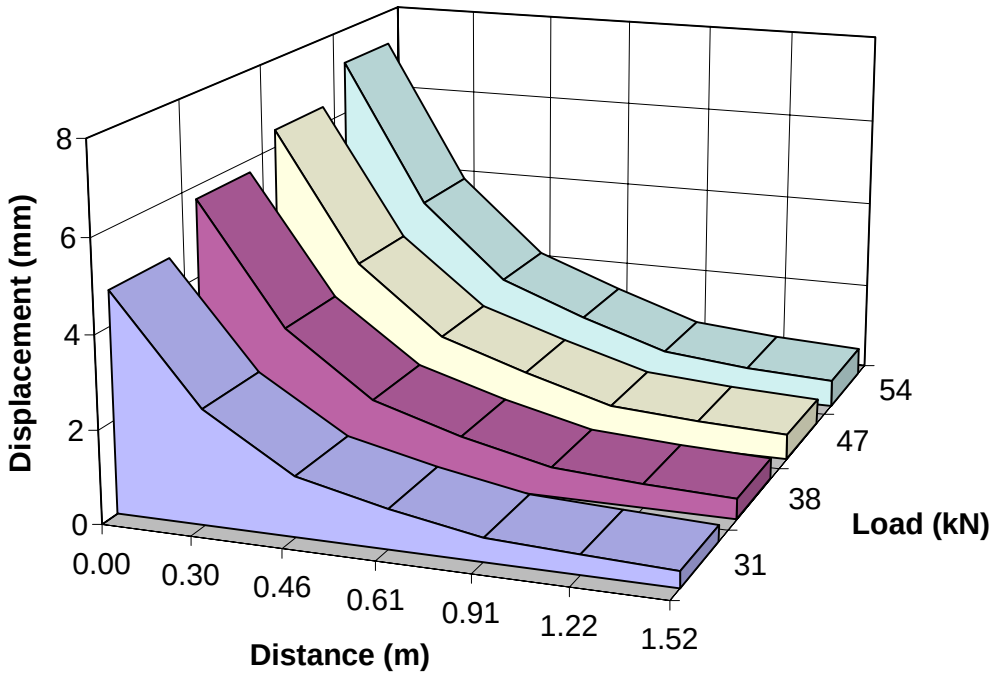


**Figure G 72 Displacement as a function of distance for different FWD load levels (July 1997, section 9).**

# APPENDIX H

# GROUND PENETRATION RADAR

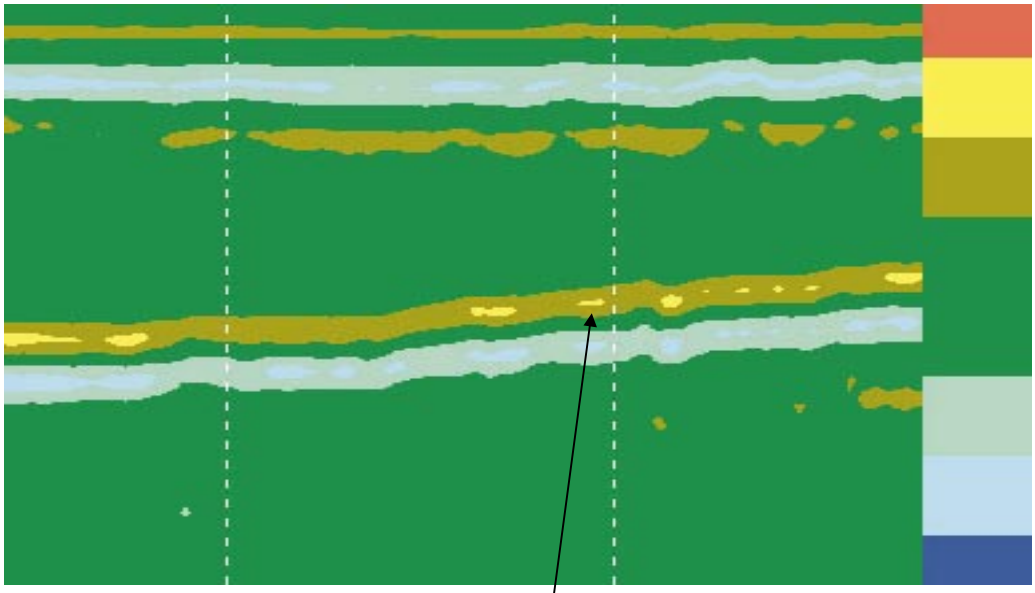


**Figure H 1  GPR scans over section 4 (June 1997).**

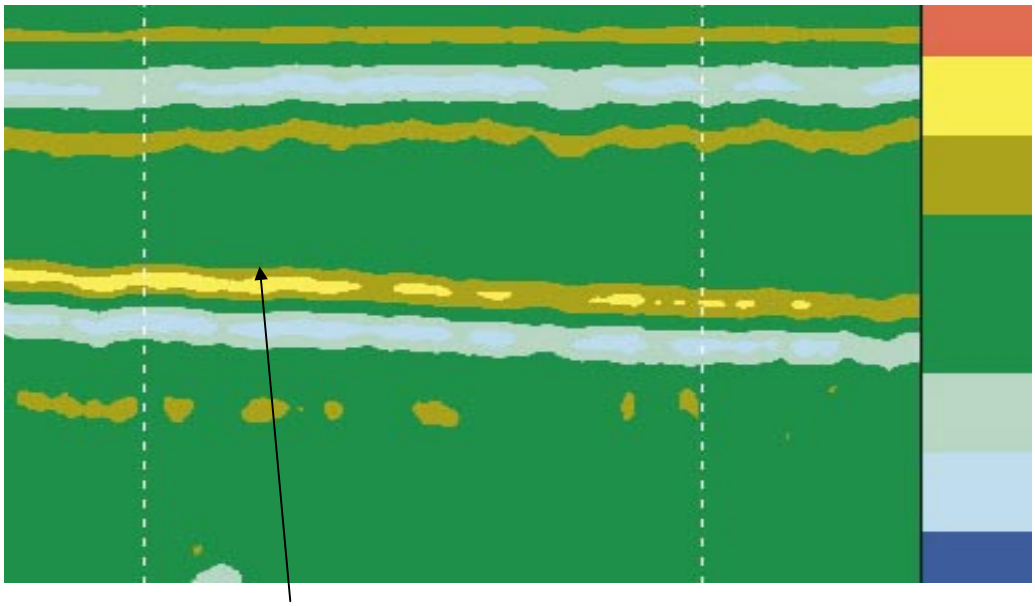


**Figure H 2  GPR scans over section 5 (June 1997).**

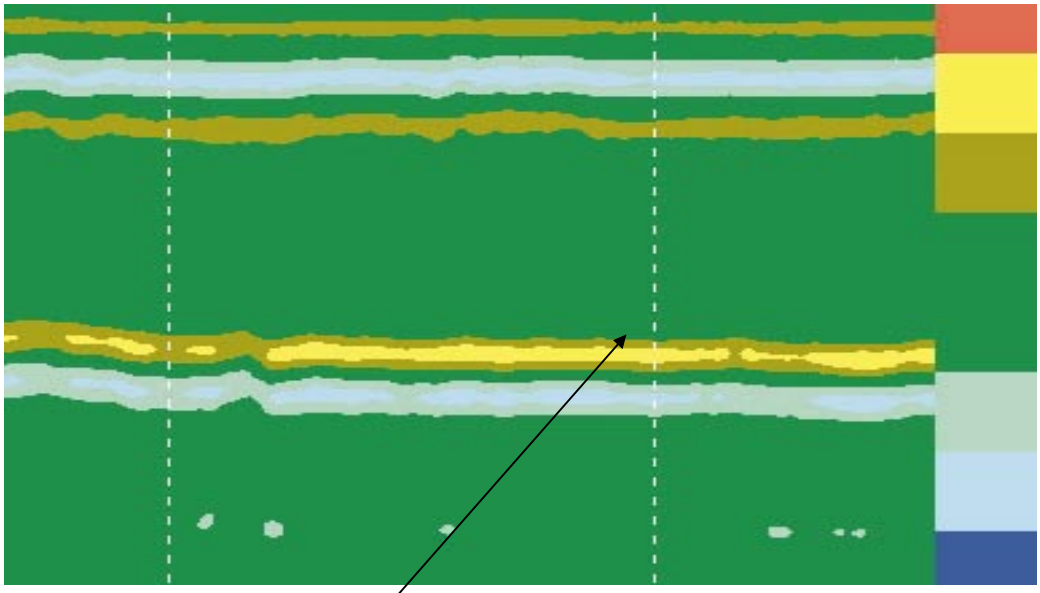


**Figure H 3  GPR scans over section 6 (June 1997).**

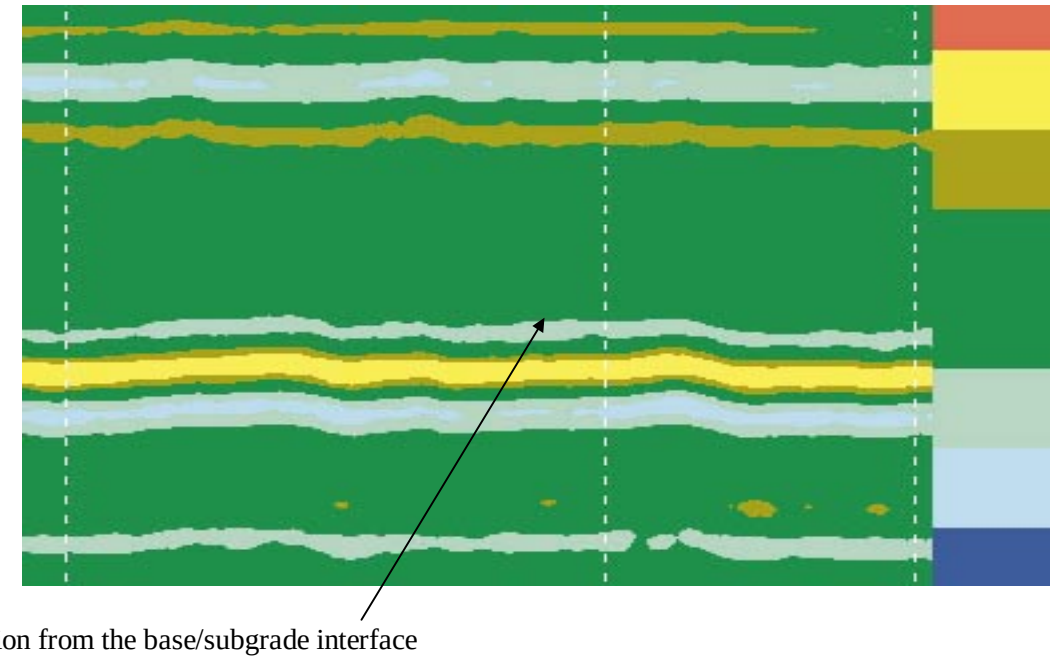


**Figure H 4  GPR scans over section 7 (June 1997).**

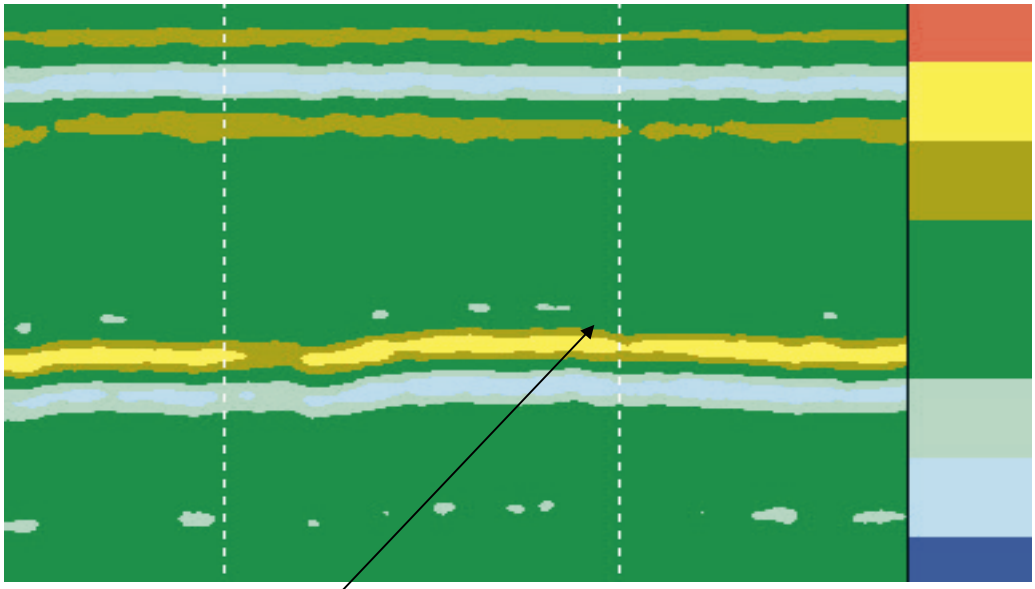

Reflection from the base/subgrade interface

**Figure H 5  GPR scans over section 8 (June 1997).**

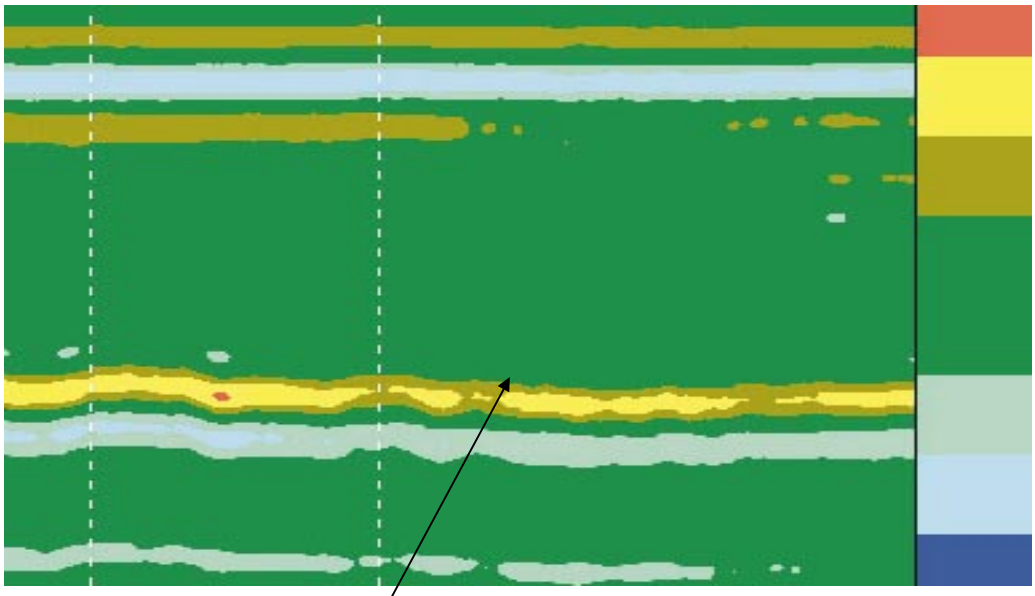

Reflection from the base/subgrade interface

**Figure H 6  GPR scans over section 9 (June 1997).**

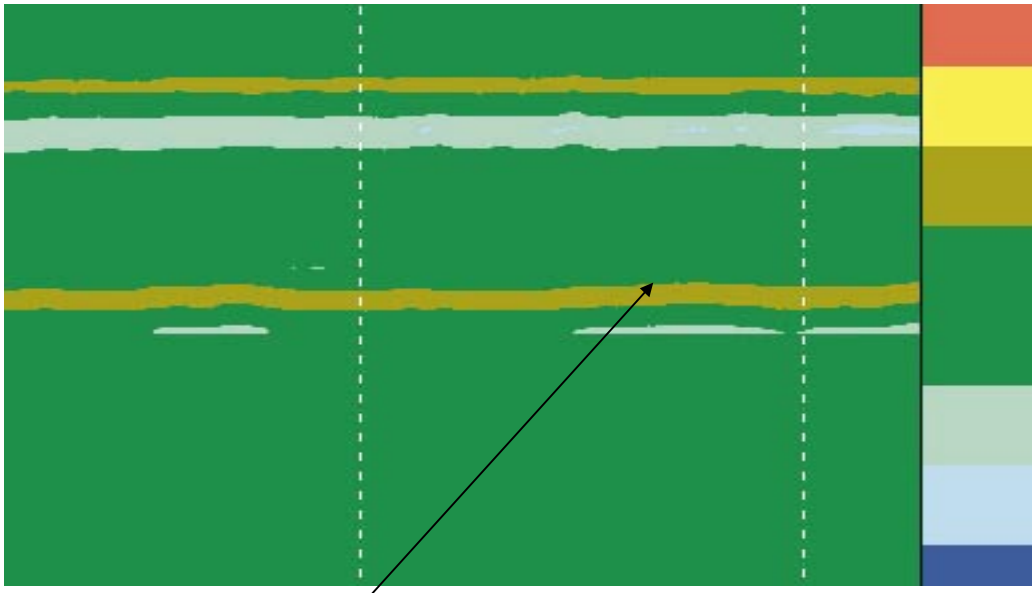

Reflection from the base/subgrade interface

**Figure H 7  GPR scans over section 1 (August 1996).**

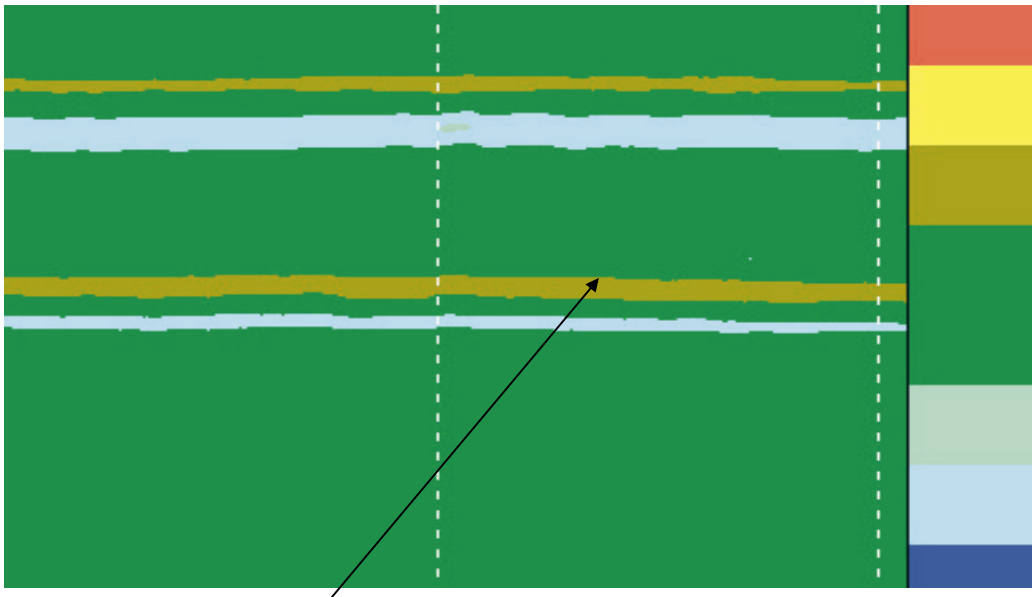

Reflection from the base/subgrade interface

**Figure H 8  GPR scans over section 2 (August 1996).**

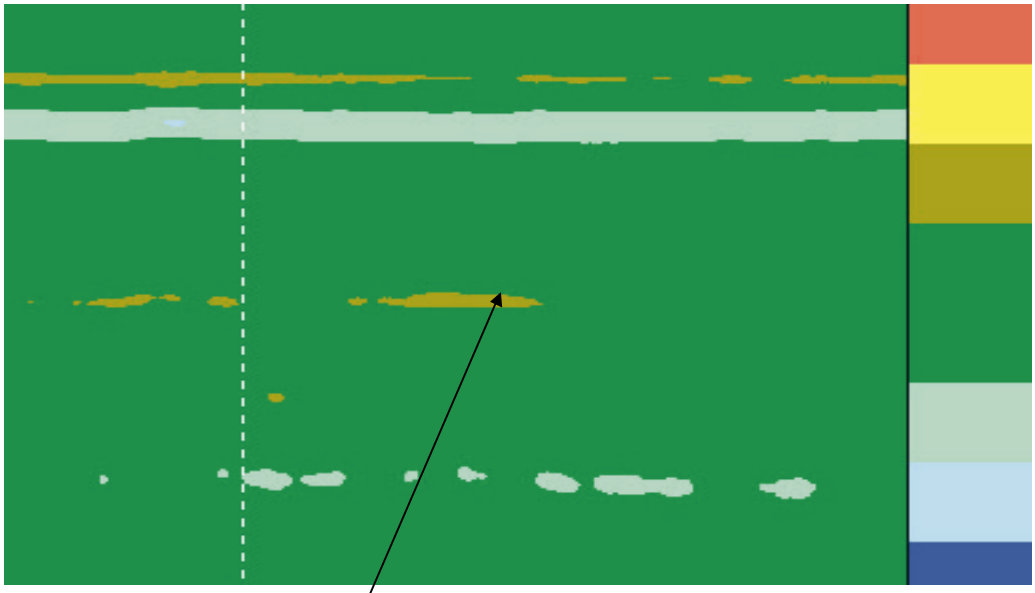

Reflection from the base/subgrade interface

**Figure H 9  GPR scans over section 3 (August 1996).**

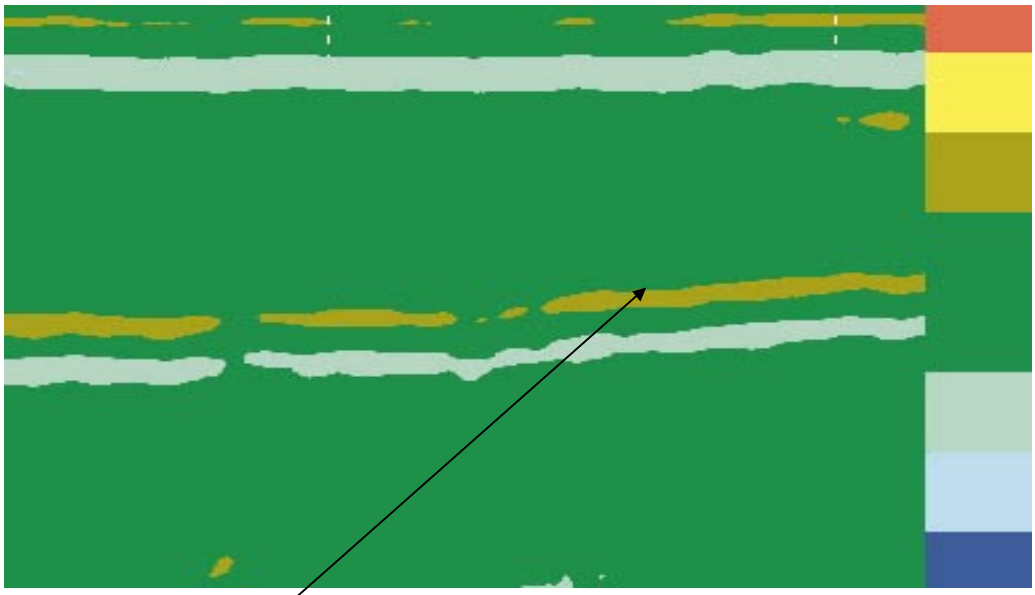

Reflection from the base/subgrade interface

**Figure H 10  GPR scans over section 4 (August 1996).**

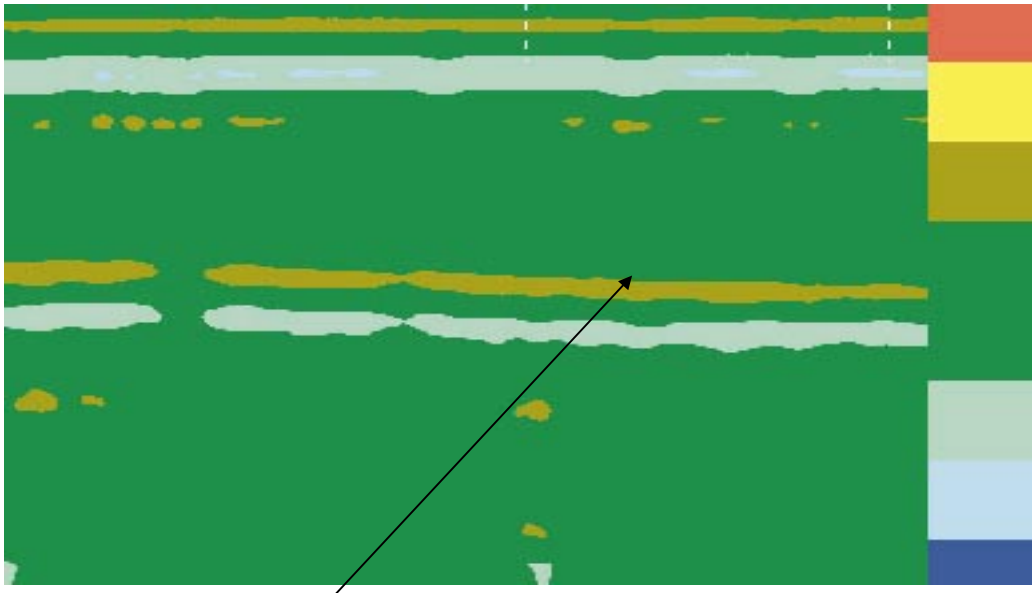

Reflection from the base/subgrade interface

**Figure H 11  GPR scans over section 5 (August 1996).**

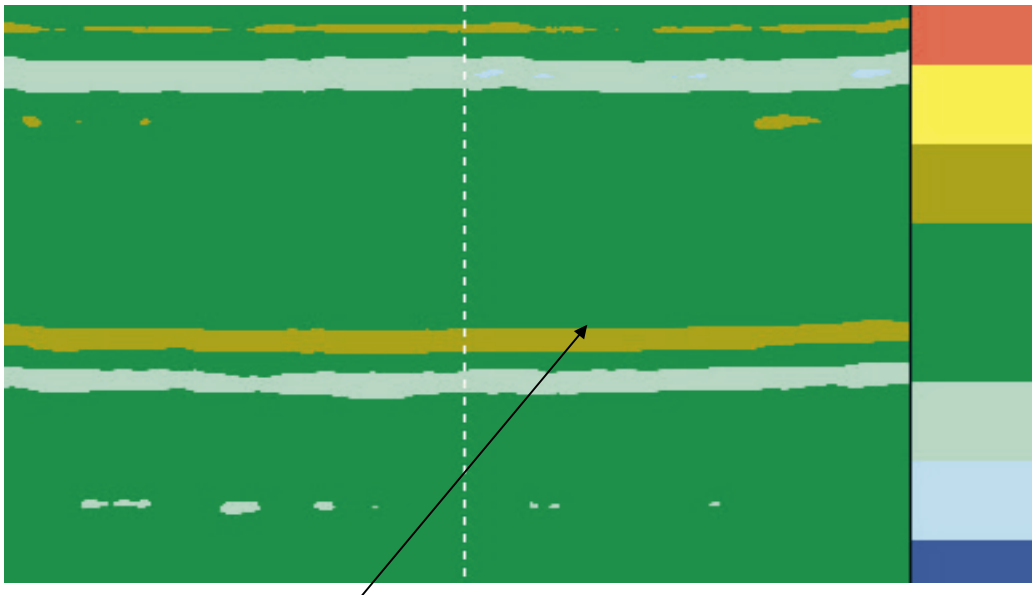

Reflection from the base/subgrade interface

**Figure H 12  GPR scans over section 6 (August 1996).**

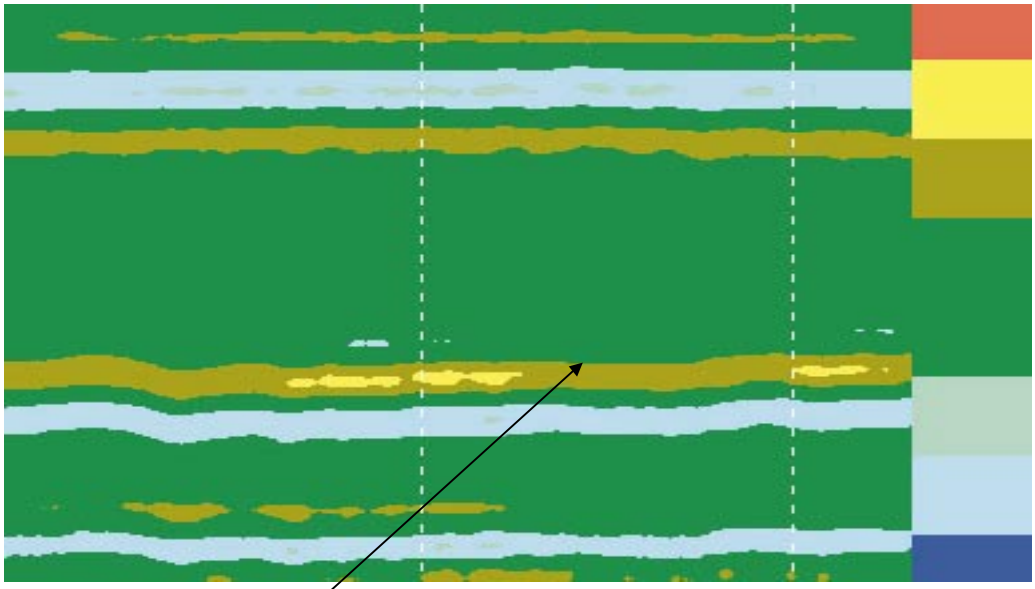

Reflection from the base/subgrade interface

**Figure H 13  GPR scans over section 7 (August 1996).**

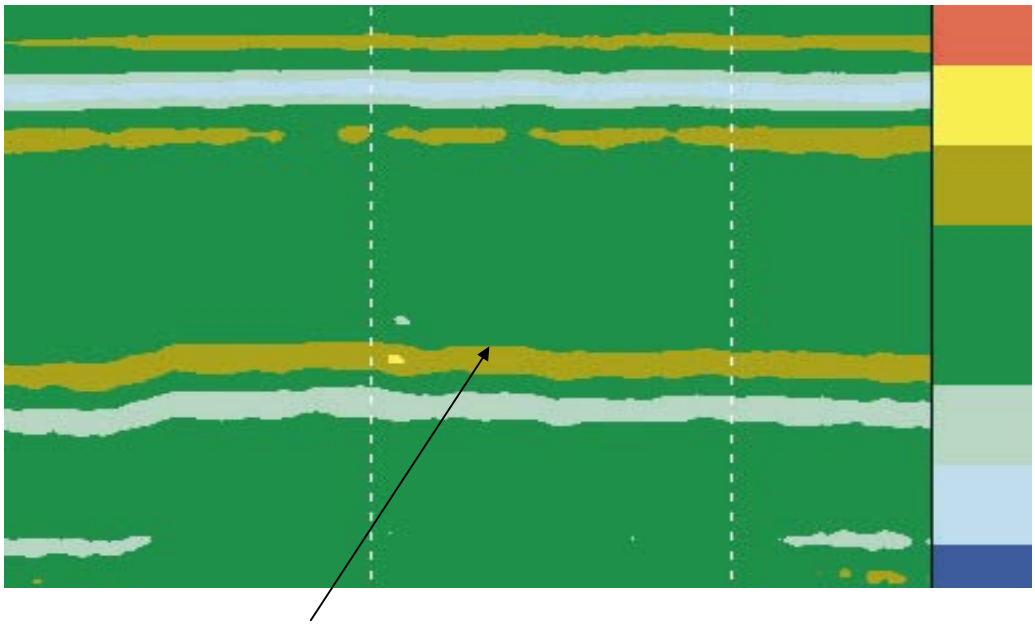

Reflection from the base/subgrade interface

**Figure H 14  GPR scans over section 8 (August 1996).**

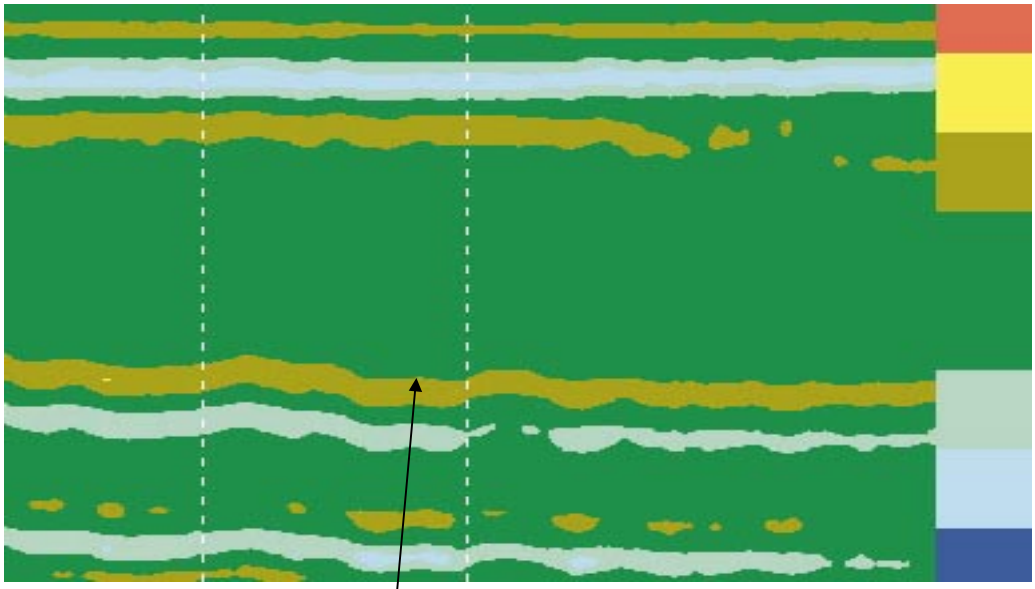


**Figure H 15  GPR scans over section 9 (August 1996).**

# APPENDIX I

# CALIBRATION DATA

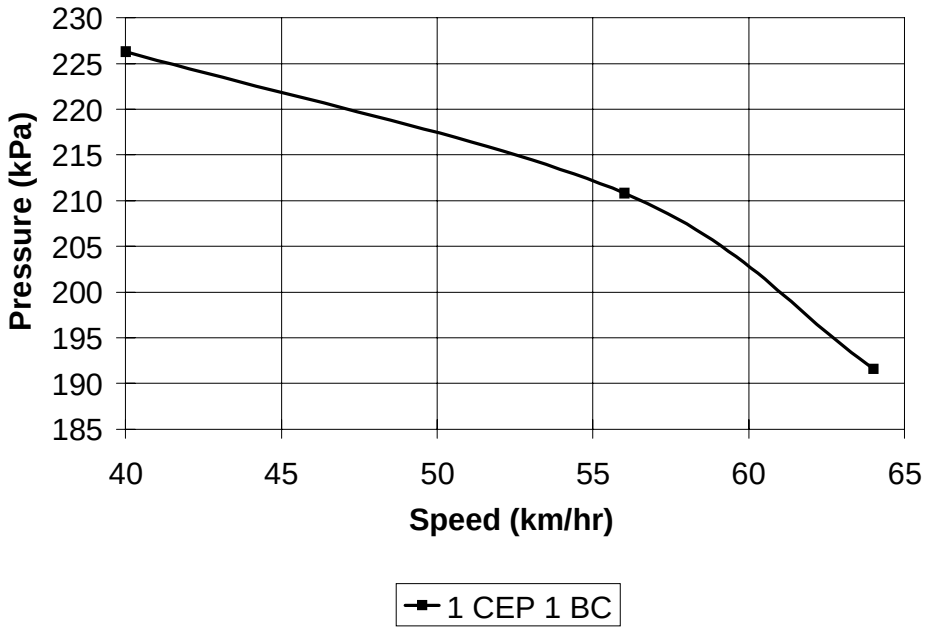


**Figure I 1 Base course pressure cell response, section 9 (80 kN axle load).**

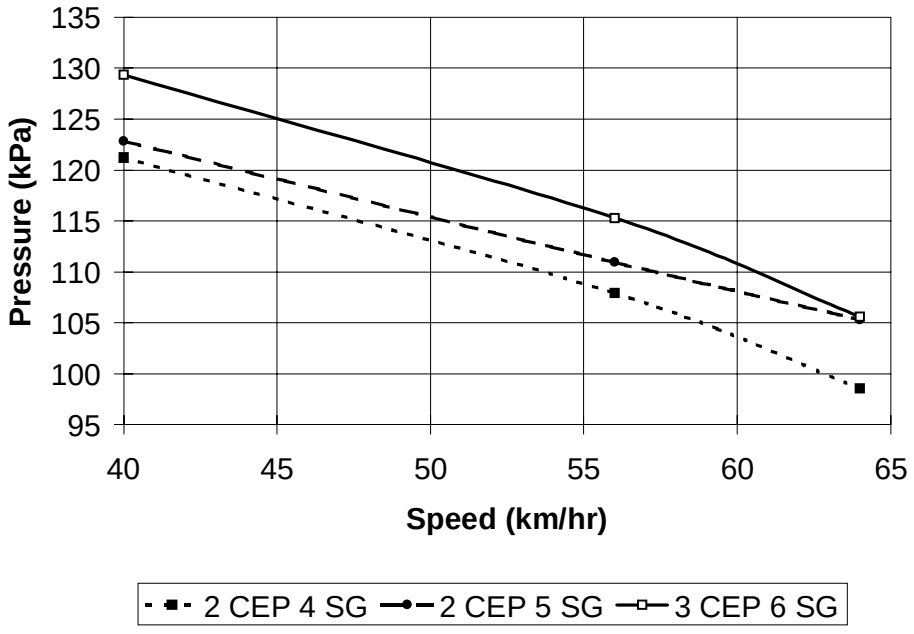


**Figure I 2 Subgrade pressure cell response, sections 2 and 3 (80 kN axle load).**

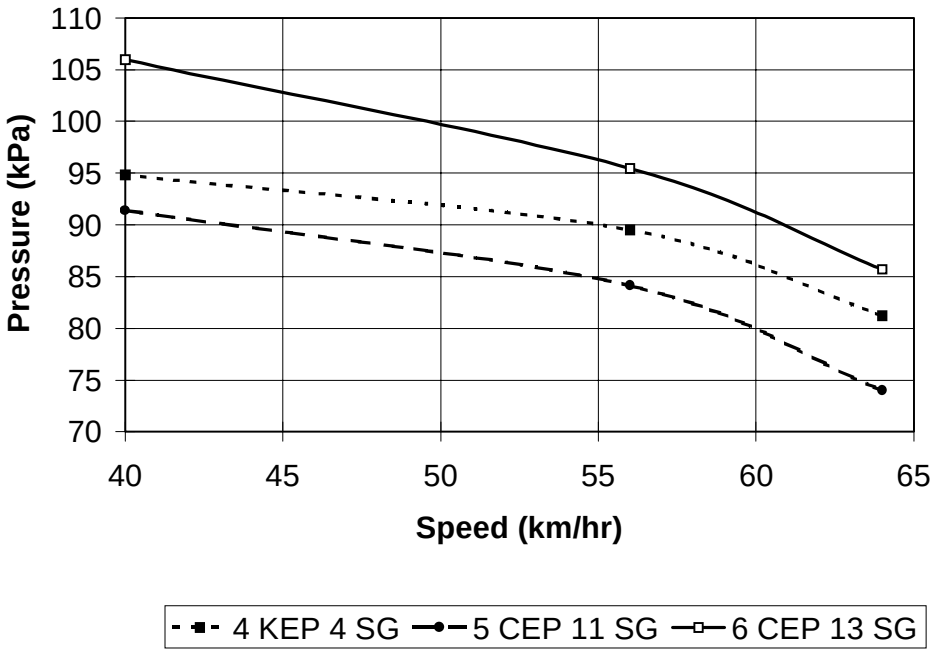


**Figure I 3 Subgrade pressure cell response, sections 4, 5, and 6 (80 kN axle load).**

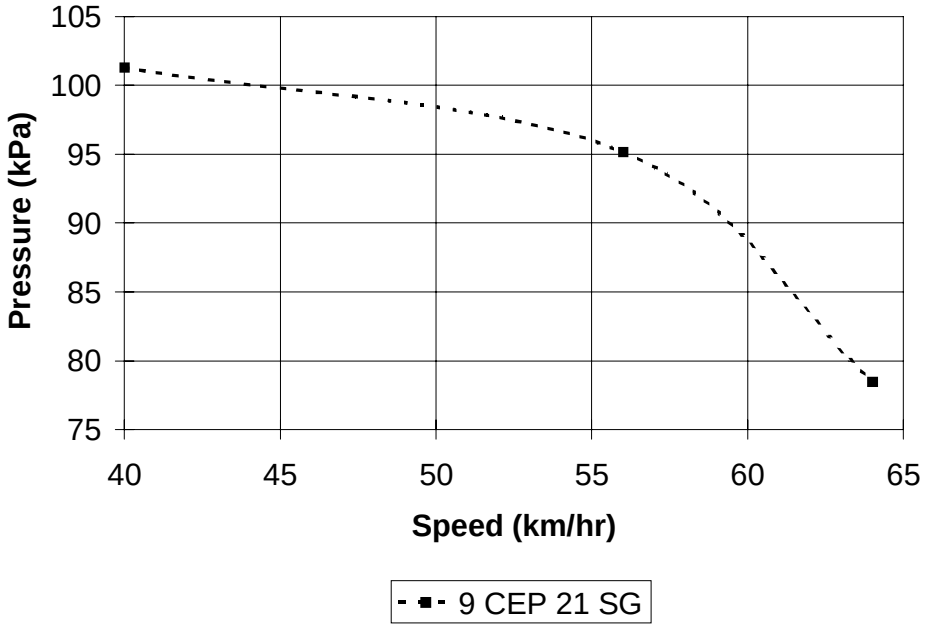


**Figure I 4 Subgrade pressure cell response, section 9 (80 kN axle load).**

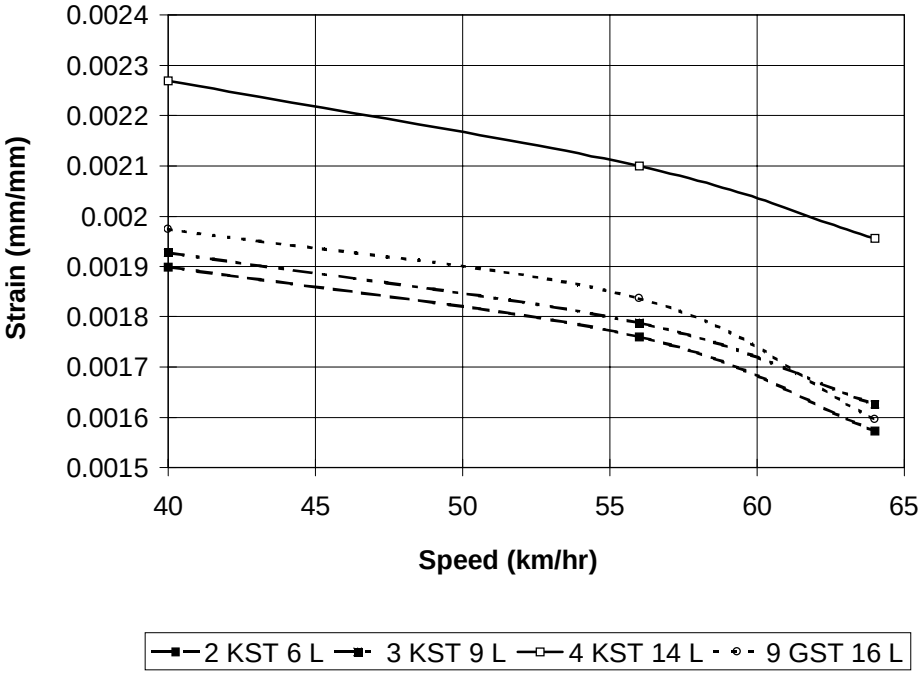


**Figure I 5 HMA strain gage response, section 2, 3, 4 and 9 (long direction, 80 kN axle load).**

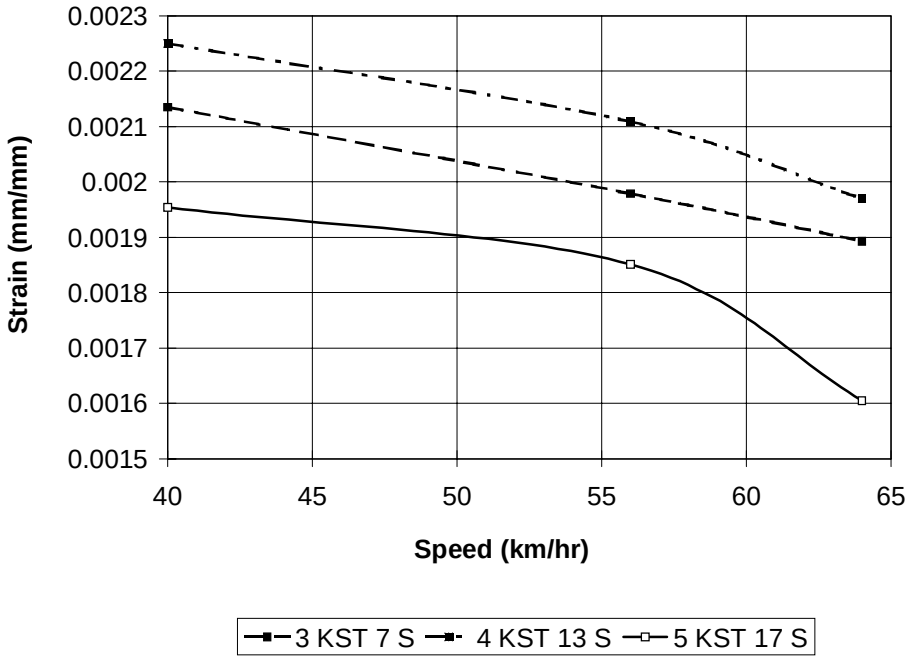


**Figure I 6 HMA strain gage response, section 3, 4, and 5 (short direction, 80 kN axle load).**

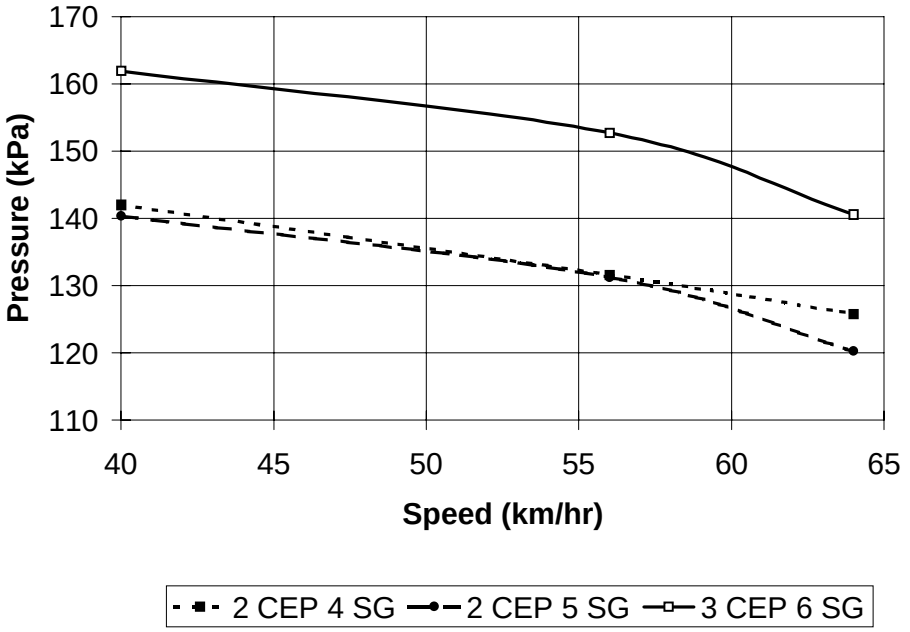


**Figure I 7 Subgrade pressure cell response, sections 2 and 3 (102 kN axle load).**

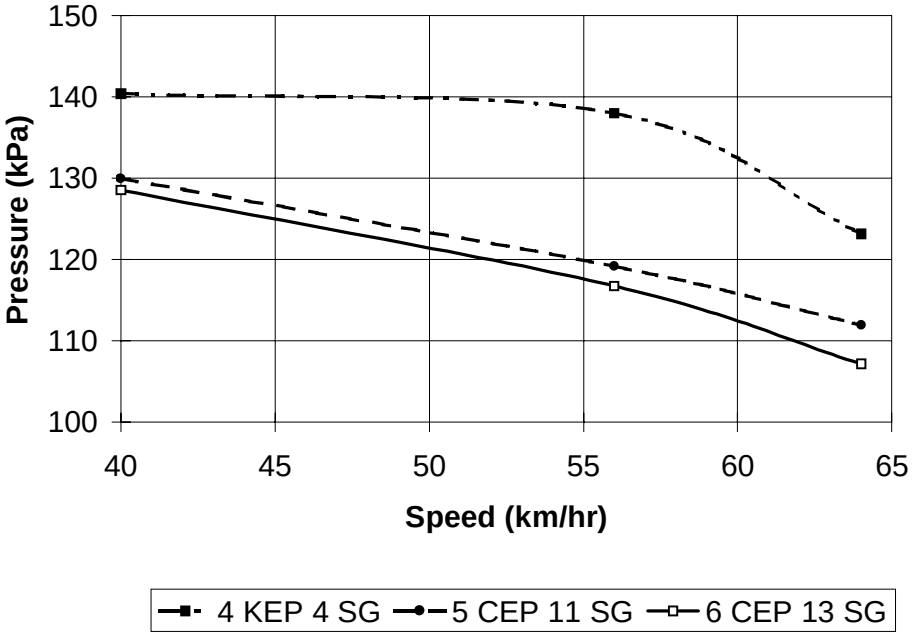


**Figure I 8 Subgrade pressure cell response, sections 4, 5, and 6 (102 kN axle load).**

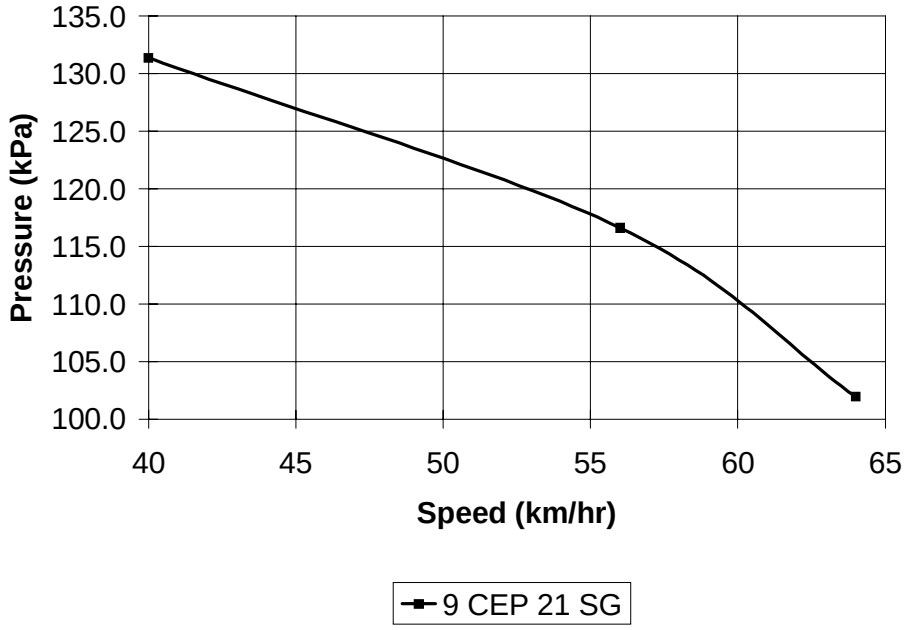


**Figure I 9 Subgrade pressure cell response, section 9 (102 kN axle load).**

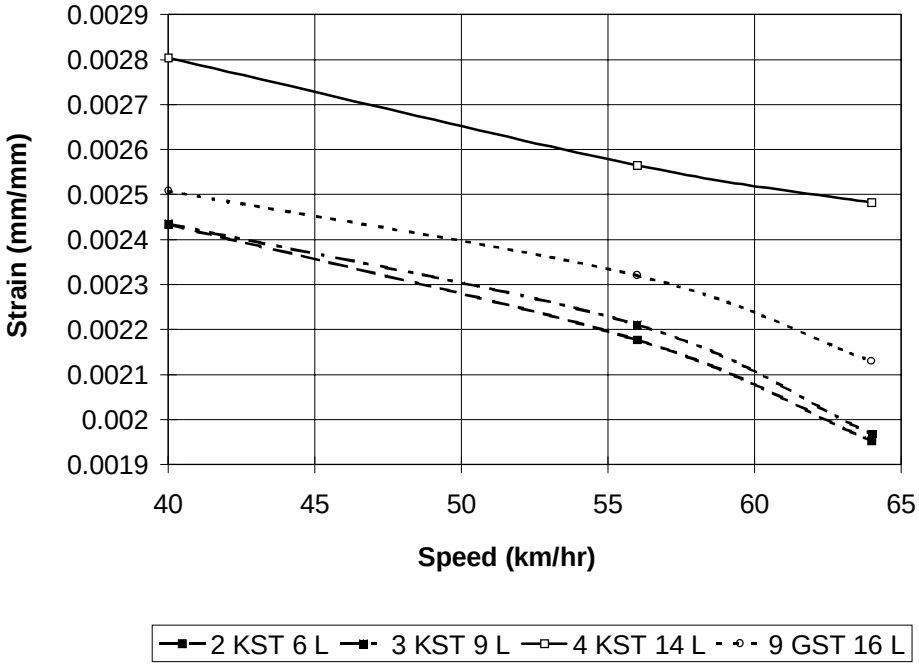


**Figure I 10 HMA strain gage response, sections 2, 3, 4 and 9 (long direction,102 kN axle load).**

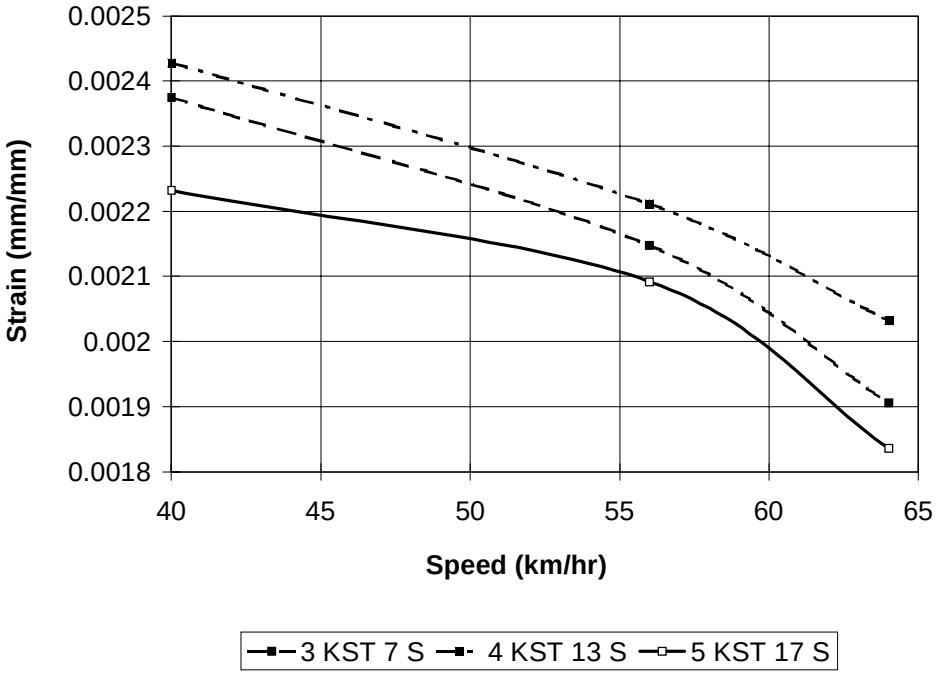


**Figure I 11 HMA strain gage response, sections 3, 4, and 5 (short direction, 102 kN axle load).**

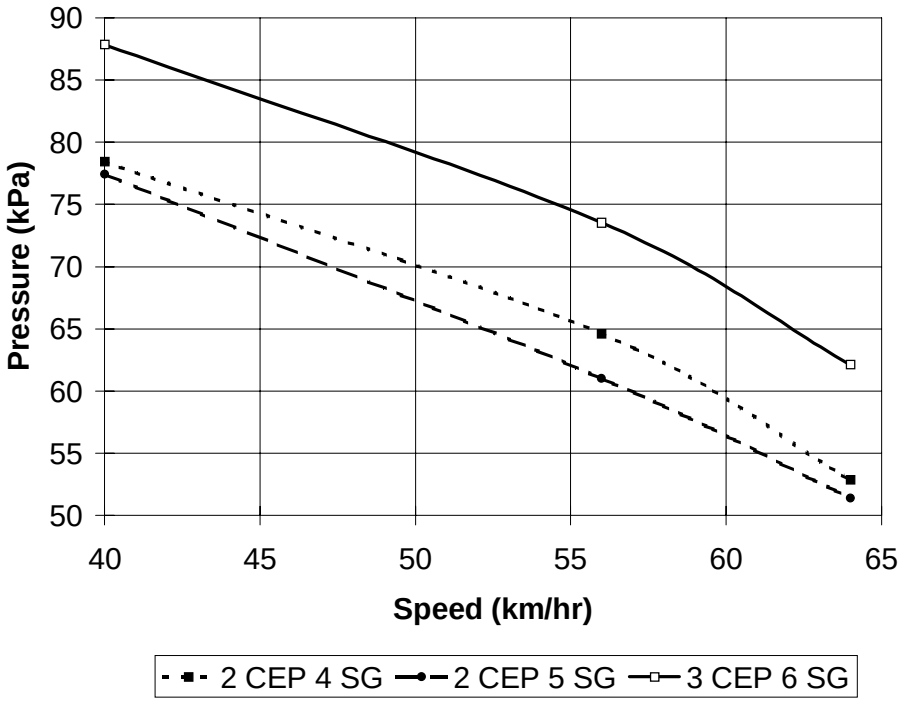


**Figure I 12 Subgrade pressure cell response, sections 2, and 3 (53 kN axle load).**

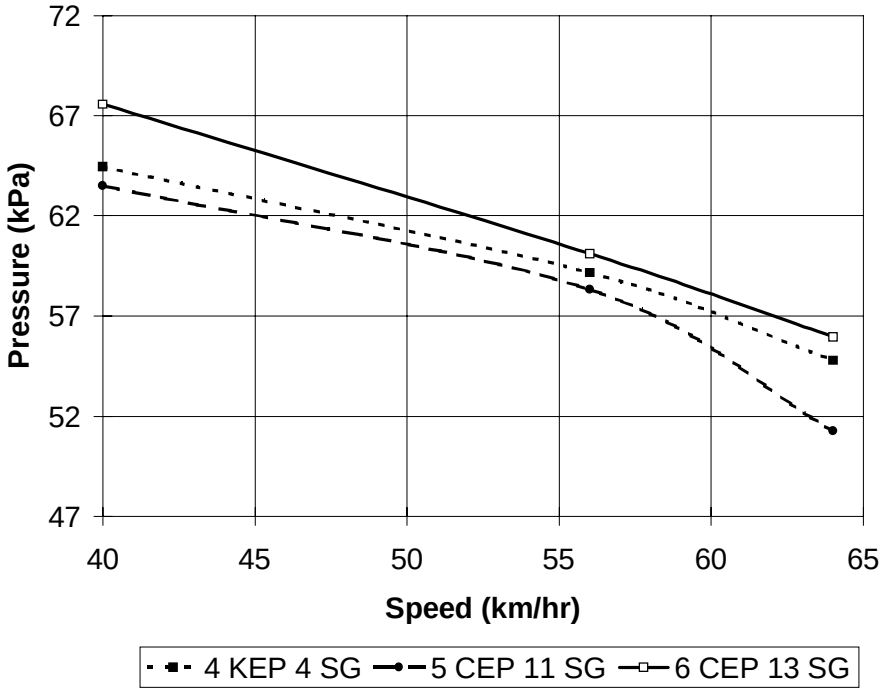


**Figure I 13 Subgrade pressure cell response, sections 4, 5, and 6 (53 kN axle load).**

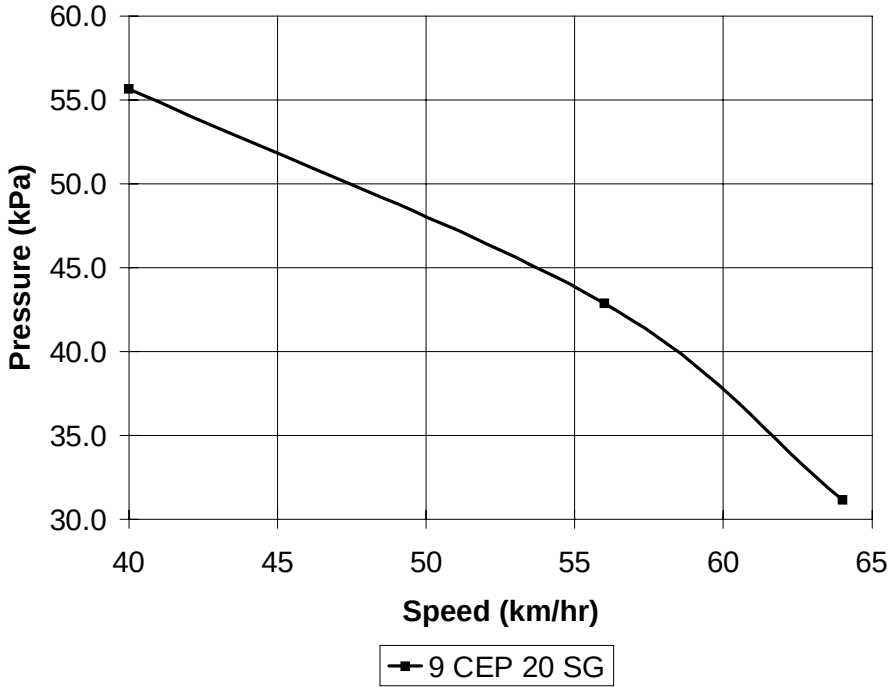


**Figure I 14 Subgrade pressure cell response, sections 4, 5, and 6 (53 kN axle load).**

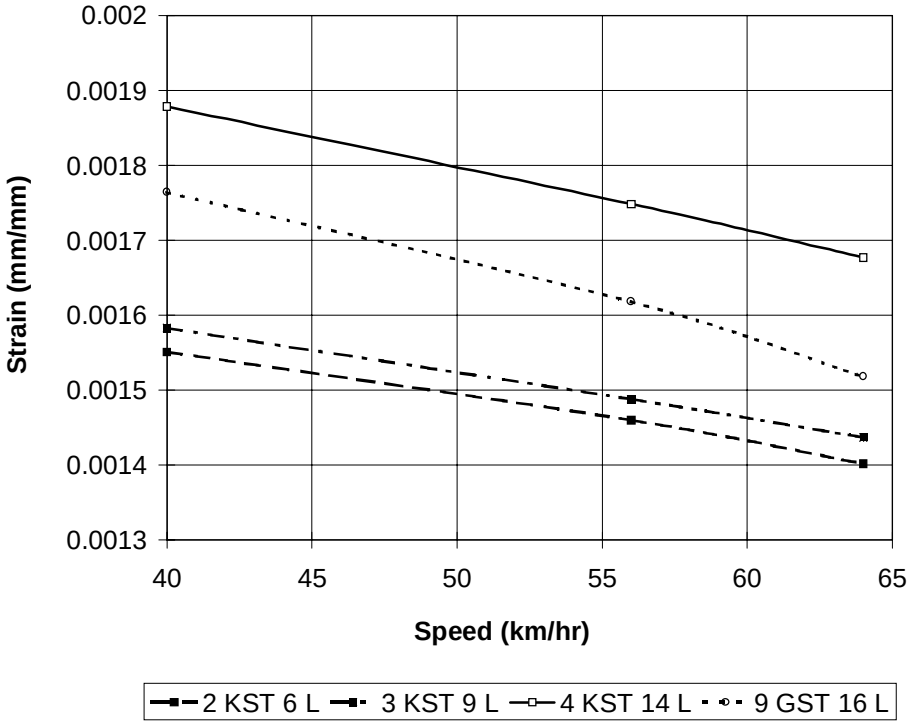


**Figure I 15 HMA strain gage response, sections 2, 3, 4 and 9 (long direction, 53 kN axle load).**

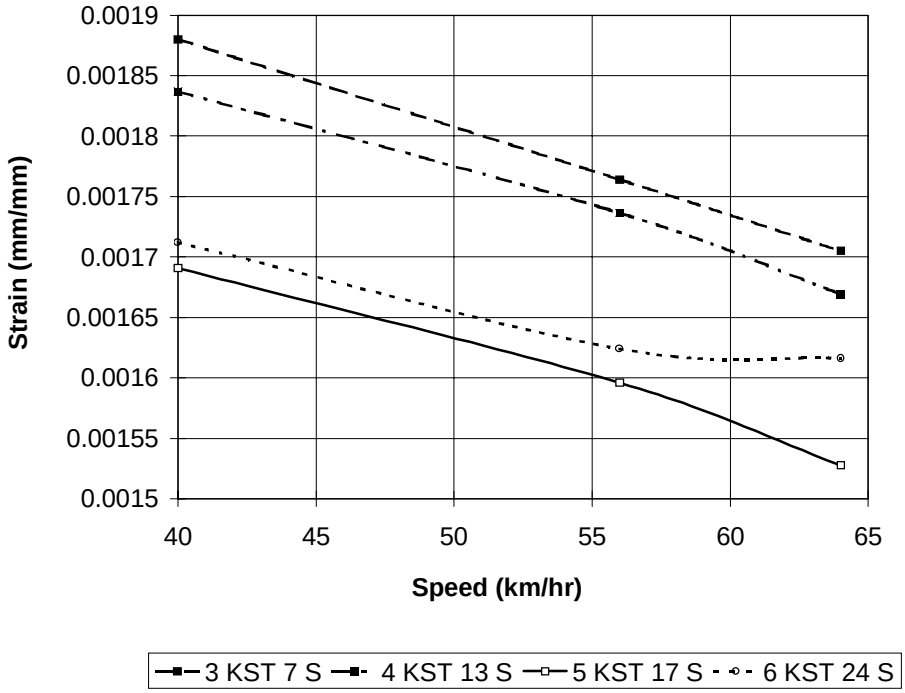


**Figure I 16 HMA strain gage response, sections 3, 4, 5 and 6 (short direction, 53 kN axle load).**

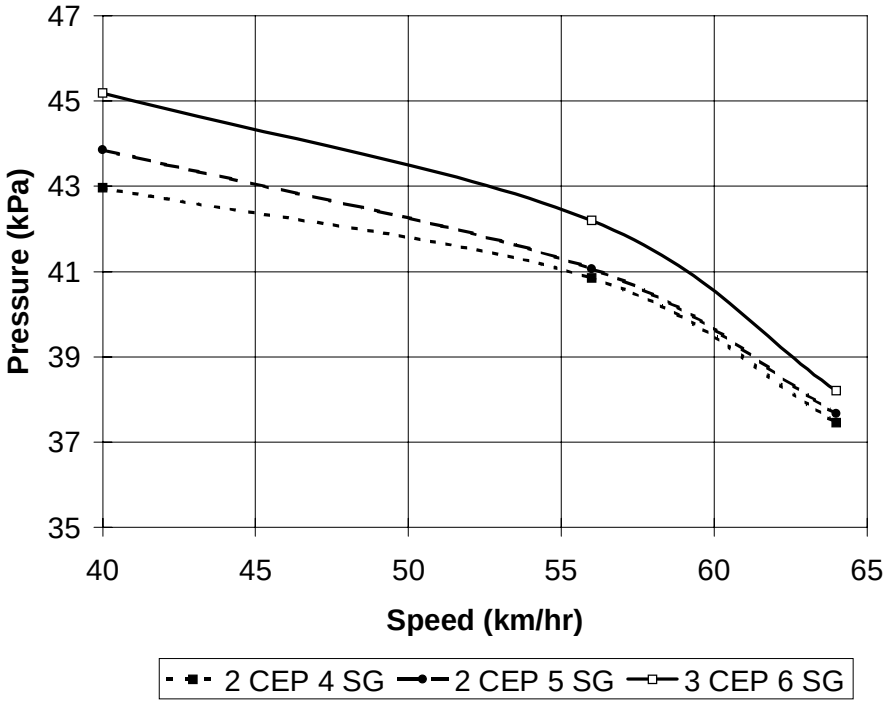


**Figure I 17 Subgrade pressure cell response, sections 2 and 3 (22 kN axle load).**

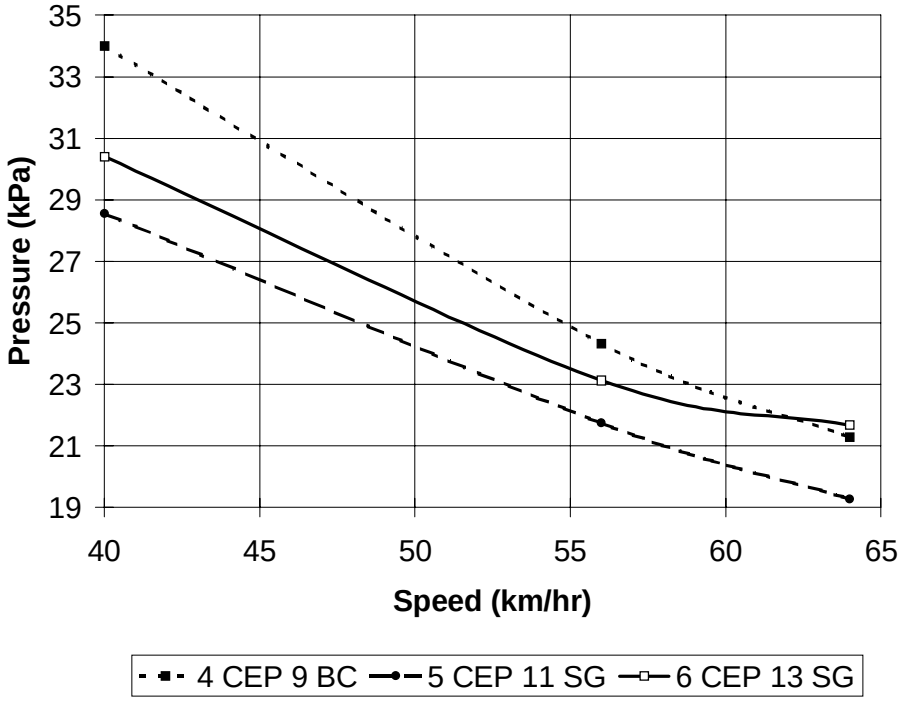


**Figure I 18 Subgrade pressure cell response, sections 4, 5, and 6 (22 kN axle load).**

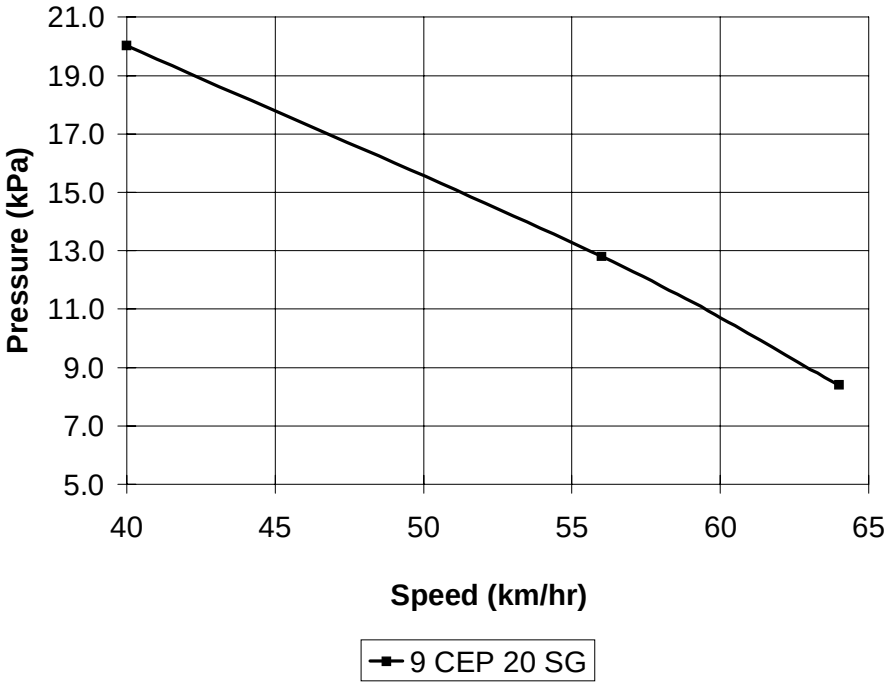


**Figure I 19 Subgrade pressure cell response, section 9 (22 kN axle load).**

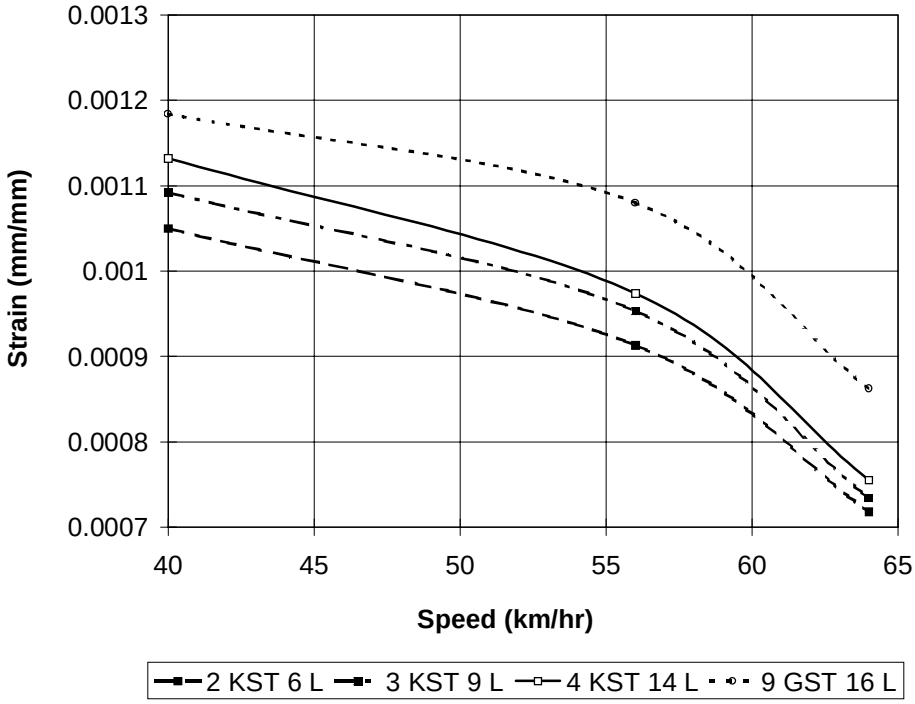


**Figure I 20 HMA strain gage response, sections 2, 3, 4 and 9 (long direction, 22 kN axle load).**

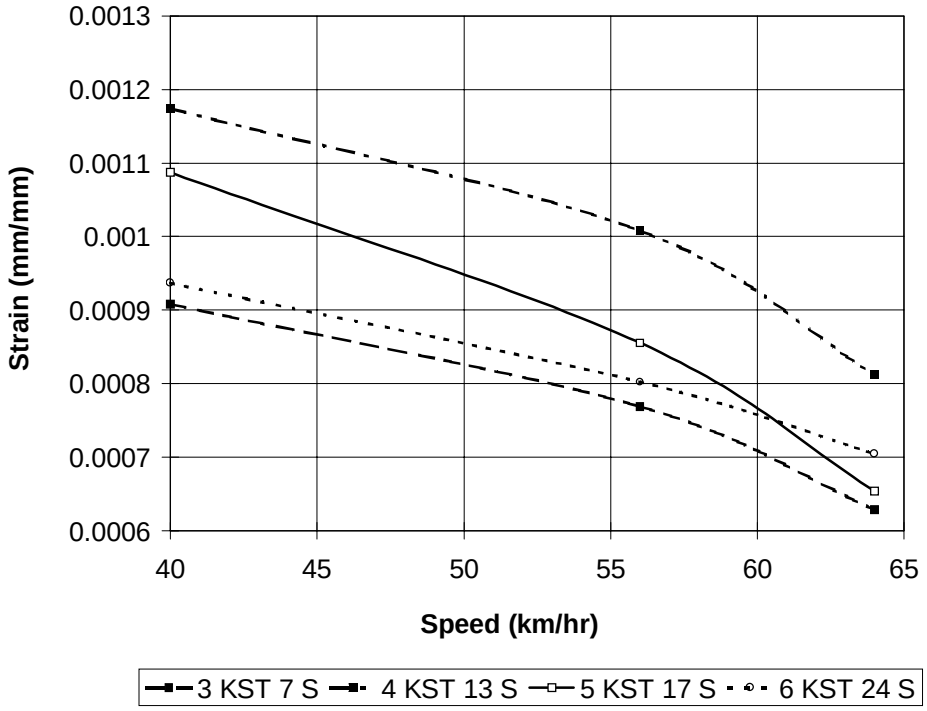


**Figure I 21 HMA strain gage response, sections 3, 4, 5, and 6 (short direction, 22 kN axle load).**

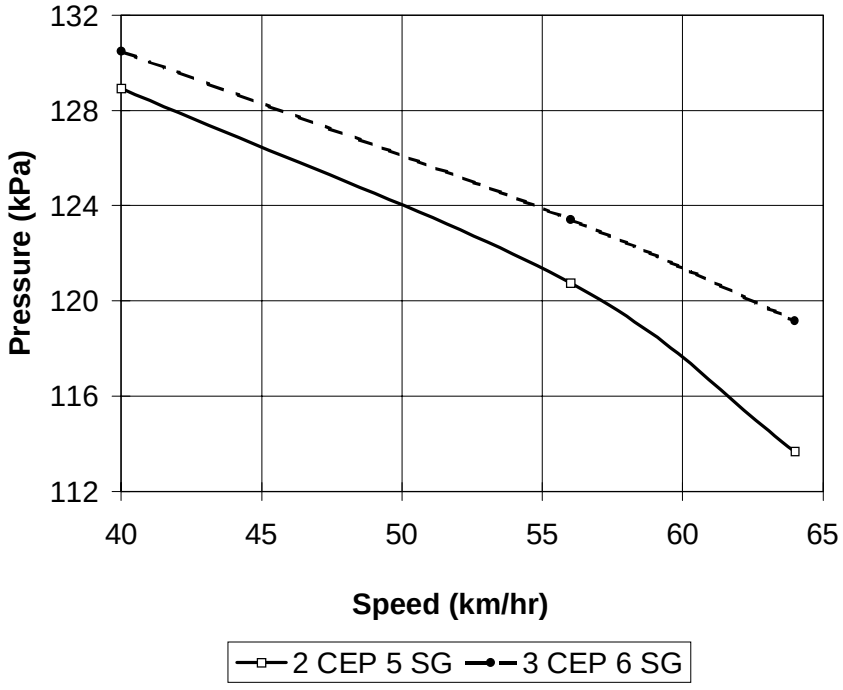


**Figure I 22 Subgrade pressure cell response, sections 2 and 3 (80 kN axle load).**

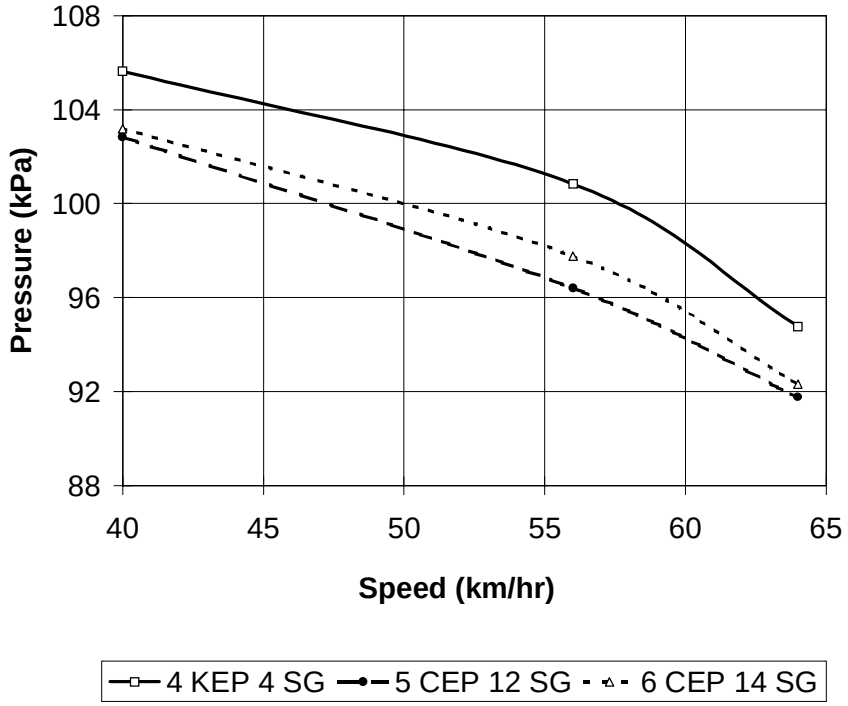


**Figure I 23 Subgrade pressure cell response, sections 4, 5, and 6 (80 kN axle load).**

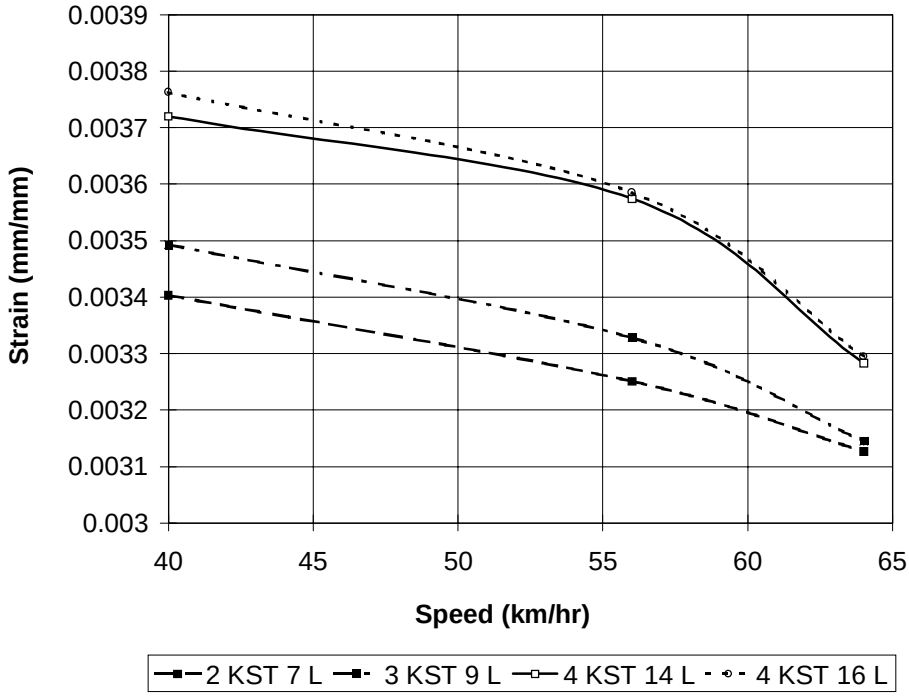


**Figure I 24 HMA strain gage response, sections 2, 3, and 4 (long direction, 80 kN axle load).**

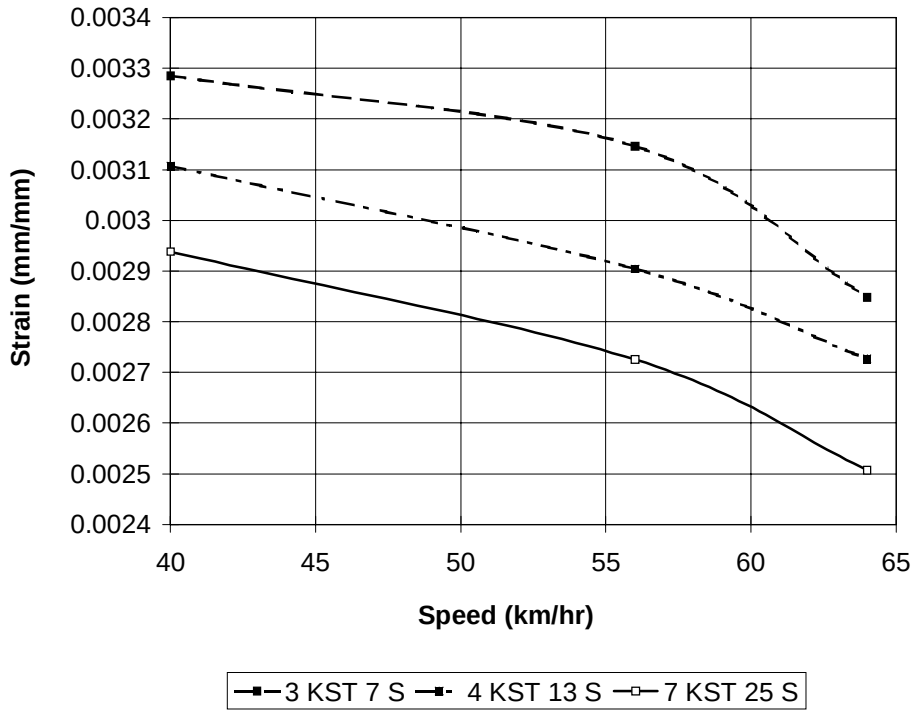


**Figure I 25 HMA strain gage response, sections 3, 4, and 7 (short direction, 80 kN axle load).**

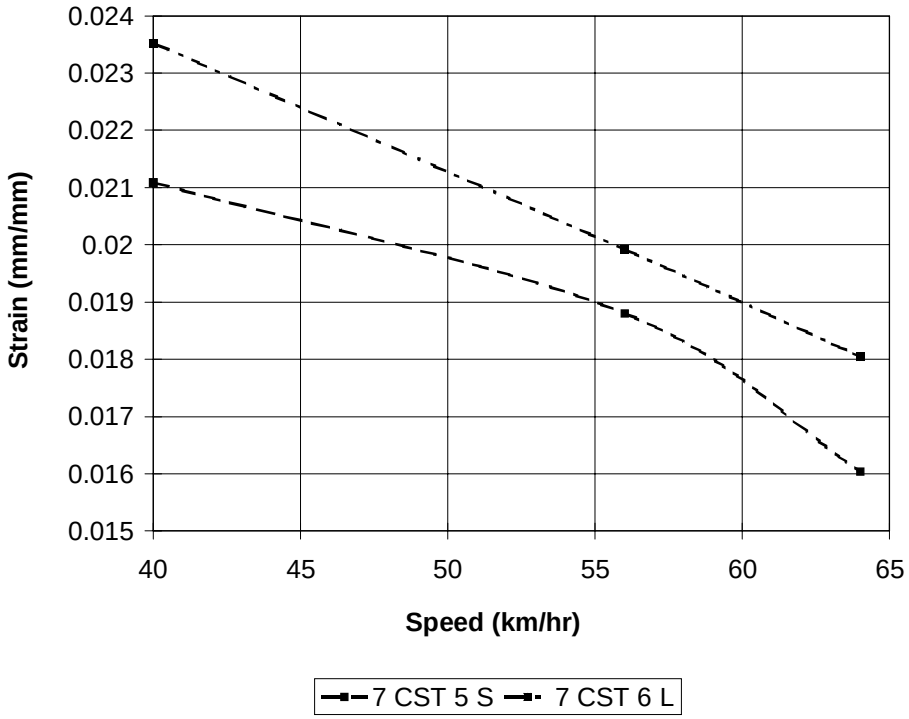


**Figure I 26 Soil strain gage response, section 7 (80 kN axle load).**

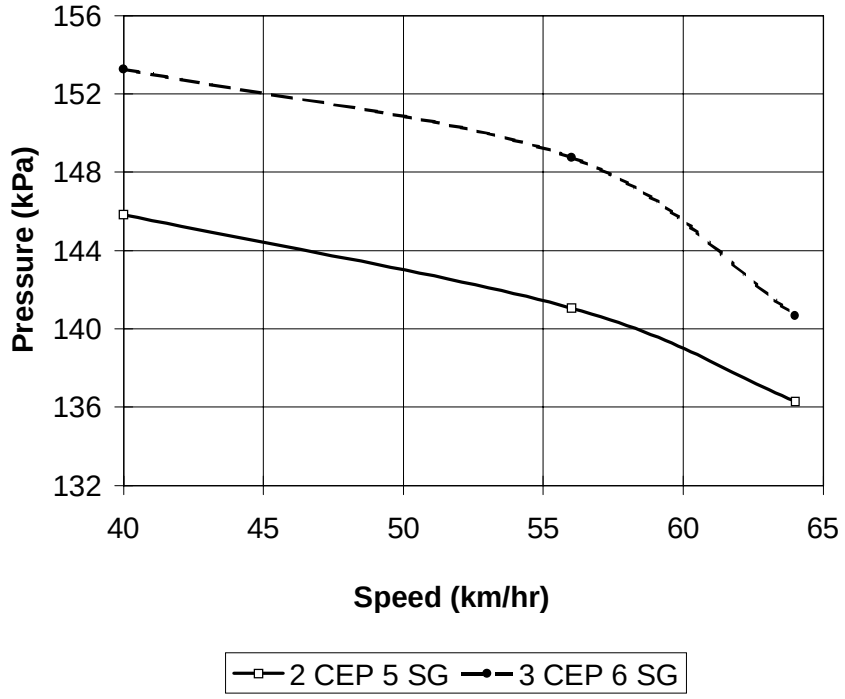


**Figure I 27 Subgrade pressure cell response, sections 2 and 3 (102 kN axle load).**

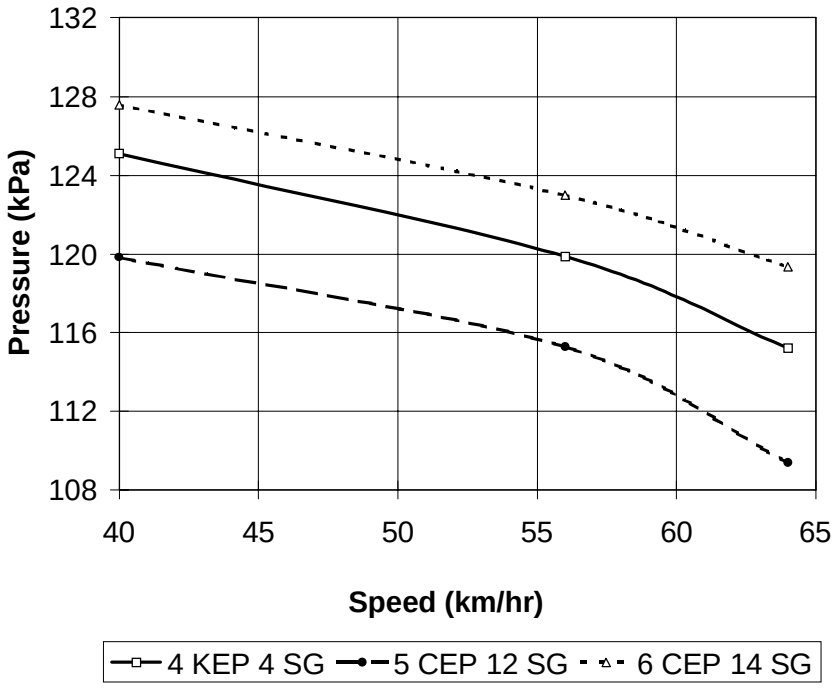


**Figure I 28 Subgrade pressure cell response, sections 4, 5, and 6 (102 kN axle load).**

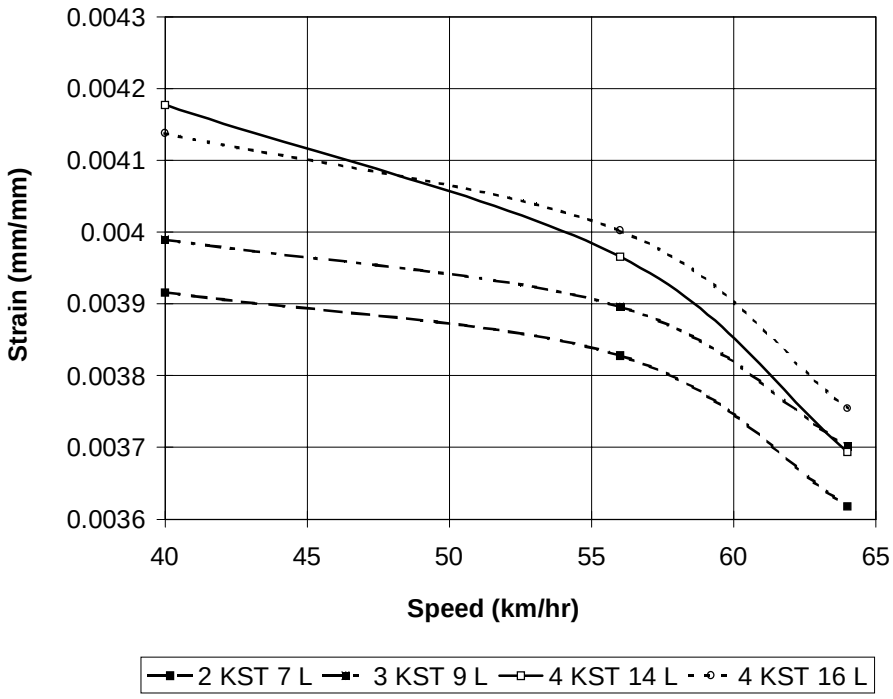


**Figure I 29 HMA strain gage response, sections 2, 3, and 4 (long direction, 102 kN axle load).**

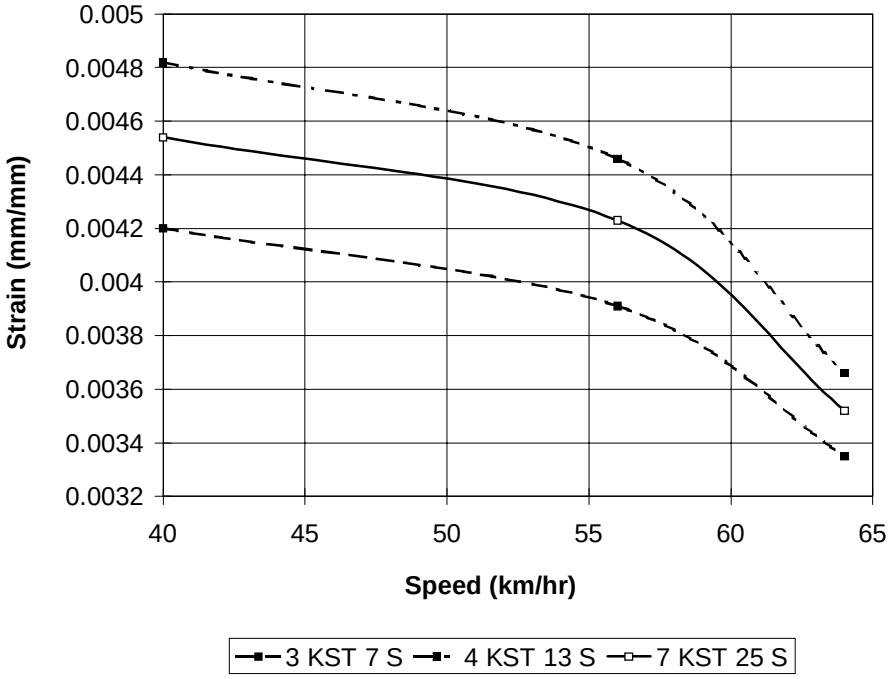


**Figure I 30 HMA strain gage response, sections 3, 4, and 7 (short direction, 102 kN axle load).**

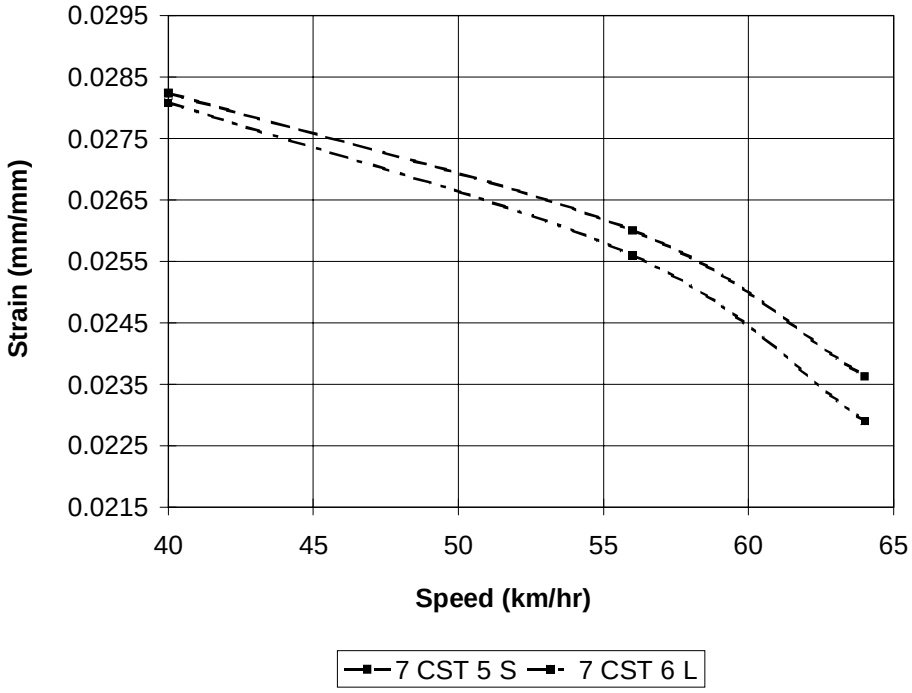


**Figure I 31 Soil strain gage response, section 7 (102 kN axle load).**

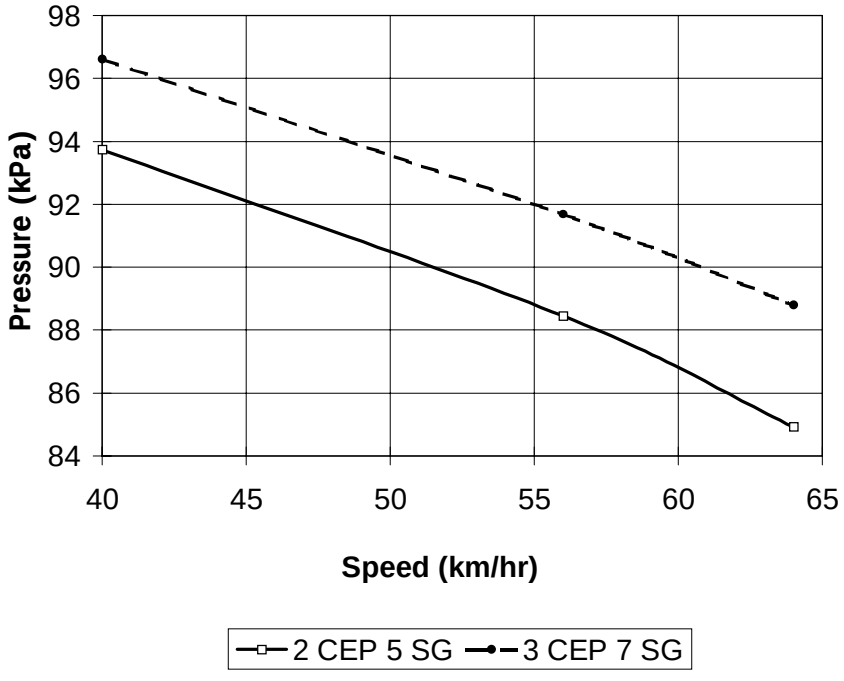


**Figure I 32 Subgrade pressure cell response, sections 2 and 3 (53 kN axle load).**

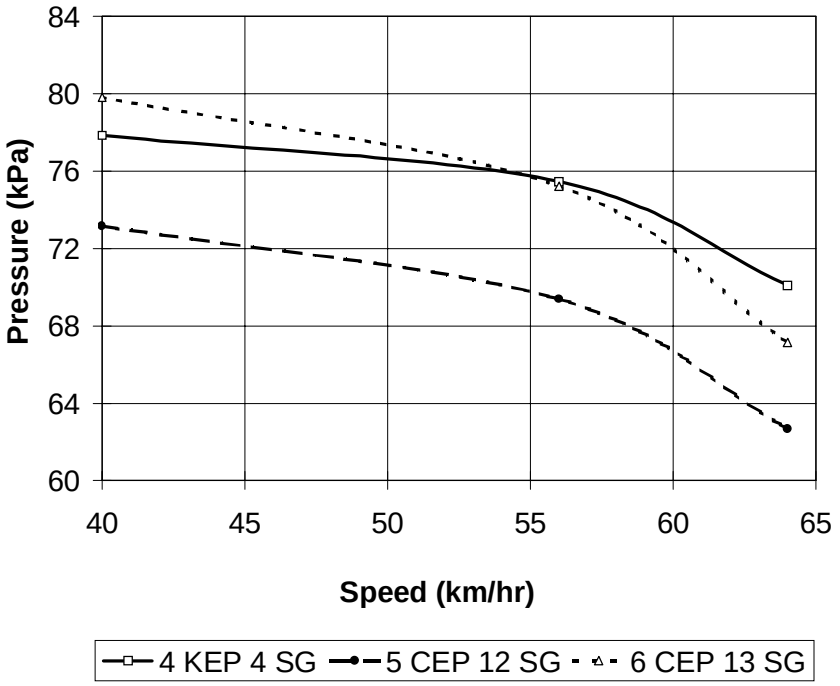


**Figure I 33 Subgrade pressure cell response, sections 4, 5, and 6 (53 kN axle load).**

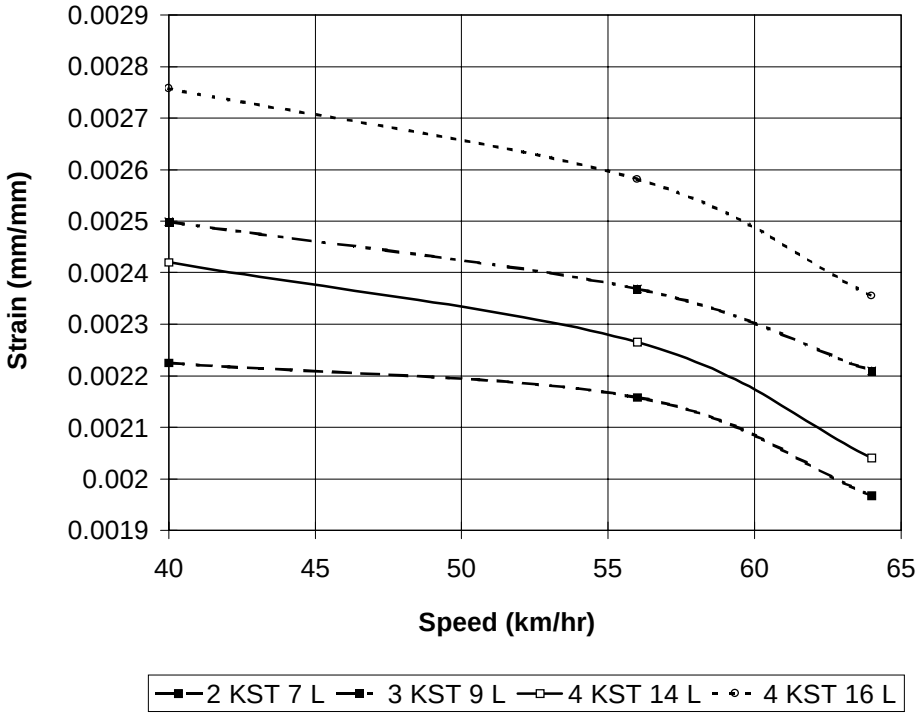


**Figure I 34 HMA strain gage response, sections 2, 3, and 4 (long direction, 53 kN axle load).**

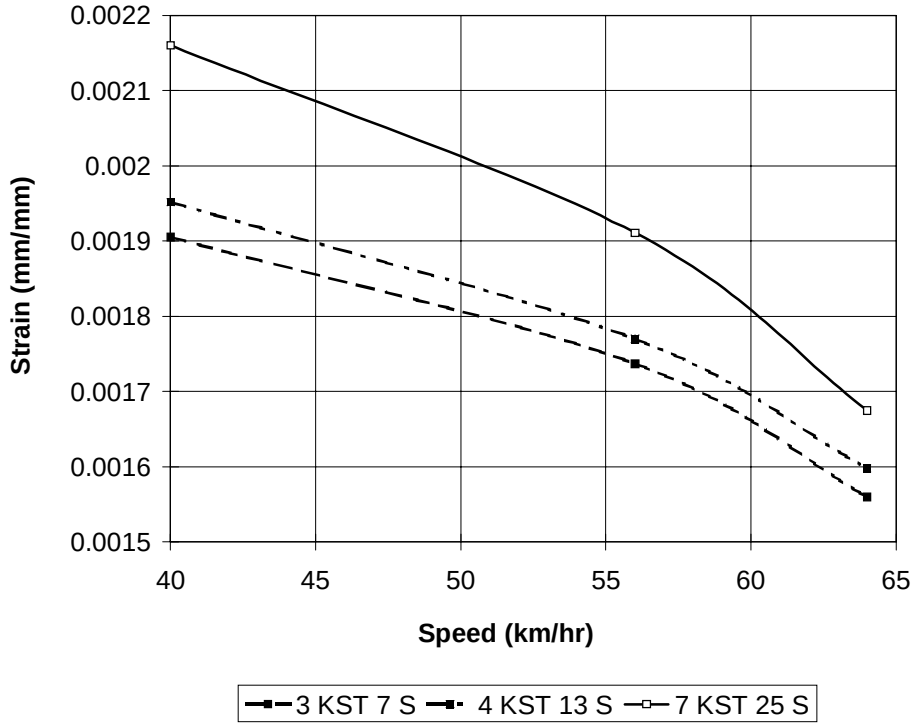


**Figure I 35 HMA strain gage response, sections 3, 4, and 7 (short direction, 53 kN axle load).**

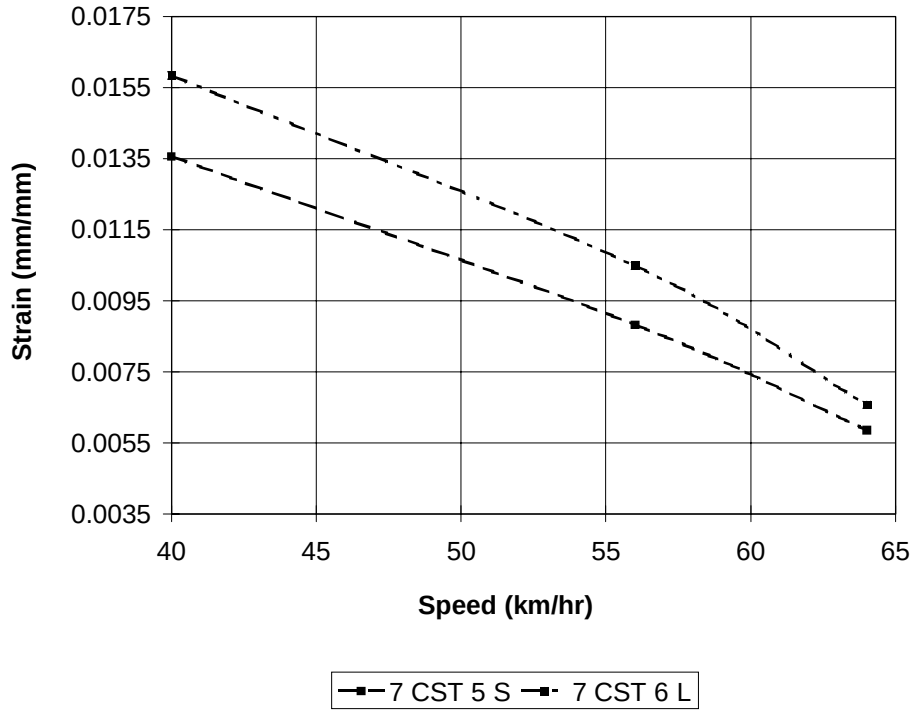


**Figure I 36 Soil strain gage response, section 7 (53 kN axle load).**

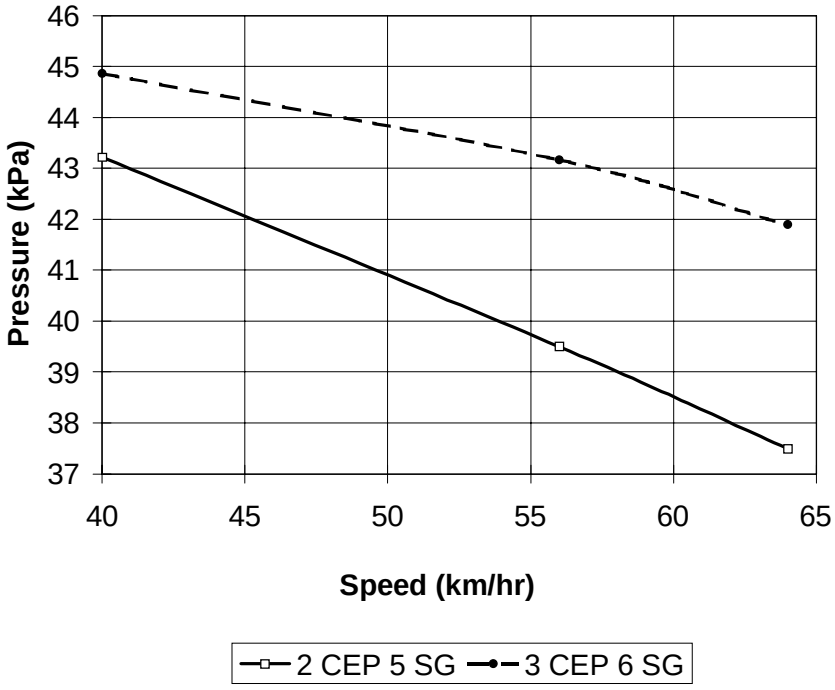


**Figure I 37 Subgrade pressure cell response, sections 2 and 3 (22 kN axle load).**

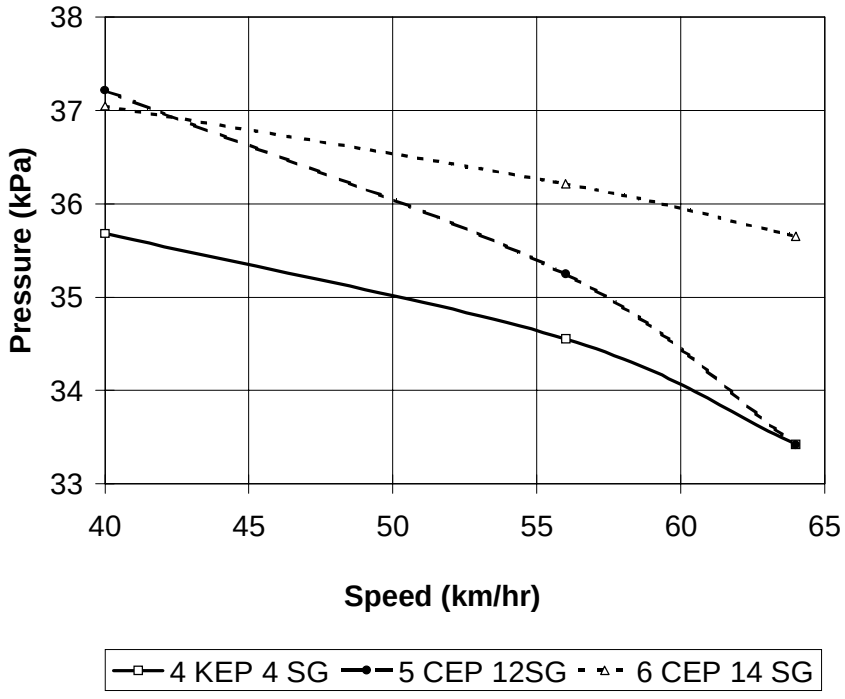


**Figure I 38 Subgrade pressure cell response, sections 4, 5, and 6 (22 kN axle load).**

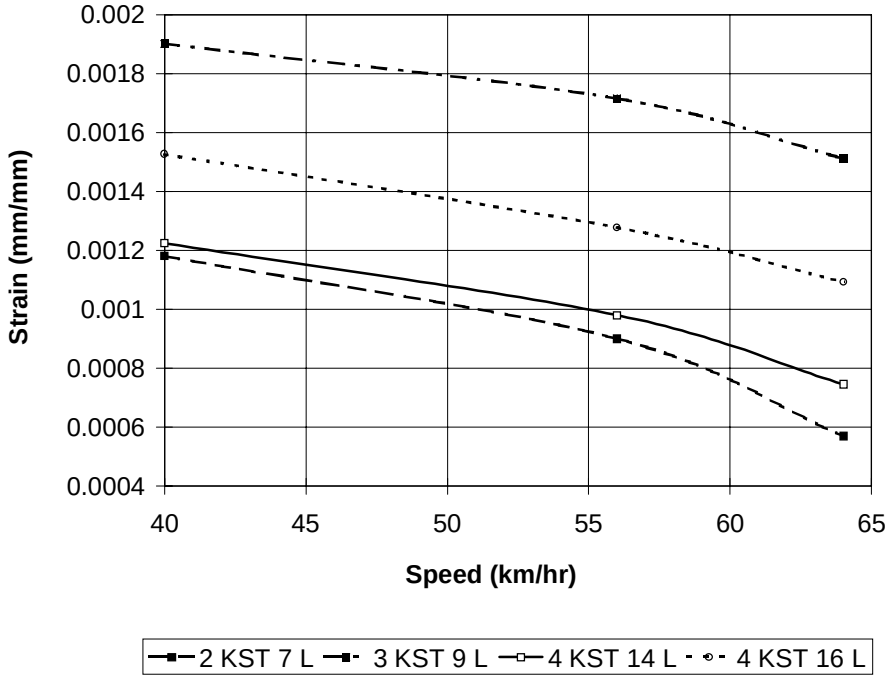


**Figure I 39 HMA strain gage response, sections 2, 3, and 4 (long direction, 22 kN axle load).**

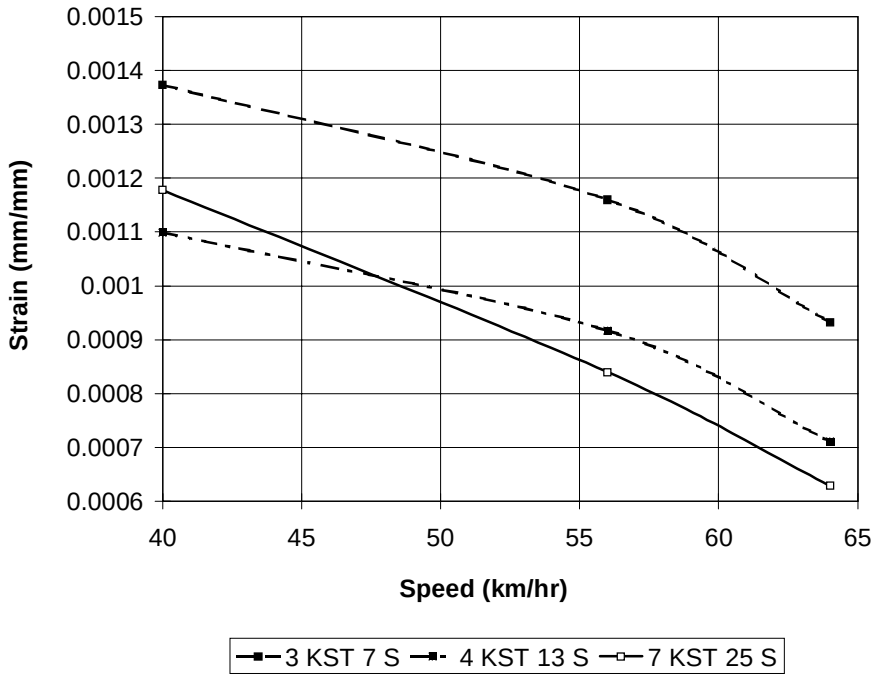


**Figure I 40 HMA strain gage response, sections 3, 4, and 7 (short direction, 22 kN axle load).**

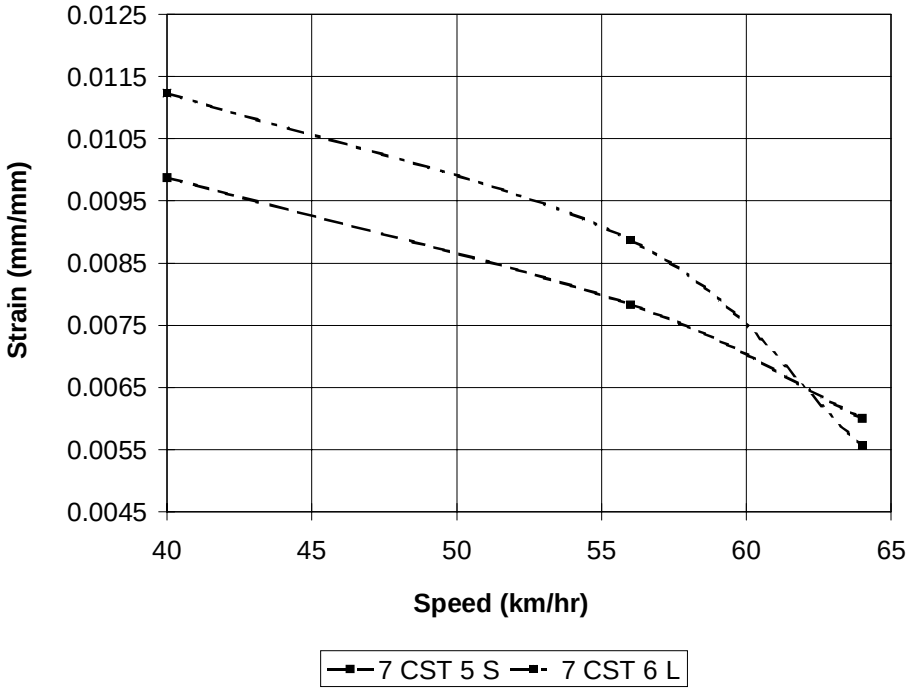


**Figure I 41 Soil strain gage response, section 7 (22 kN axle load).**

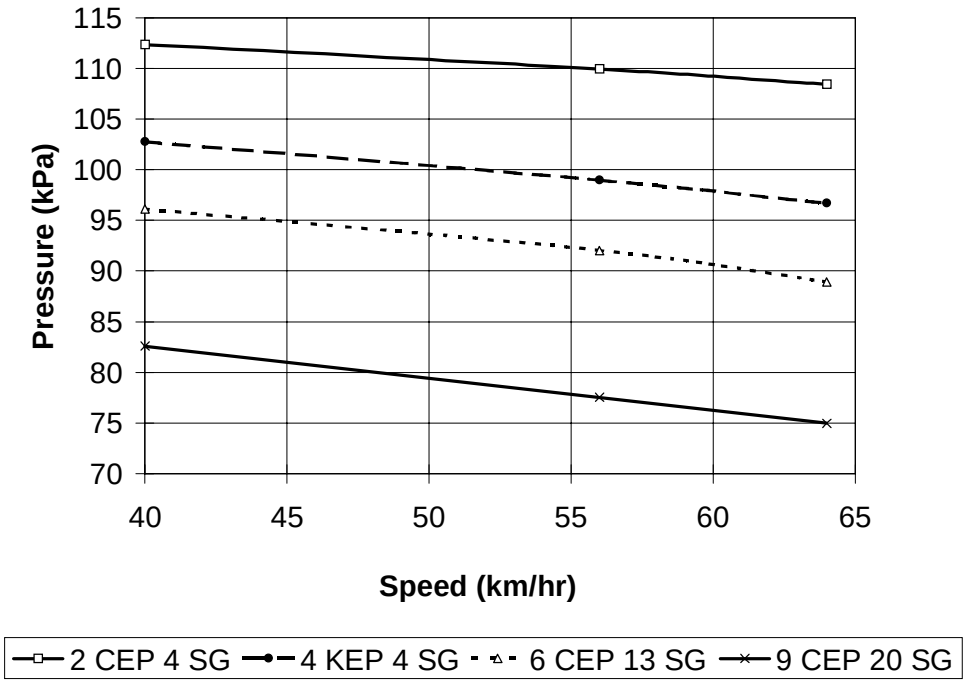


**Figure I 42 Subgrade pressure cell response, sections 2, 4, 6 and 9 (80 kN axle load).**

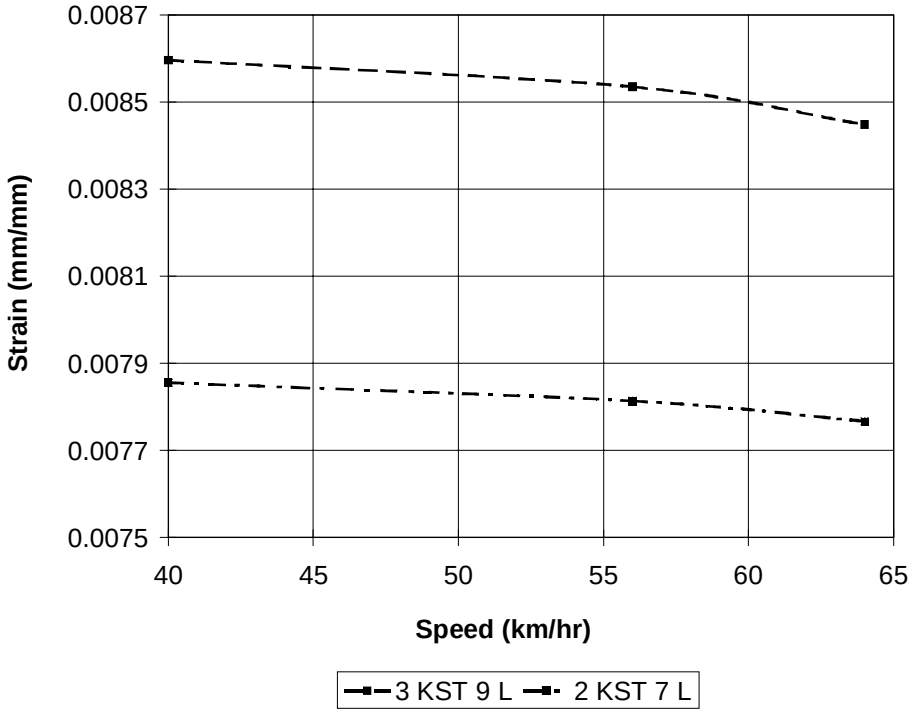


**Figure I 43 HMA strain gage response, sections 2 and 3 (long direction, 80 kN axle load).**

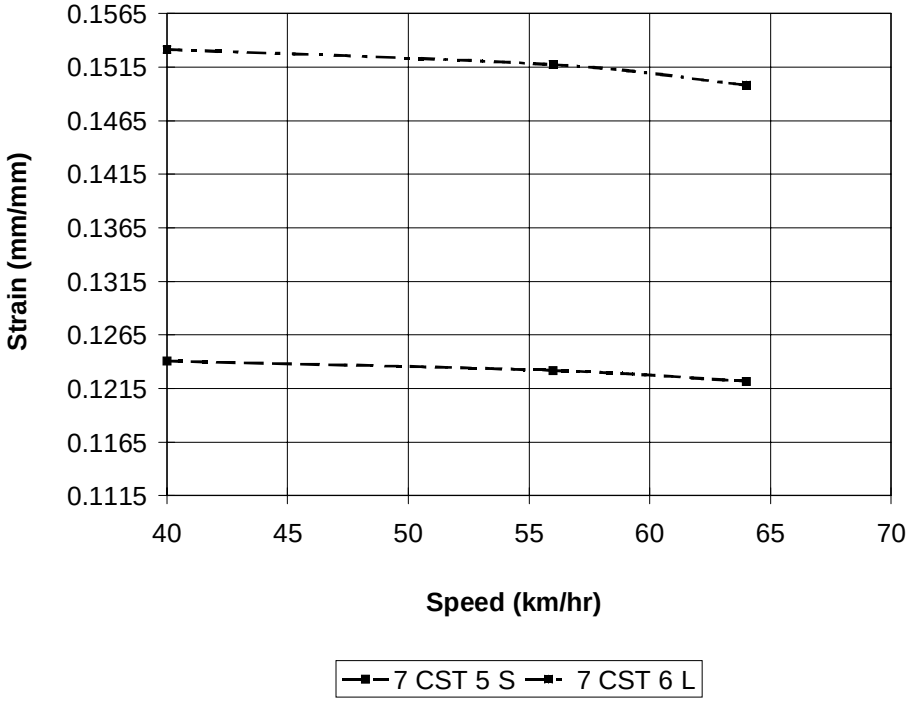


**Figure I 44 Soil strain gage response, section 7 (80 kN axle load).**

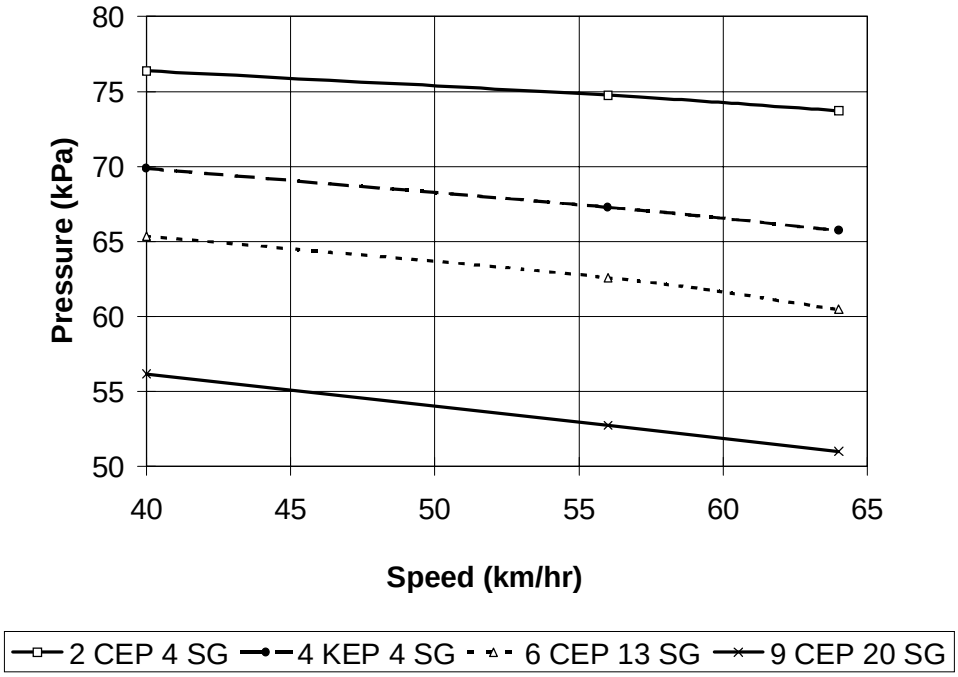


**Figure I 45 Subgrade pressure cell response, sections 2, 4, 6 and 9 (53 kN axle load).**

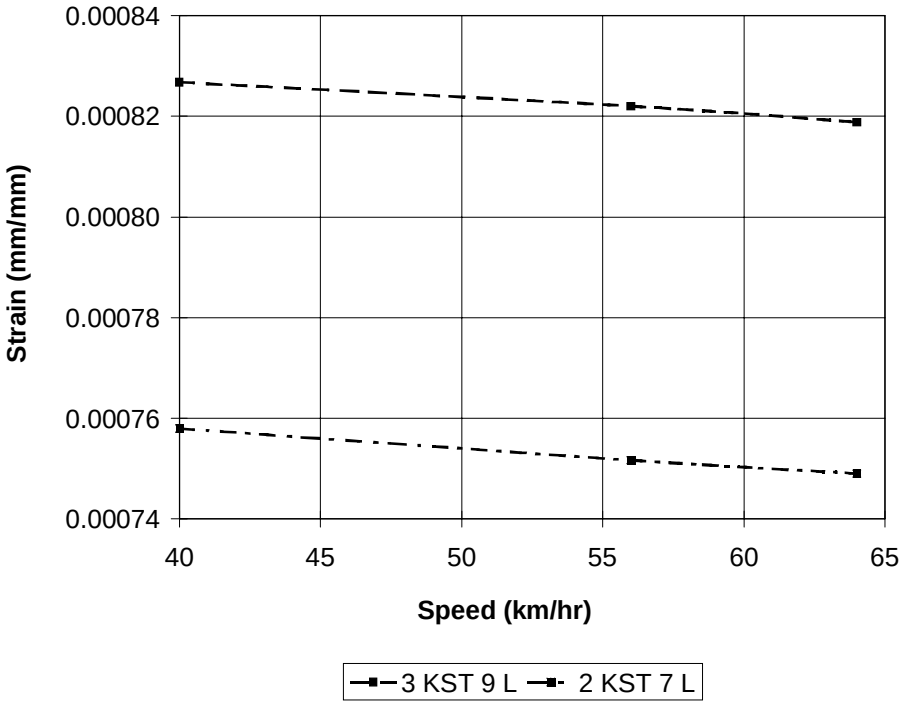


**Figure I 46 HMA strain gage response, sections 2 and 3 (long direction, 53 kN axle load).**

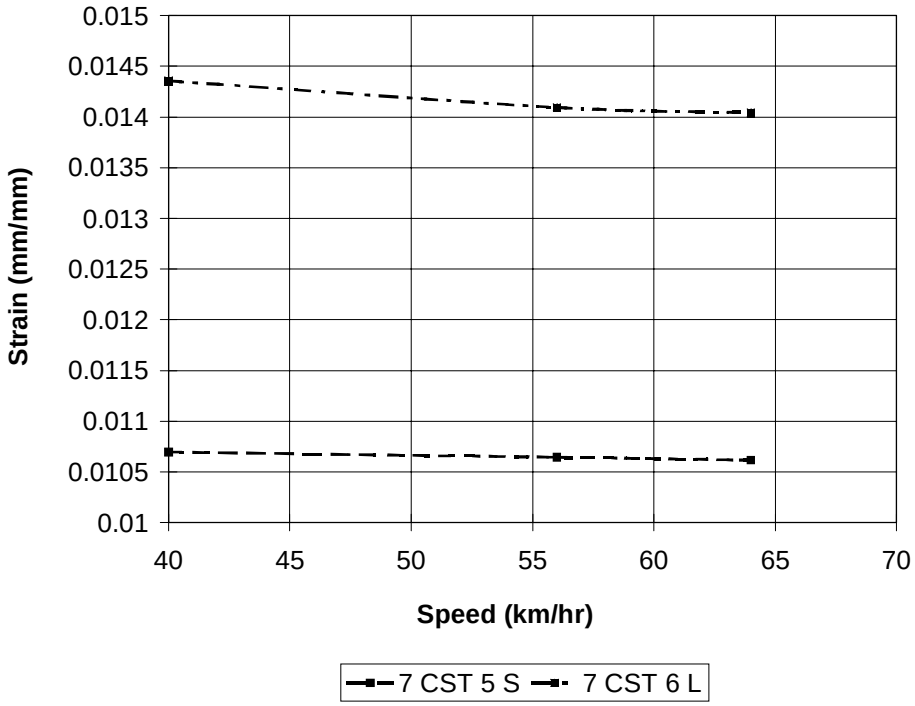


**Figure I 47 Soil strain gage response, section 7 (53 kN axle load).**

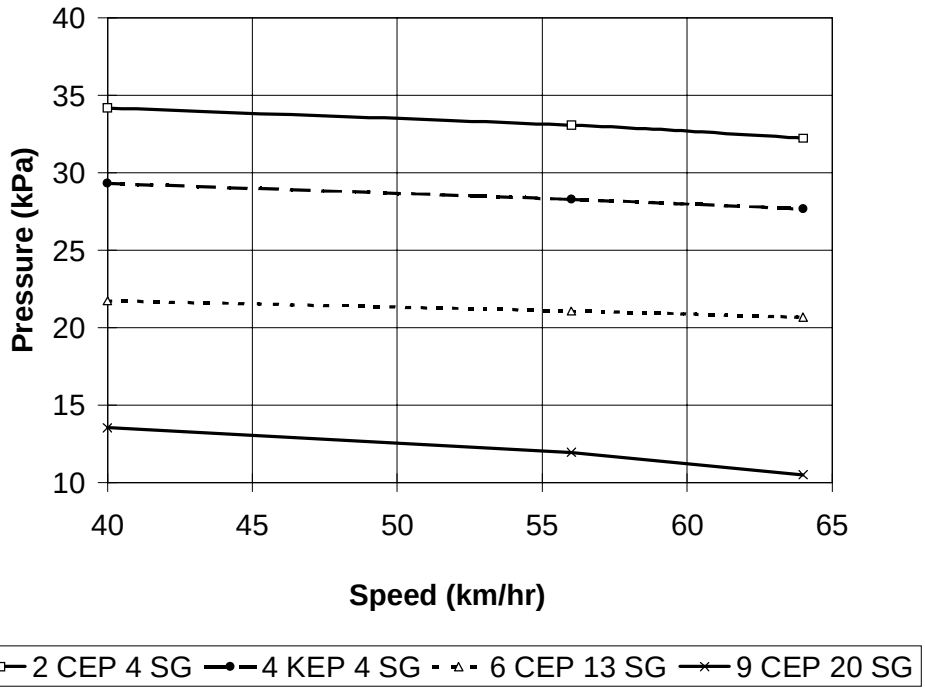


**Figure I 48 Subgrade pressure cell response, sections 2, 4, 6, and 9 (22 kN axle load).**

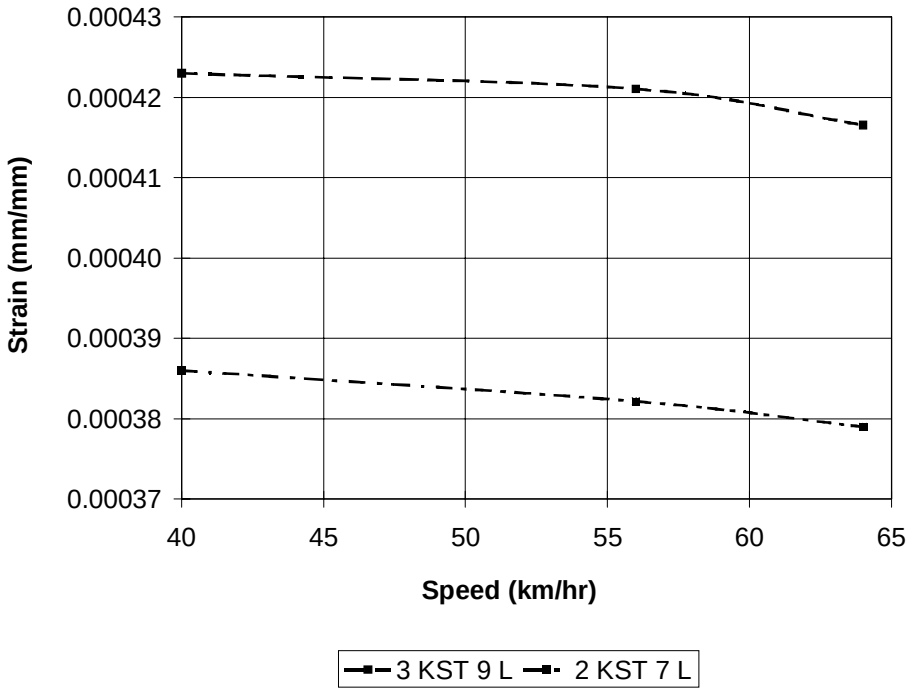


**Figure I 49 HMA strain gage response, sections 2 and 3 (long direction, 22kN axle load).**

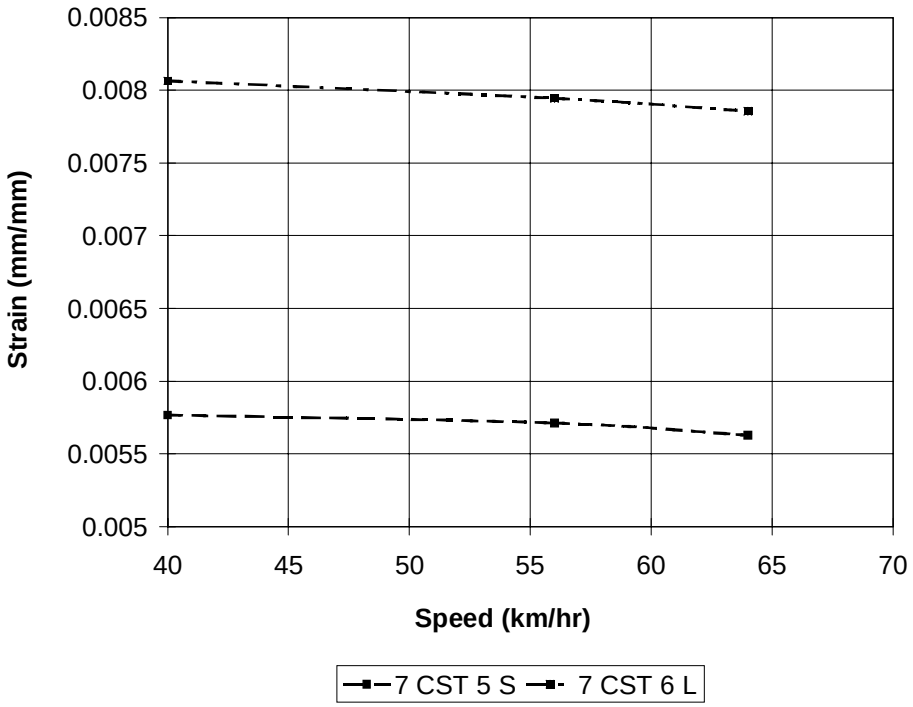


**Figure I 50 Soil strain gage response, section 7 (22 kN axle load).**

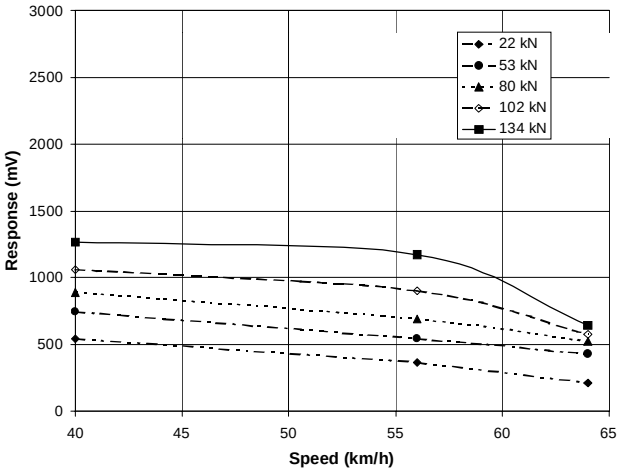


**(a) 420 kPa Tire Pressure**

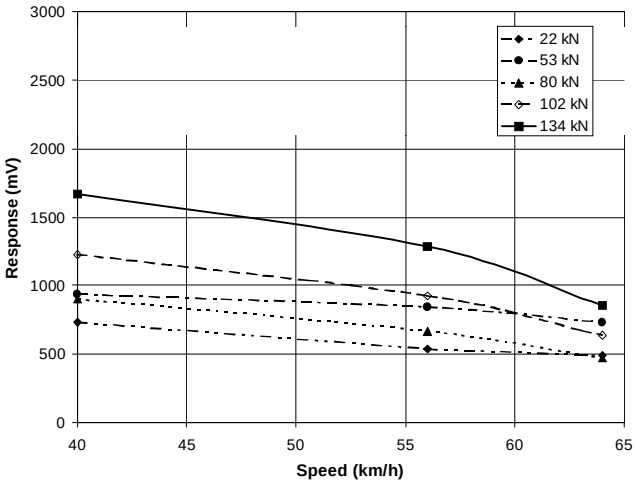


**(b) 490 kPa Tire Pressure**

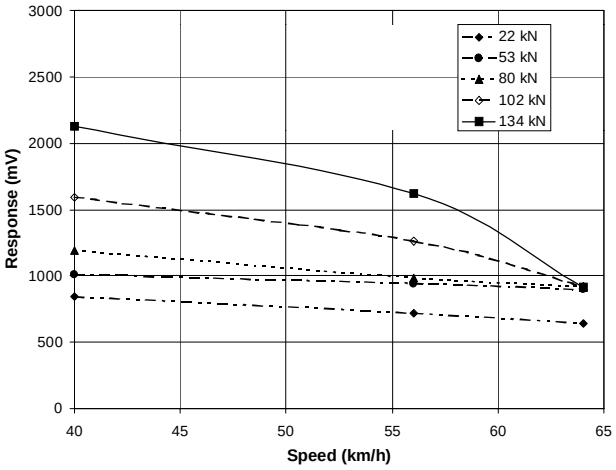


**(c) 560 kPa Tire Pressure**

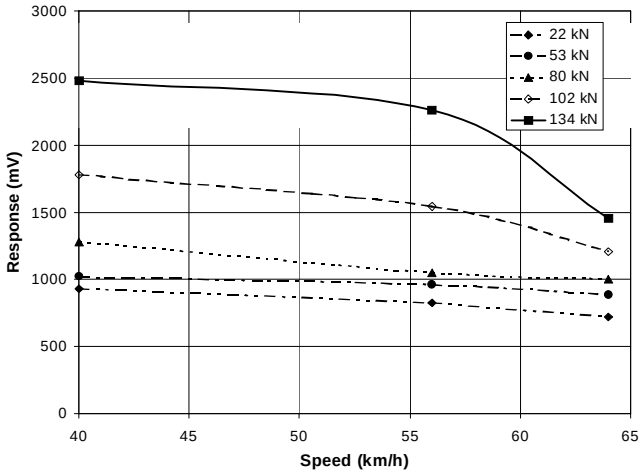


**(d) 630 kPa Tire Pressure**

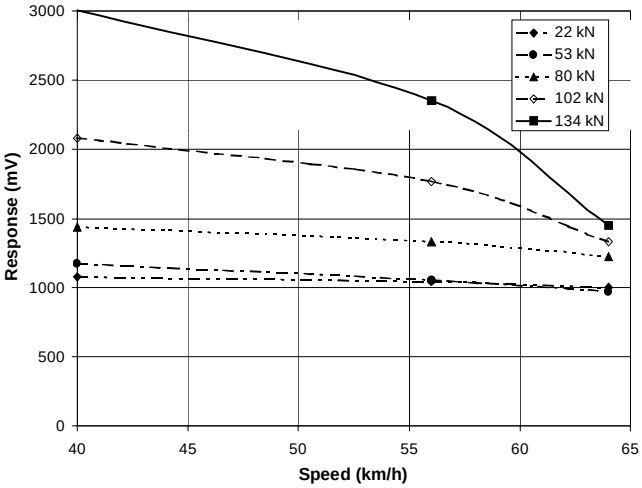


**(e) 700 kPa Tire Pressure**

**Figure I 51 Axle Load, tire pressure curves derived from calibration one.**

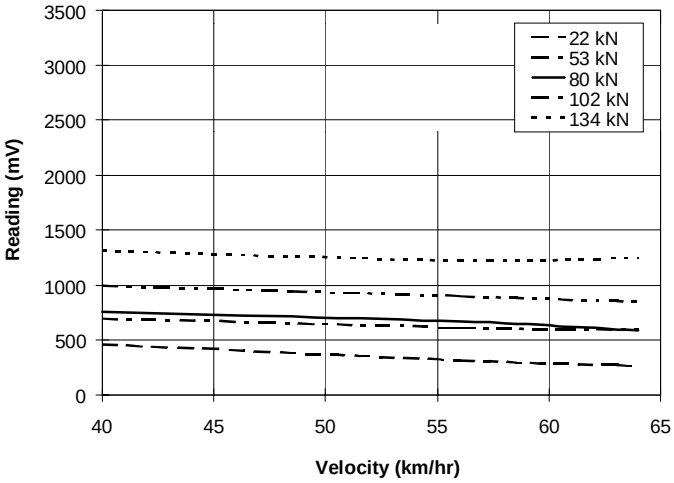


**(a) 420 kPa Tire Pressure**

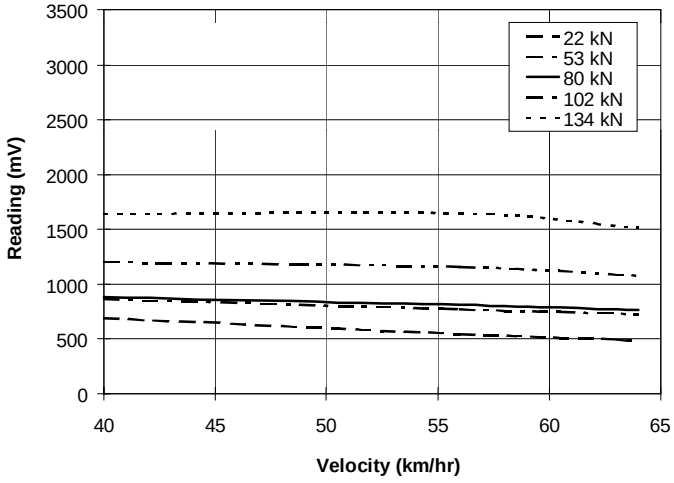


**(b) 490 kPa Tire Pressure**

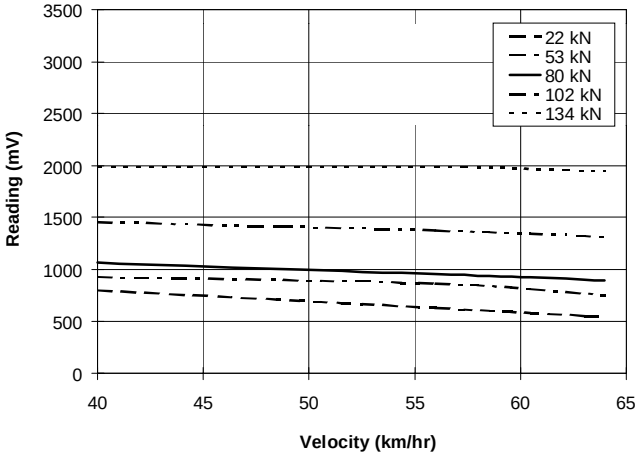


**(c) 560 kPa Tire Pressure**

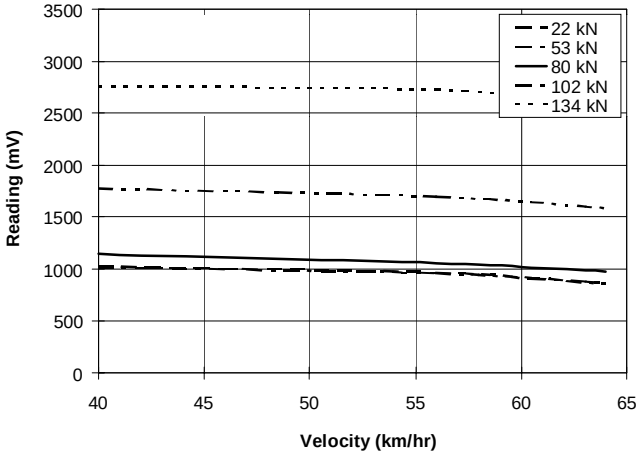


**(d) 630 kPa Tire Pressure**

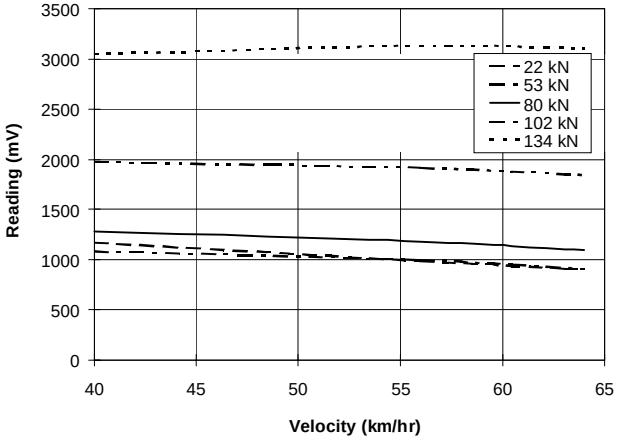


**(e) 700 kPa Tire Pressure**

**Figure I 52 Axle Load, tire pressure curves derived from calibration two.**

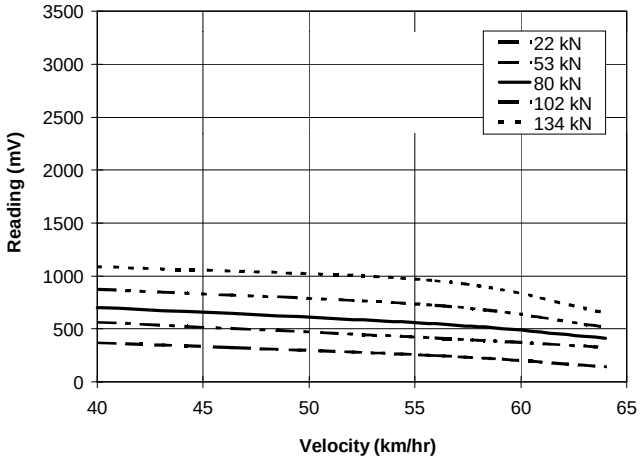


**(a) 420 kPa Tire Pressure**

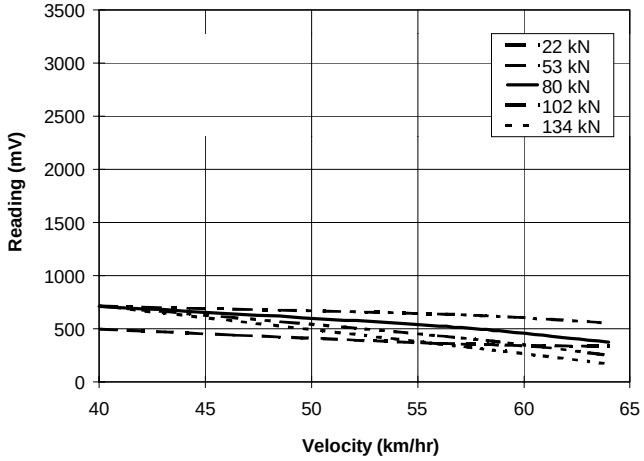


**(b) 490 kPa Tire Pressure**

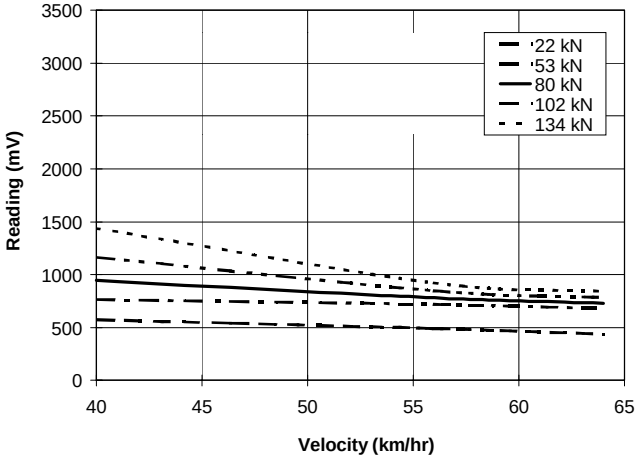


**(c) 560 kPa Tire Pressure**

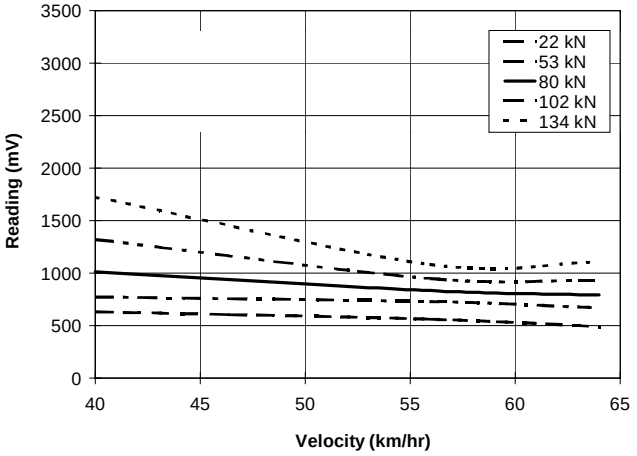


**(d) 630 kPa Tire Pressure**

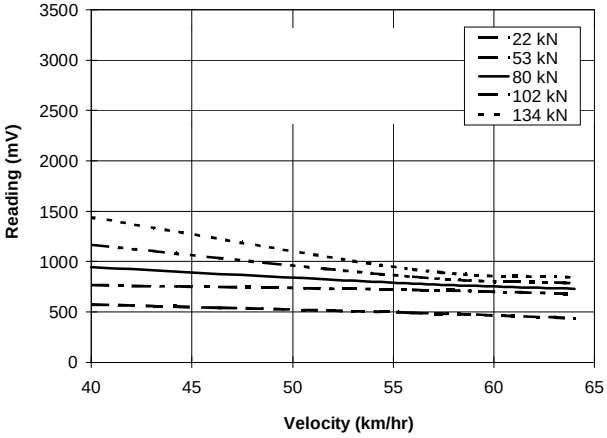


**(e) 700 kPa Tire Pressure**

**Figure I 53 Axle Load, tire pressure curves derived from calibration three.**

# APPENDIX J

# STATIC DATA

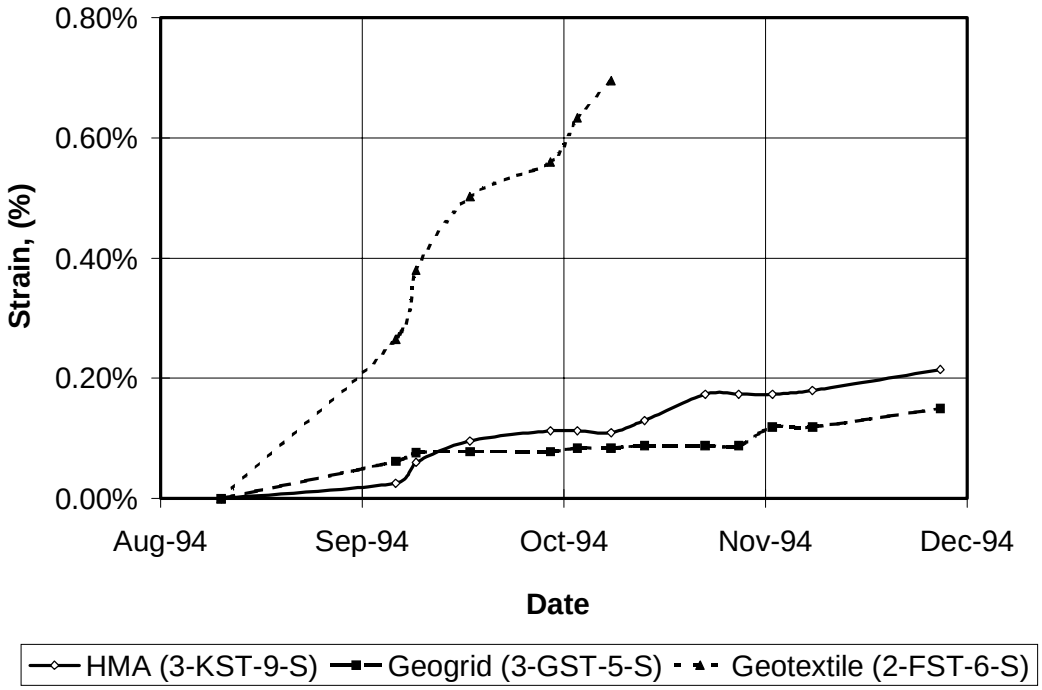


**Figure J 1 Strain development-100 mm base course (perpendicular to traffic).**

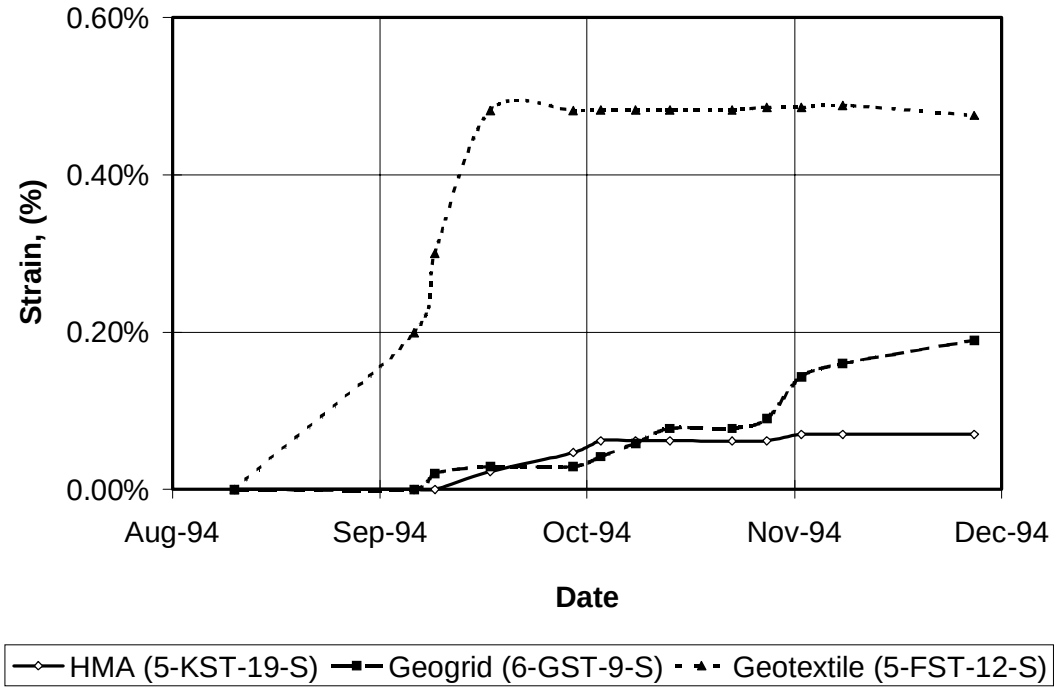


**Figure J 2 Strain development-150 mm base course (perpendicular to traffic).**

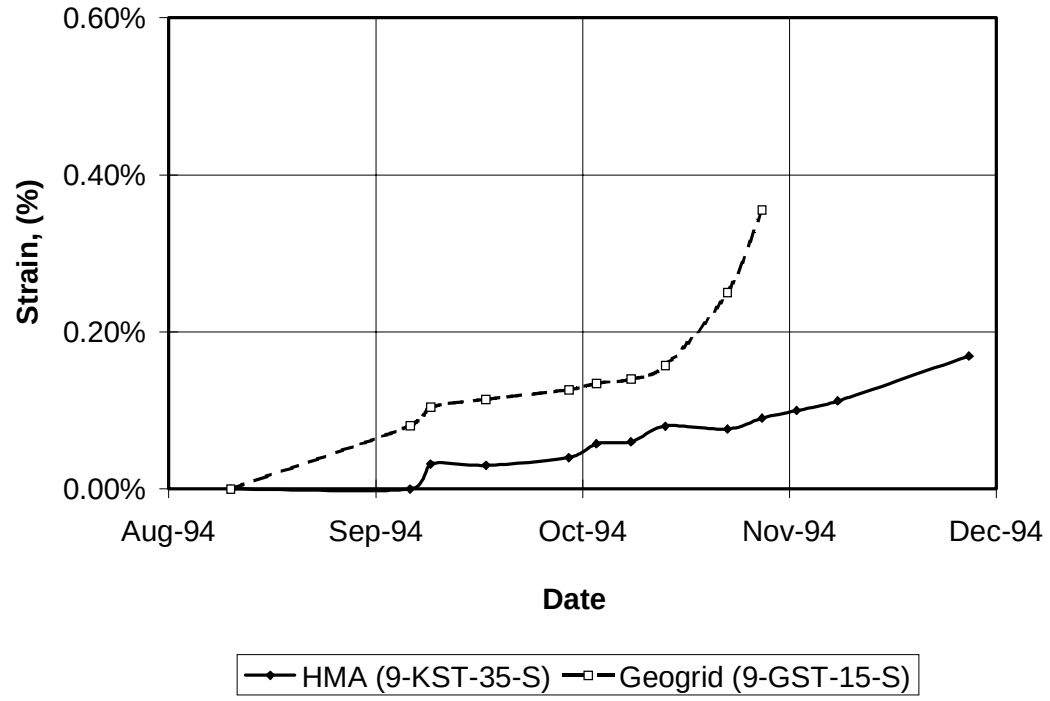


**Figure J 3 Strain development-200 mm base course (perpendicular to traffic).**

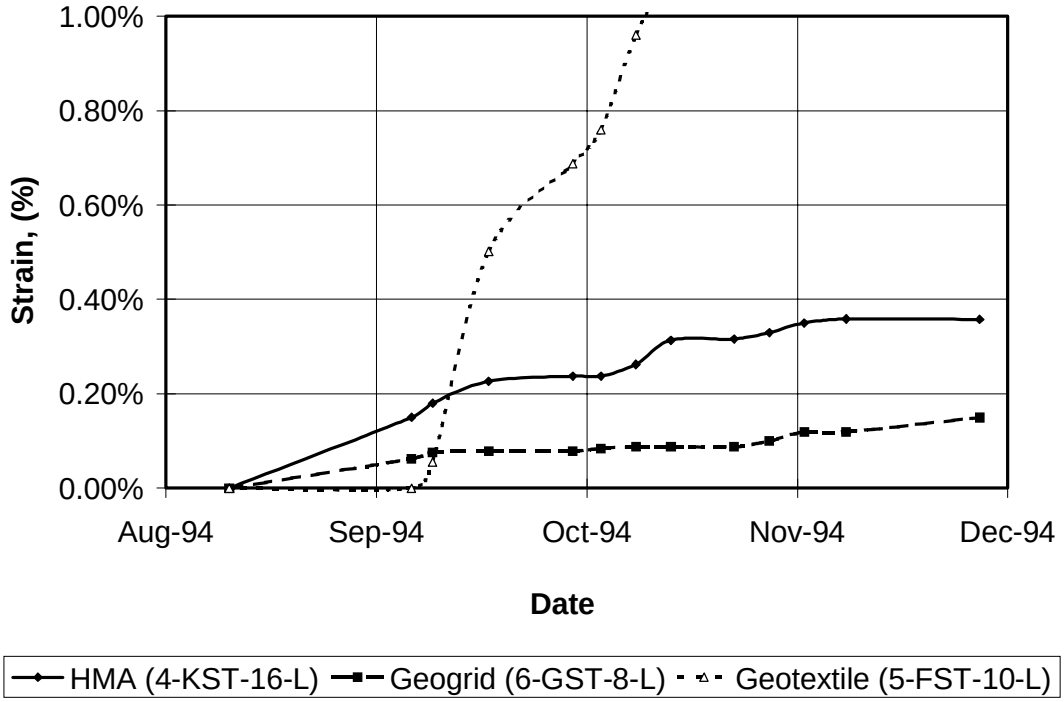


**Figure J 4 Strain development-150 mm base course (parallel to traffic).**

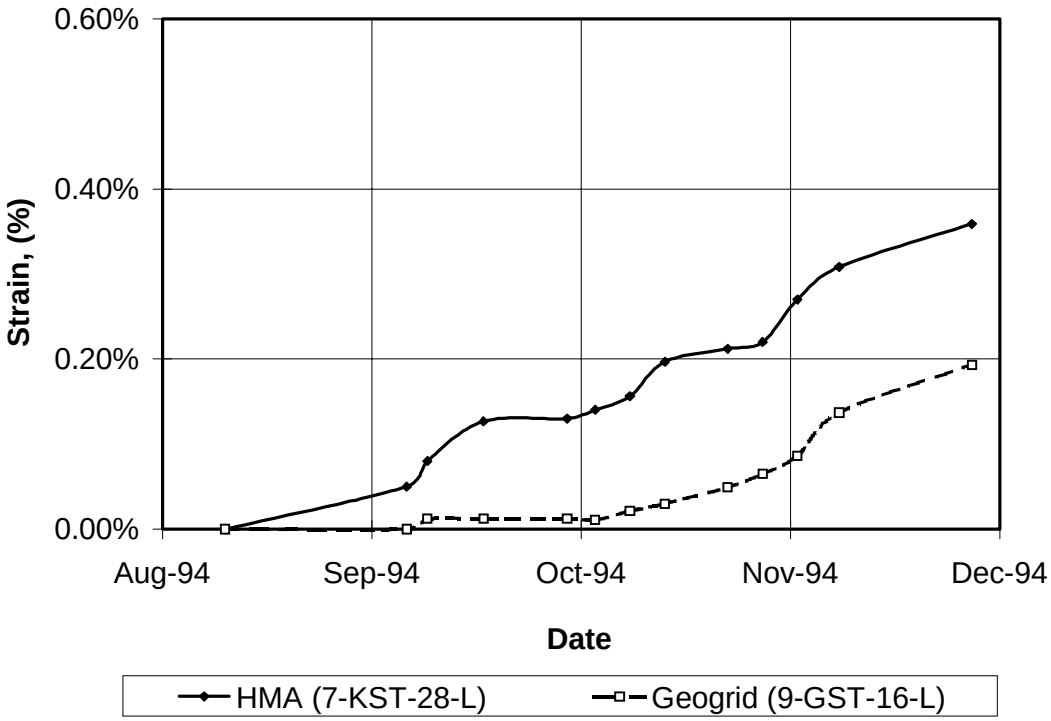


**Figure J 5 Strain development-200 mm base course (parallel to traffic).**

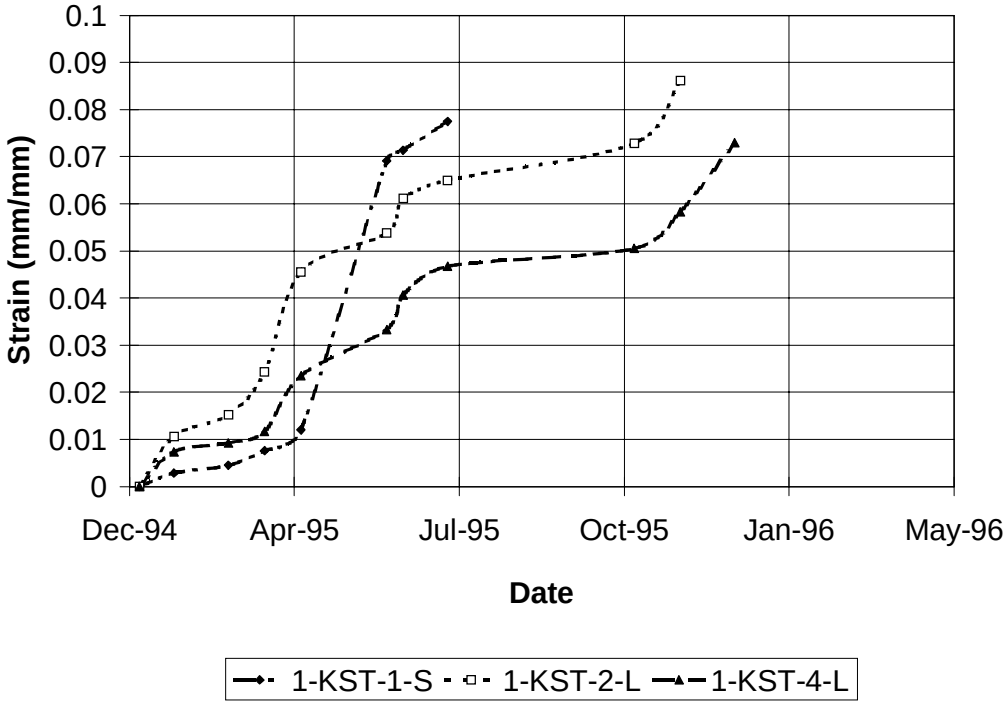


**Figure J 6 Static HMA strain accumulation in section 1.**

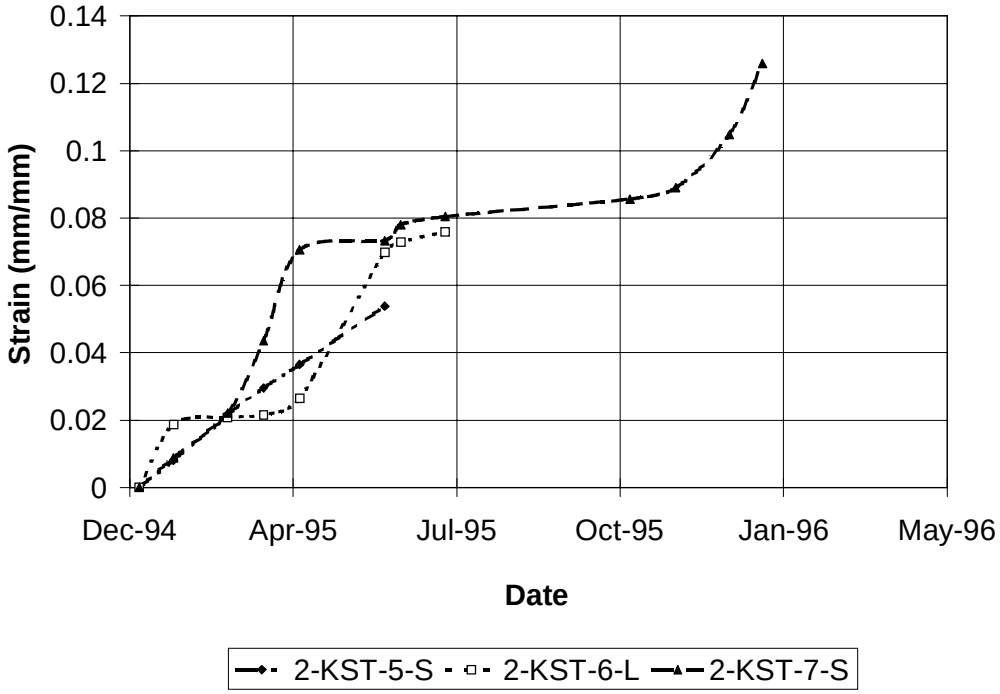


**Figure J 7 Static HMA strain accumulation in section 2.**

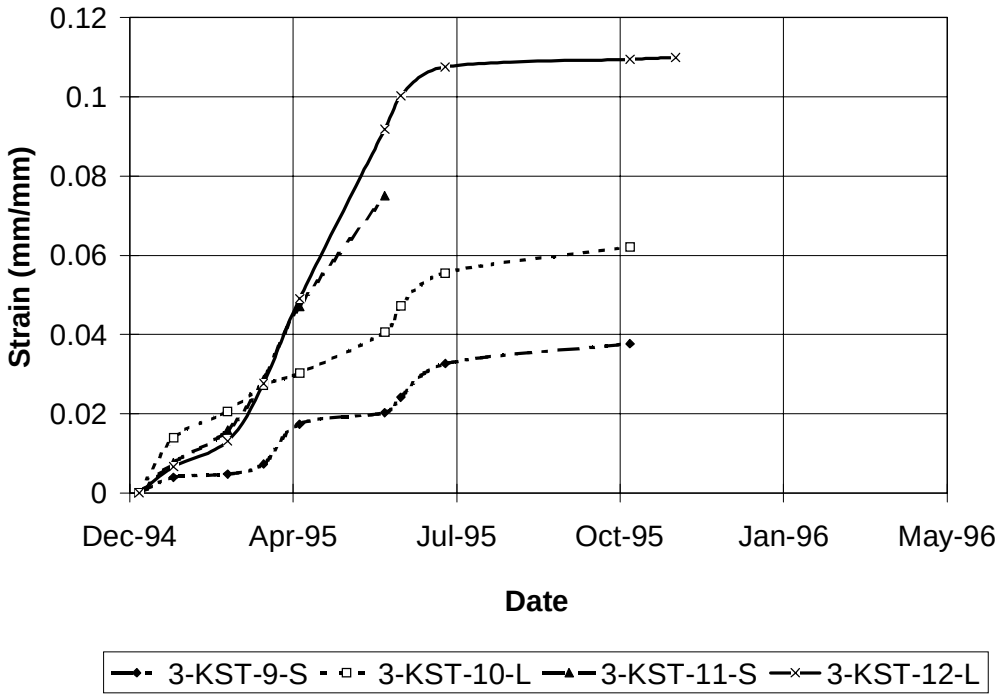


**Figure J 8 Static HMA strain accumulation in section 3.**

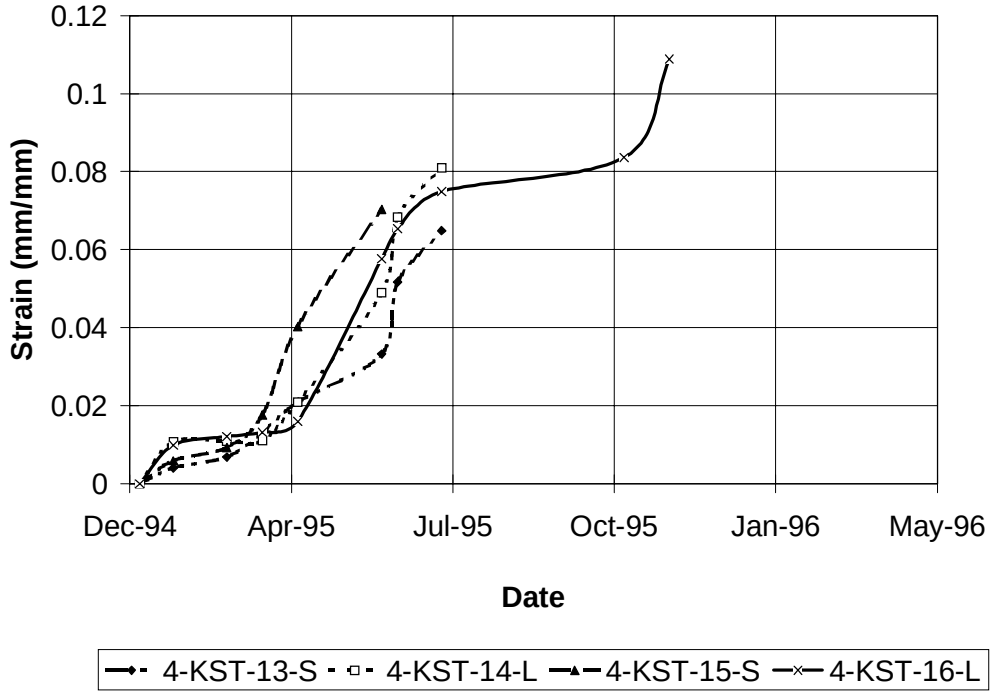


**Figure J 9 Static HMA strain accumulation in section 4.**

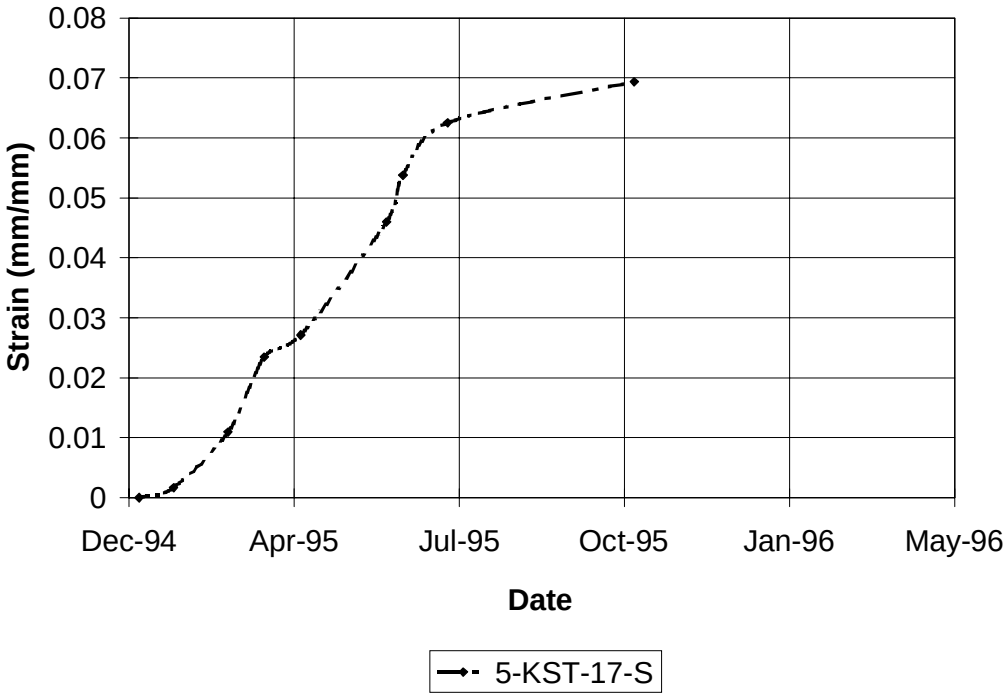


**Figure J 10 Static HMA strain accumulation in section 5.**

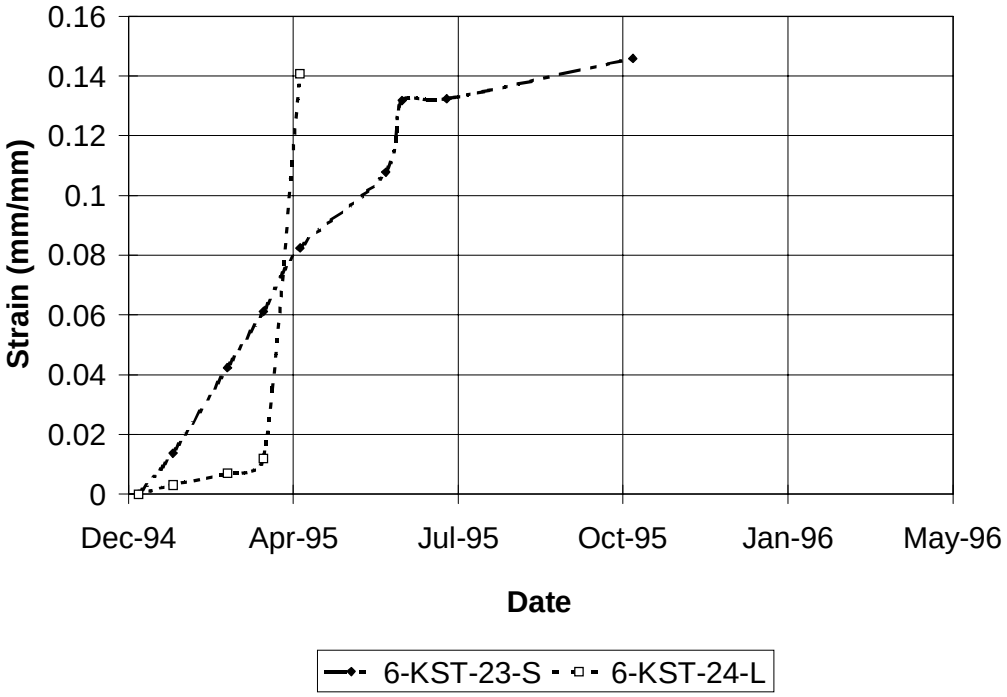


**Figure J 11 Static HMA strain accumulation in section 6.**

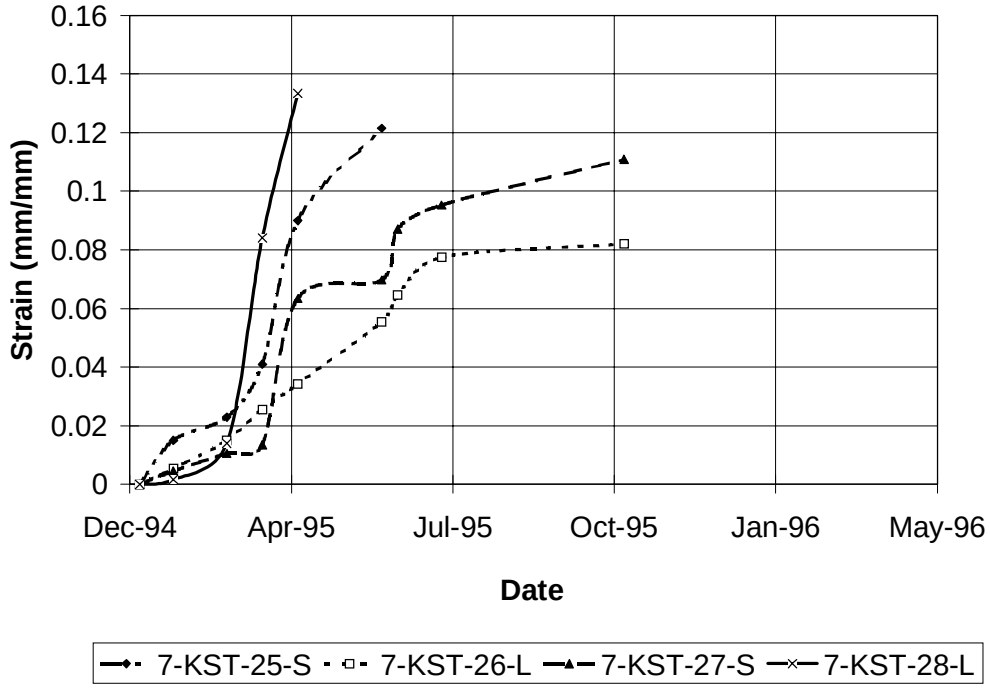


**Figure J 12 Static HMA strain accumulation in section 7.**

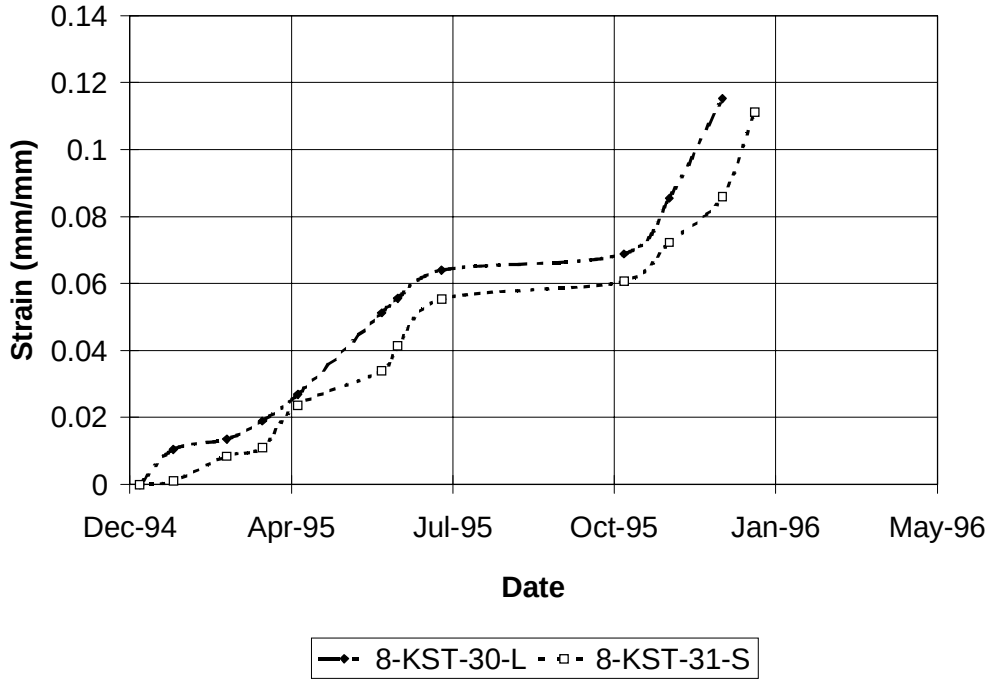


**Figure J 13 Static HMA strain accumulation in section 8.**

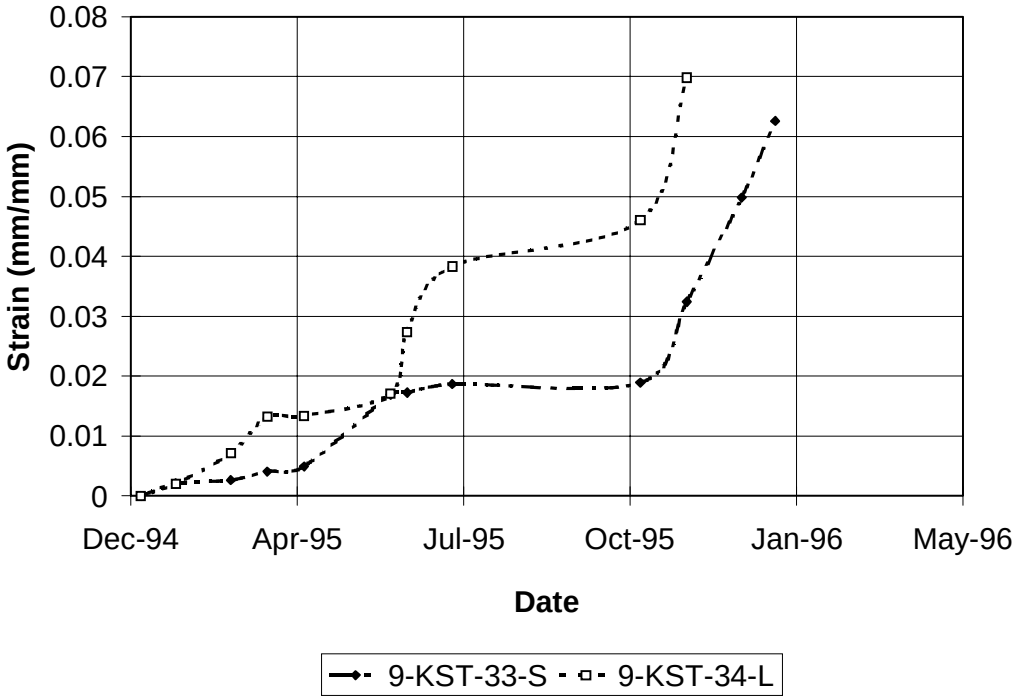


**Figure J 14 Static HMA strain accumulation in section 9.**

# APPENDIX K

# DYNAMIC FIELD DATA

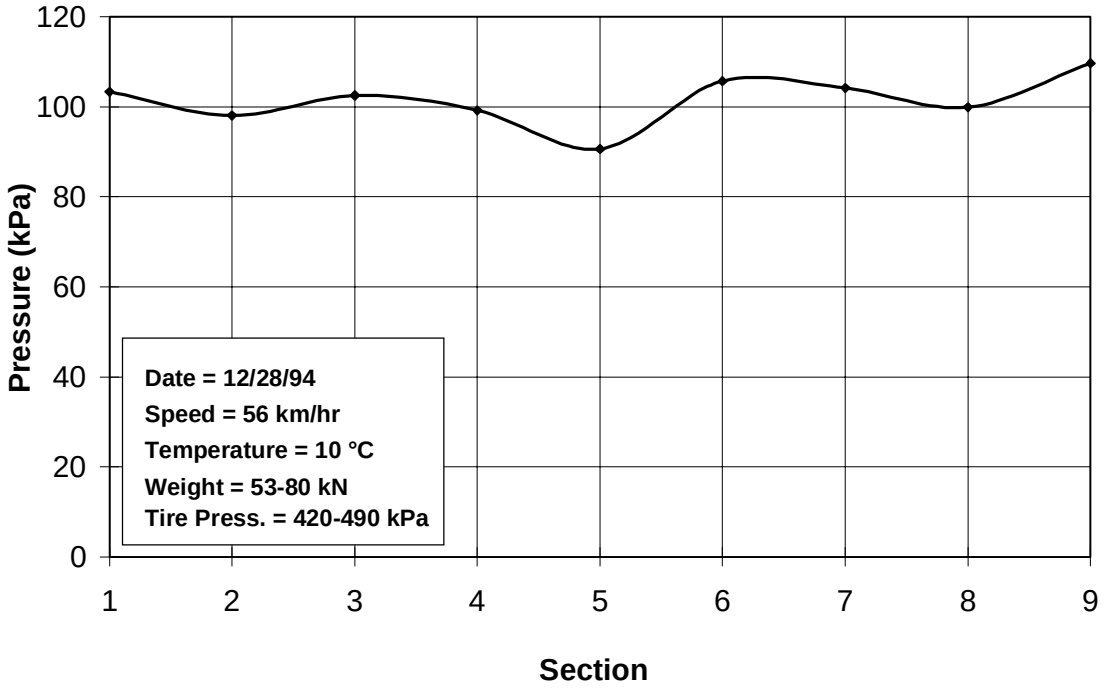


**Figure K 1 Subgrade pressure cell responses through test sections.**

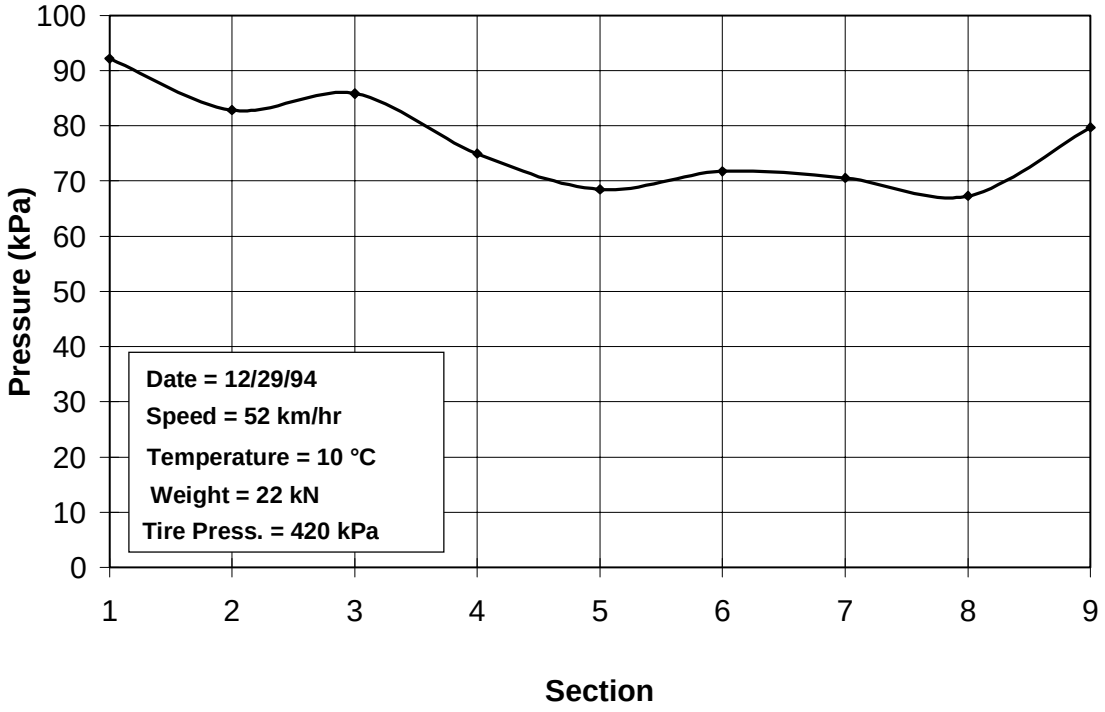


**Figure K 2 Subgrade pressure cell responses through test sections.**

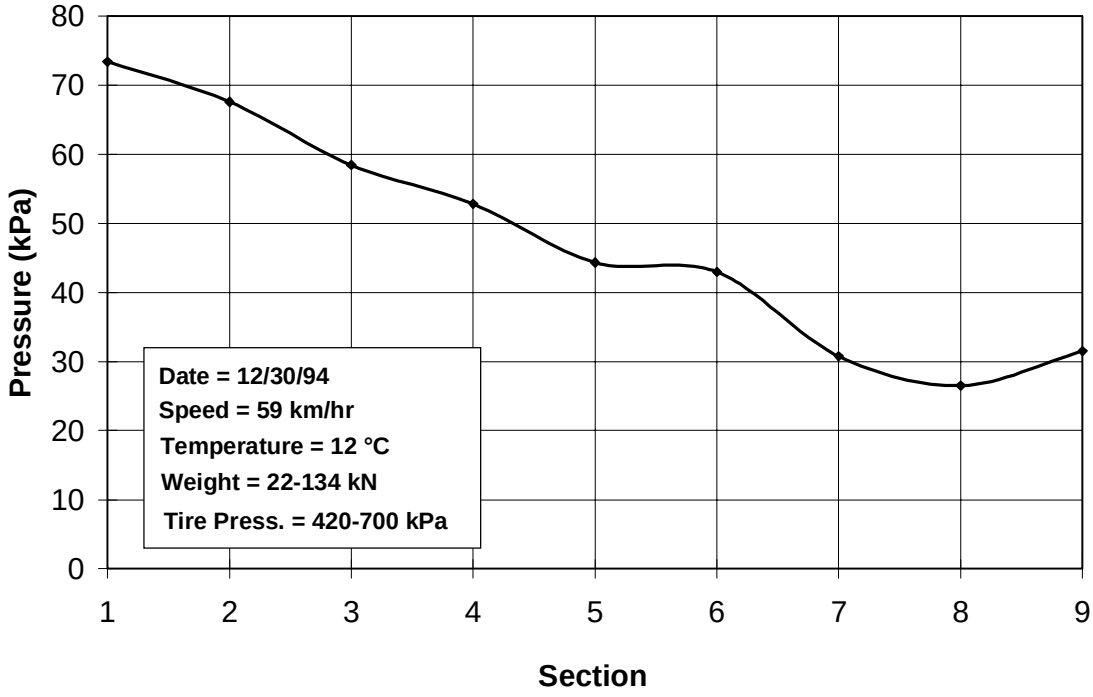


**Figure K 3 Subgrade pressure cell responses through test sections.**

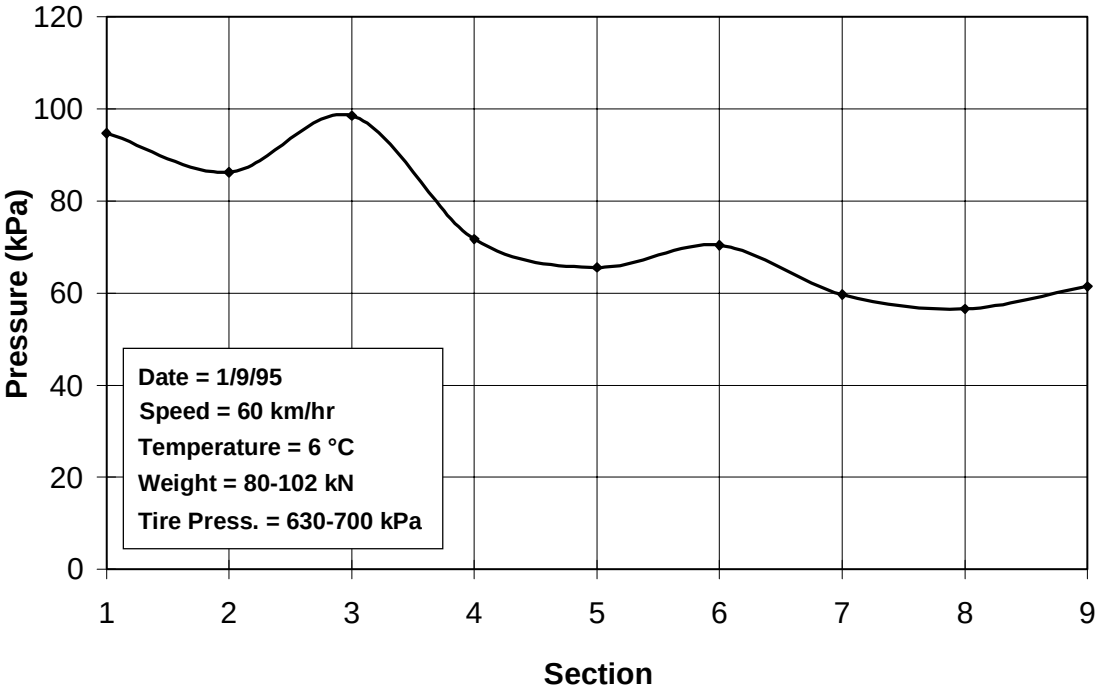


**Figure K 4 Subgrade pressure cell responses through test sections.**

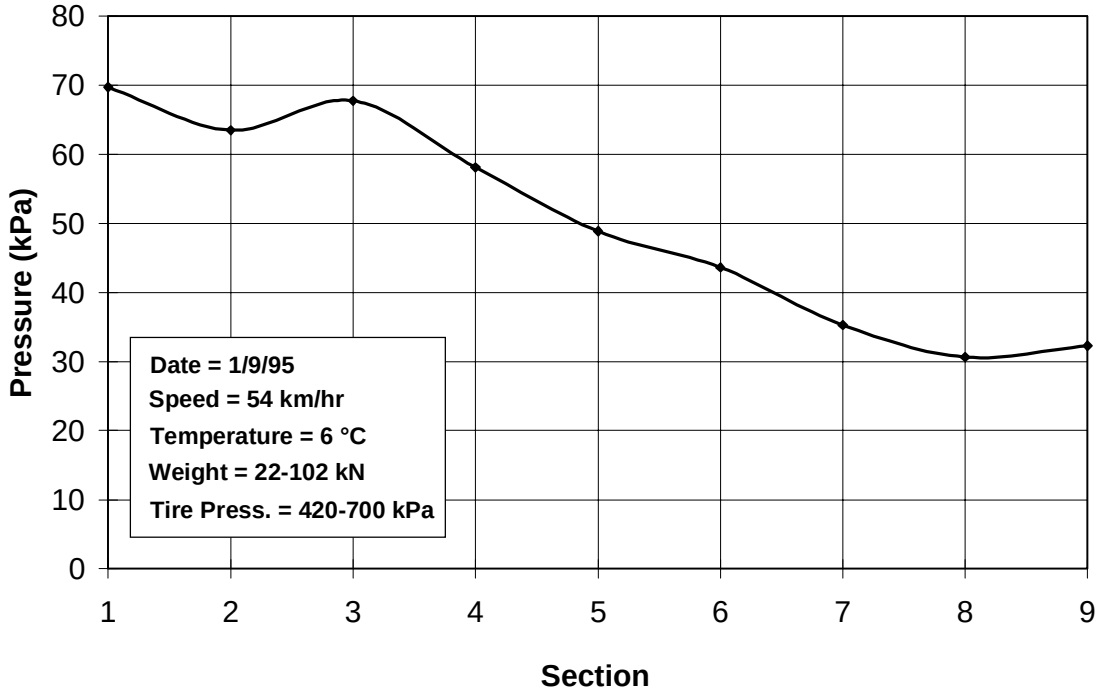


**Figure K 5 Subgrade pressure cell responses through test sections.**

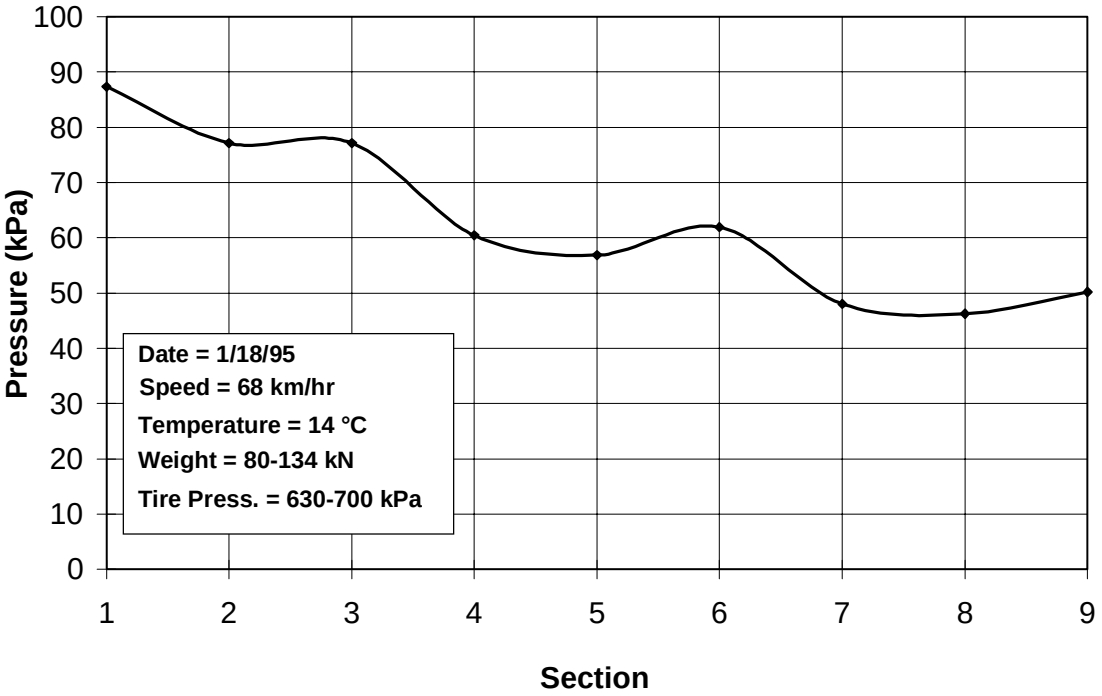


**Figure K 6 Subgrade pressure cell responses through test sections.**

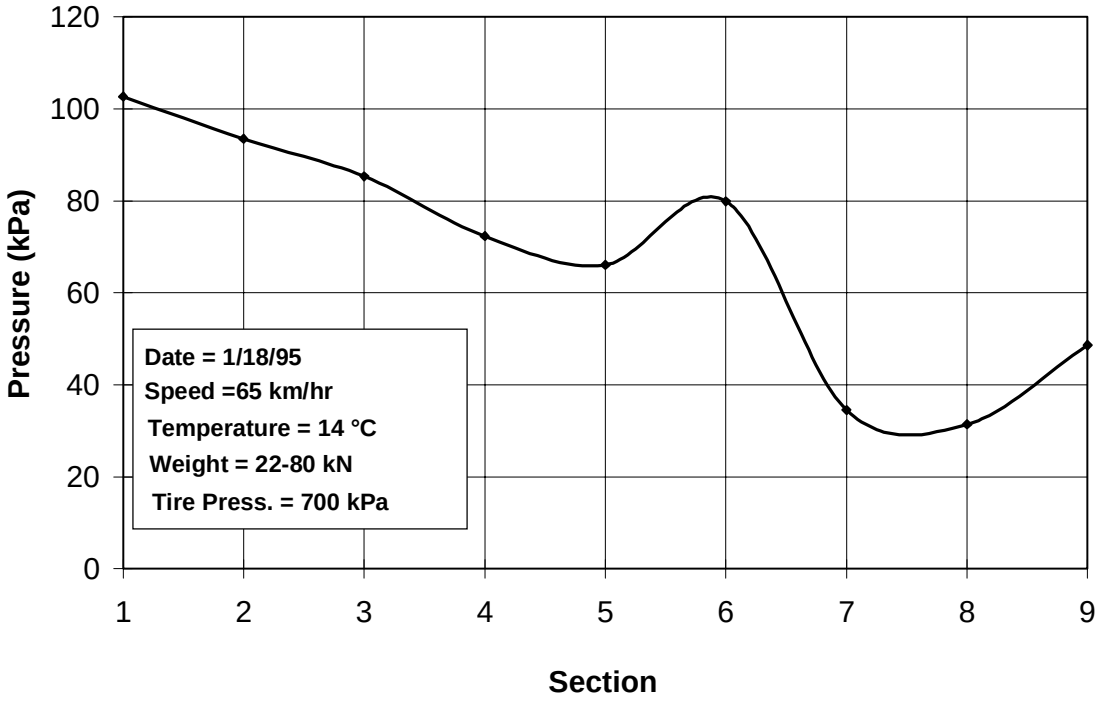


**Figure K 7 Subgrade pressure cell responses through test sections.**

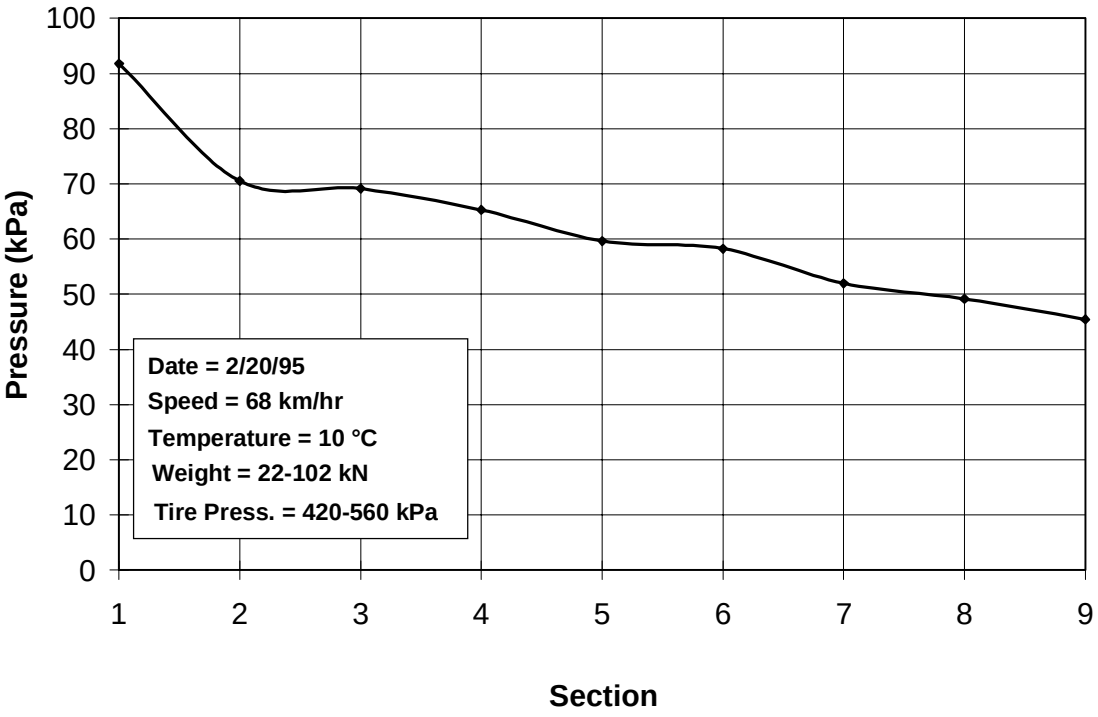


**Figure K 8 Subgrade pressure cell responses through test sections.**

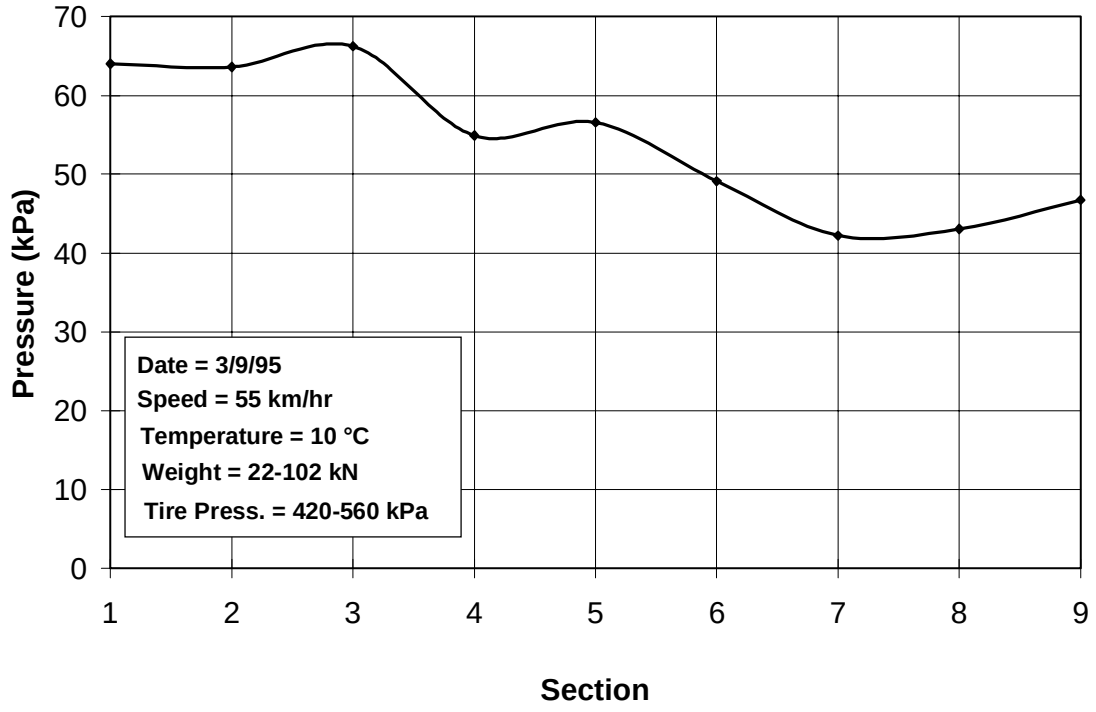


**Figure K 9 Subgrade pressure cell responses through test sections.**

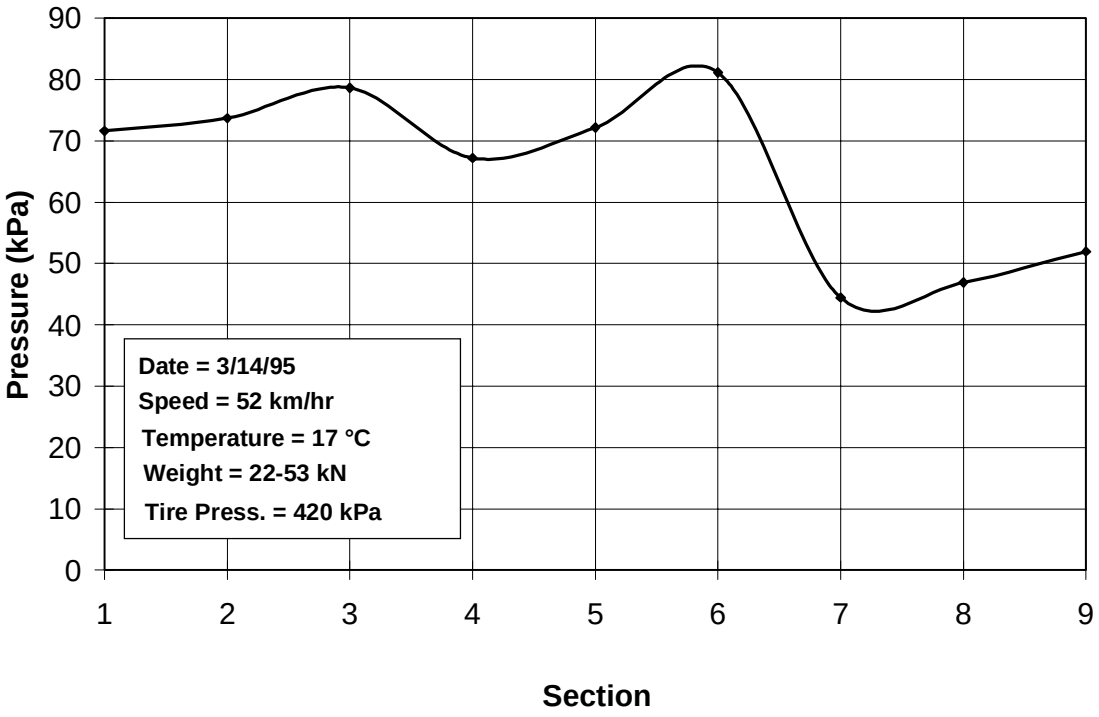


**Figure K 10 Subgrade pressure cell responses through test sections.**

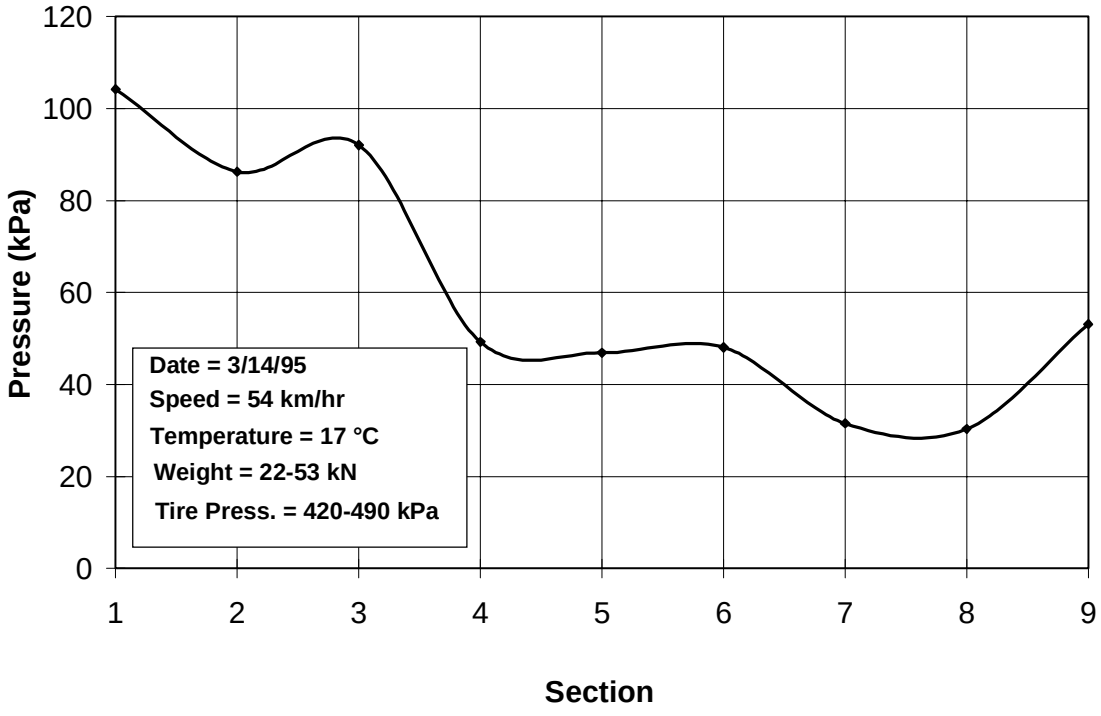


**Figure K 11 Subgrade pressure cell responses through test sections.**

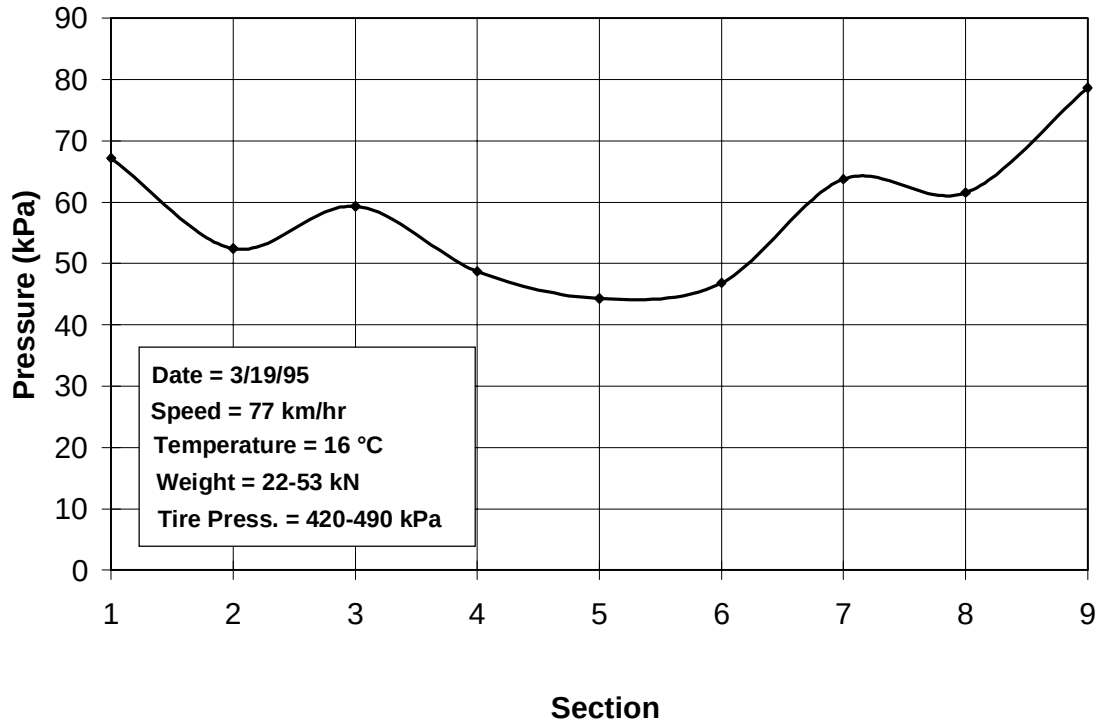


**Figure K 12 Subgrade pressure cell responses through test sections.**

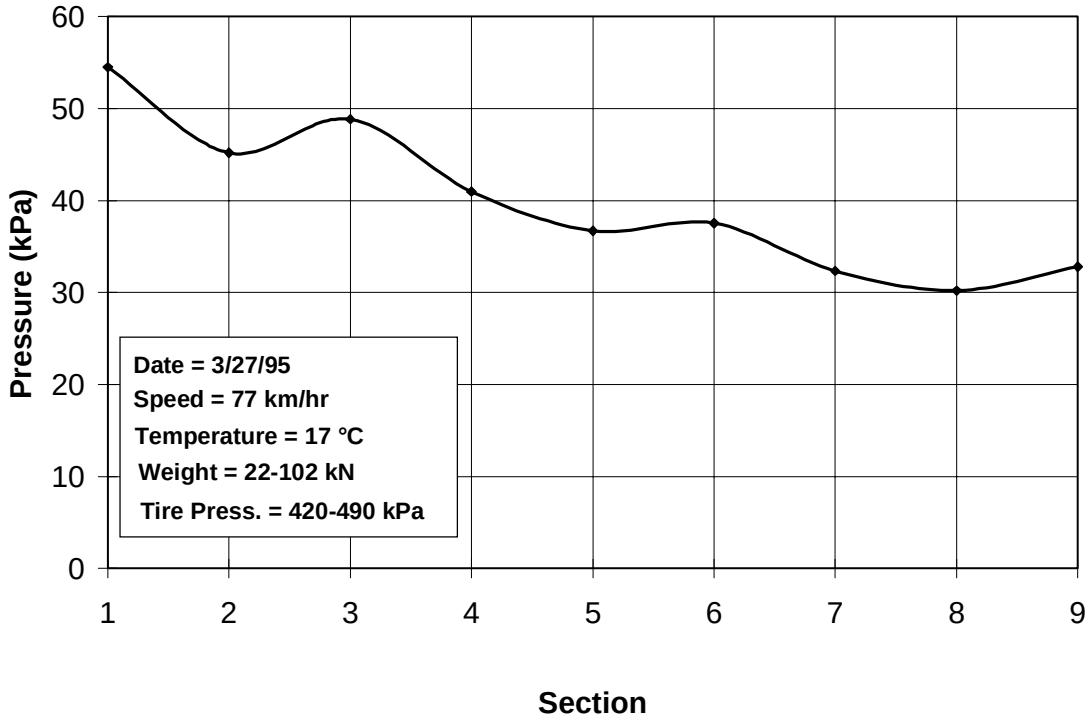


**Figure K 13 Subgrade pressure cell responses through test sections.**

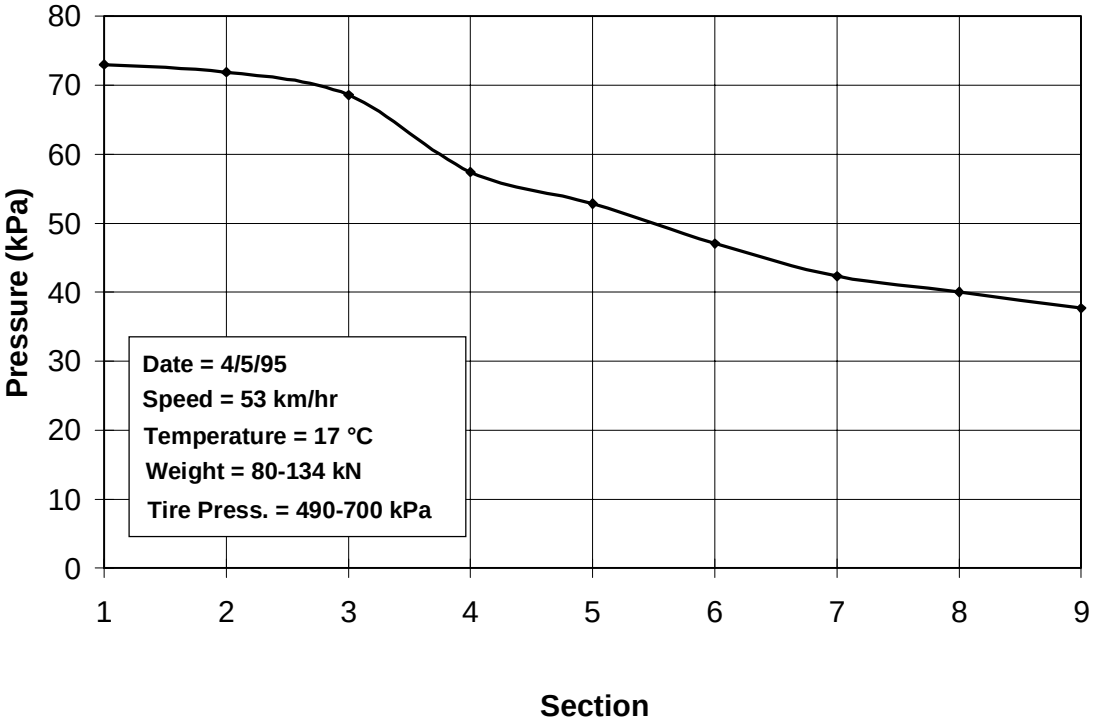


**Figure K 14 Subgrade pressure cell responses through test sections.**

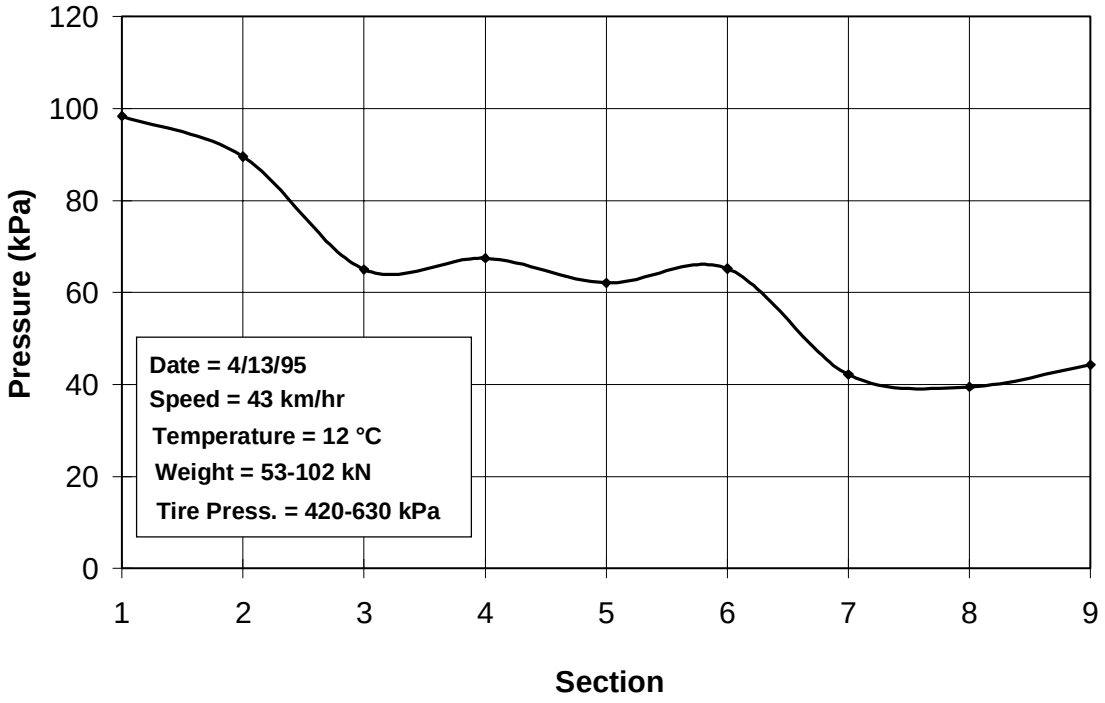


**Figure K 15 Subgrade pressure cell responses through test sections.**

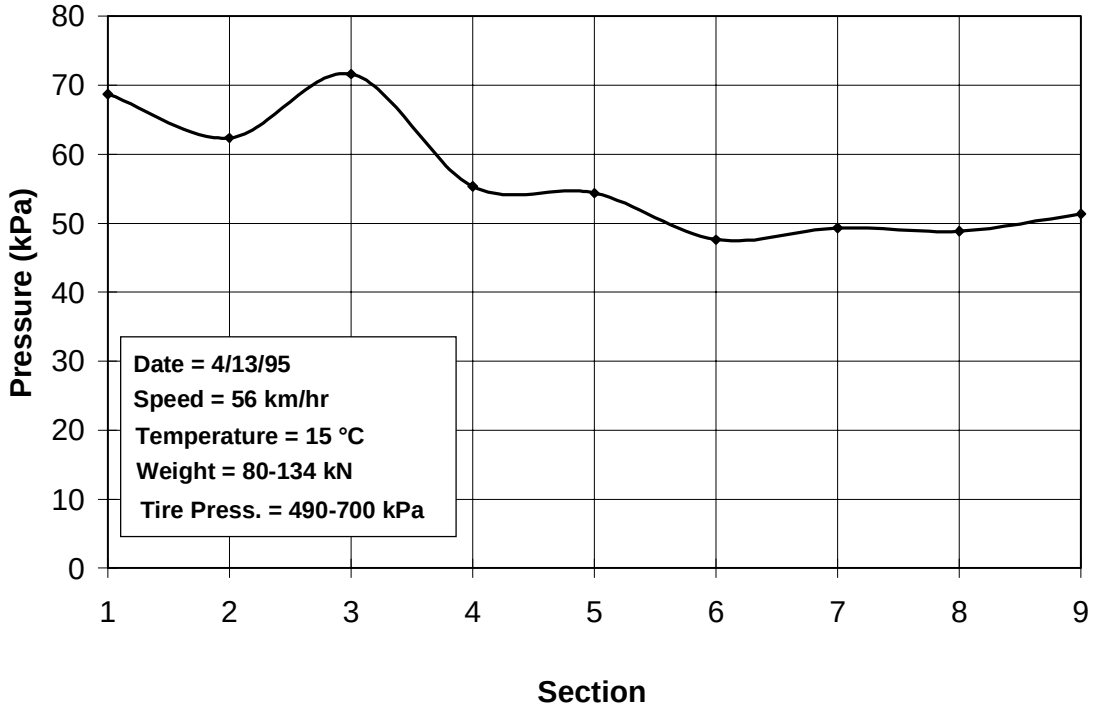


**Figure K 16 Subgrade pressure cell responses through test sections.**

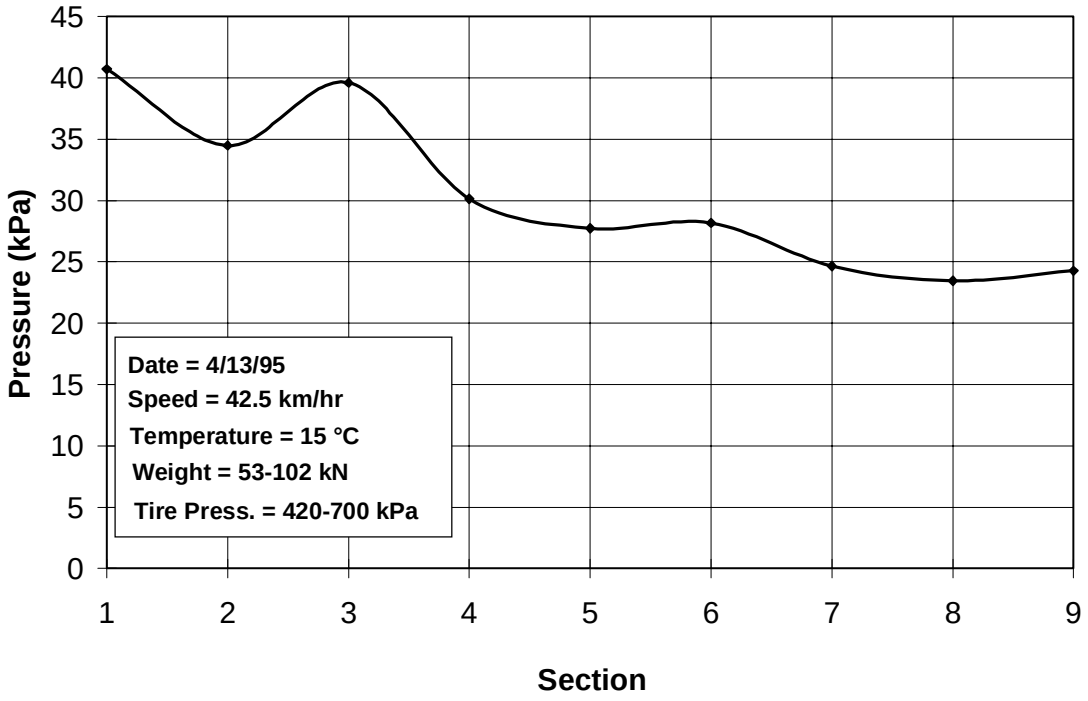


**Figure K 17 Subgrade pressure cell responses through test sections.**

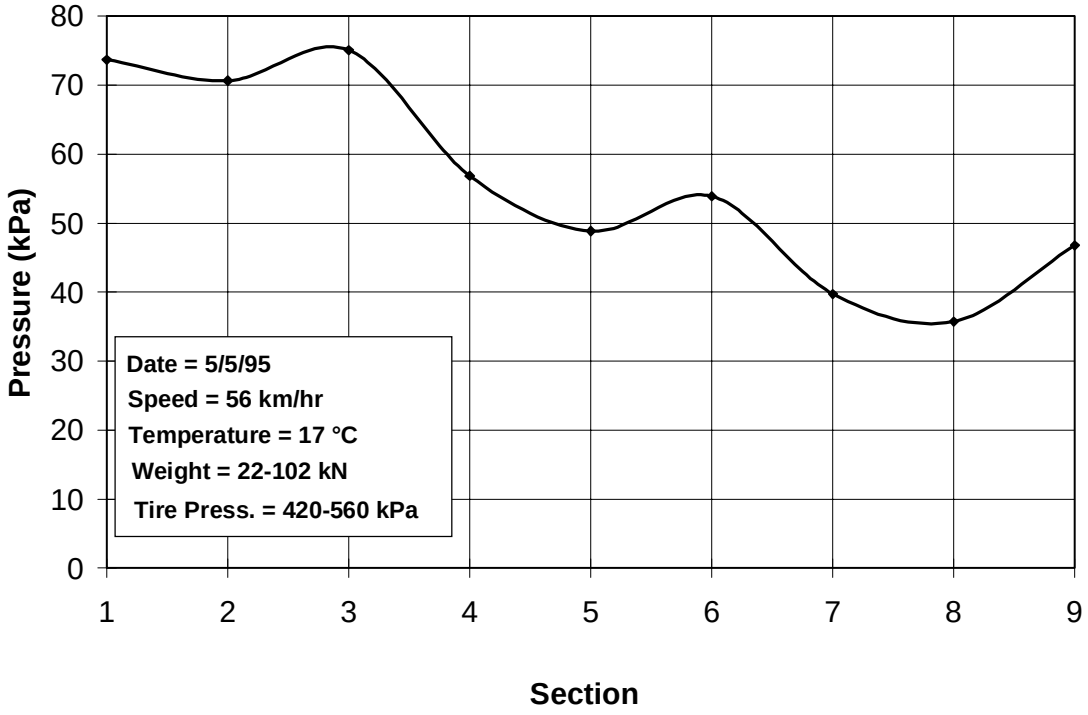


**Figure K 18 Subgrade pressure cell responses through test sections.**

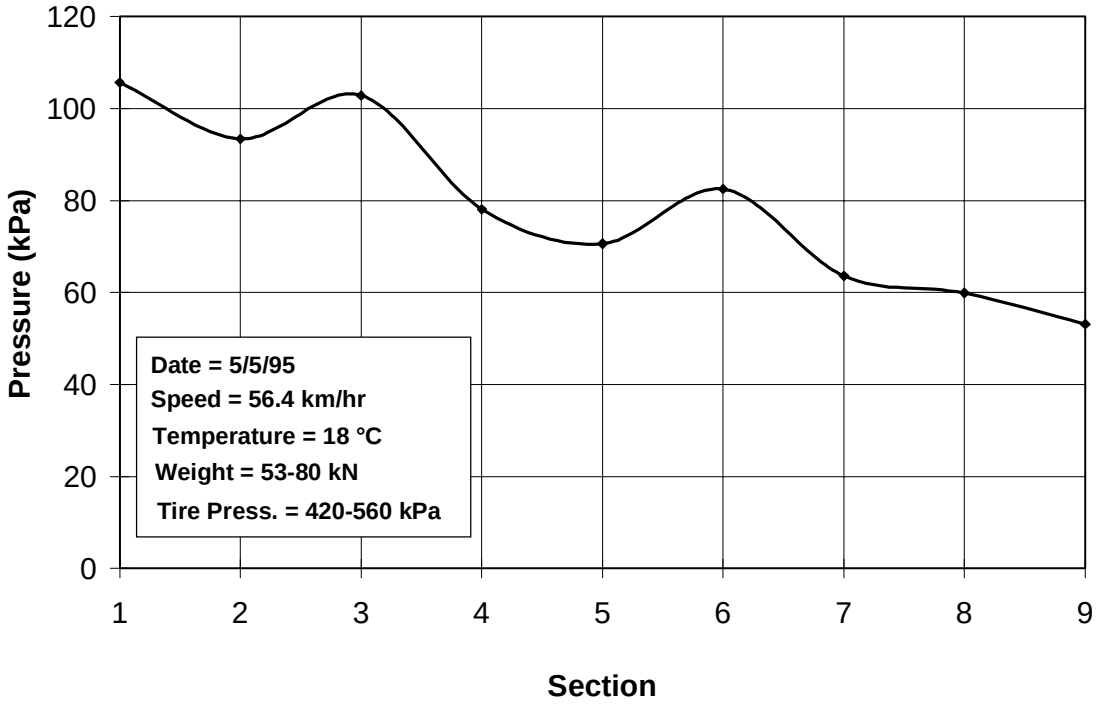


**Figure K 19 Subgrade pressure cell responses through test sections.**

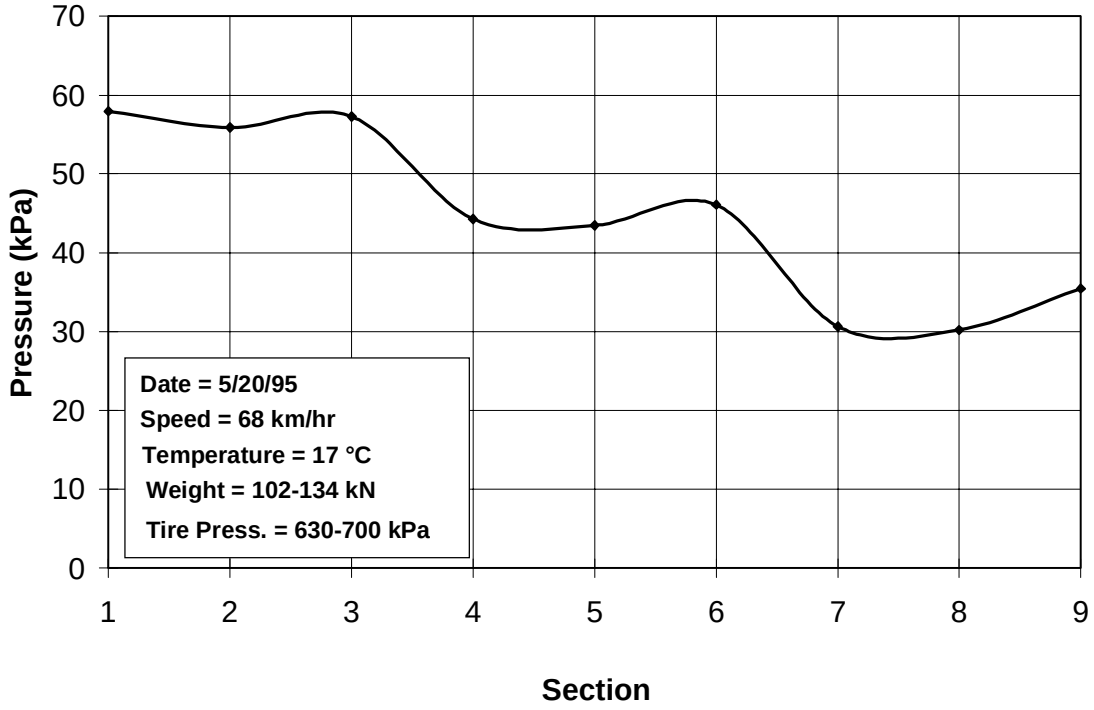


**Figure K 20 Subgrade pressure cell responses through test sections.**

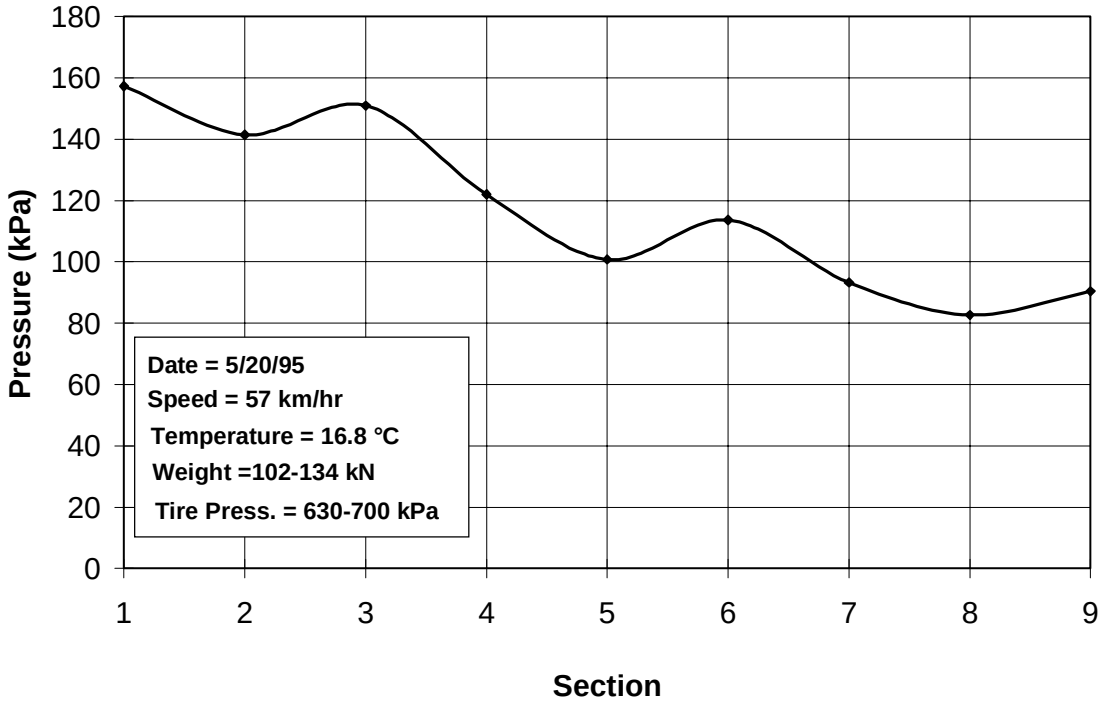


**Figure K 21 Subgrade pressure cell responses through test sections.**

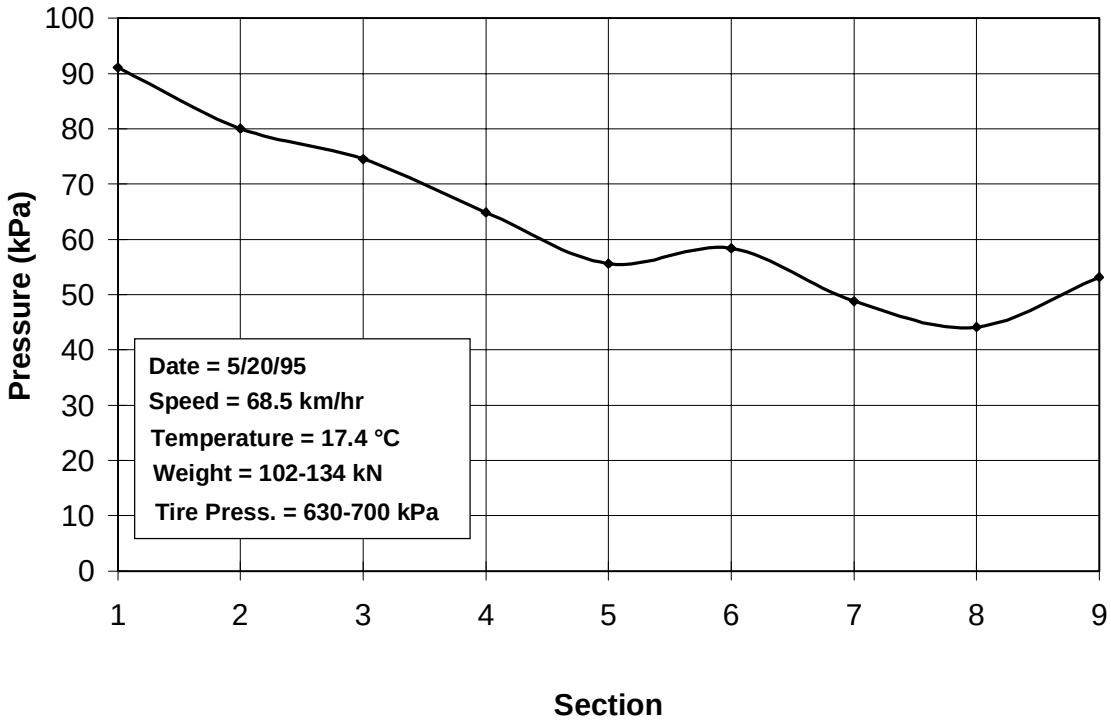


**Figure K 22 Subgrade pressure cell responses through test sections.**

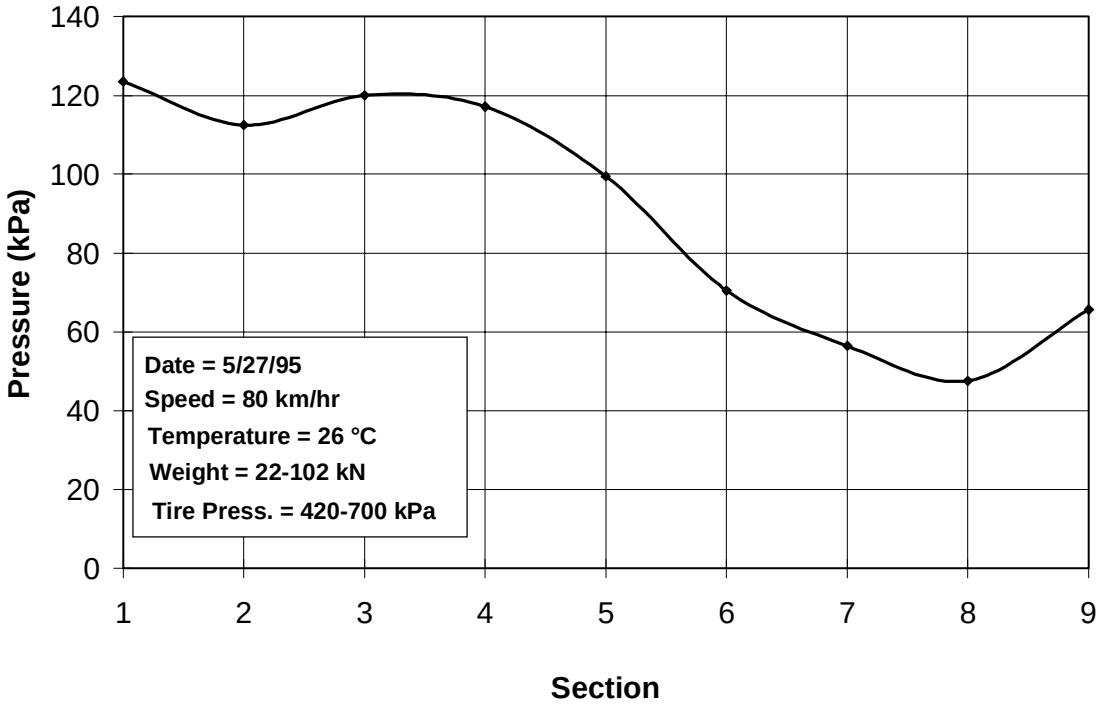


**Figure K 23 Subgrade pressure cell responses through test sections.**

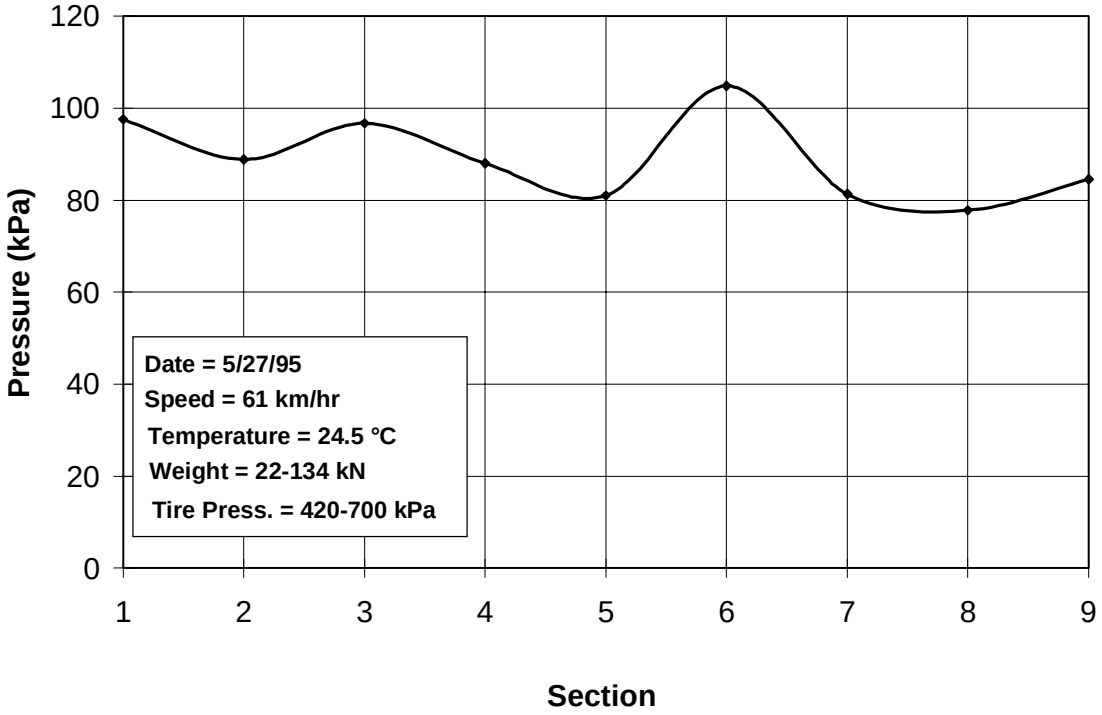


**Figure K 24 Subgrade pressure cell responses through test sections.**

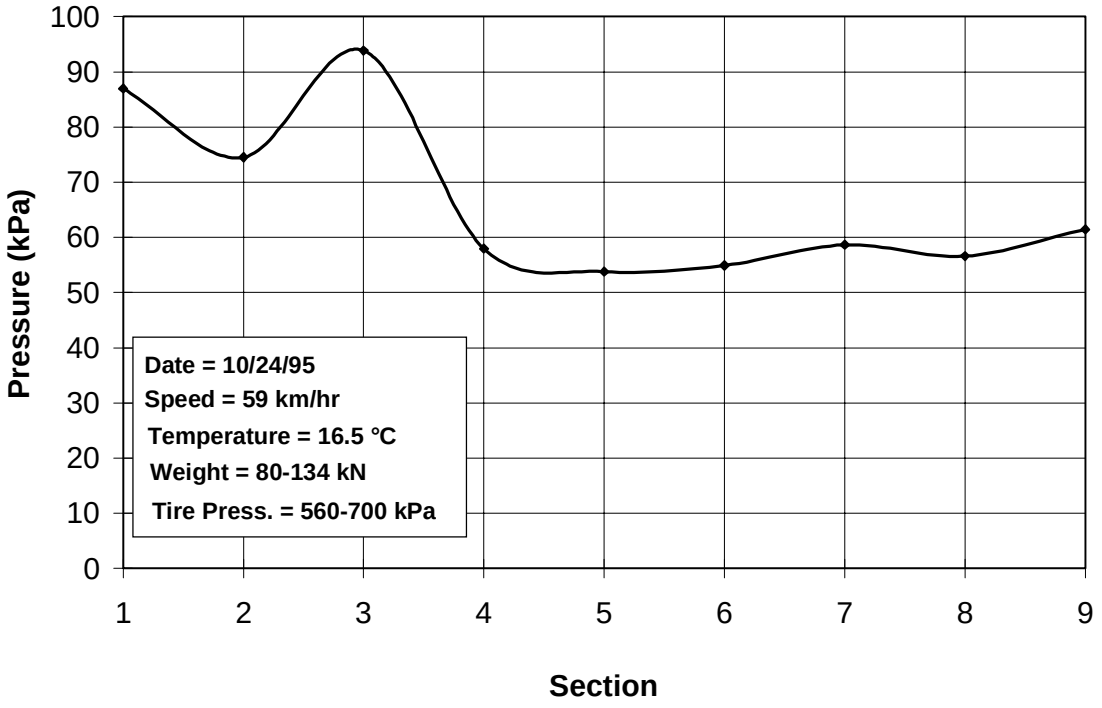


**Figure K 25 Subgrade pressure cell responses through test sections.**

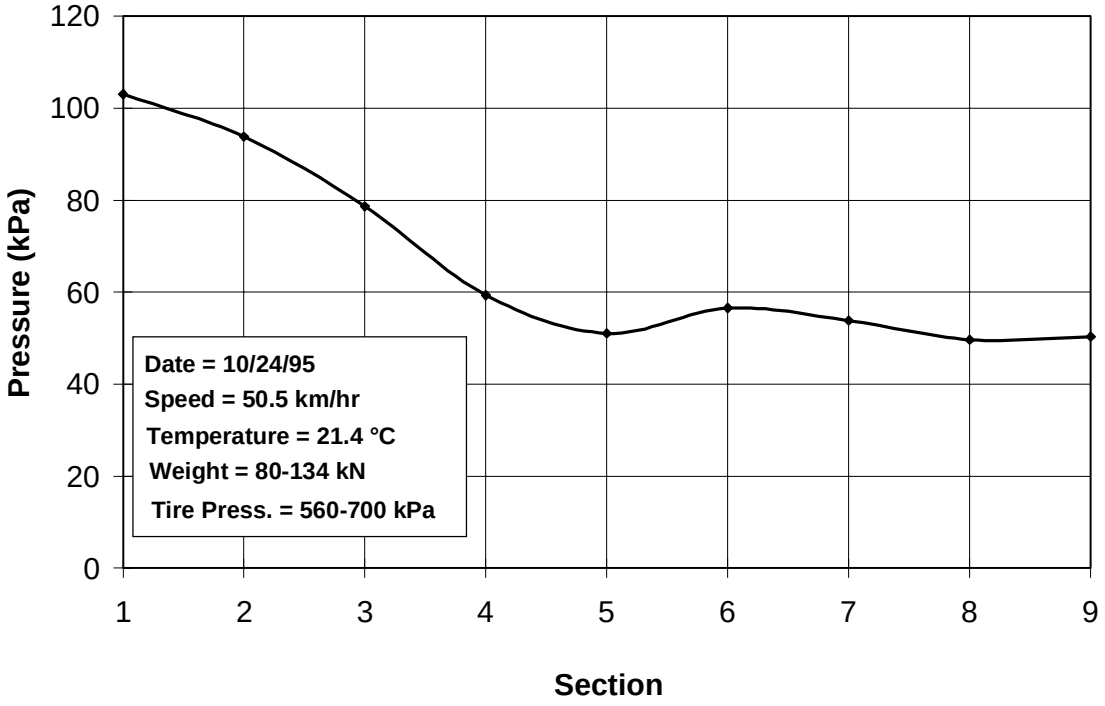


**Figure K 26 Subgrade pressure cell responses through test sections.**

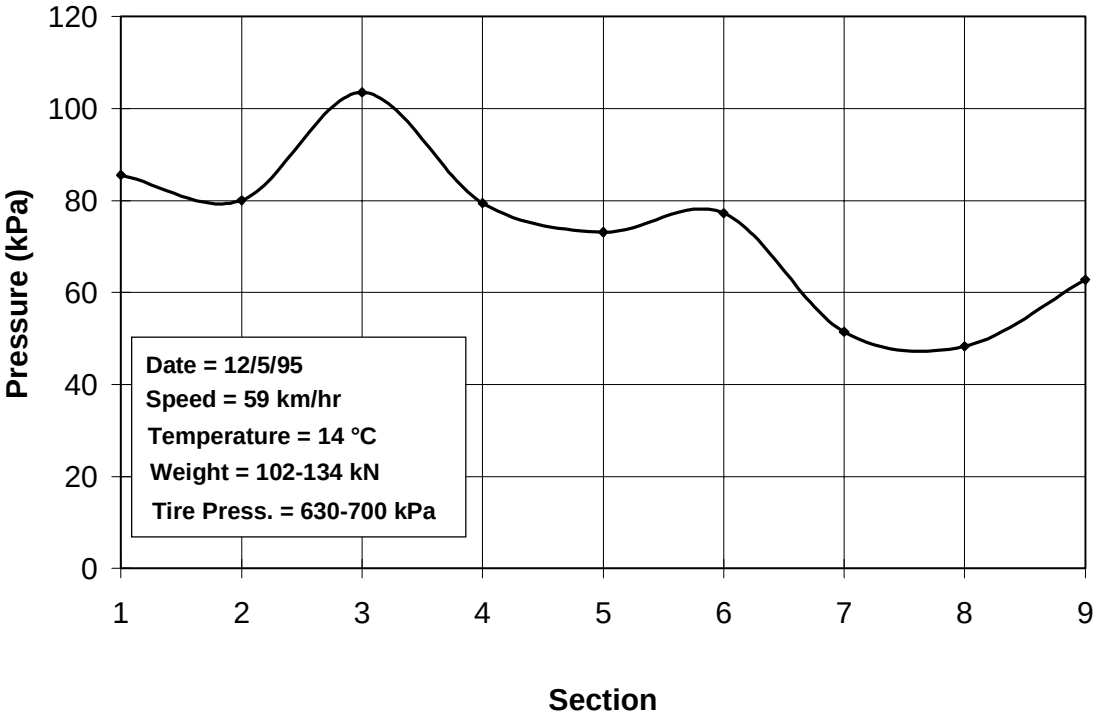


**Figure K 27 Subgrade pressure cell responses through test sections.**

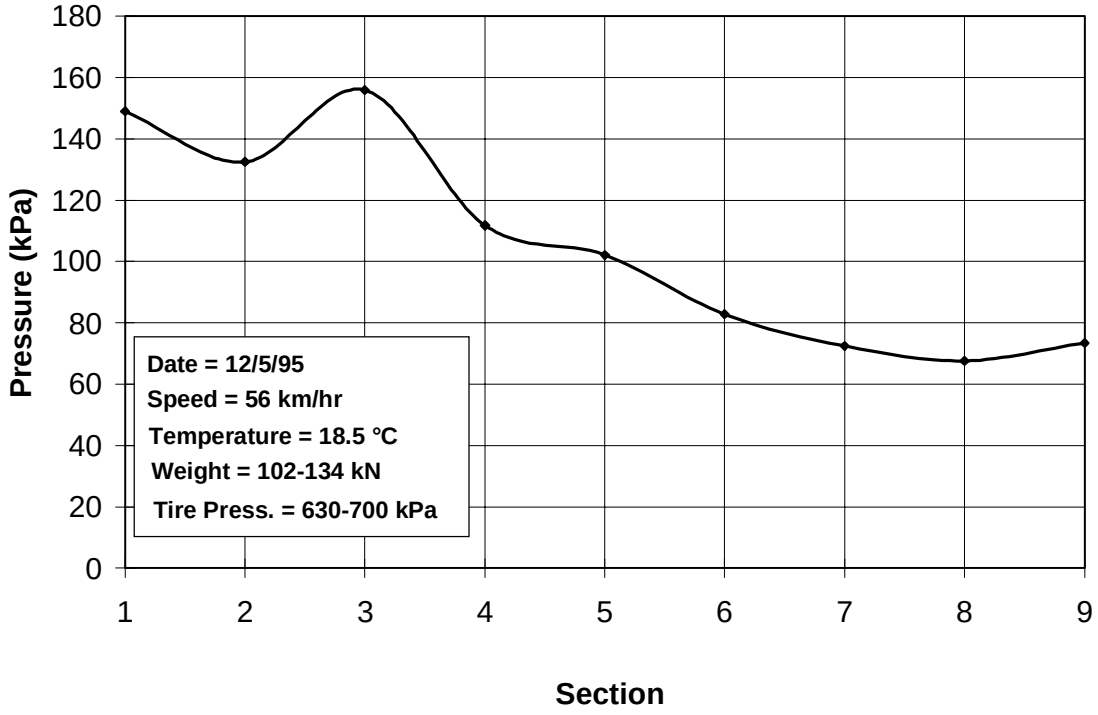


**Figure K 28 Subgrade pressure cell responses through test sections.**

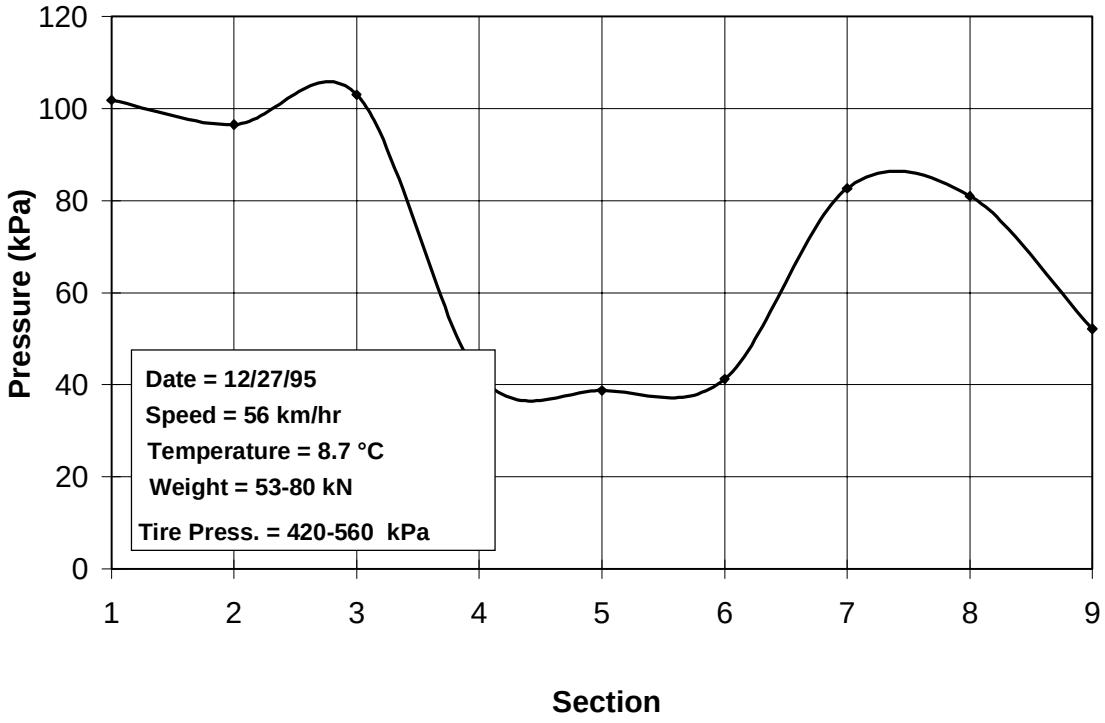


**Figure K 29 Subgrade pressure cell responses through test sections.**

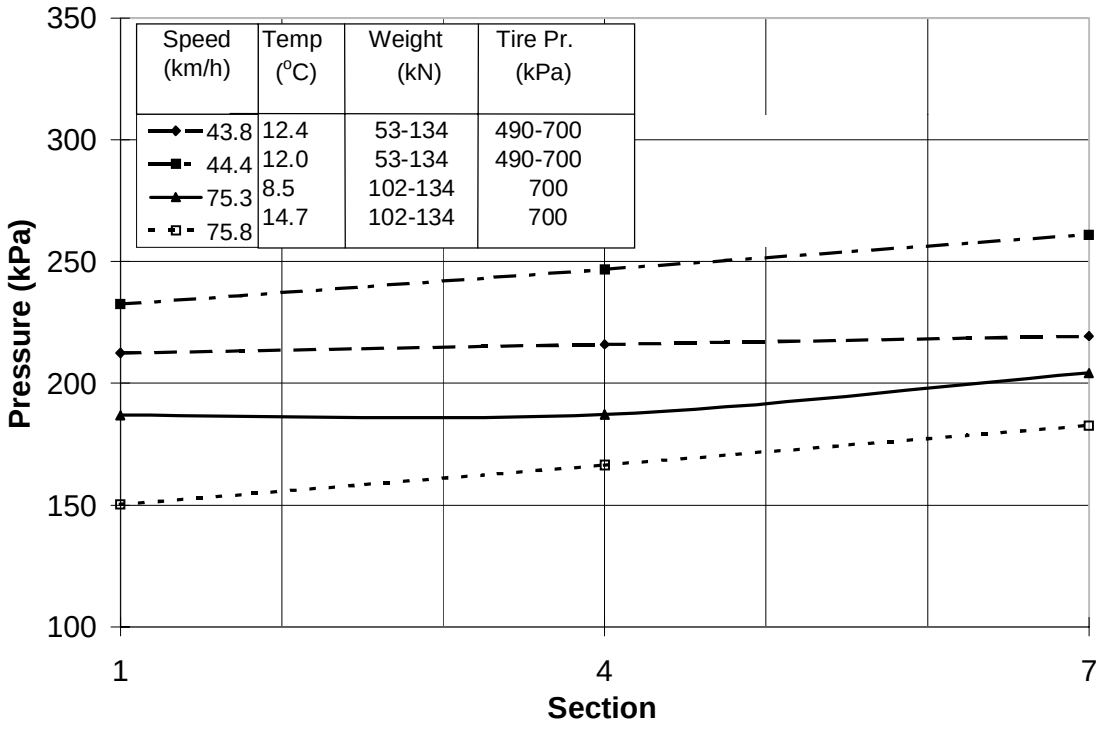


**Figure K 30 Base course pressure cell responses for sections 1, 4, and 7 (December 1994).**

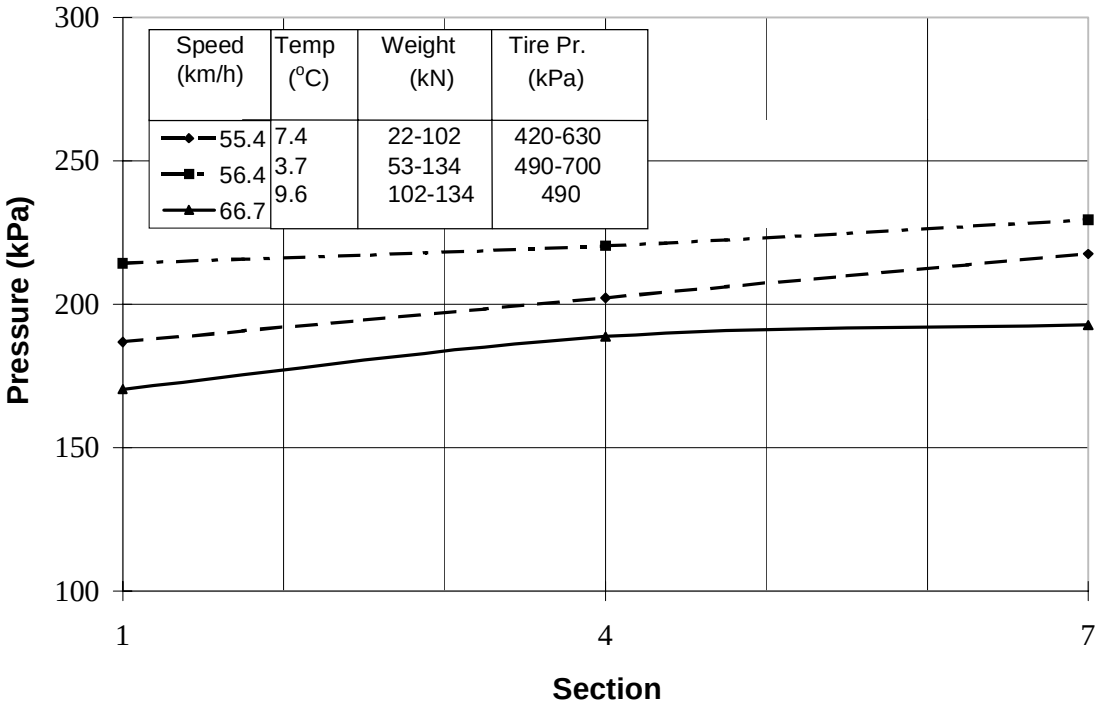


**Figure K 31 Base course pressure cell responses for sections 1, 4, and 7 (January 1995).**

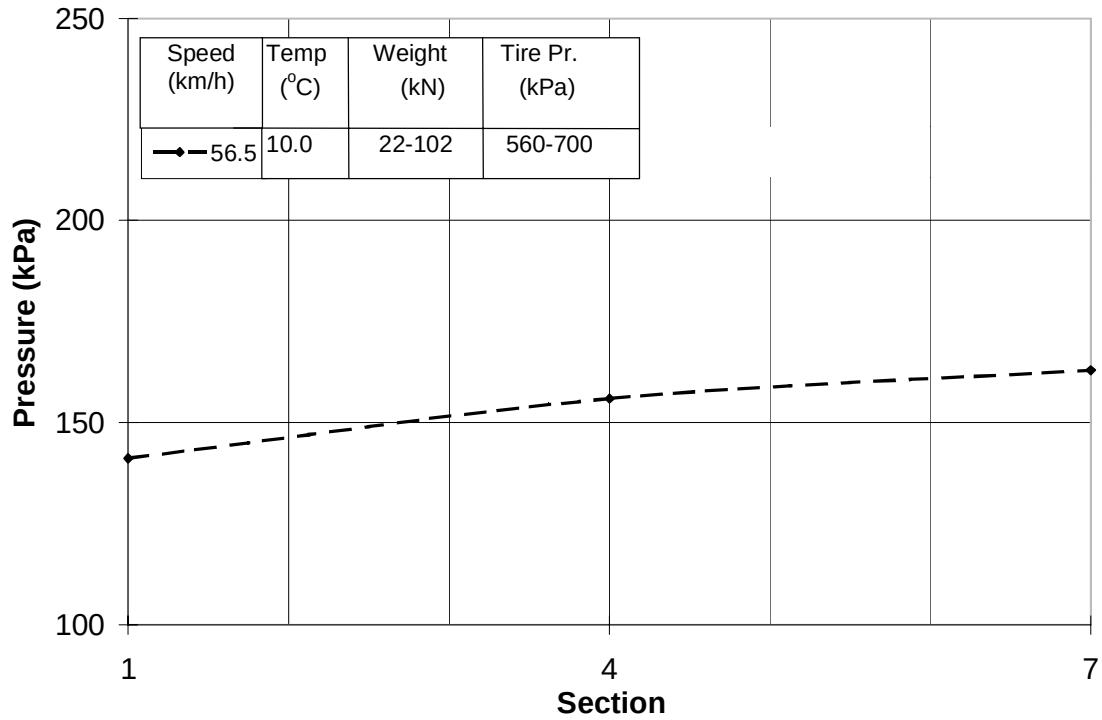


**Figure K 32 Base course pressure cell responses for sections 1, 4, and 7 (February 1995).**

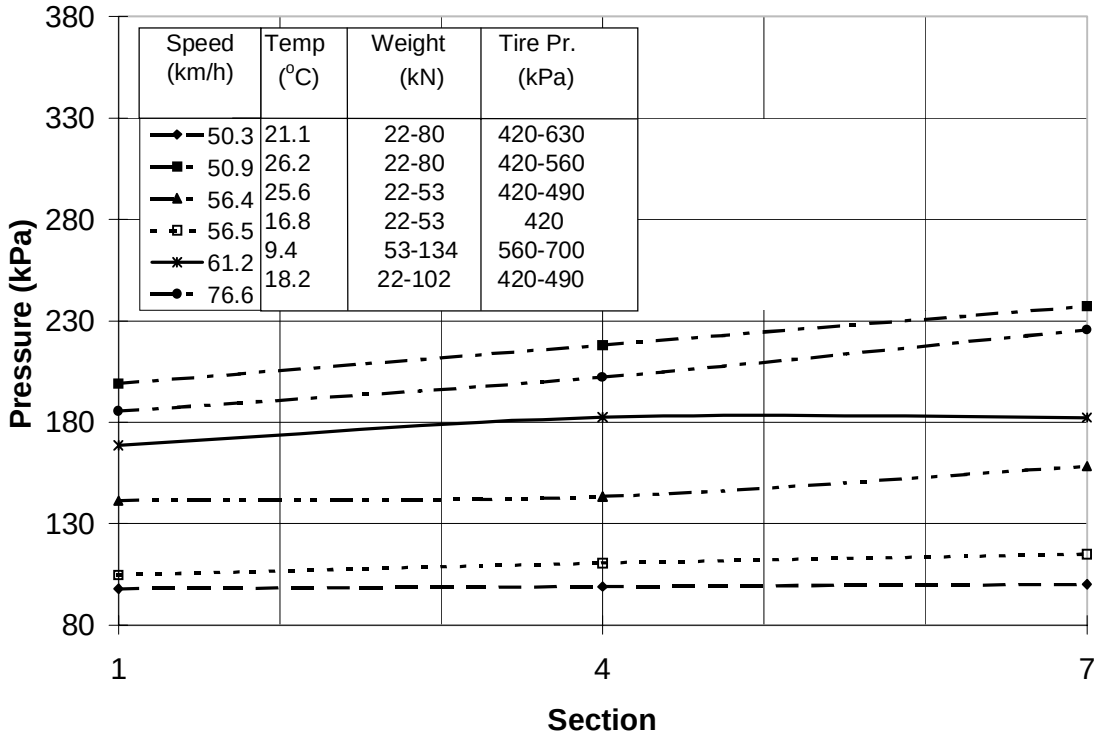


**Figure K 33 Base course pressure cell responses for sections 1, 4, and 7 (March 1995).**

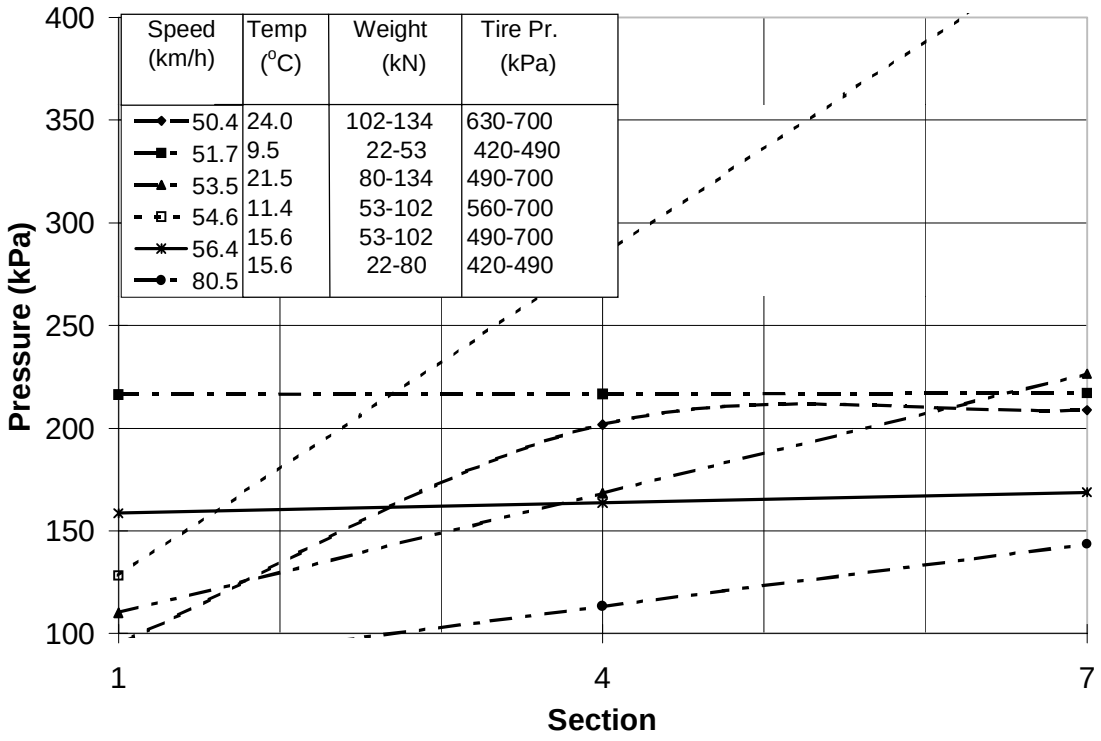


**Figure K 34 Base course pressure cell responses for sections 1, 4, and 7 (April 1995).**

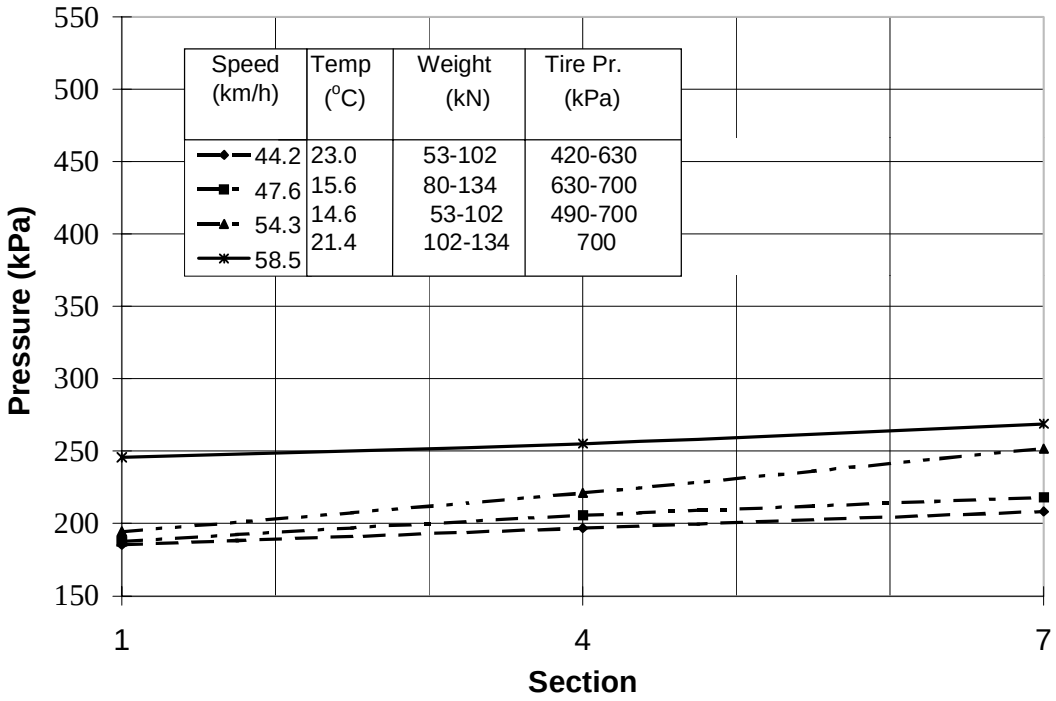


**Figure K 35 Base course pressure cell responses for sections 1, 4, and 7 (June 1995).**

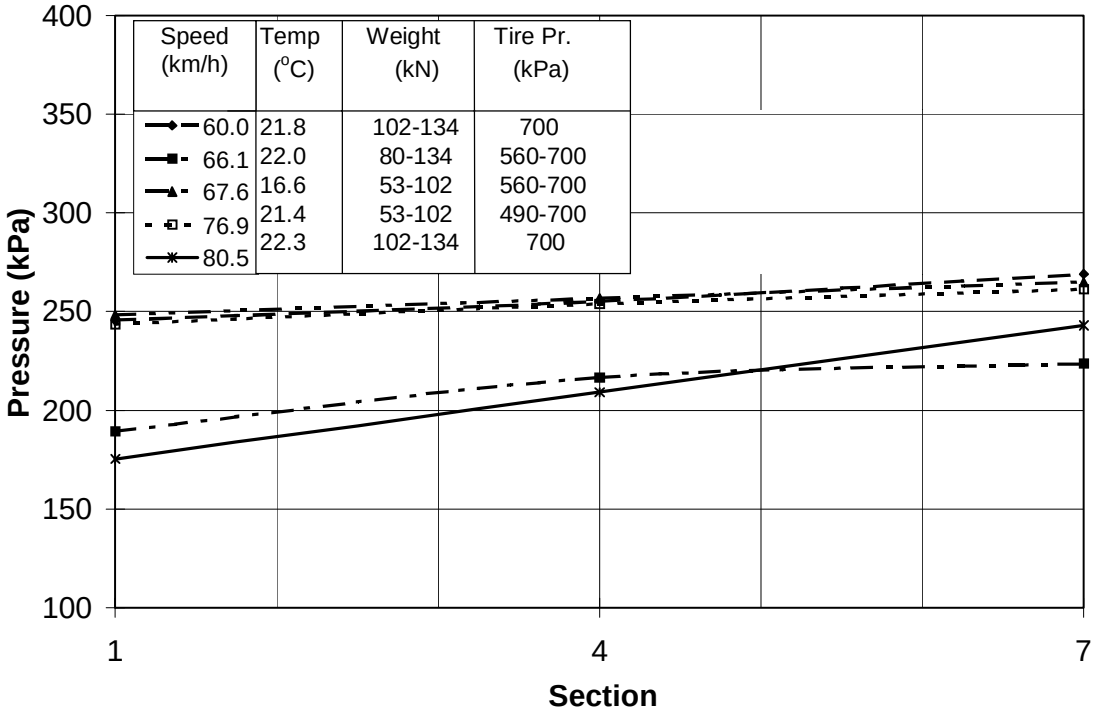


**Figure K 36 Base course pressure cell responses for sections 1, 4, and 7 (June 1995).**

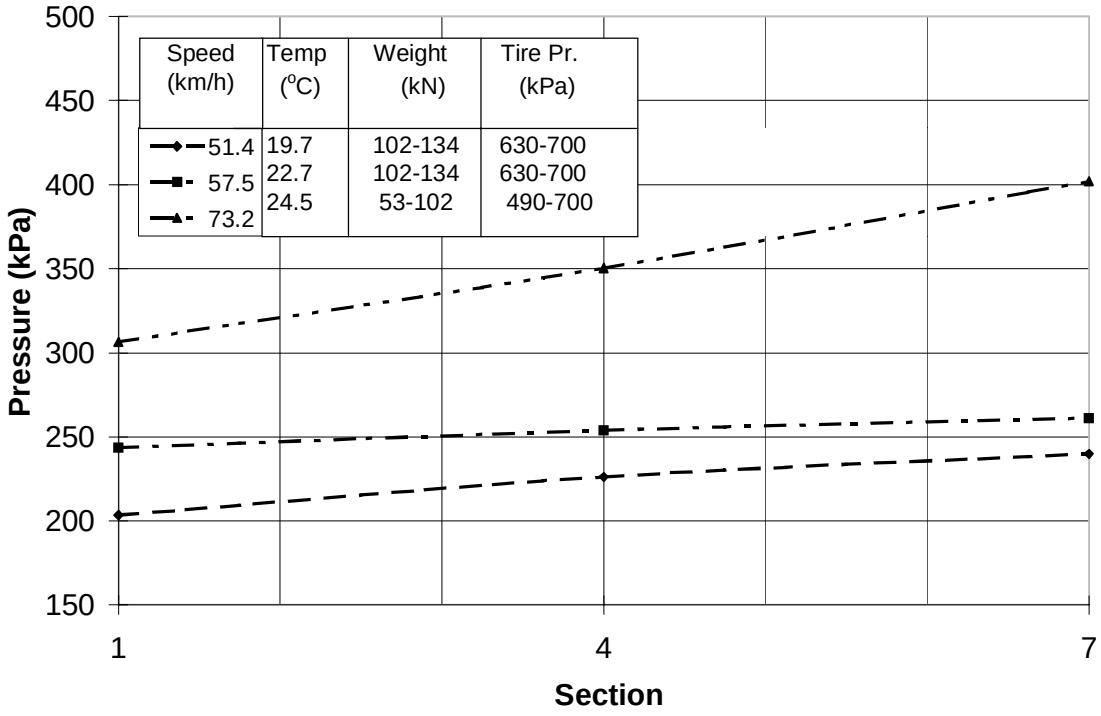


**Figure K 37 Base course pressure cell responses for sections 1, 4, and 7 (October 1995).**

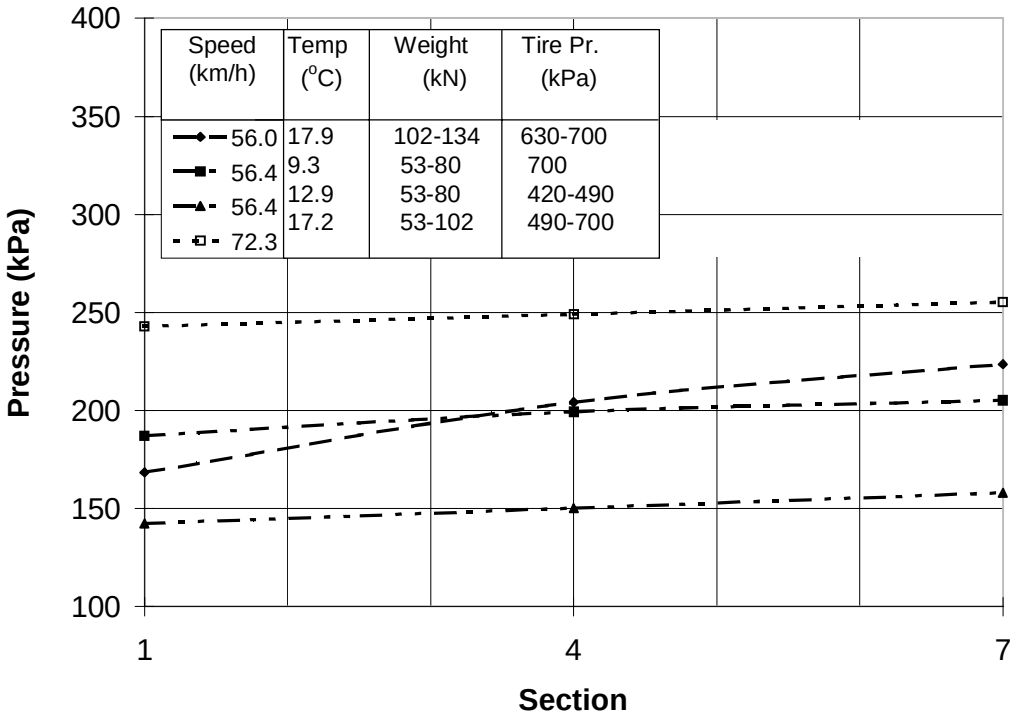


**Figure K 38 Base course pressure cell responses for sections 1, 4, and 7 (December 1995).**

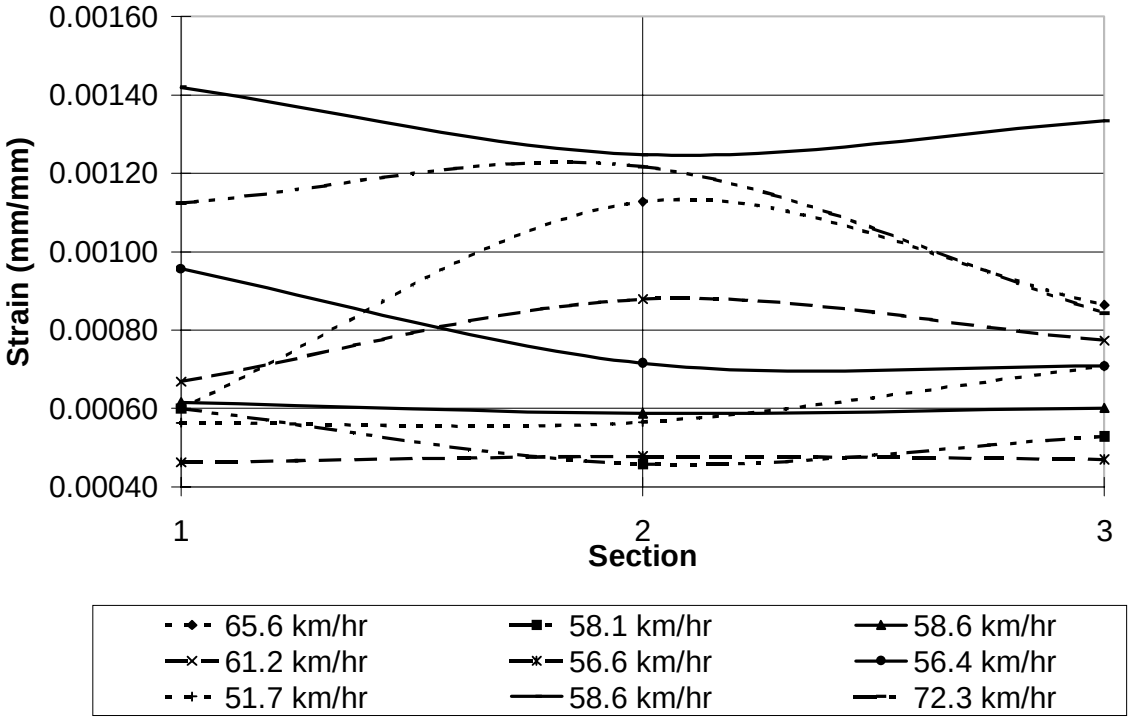


**Figure K 39 HMA strain in sections 1, 2, and 3 (**longitudinal **direction).**

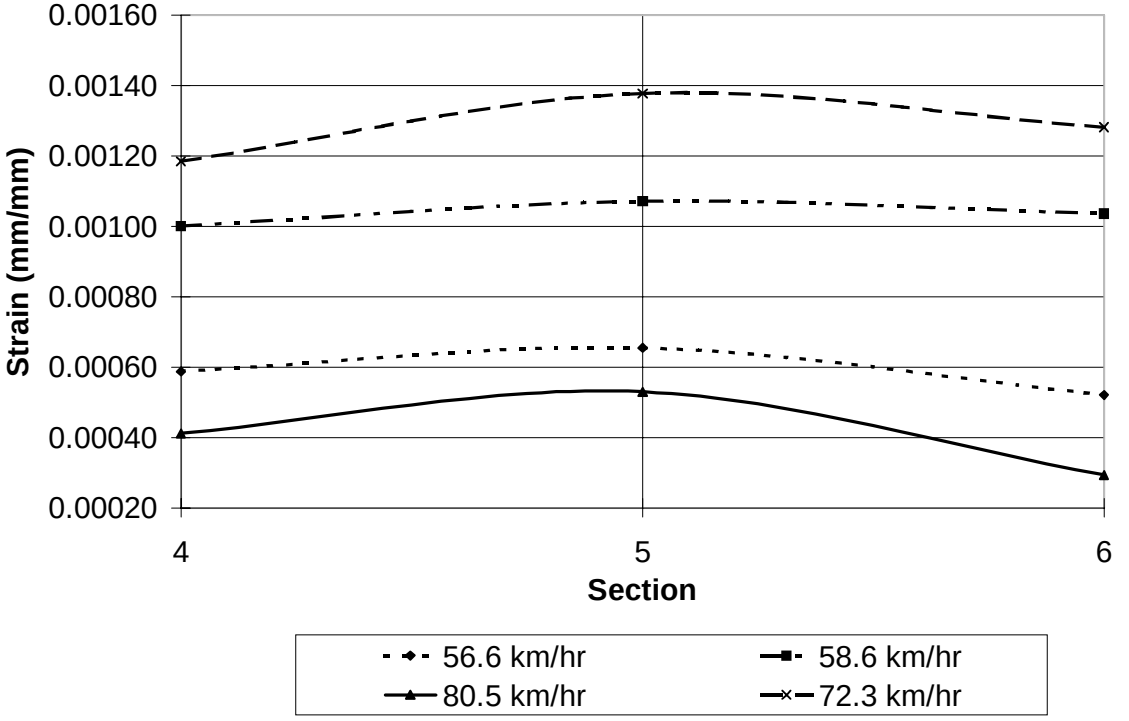


**Figure K 40 HMA strain in sections 4, 5, and 6 (longitudinal direction).**

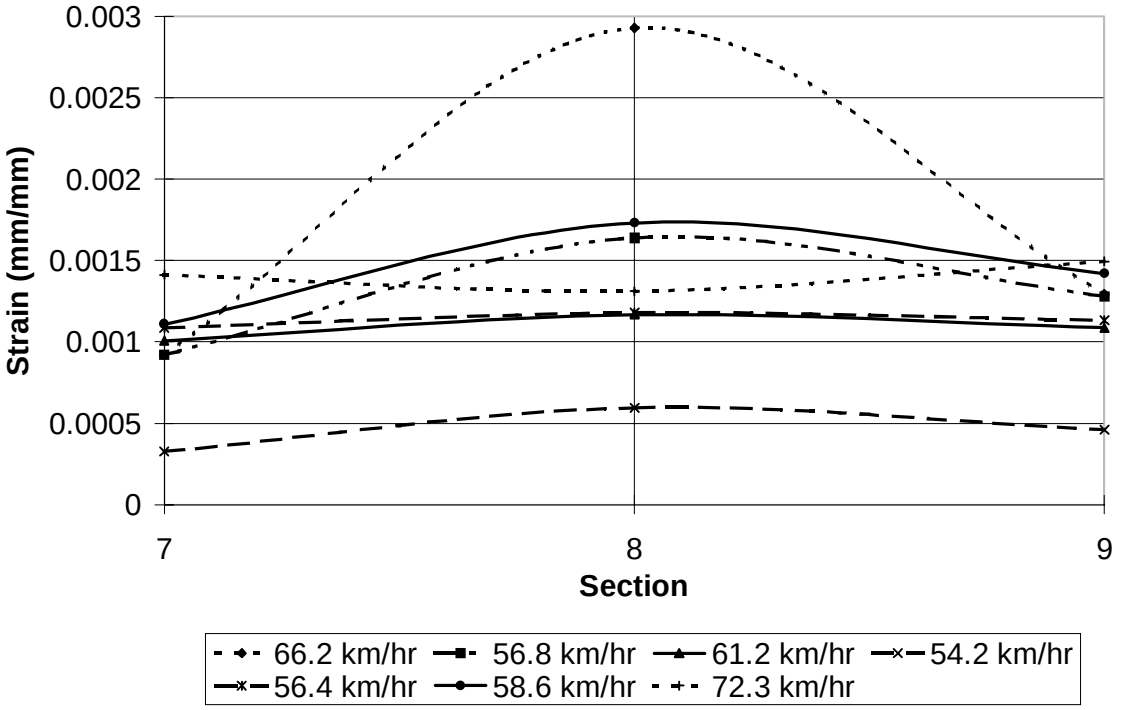


**Figure K 41 HMA strain in sections 6, 7, and 8 (longitudinal direction).**

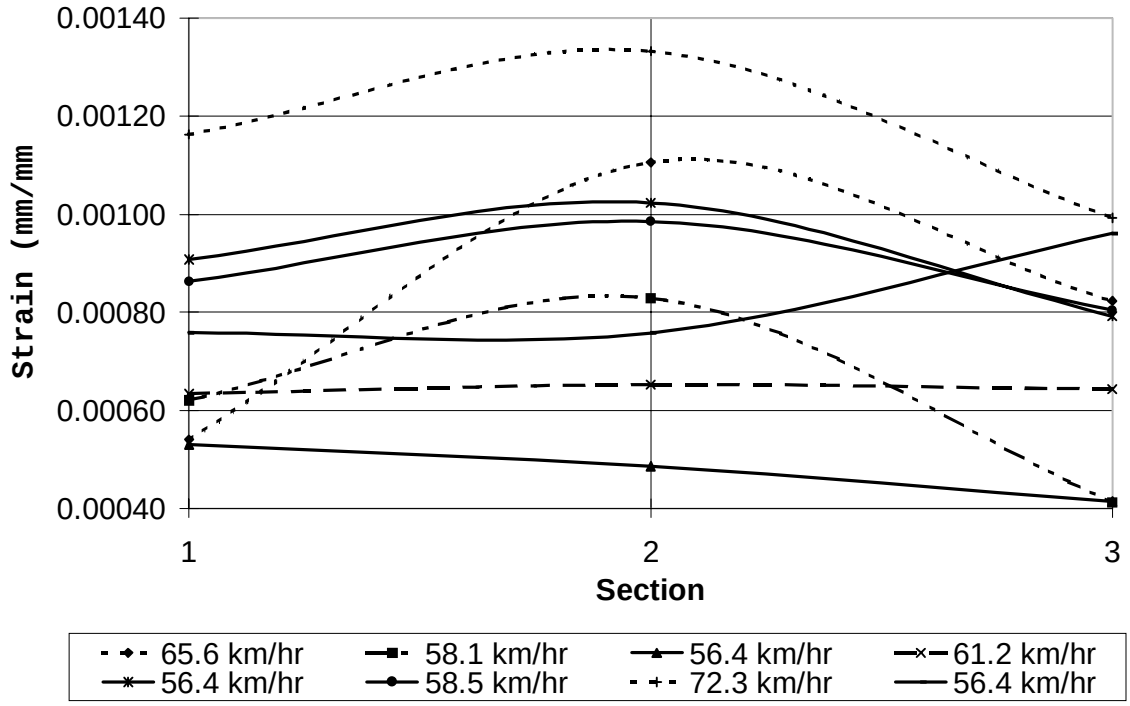


**Figure K 42 HMA strain in sections 1, 2, and 3 (transverse direction).**

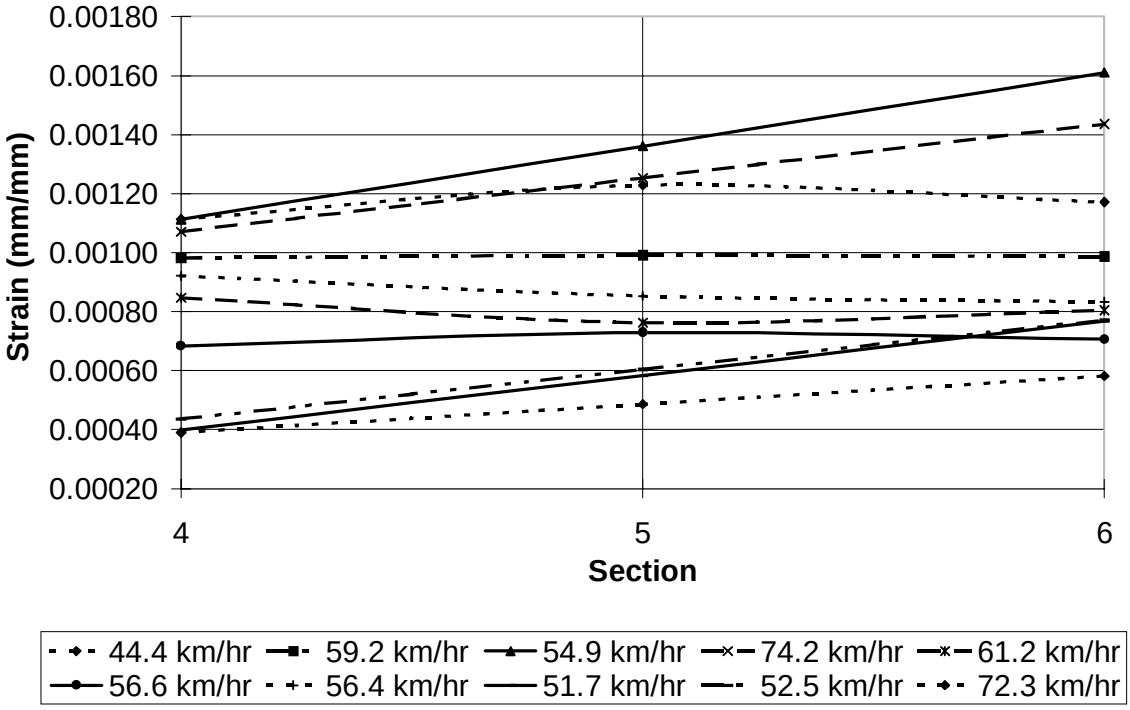


**Figure K 43 HMA strain in sections 4, 5, and 6 (transverse direction).**

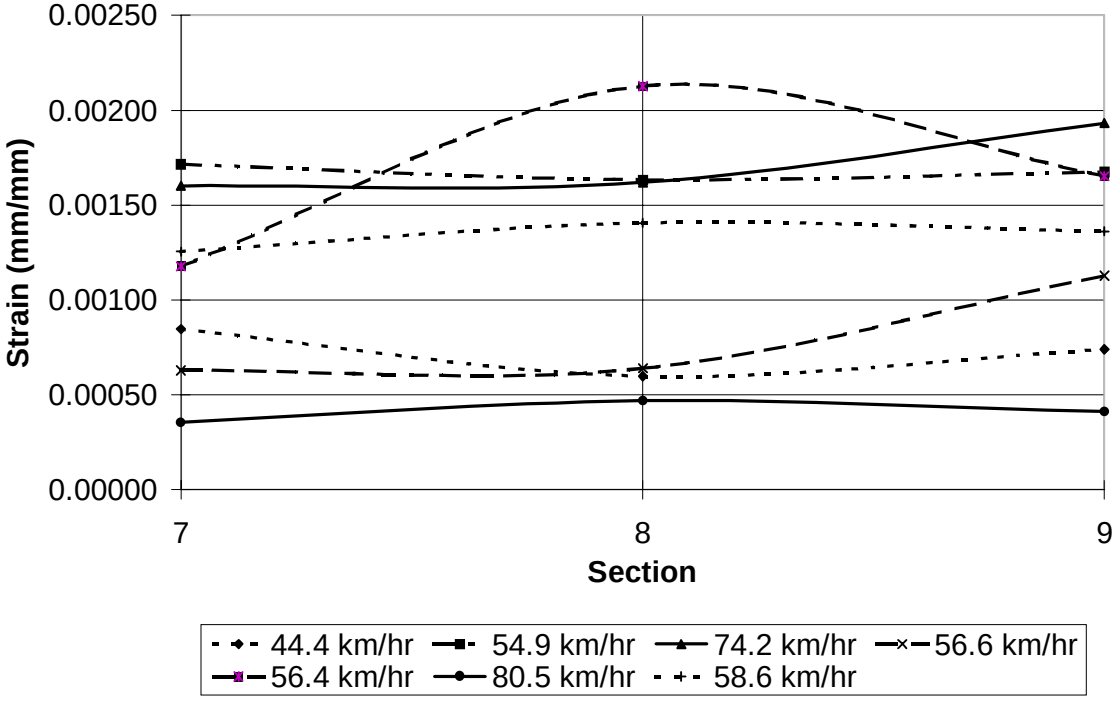


**Figure K 44 HMA strain in sections 7, 8, and 9 (transverse direction).**

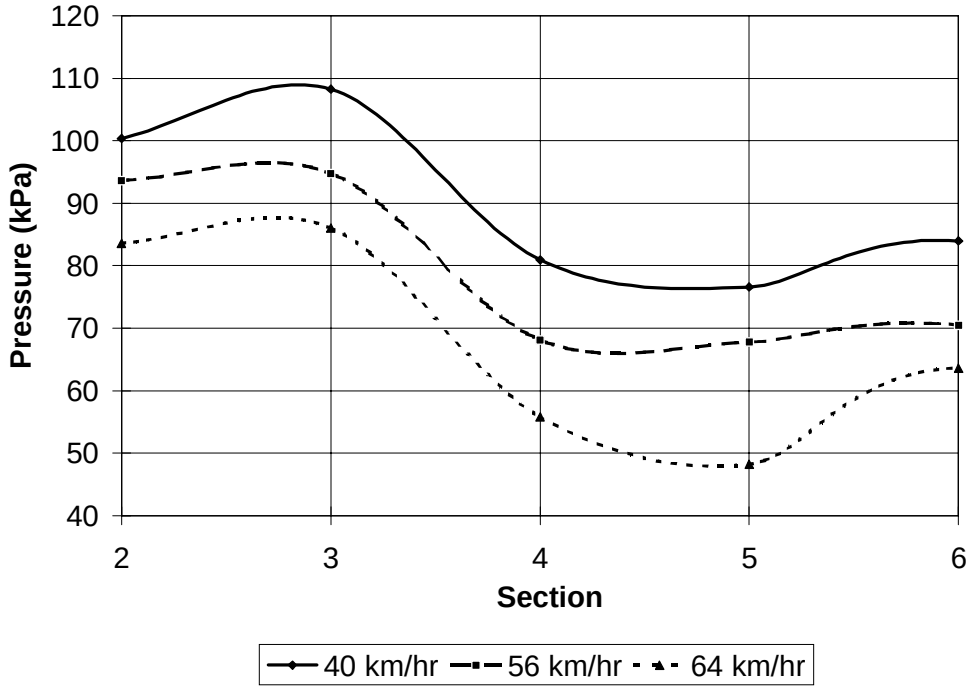


**Figure K 45 Calibration response from subgrade pressure cells, 420 kPa tire pressure.**

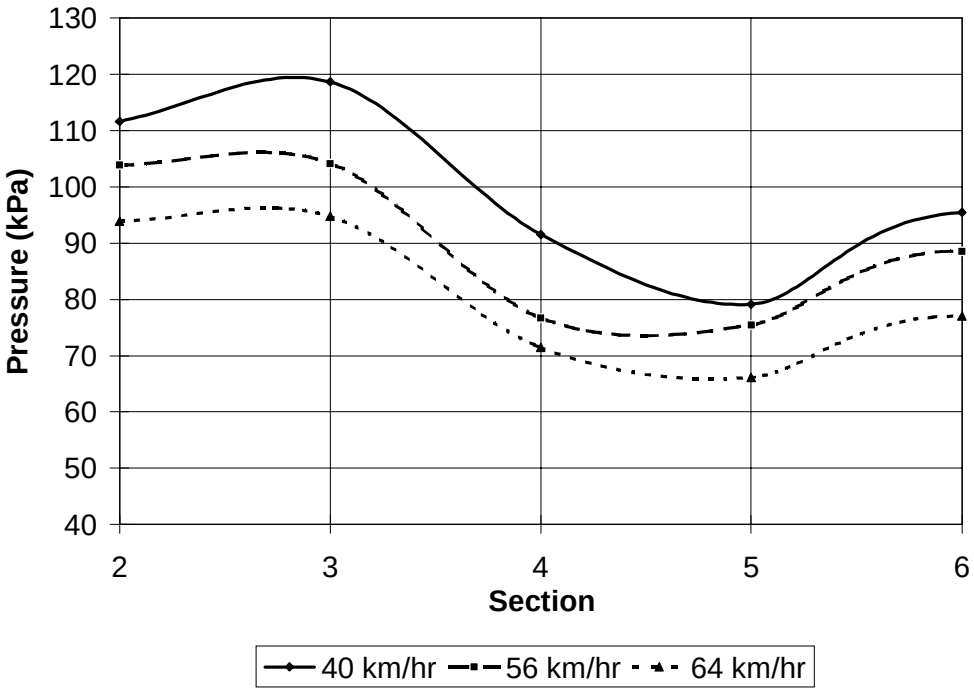


**Figure K 46 Calibration response from subgrade pressure cells, 490 kPa tire pressure.**

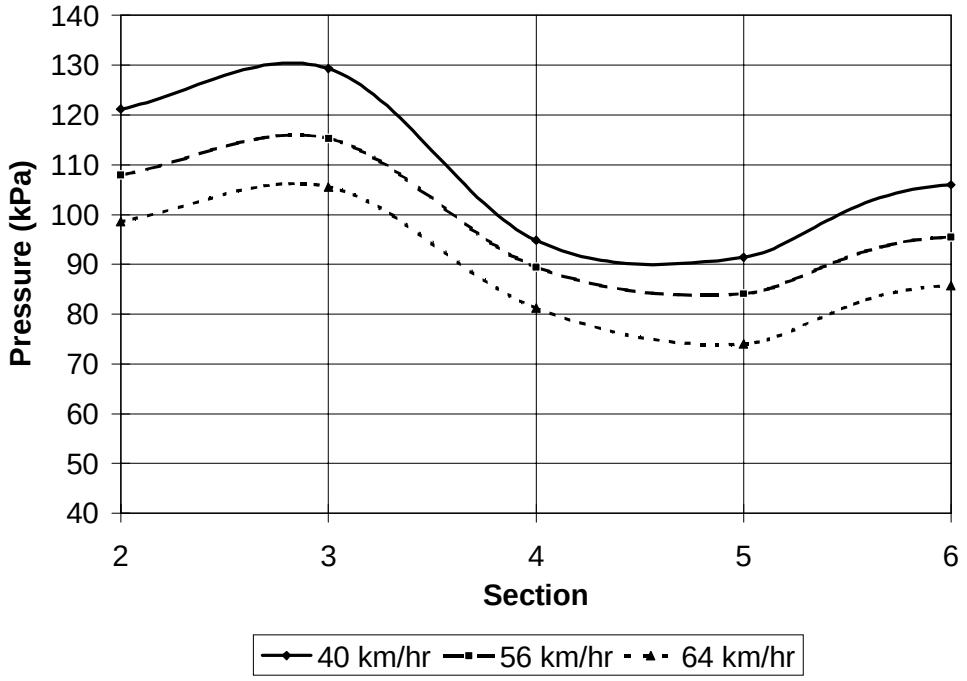


**Figure K 47 Calibration response from subgrade pressure cells, 560 kPa tire pressure.**

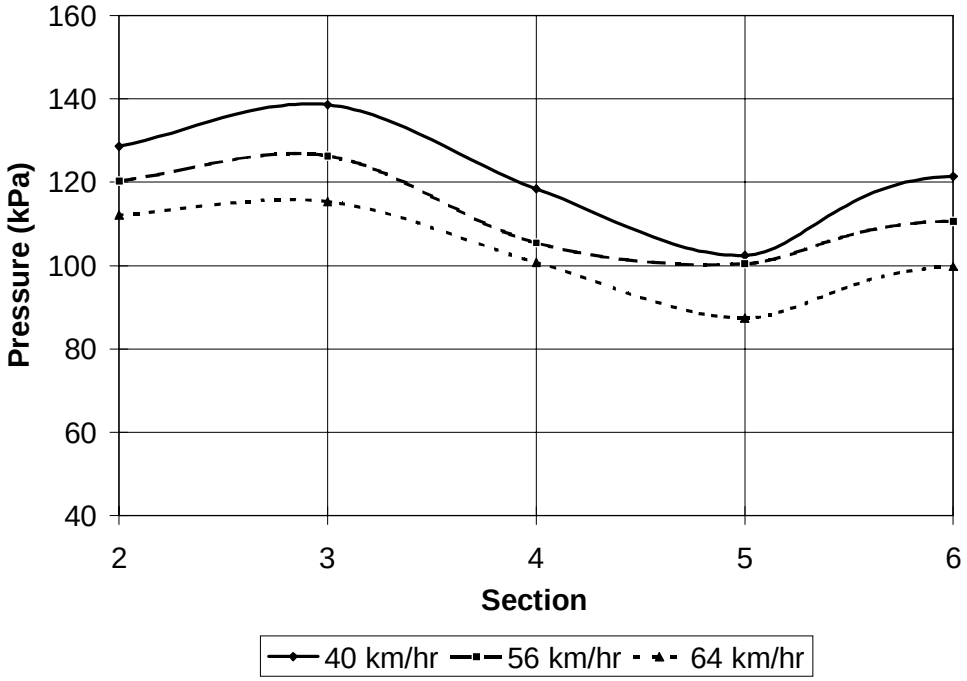


**Figure K 48 Calibration response from subgrade pressure cells, 630 kPa tire pressure.**

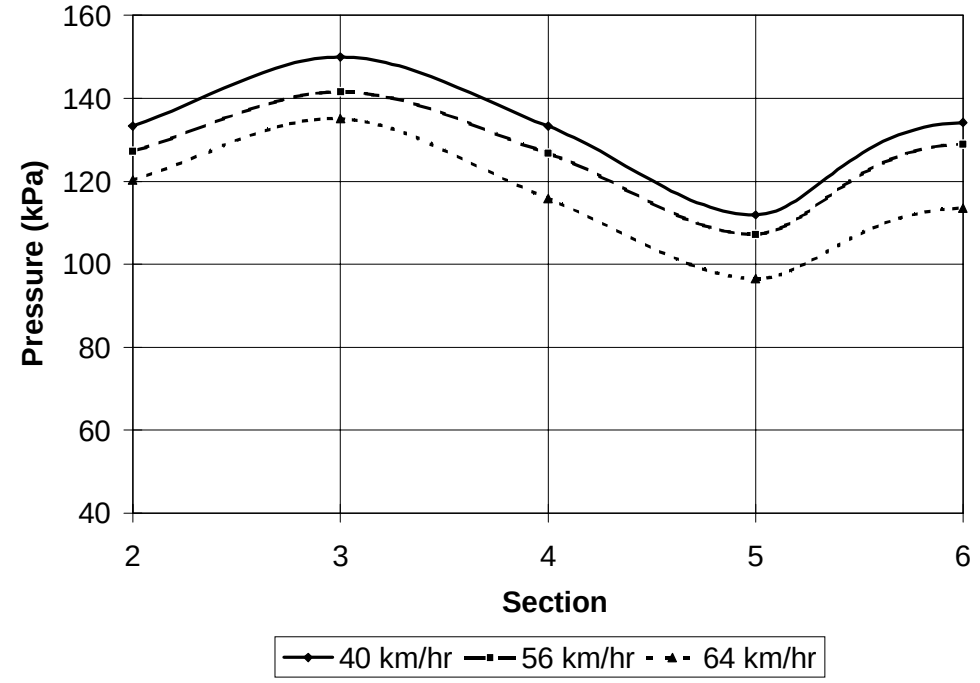


**Figure K 49 Calibration response from subgrade pressure cells, 700 kPa tire pressure.**

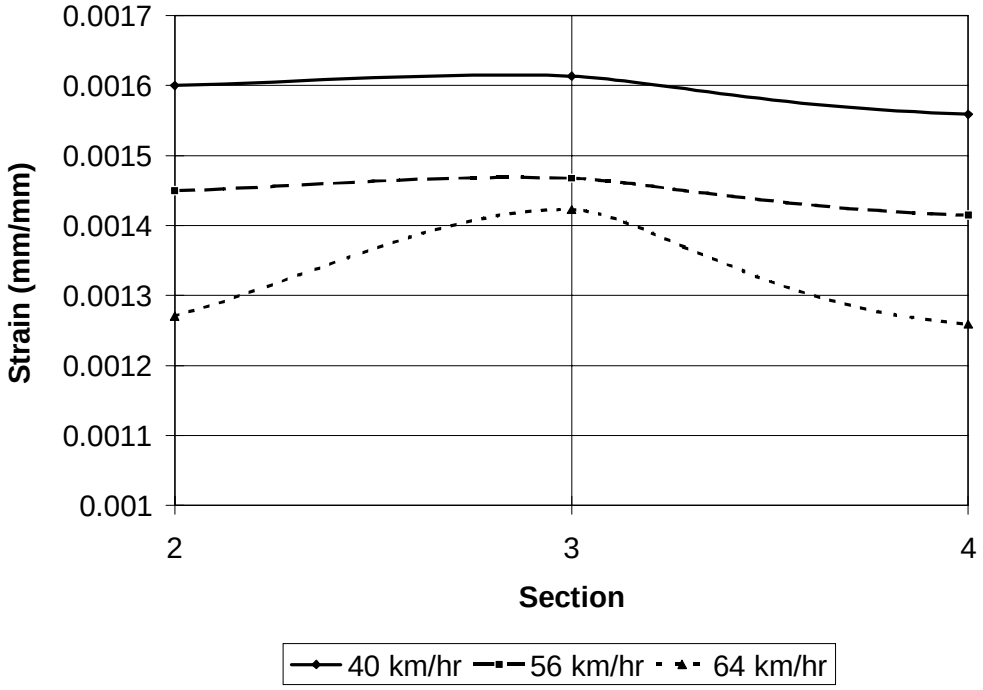


**Figure K 50 Calibration response from HMA strain gage, 420 kPa tire pressure (longitudinal direction).**

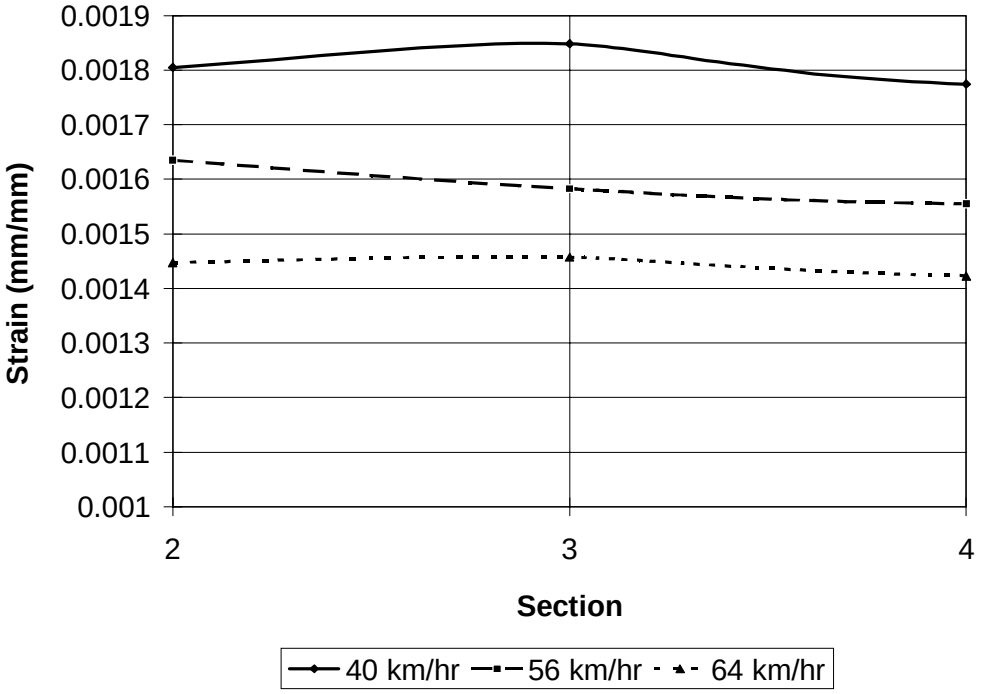


**Figure K 51 Calibration response from HMA strain gage, 490 kPa tire pressure (longitudinal direction).**

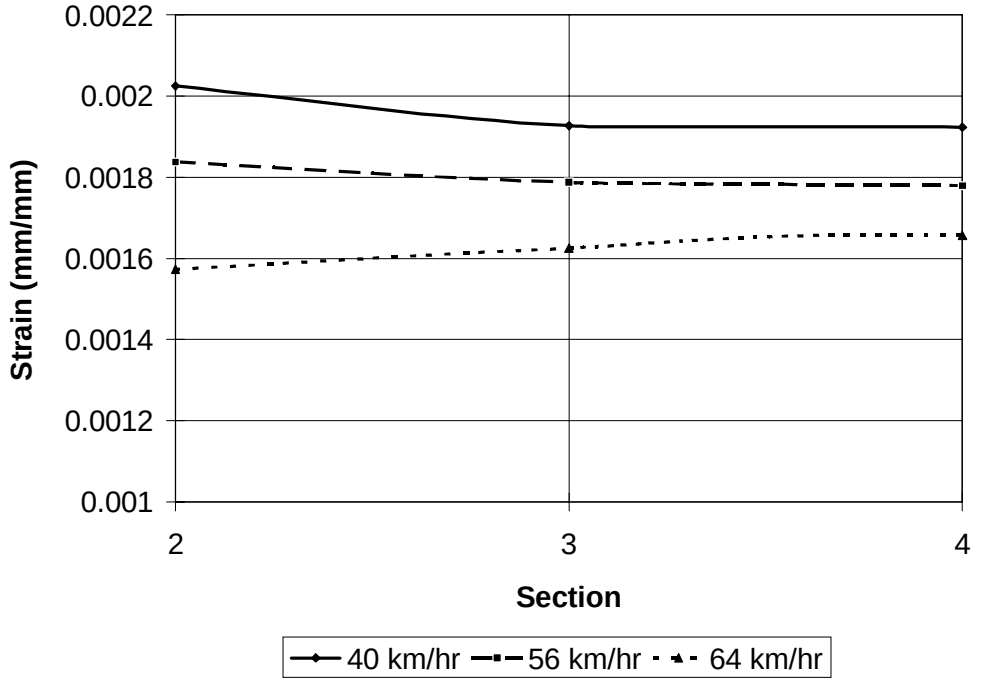


**Figure K 52 Calibration response from HMA strain gage, 560 kPa tire pressure (longitudinal direction).**

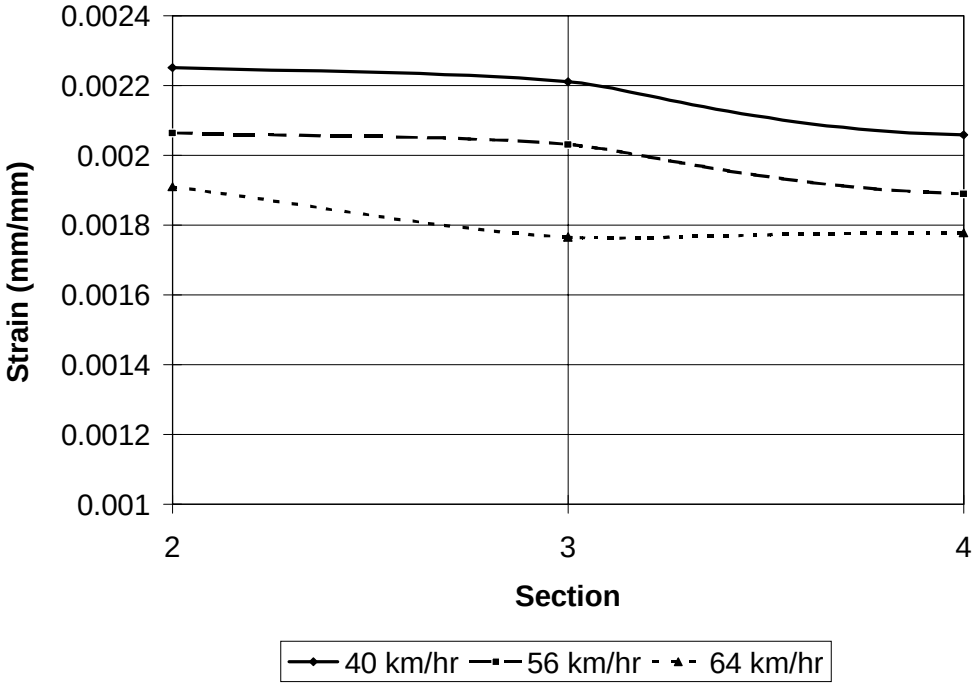


**Figure K 53 Calibration response from HMA strain gage, 630 kPa tire pressure (longitudinal direction).**

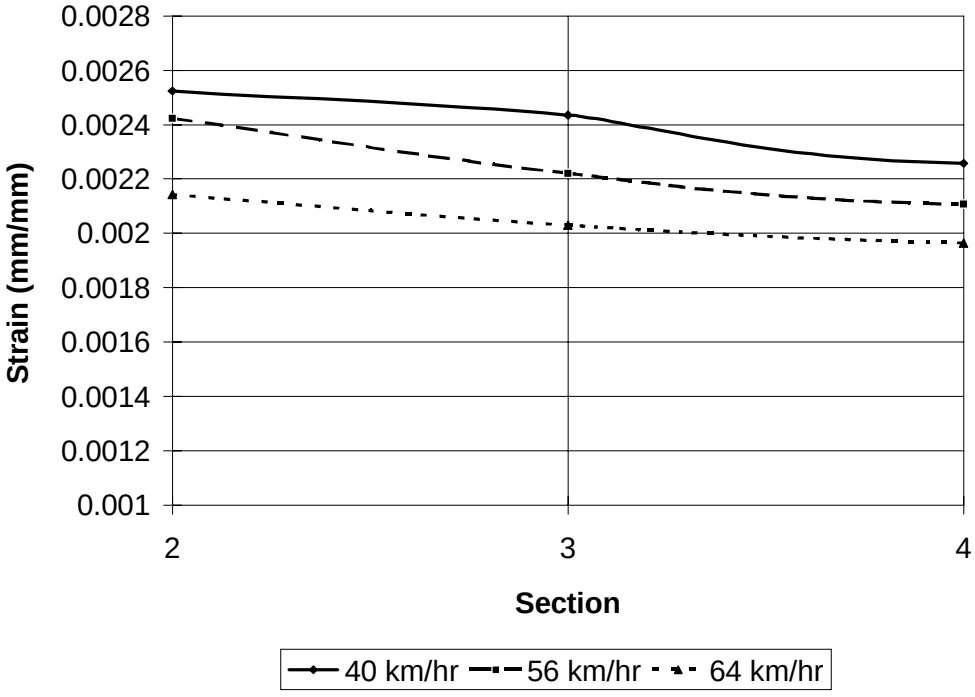


**Figure K 54 Calibration response from HMA strain gage, 700 kPa tire pressure (longitudinal direction).**

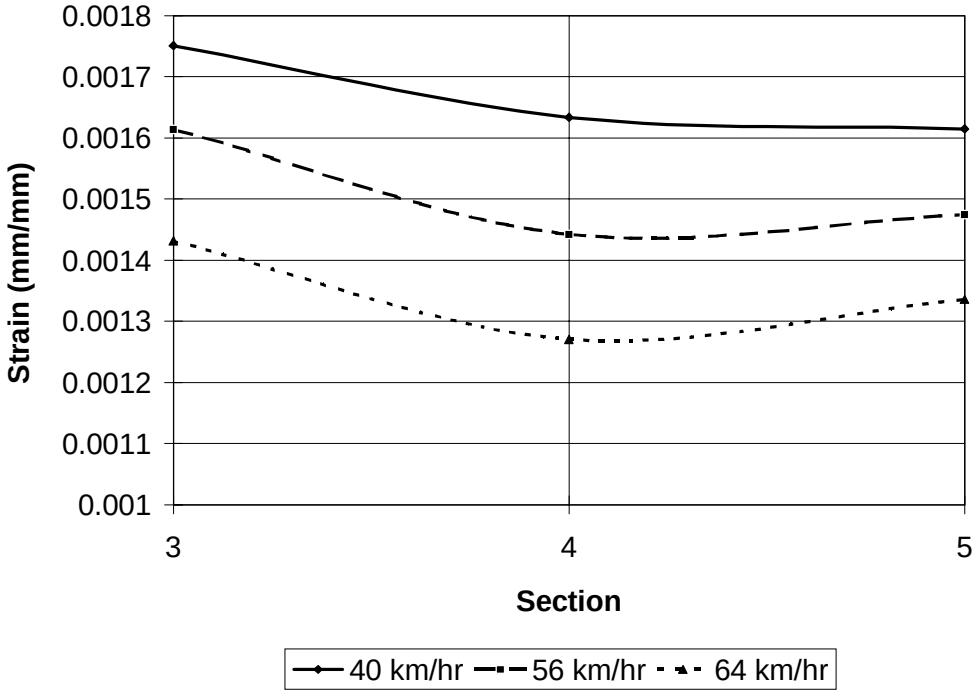


**Figure K 55 Calibration response from HMA strain gage, 420 kPa tire pressure (transverse direction).**

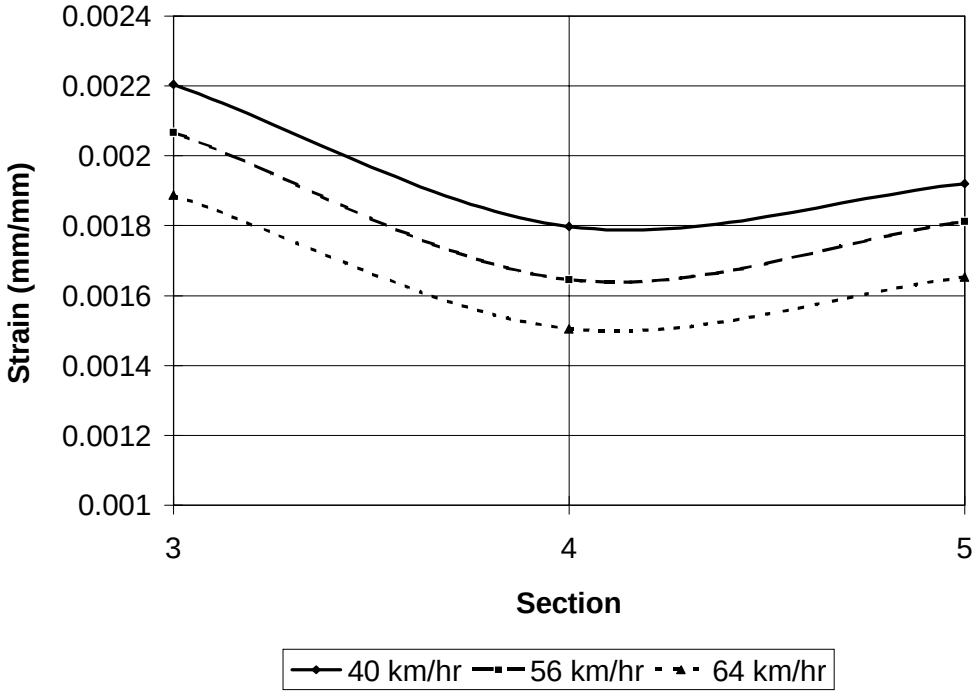


**Figure K 56 Calibration response from HMA strain gage, 490 kPa tire pressure (transverse direction).**

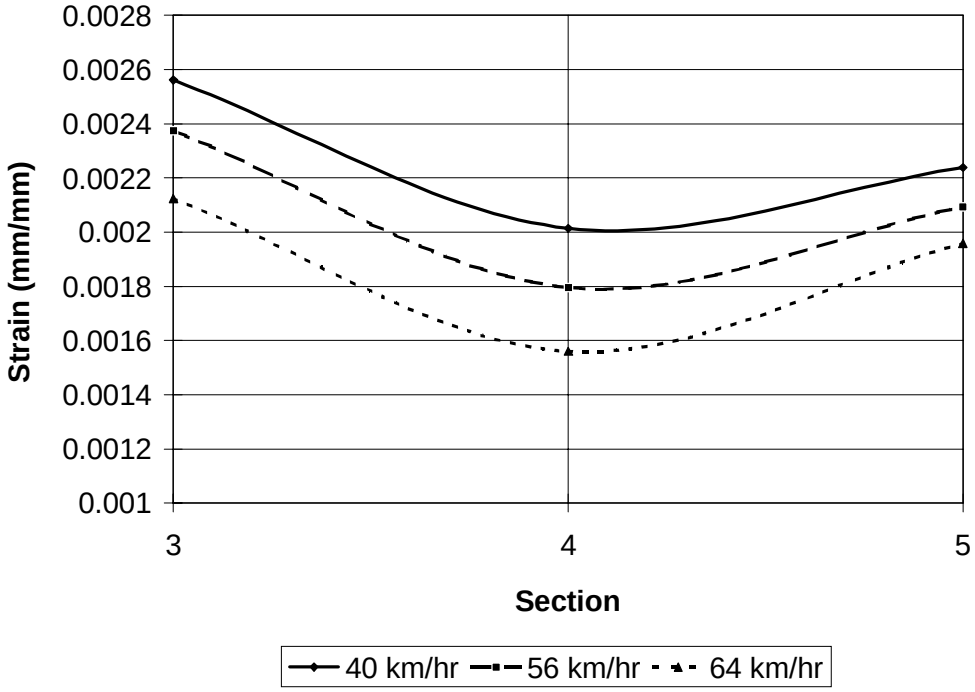


**Figure K 57 Calibration response from HMA strain gage, 560 kPa tire pressure (transverse direction).**

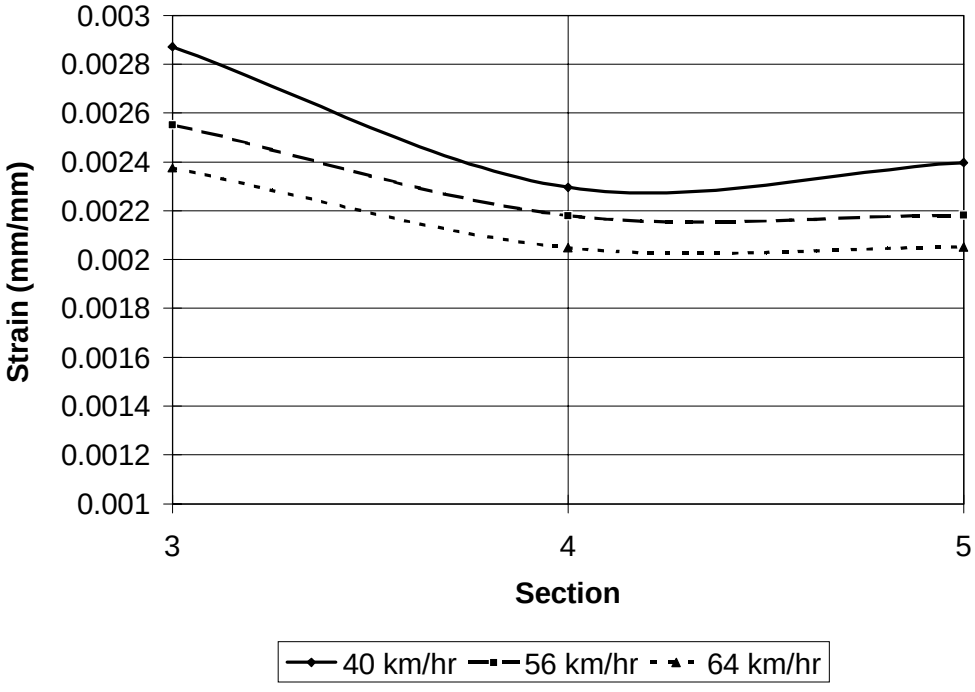


**Figure K 58 Calibration response from HMA strain gage, 630 kPa tire pressure (transverse direction).**

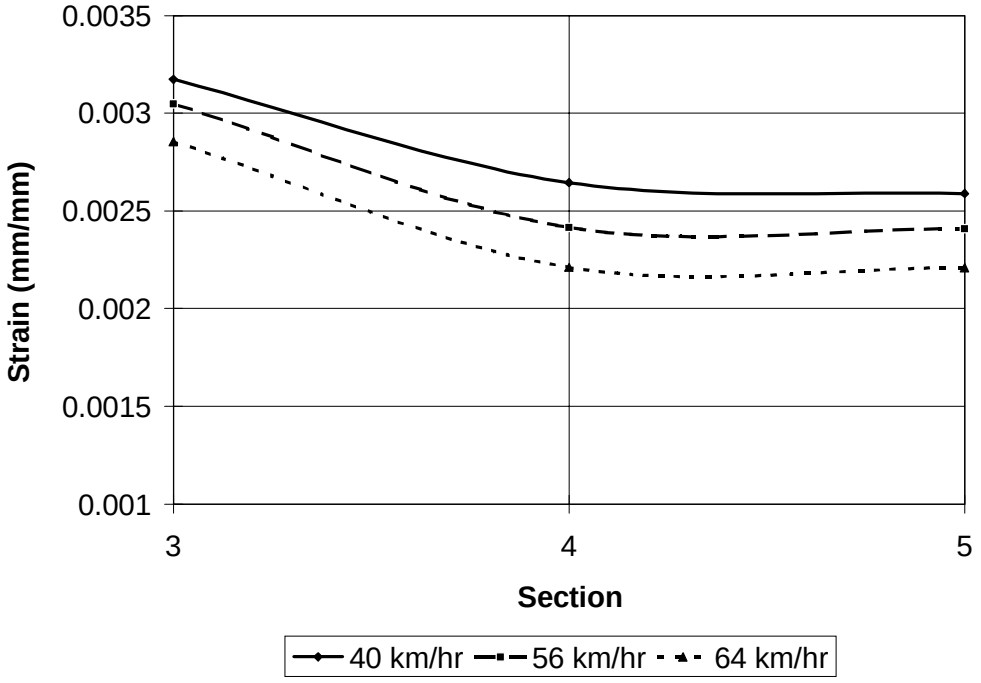


**Figure K 59 Calibration response from HMA strain gage, 700 kPa tire pressure (transverse direction).**

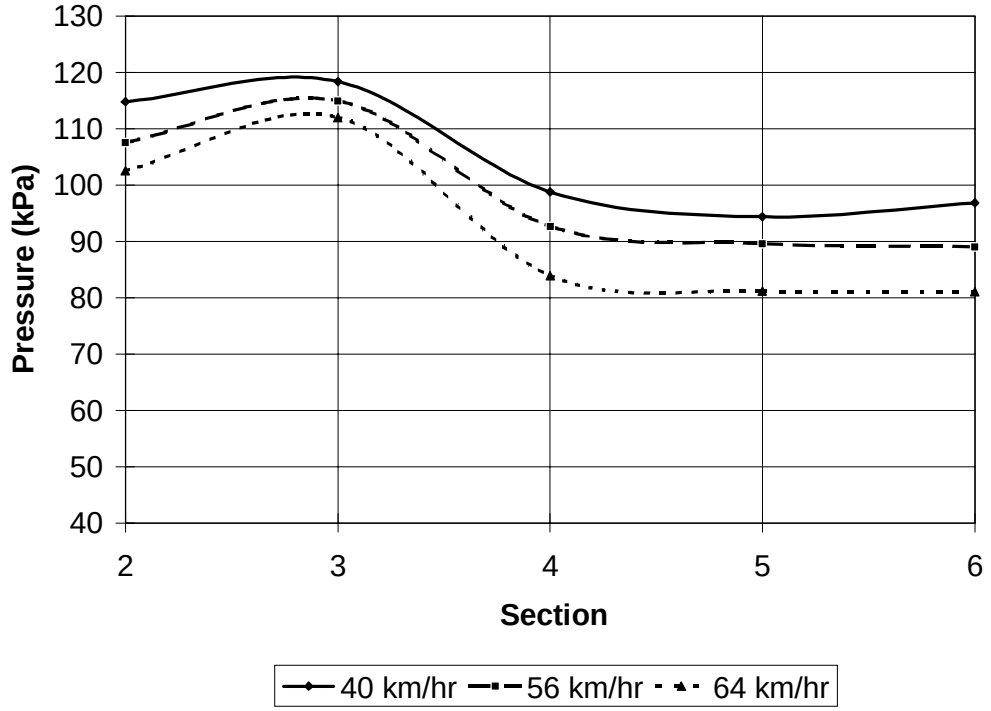


**Figure K 60 Calibration response from subgrade pressure cells, 420 kPa tire pressure.**

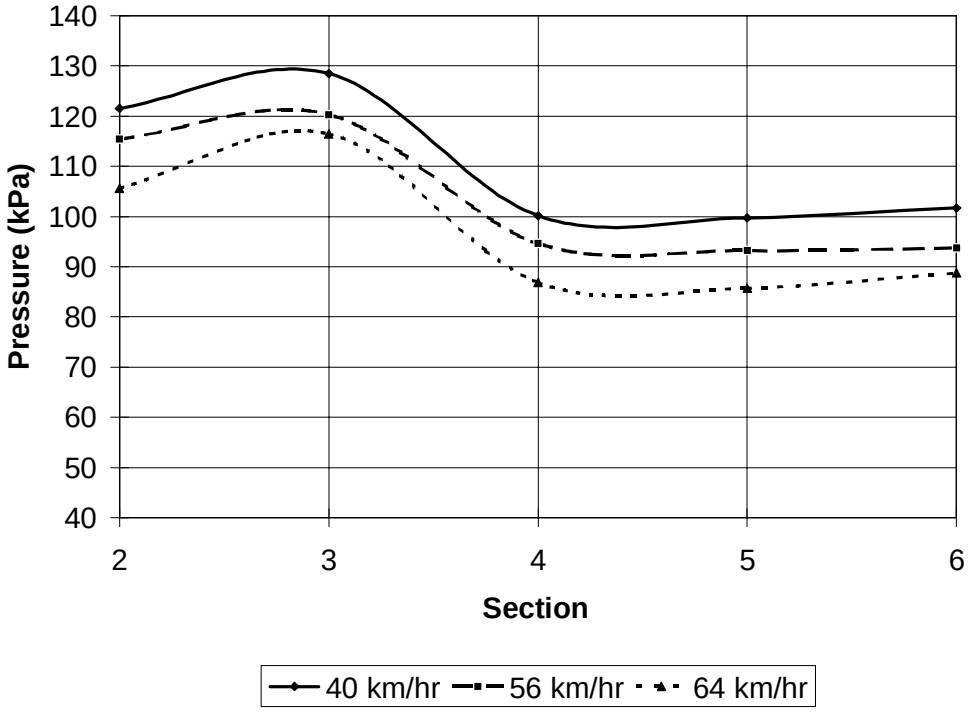


**Figure K 61 Calibration response from subgrade pressure cells, 490 kPa tire pressure.**

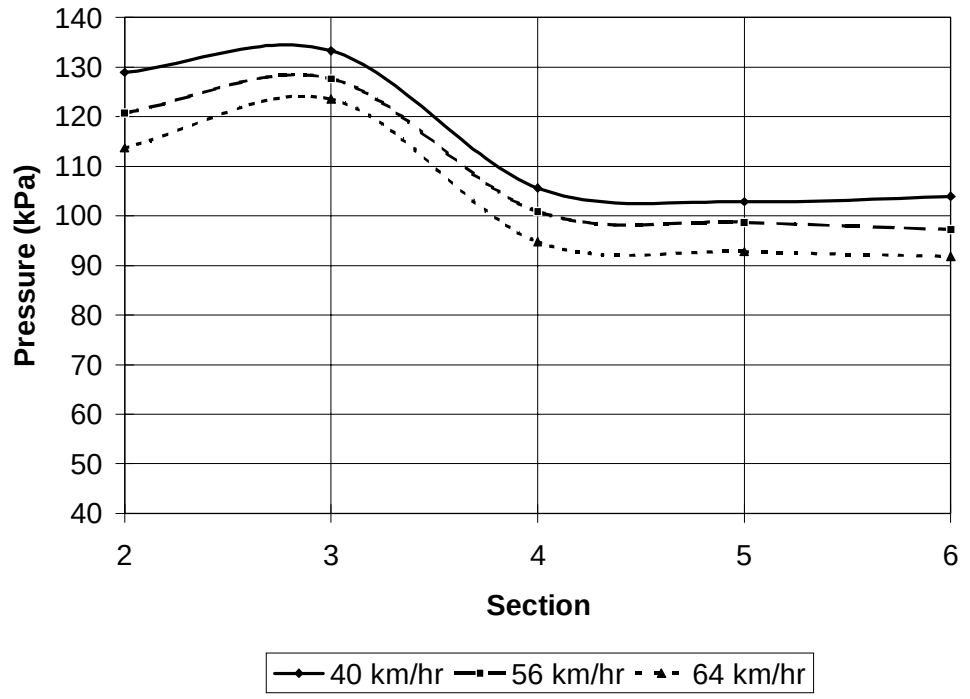


**Figure K 62 Calibration response from subgrade pressure cells, 560 kPa tire pressure.**

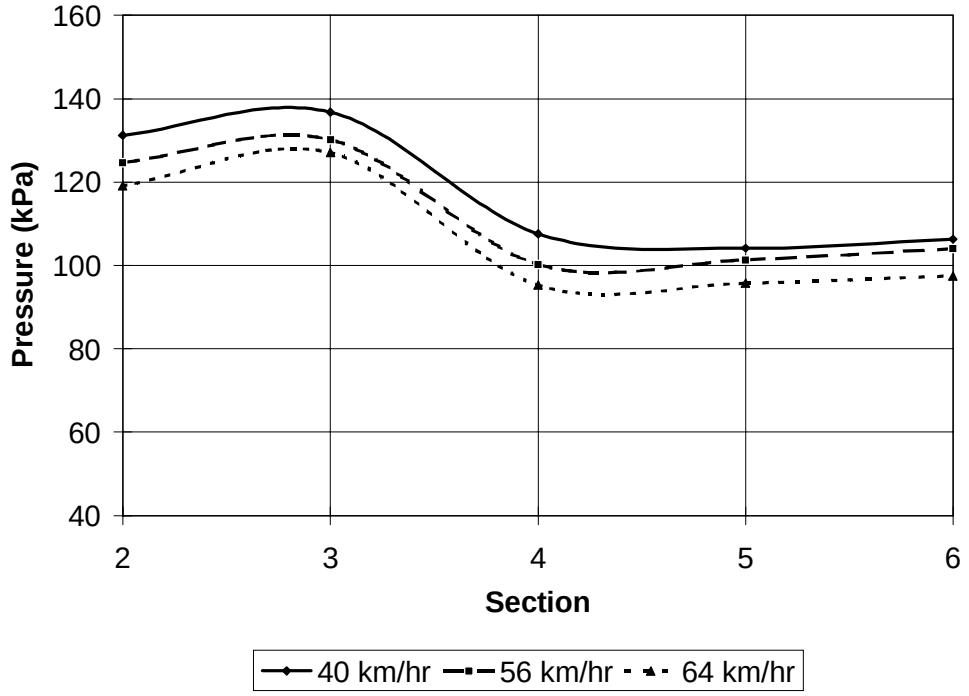


**Figure K 63 Calibration response from subgrade pressure cells, 630 kPa tire pressure.**

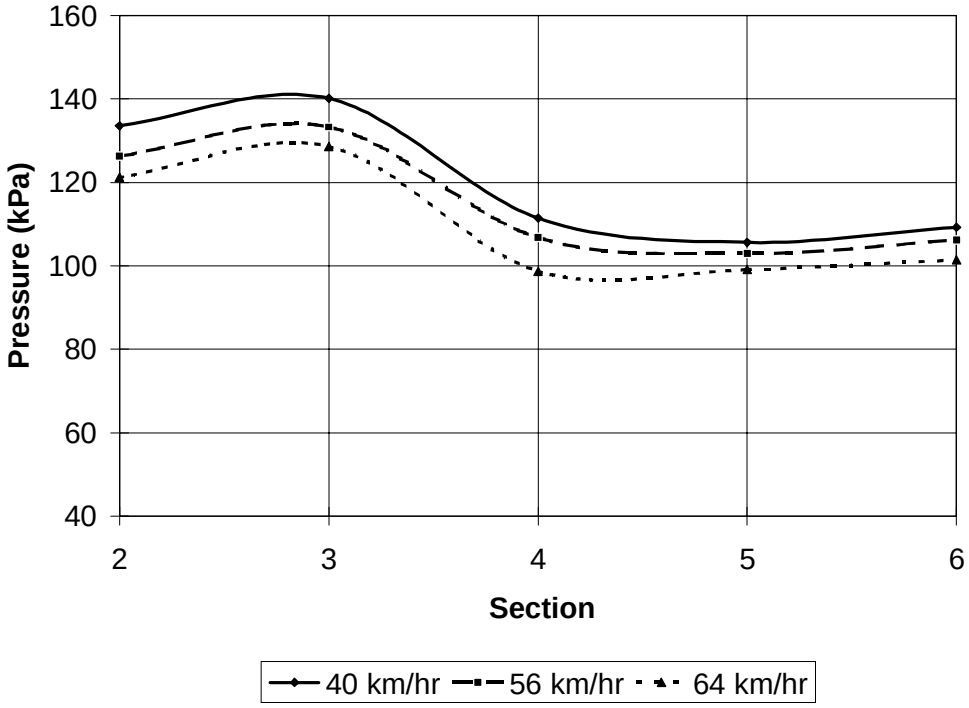


**Figure K 64 Calibration response from subgrade pressure cells, 700 kPa tire pressure.**

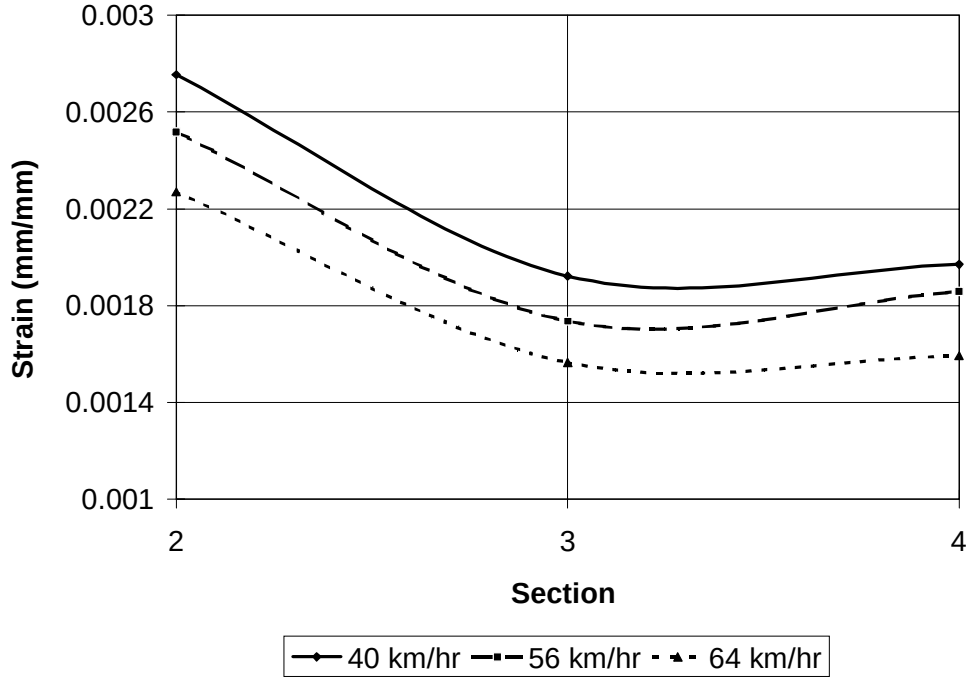


**Figure K 65 Calibration response from HMA strain gage, 420 kPa tire pressure (longitudinal direction).**

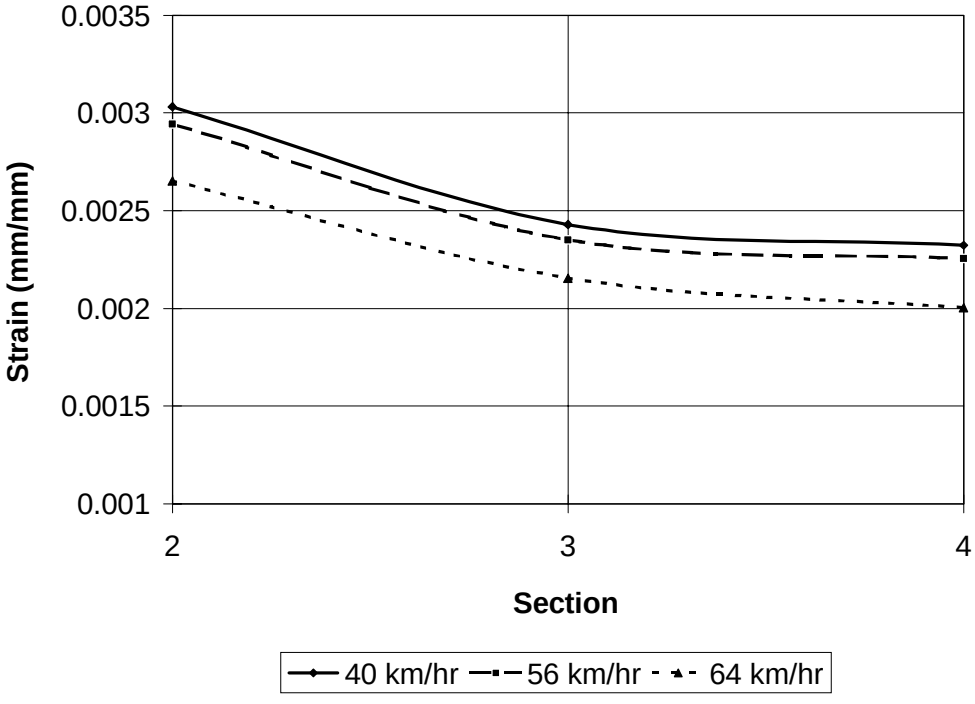


**Figure K 66 Calibration response from HMA strain gage, 490 kPa tire pressure (longitudinal direction).**

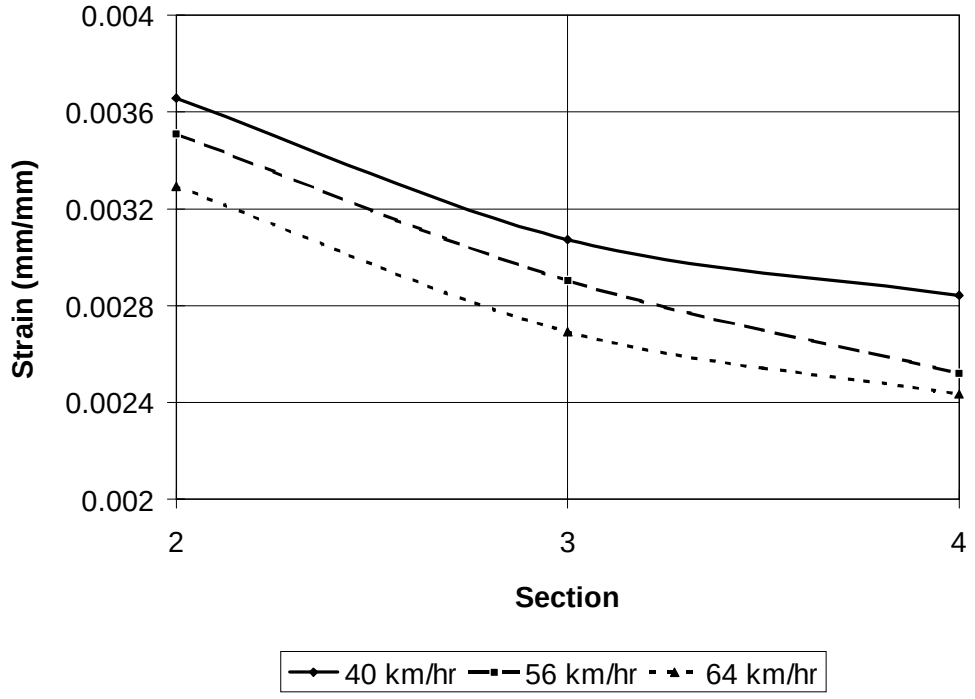


**Figure K 67 Calibration response from HMA strain gage, 560 kPa tire pressure (longitudinal direction).**

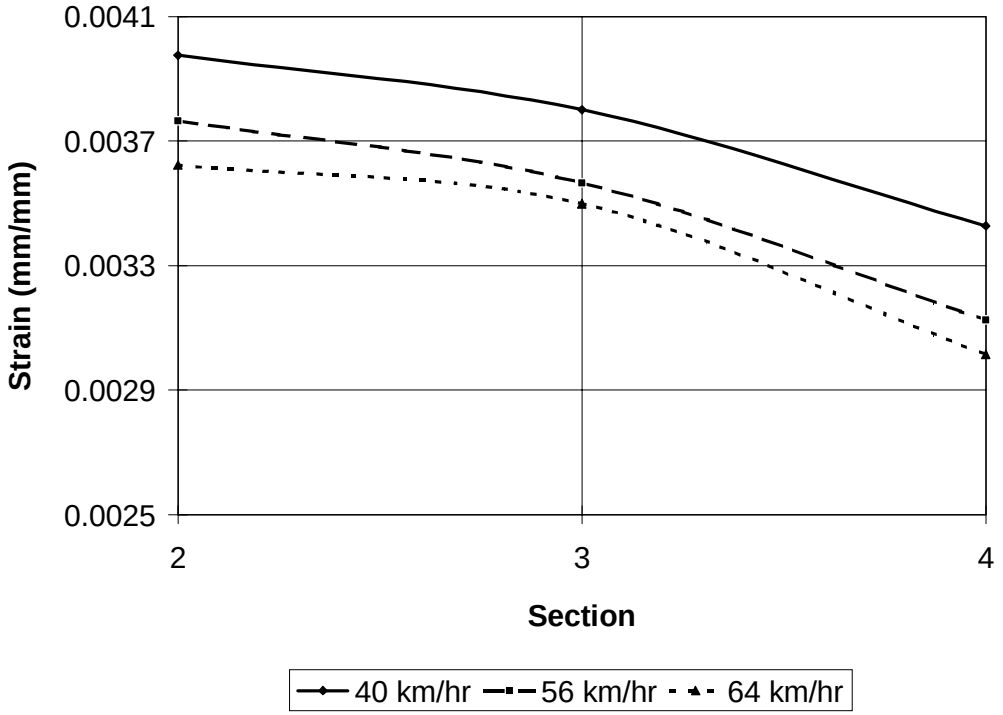


**Figure K 68 Calibration response from HMA strain gage, 630 kPa tire pressure (longitudinal direction).**

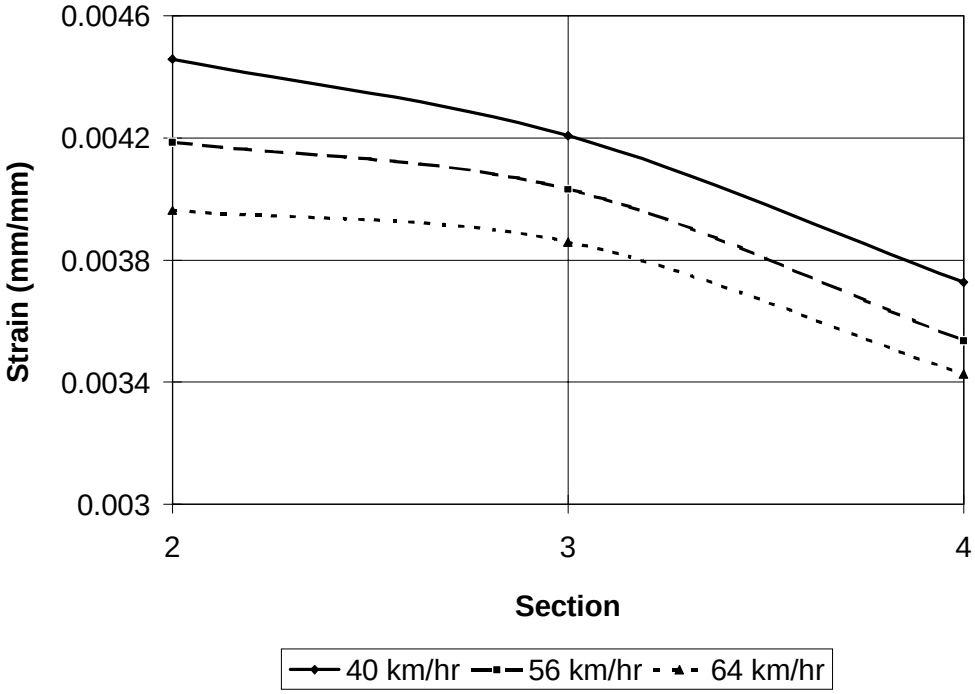


**Figure K 69 Calibration response from HMA strain gage, 700 kPa tire pressure (longitudinal direction).**

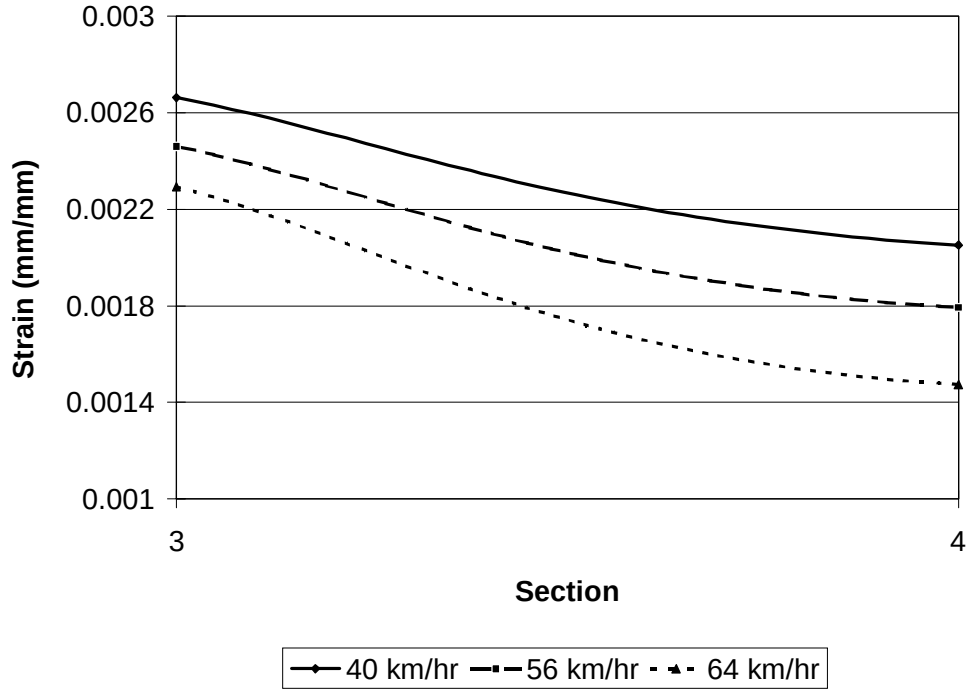


**Figure K 70 Calibration response from HMA strain gage, 420 kPa tire pressure (transverse direction).**

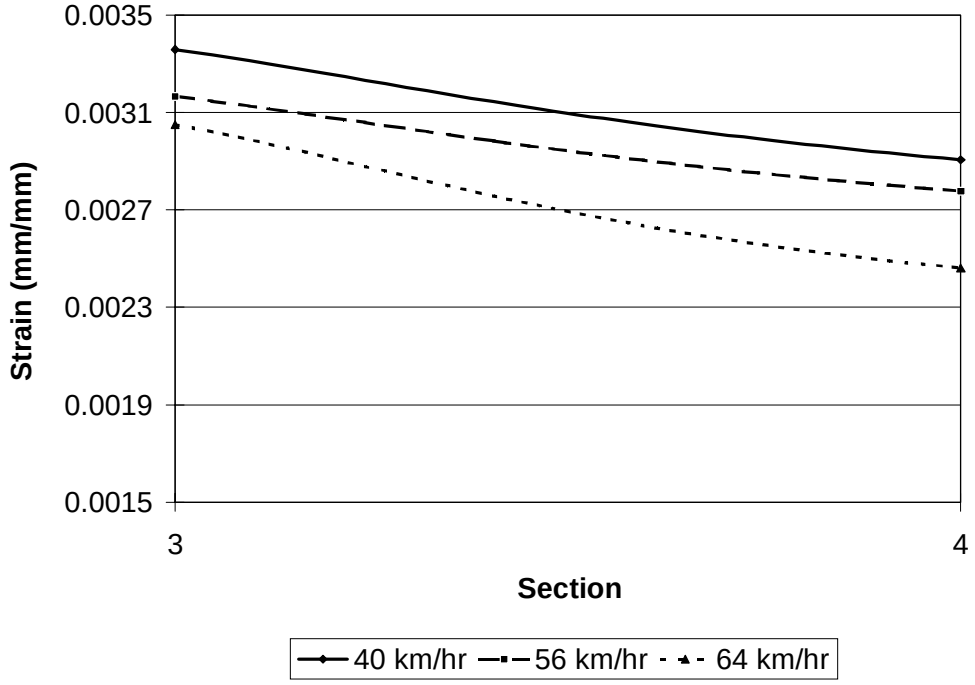


**Figure K 71 Calibration response from HMA strain gage, 490 kPa tire pressure (transverse direction).**

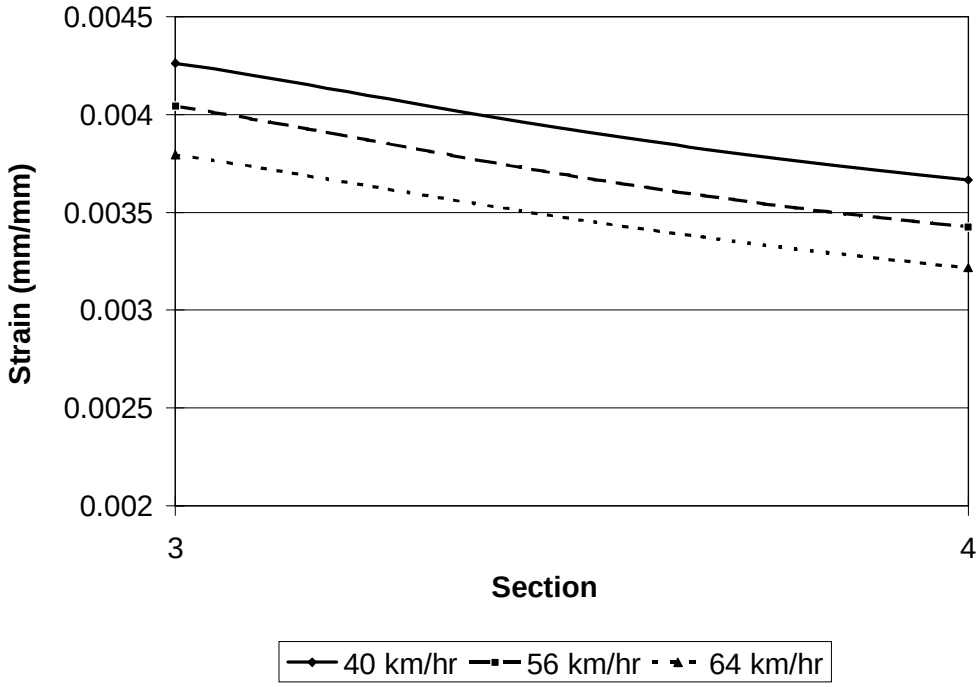


**Figure K 72 Calibration response from HMA strain gage, 560 kPa tire pressure (transverse direction).**

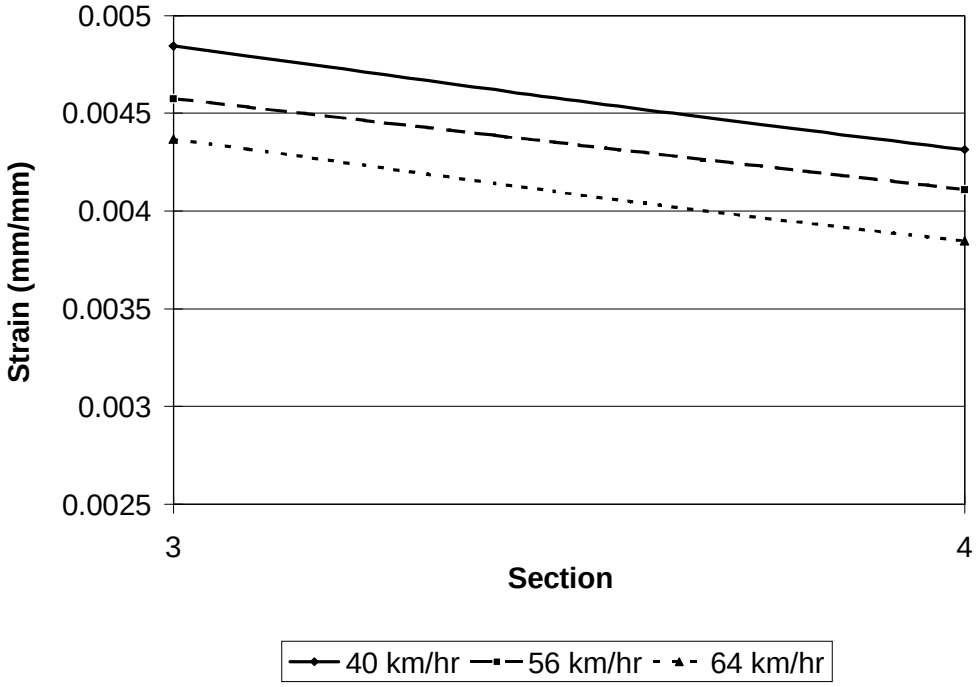


**Figure K 73 Calibration response from HMA strain gage, 630 kPa tire pressure (transverse direction).**

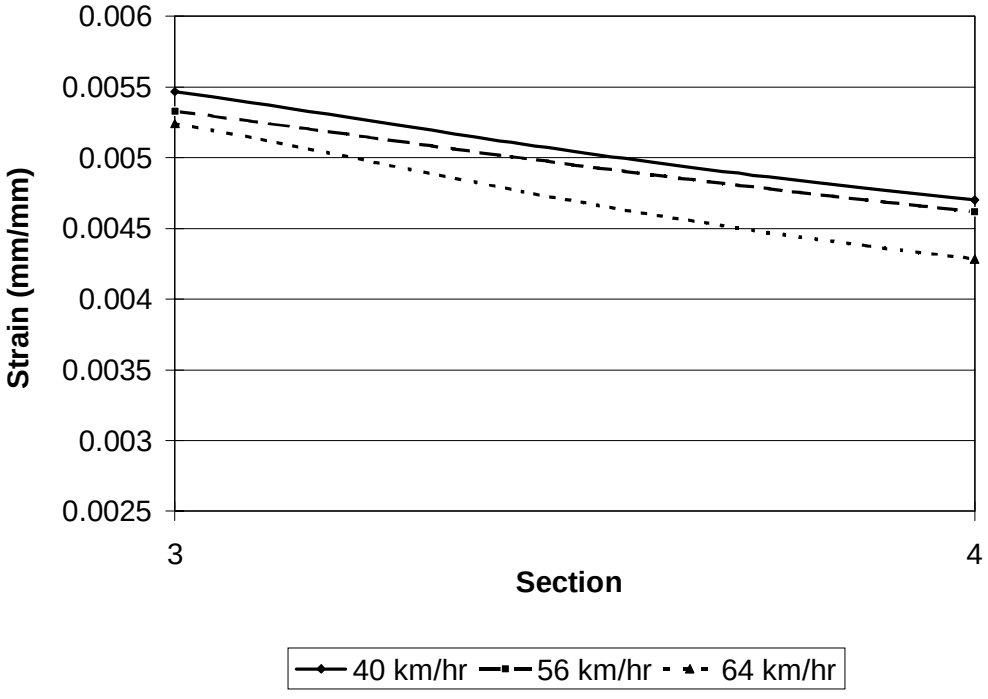


**Figure K 74 Calibration response from HMA strain gage, 700 kPa tire pressure (transverse direction).**

# APPENDIX L

# EXCAVATION DATA

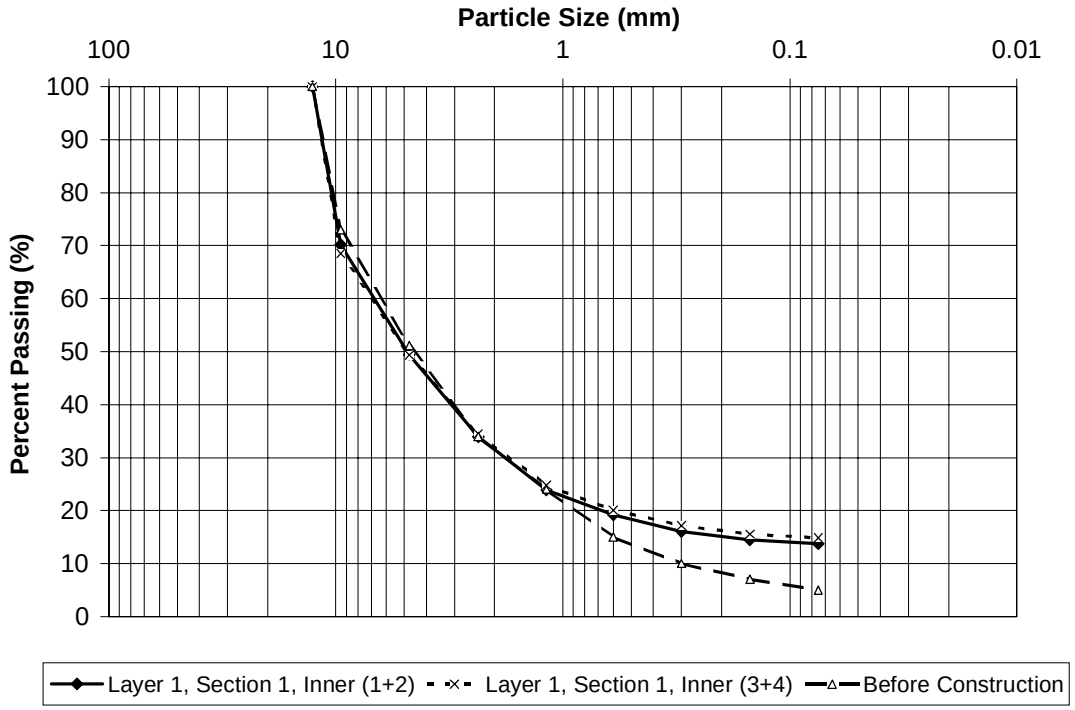


**Figure L 1 Section 1, Layer 1, inner wheel path base course gradation.**

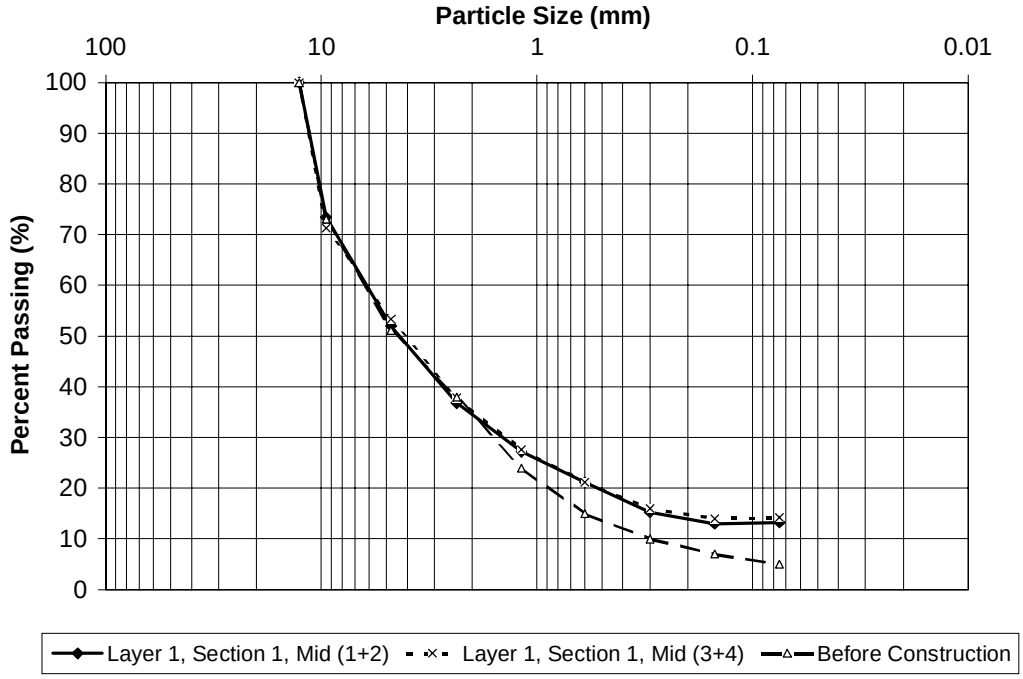


**Figure L 2 Section 1, Layer 1, middle wheel path base course gradation.**

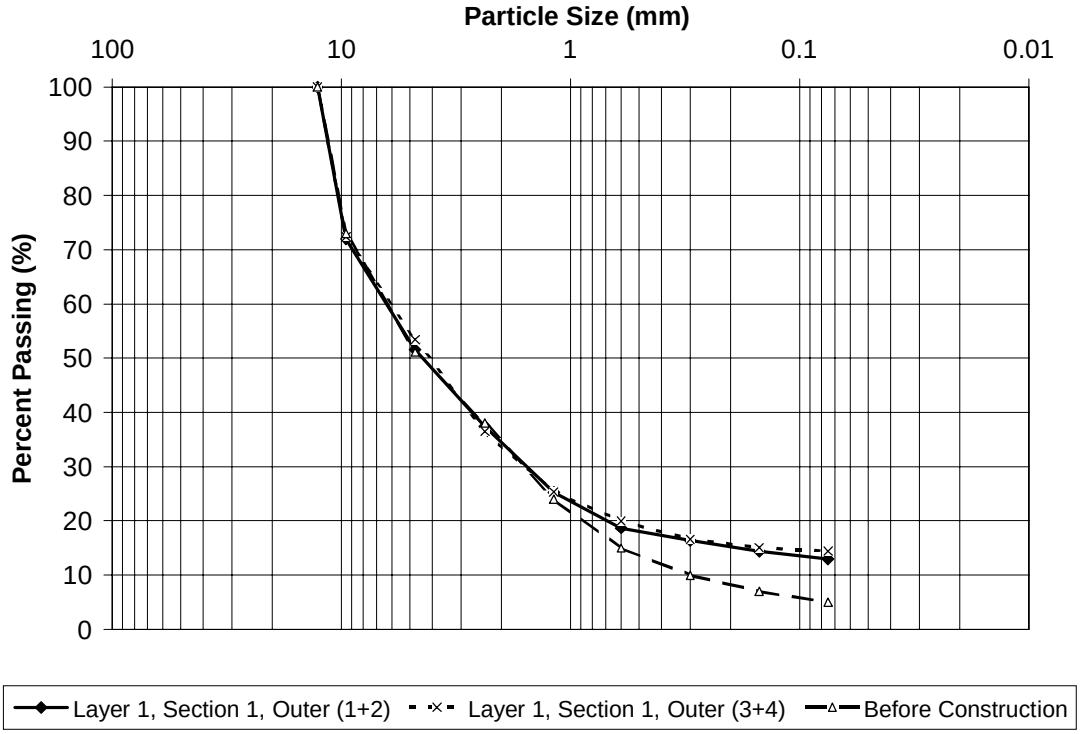


**Figure L 3 Section 1, Layer 1, outer wheel path base course gradation.**

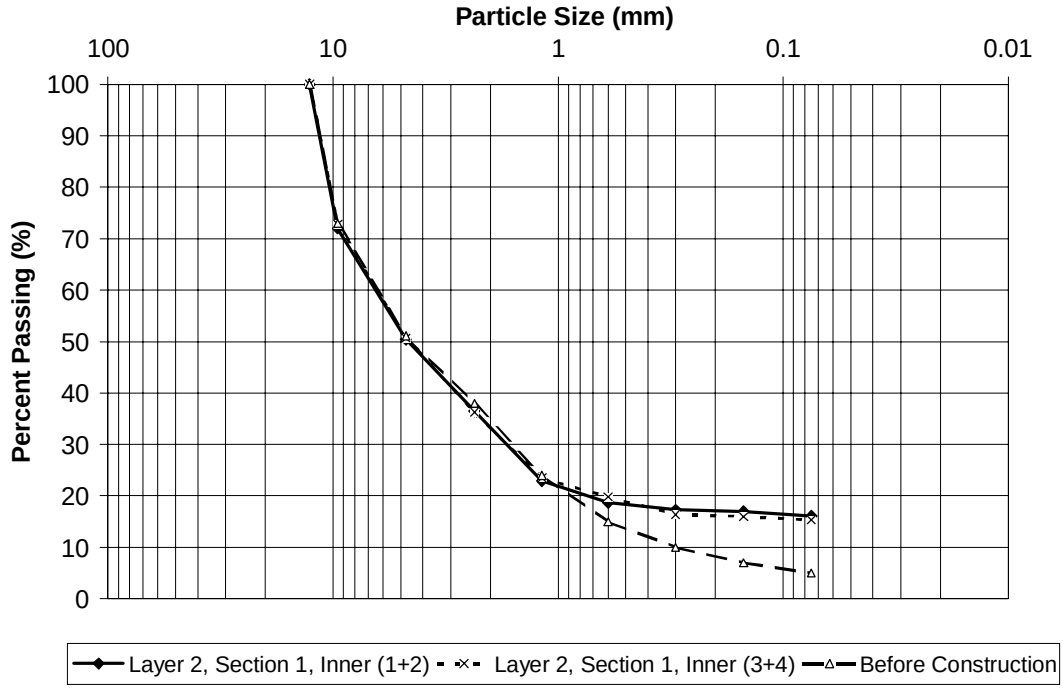


**Figure L 4 Section 1, Layer 2, inner wheel path base course gradation.**

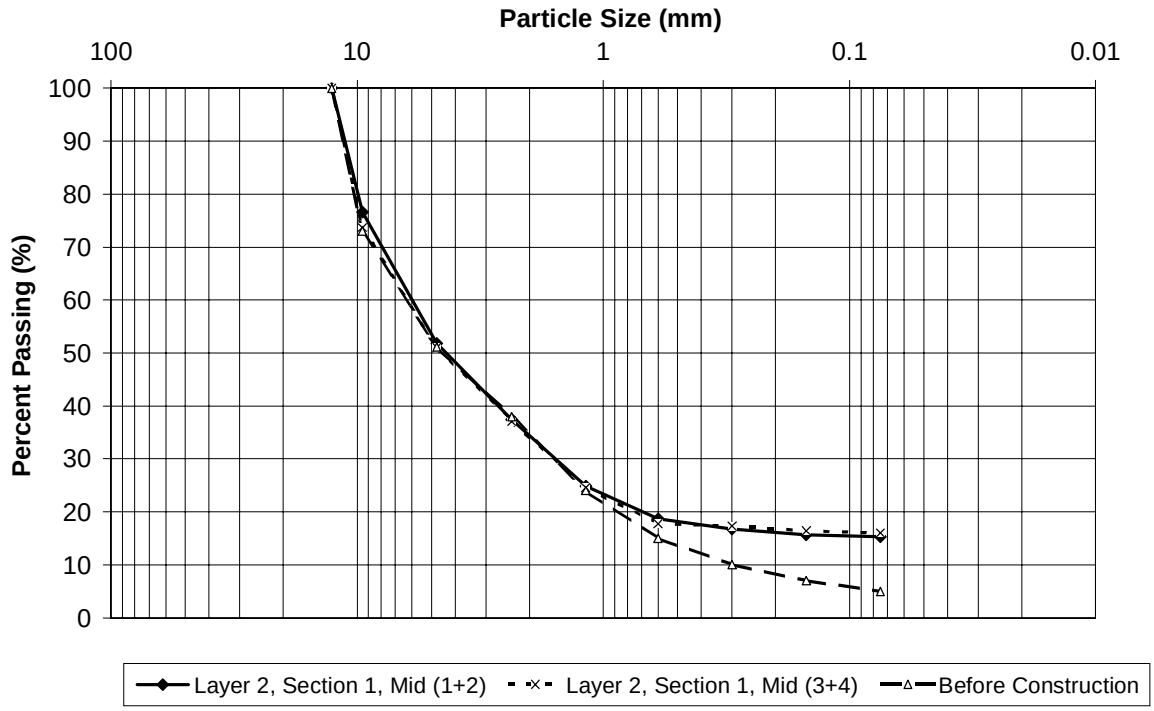


**Figure L 5 Section 1, Layer 2, middle wheel path base course gradation.**

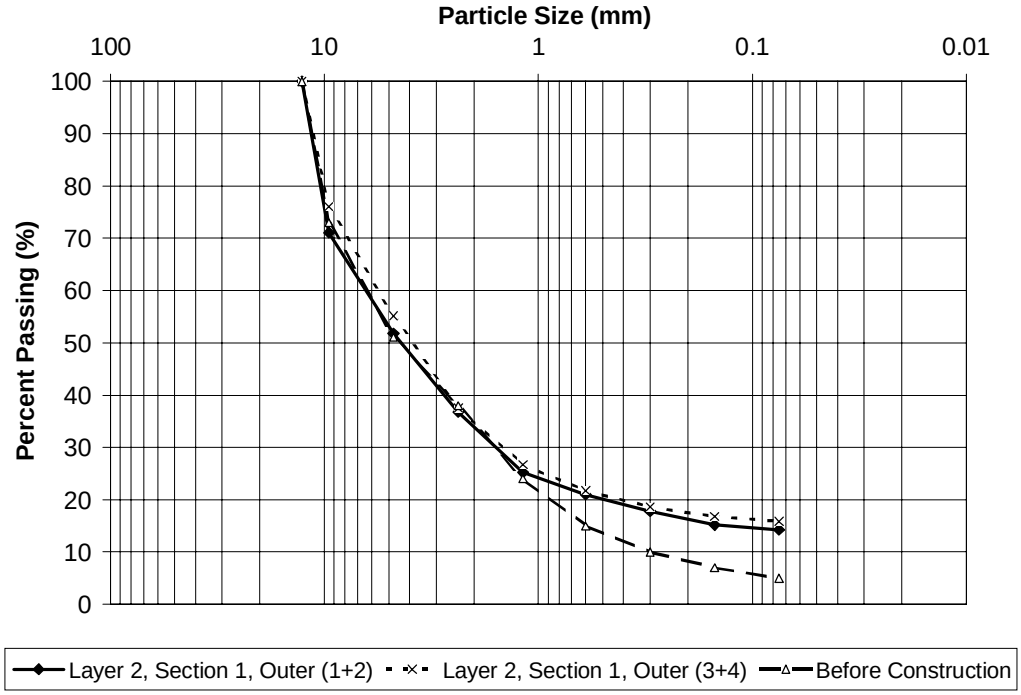


**Figure L 6 Section 1, Layer 2, outer wheel path base course gradation.**

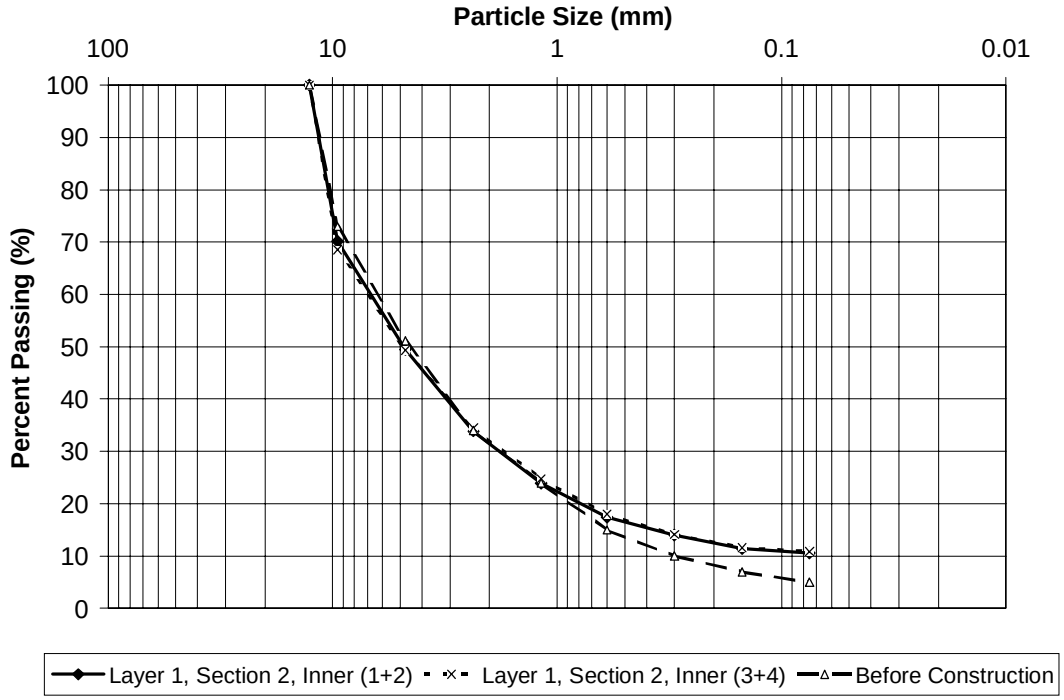


**Figure L 7 Section 2 Layer 1, inner wheel path base course gradation.**

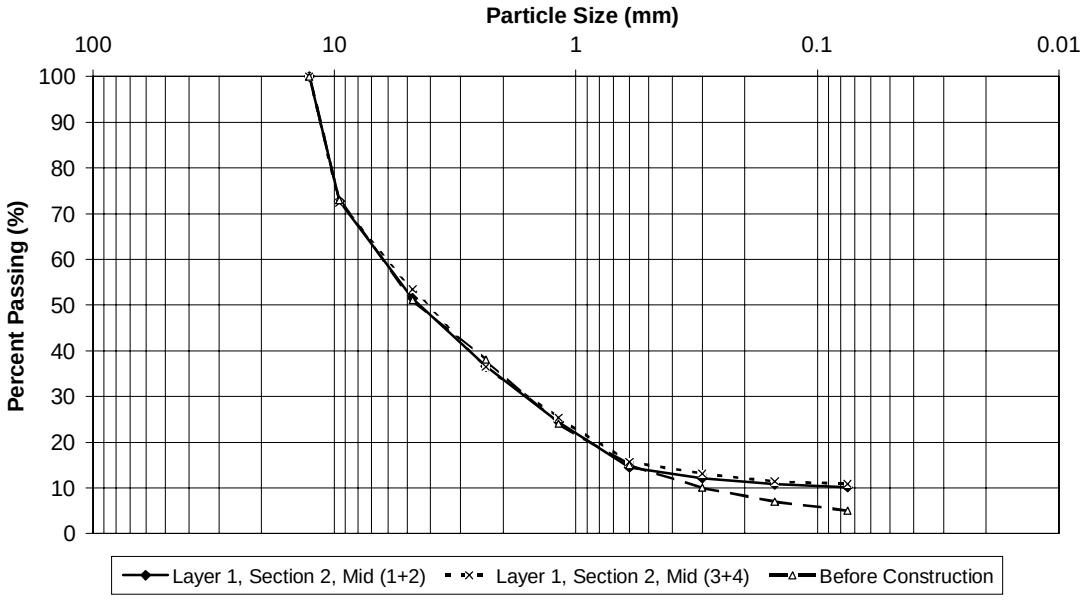


**Figure L 8 Section 2 Layer 1, middle wheel path base course gradation.**

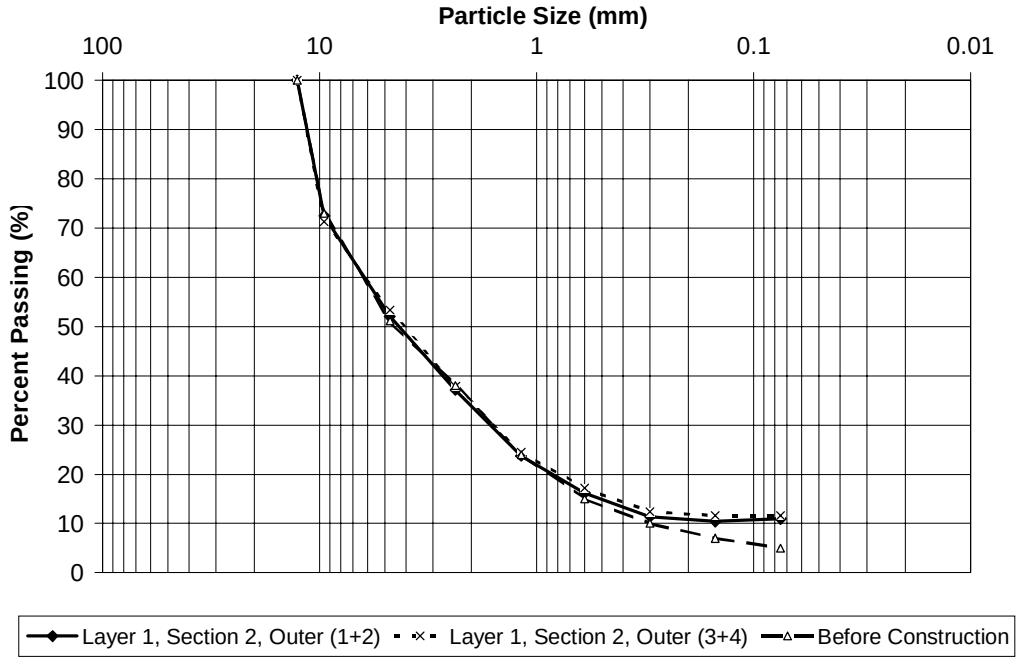


**Figure L 9 Section 2 Layer 1, outer wheel path base course gradation.**

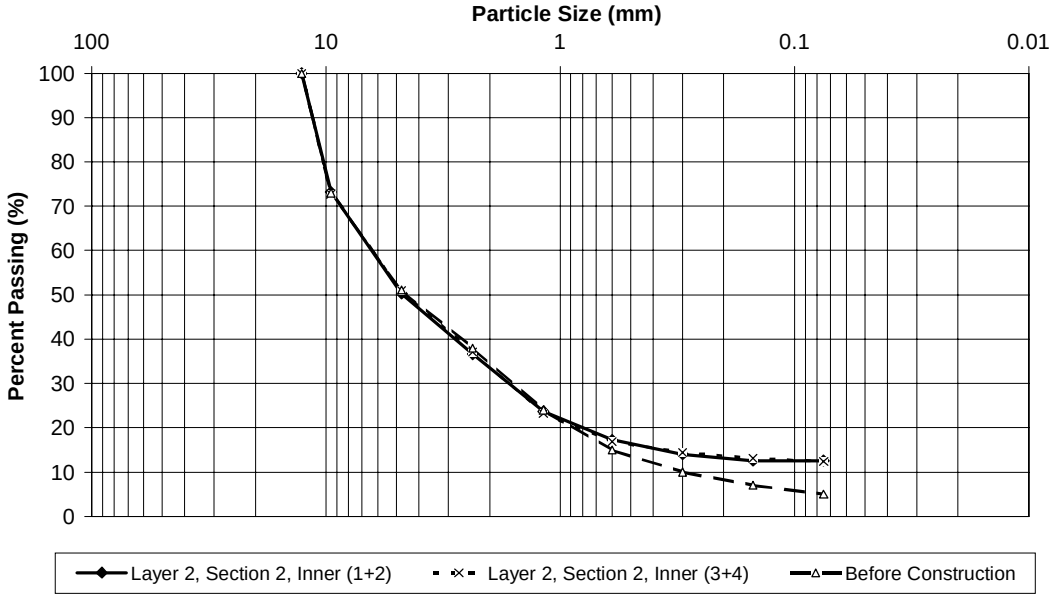


**Figure L 10 Section 2 Layer 2, inner wheel path base course gradation.**

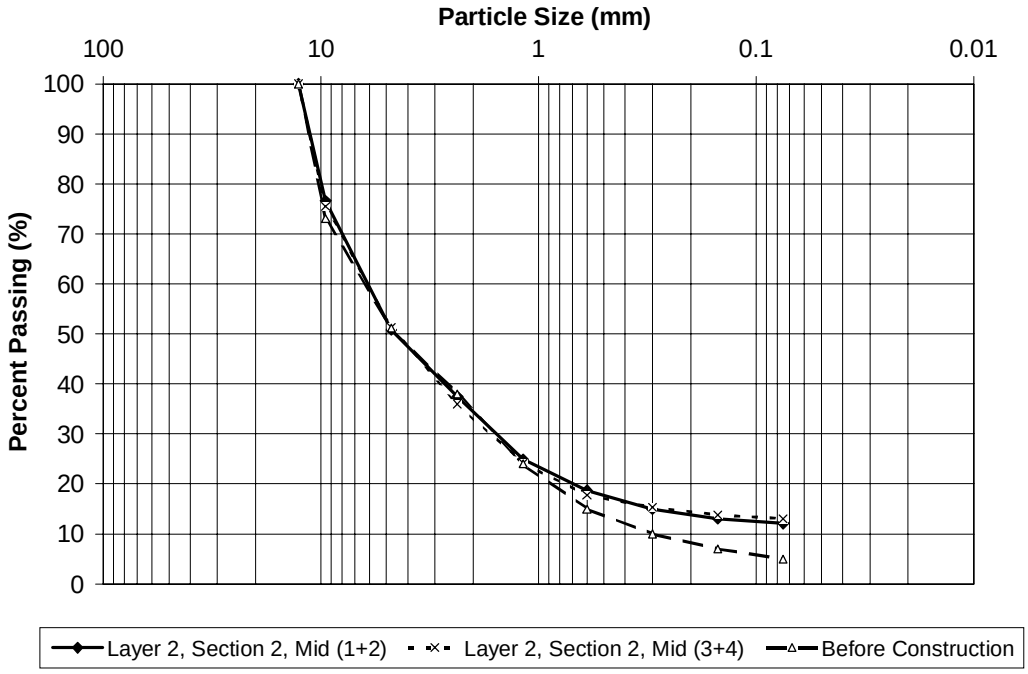


**Figure L 11 Section 2 Layer 2, middle wheel path base course gradation.**

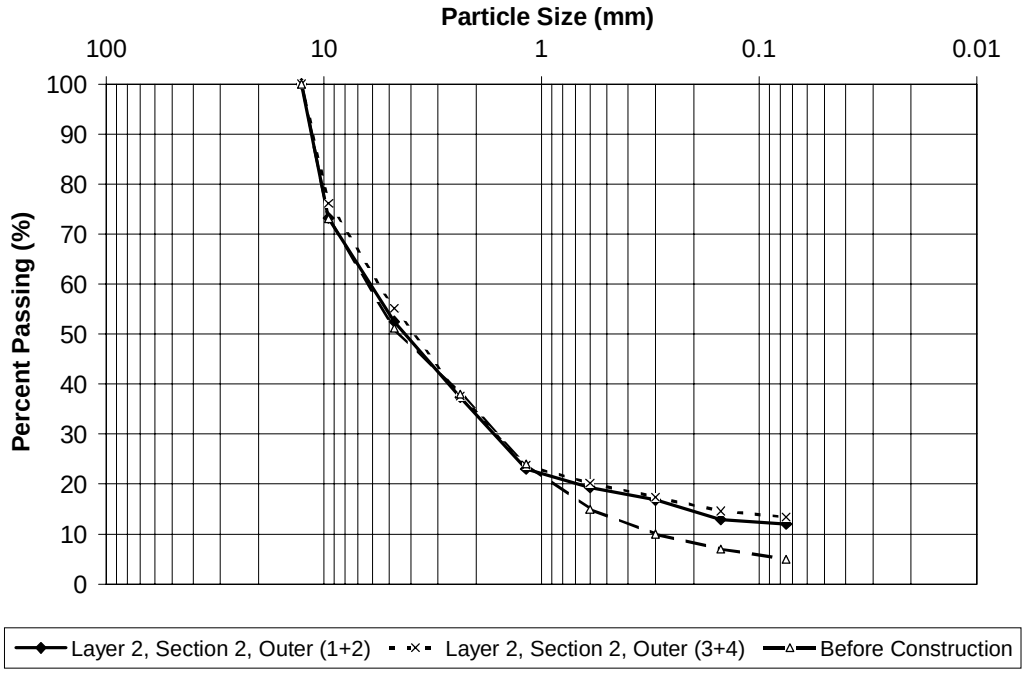


**Figure L 12 Section 2 Layer 2, outer wheel path base course gradation.**

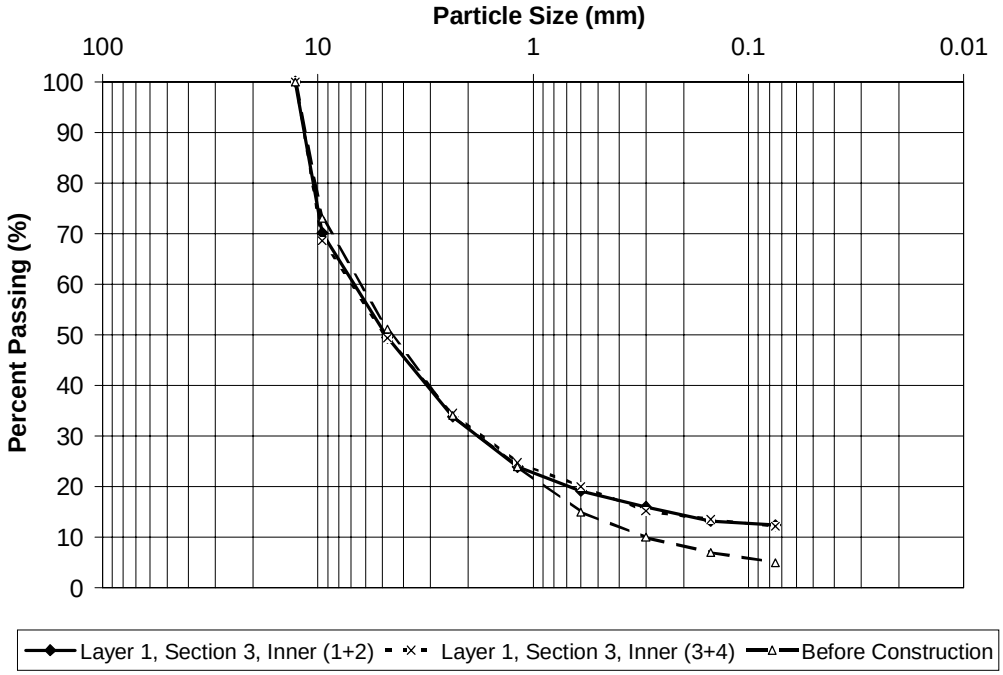


**Figure L 13 Section 3 Layer 1, inner wheel path base course gradation.**

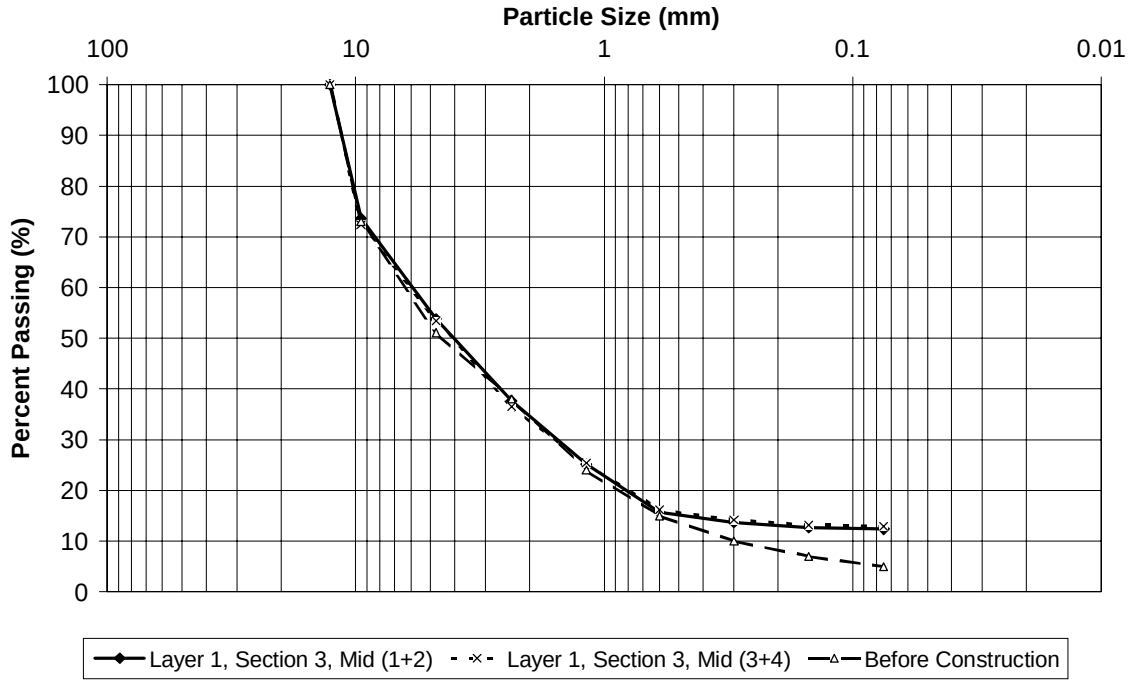


**Figure L 14 Section 3 Layer 1, middle wheel path base course gradation.**

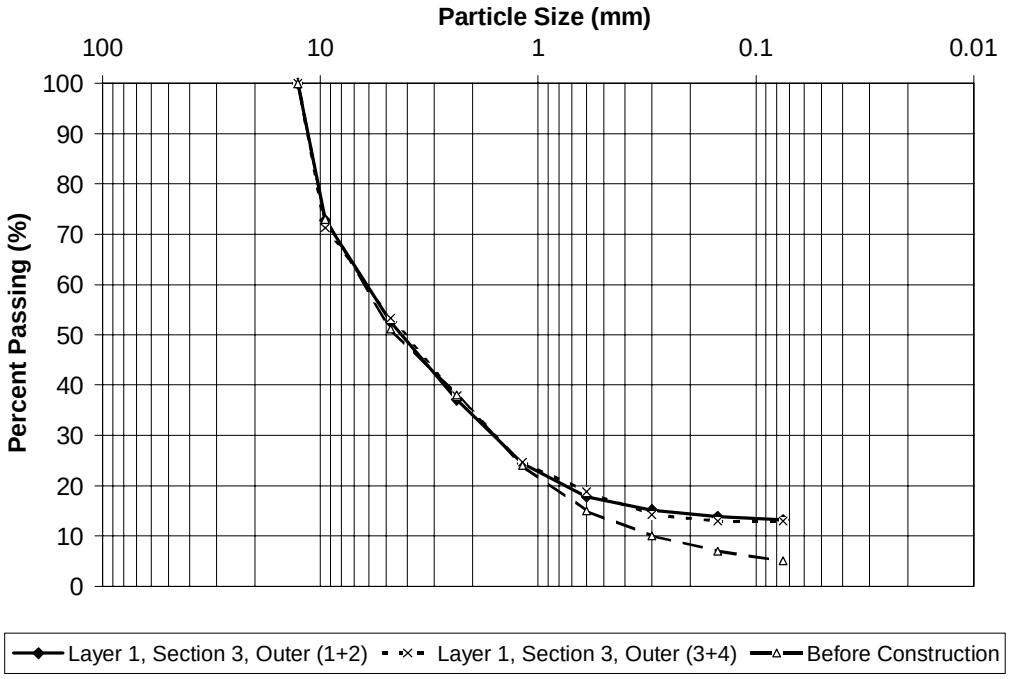


**Figure L 15 Section 3 Layer 1, outer wheel path base course gradation.**

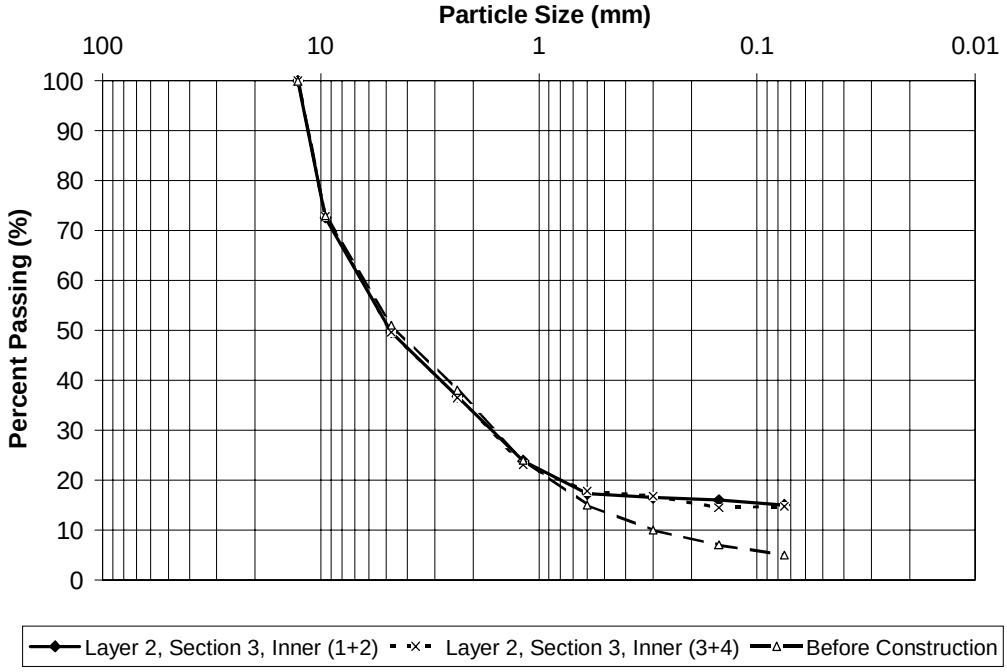


**Figure L 16 Section 3 Layer 2, inner wheel path base course gradation.**

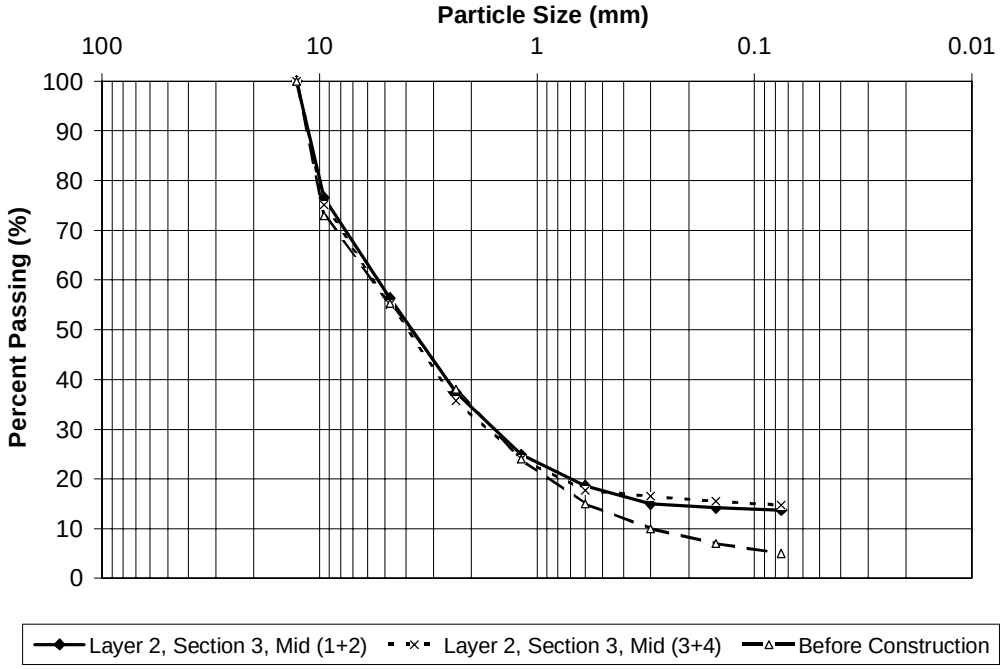


**Figure L 17 Section 3 Layer 2, middle wheel path base course gradation.**

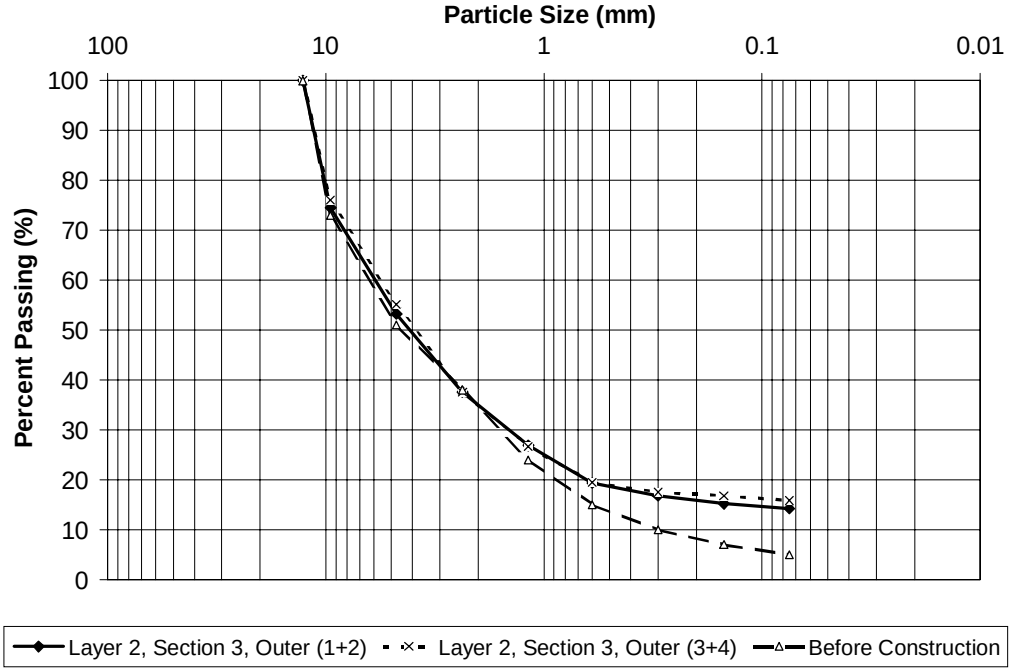


**Figure L 18 Section 3 Layer 2, outer wheel path base course gradation.**

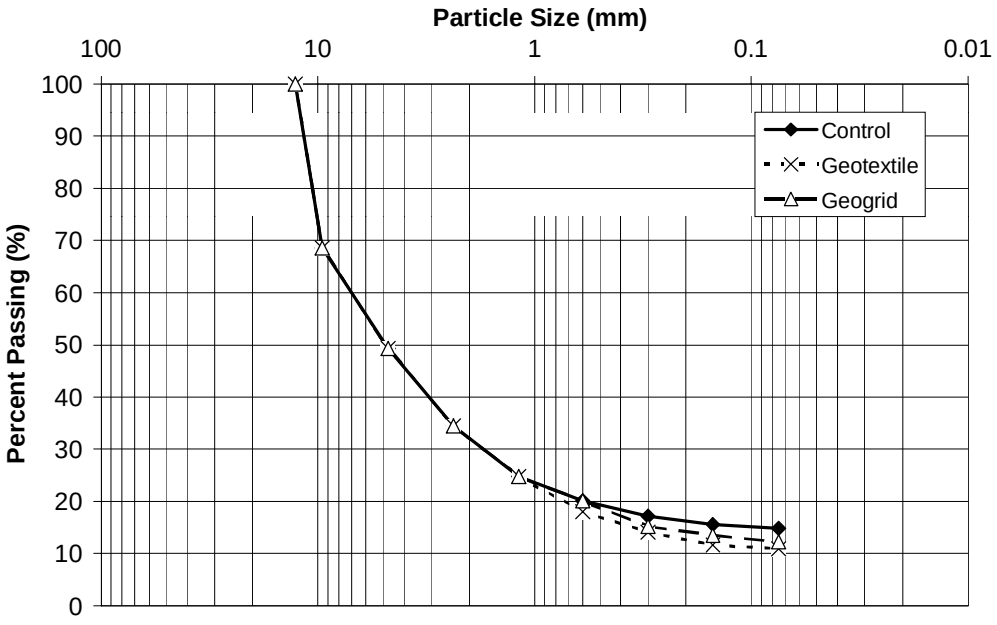


**Figure L 19 Layer 1, inner wheel path (sample, 1+2) base course gradation for all three sections.**

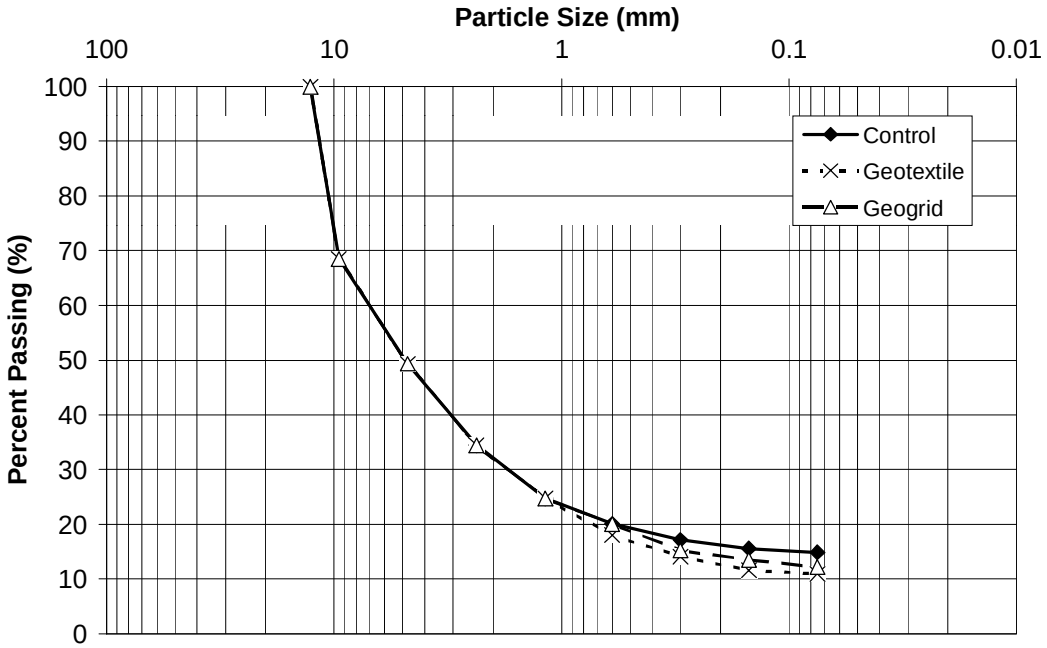


**Figure L 20 Layer 1, inner wheel path (sample, 3+4) base course gradation for all three sections.**

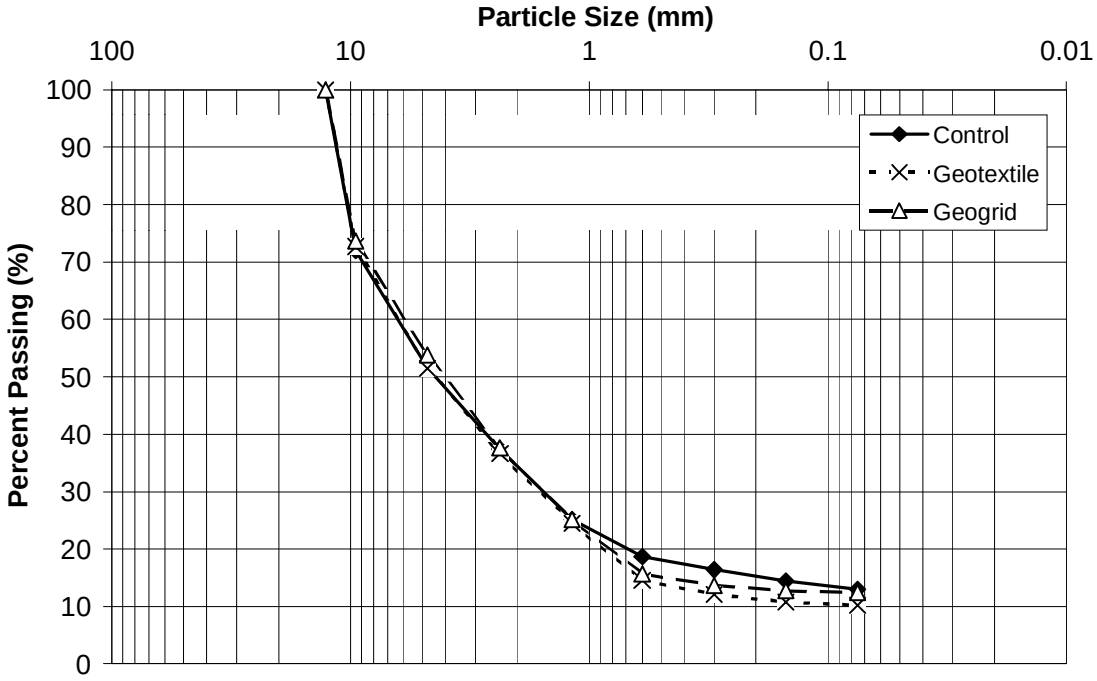


**Figure L 21 Layer 1, middle wheel path (sample, 1+2) base course gradation for all three sections.**

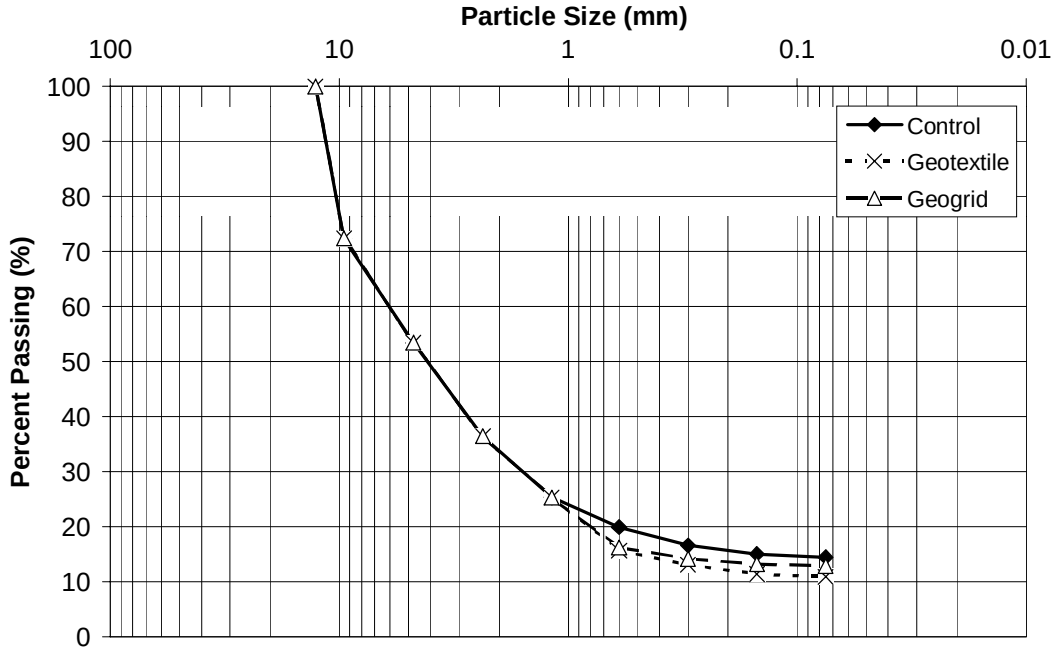


**Figure L 22 Layer 1, middle wheel path (sample, 3+4) base course gradation for all three sections.**

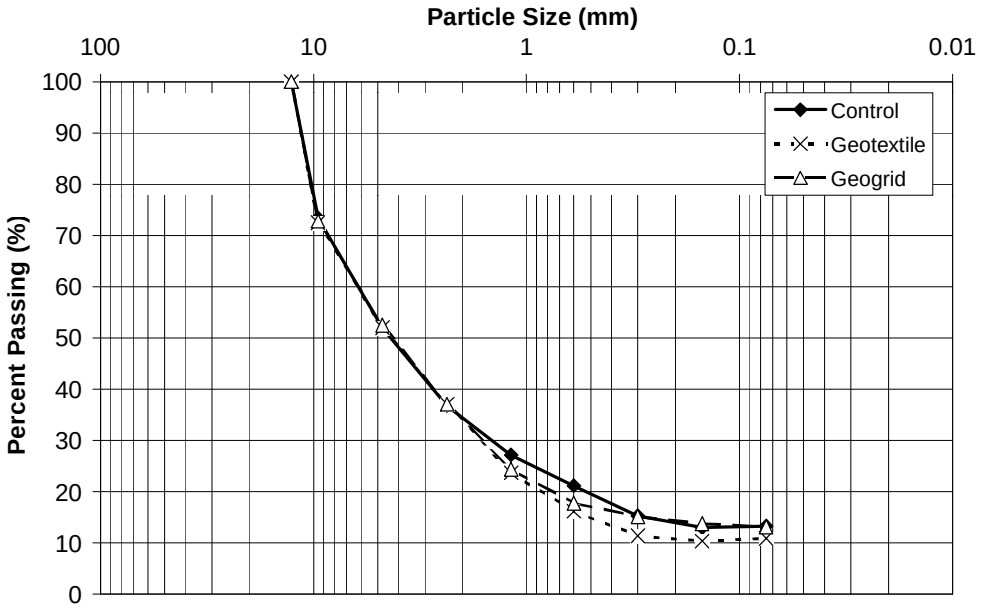


**Figure L 23 Layer 1, outer wheel path (sample, 1+2) base course gradation for all three sections.**

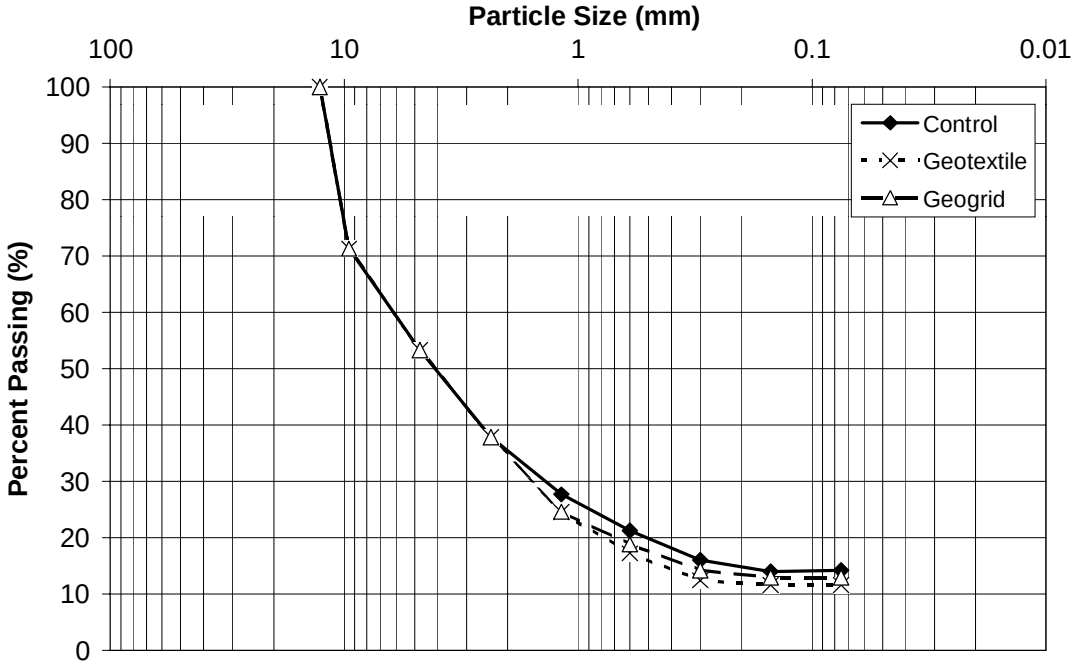


**Figure L 24 Layer 1, outer wheel path (sample, 3+4) base course gradation for all three sections.**

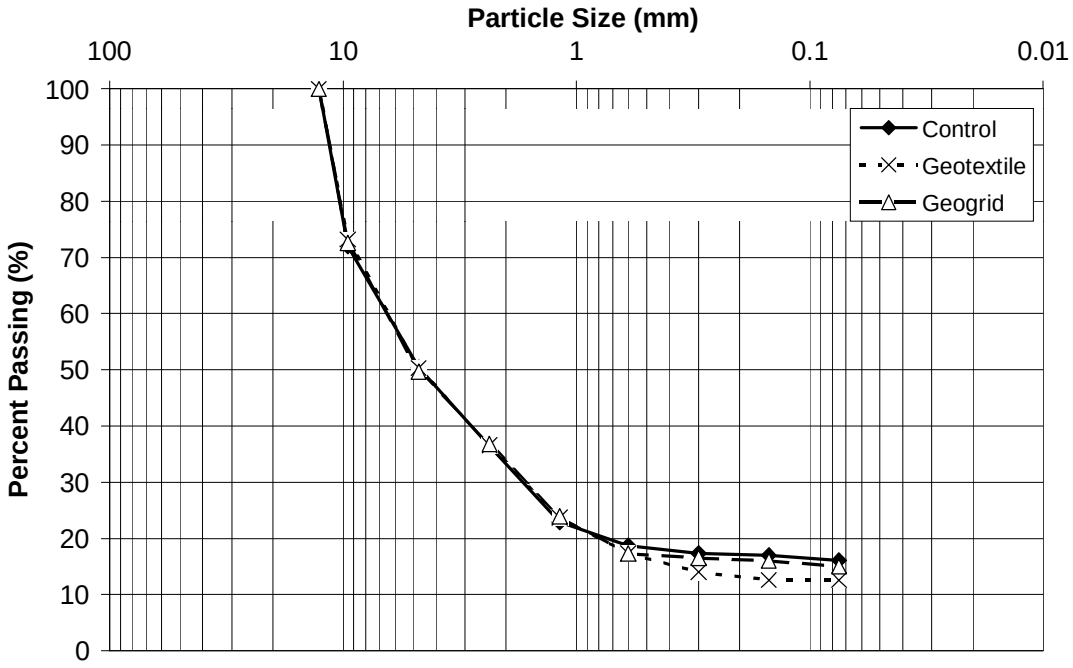


**Figure L 25 Layer 2, inner wheel path (sample, 1+2) base course gradation for all three sections.**

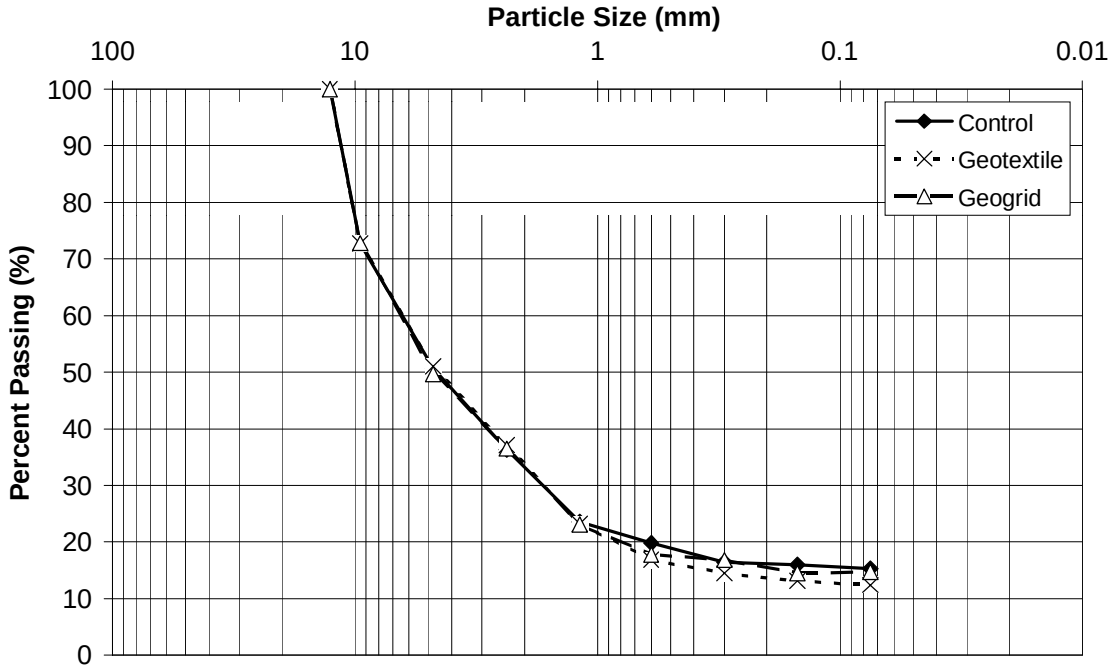


**Figure L 26 Layer 2, inner wheel path (sample, 3+4) base course gradation for all three sections.**

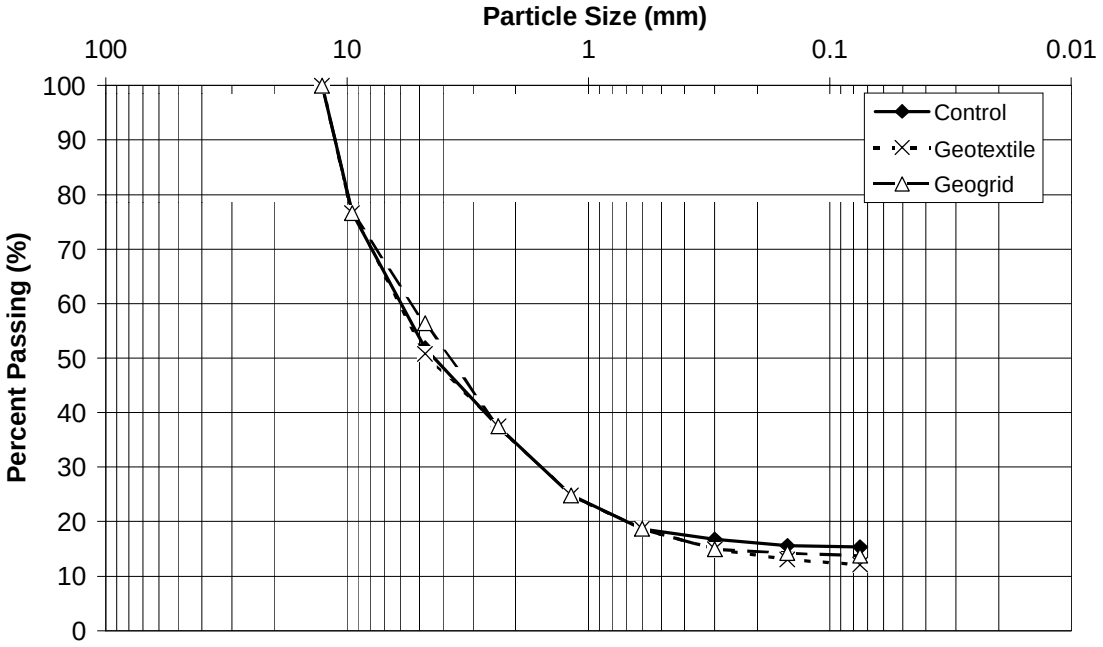


**Figure L 27 Layer 2, middle wheel path (sample, 1+2) base course gradation for all three sections.**

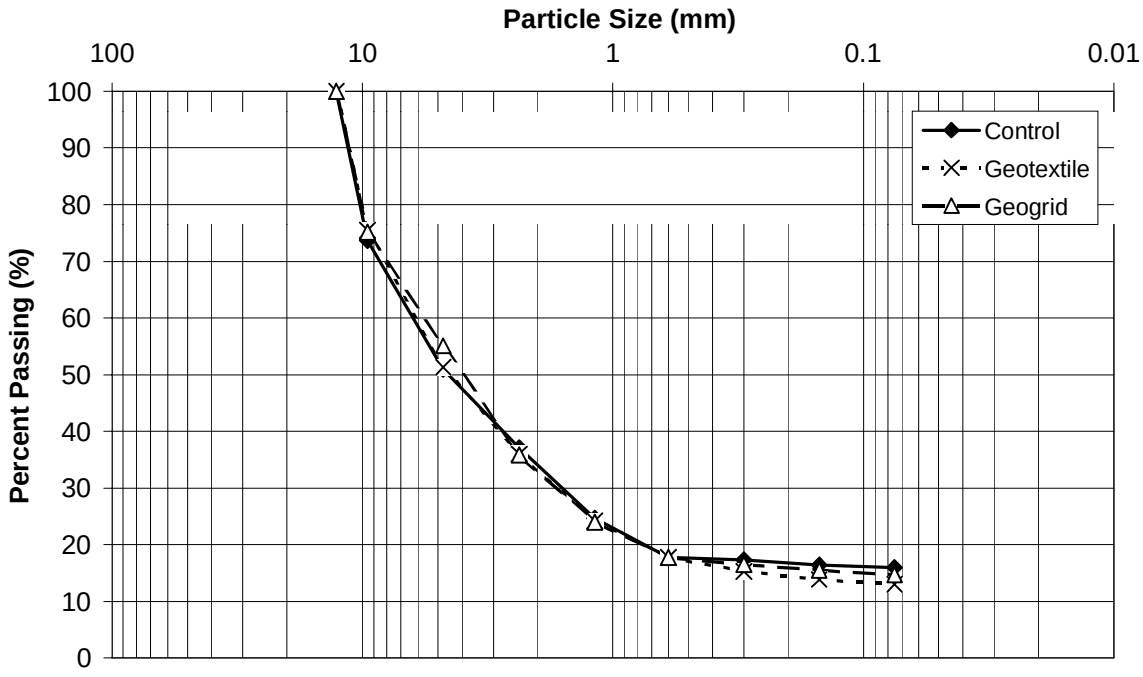


**Figure L 28 Layer 2, middle wheel path (sample, 3+4) base course gradation for all three sections.**

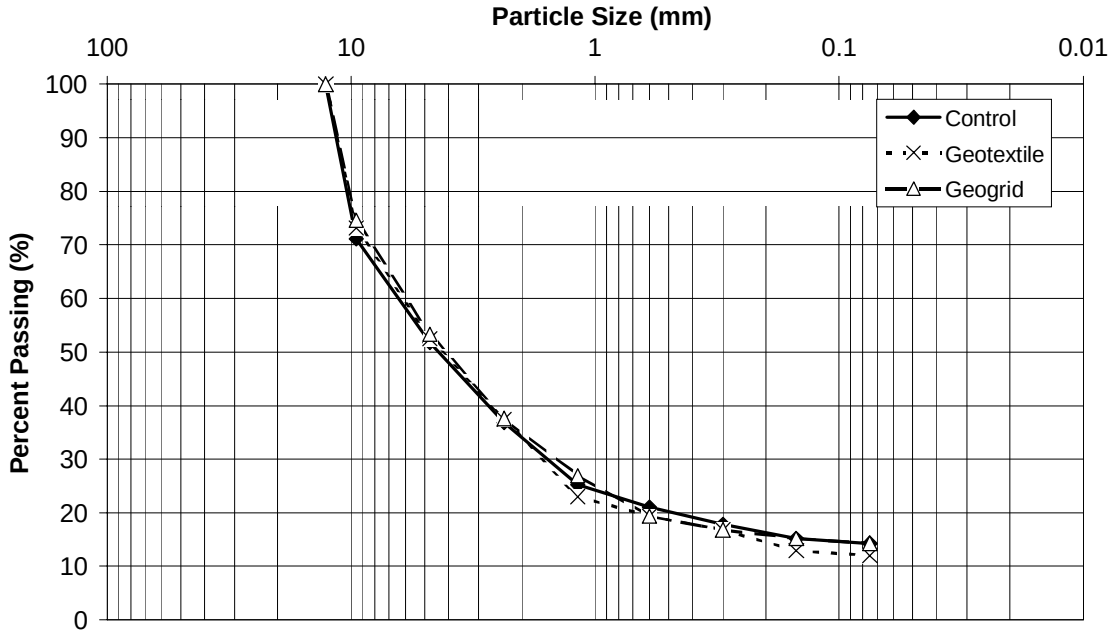


**Figure L 29 Layer 2, outer wheel path (sample, 1+2) base course gradation for all three sections.**

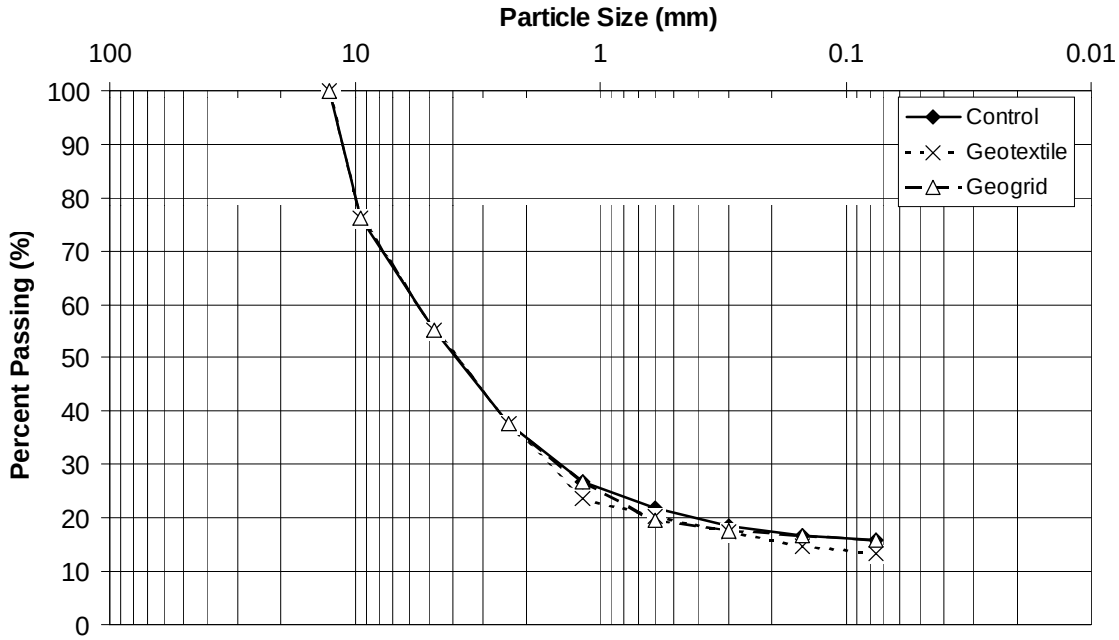


**Figure L 30 Layer 2, outer wheel path (sample, 3+4) base course gradation for all three sections.**

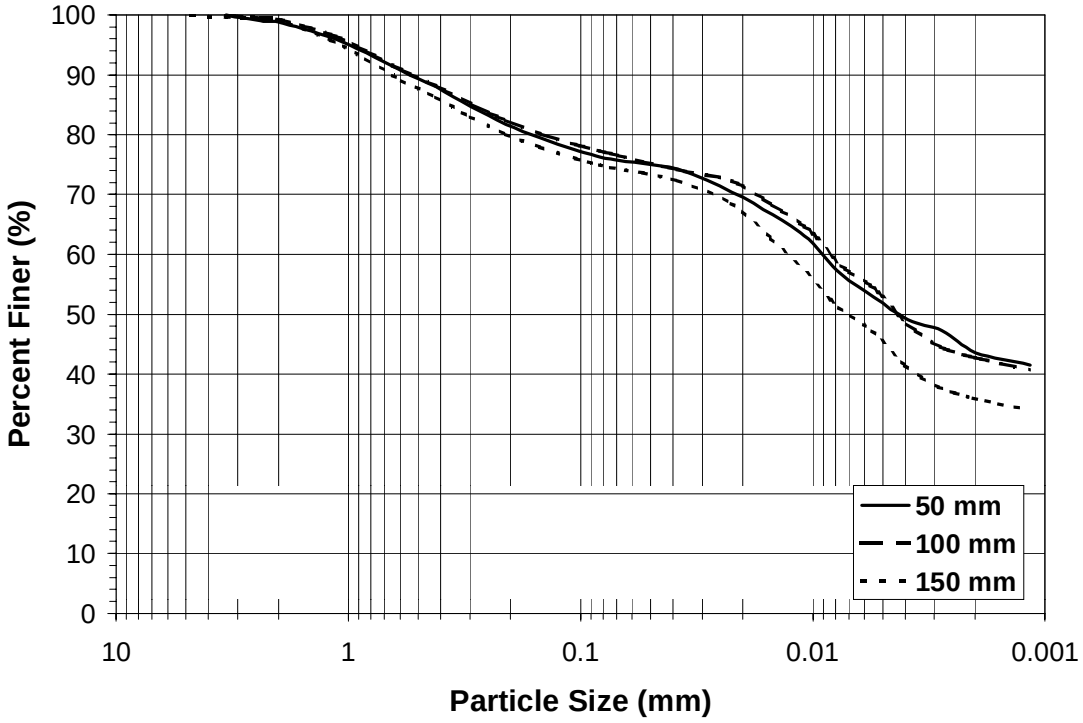


**Figure L 31 Subgrade gradation section 1 inner wheel path.**

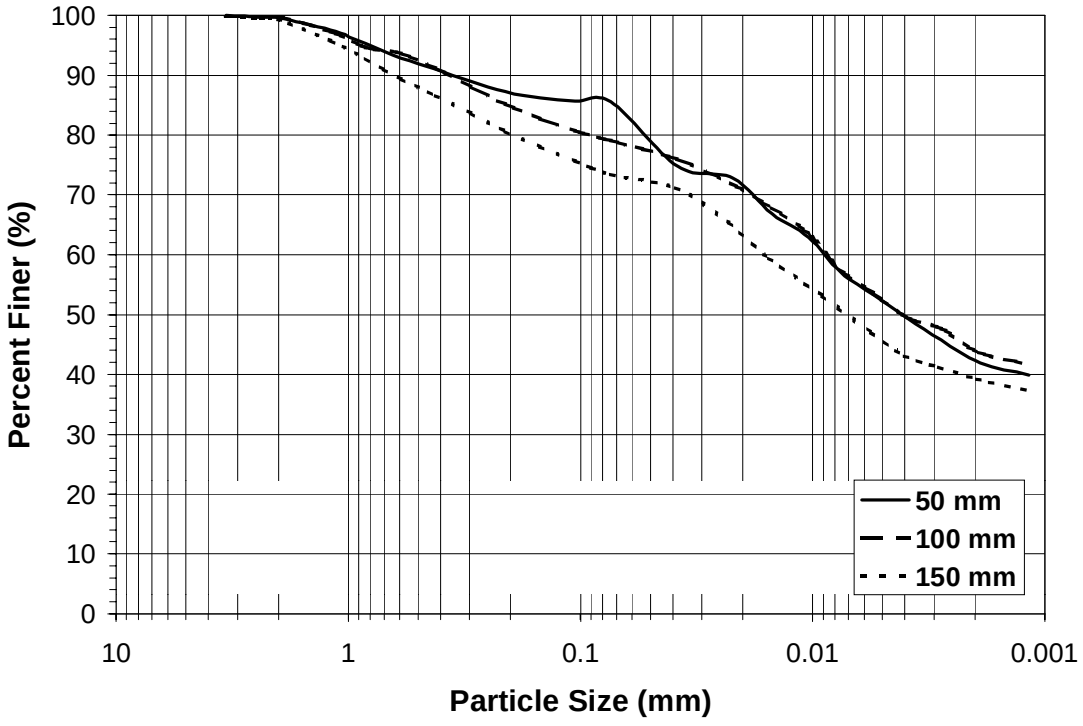


**Figure L 32 Subgrade gradation section 1 middle wheel path.**

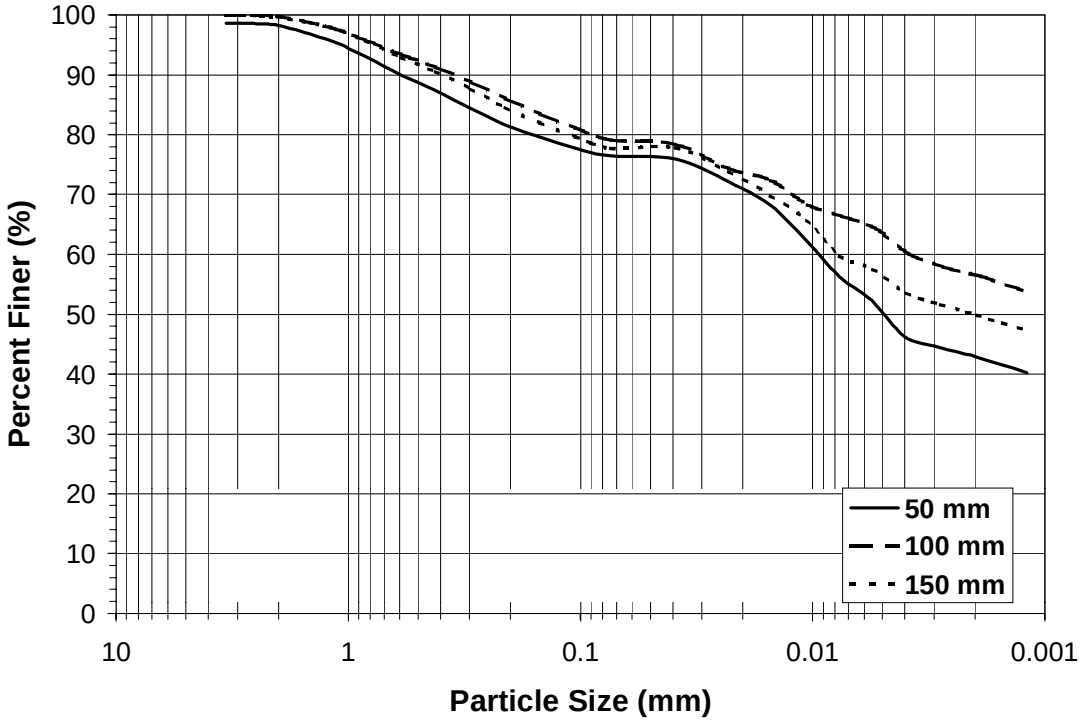


**Figure L 33 Subgrade gradation section 1 outer wheel path.**

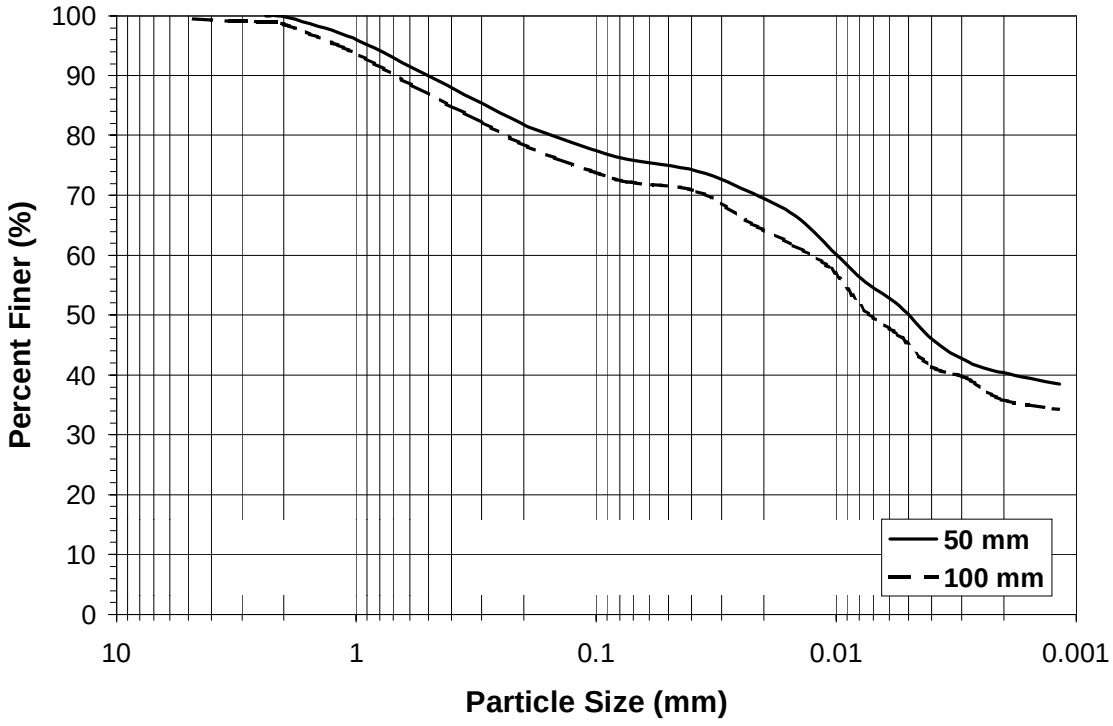


**Figure L 34 Subgrade gradation section 2 inner wheel path.**

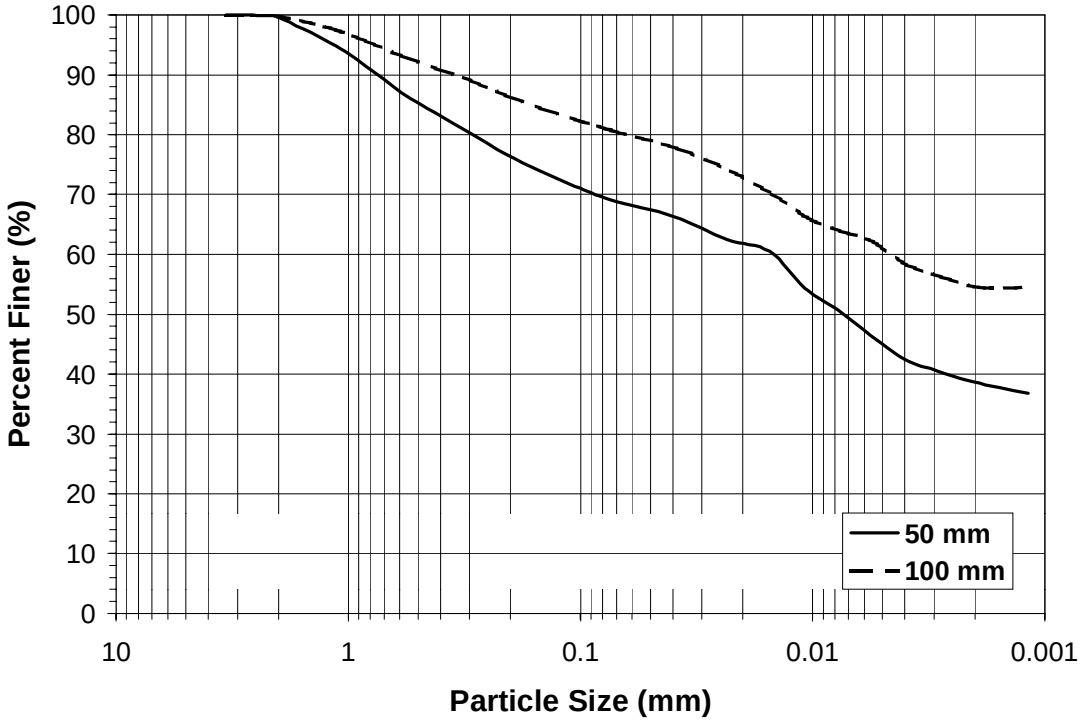


**Figure L 35 Subgrade gradation section 2 middle wheel path.**

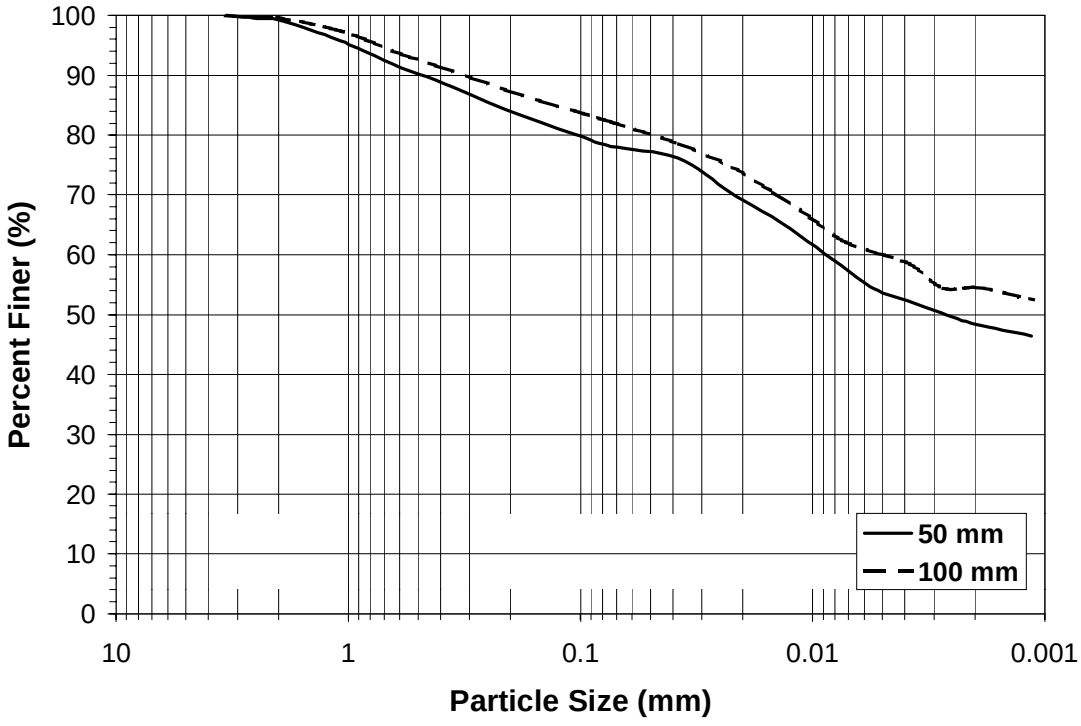


**Figure L 36 Subgrade gradation section 2 outer wheel path.**

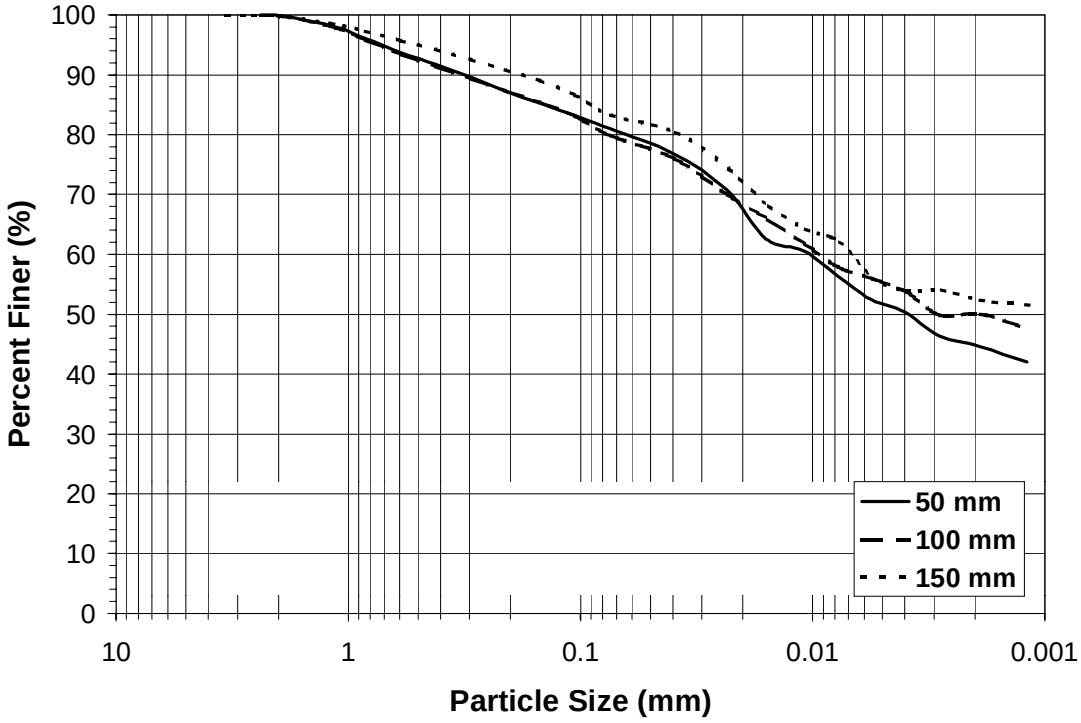


**Figure L 37 Subgrade gradation section 3 inner wheel path.**

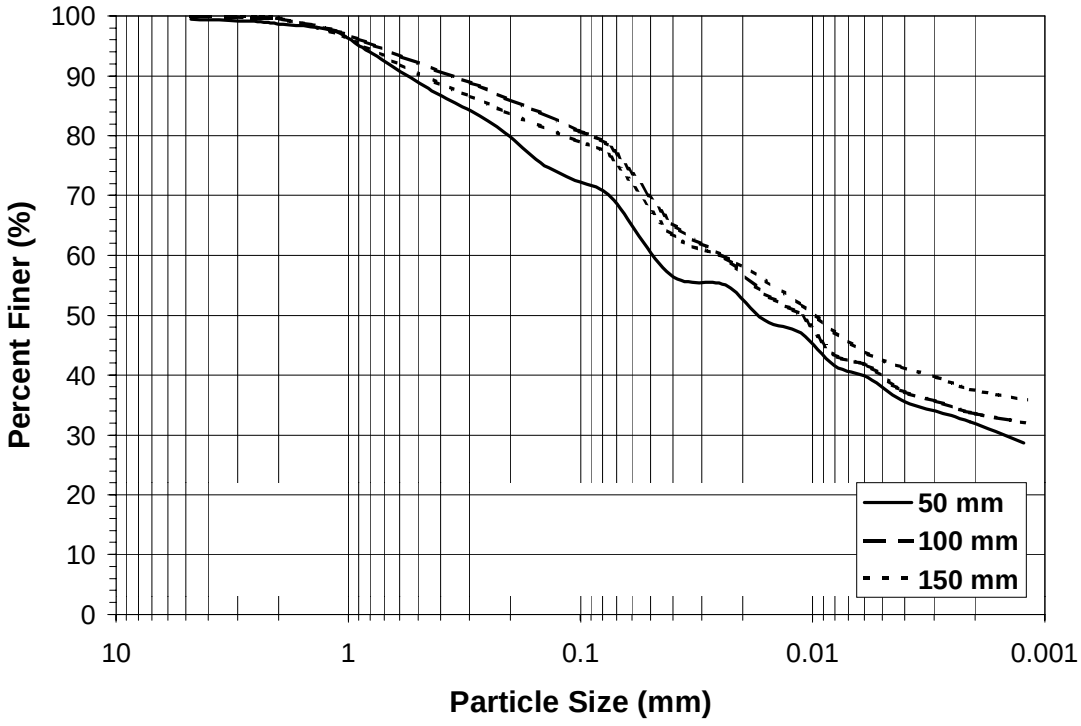


**Figure L 38 Subgrade gradation section 3 middle wheel path.**

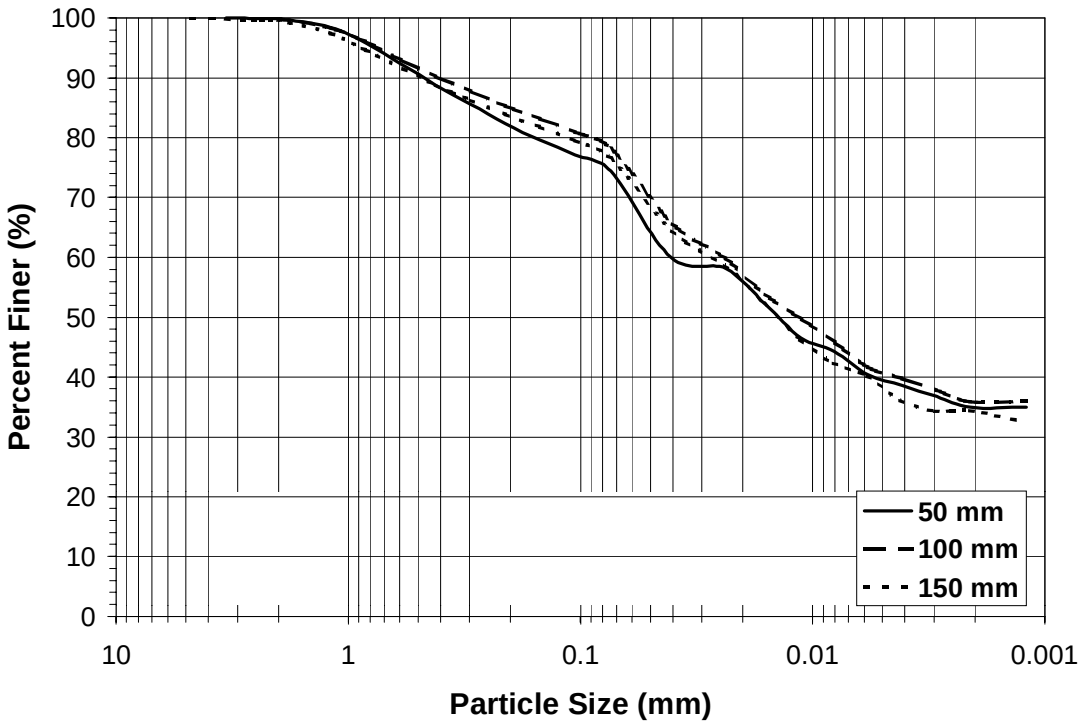


**Figure L 39 Subgrade gradation section 3 outer wheel path.**

# APPENDIX M

# COMPUTER PROGRAM

**Input file for the Secondary Road Geotextile Stabilized Section, and Explanation of Variables**

| | |
|---|---|
| 12 | No of seasons |
| 57.32d0 | Latitude of the pavement site |
| 3.50d0 | Thickness of HMA layer |
| 0.000375d0 | Coefficient of thermal expansion of HMA |
| 5.0 | Base temperature |
| 10.0,20.0 | Bottom of HMA, top of HMA temperature in season 1 |
| 35.0 | Average speed of the influencing vehicles in season 1 |
| 40 | Number of influencing vehicles |
| 7.0 | |
| 12.0,24.0 | |
| 30.0 | |
| 50 | |
| 10.0 | |
| 20.0,30.0 | |
| 35.0 | |
| 55 | |
| 20.0 | |
| 25.0,35.0 | |
| 32.0 | |
| 60 | |
| 25.0 | |
| 28.0,39.0 | |
| 30.0 | |
| 70 | The variables are defined for every season in a year |
| 30.0 | |
| 32.0,47.0 | |
| 35.0 | |
| 100 | |
| 45.0 | |
| 40.0,50.0 | |
| 30.0 | |
| 120 | |
| 47.0 | |
| 40.0,52.0 | |
| 30.0 | |
| 110 | |
| 40.0 | |
| 38.0,45.0 | |
| 32.0 | |
| 90 | |
| 35.0 | |
| 30.0,40.0 | |
| 40.0 | |
| 75 | |
| 20.0 | |
| 20.0,25.0 | |
| 35.0 | |
| 60 | |

10.0
15.0,20.0
32.0
100
2,2,0 — Number of tires on influencing axles (symmetry), number of XY location of those tires, 0 defines that data for interfaces is required

1.021d-6,1.102d-6,1.205d-6,1.383d-6,1.873d-6,4.5d-6,7.32d-6,0.32,3.5d0,3.5d0 — Creep compliance for HMA (& points), Poisson's ratio, thickness of layer 1, cumulative thickness of layer 1

| | |
|---|---|
| 35000,0.35,1.00d0,4.50d0 | Resilient modulus of layer 2, Poisson's ratio, thickness of layer 2, cumulative thickness till Bottom of Layer 2 |
| 35000,0.35,1.00d0,5.50d0 | Resilient modulus of layer 3, Poisson's Ratio, thickness of Layer 3, cumulative thickness till Bottom of Layer 3 |
| 35000,0.35,2.00d0,7.5d0 | Resilient modulus of layer 4, Poisson's Ratio, thickness of Layer 4, cumulative thickness till Bottom of Layer 4 |
| 8000,0.40 | Resilient modulus of subgrade, Poisson's ratio of subgrade |
| 1,1,1 | Interface conditions for layer 1-layer 2, layer 2-layer 3, layer 3-layer 4 (1 = Full Friction, 0 = No Friction) |
| 6.0d0,80.0d0,0.0d0,0.0d0 | Radius of tire, tire pressure, X-coordinate of Center of the Tire, Y-coordinate of the center of the tire (tire 1) |
| 6.0d0,80.0d0,13.5,0.0d0 | Radius of tire, tire pressure, X-coordinate of Center of the Tire, Y-coordinate of the center of the tire (tire 2) |
| 0.0d0,0.0d0 | XY location in the plane, where calculations are to be performed for stresses, strains, and displacements |
| 0.0d0,6.75d0 | XY location in the plane, where calculations are to be performed for stresses, strains, and displacements |
| 1,4 | Layer number for the layer 1 (HMA), and the layer the second last layer |
| 0.025,0.045,0.057,0.005 | Percentage maximum plastic strain at top of HMA in compression, maximum plastic strain at the top of HMA in tension, maximum plastic strain at the bottom of HMA in tension, maximum plastic strain at the top of subgrade in compression |
| -0.42,0.018 | Shift factors for HMA (Layer 1) at 5 °C, 25 °C and 40 °C |
| 10,5.0d0 | Number of years for analysis, Traffic growth percentage |

## How Run an Input File

Copy the entire directory called “Computer Program” into the hard-disk of the PC. Open the directory and select all files in there and right click mouse button and change the status of the files from “Read Only” to “Archive”. This step is necessary because some files need to be modified during the process of running the program. Then open the file called Data.inp (this is the input file described above) using any text editor and modify any variable(s) based upon need. Don’t change the number of seasons from 12. After necessary changes have been made, save the file Data.inp. You are all set to run the program. To Run the program double-click on the executable file by the name “Program.exe”. A small DOS window will open and you will see this statement being repeated “Start of Computation. Be Patient……..”. Once the program has completed the analysis, it will create several files (Data.buf, and Data.out are the buffer files and containing information regarding data required for the next time step, and Plastic.out, which is the output file generated by the program). Plastic.out contains information regarding accumulative deformations at the end of every season, tensile/compressive top of the HMA plastic strain, tensile plastic strain at the bottom of HMA layer and accumulative deformation at the top of the subgrade. To generate the plots in Microsoft Excel, use the sheet by the name Plots.xls. Just copy the data from the Plastic.out file into the Excel sheet, and it will generate the plots. See the next page for the listing of the computer program written in Fortran-77. If any questions arise please contact:

Salman A. Bhutta or Dr. Imad L. Al-Qadi
Department of Civil Engineering
Virginia Polytechnic Institute and State University
Blacksburg, VA 24061
E-mail: salman8@vt.edu or alqadi@vt.edu

```
**********************************************************************************************
*                    T R A N S F L E X                                                       *
*       (Transient Mechanistic Flexible Pavement Analysis and Design)                        *
*                                                                                            *
*This program is used to analyze and design flexible pavements, with and                     *
* without geosynthetics.  The program uses dynamic visco-elasto plastic                      *
* material characterization for both mechanical and thermal loading.                         *
* This program takes the input of various material properties and provides                    *
* an estimate of the rut depth, fatigue life and low temperature cracking.                    *
* The input file is called data.inp, and the output file is called plastic.out .              *
* Any questions and comments regarding the setup of the problem, processing and              *
* output can be directed towards the undersigned.  Thanks.                                    *
*  Author:  Salman A. Bhutta                                                                 *
*  Date: 20th March, 1998                                                                    *
*  Research Associate                                                                        *
*  Virginia Polytechnic Institute and State University                                       *
*  Blacksburg, VA 24060                                                                      *
*  e-mail: salman8@vt.edu                                                                    *
**********************************************************************************************
      IMPLICIT REAL(a-z)
      INTEGER i,j,k,l,l1,l2,ls,w1,w2,iii,ides,ihma,isub,ihmabot,
     -        isubtop,d,ii,traf,traffi,traff,noseas,kk,pck,yrs,
     -        traffc,thaplc
      COMMON prov(30,30,9),res(30,30,9)
      DIMENSION a(20),j1(20),ls(30),p(20),crp(10),tempr(24),ides(7,2,8)
      DIMENSION xc(20),xs(30),yc(20),ys(30),zs(30),str(7,2,8,7),
     -          mstr(7,3,4),t(7),Rt(7),Amat(7,7),Bmat(7,7),Cmat(7,7),
     -         Gmat(7),indx(7),BC(7),crpfit(7),Stgmat(4,7),
     -        lood(3),visplas(5),vismag(5),strtot(5),area(5),
     -           speeed(24),traffi(24),tmpdel1(24),Qtr(3,3),thk(3),
     -        AAmat(6,6),tmpdel2(24),Nxt(6),Nxb(6),BBmat(6,6),
     -        strptr(2),crpb(10),tme(7),crpc(10)


*************************************************************************
c     Input and Required Variable definitions:
c
c           l       Number of loads
c           l1      Number of offsets (geophone positions)
c           l2      Number of locations NOT on interfaces
c           ls      Layer number for each l2
c           a       Load radius
c           p       Load (psi, MPa NOT lb or kN)
c           xc,yc   Central coordinates of each load
c           xs,ys   X,Y coords of each point OFF 0,0 axis
c           zs      Depth z for each point NOT on interface
c           ej, uj  Elastic modulus and poisson's ratio for layer j
c           hj      Thickness of layer j
c           zj      cummulative depth of layer j
c           laj     Interface friction for interface j (= 1)
c    crp      Given creep compliance for HMA material
```

```
c             crpfit    Fitted creep compliance
c             tempr     Base temperatures for the sesons
c             tempdel1  Dynamic temperature loding per season
c             Gmat      Matrix of dilicret constants
c             speeed    Average vehicle speeds per season
c             traffi    Number of influencing vehicles per day
c             Qtr       Transformed reduced stiffness matrix
c             lood      Average vertical stress at the interfaces
c       Nxt   Applied normal forces for thermal loading
c             visplas   Megnitude of the viscoplastic strain
c             area      Area unsder the curve for Boltzman Supoerposition Integral
c             str       Matix of stresses, strains and displacements
c             strtot    Final accumulated strains and deformations
*******************************************************************************


*******************************************************************************
c     Open temporary and output files, and zero respective variables
*******************************************************************************
      OPEN(3,file="data.buf")
      OPEN(4,file="plastic.out")
      WRITE (4,9960)
      WRITE (4,9965)
      pck=0
      ptn=0
      traff=0

*******************************************************************************
c     CALL TO READ INPUT DATA FILE
c    Then loop seven times, and calculate the seven differnt results
*******************************************************************************

 5000  CALL leDOn(l,l1,l2,ls,a,p,xc,yc,xs,ys,zs,e2,e3,e4,e5,
     - u1,u2,u3,u4,u5,h1,h2,h3,h4,z1,z2,z3,z4,la1,la2,la3,noseas,
     -tempr,crpb,traffi,speeed,ihma,isub,pltpcom,pltpten,pltbtcm,
     -pltpsub,tmpdel1,tmpdel2,thkhma,alphat,latdeg,sf1,sf2,yrs,pers)

      DO 13100 i=1,7
       crpc(i)=crpb(i)
      WRITE(3,*) crpb(i)
13100 CONTINUE

      term=noseas*yrs

      DO 10100 kk=1,term

      WRITE (*,*) kk
      WRITE (3,*) kk
      IF (pck.EQ.noseas) THEN
       pck=0
       ptn=ptn+1
```

```
      END IF
      pck=pck+1
       speed=speeed(pck)
       traffc=traffi(pck)

       trfinc=0.5d0*(1+(1+pers/100.0d0)**ptn)
       traff=traffc*trfinc

       T2=tmpdel2(pck)
       T1=tmpdel1(pck)
       Tempback=T1
       temptrat=tempr(pck)


*****************************************************************************
c    Defination of Poisson's rtio as per ASTM standard
*****************************************************************************

      u1=0.0043*temptrat+0.2328

*****************************************************************************
c     CALL TO READ INPUT DATA FILE
c     Use Shift factors to calculate creep compliance as per current base
c     temperature
*****************************************************************************

      t(1)=31535.0
      t(2)=94605.0
      t(3)=315350.0
      t(4)=3.1535d6
      t(5)=31.535d6
      t(6)=9.4605d7
      t(7)=3.1535d8
      Rt(1)=31535.0
      Rt(2)=94605.0
      Rt(3)=315350.0
      Rt(4)=3.1535d6
      Rt(5)=31.535d6
      Rt(6)=9.4605d7
      Rt(7)=6.307d20
      fct=12.0/noseas
      constan=(kk-1)*fct*2.6784d6
      tme(1)=constan+fct*2.6784d6*0.003
      tme(2)=constan+fct*2.6784d6*0.005
      tme(3)=constan+fct*2.6784d6*0.008
      tme(4)=constan+fct*2.6784d6*0.01
      tme(5)=constan+fct*2.6784d6*0.1
      tme(6)=constan+fct*2.6784d6*0.3
      tme(7)=constan+fct*2.6784d6*1.0
```

```
      DO 2300 i=1,7
       Gmat(i)=0.0d0
       BC(i)=0.0d0
       DO 2400 j=1,7
        Amat(i,j)=0.0d0
        Bmat(i,j)=0.0d0
        Cmat(i,j)=0.0d0
2400  CONTINUE
2300  CONTINUE



      DO 1900 i=1,7
       DO 2000 j=1,7
        Amat(i,j)=EXP (-(t(i))/(Rt(j)))
2000  CONTINUE
1900  CONTINUE

      DO 4000 i=1,7
       DO 4000 j=1,7
        Bmat(i,j)=Amat(j,i)
4000  CONTINUE


      DO 2100 i=1,7
       DO 2100 j=1,7
         DO 2100 ii=1,7
       Cmat(i,j)=Cmat(i,j)+Bmat(i,ii)*Amat(ii,j)
 2100 CONTINUE

       DO 3100 i=1,7
        DO 3100 j=1,7
         Gmat(i)=Gmat(i)+Bmat(i,j)*crpb(j)

3100   CONTINUE


      WRITE(3,3900)
       DO 3600 i=1,7
         WRITE (3,*) Gmat(i)
3600   CONTINUE
       DO 3610 i=1,7
         WRITE (3,*) tme(i)
3610   CONTINUE

3700    FORMAT(e8.2,2x,e8.2,2x,e8.2,2x,e8.2,2x,e8.2,2x,e8.2,2x,e8.2)
3900  FORMAT(//)
3910  FORMAT('Creep for this season is:')
      CALL LUDCMP(Cmat,7,7,INDX,D)
      CALL LUBKSB(Cmat,7,7,INDX,Gmat)
```

```
      WRITE(3,3900)
       DO 3200 i=1,7
         WRITE (3,*) Gmat(i)
3200   CONTINUE

      CALL diric(Gmat,Rt,tme,crpfit)

      WRITE(3,3900)
      WRITE(3,3910)
       DO 4300 i=1,7
         WRITE (3,*) crpfit(i)
         crpc(i)=crpfit(i)
4300   CONTINUE

       py2=sf2
       py1=0.0
       px2=40.0
       px1=25.0
      slp1=(py2-py1)/(px2-px1)
      intrc1=(px2*py1-px1*py2)/(px2-px1)
       py2=sf1
       py1=0.0
       px2=5.0
       px1=25.0
      slp2=(py2-py1)/(px2-px1)
      intrc2=(px2*py1-px1*py2)/(px2-px1)

      IF (temptrat.GT.25.0) THEN
        shftfac=slp1*temptrat+intrc1
      ELSEIF (temptrat.LT.25.0) THEN
        shftfac=slp2*temptrat+intrc2
      END IF

      IF (temptrat.EQ.25.0) THEN
        shftfac=0.0
      END IF


      DO 10300 i=1,7
       crp(i)=10.0**(LOG10(crpc(i))+shftfac)
10300 CONTINUE

C     Fix the sudden dip at creep point # 6
      IF (crp(6).GT.crp(5)) THEN
       crp(6)=(crp(7)+crp(5))*0.5d0
      END IF

      WRITE(3,*) 'CREEP, VALUES FOR THE CURRENT SEASON ARE:'
      DO 10310 I=1,7
```

```
      WRITE(3,*) CRP(I)
10310 CONTINUE

*****************************************************************************
c     Calculate the time in seconds the simulation is at and shift the
c     creep compliance
*****************************************************************************

     DO 10000 iii=1,7
          l2=0
          e1=1/crp(iii)

     WRITE (3,*) 'CUREENT CREEP, MODULUS, AND POISSON RATIO'
     WRITE (3,*) CRP(III),E1,U1

*****************************************************************************
c       CALL SUBROUTINE TO SCALE DATA (This is BISAR code by van Cauwelaert, 1984)
*****************************************************************************

       CALL point(z1,z2,z3,z4,l2,zs,ls)

9      CALL echde(h1,z1,z2,z3,z4,xs,ys,zs,a,xc,yc,l1,l2,l)

c       FIND MAX OFFSET TO LATERAL POINT - rmax

     DO 106 i=1,l1
        DO 107 j=1,l
        rmax=0.
     r=SQRT((xc(j)-xs(i))*(xc(j)-xs(i))+(yc(j)-ys(i))*(yc(j)-ys(i)))
     IF(r.gt.rmax) rmax=r
107      CONTINUE
106   CONTINUE

c       FIND SMALLEST MODULUS min

     min=e1
     IF (e2.lt.min) min=e2
     IF (e3.lt.min) min=e3
     IF (e4.lt.min) min=e4
     IF (e5.lt.min) min=e5

c       IF LOWEST LAYER NOT WEAKEST MODULUS - SET INTEGRATION STEP

     IF (e5.gt.min) CALL pas1(p1,h1,a,l,ml,m,e1,e2,e3,e4,e5,
    -u1,u2,u3,u4,u5,z1,z2,z3,z4,a1,c1,a2,b2,c2,d2,a3,b3,c3,d3,
    -a4,b4,c4,d4,pr,w2,la1,la2,la3,fl,rmax)

c       IF LOWEST LAYER IS WEAKEST MODULUS - SET INTEGRATION STEP

     IF (e5.le.min) CALL pas2(p1,e1,e5,u1,u5,h1,a,l,pr,ml,rmax)
     CALL vinit(l1,l2,w1,m,m1,p1)
```

```
      CALL finit(l,l1,l2,xc,yc,xs,ys,zs,ls,e1,e2,e3,e4,e5,u1,
     -u2,u3,u4,u5,p,a,m1)

200   m=m+m1

c     COMPUTE LAYER CONSTANTS [A, B, C, D]i

      CALL const(m,e1,e2,e3,e4,e5,u1,u2,u3,u4,u5,z1,z2,z3,z4,a1,c1,a2,
     -b2,c2,d2,a3,b3,c3,d3,a4,b4,c4,d4,pr,w2,la1,la2,la3,fl)



c     COMPUTE BESSEL FUNCTION J1(x)

      CALL besj1(l,m,a,j1)

c     SET INTEGRATION SUM TO ZERO

      CALL zero(l1,l2)

c     COMPUTE FUNDAMENTAL FUNCTIONS FOR EACH DEPTH & OFFSET

      DO 100 i=1,l1
        DO 110 j=1,l
       r=SQRT((xc(j)-xs(i))*(xc(j)-xs(i))+(yc(j)-ys(i))*(yc(j)-ys(i)))
          alpha=0.
        IF(xc(j).ne.xs(i).or.yc(j).ne.ys(i))
     -  alpha=ATAN2(ys(i)-yc(j),xs(i)-xc(j))
          CALL bj0j2(m,r,j0,j2)
          CALL surfa(i,j,z1,a1,c1,u1,j0,j1,j2,m,p,a,r,alpha)
          DO 120 k=2,l2
            z=zs(k)
            IF(ls(k).eq.1) CALL couc1(i,j,k,z,p,a,j0,j1,j2,z1,u1,
     -        m,a1,c1,r,alpha)
            IF(ls(k).eq.2) CALL couc2(i,j,k,z,p,a,j0,j1,j2,z1,z2,
     -        u2,e2,m,a2,b2,c2,d2,r,alpha)
            IF(ls(k).eq.3) CALL couc3(i,j,k,z,p,a,j0,j1,j2,z2,z3,
     -        u3,e3,m,a3,b3,c3,d3,r,alpha)
            IF(ls(k).eq.4) CALL couc4(i,j,k,z,p,a,j0,j1,j2,z3,z4,
     -        u4,e4,m,a4,b4,c4,d4,r,alpha)
120         CONTINUE
110       CONTINUE
100   CONTINUE

c     PERFORM NUMERICAL INTEGRATION

      CALL simps(l1,l2,w1,m1)

c

      IF(w1.ne.0) GOTO 200
```

```
      w1=1
      IF (m.le.ml) w2=1
      IF(w2.eq.0) CALL modIF(pr,m1,l1,l2,rmax)
      IF(ABS(fl).gt..0001)GOTO 200

      CALL comsu(l,l1,a,p,u1,e1,xc,xs,yc,ys)
      CALL ccou1(l,l1,l2,ls,xc,xs,yc,ys,zs,a,p,u1,e1)
      CALL echef(h1,z1,z2,z3,z4,xs,ys,zs,a,xc,yc,l1,l2,l)

153   OPEN(1,file="DATA.OUT")
      CALL imres(l1,l2,xs,ys,zs,ls,u1,u2,u3,u4,u5,e1,e2,e3,e4,e5)
10000 CONTINUE

*****************************************************************************
c    READ the output from the analysis program (BISAR) into arrays STR and IDES
*****************************************************************************

      close(1)
      OPEN(1,file="DATA.OUT")


      DO 1100 i = 1,7
       DO 1200 j=1,2
        DO 1300 k=1,8
      READ (1,1000) str(i,j,k,1),ides(i,j,k),str(i,j,k,2),
     -str(i,j,k,3),str(i,j,k,4),str(i,j,k,5),str(i,j,k,6)
      WRITE (3,1000) str(i,j,k,1),ides(i,j,k),str(i,j,k,2),
     -str(i,j,k,3),str(i,j,k,4),str(i,j,k,5),str(i,j,k,6)


1000   FORMAT(e10.3,3x,i1,5x,e9.4,5x,e10.4,5x,e10.4,
      -5x,e10.4,5x,e10.4)
1300  CONTINUE
1200  CONTINUE
1100  CONTINUE



*****************************************************************************
c    Calculate the Maximum strains in the alREADy stored array
c     The matrix mstr(i,j,k), i=1,7 - j=1,3 - k=1,4
c          i signIFy the creep point locations (1 through 7)
c          j signIFy the top of HMA (1), bot of HMA (2), top of subgrade (3)
c          k signIFy stress-z (1), ex (2), ey (3), ez (4)
*****************************************************************************
c     Top of HMA
*****************************************************************************

      close(1)

      DO 1400 i=1,7
```

```
      IF (ABS(str(i,1,ihma,2)).GT.ABS(str(i,2,ihma,2))) THEN
       mstr(i,1,1)=str(i,1,ihma,2)
       ELSE
       mstr(i,1,1)=str(i,2,ihma,2)
      END IF
      IF (ABS(str(i,1,ihma,4)).GT.ABS(str(i,2,ihma,4))) THEN
       mstr(i,1,2)=str(i,1,ihma,4)
       ELSE
       mstr(i,1,2)=str(i,2,ihma,4)
      END IF
      IF (ABS(str(i,1,ihma,5)).GT.ABS(str(i,2,ihma,5))) THEN
       mstr(i,1,3)=str(i,1,ihma,5)
       ELSE
       mstr(i,1,3)=str(i,2,ihma,5)
      END IF
      IF (ABS(str(i,1,ihma,6)).GT.ABS(str(i,2,ihma,6))) THEN
       mstr(i,1,4)=str(i,1,ihma,6)
       ELSE
       mstr(i,1,4)=str(i,2,ihma,6)
      END IF

*****************************************************************************
c     Bottom of HMA
*****************************************************************************

      ihmabot=ihma+1

     IF (ABS(str(i,1,ihmabot,2)).GT.ABS(str(i,2,ihmabot,2))) THEN
       mstr(i,2,1)=str(i,1,ihmabot,2)
       ELSE
       mstr(i,2,1)=str(i,2,ihmabot,2)
      END IF
      IF (ABS(str(i,1,ihmabot,4)).GT.ABS(str(i,2,ihmabot,4))) THEN
       mstr(i,2,2)=str(i,1,ihmabot,4)
       ELSE
       mstr(i,2,2)=str(i,2,ihmabot,4)
      END IF
      IF (ABS(str(i,1,ihmabot,5)).GT.ABS(str(i,2,ihmabot,5))) THEN
       mstr(i,2,3)=str(i,1,ihmabot,5)
       ELSE
       mstr(i,2,3)=str(i,2,ihmabot,5)
      END IF
      IF (ABS(str(i,1,ihmabot,6)).GT.ABS(str(i,2,ihmabot,6))) THEN
       mstr(i,2,4)=str(i,1,ihmabot,6)
       ELSE
       mstr(i,2,4)=str(i,2,ihmabot,6)
      END IF

*****************************************************************************
c     Top of Subgrade
*****************************************************************************
```

```
      isubtop=isub*2

     IF (ABS(str(i,1,isubtop,2)).GT.ABS(str(i,2,isubtop,2))) THEN
       mstr(i,3,1)=str(i,1,isubtop,2)
       ELSE
       mstr(i,3,1)=str(i,2,isubtop,2)
      END IF
      IF (ABS(str(i,1,isubtop,4)).GT.ABS(str(i,2,isubtop,4))) THEN
       mstr(i,3,2)=str(i,1,isubtop,4)
       ELSE
       mstr(i,3,2)=str(i,2,isubtop,4)
      END IF
      IF (ABS(str(i,1,isubtop,5)).GT.ABS(str(i,2,isubtop,5))) THEN
       mstr(i,3,3)=str(i,1,isubtop,5)
       ELSE
       mstr(i,3,3)=str(i,2,isubtop,5)
      END IF
      IF (ABS(str(i,1,isubtop,6)).GT.ABS(str(i,2,isubtop,6))) THEN
       mstr(i,3,4)=str(i,1,isubtop,6)
       ELSE
       mstr(i,3,4)=str(i,2,isubtop,6)
      END IF

1400  CONTINUE

*****************************************************************************
c    Calculate the Maximum strains in the already stored array
c     The matrix mstr(i,j,k), i=1,7 - j=1,3 - k=1,4
c          i signify the creep point locations (1 through 7)
c          j signify the top of HMA (1), bot of HMA (2), top of subgrade (3)
c          k signify stress-z (1), ez (2), ex (3), ey (4)
*****************************************************************************

       DO 1500 i = 1,7
     WRITE (3,*) i
      DO 1600 j=1,3

     WRITE (3,1800) mstr(i,j,1),mstr(i,j,2),mstr(i,j,3),mstr(i,j,4)

1800   FORMAT(e10.4,5x,e10.4,5x,e10.4,5x,e10.4)
c 1700  CONTINUE
1600  CONTINUE
1500  CONTINUE

c*****************************************************************************
c    Calculation of Collocation Constants and calculation of Viscoplastic
c     strain and Rewrite the 7th row and column for Amat and Bmat to prepare for
c     strain fitting
c*****************************************************************************
```

```
      DO 3400 i=1,7
        Amat(7,i)= 1.0d0
        Amat(i,7)= 1.0d0
        Bmat(7,i)= 1.0d0
        Bmat(i,7)= 1.0d0
3400  CONTINUE

      DO 4700 j=1,4

       DO 4500 i=1,7
        Gmat(i) =0.0d0
4500   CONTINUE

        DO 5600 i=1,7
         DO 5600 k=1,7
          Amat(i,k)=Bmat(k,i)
 5600   CONTINUE

      IF (j.eq.1) THEN
      WRITE(3,*) j
      DO 4400 i=1,7
          Gmat(i)=ABS(mstr(i,1,2))
        WRITE (3,*) Gmat(i)
4400   CONTINUE
      END IF

      IF (j.eq.2) THEN
      WRITE(3,*) j
      DO 4800 i=1,7
          Gmat(i)=ABS(mstr(i,1,4))
        WRITE (3,*) Gmat(i)
4800   CONTINUE
      END IF

      IF (j.eq.3) THEN
      WRITE(3,*) j
      DO 4900 i=1,7
          Gmat(i)=ABS(mstr(i,2,4))
        WRITE (3,*) Gmat(i)
4900   CONTINUE
      END IF

      IF (j.eq.4) THEN
      WRITE(3,*) j
      DO 5100 i=1,7
          Gmat(i)=ABS(mstr(i,3,2))
        WRITE (3,*) Gmat(i)
5100   CONTINUE
      END IF

c**************************************************************************
```

```
c     Call Ludecomposition and backsubstitution subroutines
c*************************************************************************   CALL LUDCMP(Amat,7,7,INDX,D)
      CALL LUBKSB(Amat,7,7,INDX,Gmat)

      DO 4600 i=1,7
       Stgmat(j,i)=Gmat(i)
4600   CONTINUE


4700  CONTINUE

      DO 5200 j=1,4
      WRITE (3,*) j
      DO 5200 i=1,7
        WRITE (3,*) Stgmat(j,i)
5200   CONTINUE


      DO 5300 j=1,4
       WRITE (3,*) j
        DO 5400 i=1,7
         Gmat(i)=Stgmat(j,i)
5400   CONTINUE
      CALL diric(Gmat,Rt,t,crpfit)
      DO 5500 k=1,7
        WRITE (3,*) crpfit(k)
5500  CONTINUE
5300  CONTINUE

c*************************************************************************
c     Evaluation of dynamic viscoplastic strian using Boltzman superposition
c     Integral
c*************************************************************************


     traf=traff*31*12/noseas
     spd=speed*5280.0d0*12.0d0/3600
     span=12.0d0/noseas*31.0d0*24.0d0*3600.0d0


      DO 5800 i=1,3
       lood(i)=0.0d0
5800   CONTINUE

      DO 5700 i=1,7
        lood(1)=lood(1)+mstr(i,1,1)
        lood(2)=lood(2)+mstr(i,2,1)
        lood(3)=lood(3)+mstr(i,3,1)
5700   CONTINUE

      lood(1)=lood(1)/7.0d0
```

```
      lood(2)=lood(2)/7.0d0
      lood(3)=lood(3)/7.0d0
      spred=a(1)/spd
      pi=3.1415d0
      increm=span/traf



      area(1)=spred*lood(1)*0.5d0
      area(2)=spred*lood(1)*0.5d0
      area(3)=spred*lood(2)*0.5d0
      area(4)=spred*lood(3)*0.5d0

c*************************************************************************
c     Figure out the equation for plastic strain in HMA, from the given input
c*************************************************************************

      py22=pltbtcm
      py11=pltpten
      px22=40.0
      px11=25.0
     slp11=(py22-py11)/(px22-px11)
     intrc11=(px22*py11-px11*py22)/(px22-px11)
      py22=pltpcom
      py11=pltpten
      px22=5.0
      px11=25.0
     slp22=(py22-py11)/(px22-px11)
     intrc22=(px22*py11-px11*py22)/(px22-px11)

     IF (temptrat.GT.25.0) THEN
       vismag(1)=slp11*temptrat+intrc11
     ELSEIF (temptrat.LT.25.0) THEN
       vismag(1)=slp22*temptrat+intrc22
     END IF

     IF (temptrat.EQ.25.0) THEN
       vismag(1)=pltpten
     END IF

      vismag(2)=vismag(1)*u1
      vismag(3)=vismag(2)
      vismag(4)=pltpsub

15130 FORMAT(e10.4,5x,e10.4,5x,e10.4,5x,e10.4,5x,e10.4)

     DO 5900 i=1,4,3
      strtot(i)=0.0d0
      DO 6100 step=0.0001,span,increm
       DO 6200 j=1,7
       strtot(i)=strtot(i)+stgmat(i,j)*EXP (-(step)/Rt(j))
```

```
6200  CONTINUE
       visplas(i)=visplas(i)+vismag(i)/100*strtot(i)*area(i)/1.5d0
       strtot(i)=0.0d0
6100  CONTINUE
5900  CONTINUE

      DO 5910 i=2,3
       strtot(i)=0.0d0
       DO 5920 step=0.0001,span,increm
        DO 5930 j=1,7
       strtot(i)=strtot(i)+stgmat(i,j)*EXP (-(step)/Rt(j))
5930  CONTINUE
       visplas(i)=visplas(i)+vismag(i)/100*strtot(i)*area(i)
       strtot(i)=0.0d0
5920  CONTINUE
5910  CONTINUE

c*************************************************************************
c     write several temporary outputs in the temporary file
c*************************************************************************

      WRITE (3,3900)
      WRITE (3,6300)
      WRITE (3,*) traf
      WRITE (3,7100)
      WRITE (3,*) speed
      WRITE (3,7000)
      WRITE (3,*) span
      WRITE (3,6400)
      WRITE (3,*) lood(1),lood(2),lood(3)
      WRITE (3,6600)
      WRITE (3,*) spred
      WRITE (3,6800)
      WRITE (3,7200)
      WRITE (3,7300)
      WRITE (3,*) pltpcom,pltpten,pltbtcm,pltpsub
      WRITE (3,*) vismag(1),vismag(2),vismag(3),vismag(4)
      WRITE (3,6500)
      WRITE (3,*) area(1),area(2),area(3),area(4)
      WRITE (3,6700)
      WRITE (3,*) increm
      WRITE (3,6900)
      WRITE (3,*) visplas(1),visplas(2),visplas(3),visplas(4)
      WRITE (3,*) strtot(1),strtot(2),strtot(3),strtot(4)
      WRITE (3,7110)
      WRITE (3,*) tmpdel1(1),tmpdel1(2),tmpdel1(3),tmpdel1(4)
      WRITE (3,*) tmpdel2(1),tmpdel2(2),tmpdel2(3),tmpdel2(4)
      WRITE (3,*) T2,T1
6300   FORMAT('Traffic over the period of the Season')
6400  FORMAT('Dynamic Stress at Top & Bottom of HMA, Top of Subgrade')
6500  FORMAT('Calculated factors for dynamic load application')
```

```
6600  FORMAT('SpREAD of dynamic spike to load')
6700  FORMAT('Time increment in dynamic load application')
6800  FORMAT('Viscoplastic megnitude of strain as a fn of total strain')
6900  FORMAT('Extent of accumulated strain at critical locations')
7200  FORMAT('HMA Tesile top, HMA compressive top, HMA tensile bottom')
7300   FORMAT('Subgrade compressive top')
7000  FORMAT('Total span of analysis season in seconds')
7100  FORMAT('Average speed of the vehicles')
7110  FORMAT('Temperature 2, THEN temperature 1')

c*************************************************************************
c     Calculation of thermal visco-plastic dynamic strains using Clasical
c     Lamination Theory (CLT).
C      Calculation of Qij, and transformed Qij matrices, also temperatures top
c     and bottom of HMA based upon SHRP
C*************************************************************************

      Temptop=(T2-0.00618d0*(latdeg)**2+0.22891d0*latdeg+42.2)*
      -0.9594-17.78
      Tempbot=Temptop-10.0d0

      DO 7600 iii=1,7

      e1=1/crp(iii)

      WRITE (3,*) e1
      WRITE (3,*) u1

      G12=e1/(2*(1+u1))
      Q11=e1/(1-(u1)**2)
      Q12=u1*e1/(1-(u1)**2)
      Q22=Q11
      Q66=G12
      UU1=(3.0d0*Q11+3.0d0*Q22+2*Q12+4.0d0*Q66)/8.0d0
      UU2=(Q11-Q22)/2.0d0
      UU3=(Q11+Q22-2.0d0*Q12-4.0d0*Q66)/8.0d0
      UU4=(Q11+Q22+6.0d0*Q12-4.0d0*Q66)/8.0d0
      UU5=(Q11+Q22-2.0d0*Q12+4.0d0*Q66)/8.0d0
      Qtr(1,1)=UU1+UU2+UU3
      Qtr(1,2)=UU4-UU3
      Qtr(2,1)=Qtr(1,2)
      Qtr(2,2)=UU1-UU2+UU3
      Qtr(1,3)=0.0d0
      Qtr(2,3)=0.0d0
      Qtr(3,1)=0.0d0
      Qtr(3,2)=0.0d0
      Qtr(3,3)=UU5-UU3

      WRITE(3,*) thkhma
      WRITE(3,*) alphat
```

```
c*************************************************************************
c     Using SHRP temperature equation to evaluate the maximum pavement
c     temperature from air (both at the top and the bottom of HMA)
c     Calculation of A matrix B matrix and D matrix
c*************************************************************************

      WRITE(3,*) Temptop
      WRITE(3,*) Tempbot

      DO 7700 i=1,3
       thk(i)=0.0d0
7700  CONTINUE

      hmaunt =thkhma/4.0d0
      tophma=hmaunt
      bothma=tophma
      thk(1)=-hmaunt/2.0d0
      thk(2)=0.0d0
      thk(3)=-thk(1)

      DO 7900 i=1,6
       DO 7900 j=1,6
       AAmat(i,j)=0.0d0
       BBmat(i,j)=0.0d0
7900  CONTINUE

      DO 7800 i=1,3
       DO 7800 j=1,3
        DO 7800 k=1,2
            AAmat(i,j)=AAmat(i,j)+Qtr(i,j)*(thk(k+1)-thk(k))
7800  CONTINUE

      DO 8200 i=1,3
       DO 8200 j=4,6
        DO 8200 k=1,2
            AAmat(i,j)=AAmat(i,j)+Qtr(i,j-3)*((thk(k+1))**2-(thk(k))**2)
8200  CONTINUE

      DO 8400 i=4,6
       DO 8400 j=1,3
        DO 8400 k=1,2
            AAmat(i,j)=AAmat(i,j)+Qtr(i-3,j)*((thk(k+1))**2-(thk(k))**2)
8400  CONTINUE

      DO 8300 i=4,6
       DO 8300 j=4,6
        DO 8300 k=1,2
            AAmat(i,j)=AAmat(i,j)+Qtr(i-3,j-3)*((thk(k+1))**3-(thk(k))**3)
8300  CONTINUE

      DO 8900 i=1,3
```

```
      DO 8900 j=4,6
       AAmat(i,j)=0.5d0*AAmat(i,j)
       AAmat(j,i)=0.5d0*AAmat(j,i)
8900  CONTINUE

     DO 8500 i=4,6
      DO 8500 j=4,6
       AAmat(i,j)=0.333d0*AAmat(i,j)
8500  CONTINUE

c*************************************************************************
c    Backup AAmat into BBmat
c     Estimation of applied inplane thermal load Nx, Ny, and Nxy
c*************************************************************************

     DO 8050 i=1,6
      DO 8050 j=1,6
       BBmat(i,j)=AAmat(i,j)
8050  CONTINUE

     T2=Temptop
     T1=Tempback

     WRITE (3,9005)
9005   FORMAT('Temperature T2, and T1 at the top of HMA')
     WRITE (3,*) T2,T1
     DO 9010 i=1,6
      Nxt(i)=0.0d0
9010  CONTINUE


     DO 9000 i=1,3
      DO 9000 k=1,2
       Nxt(i)=Nxt(i)+(Qtr(i,1)+Qtr(i,2)+Qtr(i,3))*alphat*
    -(thk(k+1)-thk(k))
9000  CONTINUE

     DO 9100 i=1,3
      Nxt(i)=(T2-T1)*Nxt(i)
9100  CONTINUE

     WRITE (3,9020)
9020  FORMAT('Applied loads due to Thermal loading')
     WRITE (3,*) Nxt(1),Nxt(2),Nxt(3),Nxt(4),Nxt(5),Nxt(6)

     DO 9300 i=1,6
      DO 9300 j=1,6
       AAmat(i,j)=BBmat(i,j)
9300  CONTINUE

      CALL LUDCMP(AAmat,6,6,INDX,D)
```

```
      CALL LUBKSB(AAmat,6,6,INDX,Nxt)

     strptr(1)=0.0d0
     strptr(2)=0.0d0

     WRITE (3,9200)
9200  FORMAT('Mid Axis Strains and curvatures')
     WRITE (3,*) Nxt(1),Nxt(2),Nxt(3),Nxt(4),Nxt(5),Nxt(6)

     strptr(1)=Nxt(2)+thk(1)*Nxt(5)

     WRITE (3,9220)
9220  FORMAT('Tensile Strains at the top of HMA')
     WRITE (3,*) strptr(1)

     T2=Tempbot
     T1=Tempbot-5.0d0

     WRITE (3,9210)
9210   FORMAT('Temperature T2, and T1 at the bottom of HMA')
     WRITE (3,*) T2,T1

     DO 9400 i=1,6
      Nxb(i)=0.0d0
9400  CONTINUE

     DO 9500 i=1,3
      DO 9500 k=1,2
       Nxb(i)=Nxb(i)+(Qtr(i,1)+Qtr(i,2)+Qtr(i,3))*alphat*
    -(thk(k+1)-thk(k))
9500  CONTINUE

     DO 9600 i=1,3
      Nxb(i)=(T2-T1)*Nxb(i)
9600  CONTINUE

     WRITE (3,9700)
9700  FORMAT('Applied loads due to Thermal loading')
     WRITE (3,*) Nxb(1),Nxb(2),Nxb(3),Nxb(4),Nxb(5),Nxb(6)

     DO 9800 i=1,6
      DO 9800 j=1,6
       AAmat(i,j)=BBmat(i,j)
9800  CONTINUE


      CALL LUDCMP(AAmat,6,6,INDX,D)
      CALL LUBKSB(AAmat,6,6,INDX,Nxb)

     WRITE (3,9900)
9900  FORMAT('Mid Axis Strains and curvatures')
```

```
      WRITE (3,*) Nxb(1),Nxb(2),Nxb(3),Nxb(4),Nxb(5),Nxb(6)

      strptr(2)=Nxb(2)+thk(3)*Nxb(5)

      WRITE (3,9910)
9910  FORMAT('Tensile Strains at the bottom of HMA')
      WRITE (3,*) strptr(2)

7600   CONTINUE

c**************************************************************************
c     Calculation of accumulated plastic thermal strain, and
c     adding up the final values to their mechanical counter parts
c     also writing the necessary output to the temp file and the plastic.out
c     file
c**************************************************************************

      thaplc=31.0d0*12.0d0/noseas
      tthrvp=0.0d0

      DO 9920 i=1,thaplc
       tthrvp=tthrvp+strptr(1)*0.005d0*vismag(2)
9920  CONTINUE

      tbhrvp=0.0d0

      DO 9930 i=1,thaplc
       tbhrvp=tbhrvp+strptr(2)*0.005d0*vismag(3)
9930  CONTINUE

      WRITE (3,9940)
9940  FORMAT('Accumulated thermal strain at the top of HMA')
      WRITE(3,*) tthrvp

      WRITE (3,9950)
9950  FORMAT('Accumulated thermal strain at the bottom of HMA')
      WRITE(3,*) tbhrvp

      WRITE (3,*) visplas(1),visplas(2),visplas(3),visplas(4)
      WRITE(3,*) tthrvp,tbhrvp

      visplas(2)=visplas(2)-tthrvp
      visplas(3)=visplas(3)+tbhrvp
      yls=kk/term*yrs
      WRITE (3,9960)
      WRITE (3,9965)
9960  FORMAT('Accumulated total displacemets in the pavement')
9965  FORMAT('Year, Com Top of HMA, Ten Top of HMA, Ten Bott of HMA,
     - Comp Top Subgrade')
      WRITE (3,15000) yls,visplas(1),visplas(2),visplas(3),visplas(4)
      WRITE (4,15000) yls,visplas(1),visplas(2),visplas(3),visplas(4)
```

```
15000  FORMAT(e10.4,5x,e10.4,5x,e10.4,5x,e10.4,5x,e10.4)

      WRITE (3,*)slp1,intrc1
      WRITE (3,*)slp2,intrc2
      WRITE(3,10410)
      WRITE(3,10420)
      WRITE(3,10430)
      WRITE(3,10440)
      WRITE(3,10460)
10410 FORMAT ('Given ShIFt factors, 1st 40 deg C THEN 5 Deg C')
      WRITE(3,*) sf1,sf2
10420 FORMAT ('Base Temperature in this season')
      WRITE(3,*)temptrat
10430  FORMAT ('Current ShIFt factor')
      WRITE(3,*)shftfac
10440 FORMAT ('Current Creep Compliance')
      WRITE(3,*) crpb(1),crpb(2),crpb(3),crpb(4),crpb(5),crpb(6),crpb(7)
      WRITE(3,*) crp(1),crp(2),crp(3),crp(4),crp(5),crp(6),crp(7)
      WRITE(3,*) u1
10460 FORMAT('poisson ratio at this temperature')
      WRITE(3,10450)

10450 FORMAT('*******************************************************')

10100 CONTINUE
      close(3)
      close(4)
      END
c*************************************************************************
c    Calculate the creep dilitrict fit eqaution of the form e^-t/Ti, using
c     the Gi's previously calculated
C*************************************************************************
      SUBROUTINE diric(Gmat,Rt,tme,crpfit)
      IMPLICIT REAL (a-z)
      INTEGER i,j
      DIMENSION Gmat(7), Rt(7),tme(7),crpfit(7)

      DO 4200 i=1,7
        crpfit(i)=0.0d0
4200  CONTINUE


       DO 4100 i=1,7
        DO 4100 j=1,7
        crpfit(i)=crpfit(i)+Gmat(j)*EXP (-(tme(i))/(RT(j)))
 4100  CONTINUE
      END
C*************************************************************************
c    Solve  Cmat(i,j).(Dilitriet constants 1-7)= Gmat(i)
C     SUBROUTINE LUDCMP
C     PERFORMS LU DECOMPOSITION OF THE KG MATRIX
```

```
C*****************************************************************************
      SUBROUTINE LUDCMP(AC,N,NP,INDX,D)
      IMPLICIT REAL (a-z)
      INTEGER   D,NP,N,I,J
      DIMENSION AC(NP,NP),VV(10),INDX(N)

      TINY=1.0E-20
      D=1
      DO 2200 I=1,N
         AAMAX=0.
         DO 2300 J=1,N
            IF (ABS(AC(I,J)).GT.AAMAX) AAMAX=ABS(AC(I,J))
2300       CONTINUE

         IF (AAMAX.EQ.0.) PAUSE 'SINgular matrix.'
            VV(I)=1./AAMAX

 2200    CONTINUE

     DO 2400 J=1,N
         IF (J.GT.1) THEN
            DO 2900 I=1,J-1
               SUM=AC(I,J)
               IF (I.GT.1)THEN
                  DO 3000 K=1,I-1
                     SUM=SUM-AC(I,K)*AC(K,J)
3000                 CONTINUE

                  AC(I,J)=SUM
               END IF
2900           CONTINUE

         END IF
        AAMAX=0.
         DO 2700 I=J,N
            SUM=AC(I,J)
            IF (J.GT.1)THEN
               DO 2800 K=1,J-1
                  SUM=SUM-AC(I,K)*AC(K,J)
2800              CONTINUE

               AC(I,J)=SUM
            END IF

            DUM=VV(I)*ABS(SUM)
            IF (DUM.GE.AAMAX) THEN
               IMAX=I
               AAMAX=DUM
            END IF

2700       CONTINUE
```

```
      IF (J.NE.IMAX)THEN
         DO 2600 K=1,N
            DUM=AC(IMAX,K)
            AC(IMAX,K)=AC(J,K)
            AC(J,K)=DUM
2600        CONTINUE

         D=-D
         VV(IMAX)=VV(J)
      END IF

      INDX(J)=IMAX
      IF(J.NE.N)THEN
         IF(AC(J,J).EQ.0.) AC(J,J)=TINY


         DUM=1./AC(J,J)
         DO 2500 I=J+1,N
            AC(I,J)=AC(I,J)*DUM
2500        CONTINUE

      END IF

2400  CONTINUE

   IF(AC(N,N).EQ.0.) AC(N,N)=TINY

   RETURN
   END

C*************************************************************************
C    SUBROUTINE LUDBKSB
C    PERFORMS BACKSUBSTITUTION TO SOLVE [A][X]=[B], FOR [X], WHICH ACTUALLY
C    DESTROYS THE ORIGINAL GLOBAL FORCE MATRIX
C*************************************************************************

   SUBROUTINE LUBKSB(AC,N,NP,INDX,B)
   IMPLICIT REAL (a-z)
   INTEGER   NP,N,I,J,ii
   DIMENSION AC(NP,NP),B(N),INDX(N)

   II=0


   DO 3200 I=1,N
      LL=INDX(I)
      SUM=B(LL)
      B(LL)=B(I)
      IF (II.NE.0)THEN
         DO 3100 J=II,I-1
```

```
            SUM=SUM-AC(I,J)*B(J)
3100          CONTINUE
        ELSE IF (SUM.NE.0.) THEN
           II=I
        END IF

        B(I)=SUM
3200    CONTINUE

     DO 3400 I=N,1,-1
        SUM=B(I)
        IF(I.LT.N)THEN
           DO 3300 J=I+1,N
              SUM=SUM-AC(I,J)*B(J)
3300          CONTINUE
        END IF

        B(I)=SUM/AC(I,I)
3400    CONTINUE

     RETURN
     END

SUBROUTINE pas1(p1,h1,a,l,ml,m,e1,e2,e3,e4,e5,u1,u2,u3,u4,u5,
    -z1,z2,z3,z4,a1,c1,a2,b2,c2,d2,a3,b3,c3,d3,a4,b4,c4,d4,pr,w2,
    -la1,la2,la3,fl,rmax)
     IMPLICIT REAL(a-z)
     INTEGER i,l
     DIMENSION a(20)
     max=a(1)
     DO 480 i=1,l
        IF (a(i).gt.max) max=a(i)
480   CONTINUE
     fl=2.*(1.-u1)*(1.-(1.-u5*u5)/(1.-u1*u1)*e1/e5)
     fl1=ABS(fl)
     m=0.
     m1=.02
481   m=m+m1
     pr=fl
     CALL const(m,e1,e2,e3,e4,e5,u1,u2,u3,u4,u5,z1,z2,z3,z4,a1,c1,
    -a2,b2,c2,d2,a3,b3,c3,d3,a4,b4,c4,d4,pr,w2,la1,la2,la3,fl)
     IF (fl.lt.pr) GOTO 481
     ml=m
     pr1=ABS(pr)
     IF (fl1.gt.pr1) pr1=fl1
     p1=.1*SQRT(1./pr1)*(.5*alog10(1./max)+1.)
     pr=ABS(pr/2.)
     IF (rmax.ge.2.5) THEN
        p1l=.5/rmax
                ELSE
        p1l=.2
```

```
      END IF
      IF (p1.gt.p1l) THEN
         p1=p1l
         pr=0.
      END IF
      dum=h1
      END

      SUBROUTINE pas2(p1,e1,e5,u1,u5,h1,a,l,pr,ml,rmax)
      IMPLICIT REAL(a-z)
      INTEGER i,l
      DIMENSION a(20)
      max=a(1)
      DO 499 i=1,l
        IF (a(i).gt.max) max=a(i)
499   CONTINUE
      p1=.1*SQRT(e5/e1)*(.5*alog10(1./max)+1.)
      pr=(1.-u1)*(1.-(1.-u5*u5)/(1.-u1*u1)*e1/e5)
      pr=ABS(pr)
      IF (rmax.ge.2.5) THEN
         p1l=.5/rmax
                ELSE
         p1l=.2
      END IF
      IF(p1.ge.p1l) THEN
         p1=p1l
         pr=0.
      END IF
      ml=0
      dum=h1
      END


      SUBROUTINE echde(h1,z1,z2,z3,z4,xs,ys,zs,a,xc,yc,l1,l2,l)
      IMPLICIT REAL(a-z)
      INTEGER i,l,l1,l2
      DIMENSION a(20),xc(20),xs(30),yc(20),ys(30),zs(30)
      z1=z1/h1
      z2=z2/h1
      z3=z3/h1
      z4=z4/h1
      DO 720 i=1,l
        a(i)=a(i)/h1
        xc(i)=xc(i)/h1
        yc(i)=yc(i)/h1
720   CONTINUE
      DO 721 i=1,l1
        xs(i)=xs(i)/h1
        ys(i)=ys(i)/h1
721   CONTINUE
      DO 722 i=1,l2
```

```
      zs(i)=zs(i)/h1
722   CONTINUE
      END

      SUBROUTINE vinit(l1,l2,w1,m,m1,p1)
      IMPLICIT REAL(a-z)
      INTEGER l1,l2,w1,i,j,k
      COMMON  prov(30,30,9),res(30,30,9)
      WRITE(6,498)
498   FORMAT(//,' ',' start of computat.     be patient!!',//)
      DO 100 k=1,9
        DO 101 j=1,l2
          DO 102 i=1,l1
            prov(i,j,k)=0.
            res(i,j,k)=0.
102       CONTINUE
101     CONTINUE
100   CONTINUE
      w1=1
      m=0.
      m1=p1
      END


      SUBROUTINE zero(l1,l2)
      IMPLICIT REAL(a-z)
      INTEGER i,j,k,l1,l2
      COMMON  prov(30,30,9),res(30,30,9)
      DO 710 k=1,9
        DO 711 j=1,l2
          DO 712 i=1,l1
            prov(i,j,k)=0.
712       CONTINUE
711     CONTINUE
710   CONTINUE
      END


      SUBROUTINE finit(l,l1,l2,xc,yc,xs,ys,zs,ls,e1,e2,e3,e4,e5,
     -u1,u2,u3,u4,u5,p,a,m1)
      IMPLICIT REAL(a-z)
      INTEGER i,j,k,l,l1,l2,ls
      COMMON prov(30,30,9),res(30,30,9)
      DIMENSION xc(20),yc(20),xs(30),ys(30),zs(30),ls(30)
      DIMENSION p(20),a(20)
      fw=e1*(1.+u2)/(e2*(1.+u1))
      kw=e2*(1.+u3)/(e3*(1.+u2))
      lw=e3*(1.+u4)/(e4*(1.+u3))
      jw=e4*(1.+u5)/(e5*(1.+u4))
      DO 740 k=1,l2
        DO 741 i=1,l1
```

```
          DO 742 j=1,l
          IF(ls(k).eq.1.and.zs(k).eq.0.) res(i,k,1)=res(i,k,1)+
     - p(j)*a(j)**2*m1/40.*3.*(1.-(1.-u5)/(1.-u1)*fw*kw*lw*jw)
          IF(ls(k).eq.1.and.zs(k).ne.0.) res(i,k,1)=res(i,k,1)+
     - p(j)*a(j)**2*m1*3./10.*(1.-u1)*(1.-(1.-u5)/(1.-u1)*fw*kw*lw*jw)
          IF(ls(k).eq.2) res(i,k,1)=res(i,k,1)-(1.+u2)*(1.-u5)
     -       *kw*lw*jw*p(j)*a(j)**2*m1*3./10./e2
          IF(ls(k).eq.3) res(i,k,1)=res(i,k,1)-(1.+u3)*(1.-u5)
     -       *lw*jw*p(j)*a(j)**2*m1*3./10./e3
          IF(ls(k).eq.4) res(i,k,1)=res(i,k,1)-(1.+u4)*(1.-u5)
     -       *jw*p(j)*a(j)**2*m1*3./10./e4
742       CONTINUE
741     CONTINUE
740   CONTINUE
      END


      SUBROUTINE p4442(a,b,c)
      IMPLICIT REAL(a-z)
      INTEGER i,j,k
      DIMENSION a(4,4),b(4,2),c(4,2)
      DO 300 k=1,2
        DO 301 i=1,4
          c(i,k)=0.
          DO 302 j=1,4
            c(i,k)=c(i,k)+a(i,j)*b(j,k)
302       CONTINUE
301     CONTINUE
300   CONTINUE
      END


      SUBROUTINE pct42(a,b,c)
      IMPLICIT REAL(a-z)
      INTEGER i,k
      DIMENSION b(4,2),c(4,2)
      DO 303 k=1,2
        DO 304 i=1,4
          c(i,k)=a*b(i,k)
304     CONTINUE
303   CONTINUE
      END


      SUBROUTINE p4444(a,b,c)
      IMPLICIT REAL(a-z)
      INTEGER i,j,k
      DIMENSION a(4,4),b(4,4),c(4,4)
      DO 307 k=1,4
        DO 308 i=1,4
          c(i,k)=0.
```

```
          DO 309 j=1,4
            c(i,k)=c(i,k)+a(i,j)*b(j,k)
309         CONTINUE
308       CONTINUE
307    CONTINUE
       END

       SUBROUTINE const(m,e1,e2,e3,e4,e5,u1,u2,u3,u4,u5,z1,z2,z3,z4,a1,
      -c1,a2,b2,c2,d2,a3,b3,c3,d3,a4,b4,c4,d4,pr,w2,la1,la2,la3,fl)
       IMPLICIT REAL(a-z)
       INTEGER i,j,w2
       DIMENSION m71(4,4),m8(4,2),m78(4,2),m6178(4,2),m79(4,2)
       DIMENSION m51(4,4),m52(4,4),m61(4,4),m62(4,2),m5161(4,2),
      *m5162(4,2),m5261(4,2),m31(4,4),m32(4,4)
       DIMENSION  m41(4,4),m42(4,4),m3142(4,4),m3241(4,4),
      *m11(4,4),m12(4,4),m21(4,4),m22(4,4)
       DIMENSION m1122(4,4),m1221(4,4)
       data((m51(i,j),i=1,4),j=1,4)/2*0.,1.,3*0.,-1.,3*0.,1.,3*0.,-1.,
      *0./
       data((m52(i,j),i=1,4),j=1,4)/3*0.,-1.,3*0.,-1.,3*0.,1.,3*0.,1./
       data((m61(i,j),i=1,4),j=1,4)/2*1.,14*0./
       data((m62(i,j),i=1,4),j=1,2)/1.,-1.,6*0./
       data((m31(i,j),i=1,4),j=1,4)/2*0.,1.,3*0.,-1.,3*0.,1.,3*0.,-1.,
      *0./
       data((m32(i,j),i=1,4),j=1,4)/3*0.,-1.,3*0.,-1.,3*0.,1.,3*0.,1./
       data((m41(i,j),i=1,4),j=1,4)/1.,1.,14*0./
       data((m42(i,j),i=1,4),j=1,4)/4*0.,1.,-1.,10*0./
       data((m11(i,j),i=1,4),j=1,4)/2*0.,1.,3*0.,-1.,3*0.,1.,3*0.,-1.,
      *0./
       data((m12(i,j),i=1,4),j=1,4)/3*0.,-1.,3*0.,-1.,3*0.,1.,3*0.,1./
       data((m21(i,j),i=1,4),j=1,4)/1.,1.,14*0./
       data((m22(i,j),i=1,4),j=1,4)/4*0.,1.,-1.,10*0./
       data((m8(i,j),i=1,4),j=1,2)/-1.,1.,1.,-1.,4*0./
       data((m71(i,j),i=1,4),j=1,4)/16*0./
       c2x=.0
       c2y=.0
       c2z=.0
       c2t=.0
       ctz2=.0
       cty2=.0
       ctx2=.0
       czy2=.0
       czx2=.0
       cyx2=.0
       cx=.0
       cy=.0
       cz=.0
       ct=.0
       w2=0
       fw=e1*(1.+u2)/(e2*(1.+u1))
       fu=fw*la1
```

```
kw=e2*(1.+u3)/(e3*(1.+u2))
ku=kw*la2
lw=e3*(1.+u4)/(e4*(1.+u3))
lu=lw*la3
jw=e4*(1.+u5)/(e5*(1.+u4))
x=m*z1
y=m*z2
z=m*z3
t=m*z4
l1=-3.+4.*u3-lu-2.*u3*(lw-lu)
l2=-1.-2.*lw+4.*lw*u4-lu
l3=lw-lu
l4=-1.+6.*u4-8.*u3*u4-4.*u3*lw+8.*u3*u4*lw-2.*u3*lu+lu
k1=-3.+4.*u2-ku-2.*u2*(kw-ku)
k2=-1.-2.*kw+4.*kw*u3-ku
k3=kw-ku
k4=-1.+6.*u3-8.*u2*u3-4.*u2*kw+8.*u2*u3*kw-2.*u2*ku+ku
f1=-3.+4.*u1-fu-2.*u1*(fw-fu)
f2=-1.-2.*fw+4.*fw*u2-fu
f3=fw-fu
f4=-1.+6.*u2-8.*u1*u2-4.*u1*fw+8.*u1*u2*fw-2.*u1*fu+fu
  m11(1,1)=-(1.+x)
  m11(1,2)=-(2.-4.*u1-x)
  m11(1,3)=-(2.*u1+x)
  m11(1,4)=-(1.-2.*u1-x)
  m12(2,1)=-(1.-x)
  m12(2,2)=(2.-4.*u1+x)
  m12(2,3)=(2.*u1-x)
  m12(2,4)=-(1.-2.*u1+x)
  m21(3,1)=fw
  m21(4,1)=fu
  m21(1,3)=-(1.-2.*u2-x)
  m21(2,3)=(2.*u2+x)
  m21(3,3)=-fw*(2.-4.*u2-x)
  m21(4,3)=fu*(1.+x)
  m22(3,2)=-fw
  m22(4,2)=fu
  m22(1,4)=(1.-2.*u2+x)
  m22(2,4)=(2.*u2-x)
  m22(3,4)=-fw*(2.-4.*u2+x)
  m22(4,4)=-fu*(1.-x)
  m31(1,1)=-(1.+y)
  m31(1,2)=-(2.-4.*u2-y)
  m31(1,3)=-(2.*u2+y)
  m31(1,4)=-(1.-2.*u2-y)
  m32(2,1)=-(1.-y)
  m32(2,2)=2.-4.*u2+y
  m32(2,3)=2.*u2-y
  m32(2,4)=-(1.-2.*u2+y)
  m41(3,1)=kw
  m41(4,1)=ku
```

```
      m41(1,3)=-(1.-2.*u3-y)
      m41(2,3)=(2.*u3+y)
      m41(3,3)=-kw*(2.-4.*u3-y)
      m41(4,3)=ku*(1.+y)
      m42(3,2)=-kw
      m42(4,2)=ku
      m42(1,4)=(1.-2.*u3+y)
      m42(2,4)=(2.*u3-y)
      m42(3,4)=-kw*(2.-4.*u3+y)
      m42(4,4)=-ku*(1.-y)
      m51(1,1)=-(1.+z)
      m51(1,2)=-(2.-4.*u3-z)
      m51(1,3)=-(2*u3+z)
      m51(1,4)=-(1.-2*u3-z)
      m52(2,1)=-(1.-z)
      m52(2,2)=(2.-4*u3+z)
      m52(2,3)=(2*u3-z)
      m52(2,4)=-(1.-2*u3+z)
      m61(3,1)=lw
      m61(4,1)=lu
      m61(1,3)=-(1.-2.*u4-z)
      m61(2,3)=2.*u4+z
      m61(3,3)=-lw*(2.-4.*u4-z)
      m61(4,3)=lu*(1.+z)
      m62(3,1)=-lw
      m62(4,1)=lu
      m62(1,2)=(1.-2.*u4+z)
      m62(2,2)=(2.*u4-z)
      m62(3,2)=-lw*(2.-4.*u4+z)
      m62(4,2)=-lu*(1.-z)
      m71(1,1)=-jw*jw*(t+2.*u4)*(3.-4.*u5)-jw*((1.-2.*u5)*
     -          (3.-4.*u4)+1.+t)
      m71(1,2)=-jw*jw*(1.-2.*u4-t)*(3.-4.*u5)-jw*(2.*(1.-u5)*
     -          (3.-4.*u4)-1.-t)
      m71(1,3)=jw*(1.-2.*u5-(t+2.*u4)*(3.-4.*u5))-1.-t
      m71(1,4)=-jw*(2.*(1.-u5)-(t+2.*u4)*(3.-4.*u5))-2.+4.*u4+t
      m71(3,1)=jw*jw*(3.-4.*u5)+jw
      m71(3,2)=-m71(3,1)
      m71(3,3)=m71(3,1)/jw
      m71(3,4)=-m71(3,3)
      m8(1,2)=-(1.-2.*u4+t)
      m8(2,2)=-2.*u4+t
      m8(3,2)=2.-4.*u4+t
      m8(4,2)=1.-t
     delta=1/(-jw*jw*(3.-4.*u5)-2.*jw*(5.-6.*u4-6.*u5+8.*u4*u5)
     -     -(3.-4.*u4))
     IF(ABS(-2.*x).lt.20.0) c2x=EXP(-2.*x)
     IF(ABS(-2.*y).lt.20.0) c2y=EXP(-2.*y)
     IF(ABS(-2.*z).lt.20.0) c2z=EXP(-2.*z)
     IF(ABS(-2.*t).lt.20.0) c2t=EXP(-2.*t)
     IF(ABS(-2.*(y-x)).lt.20.0) cyx2=EXP(-2.*(y-x))
```

```
IF(ABS(-2.*(z-y)).lt.20.0) czy2=EXP(-2.*(z-y))
IF(ABS(-2.*(t-z)).lt.20.0) ctz2=EXP(-2.*(t-z))
IF(ABS(-(y-x)).lt.20.0) cyx=EXP(-(y-x))
IF(ABS(-(z-y)).lt.20.0) czy=EXP(-(z-y))
IF(ABS(-x).lt.20.0) cx=EXP(-x)
IF(ABS(-y).lt.20.0) cy=EXP(-y)
IF(ABS(-z).lt.20.0) cz=EXP(-z)
IF(ABS(-t).lt.20.0) ct=EXP(-t)
CALL p4442(m71,m8,m79)
CALL pct42(delta,m79,m78)
CALL p4442(m61,m78,m6178)
CALL p4442(m51,m6178,m5161)
CALL p4442(m51,m62,m5162)
CALL p4442(m52,m6178,m5261)
p11=ctz2*m5161(1,1)+m5162(1,1)
p12=ctz2*m5161(1,2)+m5162(1,2)
p21=ctz2*m5261(2,1)
p22=ctz2*m5261(2,2)
p31=ctz2*m5161(3,1)+m5162(3,1)
p32=ctz2*m5161(3,2)+m5162(3,2)
p41=ctz2*m5261(4,1)
p42=ctz2*m5261(4,2)
f11=f1-x*f3
f13=-f4+x*(f1-f2)-x*x*f3
f22=f1+x*f3
f24=f4+x*(f1-f2)+x*x*f3
f31=f3
f33=f2+x*f3
f42=-f3
f44=f2-x*f3
k11=k1-y*k3
k13=-k4+y*(k1-k2)-y*y*k3
k22=k1+y*k3
k24=k4+y*(k1-k2)+y*y*k3
k31=k3
k33=k2+y*k3
k42=-k3
k44=k2-y*k3
l21=l1+z*l3
l22=l4+z*(l1-l2)+z*z*l3
l41=-l3
l42=l2-z*l3
CALL p4444(m31,m42,m3142)
CALL p4444(m32,m41,m3241)
q12=m3142(1,2)
q14=m3142(1,4)
q21=m3241(2,1)
q23=m3241(2,3)
q32=m3142(3,2)
q34=m3142(3,4)
q41=m3241(4,1)
```

```
 q43=m3241(4,3)
 CALL p4444(m11,m22,m1122)
 CALL p4444(m12,m21,m1221)
 r12=m1122(1,2)
 r14=m1122(1,4)
 r21=m1221(2,1)
 r23=m1221(2,3)
 r32=m1122(3,2)
 r34=m1122(3,4)
 r41=m1221(4,1)
 r43=m1221(4,3)
 a11=r21+(1.-2.*u1)*r41
 a12=r12-(1.-2.*u1)*r32
 a13=r23+(1.-2.*u1)*r43
 a14=r14-(1.-2.*u1)*r34
 a21=-r21+2.*u1*r41
 a22=r12+2.*u1*r32
 a23=-r23+2.*u1*r43
 a24=r14+2.*u1*r34
 ff11=f11-(1.-2.*u1)*f31
 ff12=f22+(1.-2.*u1)*f42
 ff13=f13-(1.-2.*u1)*f33
 ff14=f24+(1.-2.*u1)*f44
 ff21=f11+2.*u1*f31
 ff22=-f22+2.*u1*f42
 ff23=f13+2.*u1*f33
 ff24=-f24+2.*u1*f44
 b11=(k11*p11+k13*p31)*czy2+q12*(p21+l21)+q14*(p41+l41)
 b12=(k11*p12+k13*p32)*czy2+q12*(p22+l22)+q14*(p42+l42)
 b21=k22*p21+k24*p41+(q21*p11+q23*p31)*czy2
 b22=k22*p22+k24*p42+(q21*p12+q23*p32)*czy2
 b31=(k31*p11+k33*p31)*czy2+q32*(p21+l21)+q34*(p41+l41)
 b32=(k31*p12+k33*p32)*czy2+q32*(p22+l22)+q34*(p42+l42)
 b41=k42*p21+k44*p41+(q41*p11+q43*p31)*czy2
 b42=k42*p22+k44*p42+(q41*p12+q43*p32)*czy2
 kl21=k22*l21+k24*l41
 kl22=k22*l22+k24*l42
 kl41=k42*l21+k44*l41
 kl42=k42*l22+k44*l42
 c11=(a11*b11+a13*b31)*cyx2+(a12*b21+a14*b41)*c2x+(ff11*b11+
-ff13*b31)*c2y+ff12*b21+ff14*b41+(a12*kl21+a14*kl41)*c2x
 c12=(a11*b12+a13*b32)*cyx2+(a12*b22+a14*b42)*c2x+(ff11*b12+
-ff13*b32)*c2y+ff12*b22+ff14*b42+(a12*kl22+a14*kl42)*c2x
 c21=(a21*b11+a23*b31)*cyx2+(a22*b21+a24*b41)*c2x+(ff21*b11+
-ff23*b31)*c2y+ff22*b21+ff24*b41+(a22*kl21+a24*kl41)*c2x
 c22=(a21*b12+a23*b32)*cyx2+(a22*b22+a24*b42)*c2x+(ff21*b12+
-ff23*b32)*c2y+ff22*b22+ff24*b42+(a22*kl22+a24*kl42)*c2x
 fkl11=ff12*kl21+ff14*kl41
 fkl12=ff12*kl22+ff14*kl42
 fkl21=ff22*kl21+ff24*kl41
 fkl22=ff22*kl22+ff24*kl42
```

```
      denom=c11*(c22+fkl22)-c12*(c21+fkl21)+
     -fkl11*c22-fkl12*c21+(f1*f2+f3*f4)*(k1*k2+k3*k4)*(l1*l2+l3*l4)
      b4=-64.*(1.-u1)*(1.-u2)*(1.-u3)*(c22+fkl22)/denom
      d4=64.*(1.-u1)*(1.-u2)*(1.-u3)*(c21+fkl21)/denom
      a3=-(p11*b4*cz+p12*d4*cz)/4./(1.-u3)
      b3=-((p21+l21)*b4*cy+(p22+l22)*d4*cy)/4./(1.-u3)
      c3=-(p31*b4*cz+p32*d4*cz)/4./(1.-u3)
      d3=-((p41+l41)*b4*cy+(p42+l42)*d4*cy)/4./(1.-u3)
      aa3=-(p11*b4*czy2+p12*d4*czy2)/4./(1.-u3)
      bb3=-((p21+l21)*b4*cx+(p22+l22)*d4*cx)/4./(1.-u3)
      cc3=-(p31*b4*czy2+p32*d4*czy2)/4./(1.-u3)
      dd3=-((p41+l41)*b4*cx+(p42+l42)*d4*cx)/4./(1.-u3)
      a2=-(k11*a3*czy+q12*b3+k13*c3*czy+q14*d3)/4./(1.-u2)
      b2=-(q21*aa3*cx+k22*bb3+q23*cc3*cx+k24*dd3)/4./(1.-u2)
      c2=-(k31*a3*czy+q32*b3+k33*c3*czy+q34*d3)/4./(1.-u2)
      d2=-(q41*aa3*cx+k42*bb3+q43*cc3*cx+k44*dd3)/4./(1.-u2)
      a1=-(f11*a2*cyx+r12*b2+f13*c2*cyx+r14*d2)/4./(1.-u1)
      c1=-(f31*a2*cyx+r32*b2+f33*c2*cyx+r34*d2)/4./(1.-u1)
      a4=ct*(m78(1,1)*b4+m78(1,2)*d4)
      c4=ct*(m78(3,1)*b4+m78(3,2)*d4)
      b4=b4*cz
      d4=d4*cz
      fl=a1-c1*(2.-4.*u1-x)+a1*(3.-4.*u1+2.*x)*c2x-
     -c1*(2.-8.*u1+8.*u1*u1+x-4.*u1*x)*c2x
      fl1=a2*cyx-b2-c2*(2.-4.*u2-x)*cyx-d2*(2.-4.*u2+x)
      IF(ABS(fl1).gt.ABS(fl)) fl=fl1
      IF (ABS(fl).gt.pr) w2=1
      END


      SUBROUTINE besj1(l,m,a,j1)
      IMPLICIT REAL(a-z)
      INTEGER i,l
      DIMENSION a(20),j1(20)
      pi=3.141592
      DO 640 i=1,l
        mai=m*a(i)
        IF(mai.gt.16.) THEN
                    j1(i)=SIN(mai-pi/4.)*SQRT(2./pi/mai)
                ELSE
                    z9=0.
                    v1=1.
                    v2=1.
840                   z9=z9+1.
                    v2=-v2/z9*(mai/2.)**2/(z9+1.)
                    v1=v1+v2
                    IF(ABS(v2).gt..00001) GOTO 840
                    j1(i)=mai*v1/2.
                END IF
640   CONTINUE
      END
```

```
      SUBROUTINE bj0j2(m,r,j0,j2)
      IMPLICIT REAL(a-z)
      IF (r.eq.0.) THEN
                  j0=1.
                  j2=0.
                  GOTO 843
                END IF
      pi=3.141592
      mr=m*r
      IF (mr.gt.16.)THEN
                   j0=SQRT(1./(mr/2.)/pi)*COS(mr-pi/4.)
                   j2=SQRT(1./(mr/2.)/pi)*SIN(mr-pi/4.)
                ELSE
                   z9=0.
                   v1=1.
                   v2=1.
841                  z9=z9+1.
                   v2=-v2*((mr/2.)/z9)**2
                   v1=v1+v2
                   IF(ABS(v2).gt..00001) GOTO 841
                   j0=v1
                   z9=0.
                   v1=1.
                   v2=1.
842                  z9=z9+1.
                   v2=-v2/z9*(mr/2.)**2/(z9+1.)
                   v1=v1+v2
                   IF(ABS(v2).gt..00001) GOTO 842
                   j2=mr*v1/2.
                END IF
843   END


      SUBROUTINE surfa(i,j,z1,a1,c1,u1,j0,j1,j2,m,p,a,r,alpha)
      IMPLICIT REAL(a-z)
      INTEGER i,j
      COMMON prov(30,30,9),res(30,30,9)
      DIMENSION p(20),a(20),j1(20)
      x1=0.
      IF(ABS(-m*z1).lt.20.0) x1=EXP(-m*z1)
      prov(i,1,1)=prov(i,1,1)+p(j)*a(j)*j0*j1(j)*(a1-(1.-2.*u1)*c1)*x1/m
      c=p(j)*a(j)*j0*j1(j)*(a1+2.*u1*c1)*x1*(-2.*(1.+u1))
      IF(r.ne.0.) THEN
                   d=p(j)*a(j)*j1(j)*
     -              (a1+2.*u1*c1)*x1*(j0-2.*j2/(m*r))*(-2.*(1.-u1))
                   prov(i,1,4)=prov(i,1,4)+c+d*COS(2.*alpha)
                   prov(i,1,5)=prov(i,1,5)+c-d*COS(2.*alpha)
                   prov(i,1,9)=prov(i,1,9)+d*SIN(2.*alpha)
                  c=p(j)*a(j)*j2*j1(j)*(a1+2.*u1*c1)*x1/m
```

```
          prov(i,1,2)=prov(i,1,2)+c*COS(alpha)
          prov(i,1,3)=prov(i,1,3)+c*SIN(alpha)
          ELSE
             prov(i,1,4)=prov(i,1,4)+c
             prov(i,1,5)=prov(i,1,5)+c
          END IF
 END


 SUBROUTINE couc1(i,j,k,z,p,a,j0,j1,j2,z1,u1,m,a1,c1,r,alpha)
 IMPLICIT REAL(a-z)
 INTEGER i,j,k
 COMMON prov(30,30,9),res(30,30,9)
 DIMENSION p(20),a(20),j1(20)
 x1=0.
 x2=0.
 IF(ABS(-m*(z1-z)).lt.20.0) x1=EXP(-m*(z1-z))
 IF(ABS(-m*(z1+z)).lt.20.0) x2=EXP(-m*(z1+z))
 b=a1*x1-(2.-4.*u1-m*z)*c1*x1+a1*(3.-4.*u1+2.*m*z)*
-x2-c1*(2.-8.*u1*(1-u1)+m*z*(1-4.*u1))*x2
 prov(i,k,1)=prov(i,k,1)+p(j)*a(j)*j0*j1(j)*b/m
 b=a1*x1+c1*(1.+4.*u1+m*z)*x1+a1*(3.+4.*u1-2.*m*z)*
-x2-c1*(1.-4*u1*(1+2.*u1)-m*z*(1-4.*u1))*x2
 c=p(j)*a(j)*j0*j1(j)*b*(-1./2.)
  IF(r.ne.0.) THEN
             b=a1*x1+c1*(1.+m*z)*x1+a1*(3.-4.*u1-2.*m*z)*
-             x2-c1*(1.-8.*u1*(1.-u1)-m*z*(1.-4.*u1))*x2
             d=p(j)*a(j)*j1(j)*(j0/2.-j2/(m*r))*b*(-1.)
             prov(i,k,4)=prov(i,k,4)+c+d*COS(2.*alpha)
             prov(i,k,5)=prov(i,k,5)+c-d*COS(2.*alpha)
             prov(i,k,9)=prov(i,k,9)+d*SIN(2.*alpha)
          c=p(j)*a(j)*j2*j1(j)*b/m
          prov(i,k,2)=prov(i,k,2)+c*COS(alpha)
          prov(i,k,3)=prov(i,k,3)+c*SIN(alpha)
          b=a1*x1+c1*(2.*u1+m*z)*x1-a1*(1.-2.*m*z)*x2-c1*
-              (2.*u1+m*z-4.*u1*m*z)*x2
          c=p(j)*a(j)*j2*j1(j)*b*(-1.)
          prov(i,k,8)=prov(i,k,8)+c*COS(alpha)
          prov(i,k,7)=prov(i,k,7)+c*SIN(alpha)
           ELSE
             prov(i,k,4)=prov(i,k,4)+c
             prov(i,k,5)=prov(i,k,5)+c
           END IF
 b=a1*x1-c1*(1.-2.*u1-m*z)*x1-a1*(1.+2.*m*z)*x2+c1*
-(1.-2.*u1+m*z-4.*u1*m*z)*x2
 prov(i,k,6)=prov(i,k,6)+p(j)*a(j)*j0*j1(j)*b
 END


 SUBROUTINE couc2(i,j,k,z,p,a,j0,j1,j2,z1,z2,u2,e2,m,
-a2,b2,c2,d2,r,alpha)
```

```
 IMPLICIT REAL(a-z)
 INTEGER i,j,k
 COMMON prov(30,30,9),res(30,30,9)
 DIMENSION p(20),a(20),j1(20)
 y1=0.
 y2=0.
 IF(ABS(-m*(z2-z)).lt.20.0) y1=EXP(-m*(z2-z))
 IF(ABS(-m*(z-z1)).lt.20.0) y2=EXP(-m*(z-z1))
 b=a2*y1-b2*y2-c2*(2.-4.*u2-m*z)*y1-d2*(2.-4.*u2+m*z)*y2
 prov(i,k,1)=prov(i,k,1)+(1.+u2)*p(j)*a(j)*j0*j1(j)*b/(m*e2)
 b=a2*y1+b2*y2+c2*(1.+4.*u2+m*z)*y1-d2*(1.+4.*u2-m*z)*y2
 c=-p(j)*a(j)*j0*j1(j)*b/2.
 IF(r.ne.0.) THEN
              b=a2*y1+b2*y2+c2*(1.+m*z)*y1-d2*(1.-m*z)*y2
              d=p(j)*a(j)*j1(j)*b*(j2/(m*r)-j0/2)
              prov(i,k,4)=prov(i,k,4)+c+d*COS(2.*alpha)
              prov(i,k,5)=prov(i,k,5)+c-d*COS(2.*alpha)
              prov(i,k,9)=prov(i,k,9)+d*SIN(2.*alpha)
           c=-(1.+u2)*p(j)*a(j)*j2*j1(j)*b/(m*e2)
           prov(i,k,2)=prov(i,k,2)+c*COS(alpha)
                 prov(i,k,3)=prov(i,k,3)+c*SIN(alpha)
           b=a2*y1-b2*y2+c2*(2.*u2+m*z)*y1+d2*(2.*u2-m*z)*y2
           c=-p(j)*a(j)*j2*j1(j)*b
           prov(i,k,8)=prov(i,k,8)+c*COS(alpha)
           prov(i,k,7)=prov(i,k,7)+c*SIN(alpha)
           ELSE
              prov(i,k,4)=prov(i,k,4)+c
              prov(i,k,5)=prov(i,k,5)+c
           END IF
 b=a2*y1+b2*y2-c2*(1.-2.*u2-m*z)*y1+d2*(1.-2.*u2+m*z)*y2
 prov(i,k,6)=prov(i,k,6)+p(j)*a(j)*j0*j1(j)*b
 END


 SUBROUTINE couc3(i,j,k,z,p,a,j0,j1,j2,z2,z3,u3,e3,
-m,a3,b3,c3,d3,r,alpha)
 IMPLICIT REAL(a-z)
 INTEGER i,j,k
 COMMON prov(30,30,9),res(30,30,9)
 DIMENSION p(20),a(20),j1(20)
 z5=0.
 z6=0.
 IF(ABS(-m*(z3-z)).lt.20.0) z5=EXP(-m*(z3-z))
 IF(ABS(-m*(z-z2)).lt.20.0) z6=EXP(-m*(z-z2))
 b=a3*z5-b3*z6-c3*(2.-4.*u3-m*z)*z5-d3*(2.-4.*u3+m*z)*z6
 prov(i,k,1)=prov(i,k,1)+(1.+u3)*p(j)*a(j)*j0*j1(j)*b/(m*e3)
 b=a3*z5+b3*z6+c3*(1.+4.*u3+m*z)*z5-d3*(1.+4.*u3-m*z)*z6
 c=-p(j)*a(j)*j0*j1(j)*b/2.
 IF(r.ne.0.) THEN
              b=a3*z5+b3*z6+c3*(1.+m*z)*z5-d3*(1.-m*z)*z6
              d=p(j)*a(j)*j1(j)*b*(j2/(m*r)-j0/2)
```

```
            prov(i,k,4)=prov(i,k,4)+c+d*COS(2.*alpha)
            prov(i,k,5)=prov(i,k,5)+c-d*COS(2.*alpha)
            prov(i,k,9)=prov(i,k,9)+d*SIN(2.*alpha)
          c=-(1.+u3)*p(j)*a(j)*j2*j1(j)*b/(m*e3)
          prov(i,k,2)=prov(i,k,2)+c*COS(alpha)
          prov(i,k,3)=prov(i,k,3)+c*SIN(alpha)
          b=a3*z5-b3*z6+c3*(2.*u3+m*z)*z5+d3*(2.*u3-m*z)*z6
          c=-p(j)*a(j)*j2*j1(j)*b
          prov(i,k,8)=prov(i,k,8)+c*COS(alpha)
            prov(i,k,7)=prov(i,k,7)+c*SIN(alpha)
          ELSE
            prov(i,k,4)=prov(i,k,4)+c
            prov(i,k,5)=prov(i,k,5)+c
          END IF
b=a3*z5+b3*z6-c3*(1.-2.*u3-m*z)*z5+d3*(1.-2.*u3+m*z)*z6
prov(i,k,6)=prov(i,k,6)+p(j)*a(j)*j0*j1(j)*b
END


SUBROUTINE couc4(i,j,k,z,p,a,j0,j1,j2,z3,z4,u4,e4,m,
-a4,b4,c4,d4,r,alpha)
IMPLICIT REAL(a-z)
INTEGER i,j,k
COMMON prov(30,30,9),res(30,30,9)
DIMENSION p(20),a(20),j1(20)
t1=0.
t2=0.
IF(ABS(-m*(z4-z)).lt.20.0) t1=EXP(-m*(z4-z))
IF(ABS(-m*(z-z3)).lt.20.0) t2=EXP(-m*(z-z3))
b=a4*t1-b4*t2-c4*(2.-4.*u4-m*z)*t1-d4*(2.-4.*u4+m*z)*t2
prov(i,k,1)=prov(i,k,1)+(1.+u4)*p(j)*a(j)*j0*j1(j)*b/(m*e4)
b=a4*t1+b4*t2+c4*(1.+4.*u4+m*z)*t1-d4*(1.+4.*u4-m*z)*t2
c=-p(j)*a(j)*j0*j1(j)*b/2.
IF(r.ne.0.) THEN
            b=a4*t1+b4*t2+c4*(1.+m*z)*t1-d4*(1.-m*z)*t2
            d=p(j)*a(j)*j1(j)*b*(j2/(m*r)-j0/2.)
            prov(i,k,4)=prov(i,k,4)+c+d*COS(2.*alpha)
            prov(i,k,5)=prov(i,k,5)+c-d*COS(2.*alpha)
            prov(i,k,9)=prov(i,k,9)+d*SIN(2.*alpha)
          c=-(1.+u4)*p(j)*a(j)*j2*j1(j)*b/(m*e4)
          prov(i,k,2)=prov(i,k,2)+c*COS(alpha)
            prov(i,k,3)=prov(i,k,3)+c*SIN(alpha)
          b=a4*t1-b4*t2+c4*(2.*u4+m*z)*t1+d4*(2.*u4-m*z)*t2
            c=-p(j)*a(j)*j2*j1(j)*b
          prov(i,k,8)=prov(i,k,8)+c*COS(alpha)
            prov(i,k,7)=prov(i,k,7)+c*SIN(alpha)
          ELSE
            prov(i,k,4)=prov(i,k,4)+c
            prov(i,k,5)=prov(i,k,5)+c
          END IF
b=a4*t1+b4*t2-c4*(1.-2.*u4-m*z)*t1+d4*(1.-2.*u4+m*z)*t2
```

```
      prov(i,k,6)=prov(i,k,6)+p(j)*a(j)*j0*j1(j)*b
      END


      SUBROUTINE modIF(pr,m1,l1,l2,rmax)
      IMPLICIT REAL(a-z)
      INTEGER i,j,k,l1,l2
      COMMON    prov(30,30,9),res(30,30,9)
      m2=2.*m1
      pr=pr/2.
      IF (rmax.ge.2.5) THEN
        p1l=.5/rmax
                  ELSE
        p1l=.2
      END IF
      IF (m2.ge.p1l) THEN
         m2=.2
         pr=0
      END IF
      DO 690 k=1,9
        DO 691 j=1,l2
          DO 692 i=1,l1
            res(i,j,k)=res(i,j,k)+prov(i,j,k)*(m2-m1)*3./10.
692         CONTINUE
691       CONTINUE
690     CONTINUE
      m1=m2
      END


      SUBROUTINE simps(l1,l2,w1,m1)
      IMPLICIT REAL(a-z)
      INTEGER i,j,k,l1,l2,w1
      COMMON  prov(30,30,9),res(30,30,9)
      GOTO (10,20,30,40,50,60),w1
10    coef=5.
      w1=2
      GOTO 70
20    coef=1.
      w1=3
      GOTO 70
30    coef=6.
      w1=4
      GOTO 70
40    coef=1.
      w1=5
      GOTO 70
50    coef=5.
      w1=6
      GOTO 70
60    coef=2.
```

```
      w1=0
      GOTO 70
70    DO 700 k=1,9
        DO 701 j=1,l2
          DO 702 i=1,l1
            res(i,j,k)=res(i,j,k)+prov(i,j,k)*coef*m1*3./10.
702       CONTINUE
701     CONTINUE
700   CONTINUE
      END


      SUBROUTINE comsu(l,l1,a,p,u1,e1,xc,xs,yc,ys)
      IMPLICIT REAL(a-z)
      INTEGER i,j,l,l1
      COMMON prov(30,30,9),res(30,30,9)
      DIMENSION a(20),p(20),xc(20),xs(30),yc(20),ys(30)
c     WRITE(6,'(1h+,36h     be even more patient.....!! )')
      DO 680 i=1,l1
        res(i,1,1)=res(i,1,1)*(4.*(1.-u1*u1)/e1)
        res(i,1,2)=res(i,1,2)*(-4.*(1.-u1*u1)/e1)
        res(i,1,3)=res(i,1,3)*(-4.*(1.-u1*u1)/e1)
        res(i,1,6)=0.
        res(i,1,7)=0.
        res(i,1,8)=0.
        DO 681 j=1,l
        r=SQRT((xc(j)-xs(i))*(xc(j)-xs(i))+(yc(j)-ys(i))*(yc(j)-ys(i)))
          alpha=0.
        IF(xc(j).ne.xs(i).or.yc(j).ne.ys(i))
     -alpha=ATAN2(ys(i)-yc(j),xs(i)-xc(j))
          IF(r.lt.a(j)) THEN
      b=-.5
      c=1.
      z=(r/a(j))**2
      res(i,1,1)=res(i,1,1)-2.*(1.-u1*u1)*p(j)*a(j)*fonc(b,c,z)/e1
      IF(r.ne.0.) THEN
            c=(1.+u1)*(1.-2.*u1)*p(j)*r/(2*e1)
            res(i,1,2)=res(i,1,2)+c*COS(alpha)
            res(i,1,3)=res(i,1,3)+c*SIN(alpha)
              END IF
      res(i,1,4)=res(i,1,4)+(1.+2.*u1)*p(j)/2
      res(i,1,5)=res(i,1,5)+(1.+2.*u1)*p(j)/2
      res(i,1,6)=res(i,1,6)+p(j)
                      ELSE
                        IF(r.eq.a(j))  THEN
          pi=3.141592
          res(i,1,1)=res(i,1,1)-2.*(1.-u1*u1)*p(j)*a(j)*2./(pi*e1)
          c=(1.+u1)*(1.-2.*u1)*p(j)*a(j)/(2*e1)
          res(i,1,2)=res(i,1,2)+c*COS(alpha)
          res(i,1,3)=res(i,1,3)+c*SIN(alpha)
          c=(1.+2.*u1)*p(j)/4.
```

```
        d=-(1.-2.*u1)*p(j)/4.
        res(i,1,4)=res(i,1,4)+c+d*COS(2.*alpha)
        res(i,1,5)=res(i,1,5)+c-d*COS(2.*alpha)
        res(i,1,9)=res(i,1,9)+d*SIN(2.*alpha)
        res(i,1,6)=res(i,1,6)+p(j)/2.
                                  ELSE
        b=.5
        c=2.
        z=(a(j)/r)**2
        res(i,1,1)=res(i,1,1)-2.*(1.-u1*u1)*p(j)*a(j)*
     -  fonc(b,c,z)*a(j)/(2.*r*e1)
        c=(1.+u1)*(1.-2.*u1)*p(j)*a(j)**2/(2.*r*e1)
        res(i,1,2)=res(i,1,2)+c*COS(alpha)
        res(i,1,3)=res(i,1,3)+c*SIN(alpha)
        d=-(1.-2.*u1)*p(j)*a(j)*a(j)/(r*r*2.)
        res(i,1,4)=res(i,1,4)+d*COS(2.*alpha)
        res(i,1,5)=res(i,1,5)-d*COS(2.*alpha)
        res(i,1,9)=res(i,1,9)+d*SIN(2.*alpha)
                                  END IF
                    END IF
681     CONTINUE
680   CONTINUE
      END


      FUNCTION fonc(b,c,z)
      v2=.5*b*z/c
      fonc=1.+v2
      n=2.
850   v2=v2*z*(.5+n-1.)*(b+n-1.)/(n*(c+n-1.))
      fonc=fonc+v2
      n=n+1.
      IF(ABS(v2).gt..00001) GOTO 850
851   END


      SUBROUTINE ccou1(l,l1,l2,ls,xc,xs,yc,ys,zs,a,p,u1,e1)
      IMPLICIT REAL(a-z)
      INTEGER ii,i,j,k,l,l1,l2,ls,w1
      COMMON prov(30,30,9),res(30,30,9)
      DIMENSION y(9),f(6),xc(20),yc(20),xs(30),ys(30),zs(30)
      DIMENSION ls(30),a(20),p(20)
      n=500.
      pi=3.141592
      DO 666 k=1,l2
        IF (ls(k).eq.1.and.zs(k).ne.0.) THEN
                                  DO 667 i=1,l1
                  res(i,k,1)=res(i,k,1)*(1.+u1)/e1
                  res(i,k,2)=-res(i,k,2)*(1.+u1)/e1
                  res(i,k,3)=-res(i,k,3)*(1.+u1)/e1
                    DO 668 j=1,l
```

```
      r=SQRT((xc(j)-xs(i))*(xc(j)-xs(i))+(yc(j)-ys(i))*(yc(j)-ys(i)))
                  alpha=0.
       IF(xc(j).ne.xs(i).or.yc(j).ne.ys(i))
     - alpha=ATAN2(ys(i)-yc(j),xs(i)-xc(j))
                  DO 660 ii=1,9
                    y(ii)=0.
660                 CONTINUE
                IF(r.eq.0.) THEN
              y(6)=(SQRT(a(j)**2+zs(k)**2)-zs(k))*p(j)
              y(1)=y(6)/SQRT(a(j)**2+zs(k)**2)
              y(2)=a(j)*a(j)*p(j)*zs(k)/SQRT((a(j)**2+zs(k)**2)**3)
              y(3)=y(1)/2.
              y(4)=y(2)/2.
              y(7)=y(1)*zs(k)
                              ELSE
              pas1=2*a(j)/n
              pas2=pi/n
              x1=-a(j)
              x2=0.
              w1=0
860             x1=x1+pas1
              x2=x2+pas2
              IF(x1.gt.(a(j)-pas1/2)) GOTO 861
              f(1)=fonc1(x1,zs(k),a(j),r)
              f(2)=fonc2(x1,zs(k),a(j),r)
              f(3)=fonc3(x2,zs(k),a(j),r)
              f(4)=fonc4(x2,zs(k),a(j),r)
              f(5)=fonc5(x2,zs(k),a(j),r)
              f(6)=fonc6(x1,zs(k),a(j),r)
              IF(w1.eq.0) THEN
                          DO 661 ii=1,6
                          f(ii)=4.*f(ii)
661                         CONTINUE
                          w1=1
                        ELSE
                          DO 662 ii=1,6
                          f(ii)=2.*f(ii)
662                         CONTINUE
                          w1=0
                        END IF
               DO 663 ii=1,6
                 y(ii)=y(ii)+f(ii)
663              CONTINUE
               GOTO 860
861              y(1)=p(j)*(y(1)*pas1/3)/(2*pi)
              y(2)=p(j)*(y(2)*pas1/3)/(2*pi)+y(1)
              y(3)=p(j)*(y(3)*pas2/3)*(a(j)**2/pi)
              y(4)=p(j)*(y(4)*pas2/3)*(a(j)**2*zs(k)/pi)
              y(5)=p(j)*(y(5)*pas2/3)*(3*a(j)**2*r*zs(k)**2/pi)
              y(6)=p(j)*(y(6)*pas1/3)/(2*pi)
              y(7)=y(1)*zs(k)
```

```
            y(8)=y(3)*r
            y(9)=y(4)*r
                          END IF
       res(i,k,1)=res(i,k,1)-y(6)*2.*(1.-u1*u1)/e1-y(7)*(1.+u1)/e1
       c=y(1)*(1.+2.*u1)/2.-y(2)/2.
       IF(r.ne.0.) THEN
          d=(y(1)/2.-y(3))*(1.-2.*u1)-y(2)/2.+y(4)
                       res(i,k,4)=res(i,k,4)+c+d*COS(2.*alpha)
                       res(i,k,5)=res(i,k,5)+c-d*COS(2.*alpha)
                  res(i,k,9)=res(i,k,9)+d*SIN(2.*alpha)
              c=y(8)*(1.-2.*u1)*(1.+u1)/e1-y(9)*(1.+u1)/e1
              res(i,k,2)=res(i,k,2)+c*COS(alpha)
              res(i,k,3)=res(i,k,3)+c*SIN(alpha)
                   res(i,k,8)=res(i,k,8)+y(5)*COS(alpha)
                   res(i,k,7)=res(i,k,7)+y(5)*SIN(alpha)
              ELSE
                 res(i,k,4)=res(i,k,4)+c
                 res(i,k,5)=res(i,k,5)+c
              END IF
        res(i,k,6)=res(i,k,6)+y(1)+y(2)
668          CONTINUE
667                CONTINUE
                           END IF
666   CONTINUE
      END


      FUNCTION fonc1(x,z,a,r)
      fonc1=2.*z*SQRT(a**2-x**2)/((z**2+x**2+r**2-2.*x*r)*
     -SQRT(z**2+r**2+a**2-2.*x*r))
      END


      FUNCTION fonc2(x,z,a,r)
      a1=z*z+x*x+r*r-2.*x*r
      a2=z*z+a*a+r*r-2.*x*r
      fonc2=-(2.*z*(r*r+x*x-2.*r*x)*SQRT(a*a-x*x))*
     -(1./a2+2./a1)/(a1*SQRT(a2))
      fonc2=fonc2+2.*z*SQRT(a*a-x*x)/(SQRT(a2**3))
      END


      FUNCTION fonc3(x,z,a,r)
      omega=SQRT(a*a+r*r-2.*a*r*COS(x))
      fonc3=(SIN(x)**2)*(1.-z/SQRT(omega*omega+z*z))/(omega*omega)
      END


      FUNCTION fonc4(x,z,a,r)
      omega=SQRT(a*a+r*r-2.*a*r*COS(x))
      fonc4=(SIN(x)**2)/SQRT((omega**2+z*z)**3)
```

```
      END


      FUNCTION fonc5(x,z,a,r)
      omega=SQRT(a*a+r*r-2.*a*r*COS(x))
      fonc5=(SIN(x)**2)/SQRT((omega**2+z*z)**5)
      END

      FUNCTION fonc6(x,z,a,r)
      a1=SQRT(r*r-2.*x*r+a*a+z*z)
      a2=SQRT(a*a-x*x)
      fonc6=alog((a1+a2)/(a1-a2))
      END


      SUBROUTINE echef(h1,z1,z2,z3,z4,xs,ys,zs,a,xc,yc,l1,l2,l)
      IMPLICIT REAL(a-z)
      INTEGER i,j,l,l1,l2
      COMMON prov(30,30,9),res(30,30,9)
      DIMENSION a(20),xc(20),xs(30),yc(20),ys(30),zs(30)
      z1=z1*h1
      z2=z2*h1
      z3=z3*h1
      z4=z4*h1
      DO 730 i=1,l
        a(i)=a(i)*h1
        xc(i)=xc(i)*h1
        yc(i)=yc(i)*h1
730   CONTINUE
      DO 731 i=1,l1
        xs(i)=xs(i)*h1
        ys(i)=ys(i)*h1
731   CONTINUE
      DO 732 i=1,l2
        zs(i)=zs(i)*h1
732   CONTINUE
      DO 733 j=1,l2
        DO 734 i=1,l1
          res(i,j,1)=res(i,j,1)*h1
          res(i,j,2)=res(i,j,2)*h1
          res(i,j,3)=res(i,j,3)*h1
734     CONTINUE
733   CONTINUE
      END


      SUBROUTINE imres(l1,l2,xs,ys,zs,ls,u1,u2,u3,u4,u5,e1,e2,e3,e4,e5)
      IMPLICIT REAL(a-z)
      INTEGER i,j,l1,l2,ls
      COMMON prov(30,30,9),res(30,30,9)
      DIMENSION ls(30),xs(30),ys(30),zs(30)
```

```
      DO 670 i=1,l1

c*************************************************************************
c     This is how the valuses of functions are read
c     FORMAT('  depth',4x,'layer ',4x,'    sz          w(z)    ',
c     -'      ez          ex          ey',/)
c*************************************************************************

        DO 672 j=1,l2
          pi=3.141592
          i1=res(i,j,4)+res(i,j,5)+res(i,j,6)
          IF(ABS(i1).lt.0.00001.and.res(i,j,6).lt.0.00001) THEN
                                        s1=0.
                                         s2=0.
                                        s3=0.
                                        eps1=0.
                                        eps2=0.
                                        eps3=0.
                                        GOTO 672
                                      END IF
          i2=res(i,j,4)*res(i,j,5)+res(i,j,5)*res(i,j,6)-res(i,j,9)**2
          i2=i2+res(i,j,6)*res(i,j,4)-res(i,j,7)**2-res(i,j,8)**2
          i3=res(i,j,4)*res(i,j,5)*res(i,j,6)
          i3=i3+2.*res(i,j,7)*res(i,j,8)*res(i,j,9)
          i3=i3-res(i,j,4)*res(i,j,7)**2-res(i,j,5)*res(i,j,8)**2
          i3=i3-res(i,j,6)*res(i,j,9)**2
          d=(3.*i2-i1*i1)/3.
          IF(d.ge.0.) THEN
                      s1=res(i,j,4)
                      s2=res(i,j,5)
                      s3=res(i,j,6)
                      GOTO 870
                    END IF
          b=(9.*i1*i2-2.*i1**3-27*i3)/27.
          c=3.*b/(2.*d*SQRT(-d/3.))
          IF (c.lt.-1.) c=-1.
          IF (c.gt.1.) c=1.
          teta1=aCOS(c)/3.
          s1=2.*SQRT(-d/3.)*COS(teta1)+i1/3.
          s2=2.*SQRT(-d/3.)*COS(teta1+2.*pi/3.)+i1/3.
          s3=2.*SQRT(-d/3.)*COS(teta1+4.*pi/3.)+i1/3.
          IF(s1.le.s2) THEN
                       IF(s2.le.s3) THEN
                                    s=s3
                                 s3=s1
                                    s1=s
                                  ELSE
                                    IF(s1.le.s3)THEN
                                                s=s2
                                                s2=s3
                                                s3=s1
```

```
                                    s1=s
                                  ELSE
                                    s=s2
                                    s2=s1
                                    s1=s
                                  END IF
                          END IF
                    ELSE
                      IF(s2.le.s3) THEN
                            IF(s1.le.s3)THEN
                                  s=s3
                                  s3=s2
                                    s2=s1
                                    s1=s
                                  ELSE
                                    s=s2
                                    s2=s3
                                    s3=s
                                  END IF
                          END IF
                    END IF
870       IF(ls(j).eq.1) THEN
                      u=u1
                      e=e1
                    END IF
          IF(ls(j).eq.2) THEN
                      u=u2
                      e=e2
                    END IF
          IF(ls(j).eq.3) THEN
                      u=u3
                      e=e3
                    END IF
          IF(ls(j).eq.4) THEN
                      u=u4
                      e=e4
                    END IF
          eps1=(s1-u*(s2+s3))/e
          eps2=(s2-u*(s1+s3))/e
          eps3=(s3-u*(s1+s2))/e
672       CONTINUE
          DO 673 j=1,l2
          IF(ls(j).eq.1) THEN
                      u=u1
                      e=e1
                    END IF
          IF(ls(j).eq.2) THEN
                      u=u2
                      e=e2
                    END IF
          IF(ls(j).eq.3) THEN
```

```
                    u=u3
                    e=e3
                  END IF
          IF(ls(j).eq.4) THEN
                    u=u4
                    e=e4
                  END IF
          ez=(res(i,j,6)-u*(res(i,j,4)+res(i,j,5)))/e
          ex=(res(i,j,4)-u*(res(i,j,5)+res(i,j,6)))/e
          ey=(res(i,j,5)-u*(res(i,j,4)+res(i,j,6)))/e
          WRITE(1,473)zs(j),ls(j),res(i,j,6),res(i,j,1),res(i,j,1),
     -                res(i,j,3),ey
473       FORMAT(f10.3,3x,i1,5x,f9.4,5x,e10.4,5x,e10.4,
     -5x,e10.4,5x,e10.4)
673     CONTINUE
675   FORMAT(a)
670   CONTINUE
      END

c*************************************************************************
c    Input subroutine, called only once to read all necessary infromation
c
c*************************************************************************

      SUBROUTINE leDOn(l,l1,l2,ls,a,p,xc,yc,xs,ys,zs,e2,e3,e4,e5,
     - u1,u2,u3,u4,u5,h1,h2,h3,h4,z1,z2,z3,z4,la1,la2,la3,noseas,
     -tempr,crpb,traffi,speeed,ihma,isub,pltpcom,pltpten,pltbtcm,
     -pltpsub,tmpdel1,tmpdel2,thkhma,alphat,latdeg,sf1,sf2,yrs,pers)

      IMPLICIT REAL (a-z)
      INTEGER i,j,l,l1,l2,ls,noseas,traffi,ihma,isub,yrs
      DIMENSION a(20),ls(30),p(20),crpb(10),tempr(24),speeed(24),
     -          traffi(24),tmpdel1(24),tmpdel2(24)
      DIMENSION xc(20),yc(20),xs(30),ys(30),zs(30)
      OPEN (2,file="DATA.INP")
      READ(2,*)noseas
      READ(2,*)latdeg
      READ(2,*)thkhma
      READ(2,*)alphat

      DO 7400 i=1,noseas
        READ(2,*)tempr(i)
        READ(2,*)tmpdel1(i),tmpdel2(i)
        READ(2,*)speeed(i)
        READ(2,*)traffi(i)
7400   CONTINUE

      READ(2,*)l,l1,l2
      READ(2,*)crpb(1),crpb(2),crpb(3),crpb(4),crpb(5),crpb(6),crpb(7),
     -u1,h1,z1
      READ(2,*)e2,u2,h2,z2
```

```
      READ(2,*)e3,u3,h3,z3
      READ(2,*)e4,u4,h4,z4
      READ(2,*)e5,u5
      READ(2,*)la1,la2,la3
      DO 1 j=1,l
      READ(2,*)a(j),p(j),xc(j),yc(j)
1     CONTINUE
      DO 2 j=1,l1
      READ(2,*)xs(j),ys(j)
2     CONTINUE
      DO 3 j=1,l2
      READ(2,*)zs(j),ls(j)
3     CONTINUE
       READ(2,*)ihma,isub
       READ(2,*) pltpcom,pltpten,pltbtcm,pltpsub
       READ(2,*) sf1,sf2
       READ(2,*) yrs,pers
      close (2)
     END

c     intermediate depths introduction
c     --------------------------------
     SUBROUTINE point(z1,z2,z3,z4,l2,zs,ls)
     IMPLICIT REAL(a-z)
     INTEGER i,j,l2,ls
     DIMENSION zs(30),ls(30)
834   zs(l2+1)=0.
     ls(l2+1)=1
     zs(l2+2)=z1
     ls(l2+2)=1
     zs(l2+3)=z1
     ls(l2+3)=2
     zs(l2+4)=z2
     ls(l2+4)=2
     zs(l2+5)=z2
     ls(l2+5)=3
     zs(l2+6)=z3
     ls(l2+6)=3
     zs(l2+7)=z3
     ls(l2+7)=4
     zs(l2+8)=z4
     ls(l2+8)=4
     l2=l2+8
833   j=0
     DO 633 i=1,l2-1
       IF (zs(i).gt.zs(i+1)) THEN
                          e=zs(i)
                          zs(i)=zs(i+1)
                          zs(i+1)=e
                          j=ls(i)
                          ls(i)=ls(i+1)
```

```
                        ls(i+1)=j
                      END IF
      IF (zs(i).eq.zs(i+1).and.ls(i).gt.ls(i+1)) THEN
                                          j=ls(i)
                                          ls(i)=ls(i+1)
                                          ls(i+1)=j
                                        END IF
633   CONTINUE
      IF (j.ne.0) GOTO 833
      END
```

## VITA

Salman Ahmed Bhutta was born in Peshawar, Pakistan, on March 7the, 1969. He attended Pakistan Air Force Degree College, Peshawar, passing the Federal Board of Intermediate and Secondary Education Matriculation examination in 1984, and Intermediate examination in 1986. He entered N.W.F.P University of Engineering and Technology Peshawar, in August of 1986, and graduated in August, 1991 with a Bachelors of Civil Engineering Degree. Upon graduation he was also awarded the Best in Academics Honor for the Session 1989-90, Academic Gold Medal and the Merit Scholarship from the Government of Pakistan for pursuing higher education abroad. Upon graduation he joined the N.W.F.P University of Engineering and Technology as a lecturer, and later on as Assistant Director at the N.W.F.P Provincial Urban Development Board, Peshawar. He enrolled at Virginia Polytechnic Institute and State University, Blacksburg, Virginia in August, 1992, and earned a Master of Science Degree in Civil Engineering in May, 1994. He has served at Virginia Polytechnic Institute and State University since 1994 as a Research Assistant and Research Associate.